Mémoire présenté en vue de l'obtention du diplôme

d'**Habilitation à Diriger des Recherches**

Spécialité : Astrophysique

par

Clément BARUTEAU

au sein de l'Institut de Recherche en Astrophysique et Planétologie (IRAP)

Université Toulouse Paul Sabatier

FORMATION ET ÉVOLUTION ORBITALE DES SYSTÈMES PLANÉTAIRES

Mémoire d'Habilitation soutenu le 16 Juin 2020

Commission

Magali Deleuil	examinatrice
Jean-François Gonzalez	rapporteur
François Ménard	examinateur
Claire Moutou	examinatrice
Sean Raymond	rapporteur
Michel Rieutord	examinateur et parrain
Geneviève Soucail	examinatrice et présidente du jury
Caroline Terquem	rapportrice

A Sarah, Lou et Siloé,
mis vidas.

A Frédéric Masset, Douglas Lin, Richard Nelson et John Papaloizou,
pour leur bienveillance.

Clément BARUTEAU

Formation et évolution orbitale des systèmes planétaires

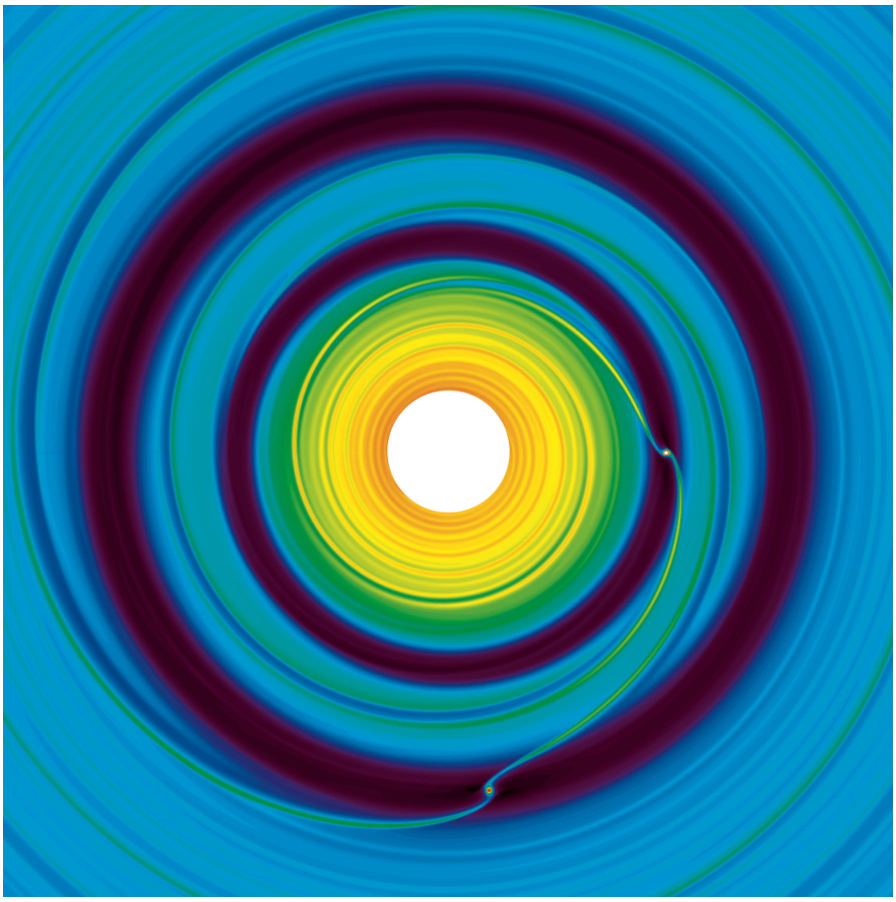

– IRAP, Université Toulouse Paul Sabatier –

Page de couverture :

Densité surfacique de masse d'un disque protoplanétaire de gaz, obtenue par une simulation hydrodynamique à deux dimensions. Le cercle blanc au milieu de l'image couvre les parties internes du disque près de l'étoile, qui ne sont pas modélisées dans cette simulation. Deux planètes de quelques masses terrestres perturbent le gaz de leur disque protoplanétaire en y excitant des ondes spirales de densité qui se propagent dans le disque, et en creusant un sillon annulaire autour de leur orbite.

Résumé

Ce mémoire d'Habilitation à Diriger des Recherches décrit mes activités de recherche sur la formation et l'évolution orbitale des systèmes planétaires et la dynamique des disques protoplanétaires. Mon travail porte sur les interactions gravitationnelles entre planètes, le disque protoplanétaire de gaz et de poussières où elles se forment, et leur(s) étoile(s). Je cherche à comprendre dans quelle mesure la migration planétaire résultant des interactions entre planètes et leur disque protoplanétaire peut rendre compte des propriétés orbitales des exoplanètes, dont la diversité révèle que les planètes peuvent se former et évoluer dans des conditions variées, parfois extrêmes. Je cherche également à comprendre si les structures observées dans l'émission du gaz et des poussières des disques protoplanétaires (succession d'anneaux sombres et brillants, spirales, asymétries etc.) peuvent être dues à des planètes, et ce que de telles structures peuvent nous apprendre sur les premières étapes de la formation planétaire. Pour cela, j'ai recours à la théorie en dynamique des fluides astrophysiques, aux simulations hydrodynamiques multi-dimensionnelles et aux calculs de transfert radiatif.

Une part importante de mes travaux vise à déterminer la direction et la vitesse de migration des planètes dans leur disque protoplanétaire. Mon travail a notamment permis (i) de trouver comment ralentir la migration rapide des planètes terrestres vers leur étoile, qui pendant longtemps avait rendu les prédictions des modèles de formation et d'évolution planétaires incompatibles avec les propriétés orbitales des exoplanètes détectées, (ii) de montrer que les planètes géantes formées à grande distance de leur étoile par instabilité gravitationnelle migrent très rapidement vers les parties internes des disques protoplanétaires, et qu'il est là aussi question de devoir ralentir leur migration afin de rendre compte des planètes observées par imagerie directe, et (iii) de montrer que la diversité des rapports de période orbitale dans les systèmes multi-planétaires détectés par le satellite spatial *Kepler* peut être expliquée par les modèles de migration planétaire.

Stimulé par les observations multi-longueurs d'onde de disques protoplanétaires, je travaille plus récemment sur la dynamique et l'émission du gaz et des poussières dans les disques. Mon travail ici a pour but de prédire d'une part le type de structures qu'une planète peut génèrer dans l'émission de son disque, et d'examiner d'autre part si les structures réellement observées peuvent s'expliquer par la présence de planètes enfouies dans ces disques. Les modèles que j'ai développés ont permis notamment (i) de proposer un scénario où la présence d'anneaux multiples sombres et brillants dans l'émission radio des poussières pourrait être due à la migration rapide d'une seule planète dans le disque protoplanétaire, et (ii) de montrer que les observations de l'émission radio de plusieurs disques (AB Aurigae, MWC 758, HD 169142) suggèrent fortement la présence de planètes massives structurant la poussière de leur disque à grande distance de l'étoile, ce qui permettrait, si ces prédictions étaient confirmées à l'avenir, d'apporter de nouvelles contraintes sur la formation et l'évolution de planètes jeunes.

Le nombre croissant d'exoplanètes très proches de leur étoile, dont certaines ont une obliquité orbitale très élevée ou un rayon physique anormalement grand, demande de mieux comprendre les effets de marée entre étoiles et planètes. C'est dans cette optique que j'étudie la propagation et la dissipation d'ondes de marée dans les fluides en rotation modélisant l'intérieur d'étoiles ou de planètes géantes, ce qui m'a permis notamment de trouver un mécanisme capable d'augmenter considérablement l'efficacité des effets de marée étoile-planète.

Mots clé : formation et migration planétaires, dynamique et émission des disques protoplanétaires, effets de marée, analyse linéaire, simulations hydrodynamiques, transfert radiatif

Table des matières

1 | Curriculum vitæ

Sommaire

Clément BARUTEAU – né le 08/07/1982 (France) pacsé, 2 enfants (2014 et 2017)
e-mail – site web

1.1 Parcours académique

2013 –	Chargé de recherche CNRS, Institut de Recherche en Astrophysique et Planétologie.
2010-2013	Herchel Smith postdoctoral fellow, Department of Applied Mathematics and Theoretical Physics, University of Cambridge, UK.
2008-2010	Postdoctoral research associate, Department of Astronomy and Astrophysics, University of California at Santa Cruz, USA (superviseur : Douglas Lin). Chercheur invité au Kavli Institute for Astronomy and Astrophysics, Beijing, Chine.
2005-2008	Doctorat de l'Observatoire de Paris, préparé au CEA Saclay (directeur de thèse : Frédéric Masset). Manuscrit : Toward predictive scenarios of planetary migration.
2005	Master II Astronomie et Astrophysique, Observatoire de Paris.
2001-2005	Magistère de physique fondamentale, École Normale Supérieure de Cachan et Université Paris XI. Reçu à l'agrégation de sciences physiques option physique (2004).
1999-2001	Classes préparatoires aux grandes écoles (MPSI puis PSI*), Lycée Descartes, Tours.

1.2 Activités de recherche

1.2.1 Aperçu

Mes activités de recherche portent sur la formation et l'évolution orbitale des systèmes planétaires, et la dynamique des disques protoplanétaires. J'étudie les interactions gravitationnelles entre planètes, le disque protoplanétaire de gaz et de poussières où elles se forment, et leur(s) étoile(s). Mon travail mêle théorie en dynamique des fluides astrophysiques et simulations hydrodynamiques multi-dimensionnelles. Je cherche à interpréter les propriétés orbitales des planètes extrasolaires, dont la diversité révèle que les planètes peuvent se former dans des conditions variées, parfois extrêmes, et voir leur distance à leur étoile varier considérablement au cours de leur évolution. Je cherche également à comprendre si les structures fréquemment observées dans l'émission du gaz et des poussières des disques protoplanétaires (succession d'anneaux sombres et brillants, spirales, asymétries etc.) peuvent être dues à des planètes enfouies dans ces disques. J'étudie par ailleurs les interactions de marée étoile-planète, qui régissent l'évolution à long terme des planètes proches de leur étoile.

1.2.2 Productions scientifiques

- 53 articles et chapitres de livre publiés dans les revues internationales avec comité de lecture depuis 2008 (14 en premier auteur, 16 en second auteur ; bibliométrie ADS : environ 2300 citations, H-index = 28). La liste de mes publications, détaillée au § 1.5, est également consultable sur NASA/ADS via ce lien.
- 43 séminaires de recherche, 32 communications orales dans les conférences et les ateliers internationaux et nationaux (dont 5 revues invitées) depuis 2007.
- PI ou co-PI de 7 demandes de temps calcul depuis 2013 sur les centres de calcul nationaux et méso-centres. Co-PI ou co-I de 32 propositions de temps télescope depuis 2015, principalement pour ALMA, NOEMA et SPHERE.

1.2.3 Prix et distinctions

- Prime d'Encadrement Doctoral et de Recherche du CNRS (2016-2019).
- Bourse IDEX "Nouveaux Entrants" de l'Université de Toulouse (2015-2016).
- Herchel Smith Postdoctoral Fellowship of the University of Cambridge (2010-2013).
- Student Stipend Award of the American Astronomical Society (2008).
- Élève de l'École Normale Supérieure de Cachan (2001-2005).

1.3 Enseignement, formation et diffusion de la culture scientifique

1.3.1 Activités d'enseignement

2019	Cours invité de 4h "dynamics of gas, dust and planets in protoplanetary discs" à l'école d'été Waves, Instabilities and Turbulence in Geophysical and Astrophysical Flows (Cargèse).
2017	Cours invité de 6h "planets-disc interactions and the early orbital evolution of planetary systems" pour les doctorants et post-doctorants de l'Université de Berne.
2016, 2018	Cours invité de 1h "les systèmes planétaires extrasolaires" à l'école d'été organisée pour des étudiants de L2 par le Labex OCEVU (Marseille et Toulouse).
2016 –	Cours de 8h "formation and evolution of planetary systems" au M2 d'astrophysique de l'Université de Toulouse.
2014	Cours invité de 1h "gas dynamics in protoplanetary discs" à l'école d'été Millenium ALMA Disk (Santiago du Chili).
2014-2016	Séminaires de recherche au M2 d'astrophysique de l'Université de Toulouse.

2012-2013	Travaux dirigés à l'Université de Cambridge : encadrement de petits groupes d'étudiants pour le cours de Master "Astrophysical Fluid Dynamics"
2006-2008	Monitorat en L1, Université Paris VI, cours "Matière et Énergie" : encadrement de travaux dirigés, travaux pratiques et interrogations orales, un cours magistral.
2004-2006	Examinateur en physique-chimie, classe préparatoire PSI*, Lycée Jacques Decour, Paris.

1.3.2 Activités d'encadrement

Depuis 2013, j'ai encadré ou co-encadré 8 stages (dont 4 de M2), contribué au co-encadrement de 4 thèses de doctorat (sans statut officiel), et ai co-dirigé la thèse de Magistère sur 2 ans d'un étudiant chilien (Universidad de Chile). Après autorisation à diriger les recherches à titre individuel, je dirige la thèse de doctorat de Gaylor Wafflard-Fernandez (IRAP) depuis Janvier 2018, et co-dirige celle d'Aurélie Astoul (CEA Saclay) depuis Septembre 2017. J'ai collaboré avec plusieurs chercheurs post-doctorants, dont 2 sur des projets que j'ai initiés.

Stages

2017	Quentin Kriaa (1ère année à ISAE/Supaero) : stage d'immersion dans la recherche, simulations numériques du piégeage de poussières dans un tourbillon formé par une planète géante dans son disque protoplanétaire (1 mois).
2017	Aurélie Astoul (M2 Observatoire de Paris), co-encadrement avec Stéphane Mathis (CEA Saclay) : *tidal dissipation in stars – differential rotation and critical layers* (3 mois).
2017	Nicolas Nesme (M2 Université Toulouse III), co-encadrement avec Laurène Jouve (IRAP) : *étoiles T Tauri – champ magnétique variable et évolution du disque protoplanétaire* (5 mois).
2016	Florian Thuillet (M2 Université Toulouse III et ISAE/Supaero) : *signatures observationnelles de la migration planétaire dans les poussières des disques protoplanétaires* (5 mois).
2016	Guillaume Cazalet (M2 Université Toulouse III), co-encadrement avec Laurène Jouve (IRAP) : *impact d'un champ magnétique variable d'une étoile sur l'arrêt de la migration planétaire* (5 mois).
2015	Ghania Medjdoub (M1 Université Toulouse III) : *évolution des particules de poussières dans les disques protoplanétaires auto-gravitants* (2 mois).
2014	Marc Pech (1ère année à ISAE/Supaero) : *évolution des disques protoplanétaires et leurs interactions avec les planètes* (2 mois).
2013	Glenn Robbins (2ème année à ENSTA/ParisTech), co-encadrement avec John Papaloizou (DAMTP) : *formation and evolution of planetary systems – application to the Kepler's space mission observations* (3 mois).

Thèses et post-doctorats

Depuis Septembre 2017, je co-dirige la thèse de doctorat d'**Aurélie Astoul** avec Stéphane Mathis (CEA Saclay). La thèse d'Aurélie porte sur l'étude du transfert de moment cinétique et l'effet du magnétisme dans les dissipations de marée au sein des étoiles de faible masse. Son travail consiste en particulier à mieux comprendre comment les ondes inertielles forcées par les effets de marée se propagent au sein de l'enveloppe convective des étoiles, et comment le champ magnétique agit sur la propagation et la dissipation de ces ondes. Dans un premier article récemment accepté à A&A (Astoul et al. 2019), Aurélie a étudié, via un code d'évolution stellaire couplé à des modèles de génération de champ magnétique par effet dynamo, l'impact d'un champ magnétique sur le forçage de marée des ondes inertielles tout au long de l'évolution stellaire. La suite de la thèse examinera l'impact de différentes topologies magnétiques sur la propagation et la dissipation d'ondes inertielles forcées dans l'enveloppe convective en rotation différentielle d'étoiles de faible masse.

Depuis Janvier 2018 je dirige la thèse de doctorat de **Gaylor Wafflard-Fernandez**, qui porte sur les signatures observationnelles de la migration planétaire dans l'émission radio des disques protoplanétaires. De nombreux disques protoplanétaires présentent plusieurs anneaux sombres et brillants dans leur émission radio (cf. figure 2.5), ce qui est souvent interprété comme étant dû à la présence d'une planète massive dans chaque anneau sombre en émission. Dans la première partie de son travail de thèse, Gaylor a étudié l'impact de la migration d'une planète géante, typiquement de la masse de Saturne, sur la dynamique et l'émission des poussières du disque où se forme la planète. Lorsque le disque est suffisamment massif, la migration procède par à-coups, avec des successions de phases de migration lente et rapide, ce qui produit des successions d'anneaux sombres et brillants dans l'émission radio du disque, très semblables aux observations. Ce travail a été présenté dans Wafflard-Fernandez & Baruteau (2020). Nous allons nous intéresser par la suite aux signatures cinématiques dans le gaz de ce scénario de migration planétaire par à-coups.

Les thèses de doctorat dont j'ai contribué à l'encadrement (sans statut officiel cependant) sont les suivantes :

- Thèse de **Jason Champion** (2014-2017), sous la direction d'Olivier Berné (IRAP). Dans la première partie de sa thèse, Jason a travaillé sur des observations Herschel de disques protoplanétaires sujets à photo-évaporation externe par des étoiles proches (proplyds). Son travail a permis de contraindre la température et la densité du gaz à la surface de ces disques, ce qui est important pour estimer le taux de perte de masse par photo-évaporation externe. Dans la deuxième partie de sa thèse, Jason a travaillé avec moi sur l'évolution dynamique de ces disques, modélisés comme des disques visqueux d'accrétion 1D avec photo-évaporations interne et externe, où le taux de perte de masse par photo-évaporation externe est directement contraint des observations de Jason. Ce travail, qui permet de quantifier l'impact de la photo-évaporation externe sur la taille et la durée de vie des disques, fait l'objet d'un article en préparation.

- Thèse de **Giovanni Mirouh** (2013-2016), sous la direction de Michel Rieutord et Jérôme Ballot (IRAP). La thèse de Giovanni a porté sur l'étude théorique et numérique des modes propres d'oscillation dans la zone radiative d'étoiles en rotation différentielle. Ces modes gravito-inertiels, qu'ils soient excités par des mécanismes internes à l'étoile, ou par interactions de marée avec un compagnon stellaire ou planétaire, influencent l'évolution à long terme de la structure interne de l'étoile et de l'orbite d'éventuels compagnons. Ce travail a généralisé celui mené dans Baruteau & Rieutord (2013), où nous avions étudié la propagation et la dissipation de l'énergie associée aux modes propres inertiels dans la région convective d'étoiles ou de planètes en rotation différentielle. Le travail de thèse de Giovanni a conduit à une publication d'envergure dans Journal of Fluid Mechanics (Mirouh et al. 2016).

- Thèse de **Mathieu Guenel** (2013-2016), sous la direction de Stéphane Mathis (CEA Saclay). La thèse de Mathieu a porté sur l'étude des interactions de marée étoile-planète pour les étoiles de faible masse. De façon similaire à la thèse de Giovanni Mirouh, nous avons réalisé une étude théorique et numérique des modes propres d'oscillation se propageant dans l'enveloppe convective d'étoiles avec une rotation différentielle conique (latitudinale), telle qu'observée dans le Soleil et prédite par de nombreuses simulations numériques de convection dans les étoiles de faible masse. Nous avons ensuite examiné la dissipation d'énergie de modes inertiels forcés par interactions de marée étoile-planète. Notre travail avec Mathieu a conduit à une publication (Guenel et al. 2016b).

- Thèse de **Stefan Lines** (2012-2016), effectuée sous la direction de Zoë Leinhardt (University of Bristol). Stefan a étudié la formation planétaire autour d'étoiles binaires, peu de temps après les premières découvertes par transit d'exoplanètes autour de telles étoiles par le satellite Kepler. La partie de la thèse de Stefan où nous avons le plus interagi a consisté à examiner la croissance de planétésimaux (objets solides de taille de l'ordre du km) dans un disque protoplanétaire de gaz entourant une étoile binaire. Le travail de Stefan a permis de montrer que les exoplanètes circumbinaires détectées ont dû se former à plus grande distance dans leur disque protoplanétaire et migrer par interactions avec le disque de gaz. Le travail de Stefan a conduit a trois publications (Lines et al. 2014; 2015; 2016).

J'ai également co-dirigé, avec Simon Casassus et Sebastián Pérez, la thèse de Magistère (*tesis de magíster*) de **Marcelo Barraza**, effectuée à Universidad de Chile (Santiago) entre 2016 et 2018. Marcelo a travaillé principalement sur la modélisation de données multi-longueurs d'onde radio (ALMA et VLA) du disque protoplanétaire autour de l'étoile MWC 758. Ce travail de modélisation a été réalisé par des simulations hydrodynamiques post-traitées par des calculs de transfert radiatif dans la poussière, et a permis de proposer un scénario où les asymétries observées dans l'émission radio des poussières de ce disque seraient dues à deux planètes géantes de plusieurs fois la masse de Jupiter. De ce travail a découlé une publication (Baruteau et al. 2019).

J'ai enfin collaboré avec plusieurs chercheurs post-doctorants, dont 2 sur des projets que j'ai initiés :

- Avec **Sareh Ataiee**, chercheuse post-doctorante à l'Université de Berne (Suisse) entre 2015 et 2018, nous avons travaillé à l'élaboration de modèles globaux de formation et d'évolution des systèmes planétaires via des simulations hydrodynamiques 2D couplées à des modèles de croissance planétaire. Ce travail implique le couplage entre le code hydrodynamique 2D Fargo-ADSG que je co-développe depuis ma thèse et le code de croissance planétaire développé à Berne par Yann Alibert et son équipe. L'objectif de ce projet à long terme est de réaliser des synthèses de population planétaires 2D pour comparer de façon statistique les propriétés des exoplanètes à celles prédites par les modèles de formation et évolution planétaires (cf. § 3.1.2). Une publication a résulté de nos travaux (Ataiee et al. 2018).

- Avec **Florian Debras**, chercheur post-doctorant à l'IRAP depuis Janvier 2019, nous travaillons sur l'impact d'une cavité dans le gaz d'un disque protoplanétaire sur l'évolution orbitale de planètes géantes (de masse comparable à celle de Jupiter) ayant migré jusque dans la cavité. Cette cavité peut être créée par exemple par photo-évaporation via l'étoile centrale. Nous trouvons que de telles planètes peuvent voir leur excentricité atteindre entre 0.2 et 0.4 une fois qu'elles se trouvent dans la cavité (cf. § 2.3.3). Cette augmentation d'excentricité n'avait été jusqu'à présent obtenue que pour des planètes 5 à 10 fois plus massives. Les excentricités que nous obtenons sont comparables à l'excentricité médiane des Jupiter tièdes (cf. § 2.1.2), ces exoplanètes de masse comparable à Jupiter et orbitant à quelques ua de leur étoile. Ces résultats font l'objet d'un article soumis à MNRAS.

1.3.3 Activités de vulgarisation

2020	Conférence grand public à distance sur les exoplanètes pour l'association *Ciel d'Occitanie*.
2018	Conférence grand public sur les exoplanètes, Fête de la Science, Valderiès.
2018	Conférence sur les exoplanètes pour l'association étudiante *UPS in Space* (Université de Toulouse).
2016	Cours de 1h sur les exoplanètes pour des professeurs de collège et lycée de Toulouse en formation continue.
2014	*Speed-dating des chercheurs* à la Nuit Européenne des Chercheurs, Albi.
2014	Conférences sur les exoplanètes au lycée Matisse de Cugnaux.
2014	Conférence sur les exoplanètes à l'École Doctorale EDSYS (Université de Toulouse).
2013 –	Accueil de collégiens et lycéens à l'IRAP (plusieurs fois par an).
2010 –	Interview par plusieurs journaux (Science & Vie, Le Monde...).
2006	Conférence grand public sur les exoplanètes, Fête de la Science, Paris.

1.4 Encadrement, animation et management de la recherche

1.4.1 Responsabilités

- Membre du conseil scientifique du Programme National de Physique Stellaire et de l'Observatoire de Haute Provence (depuis 2018).
- Membre du groupe de prospectives des moyens pour l'INSU A&A (2019).

- Co-responsable d'une Action Scientifique Transverse de l'Observatoire Midi-Pyrénées sur la formation et l'évolution des systèmes planétaires (2015-2019).
- Président de la commission informatique de l'IRAP (depuis 2017).
- Co-organisateur des séminaires du groupe Astrophysical Fluid Dynamics au DAMTP/Cambridge (2011-2013) puis à l'IRAP (depuis 2017).
- Membre interne du comité de suivi de thèse de 5 doctorants de l'IRAP depuis 2014.

1.4.2 Travaux d'expertise

- Rapporteur pour des demandes de temps télescope sur les 2 mètres nationaux du Pic du Midi et de l'Observatoire de Haute Provence (depuis 2018, environ 15 demandes par semestre).
- Rapporteur pour des demandes de temps de calcul au mésocentre CALMIP de la région Occitanie (depuis 2017, environ 25 demandes par semestre).
- Rapporteur régulier pour les journaux (Nature, ApJ, MNRAS, A&A etc.), et pour plusieurs agences de financement.
- Examinateur de 4 thèses de doctorat : J. Teyssandier (IAP/Paris, 2014), É. Hébrard (IRAP/Toulouse, 2015), F. Mogavero (IAP/Paris, 2017) et L. Yu (IRAP/Toulouse, 2019).

1.4.3 Participation à des contrats de recherche

Je participe en tant que collaborateur extérieur à l'ERC Consolidator *SPIRE* (2015-2020) de Stéphane Mathis (CEA Saclay), bourse sur laquelle ont été financés le stage de M2 puis la thèse de doctorat d'Aurélie Astoul sur les interactions de marée étoile-planète. Je participe également en tant que collaborateur extérieur à l'ERC Advanced *NewWorlds* (2017-2022) de Jean-François Donati (IRAP Toulouse), bourse sur laquelle est financé le contrat postdoctoral de Florian Debras, avec qui nous travaillons sur les interactions disque-étoile-planète.

1.4.4 Organisation de conférences

J'ai contribué à l'organisation de la SF2A en Juin 2015 à l'Université de Toulouse, en tant que membre du LOC, mais aussi en y organisant avec mon collègue Olivier Berné de l'IRAP un atelier d'une demi-journée intitulé "évolution des disques protoplanétaires : du milieu interstellaire aux systèmes planétaires". Cet atelier a rassemblé une quarantaine de participants. Je contribue également en tant que membre du LOC à l'organisation de la conférence Cool Stars 21, qui devait se tenir à Toulouse en Juin 2020 avant d'être reportée à l'été 2021 (je m'occupe notamment du site web). J'ai aussi été sollicité pour organiser à Toulouse en début d'année 2021 la seconde édition de l'atelier francophone ExoSystèmes (la première édition a eu lieu à Paris en Janvier 2020).

Avec mes collègues de l'IRAP Olivier Berné et Ghylaine Quitté, nous avons animé entre 2015 et 2019 une Action Scientifique Transverse de l'Observatoire Midi-Pyrénées, doublée d'une Action Pluridisciplinaire de l'IRAP, sur la Formation et Évolution des Systèmes Planétaires. Son but est de rassembler nos collègues de l'observatoire s'intéressant aux planètes et petits corps du Système Solaire, aux disques protoplanétaires, aux systèmes exoplanétaires, et utilisant pour ce faire différentes approches : observations astrophysiques, analyses de météorites, expérimentations de laboratoire, théorie et modélisation. Nous avons organisé des ateliers de travail, typiquement sous forme de demi-journées thématiques, où l'on passait en revue les principales problématiques d'une thématique et communauté données, tout en privilégiant les temps de discussion entre participants. Ces rencontres ont visé à partager nos savoirs et expériences, à échanger nos questions et à mettre en commun les contraintes apportées par nos différentes disciplines pour faire émerger des projets permettant d'améliorer notre compréhension de la formation et de l'évolution des systèmes planétaires. Nous nous intéressons ainsi aux questions des *origines*.

Cette Action Scientifique Transverse a permis d'organiser, en Octobre 2016, un atelier national de 2 jours intitulé Origine des planètes. L'atelier comportait trois sessions et une table ronde, portant sur quatre thématiques transverses : l'eau, les champs magnétiques, les premiers solides et l'habitabilité. Ces deux jours ont rassemblé entre 30 et 40 personnes, dont de nombreux chercheurs et étudiants de l'Observatoire Midi-Pyrénées, mais aussi des collègues de Paris, Bordeaux, Nice, etc.

Cette Action Scientifique Transverse a aussi permis d'initier la mise en place d'un nouveau cours au tronc commun du M2 d'astrophysique à Toulouse sur la formation et l'évolution des systèmes planétaires, où nous intervenons Ghylaine Quitté et moi.

1.5 Bibliographie : publications, communications orales et posters

Articles et chapitres de livre avec comité de lecture (53)

53. *Linking studies of tiny meteoroids, zodiacal dust, cometary dust and circumstellar disks*
Levasseur-Regourd, **Baruteau**, Lasue, Milli & Renard
2020, Planetary and Space Science, 186, 104896 (astro-ph)

52. *Intermittent planet migration and the formation of multiple dust rings and gaps in protoplanetary disks*
Wafflard-Fernandez & **Baruteau**
2020, MNRAS, 493, 5892-5912 (astro-ph)

51. *How do planet wakes impact the location and shape of the water ice line in a protoplanetary disk ?*
Ziampras, Ataiee, Kley, Dullemond & **Baruteau**
2020, A&A, 633, A29-42 (astro-ph)

50. *Does magnetic field impact tidal dynamics inside the convective zone of low-mass stars along their evolution ?*
Astoul, Mathis, **Baruteau**, Gallet, Strugarek, Augustson, Brun & Bolmont
2019, A&A, 631, A111-122 (astro-ph)

49. *An Ideal Testbed for Planet-disk Interaction : Two Giant Protoplanets in Resonance Shaping the PDS 70 Protoplanetary Disk*
Bae, Zhu, **Baruteau**, Benisty, Dullemond, Facchini, Isella, Keppler, Pérez & Teague
2019, ApJL, 884, L41-52 (astro-ph)

48. *Magnetic field, activity and companions of V410 Tau*
Yu, Donati, Grankin, Collier Cameron, Moutou, Hussain, **Baruteau**, Jouve & the MaTYSSE collaboration
2019, MNRAS, 489, 5556-5572 (astro-ph)

47. *Chondrule Formation by the Jovian Sweeping Secular Resonance*
Gong, Zheng, Lin, Silsbee, **Baruteau** & Mao
2019, ApJ, 883, 164-175 (astro-ph)

46. *Upper limits on protolunar disc masses using ALMA observations of directly-imaged exoplanets*
Pérez, Marino, Casassus, **Baruteau**, Zurlo, Flores & Chauvin
2019, MNRAS, 488, 1005-1011 (astro-ph)

45. *Gas accretion within the dust cavity in AB Aur*
Rivière-Marichalar, Fuente, **Baruteau**, Neri, Treviño-Morales, Carmona, Agúndez & Bachiller
2019, ApJL, 879, L14-18 (astro-ph)

44. *Dust unveils the formation of a mini-Neptune planet in a protoplanetary ring*
Pérez, Casassus, **Baruteau**, Dong, Hales & Cieza
2019, AJ, 158, 15-25 (astro-ph)

43. *Dust traps in the protoplanetary disc MWC 758 : two vortices produced by two giant planets ?*
Baruteau, Barraza, Pérez, Casassus, Dong, Lyra, Marino, Christiaens, Zhu, Carmona, Debras & Alarcon
2019, MNRAS, 486, 304-319 (astro-ph)

42. *Cm-wavelength observations of MWC758 : resolved dust trapping in a vortex and intra-cavity signal*
Casassus, Marino, Lyra, **Baruteau**, Vidal, Wootten, Perez, Alarcon, Barraza, Carcamo, Dong, Sierra, Zhu, Ricci, Christiaens & Cieza
2019, MNRAS, 483, 3278-3287 (astro-ph)

41. *The Disk Substructures at High Angular Resolution Project (DSHARP) : VII. The Planet-Disk Interactions Interpretation*
Zhang, Zhu, Huang, Guzmán, Andrews, Birnstiel, Dullemond, Carpenter, Isella, Pérez, Benisty, Wilner, **Baruteau**, Bai & Ricci
2018, ApJ, 869, L47-78 (astro-ph)

40. *How much does turbulence change the pebble isolation mass for planet formation ?*
Ataiee, **Baruteau**, Alibert & Benz
2018, A&A, 615, 110-120 (astro-ph)

39. *Probing the Cold Dust Emission in the AB Aur Disk : A Dust Trap in a Decaying Vortex ?*
Fuente, **Baruteau**, Neri, Carmona, Agúndez, Goicoechea, Bachiller, Cernicharo & Berné
2017, ApJ Letters, 846, L3-8 (astro-ph)

38. *A hot Jupiter around the very active weak-line T Tauri star TAP 26*
Yu, Donati, Hébrard, Moutou, Malo, Grankin, Hussain, Collier Cameron, Vidotto, **Baruteau**, Alencar, Bouvier, Petit, Takami, Herczeg, Gregory, Jardine, Morin & Ménard
2017, MNRAS, 467, 1342-1359 (astro-ph)

37. *A gas density drop in the inner 6 AU of the transition disk around the Herbig Ae star HD 139614 : Further evidence for a giant planet inside the disk ?*
Carmona, Thi, Kamp, **Baruteau**, Matter, van den Ancker, Pinte, Kóspál, Audard, Liebhart, Sicilia-Aguilar, Pinilla, Regály, Güdel, Henning, Cieza, Baldovin-Saavedra, Meeus & Eiroa
2017, A&A, 598, 118-146 (astro-ph)

36. *A hot Jupiter orbiting a 2-Myr-old solar-mass T Tauri star*
Donati, Moutou, Malo, **Baruteau**, Yu, Hébrard, Hussain, Alencar, Ménard, Bouvier, Petit, Takami, Doyon & Collier Cameron
2016, Nature, 534, 662-666 (astro-ph)

35. *Gravito-inertial waves in a differentially rotating spherical shell*
Mirouh, **Baruteau**, Rieutord & Ballot
2016, Journal of Fluid Mechanics, 800, 213-247 (astro-ph)

34. *Formation, Orbital and Internal Evolutions of Young Planetary Systems*
Baruteau, Bai, Mordasini & Mollière
2016, The Disk in Relation to the Formation of Planets and their Proto-atmospheres (Springer) & Space Science Reviews, 205, 77-124 (astro-ph)

33. *Modelling circumbinary protoplanetary disks : II. Gas disk feedback on planetesimal dynamical and collisional evolution in the circumbinary systems Kepler-16 and 34*
Lines, Leinhardt, **Baruteau**, Paardekooper & Carter
2016, A&A, 590, A62-73 (astro-ph)

32. *High spatial resolution imaging of SO and H2CO in AB Auriga : the first SO image in a transitional disk*
Pacheco-Vázquez, Fuente, **Baruteau**, Berné, Agúndez, Neri, Goicoechea, Cernicharo & Bachiller
2016, A&A, 589, 60-70 (astro-ph)

31. *Tidal inertial waves in the differentially rotating convective envelopes of low-mass stars – I. Free oscillation modes*
Guenel, **Baruteau**, Mathis & Rieutord
2016, A&A 589, 22-38 (astro-ph)

30. *Gas and dust hydrodynamical simulations of massive lopsided transition discs – II. Dust concentration*
Baruteau & Zhu
2016, MNRAS, 458, 3927-3941 (astro-ph)
29. *Gas and dust hydrodynamical simulations of massive lopsided transition discs – I. Gas distribution*
Zhu & **Baruteau**
2016, MNRAS, 458, 3918-3926 (astro-ph)
28. *Modelling circumbinary protoplanetary disks : I. Fluid simulations of the Kepler-16 and 34 systems*
Lines, Leinhardt, **Baruteau**, Paardekooper & Carter
2015, A&A, 582, 5-16 (astro-ph)
27. *Very Large Telescope observations of Gomez's Hamburger : Insights into a young protoplanet candidate*
Berné, Fuente, Pantin, Bujarrabal, **Baruteau**, Pilleri, Habart, Ménard, Cernicharo, Tielens & Joblin
2015, A&A Letters, 578, 8-13 (astro-ph)
26. *Protoplanetary disks including radiative feedback from accreting planets*
Montesinos, Cuadra, Perez, **Baruteau** & Casassus
2015, ApJ, 806, 253-264 (astro-ph)
25. *Forming Circumbinary Planets : N-body Simulations of Kepler-34*
Lines, Leinhardt, Paardekooper, **Baruteau** & Thébault
2014, ApJ Letters, 782, L11-16 (astro-ph)
24. *Nonlinear evolution of tidally forced inertial waves in rotating fluid bodies*
Favier, Barker, **Baruteau** & Ogilvie
2014, MNRAS, 439, 845-860 (astro-ph)
23. *Planet-disc interactions and early evolution of planetary systems*
Baruteau, Crida, Paardekooper, Masset, Guilet, Bitsch, Nelson, Kley & Papaloizou
2014, Protostars and Planets VI (University of Arizona Press), 914, 667-689 (astro-ph)
22. *Disk-planets interactions and the diversity of period ratios in Kepler's multi-planetary systems*
Baruteau & Papaloizou
2013, ApJ, 778, 7-21 (astro-ph)
21. *Influence of the circumbinary disk gravity on planetesimal accumulation in the Kepler 16 system*
Marzari, Thébault, Scholl, Picogna & **Baruteau**
2013, A&A, 553, A71-79 (astro-ph)
20. *Type I planet migration in weakly magnetised laminar discs*
Guilet, **Baruteau** & Papaloizou
2013, MNRAS, 430, 1764-1783 (astro-ph)
19. *Recent developments in planet migration theory*
Baruteau & Masset
2013, Tidal effects in Astronomy and Astrophysics (Springer) & Lecture Notes in Physics, 861, 201-253 (astro-ph)
18. *Inertial waves in a differentially rotating spherical shell*
Baruteau & Rieutord
2013, Journal of Fluid Mechanics, 719, 47-81 (astro-ph)
17. *Protoplanetary migration in non-isothermal discs with turbulence driven by stochastic forcing*
Pierens, **Baruteau** & Hersant
2012, MNRAS, 427, 1562-1573 (astro-ph)
16. *How not to build Tatooine : the difficulty of in situ formation of circumbinary planets Kepler 16b, Kepler 34b and Kepler 35b*
Paardekooper, Leinhardt, Thébault & **Baruteau**
2012, ApJ Letters, 754, L16-20 (astro-ph)

15. *No slow-plough mechanism during the rapid hardening of supermassive black hole binaries*
Baruteau, Ramirez-Ruiz & Masset
2012, MNRAS Letters, 423, L65-69 (astro-ph)

14. *Eccentricity of radiative discs in close binary-star systems*
Marzari, **Baruteau**, Scholl & Thébault
2012, A&A, 539, A98-110 (astro-ph)

13. *Corotation torques experienced by planets embedded in weakly magnetized turbulent discs*
Baruteau, Fromang, Nelson & Masset
2011, A&A, 533, A84-99 (astro-ph)

12. *Numerical convergence in self-gravitating disc simulations : initial conditions and edge effects*
Paardekooper, **Baruteau** & Meru
2011, MNRAS Letters, 416, L65-69 (astro-ph)

11. *Rapid inward migration of planets formed by gravitational instability*
Baruteau, Meru & Paardekooper
2011, MNRAS, 416, 1971-1982 (astro-ph)

10. *On the dynamics of resonant super-Earths in disks with turbulence driven by stochastic forcing*
Pierens, **Baruteau** & Hersant
2011, A&A, 535, A5-16 (astro-ph)

9. *Binaries migrating in a gaseous disk : Where are the Galactic center binaries ?*
Baruteau, Cuadra & Lin
2011, ApJ, 726, 28-46 (astro-ph)

8. *A torque formula for non-isothermal Type I planetary migration - II. Effects of diffusion*
Paardekooper, **Baruteau** & Kley
2011, MNRAS, 410, 293-303 (astro-ph)

7. *Planet–planet scattering in circumstellar gas disks*
Marzari, **Baruteau** & Scholl
2010, A&A Letters, 514, L4-6 (astro-ph)

6. *Protoplanetary migration in turbulent isothermal disks*
Baruteau & Lin
2010, ApJ, 709, 759-773 (astro-ph)

5. *A torque formula for non-isothermal Type I planetary migration - I. Unsaturated horseshoe drag*
Paardekooper, **Baruteau**, Crida & Kley
2010, MNRAS, 401, 1950-1964 (astro-ph)

4. *On the eccentricity of self-gravitating circumstellar disks in eccentric binary systems*
Marzari, Scholl, Thébault & **Baruteau**
2009, A&A, 508, 1493-1502 (astro-ph)

3. *The dynamical role of the circumplanetary disc in planetary migration*
Crida, **Baruteau**, Kley & Masset
2009, A&A, 502, 679-693 (astro-ph)

2. *Type I planetary migration in a self-gravitating disk*
Baruteau & Masset
2008 ApJ, 678, 483-497 (astro-ph)

1. *On the corotation torque in a radiatively inefficient disk*
Baruteau & Masset
2008, ApJ, 672, 1054-1067 (astro-ph)

Comptes rendus de conférence avec comité de lecture (3)

3. *Type I Planet Migration in Weakly Magnetized Laminar Disks*
   Guilet, **Baruteau** & Papaloizou
   2014, Formation, Detection, and Characterization of Extrasolar Habitable Planets, Proceedings of the International Astronomical Union, IAU Symposium, Volume 293, 256-262

2. *On type I planetary migration in adiabatic disks*
   Baruteau & Masset
   2007, Exoplanets : Detection, Formation and Dynamics, Proceedings of the International Astronomical Union, IAU Symposium, Volume 249, 397-400

1. *Type I planetary migration in a self-gravitating disk*
   Baruteau & Masset
   2007, Exoplanets : Detection, Formation and Dynamics, Proceedings of the International Astronomical Union, IAU Symposium, Volume 249, 393-396

Comptes rendus de conférence sans comité de lecture (15)

15. *Does magnetic field modify tidal dynamics in the convective envelope of Solar mass stars ?*
    Astoul, Mathis, **Baruteau**, Gallet, Augustson, Bolmont, Brun & Strugarek
    2018, Proceedings of the Annual meeting of the French Society of Astronomy and Astrophysics, Eds. : Di Matteo, Billebaud, Herpin, Lagarde, Marquette, Robin & Venot, 495-500 (astro-ph)
14. *Towards a better understanding of tidal dissipation at corotation layers in differentially rotating stars and planets*
    Astoul, Mathis, **Baruteau** & André
    2017, Proceedings of the Annual meeting of the French Society of Astronomy and Astrophysics, Eds. : Reylé, Di Matteo, Herpin, Lagadec, Lançon, Meliani & Royer, 235-240 (astro-ph)
13. *Tidal dissipation by inertial waves in differentially rotating convective envelopes of low-mass stars*
    Guenel, Mathis, **Baruteau** & Rieutord
    2016, Proceedings of the 19th Cambridge Workshop on Cool Stars, Stellar Systems, and the Sun, Edited by Feiden, 4 pages (astro-ph)

12. *Planet Formation Imager (PFI) : science vision and key requirements*
    Kraus, Monnier, Ireland, Duchêne, Espaillat, Hönig, Juhasz, Mordasini, Olofsson, Paladini, Stassun, Turner, Vasisht, Harries, Bate, Gonzalez, Matter, Zhu, Panic, Regaly, Morbidelli, Meru, Wolf, Ilee, Berger, Zhao, Kral, Morlok, Bonsor, Ciardi, Kane, Kratter, Laughlin, Pepper, Raymond, Labadie, Nelson, Weigelt, ten Brummelaar, Pierens, Oudmaijer, Kley, Pope, Jensen, Bayo, Smith, Boyajian, Quiroga-Nuñez, Millan-Gabet, Chiavassa, Gallenne, Reynolds, de Wit, Wittkowski, Millour, Gandhi, Ramos Almeida, Alonso Herrero, Packham, Kishimoto, Tristram, Pott, Surdej, Buscher, Haniff, Lacour, Petrov, Ridgway, Tuthill, van Belle, Armitage, **Baruteau**, Benisty, Bitsch, Paardekooper, Pinte, Masset & Rosotti
    2016, Proceedings of the SPIE, Volume 9907, id. 99071K, 12 pages (astro-ph)

11. *Free inertial modes in differentially rotating convective envelopes of low-mass stars : numerical exploration*
    Guenel, **Baruteau**, Mathis & Rieutord
    2015, Proceedings of the Annual meeting of the French Society of Astronomy and Astrophysics, Eds. : Martins, Boissier, Buat, Cambrésy & Petit, 371-375 (astro-ph)

10. *Gravito-inertial modes in a differentially rotating spherical shell*
    Mirouh, **Baruteau**, Rieutord & Ballot
    2015, The Space Photometry Revolution - CoRoT Symposium 3, Kepler KASC-7 Joint Meeting, Toulouse, France, Edited by García & Ballot ; EPJ Web of Conferences, Vol. 101, id.06046, 4 pages

9. *Gravito-inertial modes in a differentially rotating spherical shell*
   Mirouh, **Baruteau**, Rieutord & Ballot
   2014, Proceedings of the Annual meeting of the French Society of Astronomy and Astrophysics, Eds. : Ballet, Martins, Bournaud, Monier & Reylé, 493-496 pages (astro-ph)

8. *Inertial waves in differentially rotating low-mass starsand tides*
   Guenel, **Baruteau**, Mathis & Rieutord
   2014, Proceedings of the Annual meeting of the French Society of Astronomy and Astrophysics, Eds. : Ballet, Martins, Bournaud, Monier & Reylé, 493-496 pages (astro-ph)

7. *Circumbinary planet formation : N-body simulations of a perturbed early-phase protoplanetary disk*
   Lines, Leinhardt, Paardekooper, Thébault & Baruteau
   2013, Proceedings of the European Planetary Science Congress 2013, id.EPSC2013-267, 2 pages

6. *How is protoplanetary migration changed in weakly magnetised discs ?*
   Baruteau, Guilet & Papaloizou
   2012, Proceedings of the European Planetary Science Congress 2012, id. EPSC2012-644, 2 pages

5. *Protoplanetary migration in non-isothermal disks with turbulence driven by stochastic forcing*
   Pierens **Baruteau** & Hersant
   2012, Proceedings of the European Planetary Science Congress 2012, id. EPSC2012-285, 2 pages

4. *Planetary migration in weakly magnetized turbulent discs*
   Baruteau, Fromang, Nelson & Masset
   2011, Proceedings of the Annual meeting of the French Society of Astronomy and Astrophysics, Eds. : Alecian, Belkacem, Samadi & Valls-Gabaud, 455-458

3. *Planets formed by gravitational instability should rapidly migrate inward*
   Baruteau, Meru & Paardekooper
   2011, Proceedings of the Annual meeting of the French Society of Astronomy and Astrophysics, Eds. : Alecian, Belkacem, Samadi & Valls-Gabaud, 459-461

2. *On type I planetary migration in an adiabatic disk*
   Baruteau & Masset
   2007, Proceedings of the Annual meeting of the French Society of Astronomy and Astrophysics, Eds. : Bouvier, Chalabaev & Charbonnel, 437-442

1. *On the impact of disk gravity on planetary migration*
   Baruteau & Masset
   2006, Proceedings of the Annual meeting of the French Society of Astronomy and Astrophysics, Eds. : Barret, Casoli, Lagache, Lecavelier & Pagani, 569-572

Papier blanc (1)

1. *Observing Planetary Systems in the Making*
   Isella, Ricci, Andrews, **Baruteau**, Berger, Bergin, Birnstiel, Bowler, Brogan, Carrasco Gonzalez, Chandler, Currie, Cuzzi, D'Angelo, Dong, Duchene, Dutrey, Ercolano, Espaillat, Estrada, Flock, Gaspar, Greene, Huang, Jang-Condell, Johns-Krull, Kennedy, Kim, Kirchschlager, Kraus, Krijt, Li, Lyra, Macintosh, Monnier, Oberg, Pascucci, Perez, Petrov, Pinilla, Ridgway, Stassun, ten Brummelaar, Testi, Turner, Van Belle, van der Marel, Weinberger, White, Williams, Wilner, Wootten, Wu, Youdin, Zhang & Zhu
   2019, Astro2020 : Decadal Survey on Astronomy and Astrophysics, science white papers, no. 174 ; Bulletin of the American Astronomical Society, Vol. 51, Issue 3, id. 174

Séminaires (43), communications orales (32) et posters (7)

2020 Séminaire à distance pour University or Surrey. Revue invitée à l'atelier francophone *ExoSystèmes I* (Paris). Présentation invitée à la conférence *The building blocks of planets 2020* (à distance).

2019 Séminaires à UNAM/Cuernavaca, au CEA Saclay et au DAMTP/Cambridge. Présentation invitée à l'atelier *Planetary Exploration, Horizon 2061* (Toulouse).

2018 Séminaires au LAB/Bordeaux et à University of Leicester. Présentation invitée à la conférence *Planets, Stars and Discs : A Golden Age for Particle and Gas Dynamics* (Oxford). Présentation à l'atelier *Gravitational Instability : unsolved problems in forming planets, brown dwarfs and stellar companions* (Leicester).

2017 Séminaires à ETH Zürich, Université de Berne et IRAP/Toulouse. Présentations à la conférence *The disc migration issue : from protoplanets to supermassive black holes* (Cambridge) et à l'atelier *Star-Planet(s)-Inner Disk Interactions in young accreting stars* (Montpellier).

2016 Séminaires à Universidad de Chile/Santiago et à Leiden Observatory. Présentations invitées à l'atelier francophone *disc asymmetries* (Grenoble) et à la *SF2A* (Lyon).

2015 Séminaire au CRAL/Lyon. Revues invitées à l'atelier *Magnetic Topologies of Young Stars & the Survival of close-in massive Exoplanets* (Toulouse), à l'atelier *Protoplanetary Disk Dynamics and Planet Formation* (Yokohama), et à la conférence *Exoplanets in Lund 2015* (Lund). Présentation à la *SF2A* (Toulouse).

2014 Séminaires à ETH Zürich, Pontificia Universidad Católica/Santiago et à l'IRAP/Toulouse. Revue invitée à l'atelier *The Disk in Relation to The Formation of Planets And Their Protoatmospheres* (ISSI/Beijing). Présentations à l'atelier *PLATO Meeting Theory* (London) et à la conférence *CoRoT / KASC joint meeting* (Toulouse).

2013 Séminaires à IRAP/Toulouse, Université de Berne, UTINAM/Besançon, Institute of Astronomy / Cambridge, DAMTP/Cambridge et LESIA.

2012 Séminaire au DAMTP/Cambridge. Présentations à la conférence *Planet Formation and Evolution* (Munich), à la conférence *European Planetary Science Congress* (Madrid) et à l'atelier *Rotational dynamics for planetary and stellar applications* (IRPHE/Marseille).

2011 Séminaires au DAMTP/Cambridge, à University of Tübingen, Queen Mary University of London, University of Bristol, Nagoya University (invitation) et TiTech / Tokyo (invitation). Présentations à la *SF2A* (Paris), à l'atelier *Geophysical and Astrophysical Fluid Flows : Baroclinic Instability and Protoplanetary Accretion Disks* (Ringberg castle), et à *Winter School and Workshop on Star Formation* (NAOJ Tokyo, invitation). Posters à la conférence *Extreme Solar Systems II* (Jackson Hole, USA) et à la *SF2A* (Paris).

2010 Séminaires au LATT/Toulouse et DAMTP/Cambridge. Présentation invitée à l'atelier *Planetary Population Synthesis Workshop* (Ringberg castle). Présentations à l'école d'été *International Summer Institute for Modeling in Astrophysics* (Santa Cruz, USA), et à l'atelier *Dynamics of Astrophysical Disks* (Beijing).

2009 Séminaires au LATT/Toulouse, CEA Saclay et à UC Santa Cruz. Présentation à la conférence *Dynamics of Discs and Planets*, à la conférence *Planet Formation and Evolution* (Tübingen) et à l'atelier *Solar-Extrasolar Meeting* (NASA Ames). Posters à la conférence *From Circumstellar Disks to Planetary Systems* (Garching) et à la conférence anniversaire de Douglas Lin (Prato/Italie).

2008 Séminaires à UC Santa Cruz, University of Tübingen, MPIA/Heidelberg, OCA/Nice, LAB/Bordeaux, IAP/Paris et UNAM/México. Présentations à l'atelier *Accretion Disks Workshop* (Beijing) et à la conférence *Division on Dynamical Astronomy* (Boulder). Poster à la conférence *Origin and Evolution of Planets* (Ascona).

2007 Séminaire au GRAAL/Montpellier. Présentations au Symposium 249 de l'IAU *Exoplanets : Detection, Formation and Dynamics* (Suzhou, Chine) et à la *SF2A* (Grenoble). Posters au Symposium 249 de l'IAU *Exoplanets : Detection, Formation and Dynamics* (Suzhou, Chine) et à la conférence *Extreme Solar Systems I* (île de Santorin).

2006 Présentation à la *SF2A* (Paris).

⋆⋆⋆

2 | Synthèse des travaux de recherche

MES ACTIVITÉS de recherche portent sur la formation et l'évolution orbitale des systèmes planétaires, et la dynamique des disques protoplanétaires. J'étudie les interactions gravitationnelles entre planètes, le disque protoplanétaire de gaz et de poussières où elles se forment, et leur(s) étoile(s). Mon travail mêle théorie en dynamique des fluides astrophysiques, simulations hydrodynamiques multidimensionnelles et calculs de transfert radiatif.

Je cherche notamment à interpréter les propriétés orbitales des planètes extrasolaires, dont la diversité révèle que les planètes peuvent se former et évoluer dans des conditions variées, parfois extrêmes. Une part importante de mes travaux a pour but de déterminer la direction et la vitesse de migration des planètes en formation dans leur disque protoplanétaire. Mon travail a notamment permis (i) de trouver comment ralentir la migration rapide des planètes de masse terrestre vers leur étoile, qui pendant longtemps avait rendu les prédictions des modèles de formation et d'évolution planétaires incompatibles avec les détections d'exoplanètes, (ii) de montrer que les planètes géantes formées à grande distance de leur étoile par instabilité gravitationnelle migrent très rapidement vers les parties internes des disques protoplanétaires, et qu'il est là aussi question de devoir ralentir leur migration afin de rendre compte des planètes observées par imagerie directe, et (iii) de montrer que la diversité des rapports de période orbitale dans les systèmes multi-planétaires détectés par le satellite spatial *Kepler* peut être expliquée par les modèles de migration planétaire.

Stimulé par les observations multi-longueurs d'onde de disques protoplanétaires, je travaille plus récemment sur la dynamique et l'émission du gaz et des poussières dans les disques. Je cherche en particulier à déterminer si les structures observées dans l'émission des disques (succession d'anneaux sombres et brillants, spirales, asymétries etc.) peuvent être dues à des planètes enfouies dans ces disques. Les modèles que j'ai développés ont permis notamment (i) de proposer un scénario où la présence d'anneaux multiples sombres et brillants dans l'émission radio des poussières pourrait être due à la migration rapide d'une seule planète dans le disque protoplanétaire, et (ii) de montrer que les observations de l'émission radio de plusieurs disques suggèrent fortement la présence de planètes massives structurant la poussière de leur disque à grande distance de l'étoile, ce qui permettrait, si ces prédictions étaient confirmées à l'avenir, d'apporter de nouvelles contraintes sur la formation et l'évolution de planètes jeunes.

Le nombre croissant d'exoplanètes très proches de leur étoile, dont certaines ont une obliquité orbitale très élevée ou un rayon physique anormalement grand, demande de mieux comprendre les effets de marée entre étoiles et planètes. C'est dans cette optique que j'étudie la propagation et la dissipation d'ondes de marée dans les fluides en rotation modélisant l'intérieur d'étoiles ou de planètes géantes, ce qui m'a permis notamment de trouver un mécanisme capable d'augmenter considérablement l'efficacité des effets de marée étoile-planète.

Sommaire

2.1 Contexte observationnel

L'astrophysique des systèmes planétaires connaît une expansion fulgurante, soutenue par la découverte de plus de 4000 planètes extrasolaires en 25 ans, dont environ un tiers fait partie de systèmes multi-planétaires. Grâce notamment à SPIRou au CFHT, ESPRESSO au VLT, Gaia, TESS, PLATO, JWST ou encore WFIRST dans l'espace, de nombreuses autres planètes seront découvertes dans un futur proche, planètes qui sont trop petites ou trop lointaines pour être détectées aujourd'hui. Les détections d'exoplanètes à ce jour indiquent que la formation planétaire accompagne naturellement la formation d'étoiles, avec plus de 40% des étoiles proches de type solaire possédant au moins une planète plus légère que Saturne (Mayor et al. 2009). Ces découvertes prolifiques ont révélé des mondes bien différents de notre Système Solaire, comme l'illustre la figure 2.1, qui représente le rapport de masse planète-étoile pour les $\sim$1700 exoplanètes dont la masse a été déterminée ou estimée, ainsi que pour 6 des 8 planètes du Système Solaire, en fonction de leur période orbitale et leur excentricité.

La grande diversité de périodes orbitales et d'excentricités, en particulier pour les planètes géantes, montre que les planètes peuvent se former et/ou évoluer dans des conditions variées, parfois extrêmes. Par exemple, la planète qui orbite actuellement le plus rapidement autour d'une étoile de type solaire le fait en seulement un peu plus de 4 heures (K2-137b, Smith et al. 2018), elle n'est d'ailleurs distante de son étoile que de 3 rayons stellaires environ. Et celle qui orbite le plus lentement a une période de révolution de presque 900 ans et est située à environ 115 Unités Astronomiques (ua) de son étoile (Fomalhaut b, Kalas et al. 2008). Une des questions auxquelles je tente de répondre par mes activités de recherche est de savoir quel rôle les interactions entre planètes et leur disque protoplanétaire peuvent jouer dans cette diversité. C'est ce que nous allons discuter pour les trois grandes populations de planètes que le diagramme de la figure 2.1 fait ressortir, en dépit des biais observationnels inhérents aux méthodes de détection.

2.1.1 Jupiter chauds

Les Jupiter chauds sont des planètes de masse comparable à Jupiter et orbitant autour de leur étoile en typiquement 1 à 10 jours. Même si ce sont globalement les premières exoplanètes à avoir été détectées autour d'étoiles de type solaire par spectro-vélocimétrie (Mayor & Queloz 1995, Butler et al. 1997), on sait aujourd'hui que les Jupiter chauds sont rares, avec une probabilité d'occurrence d'environ 1% autour des étoiles de type solaire (Mayor et al. 2011, Wright et al. 2012). Bien que ce soient des objets rares, ils donnent un bon

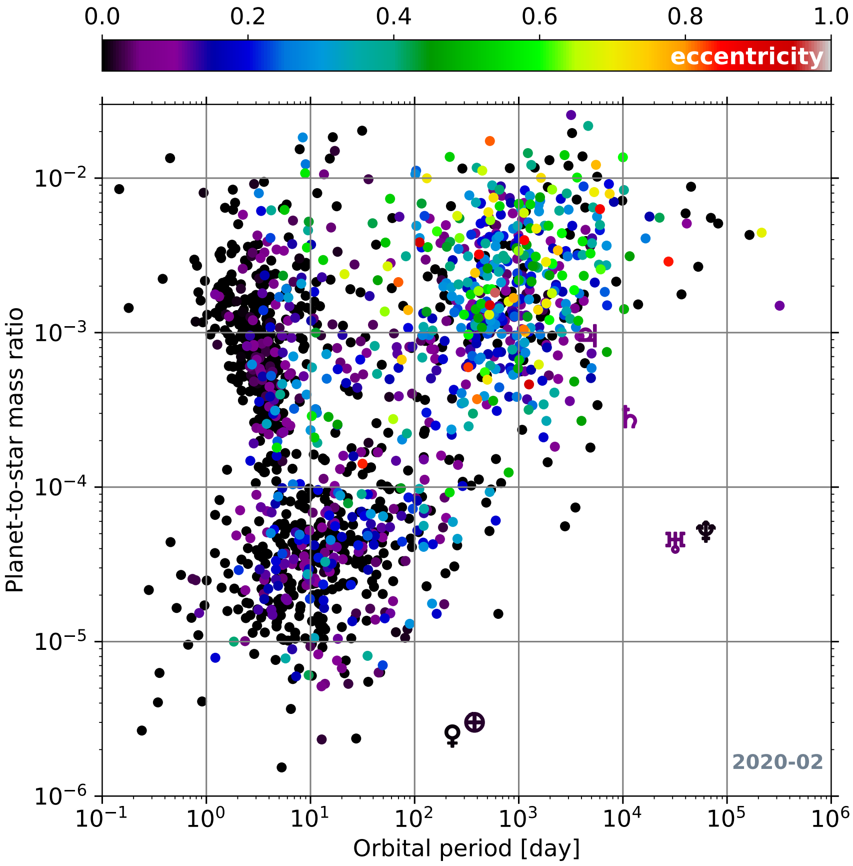

FIGURE 2.1 – *Période orbitale des exoplanètes et de 6 des 8 planètes du Système Solaire en fonction du rapport de masse des planètes à leur étoile (valeurs médianes). La couleur de chaque symbole varie avec l'excentricité de la planète qu'il représente (voir l'échelle de couleur au-dessus du graphe). Données extraites de exoplanet.eu.*

aperçu de la diversité d'évolution orbitale permise par les interactions disque-étoile-planètes. En particulier, les Jupiter chauds ont dans l'ensemble une excentricité relativement faible, ce qui peut suggérer que leur orbite reflète une évolution directement héritée de leur formation dans le disque protoplanétaire, étant donné que les planètes qui se forment seules dans un disque ont généralement une excentricité très faible, voire nulle. Il est néanmoins possible que les interactions de marée avec l'étoile aient pu amortir l'excentricité de ces planètes et ainsi cacher une évolution plus dynamique dans le passé, résultant par exemple d'interactions planète-planète.

Cette évolution dynamique passée est en fait suggérée par les mesures de l'obliquité orbitale des Jupiter chauds, c'est-à-dire l'angle entre l'axe de rotation de l'étoile et la direction perpendiculaire au plan orbital, dont on mesure le plus souvent la projection dans le plan du ciel par l'effet Rossiter McLaughlin en combinant observations par transit et par spectro-vélocimétrie (Winn et al. 2005). Cet effet correspond à une distorsion des raies d'absorption de la photosphère de l'étoile à mesure qu'une planète occulte le disque stellaire. L'obliquité orbitale projetée a été mesurée pour environ 140 planètes à ce jour, principalement pour des Jupiter chauds dont la période orbitale est inférieure à 10 jours. Comme on peut le voir sur l'image de gauche à la figure 2.2, environ un tiers des Jupiter chauds a une obliquité orbitale projetée supérieure à 30°. Elle peut même excéder 90°, on parle alors de planètes en orbite rétrograde. Même si la tendance n'est pas évidente sur l'image de droite à la figure 2.2, il y a souvent été vu une corrélation entre obliquité orbitale projetée et température effective de l'étoile : les Jupiter chauds autour d'étoiles chaudes auraient tendance à avoir une obliquité orbitale plus élevée (voir, par exemple, la revue par Winn & Fabrycky 2015). Notons qu'il est possible, sous certaines circonstances, de mesurer l'inclinaison de l'étoile par rapport à la ligne de visée, $i_{\star}$, par exemple par astérosismologie, ce qui permet de contraindre l'obliquité orbitale réelle d'une planète (une faible valeur de $i_\star$ impliquant une obliquité orbitale réelle élevée ; Huber et al. 2013, Chaplin et al. 2013), voire de la déterminer (Benomar et al. 2014). A ce jour, l'obliquité orbitale réelle de 25 planètes a été mesurée : elle excède 30° pour 11 d'entre elles. Le lecteur pourra consulter les statistiques mises à jour sur ce site.

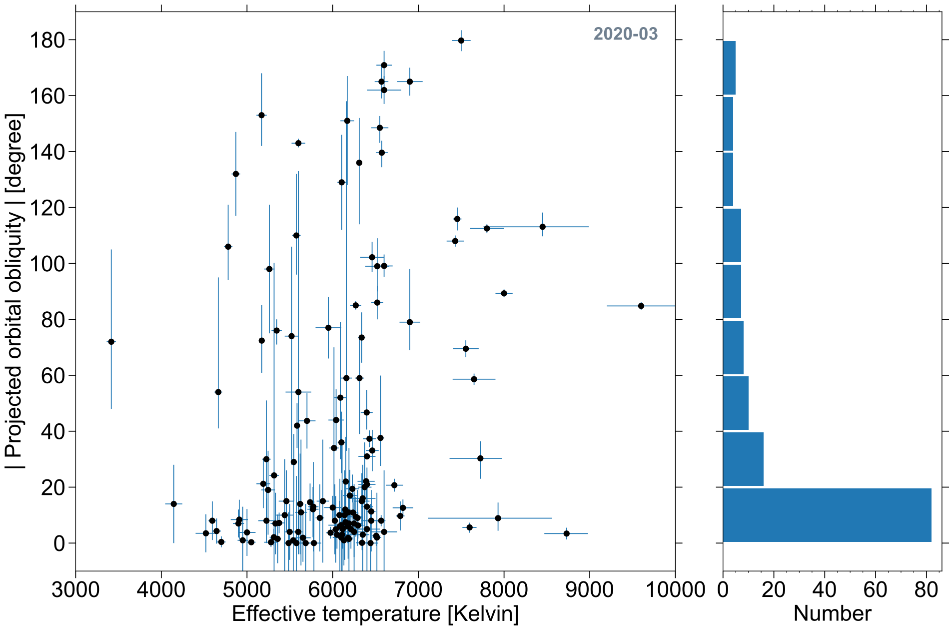

FIGURE 2.2 – *Gauche : obliquité orbitale projetée de 142 exoplanètes, la grande majorité étant des Jupiter chauds, en fonction de la température effective de leur étoile. Les barres d'erreur sont celles à 1σ. Droite : distribution de l'obliquité orbitale projetée. Données extraites du catalogue TEPCat.*

Qu'en est-il maintenant des Jupiter chauds ayant une faible obliquité ? Est-ce que ce sont des planètes qui ont toujours eu une obliquité orbitale faible, et donc quelque part une inclinaison orbitale faible, compatible avec une architecture orbitale héritée de leur disque protoplanétaire ? Ou bien ces planètes ont-elles vu leur inclinaison et obliquité orbitale amorties par interactions de marée avec leur étoile, cachant là encore une évolution passée dynamique ? Il s'agit, de mon point de vue, de l'une des questions clés sur l'évolution des Jupiter chauds, et qui demande notamment de mieux comprendre l'évolution de l'obliquité orbitale des planètes par effets de marée avec leur étoile, et ce dès lors que l'étoile est en phase de pré-séquence principale (p.e., Bolmont & Mathis 2016).

Il est par ailleurs tout particulièrement intéressant de noter que deux Jupiter chauds ont été détectés autour d'étoiles de type "weak-line T Tauri", âgées de quelques millions d'années seulement (Donati et al. 2016, Yu et al. 2017). Il est très peu probable que les effets de marée aient eu le temps de modifier significativement l'orbite de ces planètes, qui doivent refléter et donc contraindre une évolution orbitale conditionnée par le disque protoplanétaire. Nous y reviendrons au § 2.3.3.

2.1.2 Jupiter tièdes

On entend par Jupiter tièdes les planètes géantes avec des périodes orbitales excédant ~100 jours. Présentes autour de ~10% des étoiles de type solaire (Cumming et al. 2008, Mayor et al. 2011), ces planètes ont une excentricité médiane d'environ 0.25. Cette valeur élevée est souvent interprétée comme le signe d'un processus dynamique générique rendant excentrique l'orbite de ces planètes massives une fois initiée la dissipation du disque protoplanétaire. Cela peut être dû à des interactions résonantes planète-planète, et on sait que les interactions disque-planètes conduisent souvent à former des paires de planète en résonance de moyen mouvement, on en reparlera par la suite. Cela peut aussi être dû à des interactions avec des compagnons (sub-)stellaires, par exemple via des résonances de Kozai (Naoz et al. 2012).

De façon remarquable, des campagnes d'observations par spectro-vélocimétrie et par imagerie directe ont cherché des compagnons planétaires et (sub-)stellaires aux Jupiter tièdes et chauds, et n'ont pas trouvé de corrélation entre la présence d'un compagnon et une excentricité élevée et/ou une obliquité orbitale projetée élevée pour les Jupiter tièdes ou chauds (Knutson et al. 2014, Ngo et al. 2015). Cela n'indique pas nécessairement que des interactions gravitationnelles avec ces compagnons n'aient pas pu se produire dans le passé, mais cela peut suggérer que la présence de compagnons aux Jupiter tièdes est une explication circonstancielle plus que générique à leur excentricité médiane élevée. Nous reviendrons sur l'origine de l'excentricité élevée des Jupiter tièdes au § 2.3.3, où nous discuterons d'un scénario plausible pour croître de manière générique l'excentricité des planètes géantes par interactions avec leur disque protoplanétaire.

2.1.3 Super-Terres

Le télescope spatial *Kepler* a permis de détecter les transits d'une population conséquente de planètes de rayon physique compris entre celui de la Terre et celui de Neptune, et de période orbitale entre 1 et 100 jours (cf. figure 2.3). Comme le montrent les histogrammes de cette figure, les planètes détectées par Kepler se distinguent en deux populations de rayon typique ∼1.3 $R_\oplus$ (planètes qu'on appelle généralement super-Terres) et ∼2.3 $R_\oplus$ (planètes qu'on appelle généralement mini-Neptunes), avec une diminution significative du nombre de planètes aux environs de 1.8 $R_\oplus$ (Fulton et al. 2017, Fulton & Petigura 2018). Toutes ces planètes, que nous appellerons simplement super-Terres par la suite, constituent actuellement la population la plus fréquente d'exoplanètes, présente autour de 50% des étoiles de type solaire (Fulton et al. 2017). Environ la moitié des super-Terres fait partie de systèmes multi-planétaires. La plupart forme des systèmes compacts, c'est-à-dire

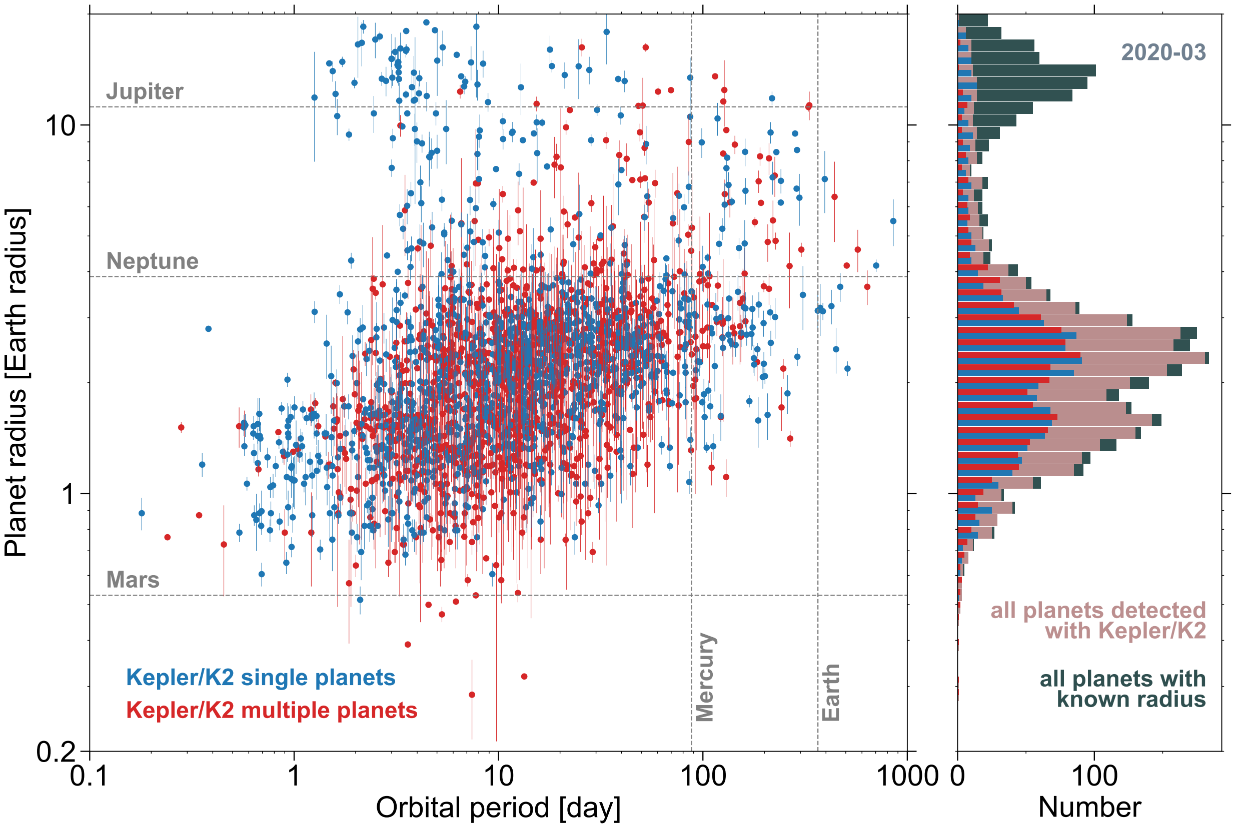

FIGURE 2.3 – *Rayon physique et période orbitale des planètes détectées par transit avec le télescope spatial Kepler (2404 planètes dont le statut est confirmé, incluant celles de la campagne K2). Les planètes dans des systèmes multi-planétaires sont représentées en rouge, les autres en bleu. Les barres d'erreur sont celles à 1σ. La partie droite de la figure compare la distribution du rayon physique de ces planètes avec celle de toutes les planètes dont le rayon physique est connu (histogramme gris, 3083 planètes). Données extraites de exoplanet.eu.*

que le rapport de période orbitale entre deux planètes consécutives est typiquement inférieur à 2. Leur excentricité reste pourtant relativement faible, de quelques pourcents typiquement, ce qui peut là encore suggérer une architecture orbitale héritée du disque protoplanétaire.

Une observable intéressante de ce point de vue est le rapport de période orbitale entre paires adjacentes de planètes d'un même système, que l'on montre à la figure 2.4 pour toutes les planètes confirmées dans les systèmes multi-planétaires détectés par *Kepler*. Cette figure illustre essentiellement deux points. D'une part, il y a beaucoup de paires adjacentes de planètes en dehors des résonances de moyen mouvement, c'est-à-dire là où le rapport de période orbitale entre planètes est un nombre rationnel, comme 2 (résonance 2:1), 3/2 (résonance 3:2), 4/3, 5/3 etc. D'autre part, les paires adjacentes de planètes proches des résonances tendent à avoir un rapport de période orbitale légèrement supérieur à celui de la résonance en question. Par exemple, on voit clairement à la figure 2.4 qu'il y a plus de paires de planètes avec un rapport de période orbitale un peu plus grand que 1.5 qu'un peu plus petit. Notons que, malgré une statistique plus faible, une tendance similaire peut être vue sur les paires de planètes détectées par spectro-vélocimétrie autour des résonances de moyen mouvement 3:2 et 2:1 (Deleuil et al., en préparation). Notons encore que l'histogramme de la figure 2.4 n'est pas exempt de biais, en particulier certains pics dans la distribution pourraient être des artefacts de planètes additionnelles non détectées par transit (Steffen 2013). Par exemple, un système avec deux planètes en transit dont le rapport de période orbitale est d'environ 1.9 pourrait en fait être constitué de trois planètes dont celle du milieu ne transite pas si elle est a une inclinaison suffisante, et qui serait en résonance en moyen mouvement 4:5 avec la planète la plus interne, et en résonance 3:2 avec celle la plus externe.

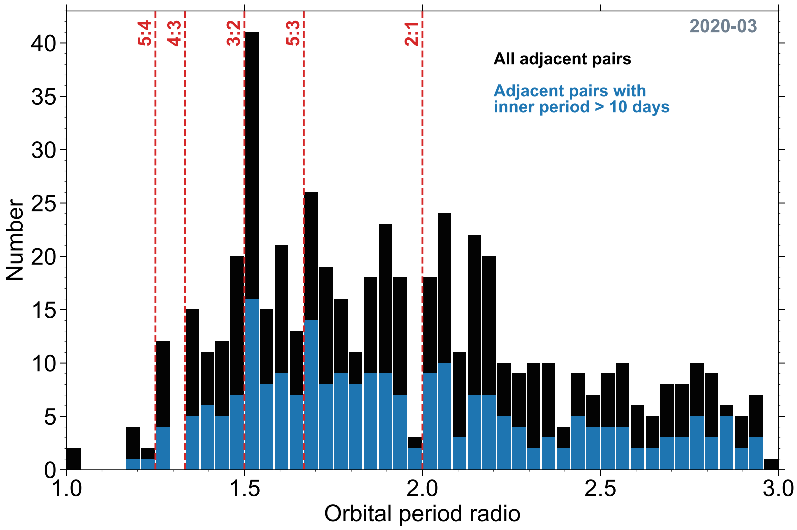

FIGURE 2.4 – *Histogramme du rapport de période orbitale entre chaque paire adjacente de planètes parmi les systèmes multi-planétaires confirmées par Kepler (noir). L'histogramme bleu concerne uniquement les paires adjacentes de planètes pour lesquelles la planète interne a une période orbitale excédant 10 jours. Figure adaptée de Baruteau & Papaloizou (2013) avec les données extraites de exoplanet.eu.*

Par ailleurs, on constate à la figure 2.4 la présence de deux paires de planètes ayant un rapport de période orbitale très proche de 1. Il ne s'agit pas de planètes co-orbitales, mais d'erreurs dans la base de données. Dans le cas de Kepler-271, la planète d, qui a une période orbitale distincte d'à peine 1% de celle la planète b, n'a en fait pas été confirmée (Rowe et al. 2014). Dans le cas de Kepler-132, l'étoile s'avère être une binaire, et les planètes b et c orbitent chacune autour d'une composante de la binaire (Kepler-132 A pour l'une, Kepler-132 B pour l'autre ; Lissauer et al. 2014). Le fait qu'elles aient la même période orbitale à moins d'un pourcent près n'est vraisemblablement qu'une coïncidence.

De nombreux travaux théoriques ont examiné si la diversité de rapports de période orbitale peut s'expliquer par les interactions disque-planètes, ou au contraire refléter une architecture orbitale résultats d'interactions planète-planète après dissipation du disque. Nous aurons l'occasion de rediscuter de ce point au § 2.3.3.

2.1.4 Observations de disques protoplanétaires

Malgré la quantité et la qualité des données observationnelles sur les systèmes planétaires, dont le nôtre, la diversité des exoplanètes nous échappe toujours et il est difficile d'avoir une théorie générale sur la formation et l'évolution des systèmes planétaires. Une raison est que les mécanismes d'évolution orbitale des systèmes planétaires (interactions disque-planète, planète-planète et étoile-planète) agissent sur des échelles de temps très différentes, et qu'il est difficile, à partir des propriétés orbitales d'exoplanètes âgées de plusieurs milliards d'années, de contraindre l'importance relative de ces mécanismes, en particulier le rôle joué par le disque protoplanétaire dans les premiers millions d'années. Une autre raison est que le disque protoplanétaire incarne nombre de difficultés et incertitudes des modèles théoriques. Ces disques sont constitués en effet de poussières et de gaz faiblement ionisé, dont l'évolution magnéto-hydrodynamique dépend de processus chimiques et radiatifs complexes. Et ces processus jouent un rôle clé dans toutes les étapes de la formation et de l'évolution des planètes jeunes : (i) ils déterminent à quelle distance de l'étoile les cœurs planétaires croissent par accrétion de solides, (ii) ils influencent particulièrement la direction et la vitesse de migration des planètes, et (iii) ils impactent l'évolution interne initiale des planètes en déterminant la quantité de chaleur emmagasinée au cours de leur formation. Ces processus sont bien sûr affectés par la gravité et l'environnement stellaire local. Cette palette de processus et mécanismes physiques fait certainement écho à la diversité des systèmes exoplanétaires, et suggère qu'il n'existe pas une unique théorie de la formation et de l'évolution planétaires, mais plusieurs.

Il est possible que les observations de disques protoplanétaires puissent contraindre les scénarios de formation et d'évolution des systèmes planétaires jeunes. Ces observations ont trait à l'émission thermique des poussières dans le domaine radio, comme on peut la détecter avec NOEMA ou ALMA, l'émission diffusée des poussières dans le proche-infrarouge, comme avec SPHERE, ou encore l'émission du gaz, comme avec NOEMA, ALMA ou CRIRES+ au VLT. Comme illustré à la figure 2.5, l'émission des disques est souvent structurée, avec notamment la présence d'anneaux sombres et brillants dans l'émission radio des poussières. Cette émission peut parfois être non-axisymétriques, et même prendre la forme de spirales comme dans le cas d'Elias 27. Les disques peuvent aussi présenter des structures bien différentes selon qu'on les observe en radio ou en proche-infrarouge, comme illustré à la figure 2.5 dans le cas de MWC 758.

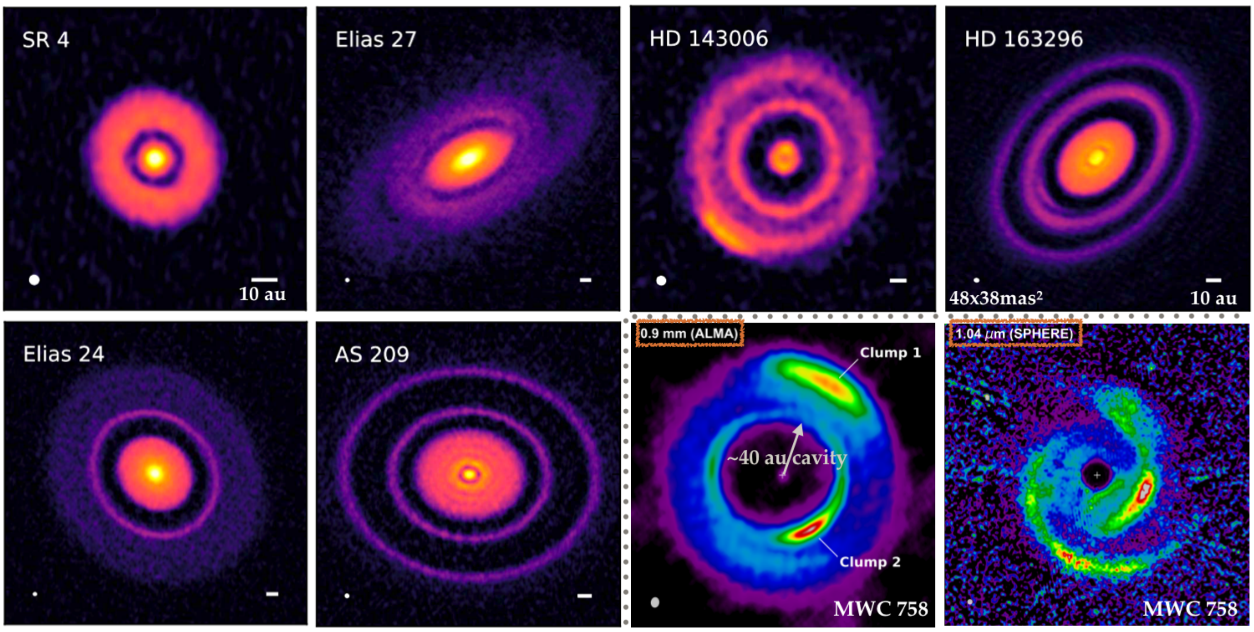

FIGURE 2.5 – *Galerie d'observations de disques protoplanétaires. Les 4 images du haut et les 2 en bas à gauche montrent le continuum d'émission en poussière à une longueur d'onde de 1.3 mm, observé par ALMA pour quelques disques du Large Programme DSHARP (Andrews et al. 2018). Les deux images en bas à droite, adaptées de Baruteau et al. (2019), montrent, à la même échelle, le disque de MWC 758 observé dans le continuum d'émission en poussière à 0.9 mm avec ALMA (données de Dong et al. 2018) et en lumière diffusée polarisée à 1.04 μm avec SPHERE (données de Benisty et al. 2015).*

Que ce soient les anneaux, les asymétries, les spirales, toutes ces structures en émission rappellent le type de perturbations qu'une planète peut générer dans la distribution des poussières ou solides de son disque. La première question qui se pose est de savoir quelles structures observées sont la signature indirecte de planètes, car à l'exception du disque autour de PDS 70 observé par SPHERE (Müller et al. 2018, Haffert et al. 2019, cf. figure 2.6), il n'y a pas, à ce jour, de détection observationnelle *directe* de planètes dans leur disque protoplanétaire. Si ces structures sont bien dues à des planètes en formation dans leur disque et non, par exemple, à la dynamique du gaz et des poussières du disque, la seconde question qui se pose est de savoir ce que ces structures nous apprennent sur la formation et éventuellement la migration de telles planètes. Nous reviendrons sur ces questions au § 2.4.

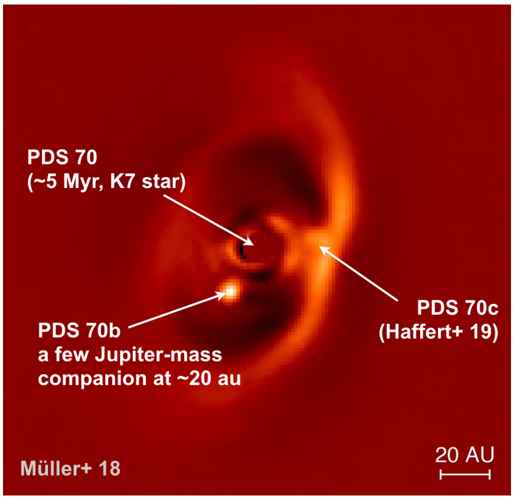

FIGURE 2.6 – *Observation avec SPHERE à 2.1 µm par imagerie différentielle angulaire du disque protoplanétaire autour de PDS 70, qui présente la particularité d'avoir une cavité assez large où a été clairement détecté un compagnon (PDS 70b), dont la masse est estimée à environ 5-10 fois la masse de Jupiter. Image adaptée de Müller et al. (2018). Un second compagnon (PDS 70c) a été détecté par émission de la raie Hα avec MUSE près du bord externe de la cavité (Haffert et al. 2019).*

2.2 Formation et évolution orbitale des planètes

Nous commençons cette section par un panorama assez général et volontairement succinct des mécanismes régissant la formation et l'évolution orbitale des planètes, avant de décrire le contexte et les résultats de mes contributions sur la formation planétaire. Mes activités de recherche sur l'évolution orbitale des planètes seront présentées dans les sections suivantes.

2.2.1 Un bref aperçu

Les planètes commencent à se former dans un disque protoplanétaire de gaz et de poussières autour d'une étoile de pré-séquence principale. La masse du disque est alors largement dominée par celle du gaz. Deux scénarios sont classiquement invoqués pour la formation des planètes :

- Le modèle d'accrétion de cœur (*core accretion*), où les cœurs planétaires croissent par accrétion de solides, qui peuvent être des planétésimaux de taille de l'ordre du km comme des solides plus petits de taille inférieure au mètre (*pebbles*). Lorsqu'un cœur planétaire atteint une dizaine de masses terrestres, il peut rapidement accréter le gaz du disque protoplanétaire autour de son orbite, et évoluer ainsi en planète géante de gaz.
- Le modèle d'instabilité gravitationnelle, où les parties externes des disques protoplanétaires jeunes et massifs peuvent fragmenter à cause de l'instabilité gravitationnelle, et former rapidement des sortes de cocons de gaz massifs, de masse initiale de l'ordre de la masse de Jupiter. Ces cocons peuvent ensuite évoluer également en planètes géantes de gaz.

Quelle que soit la manière dont se forment les planètes dans leur disque protoplanétaire, elles interagissent par la gravité avec le gaz du disque. Cette interaction change le demi-grand axe des planètes, c'est ce qu'on appelle la migration planétaire. De nombreux travaux théoriques ont examiné la direction et la vitesse de migration des planètes selon les propriétés physiques des disques (comme leur densité de masse, leur température, l'impact du transport turbulent de masse dans les disques etc.). Nous en reparlerons en détail au § 2.3. Les interactions disque-planète conduisent le plus souvent à amortir l'excentricité et l'inclinaison des planètes. Toutefois, les planètes ne se forment pas seules dans leur disque protoplanétaire, et les planètes peuvent interagir entre elles par la gravité. Ces interactions planète-planète peuvent également changer le demi-grand axe des planètes, de même qu'elles croissent leur excentricité et leur inclinaison.

Le gaz du disque protoplanétaire est dissipé au bout de quelques millions d'années, soit parce qu'il est progressivement accrété par l'étoile ou les planètes, soit parce qu'il est éjecté sous forme de vents, par exemple par photo-évaporation. Cela ne sonne pas pour autant la fin de la formation et de l'évolution planétaires. D'une part, l'orbite des planètes peut évoluer par les interactions de marée avec l'étoile centrale pour les planètes les plus proches de leur étoile, ou bien par interactions gravitationnelles avec d'autres étoiles proches. D'autre part, les interactions planète-planète peuvent perdurer et croître l'excentricité et l'inclination des planètes sans l'effet d'amortissement du disque protoplanétaire, ce qui peut notamment induire une croissance planétaire par collisions. Enfin, les interactions entre planètes et planétésimaux résiduels de la formation planétaire peuvent également changer l'architecture des systèmes planétaires, comme dans le modèle de Nice du Système Solaire. Pour une description détaillée de tous ces processus, le lecteur pourra consulter, par exemple, la revue récente de Raymond & Morbidelli (2020).

2.2.2 Travaux sur la formation planétaire

Je décris dans ce paragraphe trois problèmes spécifiques de la formation planétaire sur lesquels j'ai travaillé : (i) la croissance des planétésimaux dans les disques protoplanétaires circumbinaires, (ii) la masse maximale qu'une planète peut atteindre dans son disque protoplanétaire par accrétion de solides de taille de l'ordre du centimètre (*pebble accretion*), et (iii) la formation des chondres dans le Système Solaire primordial.

Croissance des planétésimaux dans les disques circumbinaires

Les découvertes récentes par transit d'une dizaine de planètes orbitant à proximité d'étoiles binaires ont souligné une fois encore que les planètes peuvent se former et/ou évoluer dans des environnements extrêmes. C'est le cas notamment de Kepler-38(AB)b (Orosz et al. 2012), une planète de taille comparable à Saturne dont le demi-grand axe, $\sim$0.5 ua, est à peine trois fois supérieur à celui de l'étoile binaire, la plaçant donc à la limite de stabilité du système à trois corps. Une des questions clés ici est de déterminer à quelle distance de leur binaire de telles planètes peuvent se former. Peuvent-elles se former *in situ* dans leur disque protoplanétaire *circumbinaire*, là où les perturbations gravitationnelles de la binaire génèrent des vitesses relatives élevées entre planétésimaux, favorisant a priori leur destruction au cours de collisions plutôt que leur croissance en protoplanètes ? Ou ces planètes se sont-elles formées à plus grande distance de la binaire dans le disque et s'en sont rapprochées par interactions disque-planète ? Il s'agit d'une thématique de recherche sur laquelle je collabore avec Zoë Leinhardt (University of Bristol), spécialiste des scénarios de collisions entre planétésimaux, et qui a motivé la thèse de Stefan Lines entre 2012 et 2016.

Étudier la croissance des planétésimaux dans un disque de gaz circumbinaire est un problème complexe, notamment en raison du coût numérique à modéliser à la fois l'évolution hydrodynamique du gaz du disque circumbinaire, l'évolution dynamique des planétésimaux et leurs collisions (Paardekooper et al. 2012, Lines et al. 2014). Dans la thèse de Stefan Lines, nous avons attaqué ce problème en plusieurs étapes.

Dans un premier temps, nous avons étudié la réponse du seul disque de gaz circumbinaire aux perturbations gravitationnelles de l'étoile binaire, sans planétésimaux, via des simulations hydrodynamiques 2D avec le code public Fargo-ADSG que je co-développe depuis ma thèse. Stefan y a implémenté le potentiel gravitationnel d'une étoile binaire et a mené une exploration relativement large de l'espace des paramètres (viscosité turbulente du disque de gaz, impact de son auto-gravité etc.) afin de déterminer quelles régions du disque maintiennent un faible niveau d'excentricité, condition a priori nécessaire pour favoriser la croissance des planétésimaux au cours de leurs collisions (Lines et al. 2015, cf. figure 2.7a).

Dans un second temps, Stefan a incorporé les champs de densité et de vitesse du gaz de ses simulations hydrodynamiques en état stationnaire dans un code de simulations à N corps (PKDGRAV) modélisant les

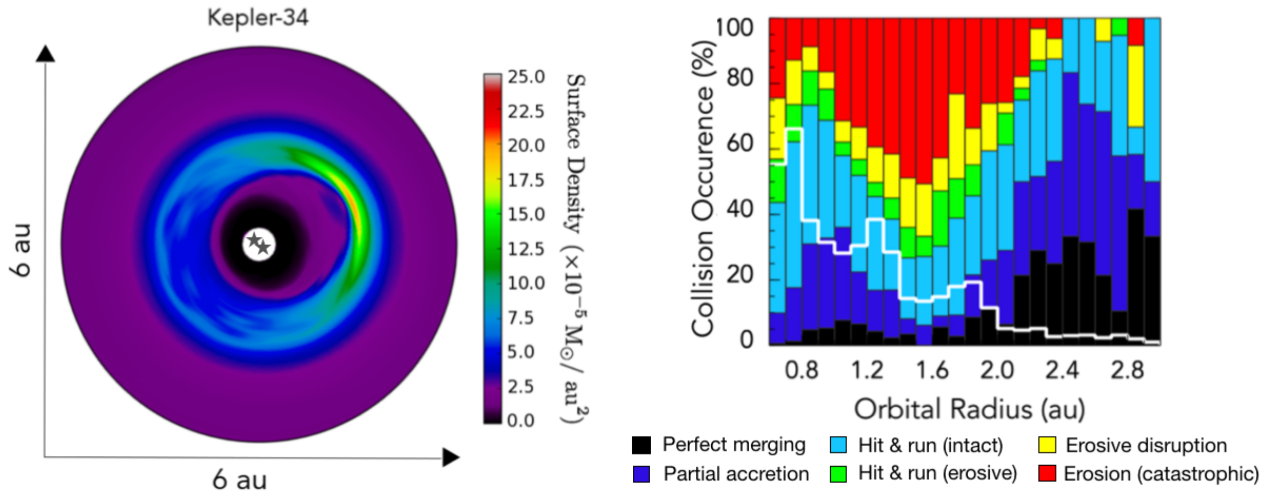

(a) (b)

FIGURE 2.7 – *(a) Densité surfacique de gaz dans une simulation hydrodynamique 2D modélisant le disque circumbinaire autour de l'étoile Kepler-34, où l'on constate que les parties internes du disque acquièrent une excentricité assez large à cause de la proximité de la binaire. Figure tirée de Lines et al. (2015). (b) Impact des collisions entre planétésimaux dans une simulation à N corps incluant une modélisation simplifiée du gaz du disque circumbinaire autour de Kepler-34. Figure tirée de Lines et al. (2016).*

collisions entre planétésimaux (différents types d'érosion ou d'accrétion). Ce travail a permis de quantifier le fait que la grande majorité des collisions entre planétésimaux dans les parties internes excentriques du disque circumbinaire conduisent à leur érosion et non à leur croissance, notamment aux distances auxquelles la plupart des planètes circumbinaires sont détectées (Lines et al. 2016, cf. figure 2.7b). Ce travail donne donc un support quantitatif à l'hypothèse que la plupart des planètes circumbinaires ont dû se former à plus grande distance de leur binaire dans leur disque et s'en rapprocher par interactions disque-planète.

D'autres études numériques ont examiné la migration planétaire dans les disques circumbinaires afin, notamment, de déterminer jusqu'à quelle distance de la binaire les planètes peuvent se rapprocher, et s'il est possible d'expliquer l'architecture orbitale des planètes circumbinaires observées (p.e., Kley & Haghighipour 2015, Mutter et al. 2017, Thun & Kley 2018). Ces études ont mis en avant la sensibilité des prédictions des modèles à la structure et l'excentricité de la cavité générée dans le gaz du disque par la binaire (impact de l'auto-gravité du disque, de l'équation d'énergie, de la viscosité turbulente, des conditions aux limites etc.). De manière générale, les simulations montrent que les planètes arrêtent leur migration à plus grande distance de leur binaire que dans les systèmes observés modélisés (Thun & Kley 2018). La formation et l'évolution orbitale des planètes circumbinaires est donc certainement un axe de recherche qu'il faut continuer à développer.

Par ailleurs, une trentaine d'exoplanètes ont été détectées autour d'étoiles possédant un compagnon stellaire à moins de 100 ua (voir, par exemple, la revue Marzari & Thebault 2019). Pour ces planètes comme pour les planètes circumbinaires se pose la question de leur formation et de leur évolution orbitale à proximité d'une étoile secondaire proche. Un exemple assez extrême est celui de γ Cep Ab, une planète d'environ 9 masses de Jupiter (Benedict et al. 2018, masse déprojetée) orbitant à $\sim$2 ua de son étoile hôte, une étoile d'environ $1.4 M_\odot$ possédant par ailleurs un compagnon stellaire ($\sim 0.4 M_\odot$) proche ($a \sim 20$ ua) et excentrique ($e \sim 0.4$, Neuhäuser et al. 2007). Encore une fois, la présence d'un compagnon stellaire proche pourrait générer des vitesses relatives élevées entre planétésimaux en rendant excentriques les parties externes du disque protoplanétaire autour de l'étoile primaire. Sur ce sujet, nous avons montré avec mes collaborateurs que la prise en compte de l'auto-gravité et des propriétés radiatives du disque conduit à diminuer l'excentricité du disque (Marzari et al. 2009; 2012; 2013). Reste à voir la possibilité de croissance des planétésimaux dans ce type de disques par des simulations à N corps dédiées.

Masse maximale d'une planète par accrétion de solides sub-métriques (pebble accretion)

Le scénario classique de croissance des cœurs planétaires par accrétion de planétésimaux de taille de l'ordre du kilomètre (*core accretion*) peine à expliquer la formation des planètes géantes au-delà de 5 à 10 ua d'étoiles de type solaire. Les détections de telles planètes vont pourtant bon train, que ce soit par imagerie directe, par astrométrie, ou par l'accumulation de données spectro-vélocimétriques depuis une vingtaine d'années. L'une des difficultés de ce scénario est d'atteindre une masse de cœur solide suffisante pour initier l'accrétion rapide d'une atmosphère massive de gaz avant la dissipation du gaz du disque protoplanétaire en quelques millions d'années. Des scénarios alternatifs de formation des planètes géantes ont été examinés de près, comme la fragmentation par instabilité gravitationnelle des parties externes des disques lorsqu'ils sont encore jeunes et massifs, ou encore la formation de plusieurs planètes géantes plus près de leur étoile par le scénario d'accrétion de cœur (*core accretion*), suivie d'une déstabilisation gravitationnelle de l'orbite des planètes lors de la dissipation du disque protoplanétaire.

Peut-être paradoxalement, l'accrétion de solides de taille de l'ordre du centimètre, bien plus petits que les planétésimaux, pourrait accélérer nettement la formation des cœurs solides des planètes géantes (Lambrechts & Johansen 2014, Bitsch et al. 2015b). Ces solides, que l'on désigne souvent sous le nom de *pebbles* en anglais, sont bien plus efficacement accrétés par une planète dans son disque protoplanétaire que les planétésimaux. Cela est dû au couplage entre les solides et le gaz du disque qui permet à ces solides (i) de dériver rapidement vers une planète depuis les parties externes du disque, et (ii) de voir leur excentricité efficacement amortie lors de leur interaction gravitationnelle avec la planète (Ormel & Klahr 2010). Toutefois, le taux d'accrétion des solides diminue à mesure que la planète croît en masse et que les sillages qu'elle génère dans le disque deviennent des ondes de choc à proximité de la planète. Les sillages de la planète lui permettent alors de creuser un sillon autour de son orbite (cf. § 2.3.2), et, un peu comme un chasse-neige, la planète crée une accumulation de gaz juste au-delà de son orbite, où se constitue un maximum de pression du gaz *capable* de piéger les solides. Les solides ainsi piégés, le cœur solide de la planète atteint sa masse maximale par *pebble accretion*.

Avec Sareh Ataiee, chercheuse post-doctorante à l'Université de Berne avec qui j'ai travaillé à l'élaboration de modèles globaux de formation et d'évolution planétaires (cf. § 3.1.2), nous avons étudié comment la masse maximale d'un cœur planétaire par *pebble accretion* dépend de la turbulence du disque protoplanétaire, modélisée comme un processus diffusif (Ataiee et al. 2018). L'idée principale de l'article est que la formation d'un maximum de pression du gaz au-delà de l'orbite de la planète est une condition nécessaire à l'arrêt de l'accrétion de solides, mais non-suffisante : les solides situés au niveau du maximum de pression peuvent diffuser vers la planète (et donc être possiblement accrétés) si la vitesse caractéristique des fluctuations turbulentes des solides excède la vitesse de dérive radiale des solides vers le maximum de pression par la force de friction du gaz. Nous avons ainsi établi une formule analytique simple permettant d'estimer la masse maximale qu'un cœur planétaire peut atteindre par *pebble accretion*. Nous avons également réalisé un grand nombre de simulations hydrodynamiques 2D modélisant l'interaction d'un disque de gaz et de solides avec une planète, dont les résultats sont en bon accord avec notre formule analytique.

Formation des chondres dans le Système Solaire primordial

Les chondres sont des petits grains solides sub-millimétriques que l'on retrouve dans les météorites primitives, et dont la structure implique qu'ils ont été soumis à des pics de température très élevée ($\gtrsim$ 1500 K ; Desch et al. 2012). De nombreux mécanismes ont été proposés pour expliquer ces pics de température, notamment les chocs induits par des planétésimaux excentriques (*bow shocks*, Ciesla et al. 2004). Hors, seuls des planétésimaux très excentriques ($e > 0.6$) et de grande taille (entre 50 et 500 km) peuvent générer des chocs à même d'augmenter suffisamment la température des chondres à leur traversée. Dans Gong et al. (2019), nous avons montré, par des arguments analytiques et des simulations à N corps, que la résonance séculaire entre les fréquences de précession de l'orbite de Jupiter et des planétésimaux de la ceinture d'astéroïdes a pu, au cours de la dissipation du disque protoplanétaire, exciter suffisamment l'excentricité des dits planétésimaux pour que les chocs induits puissent générer des pics de température nécessaires pour rendre compte de la formation des chondres. Cet article est l'aboutissement d'un projet démarré en 2010 à l'occasion du stage de Master de Munan Gong que j'avais co-encadré avec Douglas Lin lors de mon premier post-doctorat.

2.3 Prédictions des modèles de migration planétaire

Les *Jupiter chauds* ont révolutionné les modèles de formation planétaire qui, jusqu'alors, tentaient de reproduire l'architecture du Système Solaire, avec des planètes terrestres près de l'étoile et des planètes géantes loin de l'étoile. Selon les modèles actuels, il est peu probable que les Jupiter chauds se soient formés in situ. S'il est possible qu'une quantité suffisante de solides puisse dériver jusqu'à proximité de l'étoile par friction avec le gaz et y former des cœurs planétaires, et que, sous certaines conditions, ces cœurs puissent déclencher l'accrétion emballée de gaz autour de leur orbite (Batygin et al. 2016), il est en revanche nettement moins clair si une quantité suffisante de gaz peut y accéder et être accrétée par ces cœurs au point de devenir des Jupiter chauds. On pense donc plutôt que les Jupiter chauds se seraient formés à quelques ua de leur étoile dans leur disque protoplanétaire, et se seraient rapprochés de l'étoile en interagissant avec le disque ou avec d'autres compagnons planétaires. La migration planétaire due aux interactions disque-planète est rapidement devenue un ingrédient essentiel des théories de formation et d'évolution planétaires (Lin et al. 1996). Néanmoins, le nombre élevé d'exoplanètes permet à présent de comparer de manière statistique observations et prédictions théoriques, et de telles comparaisons montrent qu'il est nécessaire de progresser sur les modèles de migration planétaire (Ida & Lin 2008, Benz et al. 2014).

L'objectif de cette section est d'introduire la physique des interactions disque-planète, et en particulier leur manifestation la plus connue : la migration des planètes. Son contenu est grandement inspiré du chapitre de livre sur la formation et l'évolution des systèmes planétaires que nous avons rédigé suite à une conférence invitée organisée par l'International Space Science Institute à Beijing en 2014 (Baruteau et al. 2016).

2.3.1 Migration des planètes terrestres

La migration des planètes résulte de leur interaction gravitationnelle avec le disque protoplanétaire où elles se forment. Le disque est lui-même constitué de gaz et de matériel solide de toute taille, des poussières sub-micrométriques aux planétésimaux de taille de l'ordre du kilomètre. Dans les phases jeunes des disques protoplanétaires, le gaz représente l'essentiel de la masse des disques, bien que le rapport de masse entre gaz et solides, que l'on suppose typiquement entre 10 et 100, soit finalement assez mal contraint par les observations. Nous aurons l'occasion d'y revenir au § 2.4. Toujours est-il que, pour cette raison, on suppose que l'interaction gravitationnelle entre une planète et son disque se limite à l'interaction avec le gaz de ce disque. L'essentiel des interactions disque-planète peut donc être appréhendé en inspectant la perturbation de densité du gaz induite par une protoplanète.

La figure 2.8 montre la perturbation relative de la densité surfacique de masse du gaz d'un disque protoplanétaire où se forme une planète de 5 masses terrestres. Cette figure, qui est tirée de notre revue dans *Protostars and Planets VI* (Baruteau et al. 2014), a été obtenue par une simulation hydrodynamique 2D d'interactions disque-planète. Par 2D, on entend un modèle de disque infiniment mince pour lequel on résout les équations de Navier-Stokes intégrées sur la dimension verticale du disque. La planète, elle, correspond à un potentiel gravitationnel ressenti par le disque. Comme on peut le voir sur la figure, la planète génère deux types de perturbations dans le disque : (i) des ondes spirales de densité, que l'on appelle les sillages de la planète, et qui se propagent dans tout le disque, et (ii) des perturbations de densité localisées autour du rayon orbital de la planète, que l'on appelle pour cette raison perturbations co-orbitales, et qui sont confinées dans la région fer-à-cheval de la planète. Comme son nom l'indique, cette région fer-à-cheval englobe le gaz qui décrit des orbites en forme de fer-à-cheval par rapport à la planète (cf. partie droite de la figure 2.8).

Le principe de base de la migration planétaire est la loi de l'action et de la réaction : le disque réagit à la gravité de la planète en lui communiquant une force gravitationnelle qui change le demi-grand axe, l'excentricité et l'inclinaison de la planète. Considérons le cas le plus simple où la planète est sur une orbite circulaire et coplanaire, c'est-à-dire d'excentricité et d'inclinaison nulles. Dans ce cas, la composante du moment cinétique

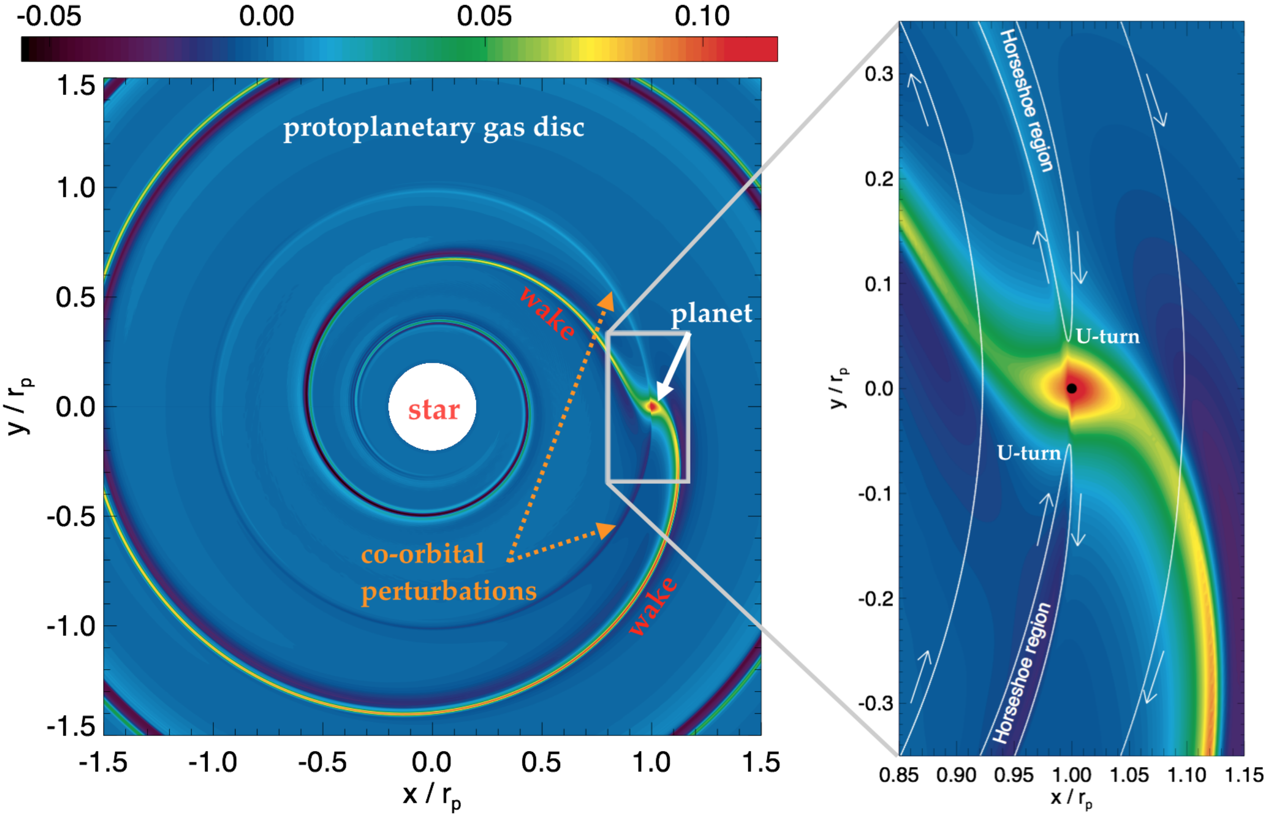

FIGURE 2.8 – *Perturbation relative de la densité surfacique de masse du gaz d'un disque protoplanétaire où se forme une planète de 5 masses terrestres. Par perturbation relative, on entend la quantité* $(\Sigma - \Sigma_0)/\Sigma_0$*, où* Σ *désigne la densité surfacique instantanée du gaz et* Σ_0 *sa valeur initiale. La position de la planète est repérée par une flèche blanche sur l'image de gauche, et par un point noir sur celle de droite. La planète génère un onde spirale de densité à un bras, le sillage ('wake'), se propageant dans tout le disque, et des perturbations de densité co-orbitales à la planète, à l'intérieur de sa région fer-à-cheval. Les lignes de courant, ou ici trajectoires, du gaz relatives à la planète sont représentées par des courbes et flèches blanches sur l'image de droite. Figure tirée de Baruteau et al. (2016) et adaptée de Baruteau et al. (2014).*

orbital de la planète perpendiculaire au plan de l'orbite s'écrit $J_p = M_p \sqrt{GM_\star r_p}$, où M_p désigne la masse de la planète, $M_\star$ celle de l'étoile, G la constante gravitationnelle, et r_p la distance de l'étoile à la planète. Notons Γ le couple exercé par le disque sur la planète, en projection suivant l'axe perpendiculaire au plan de l'orbite. Supposons la masse de la planète stationnaire, ce qui revient à supposer que le temps caractéristique d'accrétion de gaz et de solides par la planète est long devant celui d'évolution son orbite. La variation du moment cinétique (orbital) de la planète, régie par l'équation $\Gamma = dJ_p/dt$, nous donne $dr_p/dt = \Gamma \times 2r_p/J_p$. Si $\Gamma < 0$, $dr_p/dt < 0$ et la planète se rapproche de son étoile, tandis que si $\Gamma > 0$, $dr_p/dt > 0$ et la planète s'éloigne de son étoile. Nous voyons donc que pour connaître la direction et la vitesse de migration planétaire, il suffit de déterminer le signe et l'amplitude de Γ. C'est pourquoi la grande majorité des études d'interactions disque-planète ont considéré des planètes en orbite fixe (de demi-grand axe, d'excentricité et d'inclinaison donnés) et ont cherché à en déterminer l'évolution orbitale en calculant le couple exercé par le disque. Cependant, comme nous le verrons plus bas dans cette sous-section, le couple du disque sur la planète peut dépendre de l'historique et de la vitesse de migration planétaire, avec pour conséquence l'emballement de la migration. Mais décrivons pour l'instant les deux composantes du couple ressenti par la planète.

Couple dû au sillage : le couple de Lindblad

La première composante du couple du disque sur la planète est celle du sillage que la planète génère dans le disque. On peut la décomposer en deux parties. D'une part, le couple dû au sillage interne, qui se propage depuis la planète vers l'étoile. L'essentiel du couple exercé par ce sillage interne provient de l'excès de gaz situé juste devant la planète dans la direction azimutale, à quelques échelles de pression[1] de la planète. Cet excès de gaz exerce une force gravitationnelle sur la planète dont la composante azimutale F_φ est positive, ce qui correspond donc à un couple $\sim r_\mathrm{p} F_\varphi$ sur la planète lui aussi positif. D'autre part, le couple exercé par le sillage externe de la planète est dû à un excès de gaz situé juste derrière la planète dans la direction azimutale. Cet excès de gaz exerce une force $F_\varphi < 0$ sur la planète, et donc un couple négatif sur la planète.

Nous voyons ainsi que le couple total exercé par le sillage sur la planète a deux contributions de signe opposé : le couple positif du sillage interne, qui tend à éloigner la planète de son étoile, et le couple négatif du sillage externe, qui tend à rapprocher la planète de son étoile. En regardant de plus près l'image de droite sur la figure 2.8, on voit que la surdensité de gaz liée au sillage externe est un peu plus élevée et située un peu plus près de la planète que la surdensité liée au sillage interne. Le couple dû au sillage externe est donc plus fort, ce qui nous dit que le couple total dû au sillage est négatif et favorise la migration interne des planètes (c'est-à-dire, dirigée vers l'étoile). Bien que cela soit effectivement le cas en général, il s'avère que ce résultat dépend du profil de densité et surtout de température du gaz dans la direction radiale autour de la planète, ces profils agissant directement sur la position des sillages interne et externe et leur densité perturbée. Ceci peut être quantifié en résolvant les équations linéarisées des perturbations d'une planète dans un disque, en 2D (Korycansky & Pollack 1993, Ward 1997, Paardekooper et al. 2010, Masset 2011) ou en 3D (Tanaka et al. 2002). Le formalisme linéaire montre d'ailleurs que la perturbation de la planète génère des ondes acoustiques se propageant depuis ce que l'on appelle les *résonances de Lindblad*, où la vitesse du gaz par rapport à la planète est égale, en valeur absolue, à la vitesse de phase des ondes acoustiques dans la direction azimutale. C'est pour cette raison que le couple dû au sillage est souvent appelé *couple de Lindblad*. Le lecteur intéressé pourra lire la section 2.1.1 de Baruteau et al. (2014) pour plus de détails sur le couple de Lindblad et son expression en fonction des gradients des profils de température et de densité du disque.

Couple dû à la région fer-à-cheval de la planète : le couple de corotation

Comme on l'a déjà vu, le gaz situé dans la région fer-à-cheval de la planète suit des trajectoires en forme de fer-à-cheval par rapport à la planète. Au moment où le gaz est au plus proche de la planète, il subit une déflection gravitationnelle par la planète. Le gaz situé juste à l'intérieur de l'orbite de la planète dans la direction radiale, derrière elle en azimuth, reçoit du moment cinétique de la planète qui l'emmène juste à l'extérieur de l'orbite de la planète. Vu de la planète, ce gaz effectue des demi-tours vers l'extérieur du disque, et exerce donc (loi de l'action et de la réaction) un couple négatif sur la planète. Au même moment, le gaz situé juste à l'extérieur de l'orbite de la planète, devant elle en azimuth, donne du moment cinétique à la planète et se retrouve juste à l'intérieur de l'orbite de la planète. Ce gaz embarque sur des demi-tours vers l'intérieur du disque vu de la planète, et exerce ainsi un couple positif sur la planète. Le couple exercé par la région fer-à-cheval, que l'on appelle couple de corotation car, en moyenne, le gaz y orbite à la même vitesse angulaire que la planète, a donc deux contributions de signe opposé, tout comme le couple dû au sillage. Le signe et l'amplitude du couple de corotation dépendent de la différence de moment cinétique entre le gaz effectuant des demi-tours fer-à-cheval vers l'intérieur et l'extérieur.

Toute la difficulté du calcul du couple de corotation est que le moment cinétique du gaz dans la région fer-à-cheval évolue au cours du temps. Jusqu'au début de ma thèse, on savait que le couple de corotation dépendait de l'advection-diffusion d'une quantité clé en dynamique des fluides appelée vorticité potentielle, ou encore *vortensité* dans les disques protoplanétaires (Ward 1991, Masset 2002). Il s'agit de la composante verticale du rotationnel du champ de vitesse divisée par la densité surfacique de masse du disque. L'advection de la vortensité le long des lignes de courant dans la région fer-à-cheval implique que le signe et l'amplitude du couple de corotation dépendent du profil radial de vortensité et donc de densité du gaz au travers de la région fer-à-cheval. La diffusion de la vortensité signifie que le couple de corotation dépend également de la

---

[1] L'échelle de pression du disque (H) est donnée par la relation $H = c_\mathrm{s}/\Omega$, où c_s désigne la vitesse du son et Ω la fréquence de rotation du disque. Dans le cas où le disque est en équilibre hydrostatique dans sa direction verticale, H représente la dimension caractéristique du disque dans cette direction.

nature et de l'efficacité du transport radial turbulent de moment cinétique au travers de la région fer-à-cheval. La modélisation de ce transport turbulent par un processus de diffusion visqueuse implique que le couple de corotation dépend de la viscosité turbulente dans le disque. D'où l'importance pour la migration planétaire de mieux comprendre comment opère le transport turbulent de moment cinétique dans les régions de formation planétaire des disques (voir, par exemple, Lesur et al. 2014, Bai 2015, Gressel et al. 2015). Les modèles 2D et 3D de disques visqueux montrent que le couple de corotation lié à l'advection-diffusion de vortensité est généralement positif et favorise, à lui seul, la migration des planètes vers les parties externes des disques.

Ralentir la migration de type I

La migration des planètes terrestres est communément appelée migration de type I, et résulte des couples exercés sur la planète par son sillage et sa région fer-à-cheval. On a vu que le premier couple était négatif, le second positif. Le problème majeur que rencontrait les modèles de migration planétaire avant ma thèse était de prédire la migration des planètes terrestres vers leur étoile en un temps très court (entre 10^4 et 10^5 ans). Typiquement un à deux ordres de grandeur plus court que le temps typique de formation des planètes géantes et que le temps de dissipation des disques protoplanétaires. Non seulement la migration planétaire peinait à rendre compte de la détection des Jupiter chauds, elle ne permettait pas non plus d'expliquer la formation de planètes géantes à plusieurs unités astronomiques de leur étoile, comme dans notre Système Solaire.

Au début de ma thèse, Paardekooper & Mellema (2006) ont proposé une solution à ce problème de longue date en montrant, par des simulations hydrodynamiques incluant une équation d'énergie, que les propriétés radiatives des disques protoplanétaires pouvaient ralentir, arrêter, voire renverser la migration de type I selon le temps de refroidissement radiatif du disque. Mes travaux de thèse de doctorat ont permis d'expliquer ces résultats de simulations, en démontrant que la prise en compte d'une équation d'énergie pour le gaz du disque protoplanétaire induisait une nouvelle composante du couple de corotation ressenti par la planète, résultant de l'advection-diffusion de l'entropie spécifique du gaz le long des lignes de courant à l'intérieur de la région fer-à-cheval de la planète (Baruteau & Masset 2008a). L'entropie spécifique du gaz est, à une constante additive près, proportionnelle à $\log(P\Sigma^{-\gamma})$ pour un modèle 2D de disque, avec P la pression thermique du gaz ($P = \Sigma c_s^2$), Σ la densité de surface du gaz, et γ l'indice adiabatique. L'advection d'entropie au sein de la région fer-à-cheval implique que le signe et l'amplitude de ce nouveau couple de corotation dépendent du profil radial d'entropie, et donc de température et de densité du gaz au travers de la région fer-à-cheval. La diffusion d'entropie signifie qu'il dépend également de la nature et de l'efficacité des processus de transport turbulent de la chaleur au travers de la région fer-à-cheval.

J'ai continué au cours de mes deux post-doctorats à étudier les propriétés physiques de ce nouveau couple de corotation. Avec mes collaborateurs, j'ai contribué à développer un modèle analytique du couple de corotation, assisté de simulations hydrodynamiques 2D, qui a permis d'exprimer ce couple en fonction des profils de densité et de température des disques au voisinage de la planète (Paardekooper et al. 2010). Nous avons effectué un travail similaire pour le couple dû au sillage. Nos résultats, d'abord obtenus pour des modèles de disques 2D adiabatiques (i.e., sans chauffage ni refroidissement du disque), ont été ensuite généralisés dans Paardekooper et al. (2011a) aux disques 2D visqueux et radiatifs (avec diffusions visqueuse et thermique). Le résultat est une expression simple et utile donnant la direction et la vitesse de migration de type I en fonction des propriétés physiques du disque. Des résultats similaires ont été publiés par Casoli & Masset (2009), Masset & Casoli (2010). Ce type d'expression est d'intérêt tout particulier pour les synthèses de population planétaire qui, en combinant les prédictions des modèles de formation et d'évolution planétaires, de structure et d'évolution des disques protoplanétaires, peuvent comparer de manière statistique les distributions observées et théoriques des propriétés des exoplanètes (masse, période orbitale, excentricité). Nous reparlerons des modèles de synthèse de population planétaire au § 3.1.2.

Le lecteur intéressé pourra lire la section 2.1.2 de Baruteau et al. (2014) pour plus de détails sur le couple de corotation. Notons qu'une expression du couple de corotation dans un modèle 3D de disque isotherme a été présentée récemment par Masset & Benítez-Llambay (2016). Une expression généralisée aux disques 3D non-isothermes (radiatifs) serait bienvenue.

Impact de la turbulence des disques protoplanétaires

Si des progrès importants ont été accomplis dans la compréhension physique de la migration planétaire, de nombreuses zones d'ombre persistent. L'une d'elles, on vient de le voir, concerne le comportement encore méconnu du couple de corotation dans les modèles 3D de disques non-isothermes. Une autre problématique est celle de l'impact de la turbulence du disque sur le couple de corotation. En effet, on a vu que le couple de corotation reposait sur un mécanisme d'advection-diffusion au travers de la région fer-à-cheval de la planète. Il est donc intimement lié à la viscosité et à la diffusion thermique dans cette région étroite du disque (une fraction de l'échelle de pression H du disque). La modélisation des effets de la turbulence par des mécanismes de diffusions visqueuse et thermique y est donc particulièrement incertaine. Je me suis spécialisé dans l'étude de la turbulence des disques protoplanétaires afin d'examiner les propriétés de la migration planétaire dans les disques turbulents.

La turbulence dans les disques protoplanétaires peut avoir plusieurs origines, notamment l'instabilité magnéto-rotationelle (MRI), dont la turbulence magnéto-hydrodynamique (MHD) induite peut conduire à des taux d'accrétion turbulente dans les disques en bon accord avec les taux d'accrétion stellaire observés, typiquement quelques $10^{-8} M_{\odot}\ \mathrm{an}^{-1}$. De nombreux travaux récents ont examiné l'efficacité de ce transport turbulent, en particulier l'impact des processus dits de MHD non-idéale (résistivité ohmique, diffusion ambipolaire, effet Hall). Nous aurons l'occasion d'en reparler au § 3.1.1.

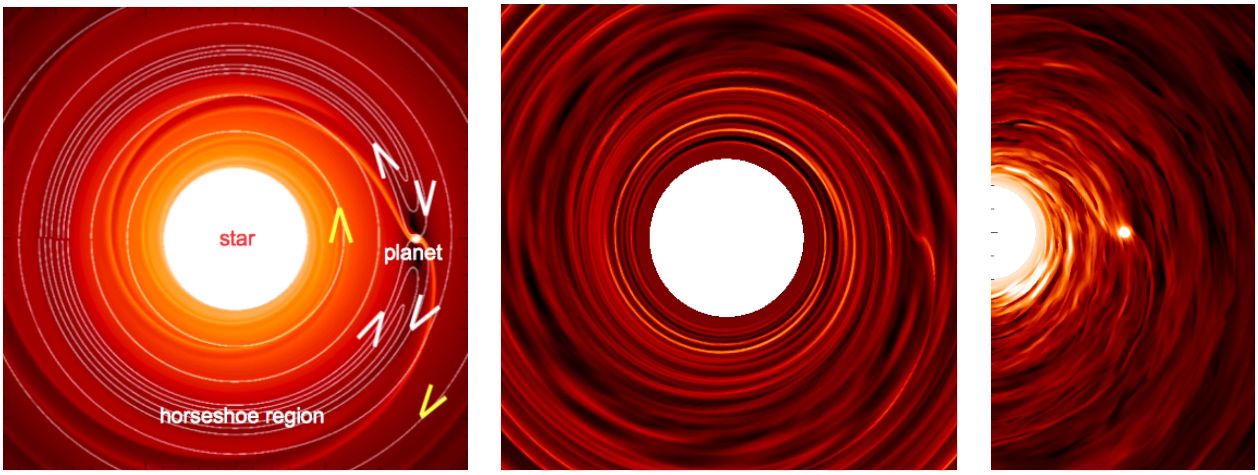

FIGURE 2.9 – *Simulations numériques d'interactions disque-planète pour des disques laminaires ou turbulents. Gauche : densité de surface obtenu pour un modèle de disque visqueux (les flèches indiquent les trajectoires du disque par rapport à la planète ; Baruteau & Masset 2013). Milieu : cas d'un disque incluant un modèle simple de turbulence générée sous forme d'ondes (Baruteau & Lin 2010). Droite : cas d'un disque envahi par la turbulence MHD générée par l'instabilité magnéto-rotationnelle (Baruteau et al. 2011b).*

Le développement de la MRI nécessite un modèle 3D de disque magnétisé impliquant des simulations coûteuses. La stratégie que j'ai adoptée pour ce champ de recherche a été de réaliser dans un premier temps des simulations hydrodynamiques 2D utilisant un modèle simple de turbulence générée sous forme d'ondes de densité (image du milieu à la figure 2.9). J'ai montré que les caractéristiques de ce modèle, inspiré de Laughlin et al. (2004), pouvaient être ajustées de sorte à reproduire les propriétés statistiques de la turbulence MHD idéale telles qu'on peut les mesurer dans les simulations 3D de disques. Cela m'a permis d'établir que le couple de corotation d'une part, et le couple de Lindblad d'autre part, ont des valeurs très similaires dans les disques turbulents ou visqueux, que le disque soit isotherme (Baruteau & Lin 2010) ou radiatif (Pierens et al. 2012). Ces résultats indiquent que le ralentissement, voire le renversement de la migration de type I par le couple de corotation restent a priori viables dans les disques turbulents. Les simulations de planètes dans des disques 3D isothermes envahis par la MRI (Baruteau et al. 2011b, cf. image de droite à la figure 2.9) tendent à le confirmer.

Un résultat important obtenu dans Baruteau et al. (2011b) a été de mettre en évidence l'existence d'un nouveau couple de corotation (encore un !) dû à la présence d'un champ magnétique toroïdal dans le disque. L'existence de ce couple a été confirmée et ses propriétés disséquées dans Guilet et al. (2013) pour des modèles de disques laminaires, où les effets de la turbulence sont modélisés par une viscosité et une résistivité magnétique. Ce nouveau couple de corotation se nourrit de l'advection-diffusion du flux magnétique au sein de la région fer-à-cheval de la planète, et, une fois n'est pas coutume, il permet de ralentir voire de renverser la migration de type I, selon l'amplitude du champ magnétique toroïdal et la résistivité magnétique au voisinage de l'orbite de la planète. Il ne dépend pas, pour autant, du gradient radial de ce champ au travers de la région fer-à-cheval, comme on aurait pu l'imaginer par analogie avec les composantes du couple de corotation liées à l'advection-diffusion de la vortensité et de l'entropie. Notons que la perturbation de densité surfacique de masse obtenue dans les simulations 2D MHD de disques laminaires par Guilet et al. (2013) est en excellent accord avec la perturbation de densité moyennée en temps des simulations 3D MHD de disques turbulents de Baruteau et al. (2011b), comme on pourra l'apprécier à la figure 2.10. Il est nécessaire de préciser que ces modèles ont été calculés pour une planète de masse de Saturne dans un disque chaud, où le rapport d'aspect du disque, c'est-à-dire la quantité H/r, est de l'ordre de 0.1. Il faudrait étendre ce type d'études à des modèles de disques froids (rapport d'aspect plus faible), plus représentatifs des régions de formation planétaire.

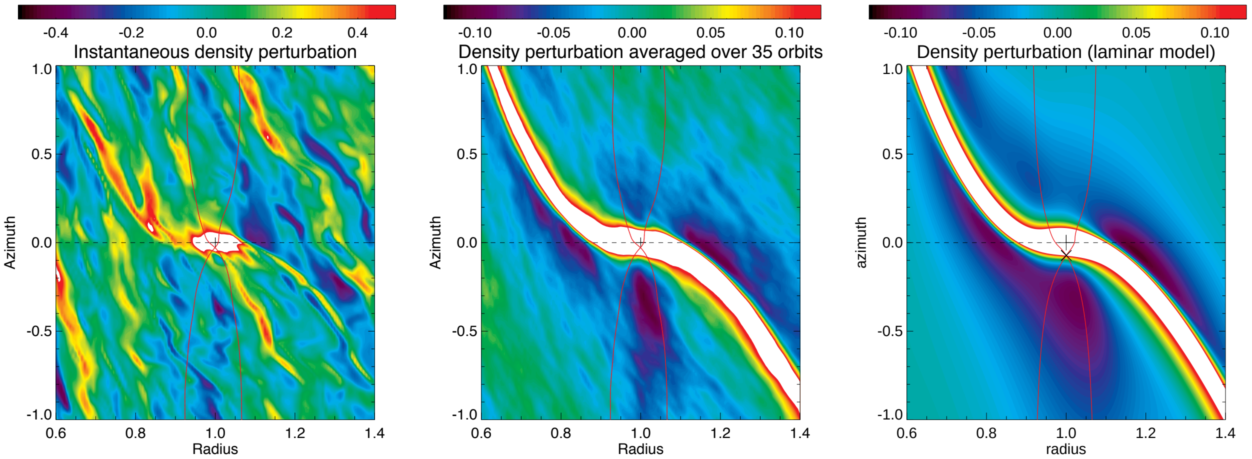

FIGURE 2.10 – *Perturbation relative de densité de surface d'un disque protoplanétaire où se forme une planète de la masse de Saturne. On compare ici les résultats obtenus pour un disque 3D envahi par la turbulence MHD générée par la MRI (images de gauche, adaptées de Baruteau et al. 2011b) avec ceux d'un modèle de disque 2D laminaire équivalent (cf. texte, image de droite tirée de Guilet et al. 2013). Le sillage de la planète est à peine discernable sur l'image de gauche à cause des larges fluctuations de densité induites par la turbulence. Lorsqu'elles sont moyennées sur 35 orbites de la planète, les perturbations de densité sont en accord remarquable avec celles de la simulation laminaire (comparer les deux images de droite). Elles montrent clairement le sillage de la planète ainsi que des sous-densités dans la région fer-à-cheval de la planète, dues à l'évolution du champ magnétique initialement toroïdal dans cette région. L'extension de la région fer-à-cheval est indiquée par les courbes en rouge. Figure tirée de Baruteau et al. (2014).*

Pour compléter ce paragraphe, mentionnons que, lorsque le disque a un champ magnétique toroïdal fort, c'est-à-dire tel que le rapport entre la pression thermique et la pression magnétique devient de l'ordre de l'unité, la région fer-à-cheval de la planète disparaît. En effet, le champ magnétique devient tellement intense que la planète ne parvient plus à défléchir le gaz autour de son orbite en leur imprimant des orbites fer-à-cheval vu de la planète. Le gaz suit donc essentiellement les lignes de champ magnétique toroïdales, mais subit des perturbations sous forme d'ondes magnéto-soniques lentes en 2D. Le couple de corotation est alors remplacé par un couple d'origine magnétique, et qui correspond au moment cinétique extrait de la planète par ces ondes magnéto-soniques lentes. Le travail récent de Uribe et al. (2015) a montré que ce couple magnétique était positif et pouvait aussi renverser la migration de type I, en accord avec les travaux pionniers analytiques et numériques de Terquem (2003) et Fromang et al. (2005).

Impact de l'auto-gravité des disques protoplanétaires

Un autre volet de mon travail de recherche sur la migration planétaire a été d'étudier l'impact de l'auto-gravité du gaz du disque protoplanétaire. L'implémentation de l'auto-gravité dans le code hydrodynamique 2D FARGO au cours de ma thèse m'a permis de confirmer par des simulations que le couple de Lindblad est légèrement renforcé par l'auto-gravité, en accord avec l'étude analytique de Pierens & Huré (2005), tandis que le couple de corotation demeure inchangé (Baruteau & Masset 2008b). J'ai expliqué que la pratique courante dans les simulations de considérer une planète migrant dans un disque non auto-gravitant conduisait à fortement surestimer la vitesse de migration (de presque un ordre de grandeur pour un disque dont la densité est 10 fois celle de la Minimum Mass Solar Nebula[2]). J'ai élaboré une méthode simple permettant aux simulations ne disposant pas de l'auto-gravité du disque d'éviter ce biais. Nous reparlerons de l'auto-gravité du gaz lorsque nous aborderons la migration des planètes massives au § 2.3.2.

Prédictions actuelles de la migration de type I

Nous avons déjà vu que la migration de type I résultait de deux couples aux aspirations opposées : le couple dû au sillage, qui vise à rapprocher les planètes de leur étoile, et le couple de corotation, qui vise à les en éloigner. Ainsi, la direction et la vitesse de migration de type I dépendent de l'amplitude relative de ces deux couples, et donc des propriétés physiques du disque au voisinage de la planète (profils de température et de densité, diffusions visqueuse et thermique etc.). Ceci est illustré à la figure 2.11, qui montre le couple total conduisant à la migration de type I, somme des couples de Lindblad et de corotation, tel que prédit par l'expression semi-analytique que nous avons formulée dans Paardekooper et al. (2011a). Le couple est représenté en fonction de la masse de la planète (ordonnée) et de la distance à l'étoile (abscisse), et est calculé pour le modèle de disque de Bitsch et al. (2013a). Dans ce modèle, des transitions d'opacité se produisent au niveau des fronts de sublimation des silicates (vers 0.7 ua) et de la glace d'eau (vers 5 ua), qui affectent le refroidissement radiatif du disque. Juste derrière ces transitions, le couple (positif) de corotation lié à l'advection-diffusion d'entropie se trouve fortement accru par la modification du profil radial de température que ces transitions génèrent. Ces transitions entraînent ainsi deux régions dans le diagramme de la figure 2.11 où le couple total exercé par le disque devient positif. Ces régions, où la migration de type I est dirigée vers l'extérieur, sont entourées en noir sur la figure 2.11. Le bord externe de ces régions, surligné en rouge sur la figure, représente un domaine de l'espace des paramètres où la migration de type I s'arrête, et que l'on appelle ainsi souvent *piège à planète*.

Le couple total représenté à la figure 2.11 peut être utilisé pour estimer le temps que met une planète à atteindre la proximité de son étoile par migration de type I. Le facteur Γ_0 par lequel le couple total est normalisé permet de définir le temps caractéristique de la migration, que nous notons τ_0, et qui est donné par $\tau_0 = \Omega_{\rm K} M_{\rm p} r_{\rm p}^2 / 2\Gamma_0$ ($\Omega_{\rm K}$ désigne la fréquence Keplerienne, à évaluer au rayon orbital de la planète). Il peut s'écrire de la façon suivante (Baruteau et al. 2016) :

$$\tau_0 \approx 1.3\,{\rm Man} \times \left(\frac{h}{0.05}\right)^2 \left(\frac{\Sigma}{200\,{\rm g\,cm^{-2}}}\right)^{-1} \left(\frac{M_\star}{M_\odot}\right)^{3/2} \left(\frac{r_{\rm p}}{5\,{\rm ua}}\right)^{-1/2} \left(\frac{M_{\rm p}}{M_\oplus}\right)^{-1}, \tag{2.1}$$

où $h = H/r = c_{\rm s}/v_{\rm K}$ est le rapport d'aspect du disque, à estimer, comme la densité surfacique de masse Σ, au rayon orbital de la planète ($r_{\rm p}$). Cette estimation montre qu'une planète d'une masse terrestre située à 5 ua d'une étoile de masse solaire, où la densité surfacique de masse du gaz est de 200 g cm^{-2} et le rapport d'aspect du disque de 5%, et qui subit un couple total $\Gamma \approx -2\Gamma_0$ d'après la figure 2.11, ne met que ~ 0.7

---

[2] La Miminum Mass Solar Nebula, ou MMSN, est un modèle classique du disque protoplanétaire à partir duquel s'est formé notre Système Solaire. Ce modèle suppose (i) un disque avec des abondances élémentaires relatives identiques à celles mesurées dans la photosphère du Soleil, tel que le suggère l'étude des chondrites carbonées, (ii) que les planètes ont accrété tout le matériel solide initialement présent (d'où le nom de masse minimale), et (iii) que les planètes se sont formées à leur distance actuelle du Soleil (pas de migration planétaire, donc !). Ce modèle aboutit à un disque entre 1% et 7% la masse du Soleil jusqu'à environ 30 ua, avec une densité surfacique de masse typique de l'ordre de 10^3 g cm^{-3} à 1 ua.

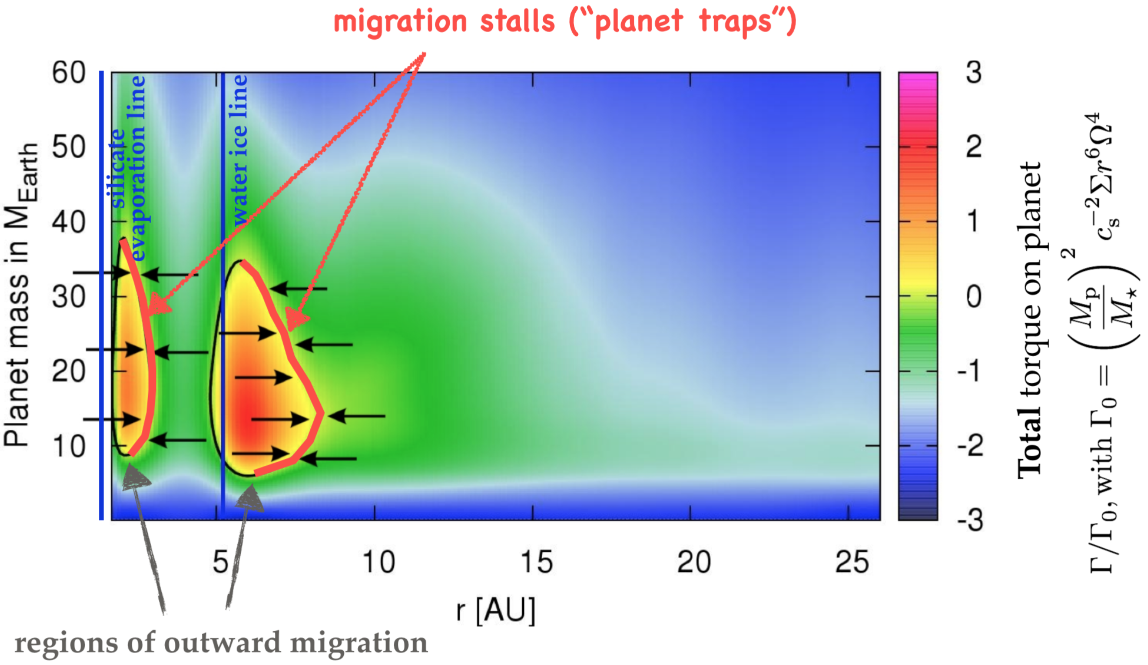

FIGURE 2.11 – *Couple total conduisant à la migration planétaire de type I, en fonction de la masse de la planète (ordonnée) et de la distance à l'étoile (abscisse). Les flèches noires montrent la direction de la migration. Figure tirée de Baruteau et al. (2016) et adaptée du papier de Bitsch et al. (2013a), dans lequel le modèle de disque protoplanétaire place la ligne de sublimation de la glace d'eau à environ 5 ua, et celle des silicates vers 0.7 ua.*

Man (million d'années) à atteindre son étoile ! Ce temps caractéristique est à comparer au temps typique de croissance planétaire dans cette gamme de masse. Le modèle de croissance par accrétion de solides sub-métriques (*pebble accretion*) prédit au plus court un temps de seulement quelques 10^4 an pour former une planète de masse terrestre à 5 ua dans un modèle de disque similaire à celui décrit ci-dessus (Lambrechts & Johansen 2012, cf. leur figure 11). Si tel était le cas, la croissance de protoplanètes de masse terrestre au-delà de la ligne de glace d'eau vers 5 ua pourrait être suffisamment rapide pour empêcher une migration significative de telles protoplanètes vers leur étoile d'après la figure 2.11. En revanche, le modèle classique de croissance par accrétion de planétésimaux prédit un temps de croissance comparable au temps de migration susmentionné : dans ce cas, la croissance pourrait ne pas empêcher la migration rapide des planètes de masse terrestre vers leur étoile. Cette constatation a permis de faire émerger un nouveau mécanisme pour ralentir ou renverser la migration des planètes de masse terrestre, qui repose sur la prise en compte de l'énergie thermique libérée par l'accrétion de matériel solide sur une planète et qui diffuse dans le disque protoplanétaire au voisinage de la planète (Benítez-Llambay et al. 2015).

Plusieurs remarques sont à faire sur la figure 2.11. D'abord, le modèle de disque qui y est adopté suppose une viscosité turbulente[3] non-dimensionnée $\alpha \sim \text{quelques} \times 10^{-3}$. Différentes valeurs de α, ou peut-être de façon plus réaliste un profil radial de α inspiré des simulations MHD de disques, pourraient affecter la position et l'apparence des régions de migration externe à la figure 2.11 (Bitsch et al. 2014). De plus, les profils de températures, de densité du disque, l'efficacité du transport dépendent du temps : au cours de son évolution, le disque perd de la masse, se refroidit, avec pour conséquence le décalage vers l'étoile et vers les plus faibles masses de planètes des régions de migration vers l'extérieur à la figure 2.11 (Bitsch et al. 2015a).

---

[3] La viscosité turbulente des disques, que nous notons ν, est très souvent exprimée sous la forme $\nu = \alpha c_s H$ suivant la formulation phénoménologique proposée par Shakura & Sunyaev (1973). Dans cette formulation, α est un paramètre sans dimension dont l'amplitude caractérise l'efficacité du transport turbulent de moment cinétique.

Couple dynamique de corotation

Nous avons vu plus haut que la direction et la vitesse de migration planétaire pouvaient se déduire directement du signe et de l'amplitude du couple total que le disque exerce sur la planète. Cette approche suppose que le taux de migration $dr_{\rm p}/dt$ dépend directement du couple du disque, et que ce dernier est indépendant du taux de migration. Toutefois, lorsqu'une planète migre, elle force continûment le gaz situé devant son orbite à traverser sa région fer-à-cheval, en effectuant un demi-tour fer-à-cheval unique par rapport à la planète. Ce gaz traversant la région fer-à-cheval contribue donc au couple de corotation. Cette contribution est proportionnelle au flux de masse du gaz traversant la région fer-à-cheval, et donc au taux de migration. Elle correspond à un couple négatif sur la planète si celle-ci migre vers l'étoile, et au contraire à un couple positif si la planète migre vers les parties externes du disque. Elle induit ainsi une *rétroaction positive* sur la migration en la faisant accélérer. Elle vient s'ajouter au couple de corotation dû au gaz piégé à l'intérieur de la région fer-à-cheval, qui se décompose dorénavant en deux parties :

- le couple dû au fait que le gaz effectue de multiples demi-tours dans la région fer-à-cheval, et qui est le même couple de corotation que celui vu plus haut lorsque la planète est en orbite fixe (le *horseshoe drag*, indépendant du taux de migration, donc sans rétroaction sur la migration).
- le couple que la région fer-à-cheval doit exercer sur la planète pour pouvoir migrer à la même vitesse qu'elle. Ce couple, que l'on appellera *couple de piégeage*, se visualise peut-être plus facilement comme l'opposé du couple que la planète doit appliquer à sa région fer-à-cheval pour la forcer à migrer de concert avec elle. Le couple de piégeage sur la planète est positif (négatif) si la planète migre vers l'intérieur (extérieur) : il induit donc une *rétroaction négative* sur la migration.

En résumé, lorsque la planète migre dans son disque, le couple de corotation a deux composantes : (i) le *couple statique de corotation* (ou *horseshoe drag*), et (ii) le *couple dynamique de corotation*, qui est la somme du couple de piégeage et du couple exercé par le gaz traversant la région fer-à-cheval de la planète (Masset & Papaloizou 2003, Paardekooper 2014). Comme l'implique cette terminologie, seul le couple dynamique de corotation dépend du taux de migration et induit une rétroaction sur la migration. Lorsque la rétroactive est positive, le couple dynamique de corotation conduit à une accélération, un emballement de la migration, qui peut devenir très rapide. Le lecteur intéressé par les circonstances pour lesquelles la migration peut s'emballer, et ce que cela implique, pourra lire la section 3.1.4 de Baruteau et al. (2016). Nous reparlerons du couple dynamique de corotation lorsque nous aborderons la migration de type III au § 2.3.2, et lorsque nous présenterons le travail de thèse de Gaylor Wafflard-Fernandez au § 2.4.

2.3.2 Migration des planètes géantes

Nous décrivons dans cette sous-section les principales prédictions des modèles d'interactions disque-planète pour les planètes massives, c'est-à-dire celles capables de creuser un sillon annulaire dans le gaz autour de leur orbite. Nous y expliquons comment le sillage d'une planète lui permet de creuser un tel sillon et quelles implications cela a sur la migration planétaire.

Ouverture d'un sillon annulaire

On a vu au § 2.3.1 que le sillage extrait du moment cinétique orbital de la planète sous forme d'ondes spirales de densité, qui se propagent de part et d'autre de la planète dans le disque. Ces ondes se transforment en chocs plus ou moins près de la planète, et finissent par déposer dans le disque le flux d'énergie et de moment cinétique qu'elles transportent (Goodman & Rafikov 2001). Plus une planète est massive, plus près de la planète les ondes deviennent des chocs et déposent leur flux d'énergie et de moment cinétique. Comme le sillage interne véhicule un flux négatif d'énergie et de moment cinétique, il tend à pousser le gaz du disque vers l'intérieur, et donc à l'éloigner de la planète. De même, le sillage externe véhicule un flux positif d'énergie et de moment cinétique qui pousse le gaz du disque vers l'extérieur, l'éloignant aussi de la planète. Sous l'effet de leur sillage, les planètes massives creusent donc un sillon annulaire autour de leur orbite, en vidant progressivement leur région co-orbitale (cf. image de gauche à la figure 2.12).

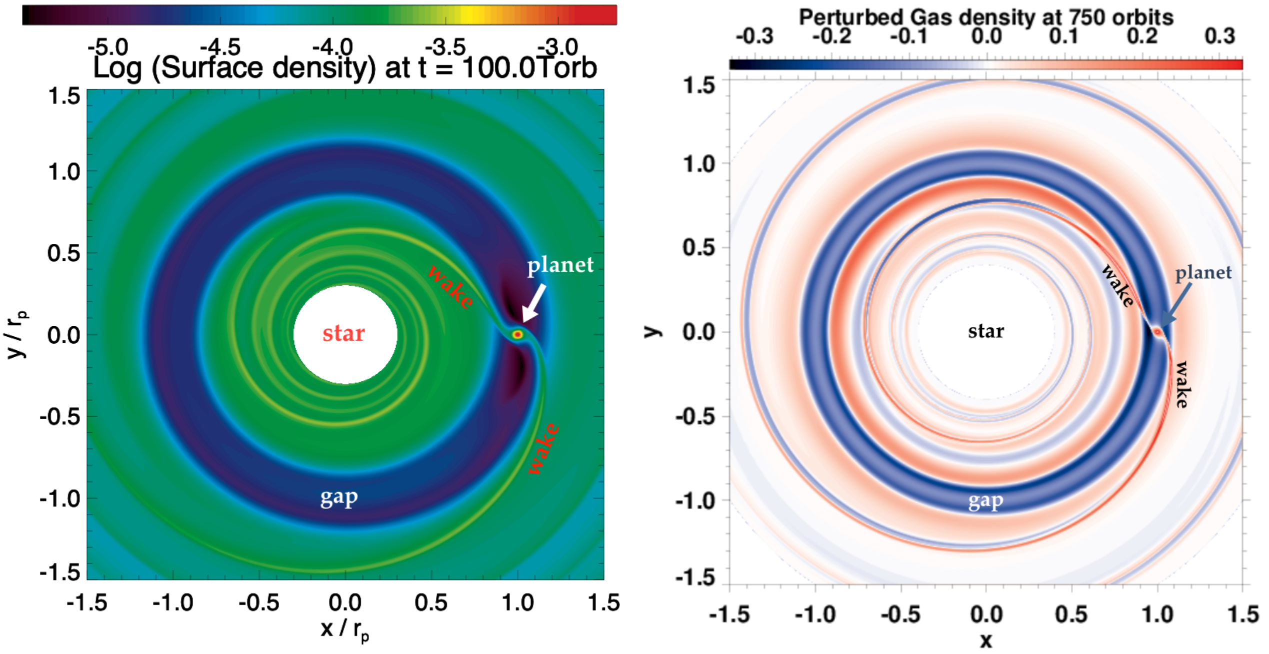

FIGURE 2.12 – *Gauche : densité surfacique de masse d'un disque en présence d'une planète de 3 masses de Jupiter (la densité est normalisée par $M_\star/r_\mathrm{p}^2$ et est représentée en échelle logarithmique). Droite : perturbation relative de densité d'un disque froid (rapport d'aspect $h = 3\%$) et inviscide en présence d'une planète de 3 masses terrestres (image adaptée de Baruteau & Lin 2010). Sur les deux images, on indique la position du sillage de la planète ('wake') et de son sillon ('gap').*

L'épaisseur du sillon, c'est-à-dire son extension radiale, est donnée par la condition d'équilibre entre le couple gravitationnel de la planète sur le disque, qui tend à creuser le sillon, et les couples visqueux et de pression du disque, qui tendent à le refermer (Lin & Papaloizou 1986a, Crida et al. 2006). Autrement dit, la capacité d'une planète à creuser un sillon dépend non seulement de sa masse, mais aussi de la vitesse du son (intervenant dans la pression thermique) et de la viscosité turbulente. Cette capacité peut être caractérisée par des paramètres sans dimension : le rapport de masse entre la planète et l'étoile ($q = M_\mathrm{p}/M_\star$), le rapport d'aspect du disque (h) et le paramètre α dans l'expression de la viscosité turbulente.

Il est difficile d'établir un critère précis définissant quand une planète ouvre un sillon autour de son orbite. Le critère formulé par Crida et al. (2006) est tel que la densité de surface du gaz dans la région co-orbitale de la planète tombe à 10% de sa valeur initiale. Cette valeur de 10% est somme toute arbitraire, et des planètes moins massives que celles satisfaisant le critère de Crida et al. (2006) peuvent tout-à-fait creuser un sillon moins profond autour de leur orbite. Cela peut même être le cas des planètes de masse terrestre dans des disques faiblement turbulents (p.e., Rafikov 2002, Muto et al. 2010, Dong et al. 2011, Duffell 2015), comme nous l'illustrons sur l'image de droite à la figure 2.12. Dans le même ordre d'idée, plusieurs études numériques, comme celle de Fung et al. (2014), ont examiné la dépendance de la profondeur du sillon (c'est-à-dire le contraste de densité de surface du gaz entre l'intérieur et l'extérieur du sillon) en fonction de q, h et α. Mentionnons à ce propos que les simulations de disques turbulents MHD montrent que l'épaisseur et la profondeur des sillons planétaires peuvent être quelque peu différentes de celles obtenues dans les modèles de disques visqueux (Papaloizou et al. 2004, Zhu et al. 2013). Ce type d'études a trouvé un cadre observationnel avec les observations d'anneaux sombres et brillants dans l'émission des disques protoplanétaire. Si ces anneaux sont effectivement dus à des planètes, il serait alors possible, en principe, d'estimer (ou au moins de contraindre) la masse de la planète dans chaque anneau sombre à partir de l'épaisseur et du contraste d'intensité des anneaux sombres. Nous reviendrons largement sur ce sujet au § 2.4.

La capacité qu'a une planète à ouvrir un sillon par les chocs générés par son sillage dépend de la vitesse de migration de la planète. Plus la planète migre lentement, plus son sillage choque de façon répétée le gaz du disque, plus le sillon s'ouvre facilement. Le critère d'ouverture de sillon mentionné ci-dessus est pour des planètes en orbite circulaire fixe, et plusieurs études numériques ont reporté sa modification par la prise en compte de la migration, notamment dans les disques massifs où la migration est rapide (Malik et al. 2015). Un cas particulier est la migration interne très rapide des planètes formées par instabilité gravitationnelle dans leur disque (p.e., Baruteau et al. 2011a). Comme nous le reverrons au § 2.3.3, ces planètes migrent tellement rapidement qu'elles n'ont en fait pas le temps de creuser de sillon autour de leur orbite, à moins qu'elles n'accrètent suffisamment de gaz pendant leur migration pour enrayer cette tendance (Zhu et al. 2012, Nayakshin & Cha 2013, Stamatellos 2015).

Au-delà de l'ouverture d'un sillon annulaire, les chocs générés par le sillage d'une planète peuvent modifier le profil de température du disque. Par exemple, dans Ziampras et al. (2020), nous avons montré, par des arguments analytiques et des simulations hydrodynamiques, que le chauffage induit par le sillage d'une planète de masse de l'ordre de Jupiter pouvait significativement déplacer, voire déformer, la ligne de glace d'eau dans le disque protoplanétaire, ligne qui, dans un disque sans planète, correspond à la distance à l'étoile où la température du gaz atteint la température de sublimation de la glace d'eau. Cette ligne de glace est importante dans les modèles de formation planétaire, car elle change les propriétés de collage des particules solides pour la formation des planétésimaux, et au-delà le contenu en eau des planétésimaux et des planètes jeunes.

Formation d'un disque circumplanétaire

A mesure que la planète ouvre un sillon annulaire autour de son orbite, une partie du gaz de la région co-orbitale de la planète se retrouve dans le disque circumplanétaire. Il s'agit en quelque sorte d'un mini disque d'accrétion en orbite autour de la planète, alimenté par le flot du disque protoplanétaire autour de l'étoile. En plus de jouer un rôle clé dans l'accrétion planétaire, le disque circumplanétaire peut largement influencer la migration planétaire. En outre, lorsque son auto-gravité est prise en compte, le disque protoplanétaire exerce un couple gravitationnel sur la planète et sur son disque circumplanétaire. Si, par commodité, l'auto-gravité est négligée, le couple ne s'applique que sur la planète, et le disque circumplanétaire demeure un spectateur passif de la migration, qu'il ralentit substantiellement, comme nous l'avons montré dans Crida et al. (2009). Nous y avons aussi proposé une méthode numérique simple pour éviter ce biais.

Les détections par imagerie directe de planètes jeunes et massives apportent de nouvelles contraintes sur les scénarios de formation et d'évolution des planètes géantes. Un exemple particulièrement intéressant est celui des deux planètes découvertes par SPHERE et MUSE dans la cavité du disque protoplanétaire autour de PDS 70 (cf. § 2.1.4). Ce type d'observations, et bien sûr d'autres précédemment, ont stimulé un grand nombre d'études récentes visant à examiner la structure, le taux d'accrétion et l'observabilité des disques circumplanétaires. On retiendra notamment que l'accrétion de gaz du disque protoplanétaire vers le disque circumplanétaire est un mécanisme intrinsèquement 3D, avec un processus de circulation méridienne impliquant un flot vertical de gaz entrant dans le disque circumplanétaire depuis les hautes latitudes du disque protoplanétaire (p.e., Tanigawa et al. 2012, Szulágyi et al. 2014), que cette accrétion peut être stochastique, et même conduire à la formation de jets depuis le disque circumplanétaire (Gressel et al. 2013). L'observabilité des disques circumplanétaires peut être étudiée par leur signatures dans la cinématique du gaz (Perez et al. 2015) ou encore dans sa distribution spectrale d'énergie, comme nous l'avons montré dans Montesinos et al. (2015).

Migration de type II

Comme pour les planètes terrestres, la migration des planètes massives ouvrant un sillon autour de leur orbite résulte des couples de Lindblad (dû au sillage de la planète) et du couple de corotation (ses composantes statique et dynamique). Le poids relatif de chacun de ces couples dépend de l'épaisseur et de la profondeur du sillon qui, comme on l'a vu plus haut, varient avec la masse de la planète, le rapport d'aspect du disque et sa viscosité turbulente. Pour les planètes qui creusent un sillon profond, qui ont typiquement une masse comparable à celle de Jupiter, ou au-delà, le couple de corotation est très largement affaibli, et le couple de Lindblad, pourtant lui aussi affaibli (mais pas autant que le couple de corotation) devient le moteur principal de la migration. C'est à ce cas de figure qu'est associée la migration planétaire dite de type II. Étant entraînée principalement par le couple de Lindblad, la migration de type II est dirigée vers l'étoile, et opère sur des temps caractéristiques somme toute assez courts, de l'ordre de 10^{4-5} ans.

Pendant longtemps, on a pensé que la migration de type II était dictée par l'évolution visqueuse du disque (Lin & Papaloizou 1986b), c'est-à-dire que les planètes massives devaient migrer à la même vitesse que celle de dérive visqueuse turbulente du disque au niveau de l'orbite de la planète. Un peu comme si la planète n'était qu'un élément fluide constitutif du disque, poussé vers l'intérieur par le couple visqueux du disque au-delà de son orbite. Comme si, finalement, le couple de Lindblad ne jouait pas de rôle dans la migration. Les simulations hydrodynamiques de Dürmann & Kley (2015) ont permis de montrer qu'une planète massive ouvrant un sillon profond pouvait migrer à une vitesse différente de celle du gaz autour de son orbite, en constatant que le gaz pouvait par exemple traverser l'orbite de la planète. Autrement dit, la migration de type II n'est pas liée à la dérive visqueuse du disque, mais bien au couple de Lindblad qui lui est exercé par le disque.

Migration de type III

Pour les planètes moins massives qui n'ouvrent qu'un sillon partiel, peu profond autour de leur orbite, l'histoire est un peu différente, le couple de corotation demeurant un acteur de premier plan de la migration. Il s'agit typiquement du cas des planètes de masse comparable à celle de Saturne. Lorsque la densité de surface du gaz proche de l'orbite de la planète est faible, c'est-à-dire tel que le paramètre de Toomre $Q \equiv c_{\rm s}\Omega_{\rm K}/\pi G\Sigma$ (sans dimension) est typiquement au-delà de 10, le régime de migration est intermédiaire entre type I et type II (p.e., Masset & Papaloizou 2003, Crida & Morbidelli 2007, D'Angelo & Lubow 2008). Pour des densités locales de gaz plus élevées ($Q \lesssim 10$), le couple dynamique de corotation conduit à un emballement de la migration, qui devient très rapide. Ce régime de migration s'appelle migration de type III (Masset & Papaloizou 2003). Une terminologie parfois contre-intuitive, puisque s'appliquant aux planètes de masse intermédiaire entre celles sujettes à la migration de type I et de type II. Toujours est-il qu'une quantité appelée déficit de masse co-orbitale, dont dépend le couple dynamique de corotation, permet de déterminer quand la migration s'emballe. Il s'agit de la masse qui devrait être ajoutée à la région fer-à-cheval de la planète afin que celle-ci ait, en moyenne, la même densité surfacique de masse que celle du gaz qui traverse la région fer-à-cheval à mesure que la planète migre. Lorsque ce déficit de masse co-orbitale excède la masse de la planète et de son disque circumplanétaire, la migration s'emballe, tandis que dans le cas contraire, le couple dynamique de corotation accélère la migration sans toutefois l'emballer (Masset & Papaloizou 2003). Le disque circumplanétaire peut grandement impacter la migration de type III (D'Angelo et al. 2005, Pepliński et al. 2008, Crida et al. 2009).

2.3.3 Comparaison des modèles de formation et évolution planétaires aux observations

Nous discutons dans cette sous-section du rôle que peuvent jouer les interactions disque-planète, et plus particulièrement la migration planétaire, dans les observations de systèmes (exo-)planétaires. Nous étendons la discussion entamée au § 2.1 à ce sujet en couvrant les grandes catégories de populations planétaires du diagramme masse - demi-grand axe à la figure 2.1, et sur lesquelles j'ai eu l'occasion de travailler : les planètes géantes lointaines, les Jupiter chauds et tièdes, et les systèmes multi-planétaires de super-Terres.

Formation et migration des planètes géantes lointaines

La découverte par imagerie directe de planètes géantes à plusieurs dizaines d'ua de leur étoile est un défi aux modèles de formation et d'évolution planétaires. Un exemple remarquable est le système planétaire HR 8799, où quatre planètes 7 à 10 fois plus massives que Jupiter se situent entre 14 et 68 ua de l'étoile (Marois et al. 2010). Seuls des disques massifs sujets à l'instabilité gravitationnelle pourraient former rapidement des planètes aussi massives et aussi loin de leur étoile. En plus d'être suffisamment massif, le disque doit pouvoir se refroidir efficacement pour déclencher l'instabilité gravitationnelle, ce qui se traduit par une distance minimale à l'étoile où l'instabilité peut se développer (entre 30 et 50 ua pour une étoile de type solaire, Rafikov 2005). Les simulations de Meru & Bate (2011) ont constaté que le temps de refroidissement du disque au-dessous duquel l'instabilité se déclenche augmentait avec la résolution des simulations. Par des simulations hydrodynamiques 2D utilisant le code FARGO, nous avons expliqué dans Paardekooper et al.

(2011b) que cette non-convergence était un artefact des conditions initiales de ce type de simulations qui imposent le disque de se refroidir soudainement.

L'instabilité gravitationnelle conduit à la formation d'un ou plusieurs fragments de gaz de masse supérieure à celle de Jupiter (Boley et al. 2010). En se refroidissant et en contractant, ces fragments forment des planètes géantes de gaz, voire des naines brunes pour des fragments très massifs ou accrétant efficacement le gaz du disque protoplanétaire. Les fragments baignent dans un disque massif et turbulent, ce qui entraîne leur migration. Dans Baruteau et al. (2011a), nous avons modélisé la migration de planètes de masse comprise entre 1 et 10 masses de Jupiter formées par instabilité gravitationnelle. Nous avons montré que les planètes ainsi formées migrent très rapidement vers les parties internes du disque, en typiquement 10^4 ans (cf. figure 2.13). La vitesse initiale de migration est en fait tellement rapide que, malgré leur masse élevée, les planètes formées par instabilité gravitationnelle n'ont pas le temps d'ouvrir un sillon annulaire autour de leur orbite. Leur migration ressemble donc beaucoup à de la migration de type I. Cette migration rapide nécessite la recherche de mécanismes alternatifs permettant au modèle de formation par instabilité gravitationnelle de rendre compte des planètes massives observées par imagerie directe.

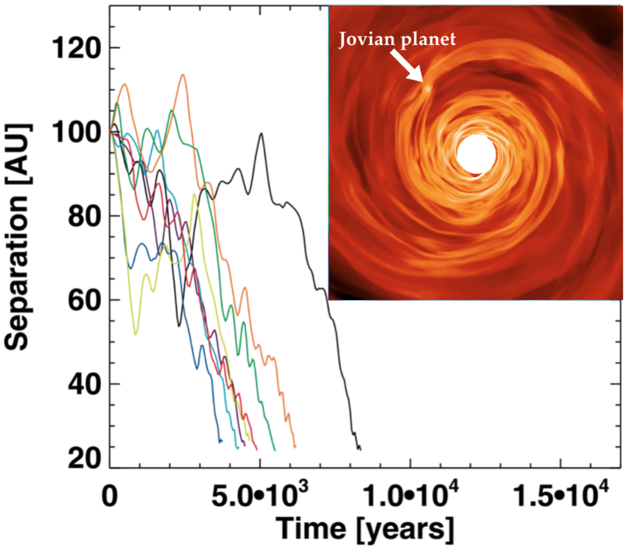

FIGURE 2.13 – *Résultat d'une simulation hydrodynamique modélisant la migration d'une planète formée par instabilité gravitationnelle. On y montre l'évolution temporelle du rayon orbital d'une planète de masse jovienne située initialement à 100 ua d'une étoile de masse solaire. Les courbes correspondent à des azimuths initiales différentes de la planète. L'image ancrée à droite montre la densité surfacique du disque. On y perçoit à peine les perturbations de densité dues à la planète, tant elles sont dominées par la turbulence générée par l'instabilité gravitationnelle. Images adaptées de Baruteau et al. (2011a).*

Obliquité et âge des Jupiter chauds : contraintes sur les scénarios de migration planétaire

Nous avons indiqué au tout début du § 2.3 que les Jupiter chauds se seraient probablement formés à plus grande distance de leur étoile dans leur disque protoplanétaire, et s'en seraient rapprochés par interactions disque-planète. L'observation d'une obliquité orbitale projetée élevée (supérieure à une trentaine de degrés) pour environ un tiers des Jupiter chauds (cf. § 2.1.1) a toutefois semé le doute sur l'importance des interactions disque-planète dans l'évolution orbitale des Jupiter chauds. Lorsque les planètes se forment dans leur disque protoplanétaire, les interactions disque-planète tendent en effet à maintenir une inclinaison orbitale faible, voire nulle, y compris pour les planètes géantes (Bitsch et al. 2013b). Une planète peut toutefois avoir une obliquité orbitale non nulle malgré une inclinaison nulle si l'axe de rotation de l'étoile et l'axe perpendiculaire au plan du disque où se trouve la planète ne sont plus alignés, ce qui peut être le cas lorsque le disque interagit gravitationnellement avec des étoiles proches (Bate et al. 2010, Batygin 2012, Picogna & Marzari 2015), ou lors des interactions de marée étoile-planète si la planète se trouve suffisamment proche de son étoile (Cébron et al. 2013, Barker & Lithwick 2014).

Autrement, une planète peut voir son inclinaison tout comme son excentricité augmenter par interaction gravitationnelle avec d'autres compagnons, planétaires (p.e., Rasio & Ford 1996, Jurić & Tremaine 2008, Marzari et al. 2010) ou stellaires (p.e., Wu & Murray 2003, Fabrycky & Tremaine 2007, Naoz et al. 2012), que le planète soit encore dans son disque protoplanétaire ou pas. Cette idée a vu émerger un scénario alternatif de migration des Jupiter chauds, appelé *high-eccentricity migration*, et que nous traduirons par *migration à haute* *excentricité*. Dans ce scénario, une planète de masse de l'ordre de Jupiter se forme à plusieurs ua de son étoile dans le disque protoplanétaire, acquiert une orbite inclinée et très excentrique (e>0.9) par interaction avec un ou plusieurs compagnons, puis l'orbite se resserre (diminution du demi-grand axe), se circularise (diminution de l'excentricité), et se réaligne (diminution de l'obliquité orbitale) par interactions de marée étoile-planète. Toute la question ici est de comparer les temps caractéristiques de resserrement, circularisation et ré-alignement de l'orbite. Il s'agit en fait d'une des questions clé dans l'étude des interactions de marée étoile-planète. Une des difficultés du modèle de migration à haute excentricité est d'amortir efficacement le demi-grand axe et l'excentricité de la planète, et ainsi rendre compte de l'excentricité faible, voire nulle des Jupiter chauds, sans amortir considérablement son inclinaison pour maintenir une obliquité projetée élevée.

A ce propos, il a été proposé que peut-être *tous* les Jupiter chauds se seraient formés par le scénario de migration à excentricité élevée, avec une obliquité (inclinaison) initiale variée qui aurait été amortie plus ou moins efficacement par interactions de marée avec l'étoile (Triaud et al. 2010, Albrecht et al. 2012)). Albrecht et al. (2012) a ainsi proposé que les Jupiter chauds d'obliquité faible auraient eu un temps caractéristique de ré-alignement orbital court devant leur âge. Ces auteurs ont fondé leur argumentation sur les travaux de Zahn (1977) concernant la synchronisation par effets de marée d'étoiles binaires proches, indiquant que le temps de ré-alignement orbital devrait être plus court pour les étoiles de plus faible masse possédant une enveloppe convective, expliquant ainsi la corrélation entre obliquité et température effective de l'étoile suggérée par la figure 2.2. Si les travaux de Zahn (1977) prédisent en effet un allongement du temps d'amortissement de l'obliquité orbitale avec la température effective de l'étoile, ils donnent en pratique des temps de ré-alignement orbital au moins un à deux ordres de grandeur plus longs que l'âge des systèmes pour lesquels l'obliquité orbitale projetée a été mesurée (Albrecht et al. 2012, Ogilvie 2014). Ceci montre la limitation à appliquer les théories d'évolution des étoiles binaires par effets de marée aux Jupiter chauds. Toujours est-il que l'étude des effets de marée étoile-planète a depuis connu un fort regain d'intérêt. En particulier, on notera que les conditions requises pour que les effets de marée conduisent à un ré-alignement de l'orbite plus rapide que son resserrement devraient produire autant de planètes alignés avec leur étoile sur des orbites progrades que rétrogrades, c'est-à-dire autant de planètes avec une obliquité orbitale égale à 0 ou 180°, ce qui n'est pas ce qu'on observe (Lai 2012, Rogers & Lin 2013). Plus vraisemblablement, les Jupiter chauds d'obliquité orbitale faible ont eu leur évolution orbitale dominée par la migration due à leur disque protoplanétaire, tandis que les Jupiter chauds d'obliquité orbitale élevée ont eu leur évolution orbitale dominée par le scénario de migration à haute excentricité suivie des effets de marée avec leur étoile. Une discussion plus détaillée de l'obliquité des Jupiter chauds pourra être trouvée dans la section 3.3.1 de Baruteau et al. (2016).

Dans ce contexte, je collabore avec Jean-François Donati à l'IRAP dans le cadre du programme MaTYSSE, dont le but est de détecter des Jupiter chauds autour d'étoiles jeunes T Tauri. Ce type de détection est très difficile car les étoiles jeunes sont très actives, avec la présence de taches sombres et de plages magnétiques à leur surface qui dominent largement le signal de vitesse radiale obtenu par spectro-vélocimétrie. Il est cependant possible de modéliser et de filtrer cette activité par spectro-polarimétrie et traquer ainsi un éventuel signal planétaire résiduel. Cette technique a porté ses fruits avec la détection d'un Jupiter chaud autour de deux étoiles "weak-line T Tauri" : $V830\tau$ (Donati et al. 2016) et TAP 26 (Yu et al. 2017), âgées d'environ 2 et 17 millions d'années, respectivement. Ces deux planètes ont une excentricité marginale, et l'âge des étoiles exclut le scénario de migration à haute excentricité pour ces planètes. Nous y concluons que ces deux planètes ont dû parvenir près de leur étoile par interactions avec leur disque protoplanétaire. Une stratégie similaire a été adoptée pour $V410\tau$, une autre étoile de type "weak-line T Tauri" (Yu et al. 2019), où la présence d'un Jupiter chaud à moins de 0.1 ua de l'étoile est exclue. Dans ce cas, il est possible que le compagnon stellaire (naine M) orbitant à quelques dizaines d'ua ait tronqué le disque protoplanétaire autour de $V410\tau$, entraînant sa dissipation rapide et limitant donc largement la possibilité de former des planètes massives proches.

Excentricité des Jupiter tièdes

Comme on l'a vu au § 2.1.2, l'excentricité médiane élevée ($\sim$0.25) des Jupiter tièdes suggère un processus dynamique générique capable de rendre relativement excentrique l'orbite de telles planètes une fois initiée la dissipation du disque protoplanétaire. Il est possible que les Jupiter tièdes aient acquis une excentricité élevée par interactions gravitationnelles avec d'autres planètes massives ou des étoiles proches. Néanmoins, comme anticipé au § 2.1.2, l'absence de corrélation observationnelle entre excentricité élevée des Jupiter chauds ou tièdes et présence d'un compagnon planétaire ou (sub-)stellaire laisse à penser que cette explication est davantage circonstancielle que générique.

Partant de cette observation, Florian Debras, chercheur post-doctorant à l'IRAP depuis Janvier 2019, a revisité l'idée communément admise qu'une planète massive se formant seule dans son disque protoplanétaire acquiert nécessairement une faible excentricité orbitale. Depuis les travaux de Papaloizou et al. (2001), on sait qu'une planète d'au moins 5 à 10 fois la masse de Jupiter, située dans une cavité d'un disque protoplanétaire, peut voir son excentricité augmenter jusqu'à 0.1-0.2. Cela est dû à la présence de la cavité qui favorise l'échange de moment cinétique entre la planète et le disque aux résonances de Lindblad excentriques, qui, comme leur nom le suggère, tendent à croître l'excentricité de la planète. Par ailleurs, les observations récentes de disques protoplanétaires ont mis en lumière une catégorie de disques, appelés disques de transition, dans lesquels on observe la présence d'une cavité dans la poussière comme dans le gaz (p.e., Carmona et al. 2017). Enfin, les modèles d'évolution des disques indiquent qu'il est assez attendu de former une cavité dans un disque protoplanétaire, que ce soit par photo-évaporation ou par l'action du champ magnétique du disque. Dans ce contexte, nous nous sommes rendus compte que le mécanisme de croissance d'excentricité initialement proposé par Papaloizou et al. (2001) pouvait s'appliquer à des planètes moins massives (d'un ordre de grandeur typiquement). Florian a réalisé de longues simulations hydrodynamiques 2D via lesquelles nous trouvons que la présence d'une cavité dans le disque peut croître l'excentricité d'une planète de masse comparable à Jupiter jusqu'à de l'ordre de 0.4, au-delà même de l'excentricité médiane des exoplanètes géantes (cf. figure 2.14). Ces résultats font l'objet d'un article soumis à MNRAS, où nous proposons que l'excentricité des exoplanètes géantes reflète un mécanisme générique lié à la structure du disque protoplanétaire (la formation d'une cavité) plutôt qu'à la présence éventuelle de compagnons planétaires ou sub-stellaires.

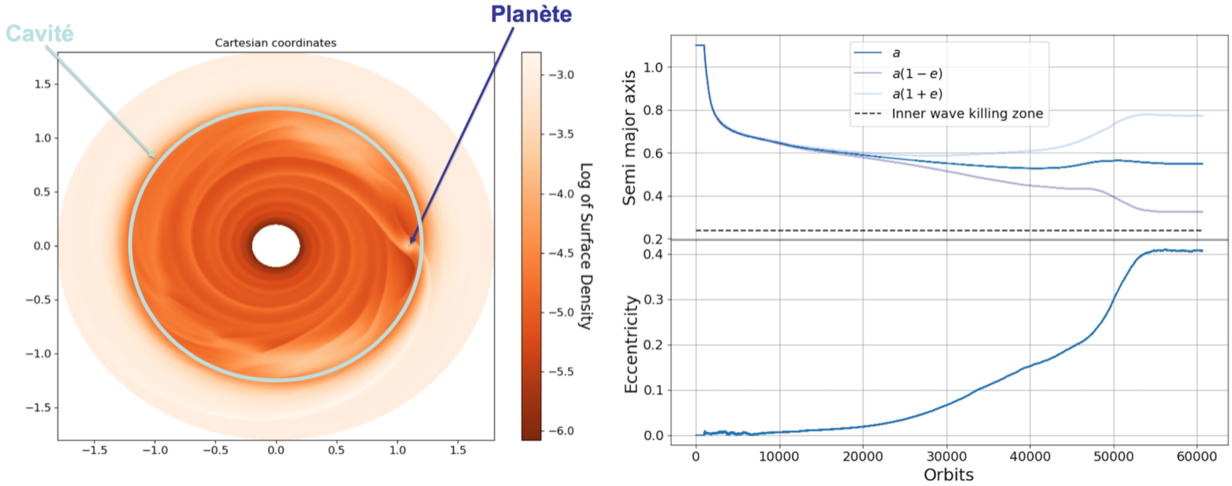

FIGURE 2.14 – *Résultats d'une simulation hydrodynamique modélisant l'évolution orbitale d'une planète de masse jovienne dans un disque protoplanétaire pourvu d'une cavité dans le gaz. Gauche : densité surfacique du disque (échelle logarithmique) au moment où la planète rentre dans la cavité et est encore peu excentrique. Droite : évolution temporelle du demi-grand axe (a) et de l'excentricité (e) de la planète à mesure qu'elle pénètre dans la cavité de son disque. Images adaptées de Debras, Baruteau & Donati (soumis à MNRAS).*

Architecture des systèmes multi-planétaires détectés par *Kepler*

Comment rendre compte de la diversité des rapports de période orbitale parmi les systèmes multi-planétaires de *Kepler*? Les modèles de migration planétaire prédisent classiquement que, lorsque deux super-Terres se rapprochent l'une de l'autre par migration de type I dans leur disque, elles finissent par se capturer en résonance de moyen mouvement. Hors, le diagramme de la figure 2.4 montre que les rapports de période orbitale peuvent être bien différents de ceux attendus aux résonances. Est-ce que cela signifie que les super-Terres des systèmes multi-planétaires de *Kepler* n'ont pas ou très peu migré dans leur disque ? Cette question a été soulevée dans plusieurs études qui ont examiné la possibilité d'une croissance in-situ de ce type de planètes. Par croissance in-situ, on entend la croissance de protoplanètes de masse typiquement comprise entre celle de Mars et la Terre, dans un environnement dépourvu de gaz (donc, après dissipation du disque protoplanétaire – notons que ces protoplanètes pourraient très bien avoir migré dans le disque protoplanétaire avant sa dissipation). La distribution de rapports de période orbitale prédite par les modèles de croissance in-situ de Hansen & Murray (2013) tendent à produire trop peu de paires de planètes proches des résonances par rapport aux observations. Celui de Ogihara et al. (2015) montre que les protoplanètes en question pourraient en fait se former rapidement dans les parties internes des disques protoplanétaires, et que dans ces conditions il est peu justifié de négliger leur migration due au disque. La prise en compte de la migration planétaire dans les calculs de croissance in-situ de Ogihara et al. (2015) produit pourtant trop de paires de planètes proches des résonances comparé aux observations !

Un autre modèle qui a été particulièrement étudié est celui de l'évolution orbitale par interactions de marée avec l'étoile d'un système multi-planétaire résonant ayant migré jusqu'à proximité de l'étoile par interactions disque-planète. Les travaux de Papaloizou & Terquem (2010), Papaloizou (2011) et Lithwick & Wu (2012) ont montré que les effets de marée de l'étoile sur la planète la plus interne conduisaient à augmenter le rapport de période orbitale du système multi-planétaire, tout en le maintenant dans un état dynamique de résonance de moyen mouvement. C'est l'amortissement de l'excentricité par les effets de marée qui permet l'augmentation du rapport de période orbitale (Papaloizou 2011). Ce modèle pourrait ainsi expliquer que certaines paires de planètes aient vu leur rapport de période orbitale augmenter légèrement par rapport à une valeur résonante. Toutefois, le temps de circularisation par effets de marée devient très long pour les planètes orbitant à typiquement plus de 10 jours de leur étoile, hors pour ces planètes également on constate une tendance à ce que les paires adjacentes de planètes aient un rapport de période orbitale légèrement supérieur à celui des résonances (Baruteau & Papaloizou 2013, cf. histogramme bleu à la figure 2.4).

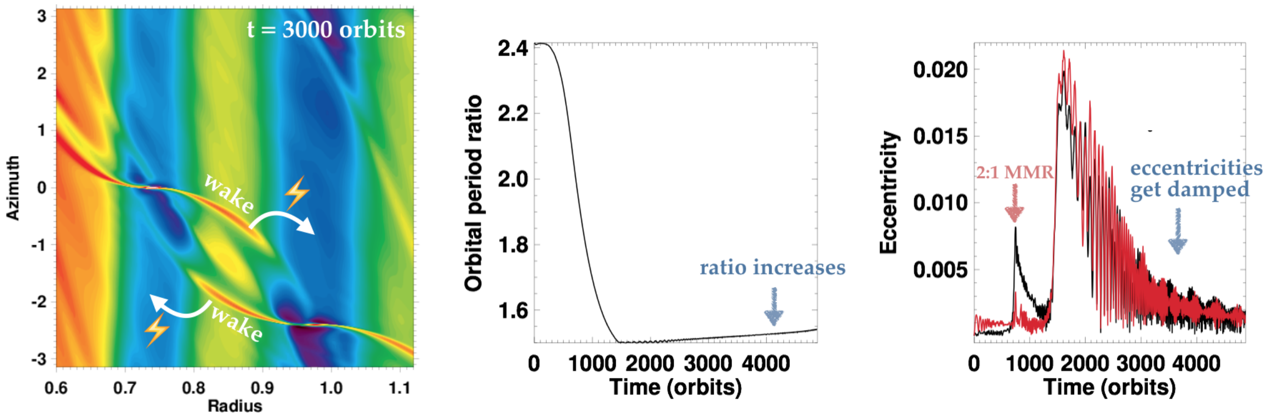

FIGURE 2.15 – *Migration de deux planètes d'environ 15 masses terrestres dans un disque de faible rapport d'aspect ($h \sim 2.3\%$) et modérément turbulent ($\alpha \sim 2 \times 10^{-3}$), représentatif des parties internes des disques aux périodes orbitales typiques où sont détectées les super-Terres de Kepler. L'image de gauche représente la densité surfacique de masse du disque (échelle logarithmique) et sert à illustrer la dissipation d'énergie ou de moment cinétique du sillage d'une planète dans la région co-orbitale de l'autre planète. Cette dissipation entraîne l'augmentation du rapport de période orbitale des planètes (image du milieu) ainsi que l'amortissement de l'excentricité des planètes (image de droite : la courbe noire montre l'excentricité de la planète interne, la rouge celle de la planète externe). Images adaptées de Baruteau & Papaloizou (2013).*

C'est dans ce contexte que j'ai revisité les prédictions des modèles de migration planétaire pour des paires de super-Terres. Dans Baruteau & Papaloizou (2013), nous avons montré qu'à la position orbitale des planètes détectées par *Kepler*, le rapport d'aspect des disques est faible (de l'ordre de 2 à 3%), et que par conséquent le sillage de ces planètes choque efficacement le gaz près de l'orbite des planètes. Cela a deux implications : (i) ce type de planètes creuse facilement un sillon annulaire partiel autour de leur orbite, et (ii) leur sillage peut déposer l'énergie et le moment cinétique qu'il transporte dans la région fer-à-cheval des autres planètes, ce qui tend à repousser progressivement les planètes les unes des autres, et donc à augmenter leur rapport de période orbitale. L'augmentation du rapport de période orbitale implique également l'amortissement de l'excentricité des planètes. Tout ceci est illustré sur la figure 2.15. Ces résultats montrent que la migration de super-Terres ne conduit pas nécessairement à former des systèmes multi-planétaires résonants, en accord qualitatif avec les observations. Notons enfin que la turbulence du disque protoplanétaire peut également déloger les systèmes multi-planétaires des résonances de moyen mouvement, comme nous l'avons étudié dans Pierens et al. (2011), et pourrait jouer un rôle clé pour expliquer la formation de systèmes multi-planétaire compacts, avec des rapports de périodes orbitales faibles, typiquement inférieurs à 4/3 (Paardekooper et al. 2013). D'autres mécanismes peuvent également déloger les planètes des résonances de moyen mouvement, qui sont discutés dans Terquem & Papaloizou (2019).

2.3.4 Applications à d'autres contextes astrophysiques

En parallèle de mes activités de recherche sur les systèmes planétaires, je me suis attaché à appliquer les prédictions des modèles de migration planétaire à d'autres contextes astrophysiques. J'ai ainsi élaboré un modèle de formation et de migration de binaires d'étoiles pour expliquer les propriétés orbitales des étoiles S dans le centre galactique. J'ai aussi étudié le durcissement des binaires de trous noirs supermassifs pour prédire l'absence de rayonnement électromagnétique précédent leur coalescence.

Migration d'étoiles dans le centre galactique

Par analogie avec certains Jupiter chauds, les étoiles S près du centre galactique sont massives (de type O-B), d'excentricité élevée, d'inclinaison aléatoire, et ne devraient pas s'être formées in situ. Si la migration stellaire dans un disque de gaz pourrait expliquer la proximité de ces étoiles du trou noir supermassif au centre galactique (Sgr A*), elle ne permet pas de rendre compte de leur excentricité ou de leur inclinaison. Dans Baruteau et al. (2011c), j'ai construit un modèle où certaines étoiles S constituaient initialement une binaire massive formée dans un disque autour de Sgr A*. Par des simulations hydrodynamiques, j'ai montré que l'interaction disque-binaire permet non seulement la migration lente de la binaire vers l'objet central, mais aussi le rapprochement très rapide des deux étoiles. Cela m'a permis d'établir qu'une binaire massive, circulaire et très compacte (par l'interaction avec le disque) pouvait, après sa dislocation par supernova de l'étoile primaire, conférer à l'étoile secondaire une excentricité et une inclinaison comparables à celles des étoiles S.

Durcissement de binaires de trous noirs supermassifs

La fusion de deux galaxies de masse différente forme un système binaire de trous noirs supermassifs dans un disque d'accrétion. Pour des binaires de rapport de masse inférieur au pourcent, cette configuration est analogue à celle d'une planète géante dans un disque autour d'une étoile de type solaire. Néanmoins, à mesure qu'une binaire de trous noirs se durcit sous l'action du disque, l'émission d'ondes gravitationnelles domine le durcissement. Le durcissement de la binaire devient beaucoup plus rapide que l'accrétion du disque sur le trou noir primaire (le plus massif). Des modèles de disques 1D ont montré que cela devait augmenter rapidement la densité du disque entre les deux trous noirs et conduire à un pic de luminosité d'accrétion précédent la coalescence de la binaire, pic qui serait identifiable en conjonction avec le signal d'onde gravitationnelle détectable par l'interféromètre LISA (Chang et al. 2010). Dans Baruteau et al. (2012), nous invalidons cette prédiction par des modèles de disques 2D. Nous y avons expliqué que le durcissement rapide de la binaire devait rediriger le gaz du disque entre les deux trous noirs au-delà de l'orbite du trou noir secondaire, en embarquant sur des demi-tours fer-à-cheval par rapport à celui-ci (de façon analogue au gaz d'un disque protoplanétaire où migre rapidement une planète, cf. § 2.3.1).

2.4 Disques protoplanétaires : observations, modélisation et simulations

L'observation des disques protoplanétaires a connu un essor considérable avec l'arrivée en 2014-2015 de SPHERE, instrument dédié à la spectro-polarimétrie et l'imagerie directe à haut contraste dans le proche-infrarouge au VLT, et du radiotélescope ALMA. SPHERE et ALMA permettent aujourd'hui d'observer les disques à des résolutions angulaires de quelques dizaines de milli-arcsecondes, ce qui équivaut à des résolutions spatiales de seulement quelques ua pour les régions proches de formation d'étoiles (entre 100 et 150 pc). Étant donné la taille typique des disques, entre 50 et 100 ua (Williams & Cieza 2011), ces deux instruments permettent donc de résoudre confortablement l'émission des disques. Rappelons qu'il existe plusieurs types d'émission : (i) celle induite par la désexcitation des atomes ou molécules du gaz (classiquement, CO dans les disques, mais pas seulement !), et (ii) la diffusion et la réémission thermique de la lumière stellaire par les poussières des disques. Une poussière peut être vue en effet comme une collection de charges électriques discrètes qui, sous l'effet du champ électrique d'une onde lumineuse incidente, se mettent à osciller, un peu comme des moments dipolaires induits. L'énergie électromagnétique émise par ces charges accélérées correspond à ce que l'on appelle la lumière diffusée, qui peut être polarisée. Une partie de l'énergie électromagnétique de l'onde lumineuse incidente est également transformée en énergie thermique (la poussière s'échauffe), laquelle est réémise sous forme d'un rayonnement continu à toutes les longueurs d'onde. C'est ce qu'on appelle l'émission thermique ou continue des poussières.

Dans ce contexte observationnel riche et stimulant, mes activités de recherche se sont récemment tournées vers la modélisation de la dynamique et de l'émission des poussières dans les disques. Je cherche principalement à déterminer si les structures observées en émission (cavités, spirales, asymétries en forme de fer-à-cheval etc.) peuvent être dues à des planètes enfouies dans ces disques, et je fais des prédictions qui peuvent être testées par les observations. Je réalise pour cela des simulations hydrodynamiques modélisant les interactions planète-disque (gaz et poussières) dont les résultats sont post-traités par des calculs de transfert radiatif dans la poussière. Un aspect important de l'émission des poussières du point de vue de la modélisation est la nature et la provenance de cette émission. L'émission proche-infrarouge, telle qu'elle peut être observée avec SPHERE par exemple, est principalement celle diffusée par les poussières de taille de l'ordre du micron situées dans les parties superficielles des disques, loin de leur plan équatorial. Modéliser ce type d'émission, comme par exemple les spirales détectées à ces longueurs d'onde, nécessite des simulations hydrodynamiques 3D, et plusieurs études ont montré que les simulations 2D (coordonnées cylindriques polaires) ne donnaient pas des résultats satisfaisants (p.e., Zhu et al. 2015). L'émission dans le domaine radio, comme avec ALMA, est sensible à l'émission thermique des solides de taille comprise entre quelques dizaines de micron et quelques cm, situées essentiellement dans le plan équatorial des disques. Une modélisation 2D (coordonnées cylindriques polaires) de cette émission et de leur disque est alors justifiée, et c'est la stratégie que j'ai adoptée en premier lieu.

Je me suis donc intéressé à la modélisation de l'émission radio des disques, qui montre deux particularités étonnantes : la présence d'anneaux sombres et brillants, comme dans le disque autour d'HL Tau (ALMA Partnership et al. 2015), ou d'asymétries à grande échelle en forme de fer-à-cheval, comme dans le disque autour de AB Aur (Tang et al. 2012, Fuente et al. 2017). Je décris ces deux branches de mes activités de recherche sur les disques aux § 2.4.1 et 2.4.2.

Pour mener à bien ces travaux, j'ai implémenté l'évolution orbitale des particules de poussières dans le code hydrodynamique public 2D Fargo-ADSG. Cette implémentation a bénéficié de l'aide de Bertrand Putigny, ancien ingénieur de recherche dans mon équipe à l'IRAP, pour optimiser la parallélisation de l'évolution des poussières dans le code. J'ai par ailleurs développé et rendu public un programme python, fargo2radmc3d, qui permet, à partir des résultats des simulations hydrodynamiques gaz+poussières réalisées avec Fargo-ADSG, de calculer des cartes synthétiques de l'émission continue des poussières et de la lumière diffusée polarisée via le code public de transfert radiatif RADMC3D. Cela m'a permis de mettre en place un réseau de collaborations avec plusieurs équipes d'observateurs et de modélisateurs des disques protoplanétaires. Depuis 2015, j'ai ainsi été co-PI de deux demandes de temps d'observation pour ALMA et NOEMA, et co-l d'une trentaine d'autres demandes, principalement pour ALMA, NOEMA et SPHERE. Ces collaborations m'ont conduit à d'être co-auteur (impliqué !) de 5 papiers observationnels et de 3 papiers théoriques sur les 5 dernières années, dont j'ai contribué à l'interprétation des résultats (Montesinos et al. 2015, Berné et al. 2015, Pacheco-Vázquez et al. 2016, Carmona et al. 2017, Zhang et al. 2018, Rivière-Marichalar et al. 2019, Pérez et al. 2019b, Bae et al. 2019).

2.4.1 Asymétries dans l'émission radio des disques

Les asymétries en forme de fer-à-cheval dans l'émission radio des poussières (cf. par exemple HD 143006 ou MWC 758 à la figure 2.5) rappellent la structure en densité du gaz d'un disque protoplanétaire où se développe un vortex par une instabilité hydrodynamique appelée instabilité de Rossby (*Rossby-Wave Instability*, analogue de l'instabilité barotrope en dynamique des fluides géophysiques – cf. Lovelace et al. 1999, Li et al. 2001). Cette instabilité est bien connue des modélisateurs des interactions disque-planète car on la retrouve fréquemment dans les simulations avec une planète massive ouvrant un sillon autour de son orbite. Avec mon collaborateur Zhaohuan Zhu (University of Nevada Las Vegas), nous nous sommes intéressés au développement de cette instabilité dans les disques protoplanétaires auto-gravitants, puis nous avons étudié son impact sur la dynamique et l'émission de particules solides piégées à l'intérieur du vortex généré par ladite instabilité. Pour ce faire, nous avons réalisé des simulations hydrodynamiques 2D bi-fluides (gaz+poussières) utilisant le code Fargo-ADSG. De la distribution spatiale des poussières de différentes tailles obtenue dans les simulations, nous avons produit des images synthétiques du flux d'émission thermique des poussières à différentes longueurs d'onde radio.

Dans un premier temps, l'instabilité de Rossby a été générée sans planète, mais par un profil initial de densité du gaz sous forme d'anneau étroit (c'est une façon relativement générique de déclencher et d'étudier l'instabilité de Rossby dans les simulations comme dans les études analytiques). Dans Zhu & Baruteau (2016), nous avons étudié en détail les conditions de croissance de l'instabilité et les propriétés du ou des vortex en découlant, et examiné en particulier l'influence de l'auto-gravité du gaz. Même pour des disques modérément massifs, l'auto-gravité du gaz change nettement la structure et l'évolution du vortex (cf. les deux images de gauche à la figure 2.16). Dans Baruteau & Zhu (2016), nous avons expliqué que, quelle que soit la masse du

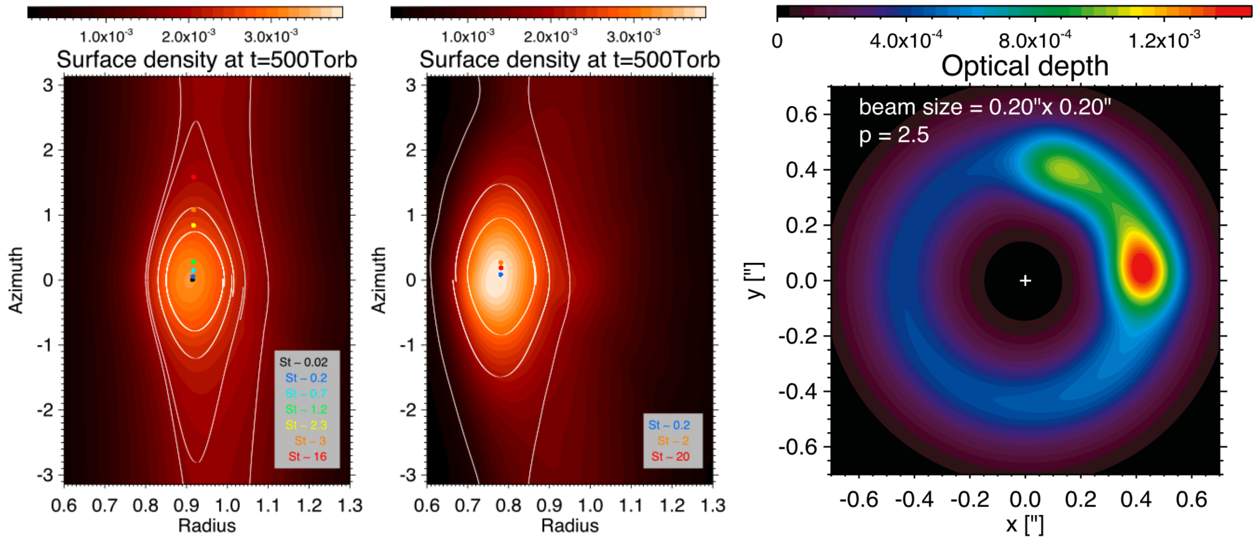

FIGURE 2.16 – *Densité de surface du gaz d'un disque protoplanétaire (en coordonnées cylindriques polaires) où un vortex se développe par l'instabilité de Rossby, avec prise en compte de l'auto-gravité du gaz (gauche) et sans (milieu). Les cercles de couleur montrent la position où sont piégées des poussières de différente taille (le nombre de Stokes St apparaît dans la légende, il croît proportionnellement à la taille des particules). Droite : image synthétique de la profondeur optique à une longueur d'onde de 8 mm de l'émission des poussières d'un disque situé à 140 pc et observé à une résolution angulaire de 0.″2. Tiré de Baruteau & Zhu (2016).*

vortex, son auto-gravité le conduit à piéger différemment les particules solides selon leur taille. Pour les vortex de faible masse, les particules piégées tendent toutes vers le rayon orbital du vortex (maximum de pression du gaz dans la direction radiale), mais plus elles sont grandes et plus elles se trouvent en amont du vortex dans la direction azimutale (cf. figure 2.16, image de gauche). Les particules de taille de l'ordre de 10 cm se trouvent ainsi décalées d'environ 90° par rapport au centre du vortex. Cela nous a permis de prédire que, selon la distribution de taille des particules dans le disque, le continuum d'émission à grande longueur d'onde (8 mm) pouvait soit prendre la forme fer-à-cheval souvent observée, soit présenter deux pics d'émission (un pour les petites particules piégées au centre du vortex, le second pour les grandes piégées en amont du vortex ; cf. image de droite à la figure 2.16). Pour les vortex massifs, en revanche, un phénomène un peu différent se produit : le vortex tourne de moins en moins vite à mesure que sa masse augmente, et moins vite que le gaz local, avec pour conséquence le fait que les petites particules se retrouvent piégées à un rayon orbital légèrement plus grand que celui du vortex, tandis que les grandes particules décrivent des anneaux, généralement non-axisymétriques, autour de la position radiale du vortex.

Nous avons ensuite considéré le cas où l'instabilité de Rossby est déclenchée par une planète massive dans le disque. Comme on l'a vu au § 2.2.2, le sillage d'une planète massive conduit à la formation d'un maximum de pression du gaz juste au-delà de l'orbite de la planète, au bord externe de son sillon. Si la viscosité turbulente du gaz reste faible, ce que l'on pense être le cas dans les parties externes des disques (à plusieurs dizaines d'ua d'une étoile de type Solaire, cf., par exemple, Flaherty et al. 2015, Pinte et al. 2016), l'instabilité de Rossby peut se déclencher au bord externe du sillon. Nous avons de nouveau réalisé un grand nombre de simulations hydrodynamiques gaz+poussières pour examiner la dynamique de piégeage des poussières dans le ou les vortex formé(s) par l'instabilité de Rossby. Là encore, nous avons effectué une exploration de l'espace des paramètres, notamment en variant la masse du disque, et examiné les conséquences observationnelles du piégeage des poussières. Ces résultats font l'objet d'un papier en préparation. Un exemple de résultat obtenu pour un disque massif est présenté à la figure 2.17, où la formation d'un vortex double au bord externe du sillon d'une planète de masse Jovienne implique deux zones de piégeage pour les particules solides, dont l'émission thermique à 0.4 mm prend ainsi la forme d'un anneau avec deux pics d'émission, assez similaire à ce que l'on peut observer dans certains disques massifs, comme HD 142527 (Casassus et al. 2015).

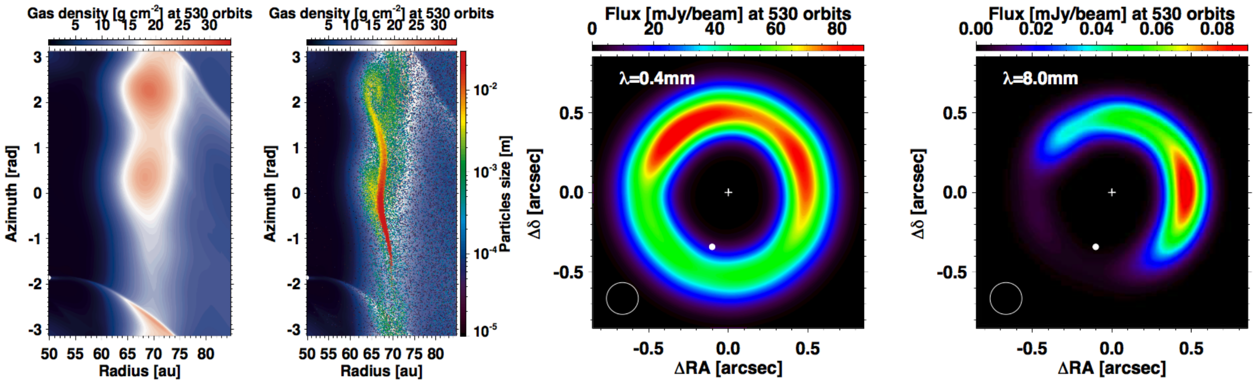

FIGURE 2.17 – *Gauche : densité de surface du gaz d'un disque protoplanétaire massif et auto-gravitant (en coordonnées cylindriques polaires) où deux vortex se développent par l'instabilité de Rossby au bord externe du sillon ouvert par une planète de masse de Jupiter (point blanc sur l'axe de gauche). Les points de couleur sur la deuxième image à partir de la gauche montrent la position de particules solides de différente taille. Les deux images de droite montrent les cartes synthétiques du continuum d'émission (flux en mJy/beam) à 0.4 mm et à 8 mm pour un disque situé à 140 pc et qui serait observé à une résolution angulaire de* $0''\!.2$.

Un autre résultat obtenu a trait à l'évolution temporelle du ou des vortex formés par l'instabilité de Rossby. On s'attend d'ordinaire à ce que plus les particules sont grandes, plus elles sont marginalement couplées avec le gaz, et plus elles sont concentrés à l'intérieur du vortex. Ainsi, le continuum d'émission à grande longueur d'onde radio, qui est davantage sensible aux particules de plus grande taille, devrait être plus piqué qu'à plus faible longueur d'onde radio. Dit d'une autre façon, le contraste azimutal de flux le long de l'anneau où émettent les poussières du disque devrait augmenter avec la longueur d'onde des observations radio. C'est ce que l'on observe par exemple pour le disque autour de Oph IRS 48 (van der Marel et al. 2015). Nous avons trouvé que la décroissance du vortex pouvait produire l'effet observationnel opposé. En effet, le vortex a une durée de vie finie, qui dépend de la viscosité turbulente du disque et du profil de densité du gaz dans le sillon de la planète. Lorsque le vortex décroît, il s'allonge de plus en plus dans la direction azimutale : les particules solides perdent progressivement le piégeage du vortex dans cette direction, ce qui se produit plus rapidement pour les grandes particules que les petites. Les petites particules restant concentrées plus longtemps que les grandes, la décroissance du vortex implique que le contraste azimutal de flux le long de l'anneau où émettent les poussières du disque diminue avec la longueur d'onde des observations radio.

De façon intéressante, avec ma collaboratrice Asunción Fuente (Observatorio Astronómico Nacional, Madrid), nous avons obtenu à peu près au même moment des observations radio du disque autour d'AB Auriga via NOEMA, qui montrent précisément le résultat précédent : le contraste azimutal du continuum d'émission à 2.2 mm (égal à 2.5 ± 0.2) est significativement plus faible qu'à 1.1 mm (où il vaut 3.6 ± 0.3). Nous avons donc proposé que l'émission radio asymétrique dans le disque d'AB Auriga indique la présence d'un ancien vortex dans le gaz du disque, formé par une planète de 2 masses de Jupiter située à presque 100 ua de l'étoile. J'ai effectué une batterie de simulations hydrodynamiques gaz+poussières de ce modèle, post-traitées par des calculs de transfert radiatif dans la poussière, qui permettent de reproduire de façon satisfaisante nos contraintes observationnelles (contraste de flux et flux total à chaque longueur d'onde, cf. figure 2.18). Ces résultats ont été publiés dans Fuente et al. (2017).

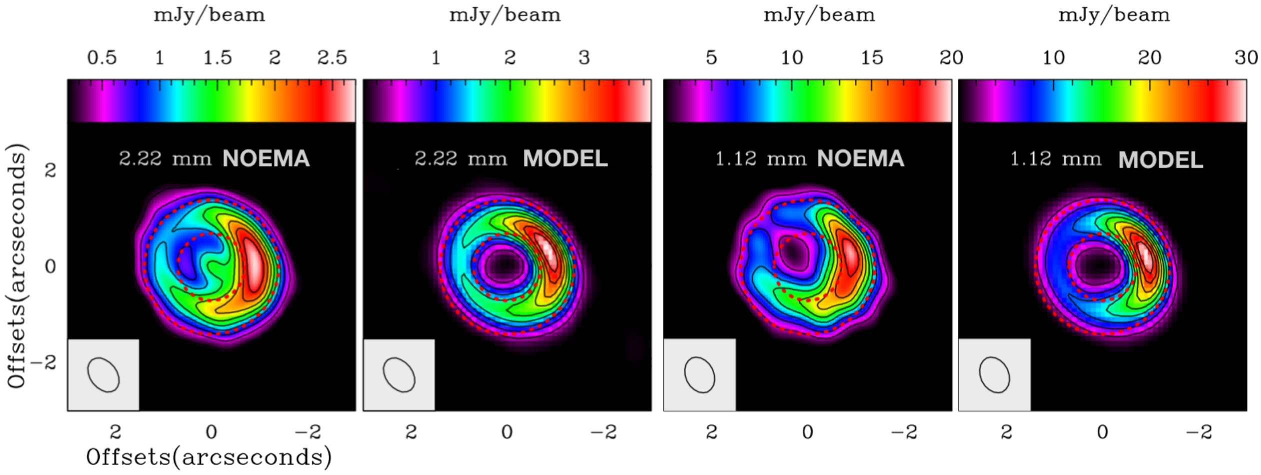

FIGURE 2.18 – *Continuum d'émission (flux en mJy/beam) du disque protoplanétaire autour de l'étoile AB Auriga, observé à 1.1 mm et 2.2 mm avec NOEMA, comparé aux images synthétiques aux mêmes longueurs d'onde obtenues à partir de nos simulations hydrodynamiques gaz+poussières. Adapté de Fuente et al. (2017).*

J'ai également eu l'opportunité de collaborer avec le groupe de Simon Casassus à Universidad de Chile (Santiago), afin de modéliser le disque autour de l'étoile MWC 758. Ce disque présente la particularité d'avoir deux anneaux d'émission asymétriques et modérément excentriques lorsqu'il est observé avec ALMA (cf. image en haut à gauche à la figure 2.19). Avec mes collaborateurs, nous avons obtenu des observations de ce même disque à plus grande longueur d'onde avec le VLA, qui montrent essentiellement un seul croissant d'émission (cf. image en bas à gauche de la figure 2.19, tirée de Casassus et al. 2019). Même si des planètes ne sont pas directement détectables dans ce disque, l'excentricité des anneaux observée avec ALMA en suggère fortement la présence. Nous avons donc proposé un modèle avec deux planètes de masse comparable à Jupiter enfouies dans ce disque protoplanétaire. Chacune de ces planètes ouvre un sillon en forme d'anneau dans le gaz autour de leur orbite. Nos simulations ont permis de montrer que chaque planète développe un vortex aux bords de son sillon par l'instabilité de Rossby. Nous avons en outre étudié la stabilité de ces vortex, et notamment leur décroissance lorsque le gaz devient modérément excentrique par la présence des planètes.

Les images synthétiques de l'émission thermique des poussières obtenues à partir de nos simulations rendent globalement bien compte de la morphologie et du flux des structures asymétriques observées dans le disque autour de MWC 758, comme on peut le voir sur les images de droite à la figure 2.19. Ces résultats ont fait l'objet de la thèse de Magistère en 2 ans de Marcelo Barazza (étudiant en Master à l'Universidad de Chile), que j'ai co-encadrée avec Simon Casassus et Sebastián Pérez. Ils ont été décrits dans Baruteau et al. (2019).

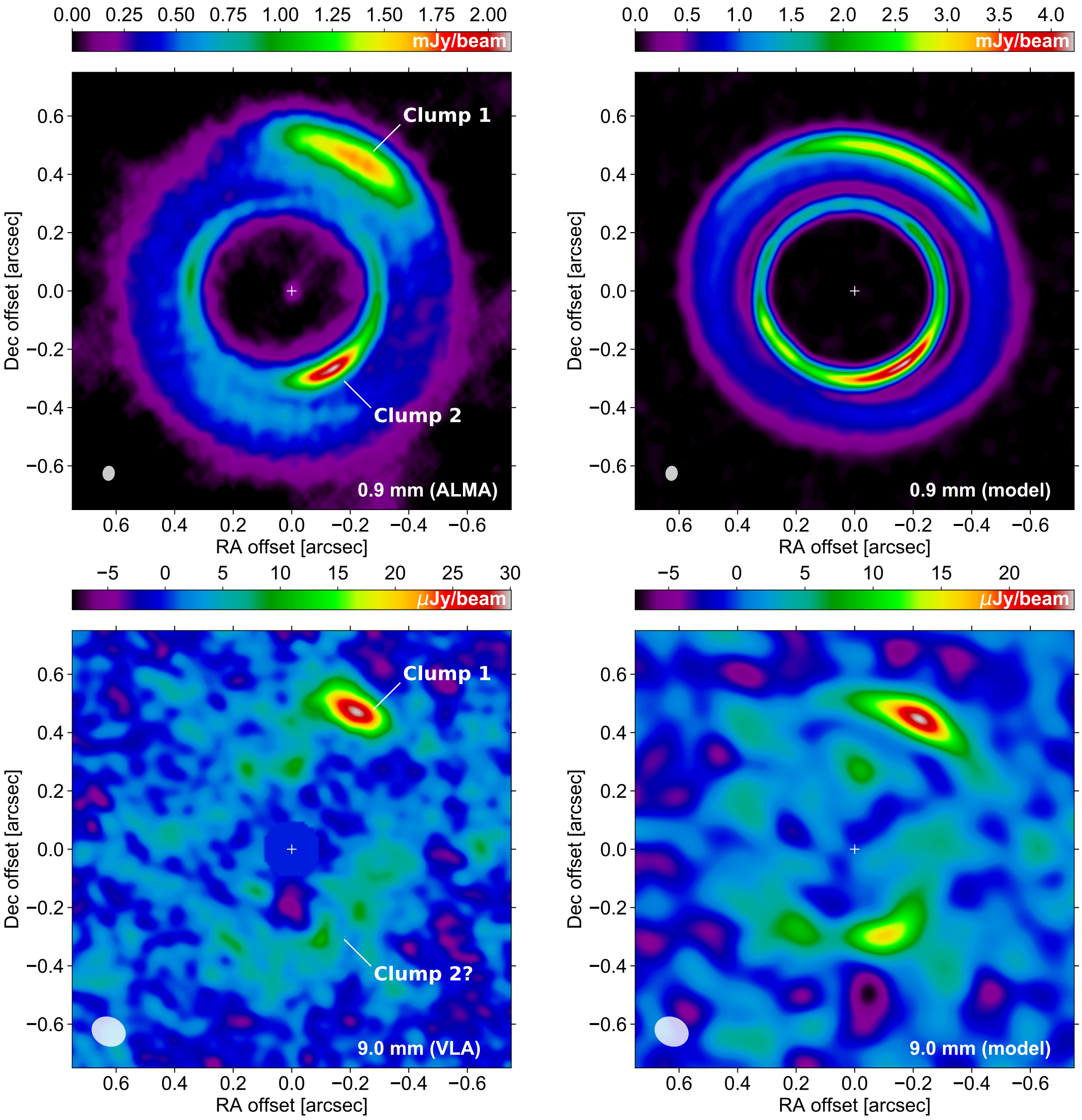

FIGURE 2.19 – *Flux d'émission thermique des poussières du disque protoplanétaire autour de l'étoile MWC 758, observé à 0.9 mm et 9 mm avec les interféromètres radio ALMA et VLA (images de gauche), comparé aux images synthétiques aux mêmes longueurs d'onde obtenues par calculs de transfert radiatif dans la poussière à partir de simulations hydrodynamiques gaz+poussières (images de droite). Les images synthétiques incluent également une modélisation simple du bruit des observations. Images tirées de Baruteau et al. (2019).*

2.4.2 Anneaux sombres et brillants dans l'émission radio des disques

La détection récente de multiples anneaux sombres et brillants dans le continuum d'émission radio des disques a également suscité beaucoup d'activité de la part des modélisateurs des disques protoplanétaires. Il est souvent imaginé que chaque anneau sombre correspond au sillon ouvert par une planète dans le disque (il n'y a pas encore de détection observationnelle directe de la présence de telles planètes). De l'extension radiale et de la profondeur de l'anneau sombre, il est possible d'estimer la masse de la planète qui créerait le sillon. Il y a plusieurs difficultés à cela : (i) aux longueurs d'onde radio auxquelles sont observés les anneaux, l'émission peut être optiquement épaisse, donc sensible aux variations de la température des poussières plutôt qu'à leur distribution spatiale, (ii) quand bien même l'émission ne serait pas optiquement épaisse, elle est la signature de poussières découplées du gaz, ce qui implique que les prédictions sur la masse de planète responsable d'un anneau sombre nécessitent des simulations bi-fluides (gaz+poussières) et pas seulement du gaz du disque, et (iii) les poussières dérivent à des vitesses différentes de celle de migration de la planète dans le disque.

Ce dernier point constitue le sujet de thèse de doctorat de Gaylor Wafflard-Fernandez, qui vise à prédire les signatures de la migration planétaire dans l'émission des poussières des disques protoplanétaires. Gaylor s'est d'abord concentré sur le cas limite où une planète migre rapidement (en quelques dizaines de milliers d'années) vers l'étoile dans son disque protoplanétaire. Ce type de migration rapide est attendu pour les planètes de masse comparable à celle de Saturne dans des disques protoplanétaires jeunes et massifs (Masset & Papaloizou 2003). Via une exploration de l'espace des paramètres (densité, température, viscosité turbulente du disque etc.), Gaylor a trouvé que la migration rapide des planètes de masse de l'ordre de Saturne pouvait se faire par à-coups (cf. image de gauche à la figure 2.20). Le travail de Gaylor a permis de bien comprendre le mécanisme hydrodynamique derrière ces à-coups, qui implique l'amplitude des chocs générés par les sillages de la planète selon sa vitesse de migration. La présence de ces à-coups a une implication forte sur la signature de la migration planétaire : à chaque ralentissement de la migration, la planète génère un maximum de pression dans le gaz juste au-delà de son orbite, qui y piège efficacement les poussières les plus larges (cf. image de milieu à la figure 2.20) et entraîne la formation d'un anneau brillant dans le flux d'émission thermique en radio. Au final, une seule planète se formant et migrant par à-coups dans son disque peut former une succession d'anneaux sombres et brillants en émission thermique radio, comme illustré sur l'image de droite à la figure 2.20. Dit d'une autre façon, notre modèle prédit l'alternance d'anneaux sombres et brillants dans le continuum radio *avec une seule planète* migrant dans le disque, alors que d'ordinaire les modèles tentent de rendre compte de ladite alternance en supposant une planète par anneau sombre (ce qui nécessiterait la formation d'au moins 3 ou 4 planètes de la masse de Neptune entre environ 10 et 70 ua de l'étoile dans un disque d'à peine quelques millions d'années, ce qui serait un défi pour les scénarios de formation et évolution planétaires). Cette prédiction est importante car de nombreux disques protoplanétaires

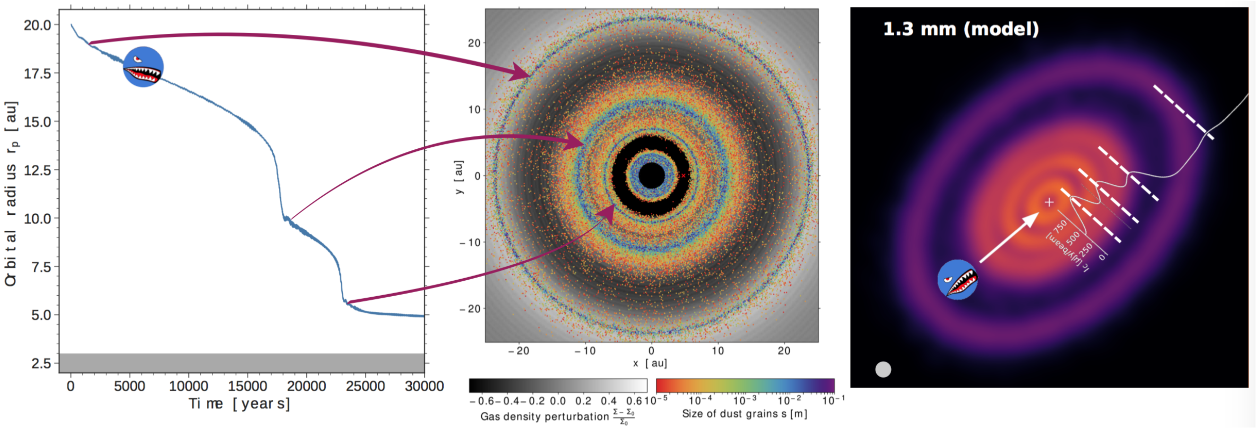

FIGURE 2.20 – *Résultat de simulation de la migration rapide d'une planète de masse de l'ordre de Saturne dans un disque protoplanétaire massif (images adaptées de Wafflard-Fernandez & Baruteau 2020). Gauche : évolution temporelle du rayon orbital de la planète, montrant une alternance de phases de migration lente et rapide. Milieu : perturbation relative de la densité de surface du gaz (noir et blanc) et position des poussières dans la simulation (points de couleur). Droite : image synthétique de l'émission radio du disque à 1.3 mm de longueur d'onde, obtenue par calcul de transfert radiatif dans la poussière. La résolution angulaire supposée pour le télescope* $(0.''02)$ *est comparable à la meilleure résolution accessible avec ALMA à la longueur d'onde considérée. La courbe blanche montre le profil radial du flux d'émission axi-symétrisé. La position de la planète à cet instant dans la simulation est indiquée par la croix rouge sur l'image du milieu.*

présentent ce type de structure lorsqu'ils sont observés en radio (comme par exemple HL Tau). Ces résultats ont été présentés dans Wafflard-Fernandez & Baruteau (2020).

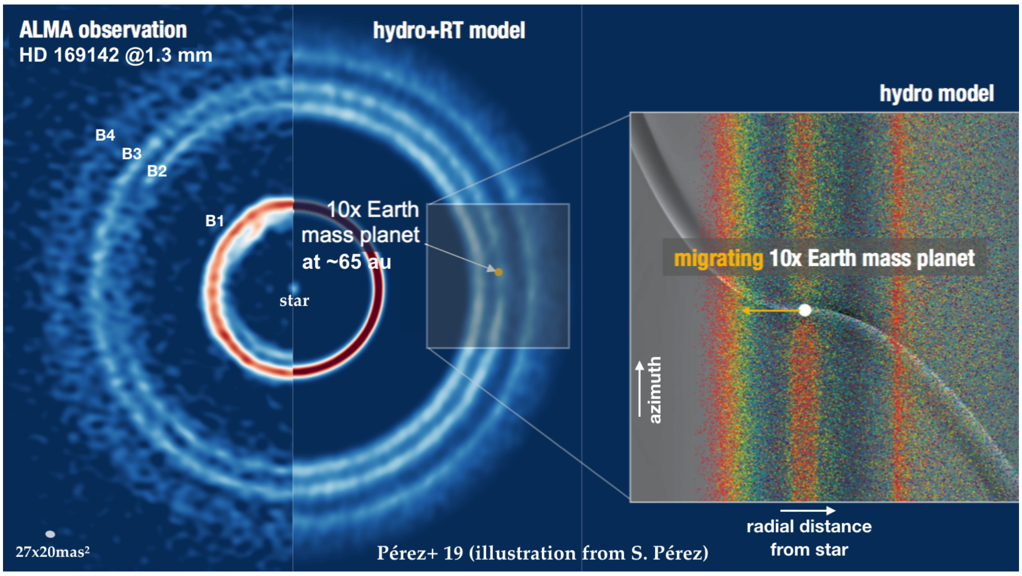

FIGURE 2.21 – *Modélisation de l'émission radio du disque protoplanétaire autour de l'étoile HD 169142. Images adaptées de Pérez et al. (2019a).*

Avec mes collaborateurs à Santiago nous avons également travaillé sur la modélisation du disque protoplanétaire autour de l'étoile HD 169142, pour lequel mes collaborateurs ont obtenu des observations radio à très haute résolution angulaire via le radio-interféromètre ALMA, montrant les anneaux de poussières les plus fins observés dans un disque protoplanétaire à ce jour. En particulier, ce que l'on pensait être un seul anneau brillant dans la partie externe du disque s'est révélé être une séquence de trois anneaux fins brillants, entourant deux anneaux sombres. L'asymétrie dans la distance à l'étoile des trois anneaux brillants est précisément quelque chose que l'on attend de la structure en poussières générée par une planète migrant cette fois ci *lentement* dans son disque protoplanétaire. J'ai réalisé un grand nombre de simulations hydrodynamiques, post-traitées par des calculs de transfert radiatif dans la poussière, qui ont permis de proposer qu'une planète d'environ dix masses terrestres, migrant vers les parties internes de son disque, soit responsable des anneaux fins observés (cf. figure 2.21). Ces résultats ont été décrits dans Pérez et al. (2019a).

2.5 Interactions étoile-planète : évolution ultime des exoplanètes chaudes

Tandis que la formation et la migration des Jupiter chauds ont reçu une attention particulière, leur évolution à long terme par les interactions étoile-planète reste encore assez mal connue. Les découvertes récentes d'exoplanètes dotées d'un rayon physique large, ou d'une obliquité élevée (cf. figure 2.2), demandent de mieux comprendre les interactions de marée étoile-planète. Après dissipation du disque protoplanétaire, les effets de marée déterminent l'évolution finale de l'orbite d'une planète proche (migration orbitale, amortissement de l'excentricité et de l'inclinaison) ainsi que les périodes de rotation de l'étoile et de la planète. Par exemple, WASP-12b, un Jupiter chaud situé à environ 3 rayons stellaires de son étoile (Hebb et al. 2009, correspondant à une période orbitale $P_{\rm orb} \approx 1.1$ jours), présente des variations de périodicité de ses transits sur une dizaine d'années environ qui indiquent que la planète se rapproche de son étoile avec un taux de variation de sa période orbitale $dP_{\rm orb}/dt \sim 10^{-9}$ (Maciejewski et al. 2016), ce qui signifie que la planète sera disloquée par son étoile d'ici quelques centaines de milliers d'années. Il s'agit du reste du seul exemple de planète dont les variations de périodicité des transits indiquent nettement un déclin de la période orbitale (Patra et al. 2020).

Les interactions de marée entre deux corps (par exemple, une étoile et sa planète proche) se décomposent classiquement en deux effets (Ogilvie 2014). D'une part, la déformation à grande échelle et quasi hydrostatique de chaque corps par le potentiel gravitationnel de son compagnon. La dissipation interne d'énergie (ou de moment cinétique) associée à cette déformation s'appelle la *marée d'équilibre*. A cette déformation est également associée la propagation d'ondes, dont la nature dépend de la force de rappel s'opposant à la déformation. Lorsqu'il s'agit de la force de Coriolis, les ondes en question sont des ondes inertielles. Lorsque c'est la poussée d'Archimède liée à la stratification du corps, ce sont des ondes de gravité. Lorsque c'est le force de Lorentz, ce sont des ondes d'Alfvén. Lorsque ces forces agissent de concert, les ondes sont de nature mixte ; par exemple, des ondes magnéto-gravito-inertielles si les trois forces susmentionnées agissent ensemble. Ces ondes transportent de l'énergie et du moment cinétique, et leur dissipation s'appelle la *marée dynamique*. Bien que la marée dynamique dans les interactions de marée étoile-planète soit souvent estimée par un nombre unique sans dimension ("tidal quality factor"), toute la difficulté réside dans le fait qu'elle dépende de façon complexe des fréquences de rotation de la planète et de l'étoile, de leur distance mutuelle, et de leur structure interne incertaine (Ogilvie 2009, Rieutord & Valdettaro 2010).

Les travaux sur les interactions de marée ont jusqu'à très récemment considéré des planètes et des étoiles en rotation solide. Hors, de la rotation différentielle est observée dans l'enveloppe convective du Soleil par héliosismologie, en surface de certaines étoiles par photométrie, à l'intérieur d'étoiles géantes rouges par astérosismologie, et est prédite par les modèles d'intérieur stellaire et planétaire. Je m'intéresse à l'impact de la rotation différentielle sur la propagation et la dissipation d'ondes de marée dans les interactions de marée étoile-planète. C'est une thématique de recherche sur laquelle je travaille avec Michel Rieutord à l'IRAP et avec Stéphane Mathis du CEA Saclay. Dans un premier temps, j'ai examiné dans Baruteau & Rieutord (2013) les propriétés des modes propres inertiels dans un modèle simple de fluide en rotation différentielle (fluide visqueux, incompressible, homogène, en rotation cylindrique ou sphérique). Nous y avons montré que l'énergie des modes tend à se concentrer le long de cycles périodiques se propageant dans tout ou partie du fluide, comme dans une cavité résonante (cf. figure 2.22). Nous avons également étudié la situation communément observée où les périodes de rotation de l'étoile et la période orbitale de la planète sont presque synchronisées. Nous avons montré que cette situation conduit à la formation d'une résonance de corotation (où la fréquence de l'onde de marée vue du fluide s'annule) à l'intérieur de l'étoile, où la dissipation par effets de marée est particulièrement élevée. La présence d'une résonance de corotation peut également entraîner une instabilité dans l'enveloppe convective. Nous avons étendu cette première étude par les travaux de thèse de deux doctorants de 2013 à 2016 : Giovanni Mirouh (directeurs de thèse : Michel Rieutord et Jérôme Ballot) et Mathieu Guenel (directeur de thèse : Stéphane Mathis).

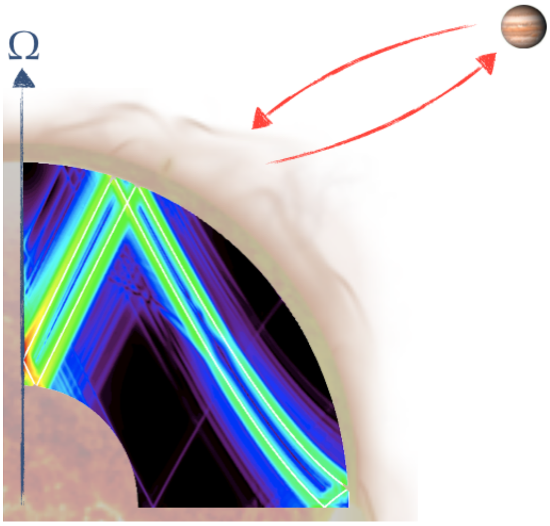

FIGURE 2.22 – *illustration schématique de l'excitation d'ondes inertielles à l'intérieur de l'enveloppe convective d'une étoile de faible masse par interaction de marée avec un Jupiter chaud. L'énergie cinétique du fluide est affichée dans une coupe méridienne d'une étoile en rotation différentielle, et s'accumule autour d'un cycle périodique (courbe blanche). Image adaptée de Baruteau & Rieutord (2013).*

Le travail de thèse de Giovanni Mirouh a examiné le cas des modes propres gravito-inertiels se propageant dans l'enveloppe radiative d'une étoile massive ou d'une planète en rotation différentielle sphérique (type de rotation différentielle permise par la stratification de l'enveloppe radiative et un choix approprié de conditions aux limites). Nous avons étudié les propriétés de propagation de ces modes par une étude semi-analytique

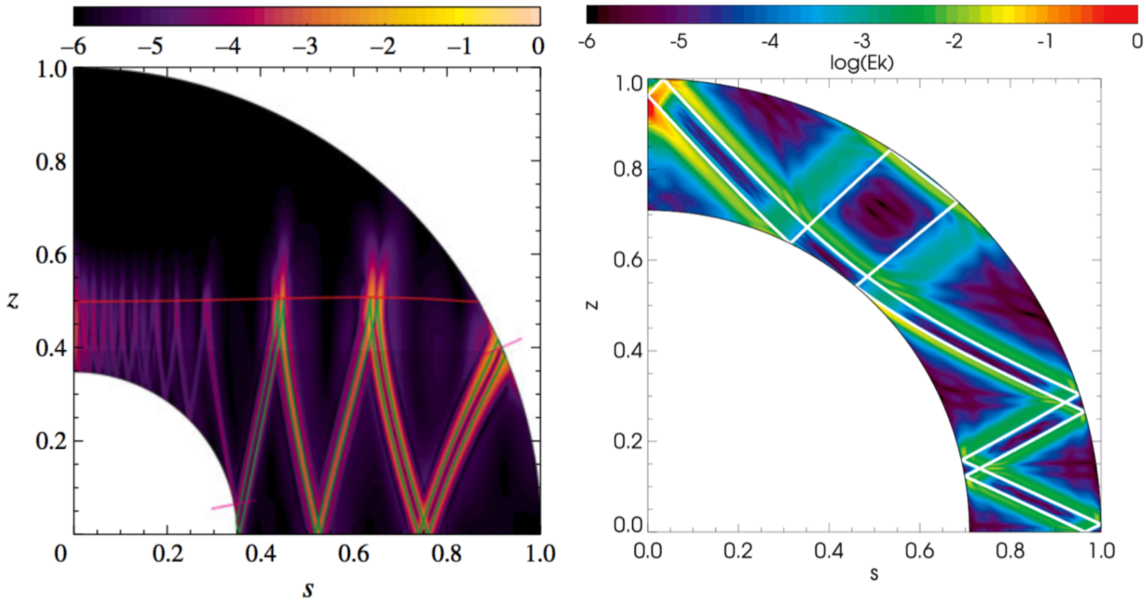

FIGURE 2.23 – *Gauche : énergie cinétique d'un mode propre gravito-inertiel dans l'enveloppe radiative d'une étoile massive en rotation différentielle sphérique (coupe méridienne ; image tirée de Mirouh et al. 2016). Droite : énergie cinétique d'une mode propre inertiel dans l'enveloppe convective d'une étoile de faible masse en rotation différentielle conique (tiré de Guenel et al. 2016b).*

de l'équation des caractéristiques dans l'approximation des courtes longueurs d'onde (WKB) et dans la limite d'un fluide sans dissipation (pas de viscosité turbulente ni diffusion thermique). Cela nous a permis d'établir l'existence de différentes classes de modes propres selon leur fréquence et la stratification du fluide (quantifiée par la fréquence de Brünt-Väisälä). Leur énergie peut se concentrer le long de cycles périodiques ou de résonances de corotation (comme pour les modes inertiels se propageant dans une enveloppe convective), ou bien se focaliser à l'interface entre deux surfaces où les ondes se réfléchissent (comportement différent des modes inertiels). Nous avons confirmé et étendu ces résultats par des simulations numériques utilisant un code spectral (cf. figure 2.23, image de gauche). Ces simulations nous ont permis en outre d'étudier la dissipation et la stabilité de ces différents types de modes propres envers les diverses instabilités hydrodynamiques attendues, et d'étudier leur comportement en fonction des propriétés dissipatives de l'enveloppe radiative (viscosité turbulente et diffusion thermique). C'est une étape importante pour rendre compte des oscillations de surface des étoiles massives observées par astérosismologie (qui nécessitent le développement de modes propres instables en surface de l'étoile), mais aussi pour comprendre l'évolution orbitale de planètes par interactions de marées étoile-planète (qui dépendent de la dissipation des modes propres excités). Les travaux de thèse de Giovanni sont décrits dans Mirouh et al. (2016).

Le travail de thèse de Mathieu Guenel a considéré le cas des modes propres inertiels se propageant dans l'enveloppe convective d'étoiles de faible masse (de type spectral M à F) ou de planètes géantes gazeuses similaires à Jupiter et Saturne. Nous avons examiné le cas d'une rotation différentielle conique (*i.e.* en latitude), inspirée des nombreuses simulations d'étoiles de faible masse ou encore du profil de rotation observée dans l'enveloppe convective solaire. Ici aussi, nous avons commencé par étudier les propriétés de propagation des modes propres d'oscillation par une étude semi-analytique de l'équation des caractéristiques dans l'approximation des courtes longueurs d'onde (WKB) et dans la limite d'un fluide sans dissipation. Nous avons trouvé que la rotation différentielle conique ne permet le développement de modes propres résonants que si ceux-ci se propagent dans l'intégralité de l'enveloppe convective, contrairement à ce que nous avions pu trouver pour des rotations différentielles cylindrique et sphérique dans Baruteau & Rieutord (2013). Là encore, ces résultats ont été confirmés et analysés par des simulations numériques utilisant un code spectral, permettant d'en étudier la dissipation et la stabilité en fonction de la viscosité turbulente de l'enveloppe convective (cf. figure 2.23, image de droite). Ces résultats sont décrits dans Guenel et al. (2016b).

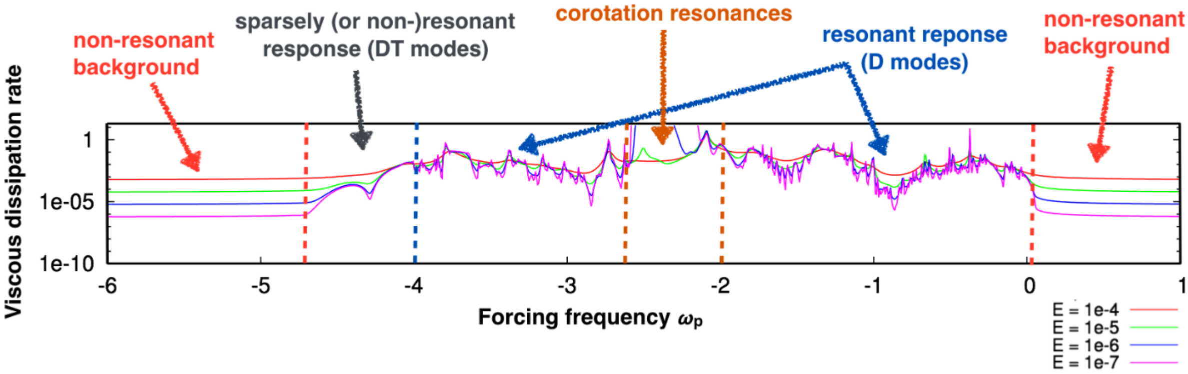

FIGURE 2.24 – *Dissipation visqueuse d'ondes inertielles de marée générées dans l'enveloppe convective d'une étoile de faible masse en rotation différentielle conique, pour différentes fréquences de forçage des ondes et pour différentes viscosités turbulentes de l'enveloppe convective (Guenel et al. 2016a).*

Dans la seconde partie de la thèse de Mathieu, nous avons commencé à étudier le comportement d'ondes inertielles forcées par un compagnon planétaire dans l'enveloppe convective d'une étoile de faible masse en rotation différentielle conique. Via des simulations numériques linéaires utilisant un code spectral, nous avons calculé l'énergie déposée par ces ondes en fonction de leur fréquence de forçage (cf. figure 2.24). Les fortes variations de la dissipation de marée en fonction de la fréquence de forçage (pics résonants et anti-résonants) indiquent que l'évolution orbitale par interactions de marée étoile-planète n'est sans doute pas un processus continu, mais opère par à-coups (p.e., Auclair-Desrotour et al. 2014). La présence d'une gamme assez large de fréquences où la dissipation de marée est grandement accrue par l'existence de résonances de corotation demande une étude spécifique pour mieux en comprendre l'origine physique. Ces résultats préliminaires ont été présentés dans un compte-rendu de conférence (Guenel et al. 2016a).

Cette étude va être poursuivie en collaboration avec Stéphane Mathis dans le cadre de la thèse d'Aurélie Astoul. Des résultats préliminaires ont déjà été obtenus au cours du stage de M2 d'Aurélie que j'ai co-encadré avec Stéphane Mathis. Au cours de son stage, Aurélie a étudié analytiquement la propagation d'ondes inertielles à travers une résonance de corotation due à une rotation différentielle conique. Ce travail a permis de mettre en exergue deux régimes de propagation : soit l'onde inertielle incidente dépose son flux d'énergie au fluide à la résonance et s'amortit, ou bien l'onde extrait de l'énergie du fluide à la résonance et s'amplifie, conduisant à une instabilité. Ces prédictions ont été illustrées par des résultats numériques préliminaires obtenus via un code spectral, qui seront poursuivis pendant la dernière année de thèse d'Aurélie.

La première partie de la thèse d'Aurélie s'est intéressée à l'impact du champ magnétique de l'étoile sur le forçage de marée d'ondes (magnéto-)inertielles dans l'enveloppe convective de l'étoile (supposée de faible masse). En l'absence de champ magnétique, c'est la force de Coriolis agissant sur la déformation à grande échelle du fluide (celle conduisant à la marée d'équilibre, comme on l'a vu plus haut) qui induit la propagation d'ondes inertielles dans l'enveloppe convective. En présence d'un champ magnétique, la force de Lorentz agissant sur cette déformation devrait également contribuer, et la question que nous nous sommes posés est de savoir si cette contribution est significative ou pas. Pour y répondre, Aurélie a estimé le rapport de ces deux contributions (Lorentz et Coriolis) pour différents âges et masses d'étoiles en utilisant des grilles de modèles stellaires obtenues par un code 1D d'évolution stellaire. Le champ magnétique à grande échelle générée dans l'enveloppe convective par effet dynamo a été estimé par des lois d'échelle. En appliquant ses prédictions aux exoplanètes détectées proches de leur étoile, Aurélie a montré que le champ magnétique stellaire a un impact relativement modéré sur le forçage d'ondes (magnéto-)inertielles dans l'enveloppe convective d'étoiles de faible masse, et de la pré-séquence principale à la fin de la séquence principale. Son travail a aussi permis de montrer que la dissipation ohmique devrait prévaloir sur la diffusion visqueuse quant à la dissipation de l'énergie transportée par les ondes. Ces résultats ont été décrits dans Astoul et al. (2019).

⋆⋆⋆

3 | Perspectives

Mes projets de recherche s'appuient sur les observations des planètes extrasolaires et des disques protoplanétaires afin d'améliorer notre compréhension de la formation et de l'évolution orbitale des systèmes planétaires. Concernant les systèmes planétaires jeunes, je propose d'avancer sur la détermination de la direction et de la vitesse de migration des planètes terrestres à la lueur des progrès récents des modèles d'évolution des disques protoplanétaires, qui suggèrent que l'accrétion dans les régions de formation planétaire est probablement davantage un processus laminaire que turbulent. Les progrès ainsi accomplis permettront d'améliorer les modèles de migration planétaire utilisés par les synthèses de population planétaire pour comparer les propriétés statistiques des exoplanètes à celles prédites par la théorie. Je compte en outre continuer les efforts entrepris dans le développement de modèles globaux de formation et d'évolution planétaires à partir de simulations hydrodynamiques de disques protoplanétaires.

Mes projets sur la dynamique et l'émission des disques protoplanétaires continueront de représenter une part importante de mes activités de recherche dans les prochaines années, toujours avec l'objectif de comprendre et de prédire les signatures de la présence de planètes dans l'émission du gaz et des poussières des disques protoplanétaires. Cette démarche est motivée par l'idée (ou peut-être l'espoir) que les observations de disques protoplanétaires permettront à l'avenir de contraindre les premières phases de la formation et de l'évolution planétaires, en complément donc des observations d'exoplanètes, qui donnent plutôt globalement une vision de l'arrivée à maturité des systèmes planétaires. Outre des projets bien ciblés, comme par exemple les signatures dans l'émission continue radio des poussières de l'instabilité gravitationnelle des disques jeunes et massifs, je propose des avancées en modélisation numérique, comme l'inclusion progressive des modèles d'évolution chimique à la dynamique du gaz et des poussières des disques, ou encore les modèles de diffusion de poussières dans les calculs de transfert radiatif.

Enfin, j'avancerai sur la compréhension des interactions entre les étoiles et leurs planètes proches à travers les différents stades de la vie de l'étoile, avec l'objectif d'interpréter les observations d'exoplanètes, comme par exemple les Jupiters chauds sous-denses ou en orbite rétrograde. Je propose des projets qui démarrent de la pré-séquence principale, avec la formation d'une cavité dans le disque protoplanétaire supposée arrêter la migration planétaire, continuent sur la séquence principale, où se pose notamment la question de l'efficacité des effets de marée étoile-planète à amortir l'obliquité orbitale des Jupiter chauds, et s'étendent au-delà de la séquence principale, avec l'évolution de planètes engouffrés dans l'enveloppe de gaz d'une étoile devenue géante rouge.

Sommaire

3.1 Evolution orbitale des systèmes planétaires jeunes

Cette section expose quelques projets dont l'objectif est d'améliorer notre compréhension de la migration des planètes en formation dans leur disque protoplanétaire. Je propose d'une part de revisiter la direction et la vitesse de migration des planètes terrestres dans des modèles réalistes de disques protoplanétaires turbulents et radiatifs. Je propose d'autre part de continuer les efforts initiés dans le développement de modèles globaux de formation et d'évolution planétaires à partir de simulations hydrodynamiques 2D d'interactions disque-planètes.

3.1.1 Migration des planètes terrestres

Comme on l'a vu au § 2.3, la migration planétaire résultant des interactions entre les planètes et leur disque protoplanétaire joue un rôle clé dans l'architecture des systèmes planétaires. Le problème majeur que rencontrait encore récemment la migration planétaire était de prédire la migration des planètes terrestres vers leur étoile en un temps très court, ce qui pendant longtemps a rendu les prédictions des modèles de formation et d'évolution planétaires incompatibles avec les observations (Ida & Lin 2008, Mordasini et al. 2009). On a vu qu'une solution possible à ce problème invoque les propriétés radiatives des disques protoplanétaires. En exacerbant le couple de corotation ressenti par la planète, les propriétés radiatives du disque peuvent en effet non seulement ralentir la migration des planètes terrestres (migration de type I), elles peuvent aussi l'arrêter, voire conduire les planètes à migrer vers les parties externes des disques (Baruteau & Masset 2008a, Paardekooper & Papaloizou 2008, Kley & Crida 2008, Masset & Casoli 2009, Paardekooper et al. 2010). Ce mécanisme prometteur est particulièrement adapté aux régions internes de formation planétaire (jusqu'à $\sim$10 ua d'une étoile de type solaire), où les planètes se forment par accrétion de cœur. Cependant, l'amplitude du couple de corotation est intimement liée à la viscosité du disque (Masset & Casoli 2010, Paardekooper et al. 2011a), qui est une représentation très courante, mais incertaine, de la turbulence dans les disques.

Des progrès importants ont été réalisés ces dernières années sur la compréhension de l'évolution dynamique des disques protoplanétaires, et en particulier le niveau de turbulence prédit dans les différentes parties des disques. On pensait encore récemment que l'évolution des disques était principalement régie par le transport radial turbulent de masse (ou de moment cinétique) via la turbulence magnéto-hydrodynamique (MHD) résultant de l'instabilité magnéto-rotationelle (MRI). Cette instabilité requiert, en plus d'un champ magnétique faible, un taux d'ionisation du gaz suffisamment élevé pour que la turbulence MHD se répercute au gaz essentiellement neutre des disques (p.e., Balbus & Hawley 1991). Hors il s'avère que le taux d'ionisation des disques n'est pas si élevé qu'on le pensait. Dans les parties denses et froides près du plan médian des disques, la diffusion ohmique, qui résulte des collisions entre électrons et neutres, empêche le développement de la MRI (Gammie 1996). Par ailleurs, on s'est aperçu ces dernières années que d'autres effets dits de MHD non-idéale agissaient notablement sur le taux d'ionisation du disque. Il s'agit de la diffusion ambipolaire ou encore de l'effet Hall, qui rendent pratiquement tout le disque inerte à la MRI. Ces résultats ont permis de proposer un nouveau paradigme de l'évolution des disques, cette fois ci dominée par le transport vertical de moment cinétique via des vents magnétiques se développant à la surface des disques (par accélération magnéto-centrifuge), et conduisant à une accrétion essentiellement laminaire du gaz en direction de l'étoile, à l'exception près des parties les plus centrales des disques, suffisamment chaudes pour que l'ionisation du gaz permette un transport turbulent par la MRI (voir, p.e., Bai 2013, Simon et al. 2013, Lesur et al. 2014, et l'illustration à la figure 3.1).

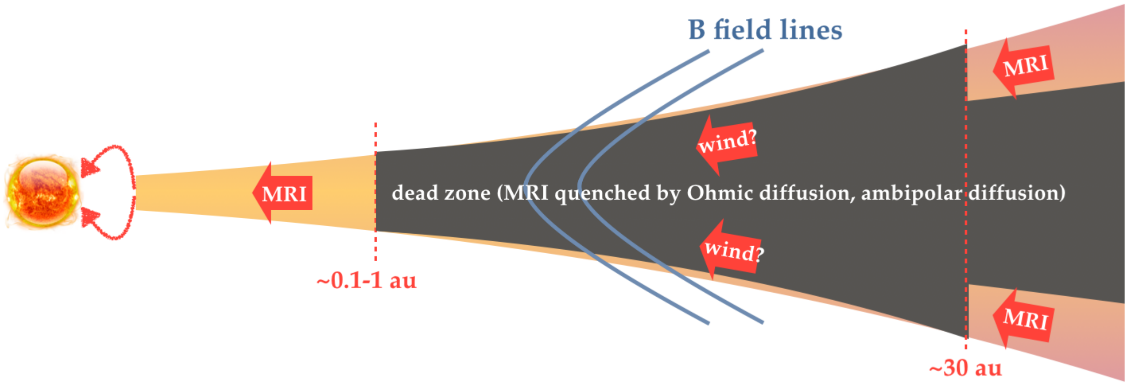

FIGURE 3.1 – *Structure schématique d'un disque protoplanétaire, montrant la position des régions turbulentes où se développe l'instabilité magnéto-rotationnelle (MRI), et des régions non turbulentes ("dead zone") où une accrétion laminaire vers l'étoile peut résulter de vents magnétiques éjectés à la surface du disque.*

Cette nouvelle vision de l'évolution des disques requiert d'en tester l'impact sur les scénarios d'évolution orbitale des planètes. Je propose de revisiter les propriétés de la migration des planètes terrestres par des simulations 3D MHD d'interactions disque-planète. L'équation d'énergie du disque sera incluse. Le code MHD Nirvana, que j'ai implémenté et utilisé de manière intensive (Baruteau et al. 2011b, Guilet et al. 2013), ou bien le code Fargo3D, successeur du code 2D Fargo, conviendraient parfaitement à cette tâche. Bien qu'ambitieuses, ces simulations sont déjà réalisables avec les supercalculateurs actuels. Les questions clés auxquelles je répondrai sont de savoir (i) si la turbulence dans les régions internes des disques protoplanétaires peut maintenir un couple de corotation suffisamment large pour ralentir ou renverser la migration de type I, et (ii) quel est l'impact d'une accrétion laminaire dans les parties non turbulentes des disques sur la migration de type I.

3.1.2 Modèles globaux de formation et d'évolution planétaires

Comparer les propriétés statistiques des exoplanètes (distributions de leur masse, période orbitale, excentricité...) avec celles prédites par les modèles de formation et d'évolution planétaires est essentiel pour améliorer les modèles théoriques, pour faire des prédictions pouvant être testées par les futures observations, et pour parvenir à comprendre la diversité des exoplanètes. C'est ce que permettent les synthèses de population planétaire qui, par des simulations de type Monte-Carlo, prédisent de manière statistique l'architecture des systèmes planétaires. Elles combinent des modèles 1D de formation, d'évolution interne et orbitale des planètes, de la structure et de l'évolution des disques protoplanétaires. Bien que l'utilisation de modèles 1D ne puisse rendre compte de toute la complexité des processus physiques mis en jeu, c'est ce qui constitue la force des synthèses de population : elles sont le seul outil permettant actuellement de comparer de manière statistique les propriétés des exoplanètes avec les prédictions théoriques. Cette comparaison est cependant délicate car elle mêle de nombreux mécanismes physiques, parfois incertains, et pour lesquels il existe encore peu de contraintes observationnelles.

L'un de mes projets de recherche à long terme, que nous avons commencé à développer en collaboration avec Yann Alibert à l'Université de Berne (Suisse), consiste à concevoir et réaliser des synthèses de population planétaire par des simulations hydrodynamiques 2D de l'évolution des disques protoplanétaires et des interactions disque-planètes, combinées à des modèles de croissance planétaire. Modéliser l'évolution d'un disque protoplanétaire en 2D sur sa durée de vie de plusieurs millions d'années est un défi numérique qui nécessitera sur le long terme l'utilisation de clusters de processeurs graphiques (GPUs). Pour le moment, nous utilisons des clusters de processeurs classiques (CPUs), sur lesquels de telles simulations requièrent typiquement plusieurs semaines de calcul. Plutôt que des synthèses de population, nous concevons donc pour le moment des modèles globaux de formation et d'évolution planétaires en 2D. Le bénéfice principal est de pouvoir modéliser précisément la migration planétaire ainsi que les interactions planète-planète, sans avoir recours à des formulations analytiques 1D approximatives et dont le domaine de validité est très limité.

Pour notre projet nous avons couplé le code hydrodynamique public Fargo-ADSG, qui modélise l'évolution d'un disque protoplanétaire en 2D ainsi que l'évolution orbitale de planètes, avec le code de formation planétaire développé à Berne par Yann Alibert et son équipe, qui modélise la croissance et l'évolution interne des planètes en 1D. Ce couplage est possible en pratique parce que les temps caractéristiques de croissance planétaire sont beaucoup plus longs que le pas de temps hydrodynamique d'une simulation de disque protoplanétaire en 2D. Après y avoir moi-même contribué initialement, ce couplage a été rendu effectif, testé et validé par Sareh Ataiee, chercheuse post-doctorante à Berne de 2015 à 2018. Ce couplage a nécessité de nombreuses modifications et implémentations dans le code Fargo-ADSG, comme par exemple la prise en compte de la photo-évaporation du disque par l'irradiation de l'étoile, ou la gestion des conditions aux limites pour permettre aux simulations de tourner sur des échelles de temps sur lesquelles le code n'avait jusqu'à présent jamais été utilisé. Toutes ces étapes ont demandé un temps conséquent et nous sommes encore au stade de résultats préliminaires, tant les simulations demandent du temps de calcul. Un exemple de résultat de nos modèles 2D globaux est montré à la figure 3.2, et comparé au résultat d'un modèle purement 1D. Pour ces modèles, le taux d'accrétion de solides sur la planète a été supposé constant. Nous pourrons étendre ces résultats en incluant un taux de croissance donné par les modèles de *pebble accretion*.

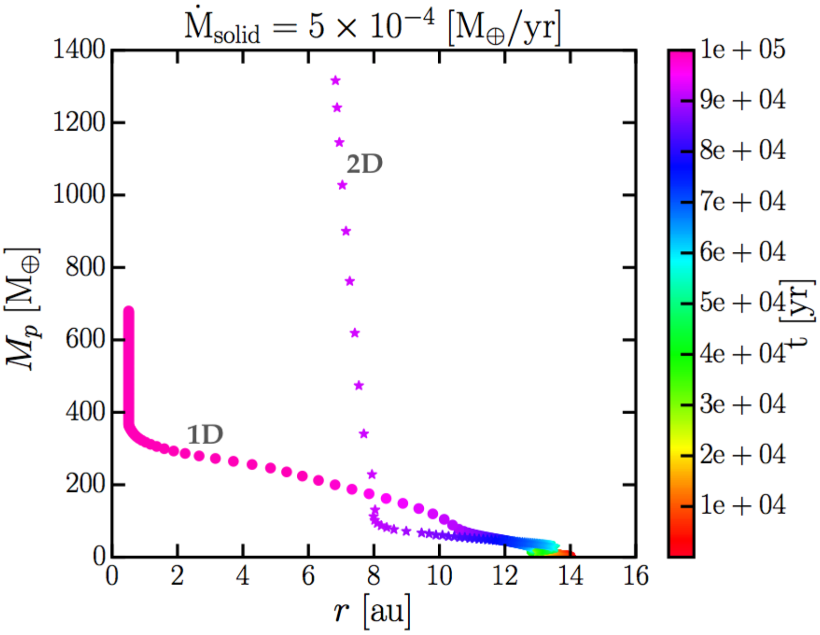

FIGURE 3.2 – *Évolution temporelle de la masse et du rayon orbital d'une planète dans un modèle global de croissance et d'évolution planétaires obtenu par une simulation hydrodynamique 2D (étoiles), et dans un modèle purement 1D utilisant des formulations analytiques approximatives pour la migration planétaire et l'évolution du disque (cercles). Les deux modèles sont en bon accord jusqu'à des masses de planète de quelques dizaines de masse terrestre, et divergent très nettement au-delà. Figure réalisée par Sareh Ataiee.*

Quelques questions clés qui seront abordées :

- Dans quelle direction et avec quelle vitesse les planètes terrestres migrent-elles dans leur disque protoplanétaire ? Quel est l'impact de la turbulence du disque ?
- Les progrès récents sur la migration des planètes terrestres peuvent-ils réconcilier observations et prédictions théoriques de l'architecture des systèmes exoplanétaires ?
- Les simulations hydrodynamiques d'interaction disque-planètes amélioreront considérablement les modèles globaux de croissance et d'évolution planétaires. Quelles prédictions donneront-ils ?

3.2 Dynamique et émission des disques protoplanétaires

Une part importante de mes travaux de recherche sur les prochaines années sera dans la continuité de mes activités de modélisation des poussières et du gaz des disques protoplanétaires, toujours avec l'objectif de prédire les signatures de la présence et de l'évolution de planètes en formation dans l'émission de leur disque. Je liste ci-dessous un certain nombre de projets ou d'idées concernant cet axe de recherche.

3.2.1 Signatures de la migration planétaire dans l'émission des disques

Nous avons présenté au § 2.4.2 les travaux de thèse en cours de Gaylor Wafflard-Fernandez sur un scénario de formation d'anneaux multiples sombres et brillants dans l'émission du continuum radio des disques par la migration d'une seule planète massive dans un disque assez massif. Ce travail pourra être poursuivi de plusieurs façons. Dans le scénario mentionné, nous nous sommes rendus compte que la position radiale (r) des anneaux brillants dans nos calculs de transfert radiatif suivait une loi de puissance (en $r^{[1.4-1.5]}$), hors c'est aussi ce qu'on constate dans la position radiale des anneaux brillants de plusieurs disques observés avec ALMA (qui plus est, avec une loi de puissance dont l'exposant est très similaire à celui de nos modèles). Nous pourrons donc chercher à appliquer les prédictions de notre scénario afin de rendre compte de l'émission radio observée de ces disques, via des calculs de transfert radiatif dans la poussière à partir de simulations hydrodynamiques gaz+poussières.

Par ailleurs, il serait intéressant de prédire les signatures observationnelles de ce scénario dans l'émission du gaz des disques protoplanétaires. On s'attend en particulier à des *signatures cinématiques* dans le gaz très différentes selon que les anneaux sombres d'un disque résultent de la migration d'une seule planète massive ayant atteint les parties internes du disque, ou bien que chaque anneau sombre soit dû à une planète ouvrant un sillon autour de son orbite. Ce projet nécessitera l'extension du programme fargo2radmc3d afin de calculer des cartes synthétiques de l'émission du gaz (par exemple, ^{12}CO, ^{13}CO ou C^{18}O) à partir des résultats de nos simulations hydrodynamiques gaz+poussières.

Enfin, suite à la visite de Gaylor et moi à la UNAM (Cuernavaca, Mexique) en Mai 2019 pour y rencontrer mon directeur de thèse, Frédéric Masset, nous avons commencé à étudier d'autres pistes de projets, notamment (i) les signatures dans l'émission de la poussière de la migration d'une planète excentrique, ou encore (ii) la présence d'une accrétion radiale laminaire (et non turbulente) du gaz induite par des vents magnétiques en surface du disque, et son impact sur la migration planétaire ainsi que sur la dynamique et l'émission des poussières du disque.

3.2.2 Émission radio des disques instables par instabilité gravitationnelle

A l'occasion du stage de M1 de Ghania Medjdoub en 2015, je m'étais intéressé à l'émission continue en radio des poussières d'un disque protoplanétaire jeune et massif instable par l'instabilité gravitationnelle. Cet intérêt faisait écho aux premières observations d'ALMA du disque protoplanétaire autour d'HL Tau (ALMA Partnership et al. 2015), où des études antérieures avaient suggéré que le disque soit gravitationnellement instable. Il était donc assez surprenant de voir que le disque soit constitué d'anneaux sombres et brillants relativement concentriques en émission radio, sans signe distinctif évident d'instabilité gravitationnelle (pas de fragments ni spirales). Une des simulations gaz+poussières que nous avons réalisées d'un disque instable par instabilité gravitationnelle (mais sans fragmentation du gaz) montrait notamment la formation initiale de spirales dans les poussières de taille de l'ordre du millimètre, spirales qui seraient donc visibles en émission radio, mais que progressivement ces poussières finissaient par former des anneaux plus ou moins axisymétriques autour de l'étoile (cf. figure 3.3). Je n'ai pas eu l'opportunité de finaliser ce projet, et j'aimerais trouver le temps de le faire à court ou moyen terme. Cela nécessitera de mieux comprendre l'évolution dynamique des poussières en présence de spirales (chocs) dans le gaz induites par l'instabilité gravitationnelle.

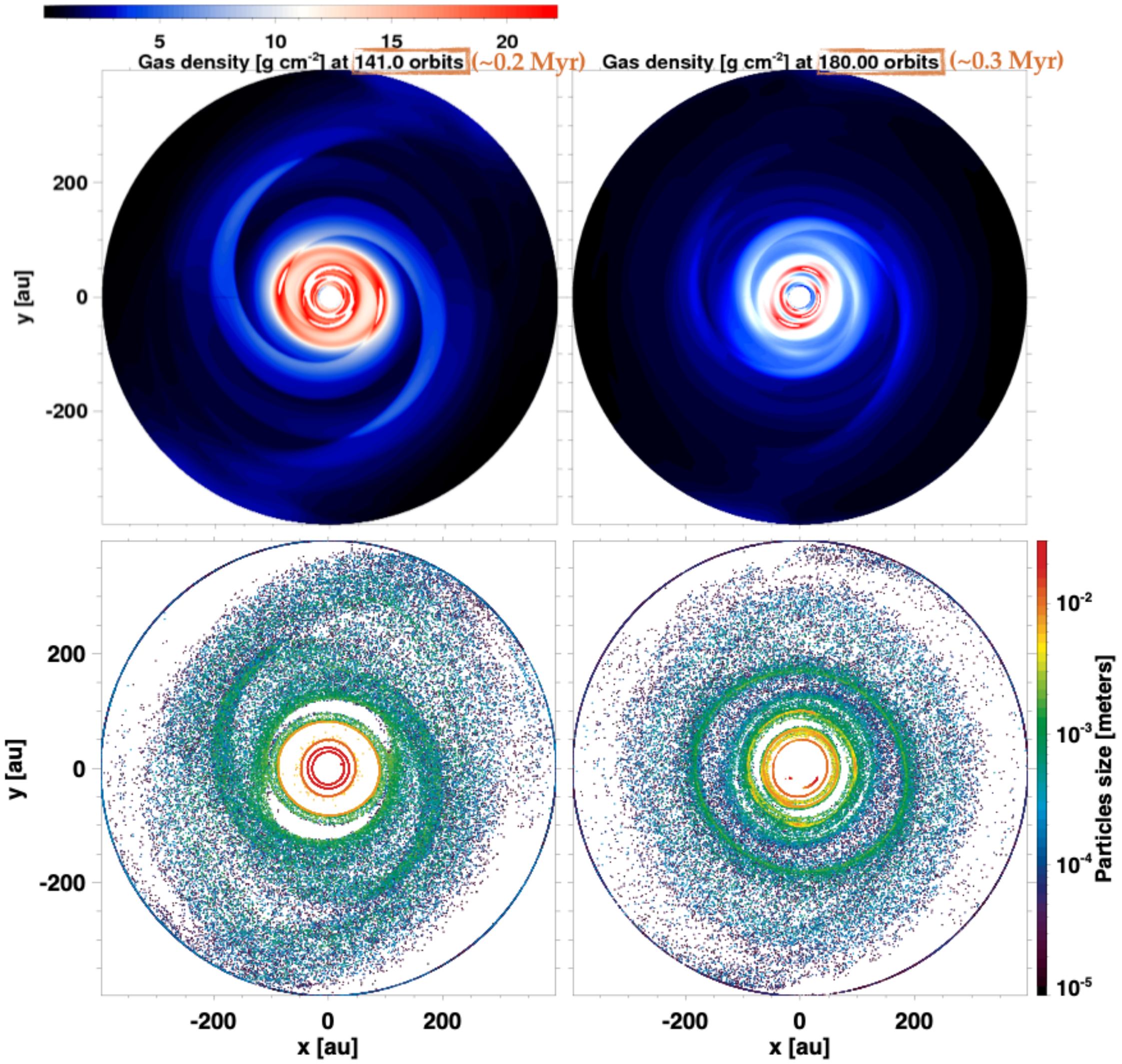

FIGURE 3.3 – *Résultats d'une simulation hydrodynamique modélisant le gaz (haut) et les poussières (bas) d'un disque protoplanétaire jeune et massif instable par instabilité gravitationnelle. Si les particules solides de taille de l'ordre du millimètre (en vert) tendent à suivre les grandes spirales du gaz au début de la simulation (gauche), elles finissent par former des anneaux concentriques et plus ou moins axisymétriques (droite).*

3.2.3 Vers des simulations 3D de la dynamique des disques

Comme nous l'avons rappelé au début du § 2.4, une modélisation 2D (rayon et azimuth en coordonnées cylindriques polaires) de la dynamique du gaz et des poussières des disques protoplanétaires est, a priori, une bonne approximation pour prédire l'émission radio des disques, car les poussières qui émettent le plus en radio, de taille (sub-)millimétrique, se situent près du plan équatorial des disques. Cela n'est plus le cas, en revanche, pour les poussières (sub-)micrométriques qui émettent ou diffusent le rayonnement en proche-infrarouge, et qui se situent dans les parties superficielles des disques par l'action de la viscosité turbulente. La modélisation de leur dynamique doit donc passer par des simulations hydrodynamiques 3D. Je compte utiliser pour cela le code Fargo3D, qui est le successeur de la version 2D de Fargo dont j'ai contribué au développement, et qui permet également la modélisation de poussières de différentes tailles. Il sera relativement facile d'étendre le programme fargo2radmc3d afin de calculer des cartes synthétiques de l'émission continue des poussières et de la lumière diffusée polarisée via le code public de transfert radiatif RADMC3D à partir des résultats de simulations hydrodynamiques gaz+poussières qui seront réalisées avec Fargo3D.

Je compte ainsi revisiter les modèles d'interactions disque-planète(s) que j'ai élaborés ces dernières années à la lumière de telles simulations 3D, non seulement pour voir les différences saillantes par rapport à des simulations 2D pour l'émission continue radio des poussières, mais aussi pour prédire plus précisément les signatures des poussières en proche-infrarouge. J'examinerai notamment le cas où une planète forme un vortex par instabilité de Rossby au bord externe de son sillon (cf. § 2.4.1), pour tester l'observabilité de spirales dues à la planète dans la lumière diffusée polarisée en proche-infrarouge. Dans le même ordre d'idée, dans le cadre de la fin de thèse de Gaylor Wafflard-Fernandez, nous pourrons revisiter le modèle de formation d'anneaux multiples de poussières par la migration d'une planète massive afin d'étudier les signatures d'un tel scénario dans l'émission proche-infrarouge des disques.

Par ailleurs, les résultats des simulations que nous avons présentés jusqu'ici ont considéré la friction du gaz sur les poussières, mais ont négligé la friction des poussières sur le gaz. Cette approximation est valide lorsque le rapport de masse entre poussières (solides) et gaz reste localement faible dans le disque, mais elle est peut être légitimement questionnée lorsque l'on s'intéresse au piégeage et/ou à la croissance des poussières dans des structures assez confinées comme des anneaux ou des vortex (Crnkovic-Rubsamen et al. 2015, Gonzalez et al. 2017). La friction des poussières sur le gaz est déjà implémentée dans le code Fargo3D, et pourra l'être dans Fargo-ADSG.

3.2.4 Couplage de la dynamique et des modèles d'évolution chimique des disques

Les observations de disques protoplanétaires montrent que l'émission continue des poussières et celle du gaz peuvent présenter des structures bien différentes, en particulier l'émission de différents traceurs du gaz (CO, HCO^+, HCN etc.). Cela montre que la chimie des molécules joue un rôle clé dans l'émission observée du gaz des disques protoplanétaires. Aussi, un projet que j'aimerais initier dans les prochaines années est celui du couplage entre les simulations hydrodynamiques gaz+poussières des disques et les modèles d'évolution chimique, avec l'objectif d'étudier les signatures chimiques observationnelles des planètes dans les disques. Je suis en contact avec Romane Le Gal, chercheuse post-doctorante au CfA/Harvard, pour ce projet. Nous pourrons démarrer par une approche simple, où la chimie n'a pas de rétroaction sur la dynamique, puis examiner par la suite les stratégies numériques possibles pour prendre en compte cette rétroaction.

3.2.5 Modèles de diffusion des poussières dans les calculs de transfert radiatif

On a vu à plusieurs reprises que l'interprétation de l'émission du continuum des disques protoplanétaires passait par des calculs de transfert radiatif à partir d'une modélisation dynamique de la poussière (par exemple, via des simulations hydrodynamiques gaz+poussières). Ceux-ci comportent de nombreux paramètres libres relatifs aux poussières du disque, dont les plus cruciaux sont (i) la distribution de taille, (ii) la porosité (ou densité interne de masse) et (iii) la composition (p.e., silicates, glaces d'eau...) qui influe sur les opacités d'absorption et de diffusion. Ces propriétés sont mal connues dans les disques protoplanétaires et souvent choisies de façon ad hoc. En particulier, les modèles de disques supposent souvent des particules solides compactes, avec une densité interne de masse de quelques g cm^{-3}.

De façon intéressante, le modèle de disque que nous avons présenté dans Baruteau et al. (2019) peut d'autant mieux expliquer les observations multi-longueurs d'onde radio du disque autour de MWC 758 que si l'on suppose les particules solides modérément poreuses, avec une densité interne de masse de l'ordre de 0.1 g cm^{-3} pour des solides de taille comprise entre quelques centaines de μm et le cm. Cette densité s'avère correspondre à celle déterminée par Rosetta pour les particules solides provenant de la comète 67P les plus poreuses dans cette gamme de tailles. Ce type de comparaison suggère que l'étude des propriétés physiques des particules cométaires peut grandement contraindre les modèles de disques protoplanétaires.

Dans ce contexte, nous avons initié en 2019 une collaboration avec Jérémie Lasue (IRAP) et Anny-Chantal Levasseur-Regourd (LATMOS), tous deux spécialistes des comètes du Système Solaire, afin d'étudier ce que les propriétés physiques des poussières cométaires peuvent nous apprendre sur la modélisation de l'émission des poussières des disques protoplanétaires (Levasseur-Regourd et al. 2020). En particulier, les calculs de transfert radiatif que j'ai réalisés dans mes publications récentes incluent une diffusion lumineuse anisotrope par les particules solides du disque, via une fonction de phase, dite de Henyey-Greenstein, qui est classiquement utilisée dans les calculs de transfert radiatif dans les disques. Cependant, cette fonction de phase ne présente pas de rétro-diffusion, ce qui est en désaccord avec les fonctions de phase cométaires observées, qui s'avèrent présenter une structure de rétro-diffusion et de diffusion vers l'avant. Il semble donc pertinent d'introduire une partie de rétro-diffusion par les poussières des disques dans les calculs de transfert radiatif. C'est l'une des tâches que nous avons initiées sur ce projet. J'ai implémenté plusieurs fonctions de phase cométaires dans le code de transfert radiatif RADMC3D, et ai testé leurs effets sur notre modèle de disque de MWC 758. Nos efforts préliminaires doivent être poursuivis par une exploration de l'espace des paramètres, notamment la longueur d'onde d'émission (vers le proche IR) et la distribution de taille des poussières.

Quelques questions clés qui seront abordées :

- Quelles sont les signatures de la présence et de l'évolution de planètes dans l'émission du gaz et des poussières des disques protoplanétaires ?
- Comment la chimie des molécules affecte-t-elle la dynamique et l'émission des disques protoplanétaires ?
- A part en proche-infrarouge, la diffusion lumineuse par les poussières joue-t-elle un rôle clé dans l'émission observée des disques protoplanétaires ?

3.3 Interactions étoile-disque-planète et l'évolution des Jupiter chauds

Les observations de Jupiters chauds d'obliquité orbitale élevée et/ou sous-denses, et de planètes autour d'étoiles évoluées, ont permis de réaliser que la physique stellaire pouvait jouer un rôle clé dans l'évolution des exoplanètes proches de leur étoile. Dans ce cadre, je continuerai mes activités de recherche sur les interactions étoile-planète dans trois directions : (i) étudier l'impact de la variabilité magnétique de l'étoile sur les régions internes des disques protoplanétaires et ses implications sur l'arrêt de la migration planétaire, (ii) étendre l'estimation de l'efficacité des effets de marée étoile-planète aux planètes excentriques et/ou inclinées, et (iii) examiner le devenir d'une planète immergée dans l'enveloppe de gaz d'une étoile géante rouge.

3.3.1 Arrêt de la migration planétaire près de l'étoile

Le champ magnétique d'une étoile jeune tend à creuser une cavité de quelques rayons stellaires dans le disque protoplanétaire l'entourant. La présence de cette cavité arrête naturellement la migration planétaire (plus de gaz, plus de migration) et pourrait expliquer le nombre élevé de Jupiter chauds orbitant leur étoile entre 1 et 5 jours. Cependant, si, comme nous le montrent les simulations numériques et les observations, le champ magnétique des étoiles jeunes varie au cours du temps, par exemple sous forme de cycles magnétiques comme pour le Soleil actuel, la cavité pourrait se remplir et se vider périodiquement, avec des implications inconnues sur l'évolution orbitale de planètes parvenues à proximité de la cavité. Ce projet de recherche, que nous avons conçu à l'IRAP avec Laurène Jouve, spécialiste des simulations MHD des étoiles, et Jean-François Donati, spécialiste des observations spectro-polarimétriques des étoiles, sera conduit par Florian Debras, chercheur postdoctorant à l'IRAP. Ce projet a déjà bénéficié du travail de deux stagiaires de M2 en 2016 et 2017.

Le travail déjà effectué sur ce projet a opté pour une modélisation simplifiée du problème, où le disque protoplanétaire est considéré comme un disque d'accrétion 1D, dont l'évolution s'effectue par le couple visqueux modélisant les effets de transport turbulent de matière dans le disque d'une part, et par le couple exercé par le champ magnétique de l'étoile d'autre part. Le champ magnétique interagissant avec le disque est obtenu par extrapolation potentielle du champ magnétique à la surface de l'étoile. Pour modéliser le champ magnétique variable de l'étoile, nous avons utilisé un code magnéto-hydrodynamique simulant l'évolution du champ magnétique d'une étoile jeune par effet dynamo pour un champ de vitesse de l'étoile prescrit.

Le travail de nos stagiaires a ainsi permis d'étudier l'impact d'un grand nombre de paramètres modélisant l'intérieur d'une étoile (profil de vitesse, période de rotation, résistivité magnétique, viscosité turbulente etc.) sur la génération de cycles magnétiques par effet dynamo. Par exemple, nous avons pu établir que le profil de rotation différentielle modifiait fortement la symétrie privilégiée du champ magnétique par rapport au plan équatorial de l'étoile, avec de potentielles fortes implications sur sa connexion avec le disque protoplanétaire. Leur travail a aussi permis d'examiner dans quelles conditions le champ magnétique variable de l'étoile peut entraîner une variabilité significative du profil de densité de surface dans la cavité du disque. Nous avons modélisé enfin la migration planétaire par des prescriptions analytiques (dont j'ai contribué à l'établissement dans Paardekooper et al. 2010; 2011a) pour étudier l'impact de la variabilité du profil de densité du disque sur la migration d'une planète dans ou proche de la cavité, mais cette partie du projet est encore peu aboutie et bénéficiera de l'investissement de Florian Debras dans le projet. Une extension prévue de ce projet est de passer par des simulations 2D, voire 3D MHD d'un disque protoplanétaire sujet au couple magnétique variable de l'étoile, qui permettraient de modéliser directement la migration planétaire sans avoir recours à des prescriptions analytiques.

3.3.2 Effets de marée étoile-planète

Si les interactions disque-planète et planète-planète ont reçu une attention particulière pour expliquer les détections des Jupiters chauds, leur évolution ultime est déterminée par les interactions avec leur étoile proche. La découverte d'exoplanètes avec un rayon physique large, ou sur une orbite très inclinée, parfois rétrograde, demande une meilleur compréhension des interactions de marée entre étoiles et planètes (Winn et al. 2010). Leur efficacité est intimement liée à la propagation et à la dissipation d'ondes de marée que l'étoile génère dans la planète, et vice versa (cf. § 2.5). C'est un problème qui dépend de façon complexe des fréquences de rotation de la planète et de l'étoile, de leur distance mutuelle, et de leur structure interne incertaine (Ogilvie & Lin 2004, Goodman & Lackner 2009, Rieutord & Valdettaro 2010). Les études sur les interactions de marée étoile-planète ont jusqu'à présent considéré des planètes d'excentricité et d'inclinaison nulles, et ont modélisé de façon très simplifiée les intérieurs stellaires et planétaires, négligeant des mécanismes physiques importants tels que la rotation différentielle, la turbulence dans les régions convectives (dont les effets sont représentés par une viscosité constante) ou l'évolution non-linéaire des ondes de marée. Je propose de progresser dans la compréhension des effets de marée étoile-planète en suivant deux orientations.

La première orientation est de déterminer l'efficacité des effets de marée pour des planètes en orbite excentrique et/ou inclinée. Je propose pour cela de calculer la réponse linéaire en fréquence d'une planète au forçage de marée de l'étoile, et la réponse de l'étoile au forçage de la planète. Pour cela, différentes harmoniques sphériques seront utilisées dans l'expression du potentiel de marée. Ces calculs seront réalisés avec le même code spectral que celui que nous avons utilisé pour étudier l'impact de la rotation différentielle sur la propagation et la dissipation des ondes de marée (gravito-)inertielles (Baruteau & Rieutord 2013, Mirouh et al. 2016, Guenel et al. 2016b).

La seconde orientation est de réaliser des simulations hydrodynamiques non-linéaires d'interactions de marée étoile-planète, dans le sillage de l'étude que nous avons réalisée dans Favier et al. (2014), dans laquelle nous avons trouvé que le développement de vent zonaux résultant de l'évolution non-linéaire des ondes inertielles de marée affectait significativement la dissipation de ces ondes par rapport au cas standard où les non-linéarités ne sont pas prises en compte dans les simulations. Je propose de poursuivre dans cette voie en étudiant l'impact de deux effets non-linéaires importants sur l'efficacité des interactions de marée. D'une part, l'évolution non-linéaire des ondes inertielles de marée sera simulée pour des couples étoile-planète proches de la rotation synchronisée. Ce projet s'inscrit dans la suite de l'étude linéaire de Baruteau & Rieutord (2013), où nous avons montré que la présence d'une résonance de corotation pour ce type de systèmes peut considérablement augmenter la dissipation des ondes inertielles de marée (cf. § 2.5). D'autre part, je propose d'examiner l'impact de la turbulence convective sur la propagation et la dissipation des ondes de marée inertielles. On pourra commencer par traiter le cas plus simple où la convection est de faible amplitude, et modélisée dans l'approximation dite de Boussinesq. L'objectif est de déterminer dans quelle mesure la convection affecte la propagation et la dissipation des ondes inertielles. Cette problématique est très analogue à celle de l'impact de la turbulence sur les ondes qu'une planète génère dans son disque protoplanétaire (cf. § 2.3.1). Ces projets pourront utiliser par exemple le code PARODY, comme dans Favier et al. (2014).

Ces différents projets ont pour objectif d'améliorer notre compréhension des mécanismes de marée qui déterminent l'évolution à long terme des exoplanètes proches de leur étoile. Ils étudieront dans quelle mesure les effets de marée peuvent rendre compte des observations de planètes dotées d'un rayon physique anormalement élevé ou d'un orbite très inclinée.

3.3.3 Au-delà de la séquence principale : planètes engouffrées par leur étoile

Le troisième volet de cet axe de recherche sur les interactions étoile-disque-planète portera sur les étoiles au-delà de la séquence principale. Le nombre croissant d'exoplanètes détectées autour de telles étoiles, notamment des étoiles de la branche horizontale du diagramme HR (Charpinet et al. 2011), a ouvert un nouveau domaine de recherche sur l'évolution planétaire en posant la question du devenir d'une planète lorsque son étoile devient une étoile géante rouge (ce scénario se produira dans le Système Solaire dans environ cinq milliards d'années). L'interaction entre la planète et l'enveloppe de gaz de l'étoile géante rouge devrait conduire la planète à migrer à l'intérieur de l'enveloppe, par analogie avec les interactions disque-planète. Un mécanisme analogue a été étudié pour l'évolution d'étoiles binaires baignant dans une enveloppe commune de gaz (Taam & Sandquist 2000). Dans le cas des planètes, les interactions avec l'enveloppe d'une étoile géante rouge ont été jusqu'ici modélisées analytiquement par une prescription simple mais incertaine de friction dynamique (Villaver & Livio 2009). Je propose de réaliser des simulations hydrodynamiques explorant le devenir d'une planète engouffrée dans une géante rouge. Un code hydrodynamique à résolution variable et adapté au traitement des chocs dans les fluides sera utilisé pour ce projet, comme par exemple le code public ATHENA.

Les questions auxquelles je compte répondre sur ce projet sont (i) de savoir dans quelles conditions une planète peut survivre à son immersion dans l'enveloppe d'une étoile géante rouge, et (ii) de déterminer la distribution des masses et périodes orbitales des planètes orbitant une étoile post-géante rouge. Ces résultats aideront à interpréter les signatures observationnelles de planètes autour d'étoiles sous-naines de type spectral B ("subdwarf B stars", Charpinet et al. 2011).

Quelques questions clés qui seront abordées :

- Comment l'activité magnétique de l'étoile affecte-t-elle la structure de la cavité l'entourant dans le disque protoplanétaire ? Quelles conséquences pour l'arrêt de la migration planétaire ?
- Quelle est l'efficacité des interactions de marée étoile-planète pour des planètes excentriques ou inclinées ? Comment dépend-elle des modèles d'intérieur stellaire et planétaire ?
- Quel est le devenir d'une planète immergée dans l'enveloppe de gaz d'une étoile géante rouge ? Quel type de planètes survit à celle évolution ?

⋆⋆⋆

Bibliographie

ALMA Partnership et al., 2015, ApJL, 808, L3
Albrecht S., et al., 2012, ApJ, 757, 18
Andrews S. M., et al., 2018, ApJL, 869, L41
Astoul A., et al., 2019, A&A, 631, A111
Ataiee S., et al., 2018, A&A, 615, A110
Auclair-Desrotour P., Le Poncin-Lafitte C., Mathis S., 2014, A&A, 561, L7
Bae J., et al., 2019, ApJL, 884, L41
Bai X.-N., 2013, ApJ, 772, 96
Bai X.-N., 2015, ApJ, 798, 84
Balbus S. A., Hawley J. F., 1991, ApJ, 376, 214
Barker A. J., Lithwick Y., 2014, MNRAS, 437, 305
Baruteau C., Lin D. N. C., 2010, ApJ, 709, 759
Baruteau C., Masset F., 2008a, ApJ, 672, 1054
Baruteau C., Masset F., 2008b, ApJ, 678, 483
Baruteau C., Masset F., 2013, in Souchay J., Mathis S., Tokieda T., eds, Vol. 861, Lecture Notes in Physics, Berlin Springer Verlag. p. 201 (`arXiv:1203.3294`), doi :10.1007/978-3-642-32961-6_6
Baruteau C., Papaloizou J. C. B., 2013, ApJ, 778, 7
Baruteau C., Rieutord M., 2013, Journal of Fluid Mechanics, 719, 47
Baruteau C., Zhu Z., 2016, MNRAS, 458, 3927
Baruteau C., Meru F., Paardekooper S.-J., 2011a, MNRAS, 416, 1971
Baruteau C., et al., 2011b, A&A, 533, A84
Baruteau C., Cuadra J., Lin D. N. C., 2011c, ApJ, 726, 28
Baruteau C., Ramirez-Ruiz E., Masset F., 2012, MNRAS, 423, L65
Baruteau C., et al., 2014, Protostars and Planets VI, pp 667–689
Baruteau C., et al., 2016, Space Science Reviews, 205, 77
Baruteau C., et al., 2019, MNRAS, 486, 304
Bate M. R., Lodato G., Pringle J. E., 2010, MNRAS, 401, 1505
Batygin K., 2012, Nature, 491, 418
Batygin K., Bodenheimer P. H., Laughlin G. P., 2016, ApJ, 829, 114
Benedict G. F., et al., 2018, Research Notes of the American Astronomical Society, 2, 7
Benisty M., et al., 2015, A&A, 578, L6
Benítez-Llambay P., et al., 2015, Nature, 520, 63
Benomar O., et al., 2014, PASJ, 66, 94
Benz W., et al., 2014, Protostars and Planets VI, pp 691–713
Berné O., et al., 2015, A&A, 578, L8
Bitsch B., et al., 2013a, A&A, 549, A124
Bitsch B., et al., 2013b, A&A, 555, A124
Bitsch B., et al., 2014, A&A, 570, A75
Bitsch B., et al., 2015a, A&A, 575, A28
Bitsch B., Lambrechts M., Johansen A., 2015b, A&A, 582, A112
Boley A. C., et al., 2010, Icarus, 207, 509
Bolmont E., Mathis S., 2016, Celestial Mechanics and Dynamical Astronomy, 126, 275
Butler R. P., et al., 1997, ApJL, 474, L115
Carmona A., et al., 2017, A&A, 598, A118
Casassus S., et al., 2015, ApJ, 812, 126
Casassus S., et al., 2019, MNRAS, 483, 3278
Casoli J., Masset F. S., 2009, ApJ, 703, 845
Cébron D., et al., 2013, Icarus, 226, 1642
Chang P., et al., 2010, MNRAS, 407, 2007
Chaplin W. J., et al., 2013, ApJ, 766, 101
Charpinet S., et al., 2011, Nature, 480, 496
Ciesla F. J., Hood L. L., Weidenschilling S. J., 2004, Meteoritics and Planetary Science, 39, 1809
Crida A., Morbidelli A., 2007, MNRAS, 377, 1324
Crida A., Morbidelli A., Masset F., 2006, Icarus, 181, 587
Crida A., et al., 2009, A&A, 502, 679
Crnkovic-Rubsamen I., Zhu Z., Stone J. M., 2015, MNRAS, 450, 4285
Cumming A., et al., 2008, PASP, 120, 531
D'Angelo G., Lubow S. H., 2008, ApJ, 685, 560
D'Angelo G., Bate M. R., Lubow S. H., 2005, MNRAS, 358, 316
Desch S. J., et al., 2012, Meteoritics and Planetary Science, 47, 1139
Donati J. F., et al., 2016, Nature, 534, 662
Dong R., Rafikov R. R., Stone J. M., 2011, ApJ, 741, 57
Dong R., et al., 2018, ApJ, 860, 124
Duffell P. C., 2015, ApJL, 807, L11
Dürmann C., Kley W., 2015, A&A, 574, A52
Fabrycky D., Tremaine S., 2007, ApJ, 669, 1298
Favier B., et al., 2014, MNRAS, 439, 845
Flaherty K. M., et al., 2015, ApJ, 813, 99
Fromang S., Terquem C., Nelson R. P., 2005, MNRAS, 363, 943
Fuente A., et al., 2017, ApJL, 846, L3
Fulton B. J., Petigura E. A., 2018, AJ, 156, 264
Fulton B. J., et al., 2017, AJ, 154, 109
Fung J., Shi J.-M., Chiang E., 2014, ApJ, 782, 88
Gammie C. F., 1996, ApJ, 457, 355
Gong M., et al., 2019, ApJ, 883, 164
Gonzalez J. F., Laibe G., Maddison S. T., 2017, MNRAS, 467, 1984
Goodman J., Lackner C., 2009, ApJ, 696, 2054
Goodman J., Rafikov R. R., 2001, ApJ, 552, 793
Gressel O., et al., 2013, ApJ, 779, 59
Gressel O., et al., 2015, ApJ, 801, 84
Guenel M., et al., 2016a, arXiv e-prints, p. arXiv :1612.05071
Guenel M., et al., 2016b, A&A, 589, A22
Guilet J., Baruteau C., Papaloizou J. C. B., 2013, MNRAS, 430, 1764
Haffert S. Y., et al., 2019, Nature Astronomy, 3, 749
Hansen B. M. S., Murray N., 2013, ApJ, 775, 53
Hebb L., et al., 2009, The Astrophysical Journal, 693, 1920
Huber D., et al., 2013, Science, 342, 331
Ida S., Lin D. N. C., 2008, ApJ, 673, 487
Jurić M., Tremaine S., 2008, ApJ, 686, 603
Kalas P., et al., 2008, Science, 322, 1345
Kley W., Crida A., 2008, A&A, 487, L9
Kley W., Haghighipour N., 2015, A&A, 581, A20
Knutson H. A., et al., 2014, ApJ, 785, 126
Korycansky D. G., Pollack J. B., 1993, Icarus, 102, 150
Lai D., 2012, MNRAS, 423, 486
Lambrechts M., Johansen A., 2012, A&A, 544, A32
Lambrechts M., Johansen A., 2014, A&A, 572, A107
Laughlin G., Steinacker A., Adams F. C., 2004, ApJ, 608, 489
Lesur G., Kunz M. W., Fromang S., 2014, A&A, 566, A56
Levasseur-Regourd A. C., et al., 2020, Planetary and Space Science, 186, 104896

Li H., et al., 2001, ApJ, 551, 874
Lin D. N. C., Papaloizou J., 1986a, ApJ, 307, 395
Lin D. N. C., Papaloizou J., 1986b, ApJ, 309, 846
Lin D. N. C., Bodenheimer P., Richardson D. C., 1996, Nature, 380, 606
Lines S., et al., 2014, ApJL, 782, L11
Lines S., et al., 2015, A&A, 582, A5
Lines S., et al., 2016, A&A, 590, A62
Lissauer J. J., et al., 2014, ApJ, 784, 44
Lithwick Y., Wu Y., 2012, ApJL, 756, L11
Lovelace R. V. E., et al., 1999, ApJ, 513, 805
Maciejewski G., et al., 2016, A&A, 588, L6
Malik M., et al., 2015, ApJ, 802, 56
Marois C., et al., 2010, Nature, 468, 1080
Marzari F., Thebault P., 2019, Galaxies, 7, 84
Marzari F., et al., 2009, A&A, 508, 1493
Marzari F., Baruteau C., Scholl H., 2010, A&A, 514, L4
Marzari F., et al., 2012, A&A, 539, A98
Marzari F., et al., 2013, A&A, 553, A71
Masset F. S., 2002, A&A, 387, 605
Masset F. S., 2011, Celestial Mechanics and Dynamical Astronomy, 111, 131
Masset F. S., Benítez-Llambay P., 2016, ApJ, 817, 19
Masset F. S., Casoli J., 2009, ApJ, 703, 857
Masset F. S., Casoli J., 2010, ApJ, 723, 1393
Masset F. S., Papaloizou J. C. B., 2003, ApJ, 588, 494
Mayor M., Queloz D., 1995, Nature, 378, 355
Mayor M., et al., 2009, A&A, 507, 487
Mayor M., et al., 2011, arXiv e-prints, p. arXiv :1109.2497
Meru F., Bate M. R., 2011, MNRAS, 411, L1
Mirouh G. M., et al., 2016, Journal of Fluid Mechanics, 800, 213
Montesinos M., et al., 2015, ApJ, 806, 253
Mordasini C., et al., 2009, A&A, 501, 1161
Müller A., et al., 2018, A&A, 617, L2
Muto T., Suzuki T. K., Inutsuka S.-i., 2010, ApJ, 724, 448
Mutter M. M., Pierens A., Nelson R. P., 2017, MNRAS, 469, 4504
Naoz S., Farr W. M., Rasio F. A., 2012, ApJL, 754, L36
Nayakshin S., Cha S.-H., 2013, MNRAS, 435, 2099
Neuhäuser R., et al., 2007, A&A, 462, 777
Ngo H., et al., 2015, ApJ, 800, 138
Ogihara M., Morbidelli A., Guillot T., 2015, A&A, 578, A36
Ogilvie G. I., 2009, MNRAS, 396, 794
Ogilvie G. I., 2014, ARA&A, 52, 171
Ogilvie G. I., Lin D. N. C., 2004, ApJ, 610, 477
Ormel C. W., Klahr H. H., 2010, A&A, 520, A43
Orosz J. A., et al., 2012, ApJ, 758, 87
Paardekooper S.-J., 2014, MNRAS, 444, 2031
Paardekooper S. J., Mellema G., 2006, A&A, 459, L17
Paardekooper S.-J., Papaloizou J. C. B., 2008, A&A, 485, 877
Paardekooper S., et al., 2010, MNRAS, 401, 1950
Paardekooper S., Baruteau C., Kley W., 2011a, MNRAS, 410, 293
Paardekooper S.-J., Baruteau C., Meru F., 2011b, MNRAS, 416, L65
Paardekooper S.-J., et al., 2012, ApJL, 754, L16
Paardekooper S.-J., Rein H., Kley W., 2013, MNRAS, 434, 3018
Pacheco-Vázquez S., et al., 2016, A&A, 589, A60
Papaloizou J. C. B., 2011, Celestial Mechanics and Dynamical Astronomy, 111, 83
Papaloizou J. C. B., Terquem C., 2010, MNRAS, 405, 573
Papaloizou J. C. B., Nelson R. P., Masset F., 2001, A&A, 366, 263
Papaloizou J. C. B., Nelson R. P., Snellgrove M. D., 2004, MNRAS, 350, 829
Patra K. C., et al., 2020, AJ, 159, 150
Pepliński A., Artymowicz P., Mellema G., 2008, MNRAS, 386, 164
Perez S., et al., 2015, ApJL, 811, L5
Pérez S., et al., 2019a, AJ, 158, 15
Pérez S., et al., 2019b, MNRAS, 488, 1005
Picogna G., Marzari F., 2015, A&A, 583, A133
Pierens A., Huré J.-M., 2005, A&A, 433, L37
Pierens A., Baruteau C., Hersant F., 2011, A&A, 531, A5
Pierens A., Baruteau C., Hersant F., 2012, MNRAS, 427, 1562
Pinte C., et al., 2016, ApJ, 816, 25
Rafikov R. R., 2002, ApJ, 572, 566
Rafikov R. R., 2005, ApJL, 621, L69
Rasio F. A., Ford E. B., 1996, Science, 274, 954
Raymond S. N., Morbidelli A., 2020, arXiv e-prints, p. arXiv :2002.05756
Rieutord M., Valdettaro L., 2010, Journal of Fluid Mechanics, 643, 363
Rivière-Marichalar P., et al., 2019, ApJL, 879, L14
Rogers T. M., Lin D. N. C., 2013, ApJL, 769, L10
Rowe J. F., et al., 2014, ApJ, 784, 45
Shakura N. I., Sunyaev R. A., 1973, A&A, 24, 337
Simon J. B., et al., 2013, ApJ, 775, 73
Smith A. M. S., et al., 2018, MNRAS, 474, 5523
Stamatellos D., 2015, ApJL, 810, L11
Steffen J. H., 2013, MNRAS, 433, 3246
Szulágyi J., et al., 2014, ApJ, 782, 65
Taam R. E., Sandquist E. L., 2000, ARA&A, 38, 113
Tanaka H., Takeuchi T., Ward W. R., 2002, ApJ, 565, 1257
Tang Y.-W., et al., 2012, A&A, 547, A84
Tanigawa T., Ohtsuki K., Machida M. N., 2012, ApJ, 747, 47
Terquem C. E. J. M. L. J., 2003, MNRAS, 341, 1157
Terquem C., Papaloizou J. C. B., 2019, MNRAS, 482, 530
Thun D., Kley W., 2018, A&A, 616, A47
Triaud A. H. M. J., et al., 2010, A&A, 524, A25
Uribe A., Bans A., Königl A., 2015, ApJ, 802, 54
Villaver E., Livio M., 2009, ApJL, 705, L81
Wafflard-Fernandez G., Baruteau C., 2020, MNRAS, 493, 5892
Ward W. R., 1991, in Lunar and Planetary Science Conference. p. 1463
Ward W. R., 1997, Icarus, 126, 261
Williams J. P., Cieza L. A., 2011, ARA&A, 49, 67
Winn J. N., Fabrycky D. C., 2015, ARA&A, 53, 409
Winn J. N., et al., 2005, ApJ, 631, 1215
Winn J. N., et al., 2010, ApJL, 718, L145
Wright J. T., et al., 2012, ApJ, 753, 160
Wu Y., Murray N., 2003, ApJ, 589, 605
Yu L., et al., 2017, MNRAS, 467, 1342
Yu L., et al., 2019, MNRAS, 489, 5556
Zahn J.-P., 1977, A&A, 57, 383
Zhang S., et al., 2018, ApJL, 869, L47
Zhu Z., Baruteau C., 2016, MNRAS, 458, 3918
Zhu Z., et al., 2012, ApJ, 755, 6
Zhu Z., Stone J. M., Rafikov R. R., 2013, ApJ, 768, 143
Zhu Z., et al., 2015, ApJ, 813, 88
Ziampras A., et al., 2020, A&A, 633, A29
van der Marel N., et al., 2015, ApJL, 810, L7

Annexes

Voici une sélection de 5 publications représentatives de mon cheminement de recherche depuis l'après-thèse, et qui illustrent bien mes activité de recherche sur la migration planétaire [1, 2, 5], la dynamique des disques protoplanétaires [1, 4, 5] et les effets de marée étoile-planète [3] :

1. *Rapid inward migration of planets formed by gravitational instability*
   Baruteau, Meru & Paardekooper
   2011, MNRAS, 416, 1971-1982 (astro-ph)

2. *Disk-planets interactions and the diversity of period ratios in Kepler's multi-planetary systems*
   Baruteau & Papaloizou
   2013, ApJ, 778, 7-21 (astro-ph)

3. *Inertial waves in a differentially rotating spherical shell*
   Baruteau & Rieutord
   2013, Journal of Fluid Mechanics, 719, 47-81 (astro-ph)

4. *Dust traps in the protoplanetary disc MWC 758 : two vortices produced by two giant planets ?*
   Baruteau, Barraza, Pérez, Casassus, Dong, Lyra, Marino, Christiaens, Zhu, Carmona, Debras & Alarcon
   2019, MNRAS, 486, 304-319 (astro-ph)

5. *Intermittent planet migration and the formation of multiple dust rings and gaps in protoplanetary disks*
   Wafflard-Fernandez & **Baruteau**
   2020, MNRAS, 493, 5892-5912 (astro-ph)

Monthly Notices of the ROYAL ASTRONOMICAL SOCIETY

Mon. Not. R. Astron. Soc. (2011) doi:10.1111/j.1365-2966.2011.19172.x

Rapid inward migration of planets formed by gravitational instability

Clément Baruteau,[1,2]★ Farzana Meru[3,4] and Sijme-Jan Paardekooper[1]

[1] *DAMTP, University of Cambridge, Wilberforce Road, Cambridge CB3 0WA*
[2] *Department of Astronomy and Astrophysics, University of California, Santa Cruz, CA 95064, USA*
[3] *School of Physics, University of Exeter, Stocker Road, Exeter EX4 4QL*
[4] *Institut für Astronomie und Astrophysik, Universität Tübingen, Auf der Morgenstelle 10, 72076 Tübingen, Germany*

Accepted 2011 June 1. Received 2011 May 30; in original form 2011 March 25

ABSTRACT

The observation of massive exoplanets at large separation ($\gtrsim$10 au) from their host star, like in the HR 8799 system, challenges theories of planet formation. A possible formation mechanism involves the fragmentation of massive self-gravitating discs into clumps. While the conditions for fragmentation have been extensively studied, little is known of the subsequent evolution of these giant planet embryos, in particular their expected orbital migration. Assuming a single planet has formed by fragmentation, we investigate its interaction with the gravitoturbulent disc it is embedded in. 2D hydrodynamical simulations are used with a simple prescription for the disc cooling. A steady gravitoturbulent disc is first set up, after which simulations are restarted including a planet with a range of masses approximately equal to the clump's initial mass expected in fragmenting discs. Planets rapidly migrate inwards, despite the stochastic kicks due to the turbulent density fluctuations. We show that the migration time-scale is essentially that of type I migration, with the planets having no time to open a gap. In discs with aspect ratio ~0.1 at their forming location, planets with a mass comparable to or larger than Jupiter's can migrate in as short as 10^4 years, that is about 10 orbits at 100 au. Massive planets formed at large separation from their star by gravitational instability are thus unlikely to stay in place, and should rapidly migrate towards the inner parts of protoplanetary discs, regardless of the planet mass.

Key words: accretion, accretion discs – hydrodynamics – turbulence – methods: numerical – planet–disc interactions – protoplanetary discs.

1 INTRODUCTION

The large majority of exoplanets have been discovered by the radial velocity and transiting techniques. Recent progress in the adaptive optics technique has revealed about 20 exoplanets by direct imaging. Since the latter requires a high brightness contrast between the planet and the parent star, massive planets have been observed at separations $\gtrsim$10 au (e.g. Kalas et al. 2008; Marois et al. 2008, 2010; Lafrenière, Jayawardhana & van Kerkwijk 2010; Lagrange et al. 2010). One such example is the HR 8799 system (Marois et al. 2010), which comprises four planets with masses evaluated between 7 and 10 Jupiter mass, and estimated separations of 14, 24, 38 and 68 au, respectively.

How can the large orbital separations of such massive planets be explained? With the standard core accretion formation scenario (e.g. Safronov 1969; Mizuno 1980; Pollack et al. 1996; Ida & Lin 2004), it is difficult to form Jupiter-like planets in isolation further than ~10 au from a Sun-like star. Still, the formation of a first gap-opening planet close to the snow line (Ida & Lin 2004) could pave the way for the formation of a second-generation planet at the outer edge of the first planet's gap (Bryden et al. 2000; Thommes 2005; Ida & Lin 2008). Provided that the second planet opens a gap, its outer edge could also trigger the formation of a third-generation planet. Subsequent planet formation could proceed as a sequence, as long as there are enough planetesimals and gas left.

The tidal interaction between a planet and its nascent protoplanetary disc alters the planet's semimajor axis, causing its orbital migration (Goldreich & Tremaine 1980). Assuming the central object is a Sun-like star, a planet typically more massive than Saturn opens a gap around its orbit and generally migrates inwards. It is thus unlikely that a massive planet formed through the core-accretion scenario within ~10 au of its host star could migrate to a separation as large as 100 au. A notable exception was proposed by Crida, Masset & Morbidelli (2009b), who showed that the tidal interaction between a pair of resonant massive planets embedded in a common gap, and their protoplanetary disc, could drive both planets to orbital separations much larger than that of their birth place, providing some specific conditions on the planets mass ratio and on the disc's turbulent viscosity.

★E-mail: C.Baruteau@damtp.cam.ac.uk

Another *in situ* formation scenario is based on the gravitational instability (e.g. Cameron 1978; Boss 1997). It involves early-stage protoplanetary discs, which are massive enough for its self-gravity to play a part in its evolution. The probability that discs form fragments is described by two dimensionless parameters. One is the Toomre Q parameter, $Q = c_s\kappa/\pi G\Sigma$, where G is the gravitational constant, c_s and Σ denote the disc's sound speed and surface mass density, and κ is the epicyclic frequency. For Keplerian discs, κ approximately equals the angular frequency Ω. Toomre (1964) showed that, for an infinitesimally thin disc to fragment, $Q \lesssim 1$. The second parameter describing the stability of a self-gravitating disc is the disc's cooling time-scale in units of the orbital time-scale, $\beta = t_{\rm cool}\,\Omega$, where $t_{\rm cool} = e({\rm d}e/{\rm d}t)^{-1}$ is the cooling time-scale and e is the disc's thermal energy density (Gammie 2001). The critical value of the cooling parameter β, below which fragmentation will occur if $Q \lesssim 1$, depends on the disc's adiabatic index (Rice, Lodato & Armitage 2005) and on the local disc to primary mass ratio (Meru & Bate 2011b). Its exact value is currently somewhat uncertain as Meru & Bate (2011a) have recently shown that previous simulations that determined this critical value were unresolved. However, current simulations show that the critical value for β could be in the range 3–18 (Gammie 2001; Rice et al. 2005; Meru & Bate 2011a,b).

The vast majority of studies of planet formation by gravitational instability have focused on the conditions to fragment discs into bound objects. It is thought to operate at separations larger than 30–50 au from the central (Sun-like) star (e.g. Matzner & Levin 2005; Rafikov 2005; Stamatellos & Whitworth 2008). However, little is known of the evolution of these objects, in particular their expected migration resulting from the gravitational interaction with the gravitoturbulent disc they are embedded in. A few numerical studies have observed that clumps could drift inwards (e.g. Mayer et al. 2002; Boss 2005; Cha & Nayakshin 2011), and some of them have focused on the early phases of disc formation and evolution following the collapse from the pre-stellar core stage (Vorobyov & Basu 2006, 2010a,b; Machida, Inutsuka & Matsumoto 2011). As these giant planet embryos migrate inwards, they may become tidally disrupted (when their radius becomes comparable to the clump's Hill radius), thereby delivering a variety of planets in the inner parts of protoplanetary discs (Nayakshin 2010).

In this paper, we examine the orbital evolution of a single planet embedded in its nascent gravitoturbulent disc, following the assumption that the planet has formed by gravitational instability. We show that the planet migrates inwards in a time-scale very similar to that of type I migration (Paardekooper & Papaloizou 2009) in the absence of turbulence. Our physical and numerical models are described in Section 2. In Section 3, we present our results of simulations. Conclusions and future directions are drawn in Section 4.

2 MODEL

We investigate the tidal interaction between a massive planet and the protoplanetary disc it formed in through the gravitational instability scenario. Once a gaseous clump has formed by fragmentation, it contracts until H_2 dissociation occurs, causing a rapid collapse of the clump down to planetary sizes. Our study does not address the formation of the planet, and we consider the clump and the planet as one object. In the following, our system of interest (clump and planet) is referred to as the planet. Our study focuses on its migration driven by the interaction with the disc, following the assumption that the planet has formed by gravitational instability. As described below, our approach is to first set up a steady-state gravitoturbulent disc, then include a single planet and follow its orbital migration.

The disc's properties after fragmentation are poorly constrained. They depend on how many clumps form, and how massive they are. In our study, we assume that the disc properties (density, temperature) are virtually unchanged by the fragmentation stage. In particular, we assume that the disc remains gravitoturbulent. This assumption is motivated by the findings of previous numerical studies on disc fragmentation (e.g. Meru & Bate 2011b), where the images of the discs show similar structures after the formation of a clump.

We carried out 2D hydrodynamical simulations using the grid-based, staggered-mesh code FARGO[1] (Masset 2000), for which a self-gravity solver based on fast Fourier transforms was presented in Baruteau & Masset (2008b). When calculating the self-gravitating acceleration, all mass is assumed to be confined to the disc midplane (the razor-thin disc approximation). The thermal energy density e satisfies the equation

$$\frac{\partial e}{\partial t} + \nabla\cdot(e\boldsymbol{v}) = -(\gamma-1)e\nabla\cdot\boldsymbol{v} + Q^{+}_{\rm bulk} - \frac{e}{\tau_{\rm cool}}, \qquad (1)$$

where $\boldsymbol{v}$ denotes the gas velocity, and γ is the adiabatic index (its value can be mapped to a 3D adiabatic index; see Gammie 2001, and references therein). In equation (1), the cooling time-scale $\tau_{\rm cool} = \beta\Omega^{-1}$, with β taken to be constant, and the heating source term $Q^{+}_{\rm bulk}$ is provided by artificial viscous heating at shocks arising from the gravitoturbulence. A von Neumann–Richtmyer artificial bulk viscosity is used, as described in Stone & Norman (1992), where the coefficient C_2 is taken equal to 1.4 (C_2 measures the number of zones over which a shock is spread over by the artificial viscosity). Providing angular momentum transport driven by gravitoturbulence occurs locally, which is not necessarily the case (Balbus & Papaloizou 1999; Cossins, Lodato & Clarke 2009); the alpha parameter associated with the angular momentum flux density is given by (Gammie 2001)

$$\alpha = \frac{4}{9}\frac{1}{\gamma(\gamma-1)\beta}, \qquad (2)$$

which indicates that varying β is equivalent to varying the viscous stress in the disc. Preliminary calculations with our fiducial set-up (initial profiles and grid's resolution are described below) showed that the critical value of β below which fragmentation occurs ranges from 10 to 15. Since we require the disc to be in a gravitoturbulent state, but we do not require further fragmentation so as to focus on the migration of a single planet, we simulated three disc models with β = 15, 20 and 30.

Each of our three models initially comprises a 0.4 $M_\odot$ 2D disc around a star of fixed mass $M_\star = 1\,M_\odot$, and spanning a radial range $20 < r < 250$ au. (As will be shown in Section 3.1, the disc mass rapidly decreases to about 0.2–0.25 $M_\odot$ after 30 orbits at 100 au.) The initial surface mass density decreases as r^{-2}, and it equals $\approx$20 g cm^{-2} at 100 au. The initial disc's temperature is $\approx$15 K at 100 au, and it decreases as r^{-1} (we assume a mean molecular weight $\mu = 2.4$ and an adiabatic index $\gamma = 5/3$). This corresponds to setting the initial disc aspect ratio h (pressure scaleheight to radius ratio H/r) equal to 0.1 at 100 au. The disc's initial Toomre Q parameter is thus uniform, $\approx$1.8. A small level ($\sim$0.1 per cent) of white noise is added initially to break the disc's axisymmetry. Here and in the following, disc and planet quantities are expressed in physical units. Since our simulations are scale-free, all the results presented

---

[1] See fargo.in2p3.fr.

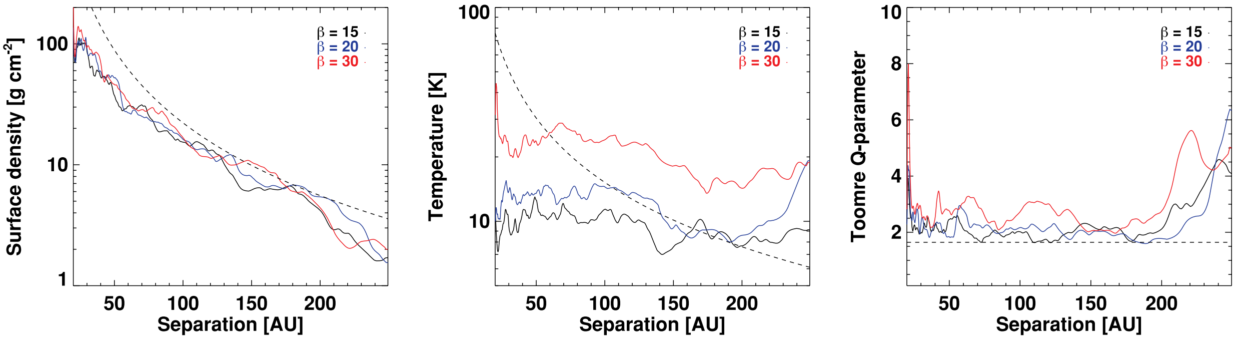

Figure 1. Azimuthally averaged surface density (left-hand panel), temperature (middle panel) and Toomre Q parameter (right-hand panel) obtained at 30 orbits for our three values of $\beta = t_{\rm cool}\,\Omega$ (solid curves). The azimuthal average of Q was calculated as $\langle c_{\rm s}\rangle\langle\Omega\rangle/\pi G\langle\Sigma\rangle$, where $\langle . \rangle$ stands for the azimuthal average. Dashed curves depict the initial value of each quantity.

throughout this paper can be easily rescaled by using different units of mass, length and temperature.

In all our simulations, the grid is covered with 512 and 1536 cells along the radial and azimuthal directions, respectively. A logarithmic spacing is used along the radial direction, as required by the self-gravity module in FARGO. Grid cells are approximately square, and the initial pressure scaleheight is resolved by about 20 cells along each direction. The radial and azimuthal components of the self-gravitating acceleration are smoothed over a softening length, $\varepsilon_{\rm sg}$. We take $\varepsilon_{\rm sg} = 3 \times 10^{-4}\, r$ throughout this study, which is a factor of 3×10^{-3} times the initial pressure scaleheight. The influence of a large $\varepsilon_{\rm sg}$, which can be seen as a crude treatment of the effects of finite thickness, will be examined in Section 3.2.4, where we find that the choice for $\varepsilon_{\rm sg}$ does not significantly alter the orbital evolution of a planet embedded in a gravitoturbulent disc. Outflow boundary conditions are used at the grid's inner and outer edges. Hydrodynamical equations are solved in the frame centred on to the central star. Since a non-inertial frame of reference is adopted, the indirect terms in the expression for the disc's gravitational potential are included.

3 RESULTS OF HYDRODYNAMICAL SIMULATIONS

Our numerical simulations were carried out in two steps. In a first step, a gravitoturbulent disc model was set up, whose properties are described in Section 3.1. We then restarted the simulations, including planets of several masses, and following the time evolution of their orbital separation. The results of the restart simulations are presented in Section 3.2. Further investigation on the impact of the disc's temperature follows in Section 3.3.

3.1 Gravitoturbulent stage

We describe in this section the results of our three disc models with cooling parameters $\beta = 15$, 20 and 30. The absence of heating source initially acts to decrease the disc's temperature, and thus the Toomre Q parameter, until gravitoturbulence sets in. As both the initial Q profile and β are taken to be uniform (the cooling time-scale thus scales proportional to the orbital time-scale), gravitoturbulence progressively develops through the disc, starting from the inner edge. After a few orbits at the disc's outer edge, a thermal quasi-equilibrium is reached over the whole disc, where cooling is approximately balanced by shock heating due to gravitoturbulence.

The disc's initial surface density that we assume does not correspond to a mechanical equilibrium with the gravitoturbulent stress. The disc therefore adjusts both its surface density and temperature profiles to satisfy a mechanical equilibrium along with a uniform Toomre Q profile. This is illustrated in Fig. 1, where the azimuthally averaged surface mass density, temperature and Toomre Q parameter are depicted at 30 orbits at 100 au. Their initial value is shown with a dashed curve. In this quasi-steady state, the surface density profile decreases approximately as $r^{-3/2}$, and the disc's temperature is almost uniform, as is the Toomre Q parameter. We comment that the high initial disc mass ($0.4\,{\rm M}_\odot$) promotes global modes that, along with the outflow boundary condition at the grid's inner edge, lead to a rapid decrease in the disc mass. After 30 orbits at 100 au, the latter ranges from 0.21 to $0.24\,{\rm M}_\odot$ for β increasing from 15 to 30. The rate at which the disc mass decreases is maximum at the onset of gravitoturbulence, and then declines (but does not vanish) as a quasi-steady state is attained.

The alpha parameters associated with the Reynolds and gravitational turbulent stresses are denoted by $\alpha_{\rm Rey}$ and $\alpha_{\rm sg}$, respectively. Details of their calculation in a 2D disc model are given in Appendix A. Fig. 2 displays the azimuthally and time-averaged radial profiles of $\alpha_{\rm Rey}$, $\alpha_{\rm sg}$ and of $\alpha_{\rm tot} = \alpha_{\rm sg} + \alpha_{\rm Rey}$. Time average is done from 30 to 60 orbits at 100 au (that is, over about eight

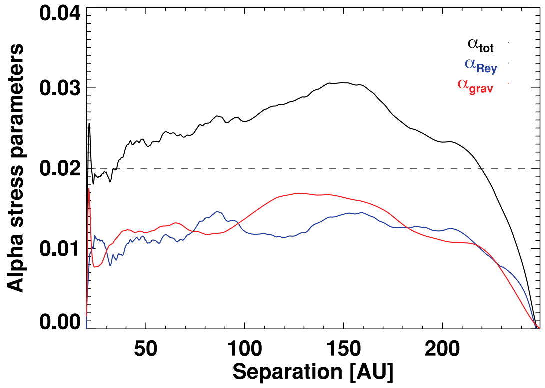

Figure 2. Gravitational, Reynolds and total alpha parameters, azimuthally and time-averaged from 30 to 60 orbits at 100 au (that is, over about eight orbits at 250 au, the location of the disc's outer edge). Results are displayed for the disc model with cooling parameter $\beta = 20$. The dashed curve shows the total alpha parameter expected from viscous transport theory, given by equation (2).

orbits at the grid's outer edge). Results are shown for $\beta = 20$. We note that $\alpha_{\rm sg}$ and $\alpha_{\rm Rey}$ take very similar values over the whole disc. The same behaviour was obtained by Gammie (2001) with 2D local shearing-sheet calculations. The decrease in both $\alpha_{\rm sg}$ and $\alpha_{\rm Rey}$ at large ($\gtrsim$200 au) separation is most probably due to the decreasing grid's resolution, as a logarithmic spacing is used along the radial direction. We comment that $\alpha_{\rm tot}$ is locally up to 50 per cent larger than the value expected from viscous (local) transport theory, given by equation (2). The difference is probably due to our large disc mass ($\gtrsim 0.2 M_\star$) and large aspect ratio ($h \sim 0.1$), which tend to foster global transport[2] of angular momentum (e.g. Lodato & Rice 2004). Although not shown here, very similar results were obtained for $\beta = 15$ and 30.

Finite resolution effects (numerical diffusion) lead to a negligible transport of angular momentum compared to gravitoturbulence (see e.g. Lin & Papaloizou 2010, who estimated the numerical 'alpha viscosity' in the FARGO code to be $\lesssim 10^{-5}$ for a number of grid cells similar to ours). Artificial bulk viscosity most likely leads to a small, if not negligible, transport of angular momentum compared to gravitoturbulence, but note that it is unclear how its contribution can be isolated in our simulations. We point out that if artificial bulk viscosity induced a net transport of angular momentum on average, it would lead to a discrepancy between the value of $\alpha_{\rm sg} + \alpha_{\rm Rey}$ measured in local, steady-state disc models and the alpha value given in equation (2). Gammie (2001) carried out 2D local shearing-sheet simulations of gravitoturbulent disc models using the ZEUS code, which is very similar to the FARGO code. In particular, both codes use the same prescription for the artificial bulk viscosity. He found that $\alpha_{\rm sg} + \alpha_{\rm Rey}$ agrees with the value given by the expression in equation (2) to within ~10 per cent, which shows that artificial bulk viscosity should lead to a small transport of angular momentum compared to gravitoturbulence. Also, although not shown here, we have checked that increasing the amount of artificial bulk viscosity (the coefficient C_2 in Stone & Norman 1992) by a factor of 3 leads to a negligible change in the values of $\alpha_{\rm Rey}$ and $\alpha_{\rm sg}$.

3.2 Restart with an embedded planet

We restarted the simulations of Section 3.1 at 30 orbits, including a single planet at 100 au. The disc's temperature and surface mass density at this location are close to their initial value for our three values of β (see Fig. 1). Note in particular that the disc aspect ratio at the planet's initial location is $\approx$0.1. Akin to the clump's contraction time-scale, the final mass of planets formed by gravitational instability is uncertain (e.g. Boley et al. 2010; Helled & Bodenheimer 2011), and may substantially differ from the clump's initial mass. The latter is estimated by Boley et al. (2010) as $\sim h_{\rm p}^3 M_\star$ for $Q \sim 1.5$, with $h_{\rm p}$ the disc aspect ratio at the clump's forming location. This estimate of the clump's initial mass, which is based on the fragmentation of spiral arms, is typically a factor of 5–10 smaller than the Toomre mass (see Boley et al. 2010, their fig. 1, and references therein). We considered three planet masses corresponding to a planet to primary mass ratio $q = M_{\rm p}/M_\star$ around $h_{\rm p}^3$: a Saturn-mass planet ($q = 3 \times 10^{-4}$, $q/h_{\rm p}^3 \sim 0.3$), a Jupiter-mass planet ($q = 10^{-3}$, $q/h_{\rm p}^3 \sim 1$) and a 5 Jupiter-mass planet ($q = 5 \times 10^{-3}$, $q/h_{\rm p}^3 \sim 5$). The planets gravitational potential is softened over a smoothing length $\varepsilon = 3 \times 10^{-2}\, r_{\rm p}$, with $r_{\rm p}$ the planet's orbital separation, and it takes its maximum value at the restart time (we do not gradually ramp up the planet's mass). We will show in Section 3.2.4 that our results are not altered by a more gentle introduction of the planet's potential in the disc over a dynamical time-scale, the typical formation time-scale of a clump. We comment that in self-gravitating discs the mass that is relevant for disc–planet interactions is the mass of the planet and of the gas envelope surrounding it. Although for simplicity the planet's mass is fixed, gas can be accreted on to its envelope (circumplanetary disc), thereby contributing to increasing the effective planet's mass. Note, however, that this accretion rate is probably not realistic due to our simple prescription for the disc cooling. Since the disc is fully self-gravitating, the calculation of the force exerted on the planet takes all the disc into account, and it does not partly exclude the planet's Hill radius (Crida et al. 2009a).

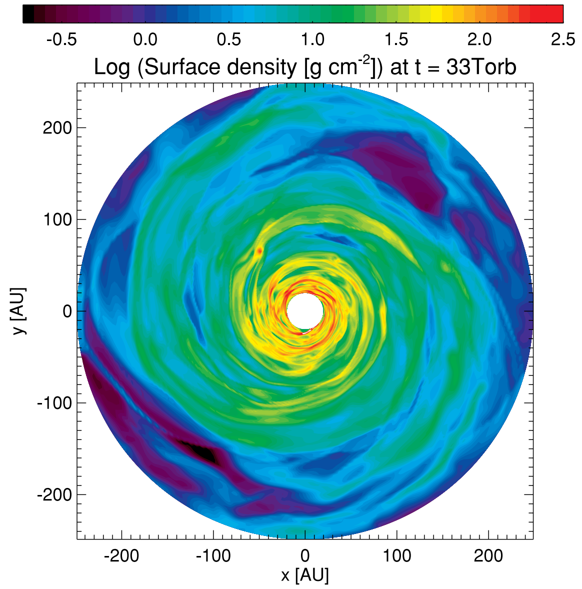

Figure 3. Contours of the disc's surface density obtained in a restart simulation with $\beta = 30$, where a Jupiter-mass planet has been introduced at 100 au. Results are displayed three orbits after the restart time. The planet is now located at about 80 au from the central star (at $x \sim -50$ au, $y \sim 60$ au).

Fig. 3 displays the surface density obtained for the disc model with $\beta = 30$, perturbed by a Jupiter-mass planet. Density contours are shown only three orbits after the restart; the planet is now located at $\approx$80 au from the central object. The density perturbation due to the planet's potential is comparable to the turbulent density perturbations. This similarity stresses that the magnitude of the stochastic torque acting on the planet can be similar to that of the disc–planet tidal torque obtained in the absence of turbulence (e.g. Nelson & Papaloizou 2004; Baruteau & Lin 2010). In such turbulent configurations, the migration time-scale must be evaluated in a statistical way, by running several simulations. For each planet mass and each value of β, we performed a suite of eight simulations, varying the planet's azimuth at restart as $\varphi_{\rm p} = \pi/4 \times i$, $i \in [0\text{–}7]$ (that is, independently of the disc's density structure at restart). The migration time-scales obtained for these series of runs are presented in Section 3.2.1. The impact of stochastic density fluctuations is described in Section 3.2.2. A comparison with predictions of laminar

---

[2] Similar gravitoturbulent disc models, but with reduced aspect ratio in a steady state, have been simulated by Paardekooper, Baruteau & Meru (2011b) with the same hydrodynamical code and similar grid resolution. Using the same method to calculate the stresses as described in Appendix A, they find an averaged value of $\alpha_{\rm tot}$ in very good agreement with the value given in equation (2).

disc models follows in Section 3.2.3, and a brief discussion on the impact of numerics is given in Section 3.2.4.

3.2.1 Migration time-scale

The time evolution of the planets' orbital separation is displayed in Fig. 4. Planet mass increases from left to right, and the cooling parameter β increases from top to bottom. In all panels, time is expressed in years (bottom x-axis) and in orbital periods at 100 au (top x-axis). Results are shown for the eight evenly spaced values of the planet's azimuth $\varphi_{\rm p}$ at restart (increases with increasing colour's wavelength).

The net trend coming out of our results is that, in spite of the stochastic kicks triggered by turbulence, planets migrate inwards very rapidly. Averaging over $\varphi_{\rm p}$ and β, the migration time-scale (defined as the time to migrate from 100 to 20 au, the location of the grid's inner edge) is typically as short as three orbits for the 5 Jupiter-mass planet, six orbits for the Jupiter-mass planet, and about eight orbits for the Saturn-mass planet. In addition, at fixed β, the amplitude of stochastic kicks increases with decreasing planet mass, and so does the spread in the migration time-scale. Both results may be qualitatively interpreted as follows. The torque exerted by the disc on the planet may be decomposed as a background tidal torque, plus a stochastic torque due to turbulent fluctuations. In the mass regime that we consider ($q/h_{\rm p}^3 \sim 1$), the amplitude of the tidal torque should increase with increasing planet mass. However, like in discs with turbulence driven by the magnetorotational instability, it is unclear if the value of the tidal torque is similar to that predicted in laminar

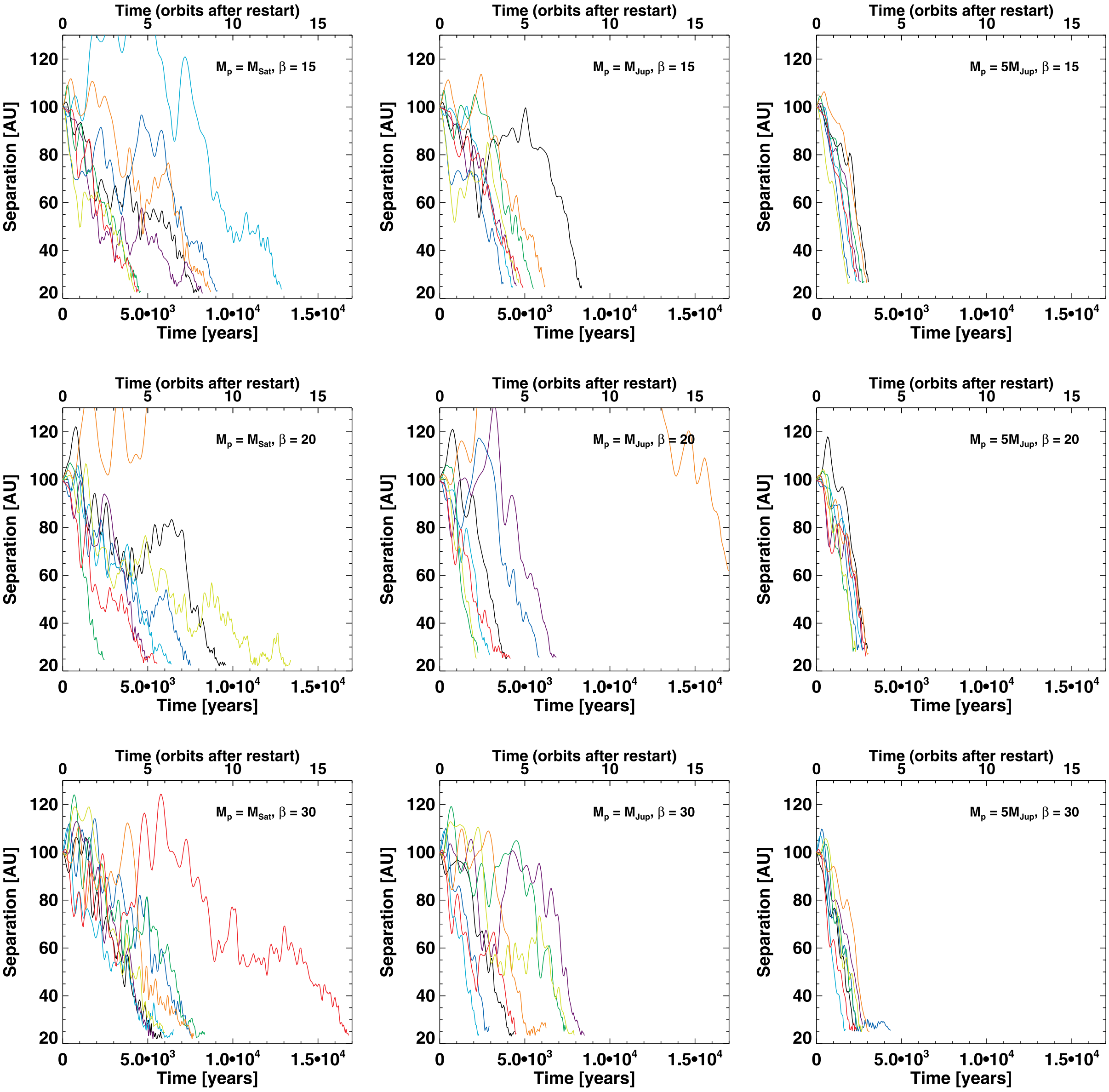

Figure 4. Time evolution of the orbital separation of a Saturn-mass planet (left column), a Jupiter-mass planet (middle column) and of a 5 Jupiter-mass planet (right column) in a gravitoturbulent disc with $\beta = 15$ (top row), 20 (middle row) and 30 (bottom row). Time is displayed in years (bottom x-axis) and in orbital periods at 100 au (top x-axis). Results are obtained for eight evenly spaced planet's azimuths at restart (azimuth increases with wavelength's colour).

disc models, in the absence of turbulence (Nelson & Papaloizou 2004). A detailed comparison with results of laminar disc models will be presented in Section 3.2.3. The standard deviation of the stochastic torque's distribution is primarily controlled by $\alpha_{\rm tot}$, and therefore by the cooling parameter β (see equation 2). For a given β, the smaller the planet mass, the smaller the tidal torque to stochastic torque ratio, the more sensitive the planet is to stochastic kicks, and therefore the larger the spread in the migration time-scale. In the same vein, at fixed planet mass, the spread in the migration time-scale should increase with decreasing β. This trend does not clearly show up in Fig. 4, most probably because our minimum and maximum values of β only differ by a factor of 2. Some further insight into the effect of stochastic kicks is given in Section 3.2.2. We finally point out that the disc's density and temperature profiles do not significantly decrease over the planets migration time-scale (for the longest simulation with the Saturn-mass planet, the disc's mass decreases by at most 10 per cent).

3.2.2 Stochastic kicks

The results of Section 3.2.1 show that planets formed by gravitational instability should rapidly migrate inwards. Even for the Saturn-mass planet, whose mass is smaller than the estimated initial clump's mass (see the first paragraph of Section 3.2), inward migration occurs in typically less than 10 orbits. As illustrated in Fig. 4, planet migration in gravitoturbulent discs is not a smooth process. Planets may experience large kicks, either inwards or outwards, depending on the local density perturbations they encounter. An example of outward kick is illustrated in Fig. 5, which displays the gas density obtained for the restart simulation with $\beta = 30$ and the Saturn-mass planet that experiences a significant episode of outward migration in the bottom-left panel of Fig. 4 (red curve). Time increases by 0.1 orbital periods at 100 au from left to right. In each panel, the planet's location is indicated with a filled black circle.

We first comment that, because the planet's mass is low enough ($q/h_{\rm p}^3 \approx 0.3$), the wakes it generates are invisible, their density contrast being much weaker than that of the turbulent perturbations. In the case depicted in Fig. 5, the planet finds itself with an underdense region behind it, and a (comparatively) overdense region in front of it. This density contrast yields a large, positive co-orbital corotation torque that is responsible for the vigorous outward kick experienced by the planet. This kick increases the planet's orbital separation from ~75 to ~95 au in only 0.2 orbital periods at 100 au (that is, in 200 years). Similarly, inward kicks are obtained as the planet experiences a negative co-orbital corotation torque induced by an underdense region ahead of it, and a (comparatively) overdense region behind it. As is shown for instance in the bottom-left panel of Fig. 4, kicks excite planets epicyclic motion, which is rapidly damped as the underlying disc–planet tidal torque takes over.

The stochastic kicks induced by gravitoturbulence are reminiscent of type III runaway migration. This migration regime relies on the formation of a co-orbital mass deficit in the planet's horseshoe region, which takes the form of an asymmetric density structure behind and in front of the planet (Masset & Papaloizou 2003). In massive ($Q \gtrsim 1$) laminar discs with moderate viscosity (α is a few × 10^{-3}), runaway migration is particularly relevant for planets with $q \sim h_{\rm p}^3$ (Masset & Papaloizou 2003), like the planets considered in our study. However, in our model, the disc's turbulent viscosity ($\alpha_{\rm tot}$ is a few per cent) is too large to allow planets to open a partial dip around their orbit before they reach the disc's inner edge. Thus, planets do not build up a co-orbital mass deficit. But, through the density fluctuations it triggers, gravitoturbulence may provide an *effective* mass deficit on each side of the planet, and induce an effective type III migration. However, this effective mass deficit is not co-orbital with the planet (as can be seen in Fig. 5), and therefore cannot lead to a runaway. Consequently, the relative fast inward migration that we obtain cannot be attributed to type III runaway migration. Also, although the planets we consider are massive, their short formation and migration time-scales compared to their gap-opening time-scale suggest they are subject to type I like migration instead of type II, perturbed by stochastic kicks. This point will be clarified in Section 3.2.3.

Stochastic kicks provide a source of very fast relative motion between the planet and the disc. Fig. 6 displays the migration speed

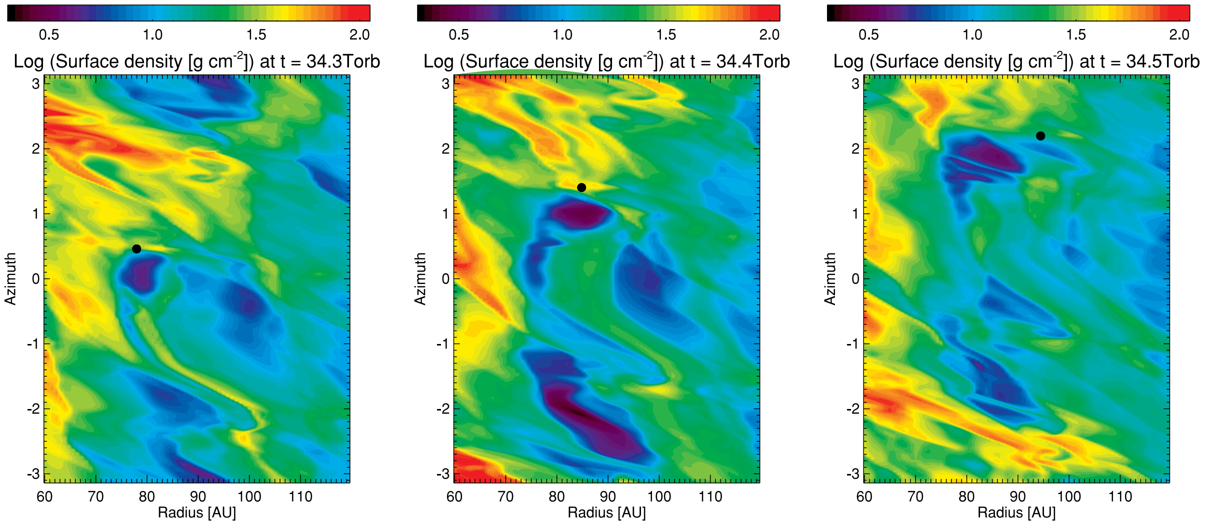

Figure 5. Contours of the gas surface density obtained for the restart simulation with $\beta = 30$, and the Saturn-mass planet with restart azimuth equal to $7\pi/4$. This simulation corresponds to the red curve in the bottom-left panel of Fig. 4, where a significant episode of outward migration occurs from three to six orbits after restart. Orbital separation is shown on the x-axis, and azimuth on the y-axis. In all panels, the planet's location is depicted with a filled black circle.

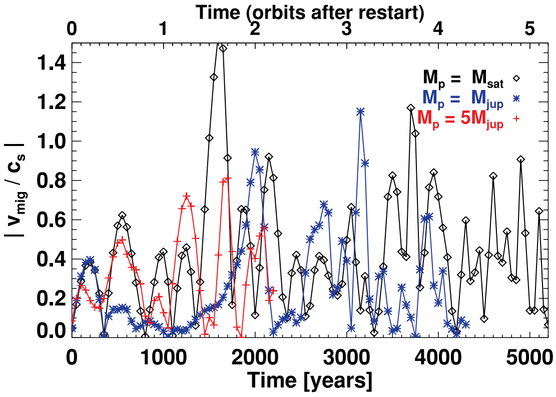

Figure 6. Time variation of the (absolute value of the) migration speed, in units of the local sound speed, obtained for the restart simulations with $\beta = 30$ and zero azimuth at restart. They correspond to the results shown with black curves in the bottom row of Fig. 4. The migration speed is measured as the time derivative of the planet's orbital separation.

in units of the local sound speed for the three runs with $\beta = 30$, and zero azimuth at restart. The migration rate can be a significant fraction of the local sound speed, and short episodes of supersonic motion are even obtained. We note that the maximum value for the migration speed to sound speed ratio tends to increase with decreasing planet mass, as less massive planets are more sensitive to stochastic kicks.

3.2.3 Comparison to laminar disc models

Our results of simulations indicate that the migration of planets embedded in gravitoturbulent discs is driven by both a vigorous (negative) tidal torque and a (positive or negative) stochastic torque. As the planet mass increases, the former prevails over the latter. In this section, we compare the results of our turbulent disc model with $\beta = 30$ to those of an equivalent laminar disc model, including the viscous force in the momentum equation. A constant alpha viscosity is used, approximately equal to 1.3 per cent. The comparison is done for the same three planet masses as previously considered. As the initial conditions for the laminar calculations, we take surface density and temperature profiles that fit those of the gravitoturbulent run with $\beta = 30$ at 30 orbits: $\Sigma \approx 15\,\mathrm{g\,cm^{-2}} \times (r/100\,\mathrm{au})^{-3/2}$, and $T \approx 25\,\mathrm{K}$.

Two series of laminar calculations were carried out: (i) one with an isothermal equation of state, where the imposed (flat) temperature profile remains constant in time, and (ii) another with an energy equation with both viscous heating ($\alpha \approx 1.3$ per cent) and β-cooling ($\beta = 30$). For the latter series, the aforementioned[3] value for α leads to an initial thermal balance between viscous heating and β-cooling (see equation 2).

All laminar calculations include the axisymmetric component of the disc's self-gravity. This is meant to avoid a large mismatch between the disc's and the planet's angular velocities due to the disc gravity, which would yield a spurious shift inwards of all Lindblad resonances, and therefore an artificial acceleration of the inward migration (Baruteau & Masset 2008b). Also, in all laminar runs, the calculation of the force exerted by the disc on the planet excludes the planet's circumplanetary disc (Crida et al. 2009a). All other parameters are otherwise the same as in the gravitoturbulent calculations.

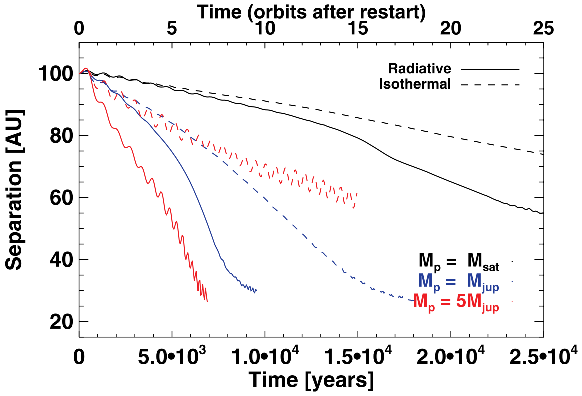

Figure 7. Time evolution of the planets' orbital separation obtained for the laminar disc model with initial profiles of surface density and temperature similar to those of the gravitoturbulent run with $\beta = 30$ before restart. Solid curves show the results with inclusion of an energy equation (with viscous heating and β-cooling), and dashed curves those with an isothermal equation of state.

The results with the laminar disc model and an energy equation are depicted in Fig. 7 as solid curves. It takes about five orbits for the 5 Jupiter-mass planet to migrate from 100 to 50 au, and about seven orbits for the Jupiter-mass planet. This corresponds to migration rates approximately half those of the gravitoturbulent calculations (see bottom row of Fig. 4). Interestingly, the difference in migration rates is larger for the Saturn-mass planet, which drifts from 100 to 60 au in 20–25 orbits in the laminar run, and (on average) in only five to six orbits in the gravitoturbulent run. We note that the migration time-scales of the Saturn- and Jupiter-mass planets differ by a factor approximately equal to their mass ratio, as expected in the type I migration regime, wherein the tidal torque encompasses the differential Lindblad torque and the horseshoe drag (Paardekooper & Papaloizou 2009). We comment that it is the large disc aspect ratio ($h \sim 0.1$) that makes the Saturn-mass planet ($q/h^3 \sim 0.3$) and the Jupiter-mass planet ($q/h^3 \sim 1$) relevant to type I migration. The 5 Jupiter-mass planet ($q/h^3 \sim 5 \gg 1$) is, however, more prone to non-linear effects (e.g. Masset, D'Angelo & Kley 2006). This is presumably why the migration time-scales of the Jupiter- and the 5 Jupiter-mass planets do not differ by a factor of their mass ratio. It may seem surprising that the 5 Jupiter-mass planet does not open a gap and migrates in a very short time-scale. The gap-opening criterion for a planet on a fixed circular orbit in a laminar viscous disc takes the form (Crida, Morbidelli & Masset 2006)

$$1.1\left(\frac{q}{h^3}\right)^{-1/3} + 50\left(\frac{\alpha}{h}\right)\left(\frac{q}{h^3}\right)^{-1} \lesssim 1, \qquad (3)$$

where α and h are to be evaluated at the planet's orbital separation. Although it is unclear to what extent the gap-opening criterion in equation (3) may be applied to planets migrating in gravitoturbulent discs, it provides some insight into the fact the planets in our disc models are not expected to clear a gap. Notwithstanding that the large values of h and α imply the 5 Jupiter-mass planet does not quite satisfy the above gap-opening criterion [the left-hand side of equation (3) typically ranges from 2 to 4 in the disc inner parts], we stress that the vigorous tidal torque exerted by the disc, which is

---

[3] As in the case with $\beta = 20$, this value of α, given by viscous transport theory, is slightly smaller than what we measured in the gravitoturbulent disc model ($\langle\alpha_{\rm tot}\rangle \approx 1.8$ per cent). We have checked that a higher value of α does not change our results of laminar calculations, presented below.

partly due to the large masses of the disc and the planet, conspires to make the planet migrate in a time-scale shorter than the time-scale required to open a gap (a few libration time-scales, which would correspond here to a few tens of orbits). In other words, the 5 Jupiter-mass planet migrates very fast because it has no time to open a gap.

The results of laminar simulations with an isothermal equation of state are overplotted as dashed curves in Fig. 7. The migration rates obtained in this series are smaller than with inclusion of an energy equation. The difference arises from a large, negative horseshoe drag obtained with an energy equation, and driven by a *positive* entropy gradient in our disc model (Baruteau & Masset 2008a; Paardekooper & Papaloizou 2008; Masset & Casoli 2009; Paardekooper et al. 2010; in our case, the radial profile of the disc entropy scales in proportion to the orbital separation).

Further insight into the impact of the horseshoe drag may be obtained by comparing the migration time-scales of our laminar calculations to those predicted by type I migration theory. Note that the predicted migration time-scales are inferred from the torque exerted on a planet held on a fixed circular orbit. In the isothermal series, where $\Sigma \propto r^{-3/2}$ and T is uniform, the total torque reduces to the differential Lindblad torque. Using equation (14) of Paardekooper et al. (2010), we find migration time-scales of about 75 and 20 orbits for the Saturn- and Jupiter-mass planets, respectively. This is in good agreement (to within ~25 per cent) with our findings (dashed curves in Fig. 7). In the series with the energy equation, the total torque comprises the differential Lindblad torque and the horseshoe drag. Despite the large value of α in our disc model, the horseshoe drag is found to be fully unsaturated, as the diffusion time-scale across the planet's horseshoe region remains larger than the U-turn time-scale (Baruteau & Masset 2008a; Masset & Casoli 2010; Paardekooper, Baruteau & Kley 2011a). Using equations (14) and (45) of Paardekooper et al. (2010), we now find migration time-scales of about 35 and 10 orbits for the Saturn- and Jupiter-mass planets, respectively. This is shorter than what we find (see solid curves in Fig. 7), although still in decent agreement. The difference presumably arises from the large velocity difference between the disc and the planet, which sets asymmetric horseshoe streamlines around the planet's orbital radius (Masset 2002), an effect that is not taken into account in the horseshoe drag expression of Paardekooper et al. (2010).

We further comment on having a positive entropy gradient in our gravitoturbulent disc model. Let us assume that the disc profiles of surface density and temperature scale as $r^{-\sigma}$ and $r^{-\varpi}$, respectively. The disc entropy s, which we define as $s \equiv p\Sigma^{-\gamma}$, where the disc pressure p verifies the ideal gas equation of state, scales as $r^{-\xi}$, with $\xi = \varpi - (\gamma - 1)\sigma$. As the disc evolves towards a steady state with approximately uniform Toomre Q profile, $\xi \sim -3 + \sigma(3 - \gamma)$. Steady-state gravitoturbulent discs may thus have a globally decreasing profile of entropy only for surface density profiles steeper than $r^{-9/4}$, assuming $\gamma = 5/3$. Furthermore, for $\gamma = 5/3$ and our fiducial softening length $0.3H(r_{\rm p})$, the fully unsaturated horseshoe drag $\Gamma_{\rm hs}$ reads (Paardekooper et al. 2010, their equation 45)

$$\gamma\Gamma_{\rm hs}/\,\Gamma_0 \approx -20.5 + 8.6\sigma, \tag{4}$$

where $\Gamma_0 = (q/h_{\rm p})^2\Sigma_{\rm p}r_{\rm p}^4\Omega_{\rm p}^2$, and all quantities with the subscript 'p' are to be evaluated at the planet's location. Equation (4) shows that, in discs with a uniform Toomre Q parameter, the horseshoe drag is negative whenever the surface density profile is shallower than $r^{-2.4}$, assuming $\gamma = 5/3$. The differential Lindblad torque $\Gamma_{\rm L}$ can be similarly recast as (Paardekooper et al. 2010, their equation 14)

$$\gamma\Gamma_{\rm L}/\,\Gamma_0 \approx 3.2 - 4.0\sigma, \tag{5}$$

and the total torque $\Gamma_{\rm tot}$ as

$$\gamma\Gamma_{\rm tot}/\,\Gamma_0 = -17.3 + 4.6\sigma. \tag{6}$$

Using equation (6), the type I migration time-scale, $\tau_{\rm I} = r_{\rm p}^2\Omega_{\rm p}M_{\rm p}/2\Gamma_{\rm tot}$, reads

$$\frac{\tau_{\rm I}}{T_{\rm orb}} \approx 5.6 \times (3.8 - \sigma)^{-1}\,\gamma Q_{\rm p}\left(\frac{q}{h_{\rm p}^3}\right)^{-1}\left(\frac{h_{\rm p}}{0.1}\right)^{-2}, \tag{7}$$

where $T_{\rm orb}$ stands for the orbital period at the planet's orbital radius. The estimate in equation (7) applies to planets with $q \sim h_{\rm p}^3$, and is approximate, since it is based on the torque expression for a planet on a fixed orbit. As we have already stressed above, the fast relative motion between the disc and planet is likely to affect this estimate. Nevertheless, it indicates that the type I migration of planets formed by fragmentation ($q \sim h_{\rm p}^3$, $Q_{\rm p} \sim 1.5$) in discs with moderate aspect ratio ($h_{\rm p} \sim 0.1$) should typically occur in a few tens of orbits at 100 au, that is a few 10^4 years.

Still, the migration time-scales in our gravitoturbulent simulations are a factor of a few shorter than obtained in laminar disc models. In addition to the stochastic kicks due to turbulence, the following two mechanisms may account for the larger migration rates in the gravitoturbulent disc model.

(i) The non-axisymmetric component of the disc's self-gravity shifts Lindblad resonances towards the planet's orbital radius (Pierens & Huré 2005). For discs close to marginal stability, and for our softening parameter ($\varepsilon/H \sim 0.3$), this shift increases the differential Lindblad torque by typically a factor of 2 (Baruteau & Masset 2008b, their fig. 10). Note, however, that this mechanism has been investigated in laminar disc models. It is therefore not straightforward whether it should behave identically with turbulence. Still, numerical simulations indicate that, on average, the Lindblad torque behaves similarly in laminar and turbulent disc models (Baruteau & Lin 2010, where wave-like turbulence is generated by stochastic forcing of the disc).

(ii) In fully self-gravitating discs, the effective mass that dictates the strength of the tidal torque and thus the migration rate not only includes the planet mass, but also the mass of the gas surrounding the planet's location. For massive planets ($q > h_{\rm p}^3$), the latter corresponds to the planet's circumplanetary disc, which is a fraction of the planet's Hill sphere (Crida et al. 2009a). It is unclear what it corresponds to for smaller planets; we speculate that it might be the planet's Bondi sphere. For illustration purposes, the time evolution of the mass inside the planet's Hill radius is shown in Fig. 8 for three gravitoturbulent runs with $\beta = 30$. It is comparable to, albeit somewhat larger than, the planet mass. It progressively grows as the planet moves inwards, despite the decrease in the planet's Hill radius with decreasing orbital separation. It is possible that the short cooling time-scales used in our simple cooling prescription (a few dynamical time-scales, depending on β) imply that the gas in the planet's Hill radius can contract more rapidly than it would do with a more realistic cooling function. Again, notwithstanding the uncertain dynamical role of the planet's Hill sphere in turbulent disc models, it is likely that the increased effective mass is responsible for an increase in the migration rate by a factor of a few compared to laminar calculations (which only include the axisymmetric component of the disc's self-gravity). We comment that both the increase in the effective planet mass and the decrease in the disc aspect ratio with radius (in discs with flat temperature profile, $h \propto r^{1/2}$) make planets less and less sensitive to stochastic kicks as they migrate inwards. This explains why in Fig. 5 the

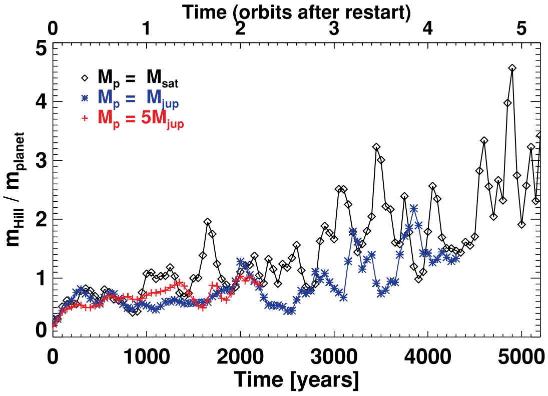

Figure 8. Time variation of the mass enclosed in the planet's Hill radius in units of the planet mass, obtained for the restart simulation with $\beta = 30$ and zero azimuth at restart. The mass ratio is displayed before the planet crosses the inner edge of the computational domain.

amplitude of the stochastic kicks decreases with decreasing orbital separation. This also implies that, if a planet undergoes a vigorous inward kick, it will be increasingly harder to reverse the trend. However, should a planet experience a large outward kick, it would take longer for the tidal torque to take over and lead to inward migration again.

3.2.4 Impact of numerics

We briefly assess in this section the impact of numerics on our results of gravitoturbulent calculations. We have performed an additional suite of simulations with the Jupiter-mass planet and $\beta = 30$, with the planet's mass first smoothly ramped up over one orbit, while the planet is held on a Keplerian orbit. After this, the planet is released in the disc. This procedure is meant to mimic the clump formation, which typically occurs over a dynamical time-scale, much shorter than the gap-opening time-scale (see Section 3.2.3). The time evolution of the planet's orbital separation is depicted in the left-hand panel of Fig. 9. It shows the very same trend as obtained without smoothly increasing the planet's mass (see the mid-bottom panel of Fig. 4).

To assess the influence of resolution on our simulation results, we have varied the grid's resolution and the softening length $\varepsilon_{\rm sg}$ over which the self-gravitating acceleration is smoothed. We have run two additional disc models with $\beta = 30$, one with an increased grid resolution (1024×2048) and another with a larger $\varepsilon_{\rm sg}$ ($3 \times 10^{-2}\, r$). In the latter case, $\varepsilon_{\rm sg}$ is 0.3 times the initial pressure scaleheight, and it can be regarded as a crude treatment for the effects of the disc's finite thickness. The value of $\varepsilon_{\rm sg}$ at $r = r_{\rm p}$ equals the softening length of the planet's gravitational potential. We have checked that before the introduction of the planet at 30 orbits the disc properties (density and temperature profiles) in both additional models are in close agreement with those of the corresponding run at our fiducial resolution and softening length value. We restarted these simulations with a Jupiter-mass planet. Again, in each case, a series of eight simulations was performed with evenly spaced values for the planet's azimuth at restart. Results with increased grid resolution and increased $\varepsilon_{\rm sg}$ are depicted in the middle and right-hand panels of Fig. 9, respectively. Overall, the amplitude of the stochastic fluctuations is somewhat larger in the high-resolution simulations. Still, except in one run that features a rather long episode of outward migration, the migration time-scale of the high-resolution simulations ranges from about three to nine orbits, which is broadly consistent with the results at our fiducial resolution. Furthermore, increasing $\varepsilon_{\rm sg}$ from $3 \times 10^{-4}\, r$ to $3 \times 10^{-2}\, r$ does not significantly change the amplitude of the stochastic kicks experienced by the planet, and the migration time-scales obtained with both values of $\varepsilon_{\rm sg}$ are in reasonable agreement. The results of both additional disc models indicate that the planet's orbital evolution is essentially unaltered by density structures arising from gravitoturbulence with typical size $\lesssim 0.3H$.

3.3 Results at lower disc temperature

As shown in Section 3.2, the migration of planets formed by gravitational instability results from a competition between the background disc–planet tidal torque and the stochastic torque due to turbulence. At least in the early stages of their evolution, such planets should have a planet-to-primary mass ratio $q \sim h_{\rm p}^3$, and be subject to type I like migration (see Section 3.2.3). As far as the tidal torque is concerned, equation (7) shows that the migration time-scale is essentially controlled by three dimensionless parameters:

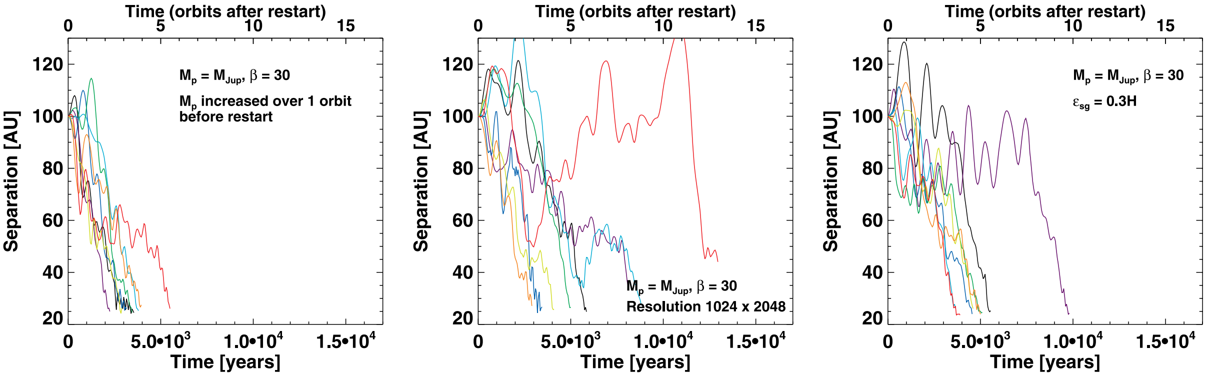

Figure 9. Migration of a Jupiter-mass planet in a disc with cooling parameter $\beta = 30$. In the left-hand panel, the planet mass is gradually ramped up over one orbit, while the planet is held on a fixed circular orbit. After this first stage (not shown in this panel), the planet is released in the disc. The middle panel shows results at higher resolution (1024×2048), and the right-hand panel shows results with increased self-gravitating softening length ($\varepsilon_{\rm sg} = 3 \times 10^{-2}\, r$). All three panels should be compared to the mid-bottom panel in Fig. 4, which displays the results of our fiducial set-up (no gradual increase of the planet mass, grid resolution is 512×1536, and $\varepsilon_{\rm sg} = 3 \times 10^{-4}\, r$).

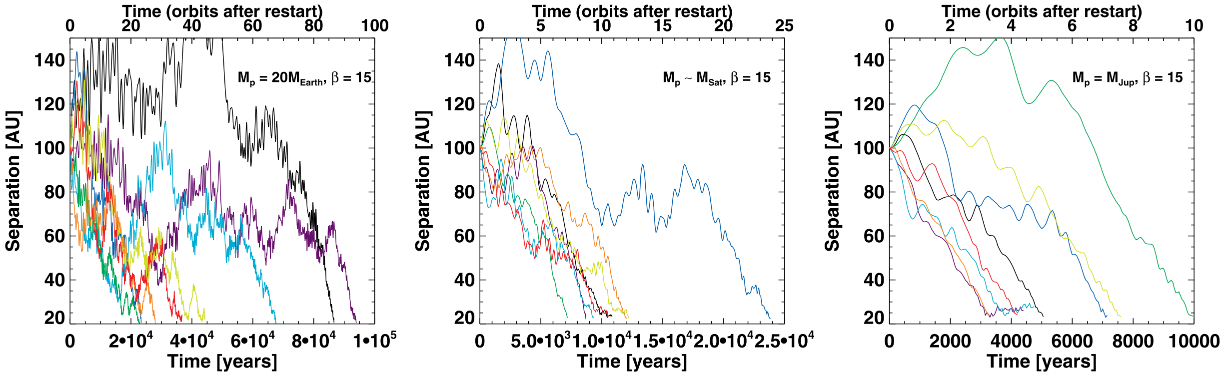

Figure 10. Time evolution of the planets' orbital separation for the disc model with $\beta = 15$ restarted at 85 orbits, when the disc aspect ratio is ≈6 per cent. From left to right, results are shown for a 20 Earth-mass planet ($q = 6 \times 10^{-5}$, $q/h^3 \sim 0.3$), a ∼ Saturn-mass planet ($q = 2 \times 10^{-4}$, $q/h^3 \sim 1.5$) and a Jupiter-mass planet ($q = 10^{-3}$, $q/h^3 \sim 5$). As in the previous figures, results are obtained for eight evenly spaced planet's azimuths at restart (increasing with increasing wavelength's colour).

q/h_p^3, which should be ∼1 in the early stages of the planet evolution, Q_p, which is $\gtrsim$1.5 in a steady state, and h_p. The disc model that we have considered so far has $h_\mathrm{p} \sim 0.1$, which leads to rapidly formed Jupiter-mass planets. However, it is possible that the disc initially has a lower aspect ratio, thereby forming less massive planets. The latter may still become Jupiter-sized objects if mass growth is efficient.

To evaluate the impact of a lower disc temperature on our results, we restarted the simulation of Section 3.1 with $\beta = 15$ at 85 orbits. At this time, the disc aspect ratio at the planet's restart location (100 au) has decreased from 0.1 to about 0.06, and the disc's mass from $0.2M_\star$ to $0.15M_\star$. We choose again three planet masses corresponding to a planet-to-primary ratio q around h_p^3: a 20 Earth-mass planet ($q = 6 \times 10^{-5}$, $q/h_\mathrm{p}^3 \sim 0.3$), a ∼ Saturn-mass planet ($q = 2 \times 10^{-4}$, $q/h_\mathrm{p}^3 \sim 1$) and a Jupiter-mass planet ($q = 10^{-3}$, $q/h_\mathrm{p}^3 \sim 5$). As previously, we take eight evenly spaced planet's azimuths at restart. The time evolution of the planets' orbital separation is shown in Fig. 10.

Compared to the results with $h_\mathrm{p} = 0.1$, planets with the same q/h_p^3 are now more sensitive to stochastic fluctuations, the tidal torque becoming less vigorous. This can be seen from equation (7), which indicates that at fixed values of q/h_p^3 and Q_p, the migration time-scale due to the tidal torque scales with h_p^{-2}. The mean migration time-scales that we obtain for $h_\mathrm{p} \sim 0.06$ (about six, 12 and 50 orbits with decreasing q/h_p^3) are typically a factor of 3–5 longer than in the corresponding runs with $h_\mathrm{p} \sim 0.1$, which is roughly consistent with the aforementioned scaling $\tau_\mathrm{I} \propto h_\mathrm{p}^{-2}$.

4 CONCLUDING REMARKS

Planets observed at large orbital separation from their host star (typically $\gtrsim$50 au) are thought to be potential candidates for the formation scenario based on the gravitational instability of massive discs. A number of studies have shown that the formation of clumps by fragmentation is possible at such separations (e.g. Matzner & Levin 2005; Rafikov 2005; Stamatellos & Whitworth 2008). The orbital evolution of clumps formed by gravitational instability has been investigated in a few studies (e.g. Mayer et al. 2002; Boss 2005; Cha & Nayakshin 2011; Vorobyov & Basu 2010a; Machida et al. 2011). Clumps are often observed to migrate inwards on short time-scales, although in some disc models the formation of several clumps and/or the use of different cooling functions has a significant impact on migration, which sometimes appears to be suppressed (Boss 2005).

In this paper, we have studied the interaction between a single planet and the gravitoturbulent disc it is embedded in, following the assumption that the planet has formed by gravitational instability. We have performed 2D hydrodynamical simulations with a simplified prescription for the disc's cooling. Three disc models with different cooling time-scales have been considered, giving rise to different levels of gravitoturbulence. After having set up a quasi-steady-state gravitoturbulent disc, we have restarted our simulations including a single planet with a range of masses approximately equal to the expected initial mass of clumps formed by fragmentation ($\gtrsim h^3 M_\star$, with h the disc aspect ratio at the fragmenting location; see Boley et al. 2010).

We find that a planet interacting with its nascent gravitoturbulent disc migrates inwards on very short time-scales, despite the stochastic kicks due to turbulent density fluctuations. In a disc with aspect ratio ∼0.1, it takes less than 10 orbits at 100 au (that is, about 10^4 years) for a Jupiter-mass planet to migrate from 100 to 20 au (the inner edge of our computational grid). Planets less massive than the expected fragmenting mass are not only more sensitive to stochastic kicks, but also migrate inwards relatively fast. Their formation and migration time-scales being shorter than their gap-opening time-scale (partly because of the disc's vigorous turbulence), planets formed by fragmentation do not open a dip or a gap around their orbit, and are therefore not subject to the type II and runaway type III migration regimes. Turbulent density fluctuations may provide an effective mass deficit in the planet's horseshoe region that kicks the planet either inwards or outwards (see Section 3.2.2). These kicks can be seen as an effective, *temporary* type III migration coming on top of the inward migration due to the background disc–planet tidal torque.

The comparison of our results with those of laminar disc models shows that the averaged tidal torque driving the net inward migration in gravitoturbulent discs is essentially the one that would lead to type I migration in the absence of turbulence (see Section 3.2.3). Part of the reason as to why planets rapidly migrate inwards in our model is due to the set-up of a positive entropy gradient in a steady state, which yields a large negative horseshoe drag, adding up to the negative differential Lindblad torque. We argue that in gravitoturbulent discs with uniform Toomre Q profiles and cooling-to-orbital time-scale ratios (that is, with a uniform alpha parameter) the horseshoe drag should be negative, unless the surface density decreases very steeply (see equation 4). Although this possibility cannot be excluded, we believe that fast inward migration should be a generic expectation for planets formed by gravitational instability.

The main conclusion of this present study is that a single planet formed by gravitational instability should migrate inwards on a time-scale much shorter than the expected lifetime of protoplanetary discs. However, it is not possible at this stage to say that massive planets at large separation from their host star, such as the HR 8799 system, *could not* have formed by gravitational instability. The simulations presented here contain a number of simplifications that need to be addressed. We have considered a simplified cooling prescription, causing the entire disc to be gravitoturbulent. In reality, we would expect the inner parts of a disc to be too hot to be gravitationally unstable, and other sources of turbulence such as the magnetorotational instability could prevail (see e.g. Clarke 2009; Rice & Armitage 2009; Zhu, Hartmann & Gammie 2009, who studied the radial dependence of the alpha viscosity parameter in self-gravitating discs with realistic cooling). It is thus possible that the rapid type I migration of planets formed by gravitational instability gets slowed down in the disc inner parts, resulting in gap formation. A more realistic cooling prescription will also impact the rate at which planets can contract, with various outcomes for the evolution of the planet mass over its orbital migration (e.g. Nayakshin 2010). Also, we have focused on the orbital evolution of a single planet assumed to have formed by fragmentation, whereas the formation of multiple clumps is a likely outcome of gravitational instability. It is fully expected that the interaction between clumps may significantly impact their migration. We will address these issues in future work.

ACKNOWLEDGMENTS

CB is supported by a Herchel Smith Postdoctoral Fellowship. FM is grateful for funding from the EC Sixth Framework Programme and also acknowledges the support of the German Research Foundation (DFG) through grant KL 650/8-2 within the Collaborative Research Group FOR 759: *The formation of Planets: The Critical First Growth Phase*. SJP is supported by an STFC Postdoctoral Fellowship. Numerical simulations were performed on the Pleiades and Grape clusters at U.C. Santa Cruz. Part of this project was done during the 2010 edition of the ISIMA summer school, whose support is gratefully acknowledged. We thank John Papaloizou and Andrew Youdin for useful discussions, Min-Kai Lin for detailed comments on a first draft of this manuscript, and the referee for useful comments.

REFERENCES

Balbus S. A., Papaloizou J. C. B., 1999, ApJ, 521, 650
Baruteau C., Lin D. N. C., 2010, ApJ, 709, 759
Baruteau C., Masset F., 2008a, ApJ, 672, 1054
Baruteau C., Masset F., 2008b, ApJ, 678, 483
Boley A. C., Hayfield T., Mayer L., Durisen R. H., 2010, Icarus, 207, 509
Boss A. P., 1997, Sci, 276, 1836
Boss A. P., 2005, ApJ, 629, 535
Bryden G., Różyczka M., Lin D. N. C., Bodenheimer P., 2000, ApJ, 540, 1091
Cameron A. G. W., 1978, Moon Planets, 18, 5
Cha S.-H., Nayakshin S., 2011, MNRAS, in press (doi:10.1111/j.1365-2966.2011.18953.x)
Clarke C. J., 2009, MNRAS, 396, 1066
Cossins P., Lodato G., Clarke C. J., 2009, MNRAS, 393, 1157
Crida A., Morbidelli A., Masset F., 2006, Icarus, 181, 587
Crida A., Baruteau C., Kley W., Masset F., 2009a, A&A, 502, 679
Crida A., Masset F., Morbidelli A., 2009b, ApJ, 705, L148
Gammie C. F., 2001, ApJ, 553, 174
Goldreich P., Tremaine S., 1980, ApJ, 241, 425
Helled R., Bodenheimer P., 2011, Icarus, 211, 939
Ida S., Lin D. N. C., 2004, ApJ, 604, 388
Ida S., Lin D. N. C., 2008, ApJ, 673, 487
Kalas P. et al., 2008, Sci, 322, 1345
Lafrenière D., Jayawardhana R., van Kerkwijk M. H., 2010, ApJ, 719, 497
Lagrange A. et al., 2010, Sci, 329, 57
Lin M.-K., Papaloizou J. C. B., 2010, MNRAS, 405, 1473
Lodato G., Rice W. K. M., 2004, MNRAS, 351, 630
Lynden Bell D., Kalnajs A. J., 1972, MNRAS, 157, 1
Machida M. N., Inutsuka S., Matsumoto T., 2011, ApJ, 729, 42
Marois C., Macintosh B., Barman T., Zuckerman B., Song I., Patience J., Lafrenière D., Doyon R., 2008, Sci, 322, 1348
Marois C., Zuckerman B., Konopacky Q. M., Macintosh B., Barman T., 2010, Nat, 468, 1080
Masset F., 2000, A&AS, 141, 165
Masset F. S., 2002, A&A, 387, 605
Masset F. S., Casoli J., 2009, ApJ, 703, 857
Masset F. S., Casoli J., 2010, ApJ, 723, 1393
Masset F. S., Papaloizou J. C. B., 2003, ApJ, 588, 494
Masset F. S., D'Angelo G., Kley W., 2006, ApJ, 652, 730
Matzner C. D., Levin Y., 2005, ApJ, 628, 817
Mayer L., Quinn T., Wadsley J., Stadel J., 2002, Sci, 298, 1756
Meru F., Bate M. R., 2011a, MNRAS, 411, L1
Meru F., Bate M. R., 2011b, MNRAS, 410, 559
Mizuno H., 1980, Progress Theor. Phys., 64, 544
Nayakshin S., 2010, MNRAS, 408, L36
Nelson R. P., Papaloizou J. C. B., 2004, MNRAS, 350, 849
Paardekooper S.-J., Papaloizou J. C. B., 2008, A&A, 485, 877
Paardekooper S.-J., Papaloizou J. C. B., 2009, MNRAS, 394, 2283
Paardekooper S.-J., Baruteau C., Crida A., Kley W., 2010, MNRAS, 401, 1950
Paardekooper S.-J., Baruteau C., Kley W., 2011a, MNRAS, 410, 293
Paardekooper S.-J., Baruteau C., Meru F., 2011b, MNRAS, in press
Pierens A., Huré J.-M., 2005, A&A, 433, L37
Pollack J. B., Hubickyj O., Bodenheimer P., Lissauer J. J., Podolak M., Greenzweig Y., 1996, Icarus, 124, 62
Rafikov R. R., 2005, ApJ, 621, L69
Rice W. K. M., Armitage P. J., 2009, MNRAS, 396, 2228
Rice W. K. M., Lodato G., Armitage P. J., 2005, MNRAS, 364, L56
Safronov V. S., 1969, Evoliutsiia Doplanetnogo Oblaka. Nakua, Moscow
Stamatellos D., Whitworth A. P., 2008, A&A, 480, 879
Stone J. M., Norman M. L., 1992, ApJS, 80, 753
Thommes E. W., 2005, ApJ, 626, 1033
Toomre A., 1964, ApJ, 139, 1217
Vorobyov E. I., Basu S., 2006, ApJ, 650, 956
Vorobyov E. I., Basu S., 2010a, ApJ, 714, L133
Vorobyov E. I., Basu S., 2010b, ApJ, 719, 1896
Zhu Z., Hartmann L., Gammie C., 2009, ApJ, 694, 1045

APPENDIX A: CALCULATION OF THE ALPHA PARAMETERS IN A 2D DISC

When mass is confined to a razor-thin disc, the calculation of the alpha parameters associated with the Reynolds and gravitational stresses may be inferred from the general 3D case by substituting the volume mass density ρ with $\Sigma\delta(z)$, where Σ is the surface mass density of the razor-thin disc, δ is Dirac's delta function and z denotes the vertical coordinate. One obtains (Lynden-Bell & Kalnajs 1972; Gammie 2001)

$$\alpha_{\rm Rey} = \frac{2}{3}\frac{\langle \Sigma \delta v_r \delta v_\varphi \rangle}{\langle \Sigma c_s^2 \rangle}, \tag{A1}$$

where $\langle . \rangle$ stands for the azimuthal average, $\delta v_r = v_r - \langle v_r \rangle$, $\delta v_\varphi = v_\varphi - \langle v_\varphi \rangle$ and

$$\alpha_{\rm sg} = \frac{2}{3} \frac{\left\langle \int_{-\infty}^{\infty} (4\pi G)^{-1} g_r g_\varphi {\rm d}z \right\rangle}{\left\langle \Sigma c_{\rm s}^2 \right\rangle}. \quad \text{(A2)}$$

In both previous equations, v_r, v_φ and $c_{\rm s}$ are to be evaluated in the razor-thin disc ($z \equiv 0$) and are therefore directly computed in a 2D simulation. However, the vertical dependence of g_r and g_φ, the radial and azimuthal components of the self-gravitating acceleration, needs to be determined as the gravitational field outside the disc contributes to the shear stress despite mass being confined to the disc. The potential Φ from which g_r and g_φ can be derived is given by

$$\Phi = -\int_{\mathcal{D}} \frac{G\Sigma(r', \varphi') r' {\rm d}r' {\rm d}\varphi'}{\sqrt{r^2 + r'^2 - 2rr' \cos(\varphi - \varphi') + z^2 + \varepsilon_{\rm sg}^2}}, \quad \text{(A3)}$$

where $\mathcal{D}$ is the domain where Σ does not vanish and $\varepsilon_{\rm sg}$ is a small softening length required to avoid numerical divergences when $z = 0$. From the surface density of our 2D simulations, $g_r(r, \varphi, z)$ and $g_\varphi(r, \varphi, z)$ can be conveniently calculated by fast Fourier transforms provided that z is taken proportional to r, condition required for g_r and g_φ to read as convolution products (another necessary condition is that a grid with logarithmic radial spacing is used). The same condition applies to $\varepsilon_{\rm sg}$ for the calculation of g_r and g_φ at $z = 0$. Writing $\varepsilon_{\rm sg} = Br$ and $z = \eta r$, with B and η constants, the expressions for $g_r(r, \varphi, z)$ and $g_\varphi(r, \varphi, z)$ are given by equations (A1) and (A3) of Baruteau & Masset (2008b) with $B^2 \rightarrow B^2 + \eta^2$. The vertical integral in equation (A2) is then numerically calculated from the values of g_r and g_φ obtained with a range of values for η.

This paper has been typeset from a TEX/LATEX file prepared by the author.

The Astrophysical Journal, 778:7 (15pp), 2013 November 20 doi:10.1088/0004-637X/778/1/7

DISK–PLANETS INTERACTIONS AND THE DIVERSITY OF PERIOD RATIOS IN *KEPLER*'S MULTI-PLANETARY SYSTEMS

Clement Baruteau and John C. B. Papaloizou
Department of Applied Mathematics and Theoretical Physics (DAMTP), University of Cambridge, Wilberforce Road,
Cambridge CB3 0WA, UK; C.Baruteau@damtp.cam.ac.uk, J.C.B.Papaloizou@damtp.cam.ac.uk

Received 2013 January 4; accepted 2013 August 29; published 2013 October 28

ABSTRACT

The *Kepler* mission is dramatically increasing the number of planets known in multi-planetary systems. Many adjacent planets have orbital period ratios near resonant values, with a tendency to be larger than required for exact first-order mean-motion resonances. This feature has been shown to be a natural outcome of orbital circularization of resonant planetary pairs due to star–planet tidal interactions. However, this feature holds in multi-planetary systems with periods longer than 10 days, in which tidal circularization is unlikely to provide efficient divergent evolution of the planets' orbits to explain these orbital period ratios. Gravitational interactions between planets and their parent protoplanetary disk may instead provide efficient divergent evolution. For a planet pair embedded in a disk, we show that interactions between a planet and the wake of its companion can reverse convergent migration and significantly increase the period ratio from a near-resonant value. Divergent evolution due to wake-planet interactions is particularly efficient when at least one of the planets opens a partial gap around its orbit. This mechanism could help account for the diversity of period ratios in *Kepler*'s multiple systems from super-Earth to sub-Jovian planets with periods greater than about 10 days. Diversity is also expected for pairs of planets massive enough to merge their gap. The efficiency of wake-planet interactions is then much reduced, but convergent migration may stall with a variety of period ratios depending on the density structure in the common gap. This is illustrated for the Kepler-46 system, for which we reproduce the period ratio of Kepler-46b and c.

Key words: accretion, accretion disks – hydrodynamics – methods: numerical – planetary systems – planet–disk interactions – protoplanetary disks

Online-only material: color figures

1. INTRODUCTION

Planetary astrophysics is undergoing an epoch of explosive growth driven by the discovery of about 850 exoplanets in two decades. Continuous improvement in detection techniques will uncover many more planets in the near future that are too small or too far from their host star to be detected at present. Observations suggest that planet formation is ubiquitous, with more than 40% of nearby Sun-like stars harboring at least one planet less massive than Saturn (Mayor et al. 2009). These discoveries have revealed the diversity of exoplanetary systems and have indicated that planets may form under a wide range of conditions and be considerably mobile.

The diversity of exoplanets has been especially highlighted by the *Kepler*'s space mission. To date, *Kepler* has detected over 2300 planet candidates (Batalha et al. 2013), from which more than a hundred are confirmed planets.[1] About one third of *Kepler*'s candidates are associated with multiple transiting systems and the vast majority of them are expected to be multi-planetary systems (Lissauer et al. 2012). Some of these systems show remarkable properties, like the five coplanar, with alternating rocky and icy planets orbiting Kepler-20 in less than 80 days (Gautier et al. 2012). Interactions between planets and their parent protoplanetary disk are likely to have played a major role in shaping such a compact system.

A striking feature of *Kepler*'s multi-planetary systems is the large number of planet pairs far from mean-motion resonances (MMR; Lissauer et al. 2011). Planet pairs near resonances tend to have period ratios slightly greater than resonant values; period ratios are defined as the outer planet's orbital period divided by the inner planet's (see Figure 1). There are almost twice as many planet pairs with period ratios between 2.0 and 2.1 than between 1.9 to 2.0. This feature could arise from tidal orbital circularization of close-in resonant planet pairs (Papaloizou 2011; Lithwick & Wu 2012; Batygin & Morbidelli 2013). However, the histograms in Figure 1 show that the same trend holds for planet pairs where the orbital period of the inner planet exceeds 10 days, especially near first-order resonances. For such systems, tidal circularization is unlikely to have caused significant divergent evolution of the planets orbits, as shown in Appendix A.

An example of a planetary system with a period ratio slightly greater than resonant is the Kepler-46 system (previously known as KOI-872). The 0.9 Solar-mass star is surrounded by a $0.8 R_{\rm J}$ transiting planet on a 33.6 day period (Kepler-46b). Large transit time variations (TTV) of Kepler-46b are caused by the presence of an outer planet, Kepler-46c, whose mass ($0.37\ M_{\rm J}$) and orbital period (57.0 days) have been determined by Nesvorný et al. (2012). The same authors have also reported the detection of a $1.7\ R_{\oplus}$ planet candidate on a 6.8 day period (Kepler-46d, not yet confirmed). The main properties of the Kepler-46 planetary system are summarized in Table 1. The low-eccentricity and quasi-coplanar orbits in this system suggest that the planets most likely reached their present location through disk–planet interactions. Still, the ratio or orbital periods between Kepler-46c and Kepler-46b is ≈1.696, which is slightly greater than 5:3. Capture in the 5:3 MMR is not a natural outcome of planet migration driven by disk–planet interactions. It requires a rate of convergent migration that is large enough to cross the 2:1 MMR, but not too large so that the planets do not reach their 3:2 MMR. Capture into a second-order resonance also requires small but not zero eccentricities, which disk–planet interactions

---

[1] http://kepler.nasa.gov

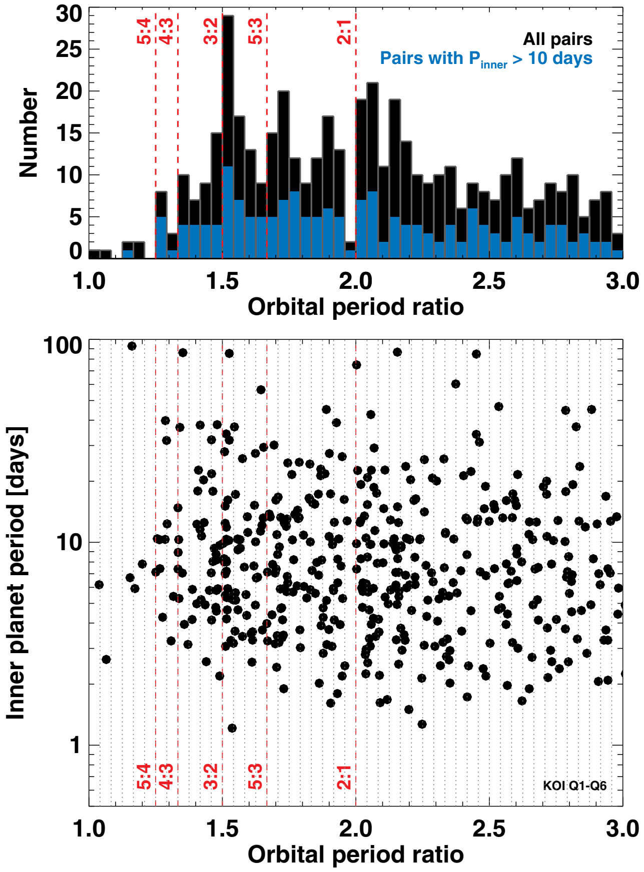

Figure 1. Bottom: ratio of orbital periods of all planet pairs among *Kepler*'s candidate multi-planetary systems detected from quarters 1 to 6 (x-axis) vs. the orbital period of the inner planet in each pair (in days, y-axis). Bins are $1/24$ wide. Top: histograms of the orbital period ratio for all planet pairs (black), and for planet pairs where the inner planet's period is greater than 10 days. For both the top and bottom graphs, from left to right, vertical dashed lines show the location of the 5:4, 4:3, 3:2, 5:3, and 2:1 mean-motion resonances. Data were extracted from http://planetquest.jpl.nasa.gov/kepler/.

(A color version of this figure is available in the online journal.)

Table 1
Kepler-46 Planetary System (Nesvorný et al. 2012)

	Mass or Radius	Period (days)	Eccentricity
Kepler-46	$0.9\,M_\odot$	...	...
Kepler-46d[a]	$\approx 1.7\,R_\oplus$	6.8	0 (assumed)
Kepler-46b	$\approx 0.8\,R_\mathrm{J}$	33.6	$\leqslant 0.02$
Kepler-46c[b]	$0.37\,M_\mathrm{J}$	57.0	≈ 0.015

Notes.
[a] Unconfirmed.
[b] Inferred from TTV signal of Kepler-46b.

tend to damp efficiently. Should disk–planet interactions have led Kepler-46b and Kepler-46c to reach their 5:3 MMR, it is unclear how their period ratio would have then increased to their present value.

The initial motivation of this work is to investigate under what circumstances disk–planets interactions may account for the orbital period ratio between Kepler-46c and Kepler-46b. In Section 2, we present results of hydrodynamical simulations modeling the early evolution of both planets as they were embedded in their parent protoplanetary disk. These Saturn-mass planets are expected to open a partial gap around their orbit. A rapid convergent migration causes the planets to merge their gap and to evolve into a common gap. The planets' convergent migration is found to stall with period ratios between 1.5 and 1.7, depending on the disk's density profile inside the common gap. The observed period ratio can be reproduced without the planets being in resonance. Furthermore, we show that disk-driven migration of partial gap-opening planets may lead to significant divergent evolution of planet pairs over typical disk lifetimes. Such divergent evolution is shown to arise from the interaction between planets and the wakes of their companions. This mechanism is illustrated for super-Earth-mass planets in Section 3 through both hydrodynamical simulations and customized three-body integrations. Divergent evolution of gap-opening planet pairs mediated by wake-planet interactions could partly account for the diversity of period ratios in *Kepler*'s multi-planetary systems. Concluding remarks are provided in Section 4.

2. HYDRODYNAMICAL SIMULATIONS OF THE KEPLER-46 PLANETARY SYSTEM

In this section, we model the early evolution of the Kepler-46 planetary system when the planets were embedded in their parent protoplanetary disk. Our study does not address the formation of the planets. We focus, instead, on the planets' orbital evolution due to disk–planet and planet–planet interactions. Two-dimensional hydrodynamical simulations of disk–planets interactions were carried out using the code FARGO (Masset 2000). The physical model and numerical setup of the hydrodynamical simulations are described in Section 2.1. Results of simulations follow in Section 2.2.

2.1. Physical Model and Numerical Setup

Disk model. We adopt a two-dimensional disk model for the protoplanetary disk in which the planets orbiting Kepler-46 formed. Disk–planets interactions determine the convergent migration rate of the planets and the damping rate of their eccentricity. Both quantities are sensitive to the disk's surface density, temperature, turbulent viscosity, and radiative properties. The parameter space is therefore particularly large, and the need to assess the planets' orbital evolution over, typically, a thousand planet orbits has led us to make simplifying assumptions for the disk model and to fix some of the disk parameters.

Disk self-gravity is discarded given the low disk masses adopted in this work (the Toomre-Q parameter associated with the unperturbed density profile does not go below 7). A locally isothermal equation of state is used where the vertically integrated pressure, P, and density, Σ, satisfy $P = \Sigma c_\mathrm{s}^2$, with the sound speed, c_s, specified as a fixed function of the cylindrical radius r. The sound speed is related to the disk's pressure scale height, H, through $H = c_\mathrm{s}/\Omega_\mathrm{K}$ with Ω_K as the Keplerian angular velocity. The fixed temperature profile is taken proportional to r^{-1} so that the disk's aspect ratio, $h = H/r$, is uniform. We take the standard value $h = 0.05$. A locally isothermal equation of state is generally not appropriate to model the migration of an embedded low-mass planet, since it underestimates the magnitude of the corotation torque that the planet experiences from the disk; see Baruteau & Masset (2013) for a recent review on planet migration. This is not an issue in this study, however, since we consider partial gap-opening planets for which the corotation torque has a rather weak effect on migration. This may be quantified through the dimensionless parameter q/h^3 (q denotes the planet-to-star mass ratio), which is $\gtrsim 2$ in our simulations. This lower limit implies that the direction and speed of planet migration are weakly sensitive to the choice for the equation of state (Kley & Crida 2008).

The effects of turbulence are modeled by a constant shear kinematic viscosity, ν. We take $\nu = 1.1 \times 10^{-5}$ in standard code units (defined below), which translates into a viscous alpha parameter $\alpha = 4.5 \times 10^{-3}$ at the initial location of the inner planet. This value of α is typical of the magnetically active regions of protoplanetary disks with magneto-hydrodynamic turbulence driven by the magneto-rotational instability. The present orbital periods of the planets in the Kepler-46 system imply that the planets have probably interacted with magnetically active regions in their parent disk. The disk's magnetic field, however, is not included in our simulations. We also point out that the planets that we consider are of large enough mass that small-scale turbulent fluctuations can be safely ignored when modeling the interaction with their parent disk. The viscous diffusion approximation is expected to be a reasonable approximation for the large planet masses we consider (Nelson & Papaloizou 2003; Baruteau et al. 2011).

The disk is set up in radial equilibrium, with the centrifugal acceleration and the radial acceleration related to the pressure gradient balancing the gravitational acceleration due to the central star. The initial gas surface density is taken proportional to $r^{-1/2}$. Its value at the initial location of the inner planet is taken as a free parameter, which we denote by Σ_0.

Planet parameters. We model the orbital evolution of the outer two planets in the Kepler-46 system: Kepler-46b (the inner planet) and Kepler-46c (the outer planet). The 1.7 $R_\oplus$ unconfirmed planet candidate with an orbital period of 6.8 days is assumed to have had a negligible impact on the orbital evolution of Kepler-46b and Kepler-46c. The planets are assumed to have already formed at the beginning of our simulations, they therefore take their present mass. The inner planet has a physical radius $\approx$0.8 $R_{\rm J}$. However, its mass could not be constrained from TTV (see Nesvorný et al. 2012). The mass–radius diagram of exoplanets detected by transiting methods indicates that the mass of the inner planet most likely lies between 0.2 $M_{\rm J}$ and 0.6 $M_{\rm J}$. Its planet-to-primary mass ratio ($q_{\rm inner}$) is therefore varied in the range [2.2×10^{-4}, 6.6×10^{-4}]. The TTV signal of the inner planet constrains the mass of the outer planet to be $\approx$0.37 $M_{\rm J}$ (Nesvorný et al. 2012). The planet-to-primary mass ratio of the outer planet is thus fixed to $q_{\rm outer} = 4 \times 10^{-4}$. The initial orbital radius of the inner planet, $r_{\rm inner}$, is taken to be the code's unit of length. That of the outer planet is arbitrarily set to $r_{\rm outer} = 1.8\, r_{\rm inner}$, so that the initial ratio of orbital periods $\approx$2.4. For the disk aspect ratio and viscosity taken in our study, the two planets are expected to open a partial gap around their orbit (Lin & Papaloizou 1993; Crida et al. 2006).

Numerical setup. The hydrodynamical equations are solved in a cylindrical coordinate system $\{r, \varphi\}$ centered on the star with $r \in [0.2\text{–}2.6] r_{\rm inner}$ and $\varphi \in [0, 2\pi]$. The computational grid has $N_{\rm r} = 400$ zones evenly spaced along the radial direction and $N_{\rm s} = 800$ azimuthal sectors. The frame rotates with the Keplerian frequency at the inner planet's location, and the indirect terms that account for the acceleration of the central star by the disk and the planets are included in the equations of motion. A standard outflow boundary condition is taken at the grid's inner edge, while damping is used in a so-called wave killing-zone extending from $r = 2.2$ to $r = 2.6$ (disk quantities are damped toward their instantaneous axisymmetric profile). To avoid a violent relaxation of the disk due to the sudden introduction of the planets, the mass of the planets gradually increases over 10 orbital periods. The gravitational potential of the planets is smoothed over a softening length, ε, equal to 0.6H with H evaluated at the planets' locations. The calculation of the force exerted by the disk on the planets excludes the content of the planets' circumplanetary disk, the size of which is about 60% of the planets' Hill radius (Crida et al. 2009). The Hill radius of each planet is initially resolved by about 10 grid cells along each direction.

Code units. Results of simulations are expressed in the standard units of disk–planet calculations: the mass unit is the mass of the central star (denoted by $M_\star$ and equal to 0.9 $M_\odot$ for the Kepler-46 system). The length unit is the initial orbital radius of the inner planet ($r_{\rm inner}$), and the time unit is the initial orbital period of the inner planet ($T_{\rm orb}$) divided by 2π. Whenever time is expressed in orbits, it refers to the orbital period at the initial location of the inner planet.

2.2. *Results of Hydrodynamical Simulations*

The free parameters in our simulations are the mass of the inner planet and the initial surface density of the disk. Both quantities determine the rate of convergent migration and the evolution of the orbital eccentricities. We consider three different masses for the inner planet: 0.2 $M_{\rm J}$, 0.4 $M_{\rm J}$, and 0.6 $M_{\rm J}$ (the mass of the outer planet is fixed at 0.37 $M_{\rm J}$). For each planet mass, a set of nine simulations was carried out varying Σ_0, the unperturbed surface density at the initial orbital radius of the inner planet. We took Σ_0 in the range [2×10^{-4}, 10^{-3}], which corresponds to an initial disk mass between 3.5×10^{-3} $M_\star$ and 1.8×10^{-2} $M_\star$. Typical outcomes of the simulations are described in Section 2.2.1. We find that disk–planets interactions may lead to significant divergent evolution of the planet orbits, which we interpret in Section 2.2.2. To obtain the evolution of the planets' orbital elements to a steady state, a simple model for disk dispersal is included; its results are presented in Section 2.2.3. The robustness of our results to variations in the assumptions made is discussed in Appendix B.

2.2.1. *A Few Illustrative Cases*

Figure 2 displays typical outcomes of our hydrodynamical simulations of the Kepler-46 system. Here, $\lambda_{\rm i,o}$ and $\varpi_{\rm i,o}$ denote the mean longitude and longitude of periastron, with the subscripts i and o referring to the inner and outer planets, respectively.

The top row shows results with $M_{\rm inner} = 0.4\, M_{\rm J}$ and $\Sigma_0 = 3 \times 10^{-4}$. As the planets progressively clear a partial gap around their orbit, convergent migration does not occur at a constant rate. In particular, the inward migration of the outer planet slightly accelerates early due to a stage of type-III migration (Masset & Papaloizou 2003) before slowing down upon approaching the 2:1 MMR with the inner planet. The planets are locked in the 2:1 MMR from about 300 orbits onward, as evidenced by the libration of the resonant angles associated with this resonance. The resonance capture increases the inner planet's eccentricity to about 0.035. The increase in the outer planet's eccentricity is much more modest, reaching about 0.005, even though the mass ratio of the planets is near unity. This modest increase in the outer planet's eccentricity is a result of the contribution of the indirect term nearly canceling the contribution from the direct term to the term that is first order in the eccentricities in the development of the disturbing function, which governs the response of the outer planet at a 2:1 MMR (see, e.g., Murray-Clay & Chiang 2005;

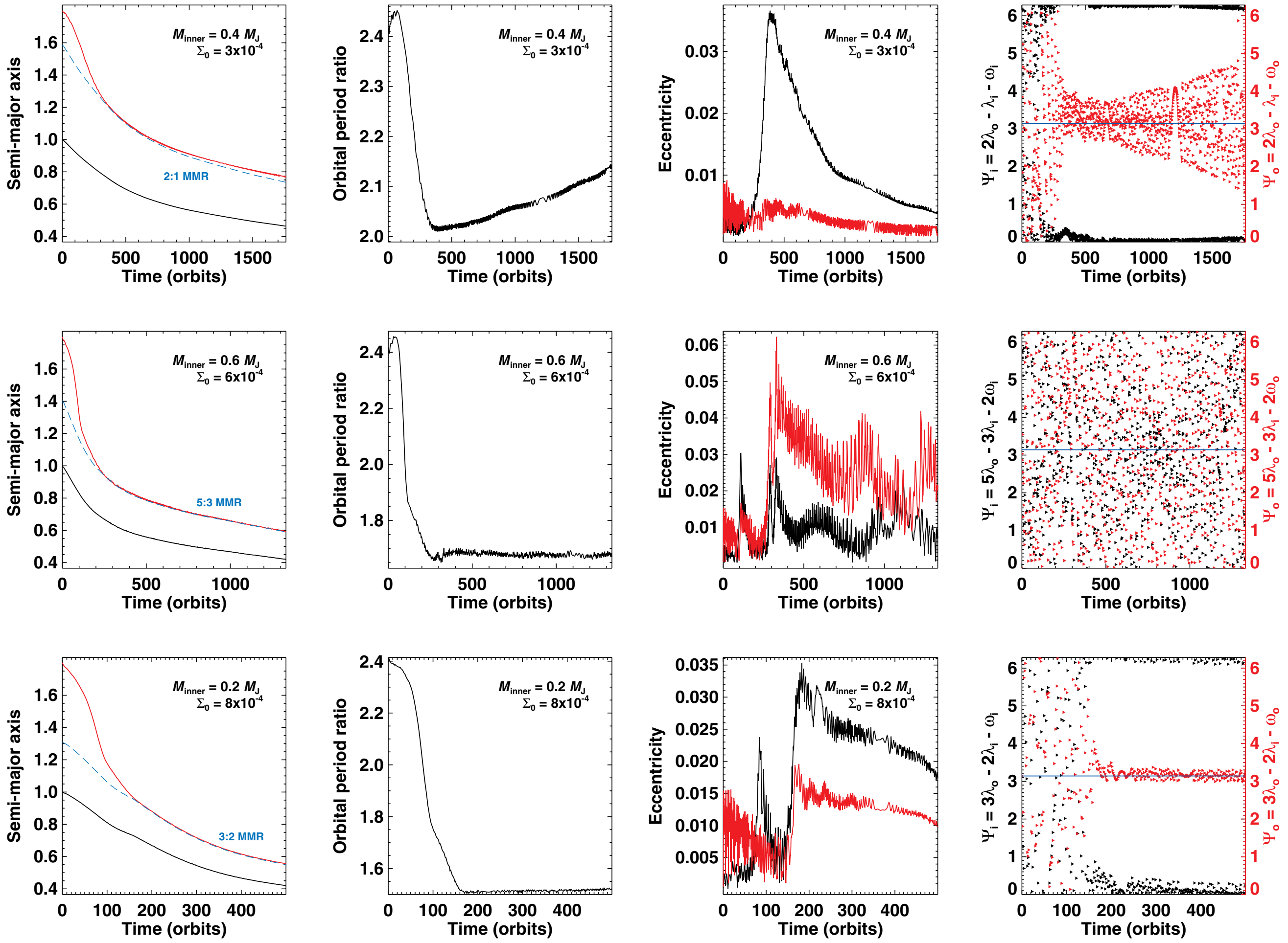

Figure 2. Results of hydrodynamical simulations of the Kepler-46 system. From left to right: time evolution of the planets' semi-major axis, orbital period ratio, eccentricity, and of the resonant angles relevant to the planets' period ratio (the horizontal line marks π). Each row corresponds to a different simulation, for which the inner planet's mass ($M_{\rm inner}$) and the disk's unperturbed surface density at $r = 1$ (Σ_0) are indicated in the top-right corner of the panels. The outer planet's mass is $0.37\,M_{\rm J}$. The location of some MMR are displayed by dashed curves in the semi-major axes panels. The first row shows an example of convergent migration toward the 2:1 MMR, followed by rapid divergent evolution. The second row shows a case where convergent migration stalls with an orbital period ratio near 1.7 (as determined by TTV). In the third row, capture into the 3:2 MMR is followed by slow divergent evolution.

(A color version of this figure is available in the online journal.)

Papaloizou & Terquem 2010). Damping of the eccentricities follows from the gravitational interaction with the background gas disk. The ratio of orbital periods increases from 2.02 to 2.15 in only 1,500 orbits, while the eccentricities are damped. The physical origin of this divergent evolution is discussed in Section 2.2.2. Resonant coupling is maintained throughout this divergent evolution, the width of the 2:1 MMR increasing as the eccentricities decrease.

The second row of panels in Figure 2 displays results for $M_{\rm inner} = 0.6\,M_{\rm J}$ and $\Sigma_0 = 6 \times 10^{-4}$. This case shows that convergent migration may stall with an orbital period ratio close to the observed value ($\approx$1.7). The accelerating inward migration of the outer planet is particularly visible in the first 100 orbits. This runaway migration is fueled by the dense gas region located between the two planet gaps. This dense material is continuously funneled beyond the outer planet's orbit through horseshoe streamlines. The density between the two planet gaps therefore decreases, and so does the migration rate of the outer planet. Convergent migration then proceeds at a slower pace and the planets merge their gap, thereby forming a common gap in the disk. This is illustrated in Figure 3, which compares the disk's surface density at 400 orbits for the two aforementioned simulations. While in the former case a narrow ring of gas is left between the two planet gaps, the latter case shows that both planets end up in a common gap.

In the second row of panels in Figure 2, we see that the orbital period ratio and the eccentricities remain approximately stationary from about 400 orbits. The time-averaged eccentricity of the inner planet is close to 0.01; that of the outer planet is $\approx$0.025. These values are consistent, albeit slightly larger than those inferred from observations (see Table 1). The critical angles show that the planets are not locked in the 5:3 MMR.

The third row of panels in Figure 2 shows $M_{\rm inner} = 0.2\,M_{\rm J}$ and $\Sigma_0 = 8 \times 10^{-4}$. Here, convergent migration is rapid enough that the planets approximately reach the nominal location of their 3:2 MMR (the minimum value of the period ratio is 1.508 at 170 orbits). The planet eccentricities increase to about 0.03 (inner planet) and 0.015 (outer planet). Subsequent damping of the eccentricities occurs along with a slight divergent evolution of the planets. The rate of divergent evolution is much reduced compared with the 2:1 MMR case shown in the top row of panels in Figure 2. We analyze this result further in Section 2.2.2. No

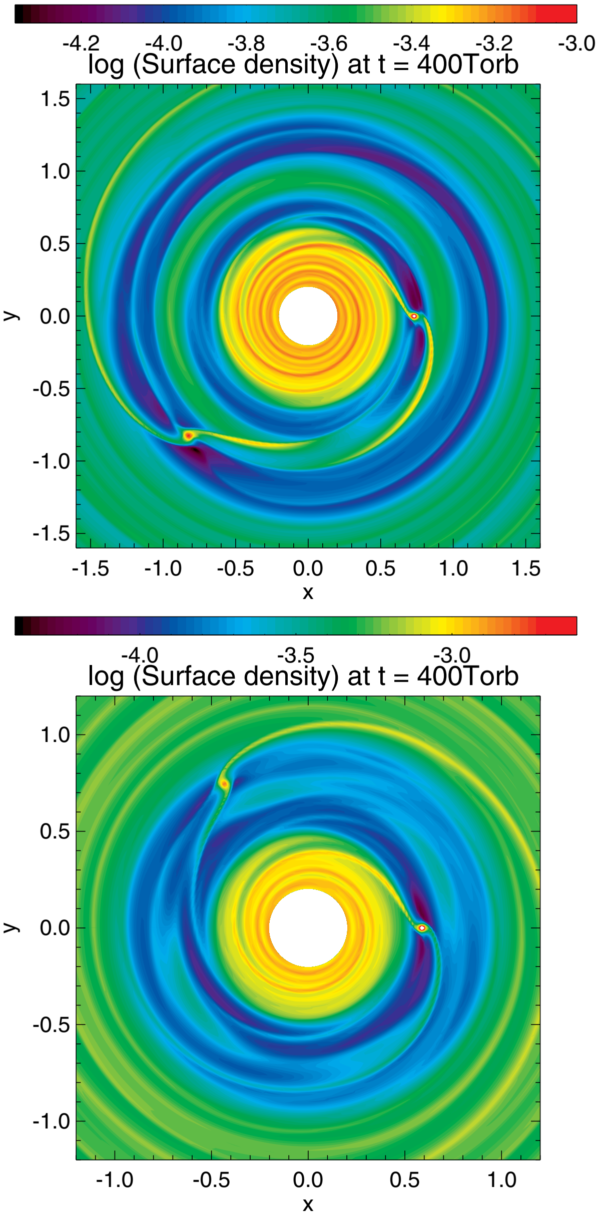

Figure 3. Disk's surface density at 400 orbits for $M_{\rm inner} = 0.4\,M_{\rm J}$ and $\Sigma_0 = 3 \times 10^{-4}$ (top), and for $M_{\rm inner} = 0.6\,M_{\rm J}$ and $\Sigma_0 = 6 \times 10^{-4}$ (bottom). The outer planet's mass is $M_{\rm outer} = 0.37\,M_{\rm J}$.

(A color version of this figure is available in the online journal.)

steady state has been reached at the end of the simulation. For this simulation, as for all simulations of the Kepler-46 system, results are shown until the inner planet reaches $r \sim 0.4$, below which the proximity of the grid's inner edge (at $r = 0.2$) starts affecting the planet's orbital evolution.

The final period ratio obtained in all our simulations is displayed in Figure 4 as a function of Σ_0 for the three masses assumed for the inner planet. By final period ratio, we mean either the period ratio obtained at the end of the simulation (after between 1500 and 2000 planet orbits), or that obtained when the inner planet's orbital radius falls below $r = 0.4$. Figure 4 highlights the three major outcomes of our simulations: (1) capture in 2:1 MMR generally followed by rapid divergent evolution, (2) capture in 3:2 MMR followed by slow divergent evolution, and (3) convergent migration stalling with a period ratio between 1.6 and 1.7, depending on the disk's density distribution inside the planets' common gap. Several simulations can reproduce the observed period ratio of Kepler-46b and Kepler-46c. The best agreement with observations is obtained for $M_{\rm inner} = 0.6\,M_{\rm J}$, our upper mass value. This mass would imply a mean density for Kepler-46b about 20% larger than Jupiter's (about 1.6 g cm^{-3}).

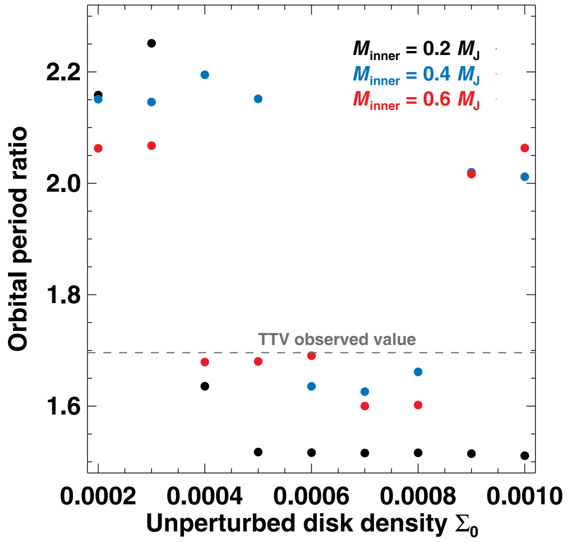

Figure 4. Summary of the results of hydrodynamical simulations for Kepler-46: ratio of orbital periods vs. the unperturbed disk's surface density at the initial location of the inner planet (Σ_0). Results are shown for the three masses assumed for the inner planet.

(A color version of this figure is available in the online journal.)

2.2.2. Disk-driven Repulsion of a Planet Pair

The results of hydrodynamical simulations in Section 2.2.1 show that the orbital period ratio of two partial gap-opening planets may increase from a near resonant value. This divergent evolution is reminiscent of the late evolution of short-period planet pairs through star–planet tidal interactions. In late evolution cases, tidal circularization causes a slow divergent evolution of the orbits (Papaloizou & Terquem 2010; Papaloizou 2011; Lithwick & Wu 2012; Batygin & Morbidelli 2013), a mechanism known as tidally driven resonant repulsion (Lithwick & Wu 2012). Tidally driven resonant repulsion is based on energy dissipation of the planet pair while its total angular momentum remains constant (Papaloizou 2011).

It is possible that there is an analogous resonant repulsion mechanism due to disk–planets interactions. To address this possibility, it is important to first look at the evolution of two embedded planets that do not interact gravitationally. In Figure 5, we compare the results of two hydrodynamical simulations: one in which the gravitational interaction between the planets is switched off (both the direct and the indirect interaction terms are discarded), and another for which the planet–planet interaction is fully accounted. The inner planet's mass is $M_{\rm inner} = 0.6 M_{\rm J}$ and the initial disk surface density at $r = 1$ is $\Sigma_0 = 2 \times 10^{-4}$. The other disk and planet parameters are those described in Section 2.1. When planet–planet interactions are on, capture into the 2:1 MMR is followed by rapid divergent evolution and damping of the eccentricities. This is similar to the case presented in the top row of panels in Figure 2.

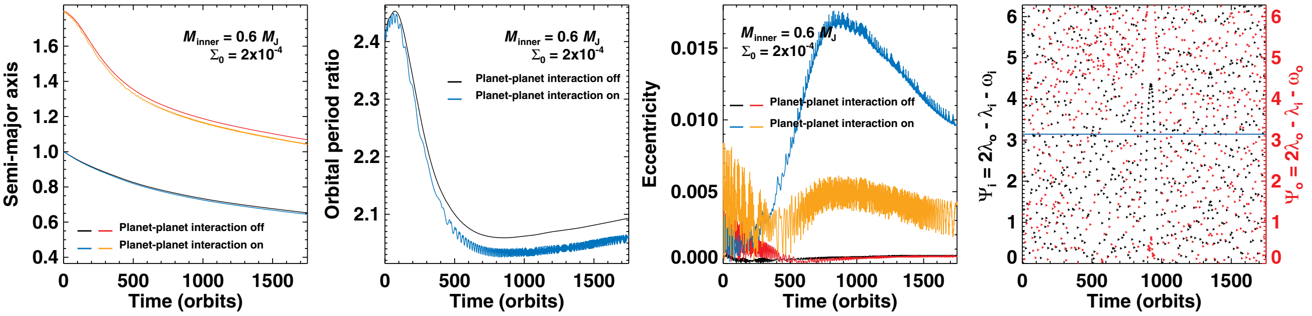

Figure 5. Time evolution of the semi-major axes, the orbital period ratio, the eccentricities and the 2 : 1 resonant angles for $M_{\rm inner} = 0.6\,M_{\rm J}$ and $\Sigma_0 = 2 \times 10^{-4}$. Two situations are compared: (1) the planets do not feel each other's gravity (planet–planet interaction off) and (2) the planets feel each other's gravity (planet–planet interaction on; our fiducial case). The resonant angles are those obtained with planet–planet interaction off.

(A color version of this figure is available in the online journal.)

We see that a similar divergent evolution is also obtained when planet–planet interactions are switched off, while the planets are not resonantly coupled (the resonant angles do not librate) and their eccentricities take vanishingly small stationary values. This comparison highlights that when disk–planet interactions are considered, eccentricity damping is not necessarily responsible for the planets' divergent evolution. The divergent evolution of a planet pair may instead be driven by changes to the disk–planet interaction brought about through the proximity of the planets, such as the development of an interaction between each planet and the wake of its companion. We argue below that the damping of the eccentricities can actually be a consequence of divergent evolution driven by wake-planet interactions.

Before describing the process of wake-planet interactions, we briefly report that in some other simulations not illustrated here, with planet–planet interactions switched off, a tiny increase in the orbital eccentricities is observed when the orbital period ratio takes near resonant values. Eccentricities may reach a few $\times 10^{-3}$ before being damped by the disk. Although this is a small effect, it suggests that planets could be weakly resonantly coupled through interaction with the wakes and/or the circumplanetary disk of their companions. In our simulations, the mass of the circumplanetary disks does not exceed one percent of the planet's mass.

Wake-planet interactions. The results of simulations shown in Figure 5 make clear that disk-driven divergent evolution of a planet pair is not necessarily driven by eccentricity damping and it may continue to operate even when the eccentricities are very small. We indicate how the interaction between a planet and the wake of its companion could act as a driving mechanism for divergent evolution. The inner planet's outer wake carries positive fluxes of angular momentum and energy. A fraction of this angular momentum flux can be deposited in the co-orbital region of the outer planet through the dissipation of shocks, and then transferred to the outer planet via an effective positive corotation torque (see Podlewska-Gaca et al. 2012). Associated with the angular momentum flux, $F_{\rm J}$, deposited in the co-orbital region of the outer planet is an energy flux, $F_{\rm E} = n_{\rm i} F_{\rm J}$, where $n_{\rm i}$ denotes the inner planet's mean motion (or angular velocity). From this energy flux, $n_{\rm o} F_{\rm J}$ is used to keep the outer planet and its co-orbital region nearly circular (see Figure 5; here, $n_{\rm o}$ is the outer planet's mean motion). The remaining energy flux, $(n_{\rm i} - n_{\rm o})F_{\rm J}$, is dissipated in the outer planet's co-orbital region. Reciprocally, a fraction of the negative inward flux of angular momentum carried by the inner wake of the outer planet can be deposited in the inner planet's co-orbital region and subsequently transmitted to the inner planet. Again, this exchange is associated with energy dissipation in the disk at a rate equal to the absolute value of the product of the flux of angular momentum transmitted to the inner planet by the outer one and the difference in the planets angular velocities. This dissipation occurs, as is usual in disk–planet interactions, through the tidally excited density waves steepening into shocks (e.g., Goodman & Rafikov 2001). Numerically, shocks are handled through a combination of numerical diffusion and the application of an artificial viscosity. As a locally isothermal equation of state is adopted in our simulations, this dissipated energy is effectively lost to the system through cooling. Though the total orbital energy of the two planets is dissipated due to the wake-planet interactions described above, their total angular momentum remains unaltered. As studied in the context of star–planet tidal interactions, energy dissipation at constant angular momentum leads to the divergent evolution of a planet pair (Papaloizou 2011; Lithwick & Wu 2012; Batygin & Morbidelli 2013).

We derive an equation satisfied by the period ratio of the two planets as a direct consequence of considering the evolution of their total orbital energy and angular momentum. We denote by $a_{\rm i}$, $e_{\rm i}$, and $M_{\rm i}$, the semi-major axis, eccentricity, and mass of the inner planet (with the subscript changed to o denoting the same quantities for the outer planet), respectively. The total angular momentum of the two planets is

$$J = J_{\rm i} + J_{\rm o} = M_{\rm i}\sqrt{GM_\star a_{\rm i}\left(1 - e_{\rm i}^2\right)} + M_{\rm o}\sqrt{GM_\star a_{\rm o}\left(1 - e_{\rm o}^2\right)}, \tag{1}$$

which gives, correct to second order in the eccentricities,

$$\dot{J} \equiv \frac{dJ}{dt} = J_{\rm i}\left(\frac{\dot{a}_{\rm i}}{2a_{\rm i}} - e_{\rm i}\dot{e}_{\rm i}\right) + J_{\rm o}\left(\frac{\dot{a}_{\rm o}}{2a_{\rm o}} - e_{\rm o}\dot{e}_{\rm o}\right). \tag{2}$$

Since we are looking for changes in the planets' semi-major axes and eccentricities that occur on similar timescales, we may therefore discard the eccentricity terms in the expressions for $\dot{J}$, $J_{\rm i}$, and $J_{\rm o}$. Denoting the torques exerted by the disk on the inner and outer planets by $\Gamma_{\rm i}$ and $\Gamma_{\rm o}$, respectively, conservation of angular momentum reads

$$\dot{J} = J_{\rm i}\frac{\dot{a}_{\rm i}}{2a_{\rm i}} + J_{\rm o}\frac{\dot{a}_{\rm o}}{2a_{\rm o}} = \Gamma_{\rm i} + \Gamma_{\rm o}. \tag{3}$$

The total orbital energy is given by

$$E = -\frac{GM_\star M_{\rm i}}{2a_{\rm i}} - \frac{GM_\star M_{\rm o}}{2a_{\rm o}},$$

and conservation of energy reads

$$\dot{E} = \frac{GM_\star M_\mathrm{i}}{2a_\mathrm{i}^2}\dot{a}_\mathrm{i} + \frac{GM_\star M_\mathrm{o}}{2a_\mathrm{o}^2}\dot{a}_\mathrm{o} = n_\mathrm{i}\Gamma_\mathrm{i} + n_\mathrm{o}\Gamma_\mathrm{o} - \frac{GM_\star M_\mathrm{i} e_\mathrm{i}^2}{a_\mathrm{i}\tau_\mathrm{c,i}} - \frac{GM_\star M_\mathrm{o} e_\mathrm{o}^2}{a_\mathrm{o}\tau_\mathrm{c,o}} - |\dot{E}|_\mathrm{wake}, \quad (4)$$

where $n_\mathrm{i,o} = \sqrt{GM_\star/a_\mathrm{i,o}^3}$ is the planet's mean motion. The right-hand side of Equation (4) contains three contributions. The first arises from the energy dissipation in the disk resulting from the action of the torques $\Gamma_\mathrm{i,o}$. Since these are negative, this energy is removed from the orbital motion. The second originates from orbital circularization due to disk–planets interactions. The quantities $\tau_\mathrm{c,i}$ and $\tau_\mathrm{c,o}$ are the circularization times for the planets that arise from the disk torque and energy dissipation acting on each planet through the effects of its own wake (Nelson & Papaloizou 2002; Papaloizou & Szuszkiewicz 2005). The third and final contribution, $-|\dot{E}|_\mathrm{wake}$, stems from the energy dissipation due to wake-planet interactions. We remark that wake dissipation in the co-orbital region of the outer planet contributes $(n_\mathrm{i} - n_\mathrm{o})|F_\mathrm{J}|$ to $|\dot{E}|_\mathrm{wake}$, in addition to a corresponding contribution arising from the co-orbital region of the inner planet, as indicated above. Terms of the order of $e_\mathrm{i,o}^2$ are retained above even though the eccentricities are small because it is assumed that $\tau_\mathrm{i,o}$ are small enough so that dissipation through circularization could be as important as, or even dominate, the other effects under some circumstances.

Combining Equations (3) and (4), we find

$$\frac{1}{3}\frac{n_\mathrm{o}}{n_\mathrm{i}}\frac{d}{dt}\left(\frac{n_\mathrm{i}}{n_\mathrm{o}}\right) = \left(\frac{\Gamma_\mathrm{o}}{J_\mathrm{o}} - \frac{\Gamma_\mathrm{i}}{J_\mathrm{i}}\right) + \frac{J_\mathrm{i} + J_\mathrm{o}}{J_\mathrm{i} J_\mathrm{o}(n_\mathrm{i} - n_\mathrm{o})} \times \left(n_\mathrm{i} J_\mathrm{i}\frac{e_\mathrm{i}^2}{\tau_\mathrm{c,i}} + n_\mathrm{o} J_\mathrm{o}\frac{e_\mathrm{o}^2}{\tau_\mathrm{c,o}} + |\dot{E}|_\mathrm{wake}\right). \quad (5)$$

When wake-planet interactions are negligible ($|\dot{E}|_\mathrm{wake} = 0$), Equation (5) shows that far from resonance, where the eccentricities are very small, the planets' period ratio $n_\mathrm{i}/n_\mathrm{o}$ decreases as a consequence of convergent migration, provided that $\Gamma_\mathrm{o}/J_\mathrm{o} < \Gamma_\mathrm{i}/J_\mathrm{i}$. As expected, the latter condition is that the inward migration rate of the outer planet should exceed the inward migration rate of the inner planet. As the eccentricities increase as resonance is approached, a steady state may be reached in which the planets' period ratio and eccentricities take stationary values. If the eccentricity damping timescales are sufficiently short, disk-driven circularization of the orbits can reverse convergent migration, thus the planets' period ratio can increase.

Equation (5) highlights that wake-planet interactions may also lead to divergent evolution of a planet pair. Divergent evolution driven by wake-planet interactions does not require the planets to be resonantly coupled, as already inferred from the simulations shown in Figure 5. Similar divergent evolution of a non-resonant planet pair embedded in a disk, comprised of a Jupiter and a super-Earth, was reported by Podlewska-Gaca et al. (2012). When divergent evolution is primarily due to wake-planets interactions, as the period ratio of the planet pair increases away from a resonant value, the distance to resonance increases, and the forced eccentricities therefore decrease (e.g., Papaloizou 2011). This means that orbital circularization is a natural consequence of divergent evolution driven by wake-planet interactions. This is a major difference between the divergent evolutions driven by wake-planet interactions and by orbital circularization (through the disk or stellar tides): eccentricity damping is the consequence of the former mechanism and the cause of the latter. With both mechanisms, the divergent evolution of a resonant planet pair maintains the libration of the resonant angles by damping the eccentricities.

We call *disk-driven resonant repulsion* the divergent evolution of a resonant planet pair embedded in a disk, following the terminology introduced by Lithwick & Wu (2012) for the divergent evolution of a resonant planet pair due to star–planet tidal interactions. We stress that disk-driven resonant repulsion can have two origins: (1) disk circularization of the orbits and (2) wake-planet interactions. Disk-driven repulsion comprises (1) *circularization-driven repulsion* and (2) *wake-driven repulsion*. The results of hydrodynamical simulations shown above indicate that for the disk and planet parameters that we have considered, wake-planet repulsion dominates circularization-driven repulsion. This point will be further illustrated in Section 3.2.1.

When is wake-driven repulsion important? We have shown that the period ratio of a planet pair embedded in a disk may increase due to angular momentum transfer between the planets through their wakes. We separate the planet pair into a donor and a recipient. The bigger the donor's mass, the stronger its wake, and the easier for the wake to deposit angular momentum in the co-orbital region of the recipient planet through the dissipation of shocks. This typically requires the dimensionless parameter q/h^3 of the donor planet to exceed unity (q is the planet-to-star mass ratio and h the disk's aspect ratio). The donor planet can thus be a partial or a deep gap-opening planet. The angular momentum that is deposited by the donor's wake is at least partly transferred to the recipient planet through an effective corotation torque (Podlewska-Gaca et al. 2012). If the recipient's mass is too big, the density in its co-orbital region will be too low for this effective corotation torque to matter. The recipient could be a partial gap-opening planet or even a type-I migrating planet. These considerations show why divergent evolution is not expected for two type-I migrating planets (the donor's wake being too weak), or for two type-II migrating planets (the recipient's gap being too deep). We have checked this with hydrodynamical simulations, not illustrated here.

The above considerations also help in understanding the different rates of divergent evolution obtained in Figure 2. The opening of a partial gap for both planets is a favorable situation for wake-planet interactions to play a significant role. In the top row of panels in Figure 2, where the planets become locked in the 2:1 MMR, the high-density region between the two gaps (see upper panel in Figure 3) causes significant deposition of angular momentum in the planets co-orbital region and, therefore, efficient divergent evolution. In contrast, as seen in the bottom row of panels in Figure 2, where the planets merge their gap and become locked in the 3:2 MMR, the moderate disk density left between the planets can only trigger slow divergent evolution. In the middle row of panels, where the period ratio stalls near 1.7, a steady state is reached with background convergent migration balanced by wake-planet divergent evolution.

Evolution toward a steady state. When the planets are widely separated, they are expected to interact with the disk independently of each other and they can then enter a convergent migration phase. As they approach each other, both planet–planet interactions and wake-planet interactions, where the planets interact with each others wakes, can occur. Both these processes involve exchanges of orbital energy and angular momentum between the planets. Planet–planet interactions can result in resonant trapping associated with the growth of eccentricities, while wake-planet interactions act to produce divergent migration without the growth of eccentricities. From Equation (5) we see that both circularization- and wake-driven resonant repulsions act together to increase the period ratio. If wake-driven repulsion dominates after the eccentricities have damped to low values, with $|\dot{E}|_{\rm wake}$ remaining constant, the period ratio should increase linearly with time; this result is roughly what is obtained in the simulation presented in the top row of panels in Figure 2. However, in the longer term, $|\dot{E}|_{\rm wake}$ should decrease with time as the planets separate, which indicates that a steady state should ultimately be reached with convergent migration driven by background disk torques balancing wake-driven repulsion. Wake-planet interactions cause a non-linear evolution of the disk's density profile near the planets, which may affect the time evolution of the background torques responsible for convergent migration. At least in the simulation without the planet–planet interaction of Figure 5, a slow decrease in the background torques could explain why the period ratio decreases and then increases, instead of reaching a stationary non-resonant value. Another possibility is that convergent migration and disk-driven repulsion behave differently as the planet pair moves closer to the star, if the torques responsible for both mechanisms have different radial dependences. These aspects require further study.

2.2.3. Disk Dispersal Model

The above simulations of the Kepler-46 system show that the planets' period ratio can take a range of values, depending on the convergent migration rate during the early evolution of the system. The limited duration of the simulations (up to a few thousand orbits) and the fact that planets still migrate at the end of the simulations, however, raise the question of the long-term evolution of the system. Even when the inward migration of the planets is stalled,[2] further evolution of the period ratio can be maintained by disk-driven resonant repulsion. A steady state may a priori be achieved after depletion of the protoplanetary disk. Disk dispersal typically occurs between 10^6 and 10^7 yr after formation of the central star. Photoevaporation, driven by extreme ultraviolet radiation from the star, opens a gap in the disk at separations of typically a few astronomical units (AU) for Sun-like stars (e.g., Owen et al. 2010; Alexander & Pascucci 2012). For planets below that separation, the background disk will be depleted over a viscous timescale at the orbital separation where photoevaporation occurs. Assuming a local viscous alpha parameter of a few $\times 10^{-3}$, viscous draining of the inner disk could operate in a few 10^4 yr, that is typically a few 10^5 orbital periods at the present location of Kepler-46b and Kepler-46c.

To assess the impact of disk evaporation on our results, we restart two simulations adopting a simple exponential decay of the surface density profile. This is done by solving $\partial_t \Sigma = -(\Sigma - \Sigma_{\rm target})/\tau_{\rm evap}$, in addition to the hydrodynamical equations, where $\overline{\Sigma}$ is the azimuthally averaged density profile at restart time (from which evaporation switches on), $\Sigma_{\rm target} = 10^{-3}\overline{\Sigma}$ is an arbitrarily small density profile in a steady state (taken to be not zero for numerical convenience), and $\tau_{\rm evap}$ is the evaporation timescale. We consider three short evaporation timescales: 100, 500, and 2000 orbits, simulations being restarted at 1000 orbits. Results are shown in Figure 6.

The upper panels are obtained with $M_{\rm inner} = 0.4\,M_{\rm J}$ and $\Sigma_0 = 3 \times 10^{-4}$, for which a rapid divergent evolution occurs after capture in the 2:1 MMR. We see that the evolution is frozen out at a few evaporation timescales after restart, the planets reaching stationary eccentricities and semi-major axes. Similarly, the lower panels in Figure 6 show the results for $M_{\rm inner} = 0.6\,M_{\rm J}$ and $\Sigma_0 = 6 \times 10^{-4}$, for which convergent migration stalls at about the observed period ratio in the Kepler-46 system. In that case, including disk evaporation stalls the migration of both planets, as expected, but it does not significantly affect the planets' eccentricities and period ratio. The final period ratio remains close to the observed value.

3. APPLICATION TO *KEPLER*'S MULTI-PLANETARY SYSTEMS

3.1. Introduction and Strategy

In Section 2, we present the results of hydrodynamical simulations modeling the early evolution of Kepler-46b and Kepler-46c as they were embedded in their parent protoplanetary disk. The variety of period ratios obtained in our simulations raises the question of whether or not disk–planets interactions could partly explain the diversity of period ratios in *Kepler*'s multi-planetary systems. Below, we review some of the processes that might account for such diversity.

3.1.1. Tidally Driven Resonant Repulsion

As highlighted in Figure 1, *Kepler*'s multi-planetary systems show a clear tendency for planet pairs near resonances to feature period ratios slightly greater than strict commensurability. Divergent evolution of a short-period resonant planet pair due to star–planet tidal interactions could partly explain this feature (Lithwick & Wu 2012; Batygin & Morbidelli 2013). Although the efficiency of tidal dissipation remains largely uncertain, it is thought that efficient tidal circularization requires the inner planet to orbit its star in less than a few days. As can be seen in Figure 1, many of *Kepler*'s candidate systems have an inner planet beyond 10 days, for which tidal circularization is unlikely to have caused significant resonant repulsion (see Appendix A). For these systems we propose that resonant repulsion driven by disk–planets interactions could have played a prominent role in determining the observed period ratios.

3.1.2. Disk-driven Type-I Migration

The vast majority of the planets in *Kepler*'s multi-planetary systems have physical radii between 0.1 and 0.3 Jupiter radii, which places them in the super-Earth to Neptune-mass range. From the mass–radius diagram of *Kepler* candidates followed up by radial velocity, the median mass of a 0.2 Jupiter-radius planet is about 10 to 15 Earth-masses.[3] Based on generally considered temperatures and viscosities in protoplanetary disks (corresponding to $h = 0.05$ and $\alpha \sim$ a few $\times 10^{-3}$), such planets are expected to experience type-I migration. Recent *N*-body experiments by Rein (2012) have shown that, in contrast with *Kepler*'s data, convergent migration of type-I migrating planets yields very little departure from strict commensurability. He showed that the inclusion of stochastic forces, in addition to type-I migration, could nicely reproduce the observed distribution of period ratios. Such agreement has been obtained

---

[2] This could be the case, for instance, when the mass of the disk inside the inner planet becomes smaller than the mass of the two gap-opening planets, a migration regime known as planet-dominated type-II migration.

[3] http://exoplanets.org

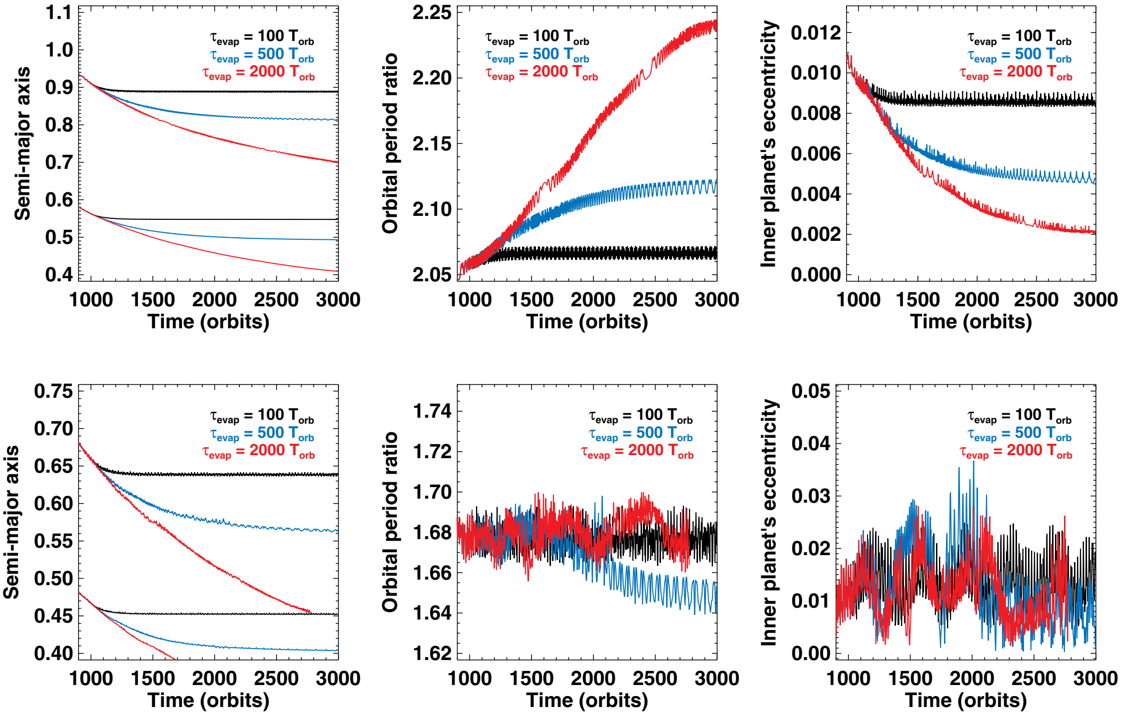

Figure 6. Time evolution of the planets' semi-major axis, period ratio, and eccentricity (for the inner planet only) with a simple model for disk dispersal (see text). Disk dispersal is switched on at 1000 orbits and the evaporation timescale ($\tau_{\rm evap}$) is varied from 100 to 2000 orbits. Results in the upper panels are for $M_{\rm inner} = 0.4\, M_{\rm J}$ and $\Sigma_0 = 3 \times 10^{-4}$. Results in the lower panels are for $M_{\rm inner} = 0.6\, M_{\rm J}$ and $\Sigma_0 = 6 \times 10^{-4}$.
(A color version of this figure is available in the online journal.)

assuming that the initial period ratio distribution is the observed one, and taking the same convergent migration timescale and the same amplitude of stochastic forces for all of *Kepler*'s multiple systems, which remains uncertain given the expected diversity of physical properties in protoplanetary disks. Still, Rein's (2012) results indicate that type-I migration alone may not be able to account for *Kepler*'s diversity of period ratios.

3.1.3. Disk-driven Repulsion of Partial Gap-opening Planets

Based on our results of hydrodynamical simulations for the Kepler-46 system, we propose that some of *Kepler*'s planet candidates in multi-planetary systems could have opened partial gaps in their parent disk, thereby escaping the type-I migration regime. This could be the case if, for instance, planets formed and/or migrated in regions of low turbulent activity (dead zones; see, e.g., Fleming & Stone 2003) or if the disk's aspect ratio takes smaller values than commonly adopted. Aspect ratios $\lesssim$3% are likely typical of the short orbital separations at which *Kepler*'s candidate systems are detected. To address this possibility, we carry out hydrodynamical simulations with two planets in the super-Earth mass range. The inner planet's mass, $M_{\rm inner} = 15\, M_\oplus$, the outer planet's mass, $M_{\rm outer} = 13\, M_\oplus$, and the central star is one Solar mass. The planet-to-primary mass ratios are therefore $q_{\rm inner} = 4.4 \times 10^{-5}$ and $q_{\rm outer} = 4 \times 10^{-5}$, that is, an order-of-magnitude smaller than those of Kepler-46b (median value) and Kepler-46c. To get similar gap depths in the super-Earths and Kepler-46 simulations, we adopt values of h and α such that the dimensionless parameters in the gap-opening criterion of Crida et al. (2006) take the same values. For the super-Earth's simulations, this yields $h = 0.023$ and $\alpha = 2.3 \times 10^{-3}$. All other simulation parameters are otherwise identical, except the grid resolution, which we increase to 600 × 1200.

Figure 7 displays the results of two simulations. In the top panels, the unperturbed disk's surface density is $\Sigma_0 = 8 \times 10^{-5}$. We see that the planets lock themselves in the 3:2 MMR from about 1300 orbits. Divergent evolution proceeds with a decrease in the planets' eccentricities. After reaching exactly 1.5 at about 1500 orbits, the period ratio increases to 1.54 at 5000 orbits. As illustrated by the screenshot of the disk surface density, the proximity of the planets allows their wakes to penetrate into each others coorbital region, where they can deposit part of their angular momentum flux. As we show in Section 2.2.2, transfer of angular momentum between planets through wake-planet interactions will result in a loss rate of the total orbital energy of the two planets. This has the consequence of increasing the period ratio and decreasing the eccentricities. In the bottom panels of Figure 7, the unperturbed disk surface density parameter is decreased to $\Sigma_0 = 3 \times 10^{-5}$. Here, convergent migration due to the background disk torques is slow enough to lock the planets in the 2:1 MMR, but, this time, the resonant capture does not lead to divergent evolution. Instead, a steady state is reached in which both the eccentricities and the orbital period ratio take stationary values. This steady state is a consequence of negligible wake-planet interactions in this case. As illustrated in the bottom-right panel of Figure 7, the planets are sufficiently far from each other that their wakes primarily transfer energy and angular momentum to regions of the disk that are not co-orbital with the planets.

3.2. Customized Three-body Simulations

The results of Section 3.1.3 support the idea that disk-driven resonant repulsion of partial gap-opening super-Earths may lead to period ratios that substantially differ from nominal resonant values. As shown in Section 2.2.2, this mechanism

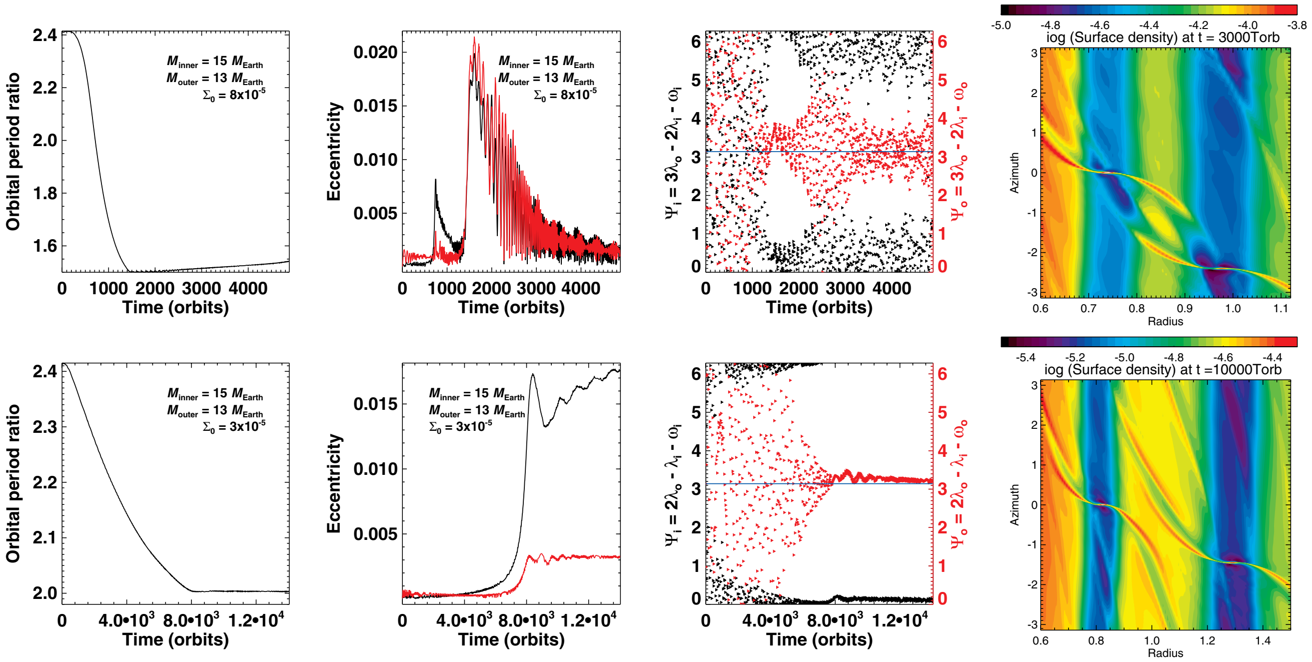

Figure 7. Results of hydrodynamical simulations with two super-Earths opening partial gaps in their disk. Top row: convergent migration leads to capture into the 3:2 MMR, followed by rapid divergent evolution. Bottom row: slow convergent migration leading to capture into the 2:1 MMR with no subsequent divergent evolution. From left to right, the panels display the time evolution of the planets orbital period ratio, eccentricities, relevant resonant angles, and a snapshot of the disk's surface density.

(A color version of this figure is available in the online journal.)

has two origins: circularization of the orbits and wake-planet interactions. The efficiency of disk-driven resonant repulsion depends on the planets' masses and the evolution of the disk's surface density. The survey of such a large parameter space is out of reach of hydrodynamical simulations, but three-body simulations with customized prescriptions for migration, eccentricity damping, and disk dispersal can help illustrate the diversity of period ratios that can be achieved. This is the strategy that we adopt. We consider fixed planet masses: $M_{\rm inner} = 15\,M_\oplus$, $M_{\rm outer} = 13\,M_\oplus$, and $M_\star = M_\odot$ (as in Section 3.1.3).

3.2.1. Method

Our three-body simulations solve the equations of motion for the two planets and the central star using a standard technique. Planets are assumed to be coplanar. Disk–planets interactions are incorporated by applying appropriate dissipative forces (for details, see Papaloizou 2011). Equation (5) shows that in order to model the planet's evolution, we need to specify (1) the rate of convergent migration before the onset of disk-driven repulsion, (2) the damping rate of the eccentricities, (3) the efficiency of wake-driven divergent evolution, and (4) the method of modeling of disk dispersal. The efficiency of wake-driven divergent evolution remains uncertain at this stage, since the term $|\dot{E}|_{\rm wake}$ in the right-hand side of Equation (5), which models energy dissipation due to wake-planet interactions, should depend sensitively on the planet masses, their mutual separation and distance from the central star, and several disk quantities (including its temperature and viscosity). A systematic study of this dependence goes beyond the scope of this paper, and is therefore left for future work. To do simple modeling and to minimize the number of free parameters, we do not attempt to parameterize the $|\dot{E}|_{\rm wake}$ term. Instead, we model disk-driven repulsion as circularization-driven repulsion only. In Equation (5), we compensate the absence of the $|\dot{E}|_{\rm wake}$ term in our three-body integrations by considering circularization timescales $\tau_{\rm c,i}$ and $\tau_{\rm c,o}$, which are shorter than in the hydrodynamical simulations. Damping of the planets' eccentricity is modeled as an exponential decay with a constant damping timescale to orbital period ratio, which we take as a free parameter (specified below).

To model the convergent migration prior to resonant repulsion, we adopt a simple prescription that reproduces the results of hydrodynamical simulations. Denoting by R, the ratio of semi-major axes ($R = a_{\rm outer}/a_{\rm inner}$), we found good agreement using

$$R(t) = R(t=0) \times 10^f \tag{6}$$

with

$$f = \log_{10}\left[\frac{({\rm pr})^{2/3}}{R(t=0)}\right] \times \frac{(t/\tau)^3}{\sqrt{1+(t/\tau)^6}}, \tag{7}$$

where pr and τ are fitting parameters. The expression in Equation (6) tends to a constant value for $t \gg \tau$, which mimics the fact that convergent migration is found to nearly stall before the onset of resonant repulsion. In Equation (7), pr denotes the period ratio at which convergent migration approximately stalls, which occurs at $t = \tau$. The good agreement between this migration prescription and our hydrodynamical simulations is illustrated in Figure 8. In the three-body simulations, disk-driven migration is applied to the outer planet only.

We display, in Figure 9, the results of a three-body simulation with pr $= 1.50$ and $\tau = 1000$ orbits, which mimics the convergent migration obtained in the hydrodynamical simulation of Section 3.1.3 with $\Sigma_0 = 8 \times 10^{-5}$ (see the right panel of Figure 8). In the top-left panel of Figure 9, only the semi-major axis of the outer planet varies in the first

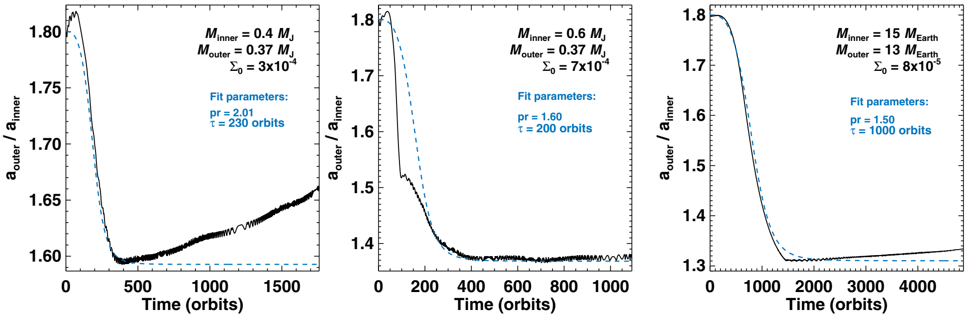

Figure 8. Time evolution of the ratio of planets semi-major axis obtained in three hydrodynamical simulations (solid curves). The planet masses and the unperturbed surface density parameter, Σ_0, are indicated in the top-right corner of each panel. The dashed curves display our fitting formula for the planets' convergent migration prior to disk-driven resonant repulsion, given by Equation (6).

(A color version of this figure is available in the online journal.)

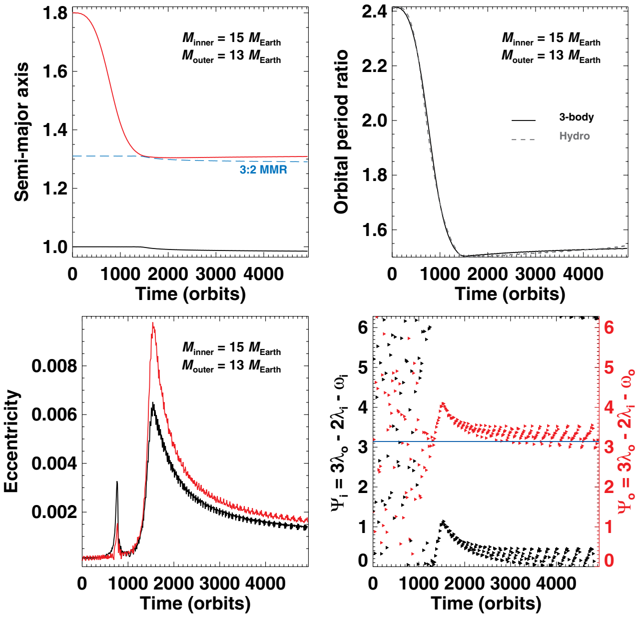

Figure 9. Results of a three-body simulation with prescribed convergent migration and eccentricity damping. The expression given by Equation (6) is used for convergent migration with $\tau = 1000$ orbits and pr $= 1.5$. The eccentricity damping timescale is 20 orbital periods. The dashed gray curve in the top-right panel shows the period ratio obtained in the hydrodynamical simulation of Section 3.1.3 with $\Sigma_0 = 8 \times 10^{-5}$.

(A color version of this figure is available in the online journal.)

1500 orbits as our prescription for disk-driven migration is applied to the outer planet. Once resonant repulsion sets in near 1500 orbits, the semi-major axis of the inner planet decreases slightly and the outer planet's increases slightly. The eccentricity damping timescale here is 20 planet orbits; this rather short timescale is found to give very similar divergent evolutions in the three-body and hydrodynamical simulations (see the top-right panel in Figure 9). At 5000 orbits, the period ratio is 1.53 in the three-body run, and 1.54 in the hydrodynamical run. This small difference can be qualitatively explained by the slightly larger pace of the repulsion in the hydrodynamical simulation than modeled in the three-body run. Furthermore, the eccentricity peaks near the 2:1 and 3:2 MMRs are about a factor of two to three smaller in the three-body simulation (compare this with the eccentricities of the hydrodynamical run shown in the second upper panel of Figure 7). The reason for this difference is most likely a reflection of the longer actual circularization time in the hydrodynamical run than that adopted in the three-body integration, consistent with the operation of wake-planet repulsion, in addition to circularization-driven repulsion as discussed above.

We also incorporate a simple model for disk dispersal, which occurs between 10^4 and 10^6 orbits. Since planets are assumed to be already formed at the beginning of the simulations, this range of timescales is meant to account for different planet formation timescales. The longest time (10^6 orbits) corresponds to a case where both planet formation and capture into resonance following convergent migration occur rapidly. The shortest one (10^4 orbits) stands for the opposite. Once disk dispersal switches on, the eccentricity damping timescale is progressively increased as an exponential growth with characteristic timescale $\tau_{\rm evap} = 2000$ orbits. This timescale is shorter than the typical viscous draining timescale of a disk inside the photoevaporation radius. As it essentially ceases to operate beyond this point, the effectiveness of disk-driven resonant repulsion is nearly entirely determined by the time from the beginning of the simulations at which dispersal switches on.

3.2.2. Results

We display in Figure 10 the results of a series of three-body simulations using the model described in Section 3.2.1. Recall that $M_{\rm inner} = 15\,M_\oplus$, $M_{\rm outer} = 13\,M_\oplus$, and $M_\star = M_\odot$, which can be thought of as being representative of *Kepler*'s sample of multi-planetary systems (the planets' mass ratio is arbitrary, it takes the same value as in the hydrodynamical simulations in Section 3.1.3). Planets are initiated with a period ratio of 2.4. The prescription for convergent migration given at Equation (6) is used with pr $= 1.50$ and $\tau = 1000$ orbits. This value of pr is meant to explore the diversity of period ratios that can be achieved by disk-driven resonant repulsion away from the 3:2 MMR. The eccentricity damping timescale varies from 20 to 200 orbits, and the time at which disk dispersal switches on from 10^4 to 10^6 orbits (see Section 3.2.1). Given the duration of disk-driven resonant repulsion, our results have very little dependence on the "convergent migration timescale," τ. Simulations were carried out over 1.2×10^6 orbits, and the period ratio time-averaged over the last 1000 orbits of the simulations is indicated by the color bar. For a given eccentricity damping timescale, the later disk dispersal occurs, the longer planets' eccentricities are damped, and, therefore, the larger the final period ratio. At a given time prior to disk dispersal, the shorter the eccentricity damping timescale, the larger the final period ratio, again as

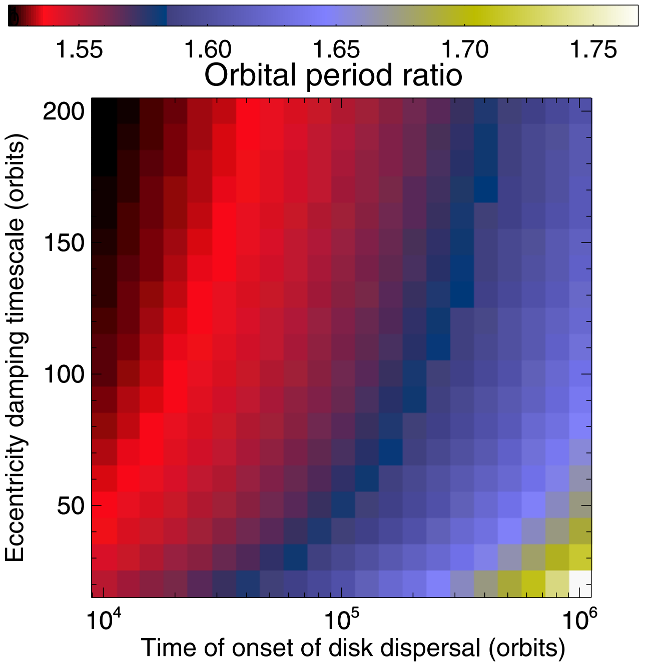

Figure 10. Results of three-body simulations with prescribed convergent migration and eccentricity damping. The central star has a Solar mass. The masses of the inner and outer planets are $M_{\rm inner} = 15\,M_{\rm Earth}$ and $M_{\rm outer} = 13\,M_{\rm Earth}$, respectively. Convergent migration is modeled using the expression in Equation (6) with pr = 1.5 and $\tau = 10^3$ orbits. The eccentricity damping timescale is varied from 20 to 200 orbits (*y*-axis), and it remains fixed until disk dispersal is switched on. The timescale of the onset of disk dispersal ranges from 10^4 to 10^6 orbits after the beginning of the simulations (*x*-axis), and the evaporation timescale is set to 2000 orbits. The orbital period ratio obtained after 1.2×10^6 orbits, and time-averaged over the last 1000 orbits, is color-coded.

(A color version of this figure is available in the online journal.)

expected. For the shortest damping timescales that we consider, period ratios can reach ∼1.75. With such short timescales, planets can evolve continuously from the 3:2 MMR to the 2:1 MMR (that is, the 2:1 resonant angles start to librate when the 3:2 resonant angles no longer librate). Had we taken even shorter damping timescales or delayed disk dispersal even more, resonant repulsion would have led to period ratios exceeding 2.

The main conclusion that can be drawn from Figure 10 is that partial gap-opening super-Earths may experience significant disk-driven resonant repulsion away from the nominal 3:2 MMR. Under favorable circumstances (particularly efficient repulsion maintained over a particularly long timescale), period ratios can easily exceed nominal resonant values. Although we consider fixed planet masses for illustration purposes, we believe that disk-driven resonant repulsion is a generic mechanism that may have occurred among *Kepler*'s multi-planetary systems.

4. CONCLUDING REMARKS

The multi-planetary systems detected by the *Kepler* mission have diverse architectures, which reflect the wide range of conditions under which planets may form and evolve. The quasi-coplanar orbits in *Kepler*'s multiple systems suggest that interactions between planets and their parent protoplanetary disk play a prominent role in shaping such diverse architectures. In particular, close planet pairs feature a variety of orbital period ratios and many of them are not in MMR. Convergent migration of multiple planets due to disk–planets interactions may lead to resonant systems in disks where turbulence is low enough not to disrupt resonances (Ketchum et al. 2011; Pierens et al. 2011; Rein 2012). Resonant planet pairs formed by disk–planet interactions may experience divergent evolution of their orbits due to tidal orbital circularization (Papaloizou & Terquem 2010; Papaloizou 2011). This tidal resonant repulsion may increase the orbital period ratio of close-in planet pairs substantially depending on the efficiency of star–planet tidal interactions (Papaloizou 2011; Lithwick & Wu 2012; Batygin & Morbidelli 2013). Tidal resonant repulsion could help account for the diversity of period ratios in *Kepler*'s close-in planet pairs.

We have shown that disk–planets interactions could also form planet pairs with a variety of period ratios. We first focus on the Kepler-46 planetary system, in which the two Saturn-mass planets, Kepler-46b and Kepler-46c, have a period ratio ≈1.69 (Nesvorný et al. 2012). We present results of hydrodynamical simulations modeling the early evolution of these planets as they were embedded in their parent disk. For typical disk temperatures and turbulent viscosities, both planets are expected to open a partial gap around their orbit. A rapid convergent migration causes the planets to merge their gaps and to evolve into a common gap. Depending on the density's structure inside the common gap, the planets' convergent migration is found to stall with a variety of period ratios between 1.5 and 1.7 (see Figure 4). The observed period ratio of the inner and outer planet can be reproduced without the planets being in MMR.

Our results also highlight that disk–planets interactions may significantly increase the orbital period ratio of a planet pair from a near-resonant value, a mechanism that we term *disk-driven resonant repulsion*. This repulsion has two origins: (1) orbital circularization by the disk and (2) the interaction between each planet and the wake of its companion. As the wake of a planet turns into a shock at some distance from the planet, it may deposit angular momentum in the co-orbital region of another planet through an effective corotation torque. We show that this mechanism can dissipate the total orbital energy of a planet pair without changing its total angular momentum, a configuration that increases the planets' period ratio and decreases their eccentricities. Resonant repulsion caused by wake-planet interactions can be particularly efficient when at least one of the planets opens a partial gap around its orbit (see Section 2.2.2). For the disk and planet parameters adopted in this work, wake-planet interactions are more efficient at driving the repulsion of a planet pair than disk circularization. However, there may be circumstances for which this balance is different.

The strength of wake-planet interactions increases as the radial separation between planets decreases, independently of their eccentricities. If wake-planet interactions are the dominant process for the divergent evolution of a planet pair, then one could expect the period ratio to reach a constant value, which could be different from a resonant ratio. Our results of simulations, however, report many cases where the period ratio nearly stalls but then increases. There could be two reasons for this behavior. First, wake-planet interactions cause a non-linear evolution of the disk's density profile near the planets, which causes the torques driving convergent migration and wake-planets interactions to change over time. Second, independent of the previous consideration, preliminary results indicate that the torques responsible for convergent migration and for wake-driven repulsion have different dependencies on the stellar distance as the planets migrate. Both effects are found to strengthen wake-driven repulsion as compared with convergent migration as planets migrate inward. This would explain why, in our simulations, the period ratio of inwardly migrating planet pairs increases after reaching a nearly constant value. The above considerations indicate that wake-planet interactions may naturally increase the period ratio of planet pairs away from resonant values.

One of our low-mass disk models for Kepler-46, in which the Saturn-mass planets are captured in the 2:1 MMR, a period ratio of 2.3 is attained in as short as a few thousand orbits. A significant divergent evolution of sub-Jovian planets was obtained in some of the hydrodynamical simulations of Rein et al. (2010) and Rein et al. (2012). The similarity between their results of simulations and ours (convergent migration nearly stalled close to resonance, followed by divergent evolution of the planets orbits alongside the damping of their eccentricity) suggests that the divergent evolution obtained in these simulations is likely to arise from wake-planet interactions.

Many planets in *Kepler*'s multiple systems are in the super-Earth to Neptune-mass range, and have orbital periods below 100 days. At these short periods, the aspect ratio of a disk should be small, thus many *Kepler*'s planet candidates could have opened partial gaps in their parent disk. In contrast to the Saturn-mass planets in the Kepler-46 system, super-Earths are not expected to merge their gaps and to evolve in a common gap, unless a fast convergent migration brings them to short mutual separations. We argue instead that close-in super-Earths are good candidates for efficient resonant repulsion caused by wake-planet interactions. For instance, one of our simulations shows that the orbital period ratio of two ∼15 Earth-mass planets increases from 1.5 to 1.55 in a few thousand orbits. Disk-driven repulsion via wake-planet interactions could explain why many planet pairs in *Kepler*'s multiple systems have period ratios slightly greater than resonant. While resonant repulsion driven by stellar tides should only be relevant to planet pairs with orbital periods below a few days, disk-driven repulsion may also apply to planets on longer periods.

The TTV signals of *Kepler*'s short-period planet pairs indicate that some of these planets have small but not zero free eccentricities (Lithwick et al. 2012). Free eccentricities get quickly damped by tidal orbital circularization. However, the presence of a disk of planetesimals or a non-smooth gas disk dispersal could give planets some free eccentricities. Close-in planet pairs that seem to have undergone resonant repulsion, but which have not zero free eccentricities, like Kepler-23b/c and Kepler-28b/c, could indicate that repulsion is primarily mediated by disk–planets interactions rather than by star–planet tidal interactions.

We foresee at least three directions to pursue work on disk-driven resonant repulsion. First, the effects of disk turbulence, which we model with a constant viscosity, need to be addressed carefully. The levels of stochastic fluctuations required to disrupt the process as planet masses decrease, and to produce some residual free eccentricity should be explored. Second, planet mass growth should be taken into account as it may also lead to some divergent evolution (Petrovich et al. 2013). Third, Monte-Carlo simulations that use three-body integrations together with simple prescriptions for the effects of disk–planets interactions should be used to compare the distribution of orbital elements among *Kepler*'s planet pairs with the synthetic distributions predicted by disk-driven resonant repulsion.

C.B. is supported by a Herchel Smith Postdoctoral Fellowship of the University of Cambridge. We thank Gwenaël Boué, Cathie Clarke, Jérôme Guilet, Cristobal Petrovich, and Yanqin Wu for useful discussions. We also thank the referee for a very helpful report. Hydrodynamical simulations were performed on the Darwin Supercomputer of the University of Cambridge High Performance Computing Service using Strategic Research Infrastructure Funding from the Higher Education Funding Council for England.

APPENDIX A

EFFICIENCY OF TIDAL RESONANT REPULSION OF A PLANET PAIR

We show that star–planet tidal interactions are unlikely to cause significant divergent evolution of two planets in the super-Earth mass range when the orbital period of the inner planet exceeds about 10 days. In the constant time lag model, taking tidal dissipation within the planet to be much larger than within the star, the orbital circularization timescale, $\tau_{\rm circ}$, is given by Equation (25) of Goldreich & Soter (1966) and can be expressed as

$$\tau_{\rm circ} = 4.5 \times 10^7\,{\rm yr} \times \left(\frac{Q^{'}_{\rm i}}{30}\right) \times \left(\frac{\rho_{\rm i}}{1\,{\rm g\,cm^{-3}}}\right) \times \left(\frac{R_{\rm i}}{0.2\,R_{\rm Jup}}\right)^{-2} \times \left(\frac{M_\star}{M_\odot}\right)^{2/3} \times \left(\frac{T_{\rm i}}{10\,{\rm days}}\right)^{13/3}, \tag{A1}$$

where $Q^{'}_{\rm i}$ is the tidal quality factor of the inner planet, $\rho_{\rm i}$ its mean density, $R_{\rm i}$ its physical radius, $T_{\rm i}$ its orbital period, and $M_\star$ is the star's mass. Divergent evolution of two resonant planets may occur as a result of tidal dissipation of orbital energy at approximately constant orbital angular momentum (Papaloizou 2011). The timescale for divergent evolution, which we denote by $\tau_{\rm div}$, satisfies

$$\tau_{\rm div} \sim \frac{\tau_{\rm circ}}{e_{\rm i}^2} \times \frac{\Delta a}{a_{\rm i}}, \tag{A2}$$

with $a_{\rm i}$ and $e_{\rm i}$ the semi-major axis and forced eccentricity of the inner planet, respectively, and Δa its change in semi-major axis during divergent evolution (it can be taken as the planet's distance from resonance). We have $e_{\rm i} = C(M_{\rm o}/M_\star) \times (\Delta a/a_{\rm i})^{-1}$, where $M_{\rm o} = \mu M_{\rm i}$ is the outer planet's mass, $M_{\rm i}$ the inner planet's mass (μ denotes the outer-to-inner planet mass ratio), and C is a constant of the order of unity that varies with the resonance (see, e.g., Equation (38) of Papaloizou 2011). Using Equation (A1) and assuming $C = 1$, we obtain

$$\tau_{\rm div} \sim 2 \times 10^{12}\,{\rm yr} \times \left(\frac{Q^{'}_{\rm i}}{30}\right) \times \mu^{-2} \times \left(\frac{\rho_{\rm i}}{1\,{\rm g\,cm^{-3}}}\right)^{-1} \times \left(\frac{R_{\rm i}}{0.2\,R_{\rm Jup}}\right)^{-8} \times \left(\frac{M_\star}{M_\odot}\right)^{8/3} \times \left(\frac{T_{\rm i}}{10\,{\rm days}}\right)^{13/3} \times \left(\frac{\Delta a/a_{\rm i}}{10^{-2}}\right)^{3}. \tag{A3}$$

This order of magnitude estimate shows that planet pairs orbiting Sun-like stars should experience negligible tidally driven resonant repulsion over gigayear timescales when the inner planet is a super-Earth, with $R_{\rm i} < 2\,R_\oplus$, $\rho_{\rm i} < 5\,{\rm g\,cm^{-3}}$, and the orbital period is greater or equal to 10 days, even if $Q^{'}_{\rm i} = 1$ and $\mu \gtrsim 1$. Moreover, if the inner planet is a Jupiter-like planet, then assuming $Q^{'}_{\rm i} \sim 10^5$ and $\rho_{\rm i} <\sim 5$ g cm^{-3},

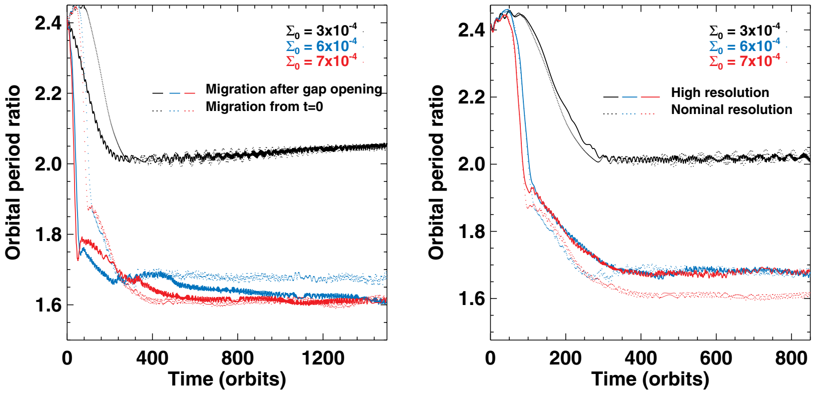

Figure 11. Ratio of orbital periods for $M_{\rm inner} = 0.6\,M_{\rm J}$ and different values of the unperturbed surface density parameter Σ_0. The left panel compares our fiducial case where planets migrate from the beginning of the simulations (dotted curves) with the case where planets are first held on fixed circular orbits for 500 orbits before migrating (solid curves). The right panel shows the overall good convergence of our results when increasing the number of grid cells from 400 × 800 (nominal resolution) to 800 × 1600 (high resolution).

(A color version of this figure is available in the online journal.)

Equation (A3) shows that divergent evolution of more than a few percent away from resonance is expected over a few gigayears as long as the inner planet's orbital period does not exceed 10 days.

APPENDIX B

HYDRODYNAMICAL SIMULATIONS OF THE KEPLER-46 SYSTEM: ROBUST RESULTS

In the course of our numerical experiments, we tested the robustness of our results by varying the assumptions made in the physical model and by varying the grid resolution.

Physical model. We performed several simulations reducing the disk's aspect ratio to 4% and 3% while keeping the same viscous alpha parameter. Although not illustrated here, these simulations show, again, a variety of outcomes, but none reproducing the observed period ratio between Kepler-46c and Kepler-46b. Decreasing the disk's aspect ratio deepens the gaps carved by the planets. When convergent migration is rapid enough for the planets to cross their 2:1 MMR and to evolve in a common gap, we find that the planets generally lock themselves into the 3:2, 4:3, or even 7:5 MMR with very little departure from exact commensurability. In these simulations, the density in the common gap is too low for wake-planet interactions to cause significant divergent evolution (see Section 2.2.2). These simulations thus suggest that partial gap opening is required to obtain a period ratio consistent with the observed value. Further, since the structure of the gaps plays a prominent role in the final evolution of the planets' period ratio, we carried out additional simulations where the planets were first held on fixed circular orbits for 500 orbits before migrating. This preliminary stage allowed enough time for each planet to build up a gap with a stationary density structure. The results of the simulations are shown in the left panel of Figure 11 for $M_{\rm inner} = 0.6\,M_{\rm J}$ and three values of Σ_0. Starting with pre-evolved gaps changes the initial rate of convergent migration. Notwithstanding quite different initial evolutions, two out of these three models follow the same evolution with or without pre-evolved gaps, and reach the same final period ratio at the end of the simulations. The model with $\Sigma_0 = 6 \times 10^{-4}$ reaches a slightly smaller period ratio (decreasing from 1.65 to 1.6 when starting with pre-evolved gaps).

Grid resolution. The effect of grid resolution was checked by doubling the number of grid cells along each direction for a few simulations. The results of three high-resolution runs (800 × 1600) are compared with the nominal-resolution runs (400 × 800) in the right panel of Figure 11. Doubling the grid resolution slightly changes the initial rate of convergent migration, leading to slightly different initial evolution. As for the above series of simulations with pre-evolved gaps, the model with capture into 2:1 MMR followed by resonant repulsion is not affected by doubling the resolution. The two models with common gap evolution seem, again, more susceptible to a variation in the initial convergent migration, but lead to small differences in the final outcome. Both high-resolution models with $\Sigma_0 = 6$ and 7×10^{-4} yield a period ratio ≈1.68, in good agreement with the observed value.

REFERENCES

Alexander, R. D., & Pascucci, I. 2012, MNRAS, 422, L82
Baruteau, C., Fromang, S., Nelson, R. P., & Masset, F. 2011, A&A, 533, A84
Baruteau, C., & Masset, F. 2013, in Tides in Astronomy and Astrophysics, ed. J. Souchay, S. Mathis, & T. Tokieda (Lecture Notes in Physics, Vol. 861; Berlin: Springer), 201
Batalha, N. M., Rowe, J. F., Bryson, S. T., et al. 2013, ApJS, 204, 24
Batygin, K., & Morbidelli, A. 2013, AJ, 145, 1
Crida, A., Baruteau, C., Kley, W., & Masset, F. 2009, A&A, 502, 679
Crida, A., Morbidelli, A., & Masset, F. 2006, Icar, 181, 587
Fleming, T., & Stone, J. M. 2003, ApJ, 585, 908
Gautier, T. N., III, Charbonneau, D., Rowe, J. F., et al. 2012, ApJ, 749, 15
Goldreich, P., & Soter, S. 1966, Icar, 5, 375
Goodman, J., & Rafikov, R. R. 2001, ApJ, 552, 793
Ketchum, J. A., Adams, F. C., & Bloch, A. M. 2011, ApJ, 726, 53
Kley, W., & Crida, A. 2008, A&A, 487, L9
Lin, D. N. C., & Papaloizou, J. C. B. 1993, in Protostars and Planets III, ed. E. H. Levy & J. I. Lunine (Tucson, AZ: Univ. of Arizona Press), 749
Lissauer, J. J., Marcy, G. W., Rowe, J. F., et al. 2012, ApJ, 750, 112
Lissauer, J. J., Ragozzine, D., Fabrycky, D. C., et al. 2011, ApJS, 197, 8
Lithwick, Y., & Wu, Y. 2012, ApJL, 756, L11
Lithwick, Y., Xie, J., & Wu, Y. 2012, ApJ, 761, 122
Masset, F. 2000, A&AS, 141, 165
Masset, F. S., & Papaloizou, J. C. B. 2003, ApJ, 588, 494
Mayor, M., Bonfils, X., Forveille, T., et al. 2009, A&A, 507, 487
Murray-Clay, R. A., & Chiang, E. I. 2005, ApJ, 619, 623
Nelson, R. P., & Papaloizou, J. C. B. 2002, MNRAS, 333, L26
Nelson, R. P., & Papaloizou, J. C. B. 2003, MNRAS, 339, 993
Nesvorný, D., Kipping, D. M., Buchhave, L. A., et al. 2012, Sci, 336, 1133
Owen, J. E., Ercolano, B., Clarke, C. J., & Alexander, R. D. 2010, MNRAS, 401, 1415

Papaloizou, J. C. B. 2011, CeMDA, 111, 83
Papaloizou, J. C. B., & Szuszkiewicz, E. 2005, MNRAS, 363, 153
Papaloizou, J. C. B., & Terquem, C. 2010, MNRAS, 405, 573
Petrovich, C., Malhotra, R., & Tremaine, S. 2013, ApJ, 770, 24
Pierens, A., Baruteau, C., & Hersant, F. 2011, A&A, 531, A5
Podlewska-Gaca, E., Papaloizou, J. C. B., & Szuszkiewicz, E. 2012, MNRAS, 421, 1736
Rein, H. 2012, MNRAS, 427, 21
Rein, H., Papaloizou, J. C. B., & Kley, W. 2010, A&A, 510, A4
Rein, H., Payne, M. J., Veras, D., & Ford, E. B. 2012, MNRAS, 426, 187

J. Fluid Mech. (2013), *vol.* 719, *pp.* 47–81. © Cambridge University Press 2013
doi:10.1017/jfm.2012.605

Inertial waves in a differentially rotating spherical shell

C. Baruteau[1],† **and M. Rieutord**[2]

[1]Department of Applied Mathematics and Theoretical Physics, University of Cambridge, Wilberforce Road, Cambridge CB3 0WA, UK

[2]Institut de Recherche en Astrophysique et Planétologie, CNRS et Université de Toulouse, 14 avenue E. Belin, 31400 Toulouse, France

(Received 19 March 2012; revised 19 October 2012; accepted 3 December 2012)

We investigate the properties of small-amplitude inertial waves propagating in a differentially rotating incompressible fluid contained in a spherical shell. For cylindrical and shellular rotation profiles and in the inviscid limit, inertial waves obey a second-order partial differential equation of mixed type. Two kinds of inertial modes therefore exist, depending on whether the hyperbolic domain where characteristics propagate covers the whole shell or not. The occurrence of these two kinds of inertial modes is examined, and we show that the range of frequencies at which inertial waves may propagate is broader than with solid-body rotation. Using high-resolution calculations based on a spectral method, we show that, as with solid-body rotation, singular modes with thin shear layers following short-period attractors still exist with differential rotation. They exist even in the case of a full sphere. In the limit of vanishing viscosities, the width of the shear layers seems to weakly depend on the global background shear, showing a scaling in $E^{1/3}$ with the Ekman number E, as in the solid-body rotation case. There also exist modes with thin detached layers of width scaling with $E^{1/2}$ as Ekman boundary layers. The behaviour of inertial waves with a corotation resonance within the shell is also considered. For cylindrical rotation, waves get dramatically absorbed at corotation. In contrast, for shellular rotation, waves may cross a critical layer without visible absorption, and such modes can be unstable for small enough Ekman numbers.

Key words: geophysical and geological flows, rotating flows, waves in rotating fluids

1. Introduction

The fluid flows that pervade the interior of stars and planets are most of the time dominated by a strong background rotation. The Earth's atmosphere, oceans or its liquid core are typical examples. Such flows are studied in a rotating frame, and the dominance of rotation arises through that of the Coriolis acceleration over all other terms in the momentum equation (the centrifugal acceleration is usually combined with the pressure gradient through the so-called reduced pressure). The Coriolis acceleration implies that the response of a rotating fluid to small-amplitude oscillations may become singular.

---

† Email address for correspondence: C.Baruteau@damtp.cam.ac.uk

It is known indeed since the work of Cartan (1922) that the pressure perturbations of an inviscid incompressible fluid obey Poincaré equation, which has the remarkable property of being spatially hyperbolic. Since boundary conditions have to be met by solutions, oscillations of bounded rotating fluids are a mathematically ill-posed problem. It means that, in most general containers, eigenmodes of inviscid incompressible fluids may simply not exist. Mathematically, the point spectrum of the operator is said to be empty. However, a few containers such as the full ellipsoid or the cylindrical layer allow the existence of such eigenmodes, because of the separation of spatial variables that is possible in these geometries. Solutions were worked out by Kelvin (1880) for the cylinder, and by Bryan (1889) for the sphere and the ellipsoid. The singular nature of the solutions to Poincaré equation have been uncovered almost a century later by the works of Stewartson & Rickard (1969) and Stewartson (1971, 1972*a*). Stewartson (1972*b*) showed that these singularities should turn into oscillating shear layers through viscosity.

New interest in the singular solutions to the Poincaré equation was put forward with the work of Maas & Lam (1995) on gravity modes in two-dimensional basins. The pressure fluctuations of internal gravity modes also satisfy the Poincaré equation, and Maas & Lam (1995) showed the crucial role of characteristic trajectories and coined the concept of attractor to describe the convergence of characteristics to special limit cycles. At the same time, Hollerbach & Kerswell (1995) and Kerswell (1995) investigated the internal shear layers spawned by the critical latitude singularity (another singularity different from that of the attractors), in relation with the precession flows of a spherical shell.

Subsequent work by Rieutord & Valdettaro (1997), Rieutord, Georgeot & Valdettaro (2001) and Rieutord, Valdettaro & Georgeot (2002) demonstrated how attractors feature the oscillations of slightly viscous rotating fluids contained in spherical shells. For very small viscosities, relevant to astrophysical and geophysical applications, oscillating flows are confined within shear layers that closely follow attractors of characteristics. In the two-dimensional limit of a spherical shell, Rieutord *et al.* (2002) derived analytical solutions for the structure of shear layers. They showed in particular that the velocity field of eigenmodes obeys the same equation as that governing the quantum states of a particle trapped in a parabolic well (the Schrödinger equation).

More recently, forced oscillations in rotating fluids have been examined in the context of tidal interactions between two celestial bodies (Ogilvie & Lin 2004; Wu 2005; Ogilvie & Lin 2007; Goodman & Lackner 2009; Ogilvie 2009; Rieutord & Valdettaro 2010). Dissipation of tidally forced modes of oscillations in each companion alters the orbital elements and spin of each body. It plays a prominent role in the late evolution of close-in extrasolar planets. The efficiency of tidal dissipation mechanisms is usually parametrized by a single, dimensionless tidal quality factor Q, which is an inverse measure of the tidal torque acting on a gravitationally perturbed body. However, tidal dissipation is extremely sensitive to the frequency and amplitude of the external tidal potential (see, e.g., Ogilvie 2009; Rieutord & Valdettaro 2010). This dependency is intimately related to the existence of singularities arising from the hyperbolic nature of the Poincaré equation. As in free modes of oscillations, these singularities consist of the critical latitude singularity and attractors of characteristics.

Works examining tidal dissipation mechanisms in rotating fluids have used simple fluid models, where the background flow disturbed by inertial modes is in pure solid-body rotation. The rotation pattern inside stars and planets is much more intricate, as may be guessed. Large-scale flows are usually present in stars and planets. Most frequently, such flows are largely axisymmetric, and include differential rotation as well as a weak meridional circulation. In light of previous works on rigidly rotating fluids, the present paper is a first study of how departure to solid-body rotation impacts the oscillation properties of rotating fluids and their associated tidal dissipation. In this first paper, we focus on free inertial modes of oscillations. Tidally forced inertial modes will be examined in a future study. As a first simplification, we discard meridional circulation, which is very weak in general, especially for very small viscosities. However, the choice for the differential rotation pattern, which we assume to be axisymmetric, remains open. The blue azimuthal velocity of the (smooth) differentially rotating background flow can be expanded into spherical harmonics,

$$u_\varphi(r,\theta) = -\sum_\ell w_m^\ell(r)\partial_\theta Y_\ell^m, \tag{1.1}$$

as for any axisymmetric azimuthal component of a vector field (Rieutord 1987). In this expression, r, θ and φ denote the usual spherical coordinates, Y_ℓ^m denotes the spherical harmonics normalized on the sphere of unit radius and $w_m^\ell(r)$ accounts for the radial variation in the flow. If differential rotation is smooth, we expect the previous expansion to be dominated by small ℓ. In the present work, we will primarily focus on a single term, the $\ell = 1$ term, such that the background velocity field takes the form

$$u_\varphi(r,\theta) = w(r)\sin\theta = r\Omega(r)\sin\theta, \tag{1.2}$$

with differential rotation along the radial direction only (Ω denotes the local angular frequency of the fluid). The obvious asset of this functional form is that it preserves the relative simplicity of the coupling of harmonics imposed by the Coriolis term. This type of flow is known in the astrophysical literature as shellular differential rotation (Zahn 1992). It originates from a simple description of the baroclinic flow (the thermal wind in geophysics), which arises in stably stratified radiative zones of rotating stars (see, e.g., Rieutord 2006). The rotation is assumed to be uniform on spheres as a consequence of some shear-induced turbulence, which erases latitudinal gradients of the velocity (Zahn 1992). Low-frequency perturbations of such flows are driven by the combined effects of the Coriolis acceleration and buoyancy. Assuming differential rotation along the radial direction therefore comes to neglecting the effects of buoyancy on the fluid perturbations. Our model approaches this astrophysical configuration in the limit of weak stratification, when the Brunt–Väisälä is small compared with the Coriolis frequency. When this is the case, some modes, called H1 by Dintrans, Rieutord & Valdettaro (1999), are essentially inertial modes slightly perturbed by buoyancy (i.e. the Coriolis acceleration is the main restoring force). In addition to giving a first look at the effect of differential rotation on inertial oscillations, shellular rotation may also provide a (partial) view on the properties of waves propagating in radiative zones inside rotating stars.

To complement the study of shellular flows, which may mimic stellar baroclinic flows, we also consider differential rotation associated with a barotropic fluid model. In this case, differential rotation only depends on the cylindrical radial coordinate $s = r\sin\theta$. Cylindrical differential rotation is expected in the convective zones of rapidly rotating stars or giant planets. It has been much investigated in the context of the Taylor–Couette instability, but in cylindrical geometry. However, recent experimental work by Kelley *et al.* (2007, 2010) and Rieutord *et al.* (2012) has raised the question of how the properties of inertial waves in spherical geometry are changed by the inclusion of cylindrical rotation. Since spherical geometry combined with cylindrical rotation results in the variables non-separability, which is a necessary condition for the existence of singularities such as attractors, some properties of the perturbations can be derived by the sole analysis of the dynamics of characteristics.

This paper is organized as follows. Our physical model is described in § 2. The ideal case of an inviscid differentially rotating fluid is first examined in § 3 through a linear analysis in the short-wavelength approximation. Cylindrical and shellular rotation profiles are considered in §§ 3.1 and 3.2, respectively. A detailed study of the dynamics of characteristics allows us to determine the range of frequencies at which inertial oscillations may exist in differentially rotating fluids. The presence of turning surfaces, critical latitudes and corotation resonances within the fluid is investigated. The full problem of a viscously rotating fluid is then investigated in § 4 with (linear) numerical calculations. Again, results with cylindrical and shellular rotation profiles are presented. Shear layers are shown to closely follow the attractors of characteristics obtained for an inviscid fluid in the short-wavelength approximation. Our simulations primarily focus on axisymmetric modes (§ 4.2), but a few examples of non-axisymmetric modes with a corotation resonance are also examined (§ 4.3). Concluding remarks and future directions are drawn in § 5.

2. Inertial modes in a differentially rotating shell: physical model

We consider a differentially rotating viscous fluid inside a spherical shell, located between radii ηR and R $(0 < \eta < 1)$. The fluid is assumed to be homogeneous, incompressible and of constant kinematic viscosity ν. We denote by $\boldsymbol{u}$ the fluid's velocity. Any quantity x is decomposed as $x = x_0 + x_1$, where x_0 describes an unperturbed background quantity and x_1 the associated disturbance $(|x_1| \ll |x_0|)$. In an inertial frame, and using the set of spherical coordinates (r, θ, φ), the linearized Navier–Stokes equation reads

$$\frac{\partial \boldsymbol{u}_1}{\partial t} + \Omega_0 \frac{\partial \boldsymbol{u}_1}{\partial \varphi} + 2\Omega_0 \boldsymbol{e}_z \times \boldsymbol{u}_1 + A(\boldsymbol{u}_1)\boldsymbol{e}_\varphi = -\nabla p_1 + \nu \boldsymbol{\Delta} \boldsymbol{u}_1, \tag{2.1}$$

with $\Omega_0 = u_0^\varphi / r \sin\theta$ the fluid's angular velocity, $u_0^\varphi = \boldsymbol{u}_0 \cdot \boldsymbol{e}_\varphi$, $\boldsymbol{e}_z = \cos\theta \boldsymbol{e}_r - \sin\theta \boldsymbol{e}_\theta$ is the unit vector along the rotation axis and p_1 denotes the pressure perturbation divided by the reference density. Since the fluid is incompressible, the linearized continuity equation reads

$$\nabla \cdot \boldsymbol{u}_1 = 0. \tag{2.2}$$

In (2.1), $A(\boldsymbol{u}_1)$ is proportional to the shear in the background flow:

$$A(\boldsymbol{u}_1) = r \sin\theta \boldsymbol{u}_1 \cdot \nabla \Omega_0. \tag{2.3}$$

In the following we consider one of two profiles.

(i) A cylindrical rotation profile, $\Omega_0 = \Omega_0(s)$, with $s = r \sin\theta$ the radial cylindrical coordinate. This rotation profile satisfies the Proudman–Taylor theorem for an incompressible homogeneous fluid in the inviscid limit, and no additional body force needs to be assumed to ensure an equilibrium state for the differentially rotating background flow;

(ii) A shellular rotation profile, $\Omega_0 = \Omega_0(r)$. In this case, differential rotation is assumed to be maintained by some appropriate body force $\boldsymbol{f}$ (arising for instance from Reynolds stresses or from a latitudinal entropy gradient), not included in our model. This body force should verify $\nabla \times \boldsymbol{f} = -s \partial \Omega_0^2 / \partial z \boldsymbol{e}_\varphi$ for Taylor–Proudman theorem to be satisfied in this case.

We seek solutions to (2.1) and (2.2) in the form $\exp(\mathrm{i}\Omega_p t + \mathrm{i}m\varphi)$, where Ω_p denotes the wave angular frequency in the inertial frame. We introduce the Ekman number $E = \nu/R^2\Omega_{ref}$, where the reference angular frequency, Ω_{ref}, refers to $\Omega_0(R)$ for shellular rotation or to $\Omega_0(s=0)$ for cylindrical rotation. Dropping all subscripts and taking the curl of (2.1), we are to solve

$$\begin{cases} \nabla \times (\mathrm{i}\tilde{\Omega}_p \boldsymbol{u} + 2\Omega \boldsymbol{e}_z \times \boldsymbol{u} + r\sin\theta(\boldsymbol{u}\cdot\nabla\Omega)\boldsymbol{e}_\varphi) = E\nabla \times \Delta\boldsymbol{u} \\ \nabla\cdot\boldsymbol{u} = 0, \end{cases} \tag{2.4}$$

where $\tilde{\Omega}_p = \Omega_p + m\Omega$ is the Doppler-shifted wave frequency (that is, the wave frequency in the frame rotating with the fluid).

We complete (2.4) with stress-free boundary conditions at both boundaries: $\boldsymbol{u}\cdot\boldsymbol{e}_r = 0$ and $\boldsymbol{e}_r \times [\sigma]\boldsymbol{e}_r = \boldsymbol{0}$, where $[\sigma]$ denotes the viscous stress tensor. As discussed by Rieutord & Valdettaro (2010), the general properties of oscillation modes are essentially unchanged by the choice of boundary conditions. We thus opt for stress-free boundaries, which are numerically less demanding.

3. Inviscid problem: paths of characteristics, existence of turning surfaces and corotation resonances

Before examining the full solutions to (2.4) by means of numerical simulations, we first study the inviscid limit and especially the dynamics of characteristics, which is known to feature the eigenfunctions of the viscous problem. For this purpose, we shall use cylindrical coordinates (s, φ, z) and eliminate the velocity perturbations in favour of the pressure perturbations (p). The partial differential equation (PDE) satisfied by p is given in the Appendix by (A 6). Retaining only the second-order terms, (A 6) becomes

$$\frac{\partial^2 p}{\partial s^2} + \frac{A_z}{\tilde{\Omega}_p^2}\frac{\partial^2 p}{\partial s \partial z} + \left(1 - \frac{A_s}{\tilde{\Omega}_p^2}\right)\frac{\partial^2 p}{\partial z^2} = 0, \tag{3.1}$$

where

$$A_s = \frac{2\Omega}{s}\frac{\partial}{\partial s}(s^2\Omega) \quad \text{and} \quad A_z = \frac{2\Omega}{s}\frac{\partial}{\partial z}(s^2\Omega). \tag{3.2}$$

Equation (3.1) matches equation (A 16) of Ogilvie (2005) for an homogeneous incompressible fluid. The equation governing the paths of characteristics in a meridional plane then reads

$$\frac{\mathrm{d}z}{\mathrm{d}s} = \frac{1}{2\tilde{\Omega}_p^2}\left(A_z \pm \xi^{1/2}\right) \quad \text{with } \xi(s,z) = A_z^2 + 4\tilde{\Omega}_p^2(A_s - \tilde{\Omega}_p^2). \tag{3.3}$$

For solid-body rotation, $A_z = 0$, $A_s = 4\Omega^2$ and (3.1) reduces to the well-known Poincaré equation for inertial waves. In this case, characteristics form straight lines in a meridional plane, and the fact that ξ is constant makes the entire shell either hyperbolic or elliptic for inertial waves. With differential rotation, however, the dependence of A_s, A_z and Ω with s and z implies that characteristics no longer form straight lines, as will be illustrated in the following. Also, ξ may vanish and change sign inside the shell. This makes possible the co-existence of hyperbolic and elliptic domains for pure inertial waves in a differentially rotating spherical shell, separated by turning surfaces. It is reminiscent of the existence of turning surfaces for gravito-inertial waves and magneto-inertial waves in rigidly rotating spherical shells, for which the perturbed pressure also satisfies a second-order PDE of mixed type in the inviscid limit (Friedlander 1982, 1987; Friedlander & Siegmann 1982; Dintrans *et al.* 1999). Equation (3.3) also shows that, in contrast to solid-body rotation, paths of characteristics with differential rotation depend on the azimuthal wavenumber m through $\tilde{\Omega}_p$. In the rest of this section, we study in more detail the dynamics of characteristics based on (3.3), considering a particular profile of cylindrical rotation in § 3.1, and of shellular rotation in § 3.2.

3.1. *Cylindrical rotation*

3.1.1. *Paths of characteristics*

To restrict the differential rotation function space to a one-parameter space, we consider the following background rotation profile:

$$\Omega(s)/\Omega_{ref} = 1 + \varepsilon\,(s/R)^2, \tag{3.4}$$

with $\Omega_{ref} = \Omega(s=0)$ the shell's angular frequency at the rotation axis, and where $|\varepsilon|$ can be seen as a Rossby number for the fluid. Equation (3.1) then takes the form

$$\frac{\partial^2 p}{\partial s^2} + \left(1 - \frac{A_s}{\tilde{\Omega}_p^2}\right)\frac{\partial^2 p}{\partial z^2} = 0, \tag{3.5}$$

where

$$\tilde{\Omega}_p(s) = \Omega_p + m\Omega(s) \tag{3.6}$$

is the Doppler-shifted frequency and

$$A_s(s) = 4\Omega^2(s) \times \left[1 + \frac{\varepsilon\,(s/R)^2}{1+\varepsilon\,(s/R)^2}\right]. \tag{3.7}$$

We will take $\varepsilon > -1/2$ so that $A_s > 0\,\forall s \in [0,R]$ (Rayleigh's stability criterion). We denote the quantity A_s by κ_s^2 (it is known as the square of the radial epicyclic frequency in astrophysical discs). We point out that (3.5) is symmetric by $z \to -z$, so that only positive values of z will be considered. From (3.3), paths of characteristics satisfy

$$\frac{\mathrm{d}z}{\mathrm{d}s} = \pm\xi^{1/2}, \tag{3.8}$$

with

$$\xi(s) = \frac{\kappa_s^2(s)}{\tilde{\Omega}_p^2(s)} - 1. \tag{3.9}$$

3.1.2. *Existence of turning surfaces: D and DT inertial modes*

The relation $\xi(s) = 0$ defines turning surfaces that separate the hyperbolic and elliptic domains. They correspond to cylinders in a meridional slice of the shell. Their location satisfies

$$\tilde{\Omega}_p^2(s) = \kappa_s^2(s), \tag{3.10}$$

with waves propagating when $\kappa_s^2(s) \geqslant \tilde{\Omega}_p^2(s)$. Here and in the following, we assume that the hyperbolic domains of the spherical shell, where ξ is positive, host inertial

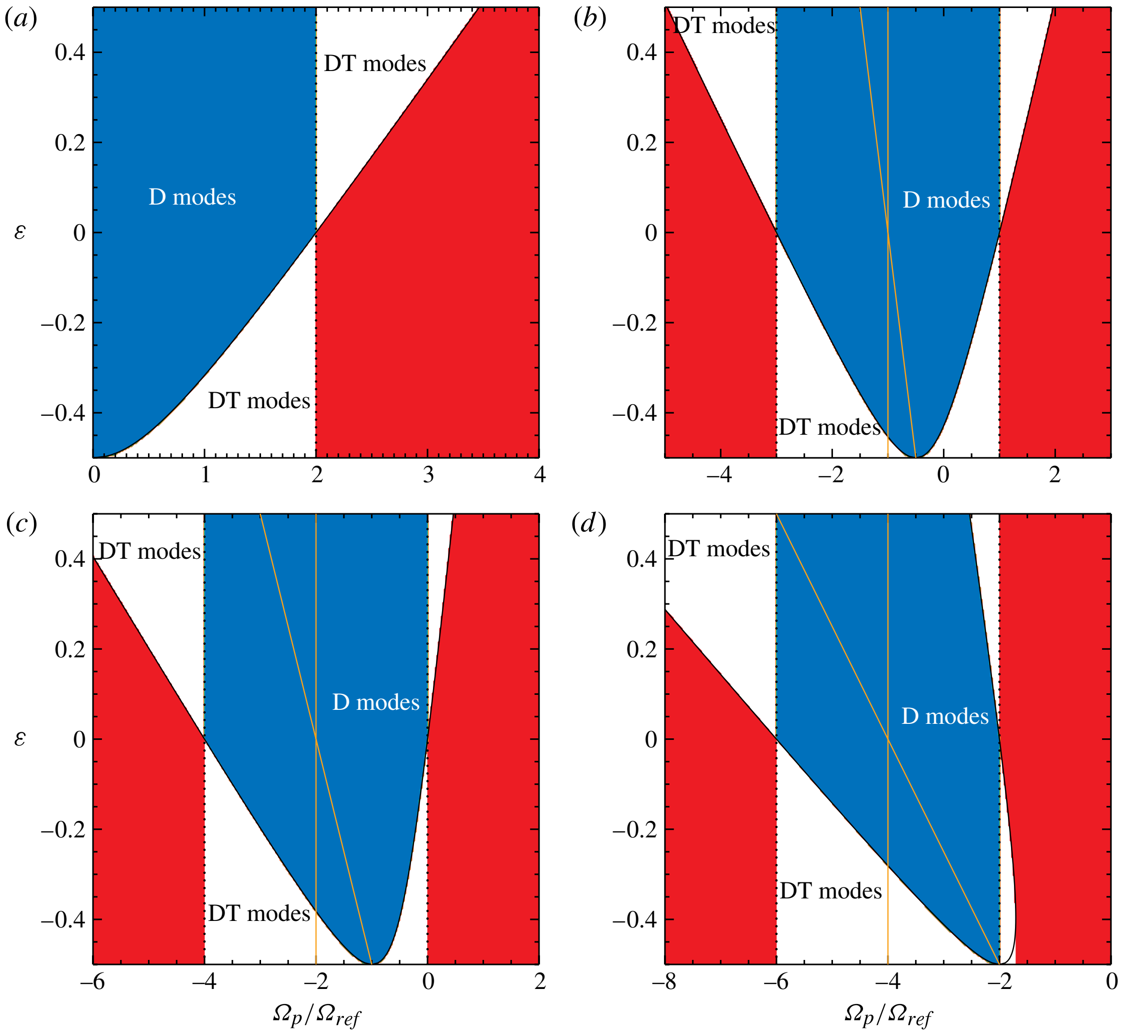

FIGURE 1. (Colour online) Illustration of the two kinds of inertial modes propagating in a differentially rotating fluid, with cylindrical rotation profile $\Omega(s)/\Omega_{ref} = 1 + \varepsilon\,(s/R)^2$ (Ω_{ref} denotes the shell's angular frequency at the rotation axis). Results are shown for azimuthal wavenumbers m equal to 0, 1, 2 and 4 (*a*–*d*). DT modes, represented by white areas, exhibit turning surfaces inside the shell. D modes correspond to the blue area and do not feature turning surfaces inside the shell. No inertial modes may propagate in the red areas. The solutions to $\xi(s=0)=0$ are shown by vertical dotted lines and the solutions to $\xi(s=R)=0$ by solid black curves. Non-axisymmetric modes that feature a critical cylinder inside the shell (corotation resonance) are located between the two orange solid curves.

modes of oscillations. The dependence of ξ on s leads to two kinds of inertial modes with cylindrical rotation:

(i) modes that exhibit at least one turning surface within the shell, which we call DT modes for future reference (D for differential rotation, and T for turning surface);

(ii) generalized inertial modes with no turning surfaces within the shell, which we name D modes.

The occurrence of axisymmetric ($m=0$) and of some non-axisymmetric D and DT modes is illustrated in figure 1. In all figures, the mode's eigenfrequency in the inertial frame (Ω_p) is shown on the x-axis, and the differential rotation parameter ε is on the y-axis. Contours are obtained by numerically calculating the right-hand side of (3.9).

DT modes, which are represented by white areas, have $\xi < 0$ at least once within the shell. D modes satisfy $\xi \geqslant 0$ everywhere in the shell and are shown by the blue area. No inertial modes can propagate if $\xi < 0$ in the entire shell, such case being depicted in red. Note that axisymmetric inertial waves may propagate for eigenfrequencies $\Omega_p > 2\Omega_{ref}$ if $\varepsilon > 0$ (see figure 1*a*). Note also that the results shown in figure 1 are independent of the shell's aspect ratio η, as is actually the dynamics of characteristics with our cylindrical rotation profile.

The transition curves that separate D and DT modes satisfy $\xi(s=0)=0$ and $\xi(s=R)=0$. The solution to $\xi(s)=0$ can be cast as $\Omega_p/\Omega_{ref} = -m[1+\varepsilon\,(s/R)^2] \pm 2\sqrt{[1+2\varepsilon\,(s/R)^2][1+\varepsilon\,(s/R)^2]}$. Applied to the following cases:

(i) $\xi(s=0)=0$, that is when the turning surface matches the location of the rotation axis, we have

$$\Omega_p/\Omega_{ref} = -m \pm 2, \tag{3.11}$$

such case being depicted by vertical dotted lines in figure 1;

(ii) $\xi(s=R)=0$, when the turning surface passes by the shell's surface, yields

$$\Omega_p/\Omega_{ref} = -m(1+\varepsilon) \pm 2\sqrt{(1+2\varepsilon)(1+\varepsilon)}, \tag{3.12}$$

which is overplotted by solid curves in figure 1.

We point out that there may exist two turning surfaces in a meridional plane. This occurs for instance for the DT modes with $m=4$ located in the (small) region of parameter space below the solid curve near $\Omega_p = -2\Omega_{ref}$ and $\varepsilon = -0.5$.

Non-axisymmetric modes may feature a corotation resonance within the shell when $\tilde{\Omega}_p(s)=0$. The location of such critical cylinders is given by

$$s_{crit} = R\sqrt{\varepsilon^{-1} \times \left(-1 - \frac{\Omega_p}{m\Omega_{ref}}\right)}. \tag{3.13}$$

For $m>0$, modes with $\varepsilon \leqslant 0$ have a critical layer if $-m \leqslant \Omega_p/\Omega_{ref} \leqslant -m(1+\varepsilon)$, and those with $\varepsilon \geqslant 0$ if $-m(1+\varepsilon) \leqslant \Omega_p/\Omega_{ref} \leqslant -m$. Modes that exhibit a critical cylinder within the shell are located between the two orange solid curves in figure 1.

The minimum and maximum frequencies at which inertial waves may propagate in a shell with cylindrical rotation is summarized in figure 2 for the four azimuthal wavenumbers considered in figure 1. These frequencies are obtained by solving $\xi(s)=0$. They correspond to the minimum and maximum frequencies amongst the four values given by (3.11) and (3.12), except for $m=4$ and ε approaching -0.5 (in which case, as already pointed out before, there are two turning surfaces inside the shell). Figure 2 highlights that the range of eigenfrequencies at which inertial modes of oscillations may exist in a spherical shell is broader with cylindrical rotation than with solid rotation, particularly if the rotation profile is an increasing function of the cylindrical radial coordinate. This is expected, because of the larger frequencies at which the fluid may rotate in this case.

3.1.3. *Dispersion relation, phase and group velocities*

We examine in this paragraph the propagation properties of local waves in a meridional plane. In the short-wavelength approximation, the general expressions for the wave dispersion relation, the phase and group velocities are given in the Appendix

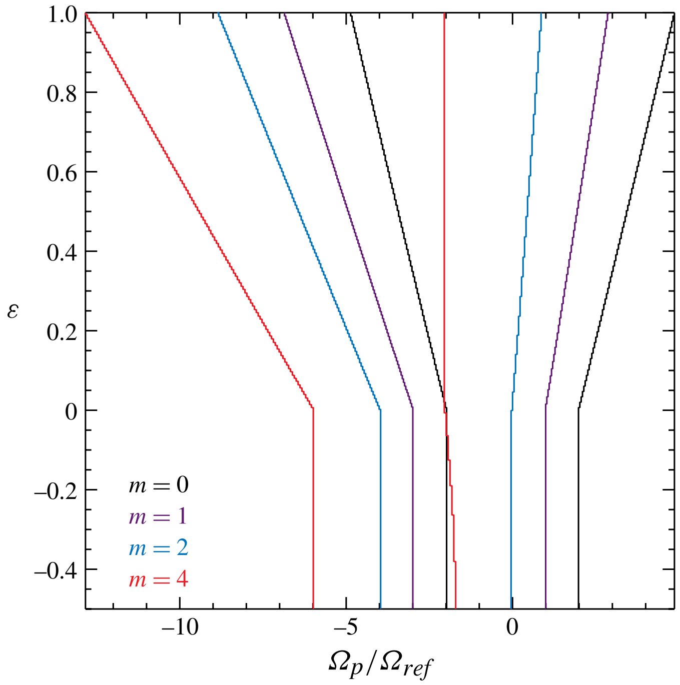

FIGURE 2. (Colour online) Range of eigenfrequencies (Ω_p, x-axis) for inertial modes of oscillations in a rotating shell with cylindrical rotation profile $\Omega(s)/\Omega_{ref} = 1 + \varepsilon\,(s/R)^2$. Eigenfrequencies are in units of Ω_{ref}, the shell's angular frequency at the rotation axis. Results are for $m = 0$, 1, 2 and 4. For a given m, the minimum and maximum frequencies at which inertial modes exist correspond to the left and right curves, respectively.

by (A 7), (A 9) and (A 10). For our cylindrical rotation profile, (A 7) reduces to

$$\tilde{\Omega}_p^2(s) = \kappa_s^2(s)\frac{k_z^2}{\|\boldsymbol{k}\|^2}, \tag{3.14}$$

where $\|\boldsymbol{k}\| = \sqrt{k_s^2 + k_z^2}$. In the frame rotating with the fluid, the phase velocity, $\boldsymbol{v}_p = \tilde{\Omega}_p\boldsymbol{k}/\,\|\boldsymbol{k}\|^2$, satisfies

$$\boldsymbol{v}_p = \pm\kappa_s(s)\frac{k_z\boldsymbol{k}}{\|\boldsymbol{k}\|^3}, \tag{3.15}$$

while the group velocity, $\boldsymbol{v}_g = \partial\tilde{\Omega}_p/\partial\boldsymbol{k}$, is given by

$$\boldsymbol{v}_g = \pm\kappa_s(s)\frac{k_s}{\|\boldsymbol{k}\|^3}(-k_z\boldsymbol{e}_s + k_s\boldsymbol{e}_z). \tag{3.16}$$

From (3.9) and (3.14), $k_s = 0$ at a turning surface (where ξ vanishes). At this location, the radial component of the phase velocity therefore vanishes, as well as the two other components of the group velocity (that is, rays are perpendicular to the turning surface).

A corotation resonance occurs inside the shell where $\tilde{\Omega}_p(s) = 0$. This formally happens if $|k_s| \to \infty$, in which case the modulus of the phase velocity and the group velocity both tend to zero, or if $k_z \to 0$, in which case the phase velocity cancels out while the radial component of the group velocity cancels out. In both cases, characteristics become more and more parallel to the rotation axis as they approach the corotation resonance (their slope $|\mathrm{d}z/\mathrm{d}s|$ increases), and they do not cross corotation (as the radial component of the group velocity tends to zero at this location). The fact that the phase velocity progressively decreases to zero upon approaching corotation suggests that nonlinear effects should become important near this location, as pointed out for instance by Barker & Ogilvie (2010) for internal gravity waves in a background shear flow, which satisfy a dispersion relation similar to that in (3.14) with the epicyclic frequency squared κ_s^2 replaced by the Brunt–Väisälä squared.

3.2. *Shellular rotation*

We now come to the propagation properties of inertial modes of oscillation in fluids with shellular rotation (the background rotation profile being a prescribed function of the spherical radius). As in the case of cylindrical rotation, we show in this section that two kinds of inertial modes can be distinguished, based on the presence or not of turning surfaces within the shell. We then discuss the range of eigenfrequencies at which inertial modes may exist, the existence of critical latitudes and corotation resonances.

3.2.1. *D and DT inertial modes*

We adopt the same strategy as in § 3.1 for cylindrical rotation and restrict the differential rotation function space to a one-parameter space. We take the following shellular rotation profile:

$$\Omega(r) = \Omega_{ref} \times (r/R)^{\sigma}, \tag{3.17}$$

where $r = \sqrt{s^2+z^2}$, $\Omega_{ref} = \Omega(r=R)$ is the angular frequency at the shell's surface, and $\sigma > -2$ to avoid centrifugal instabilities (Rayleigh's stability criterion, $A_s > 0$, is satisfied). The quantity $|1-\eta^{\sigma}|$, which measures the relative difference of angular frequencies between the inner core and the shell's surface, can be seen as a Rossby number for the fluid. Equation (3.1) being symmetric by $z \to -z$ for shellular rotation profile, only positive values of z will be considered (as with cylindrical rotation). From (3.3), paths of characteristics satisfy

$$\frac{\mathrm{d}z}{\mathrm{d}s} = A(r)\frac{sz}{R^2} \pm \xi^{1/2}, \tag{3.18}$$

where

$$\xi(s,z) = A^2(r)\frac{s^2z^2}{R^2} + 2A(r)\frac{s^2}{R^2} + \frac{4\Omega^2(r) - \tilde{\Omega}_p^2(r)}{\tilde{\Omega}_p^2(r)}, \tag{3.19}$$

$$A(r) = \sigma\frac{R^2}{r^2}\frac{\Omega^2(r)}{\tilde{\Omega}_p^2(r)}, \tag{3.20}$$

and $\tilde{\Omega}_p(r) = \Omega_p + m\Omega(r)$ is the Doppler-shifted wave frequency. Whenever paths of characteristics are calculated by solving (3.18) (or (3.8) for cylindrical rotation), reflections are imposed at the shell's inner core ($r = \eta R$) and surface ($r = R$), at the rotation ($s = 0$) and equatorial ($z = 0$) axes, and at the location of turning surfaces (where $\xi = 0$).

The possibility that ξ vanishes within the shell leads again to two kinds of inertial modes with shellular rotation: DT modes, with at least one turning surface inside the shell, and D modes, with no turning surfaces inside the shell. The occurrence of

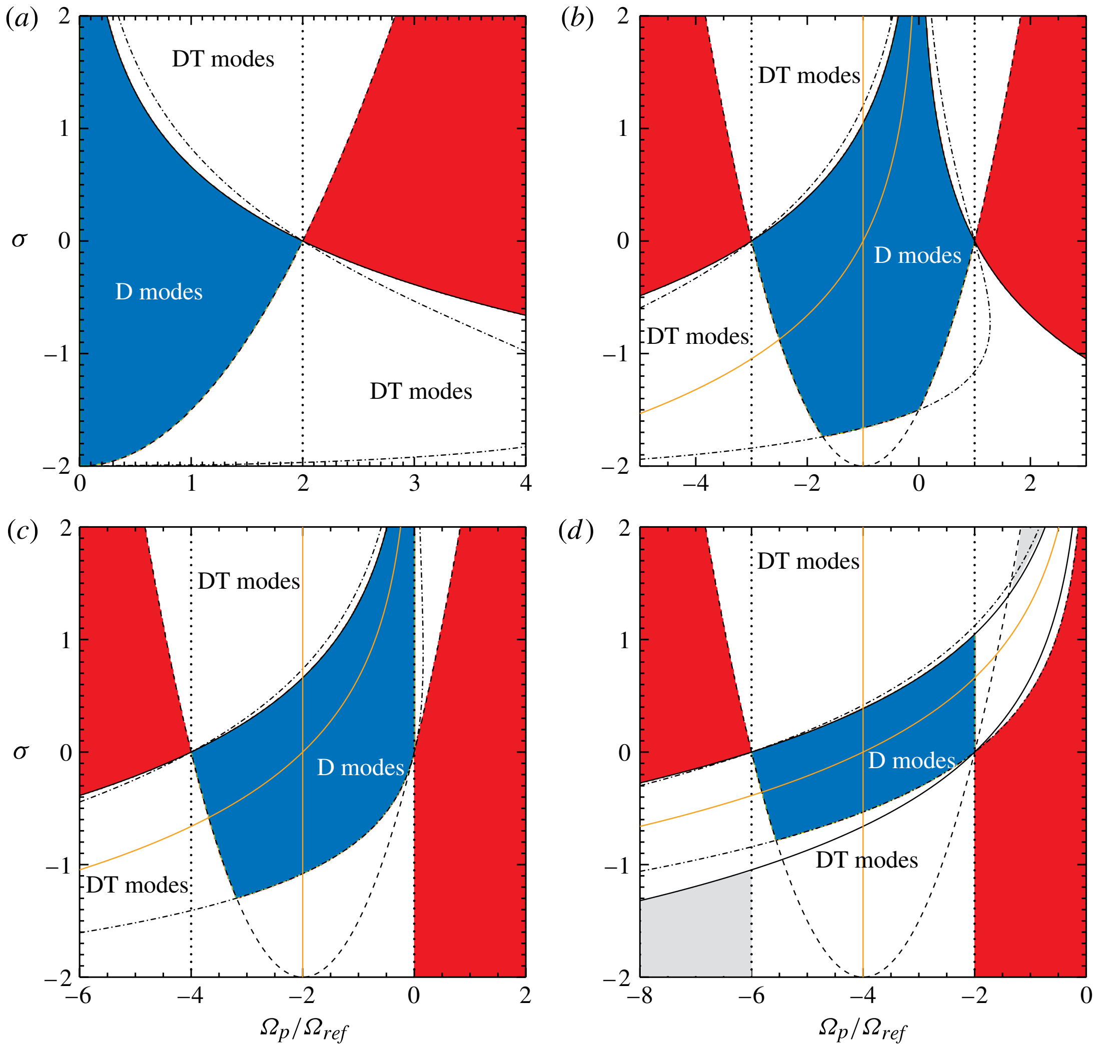

FIGURE 3. (Colour online) Occurrence of D and DT inertial modes with the shellular rotation profile $\Omega(r)/\Omega_{ref} = (r/R)^\sigma$ (Ω_{ref} denotes the angular frequency at the shell's surface). Results are obtained for $\eta = 0.35$, and $m = 0$, 1, 2 and 4 (*a*–*d*). DT modes (white areas) have at least one turning surface inside the shell. D modes (blue area) do not have turning surfaces. No inertial modes exist within the red areas. The dotted, dashed, solid and dash-dotted curves are solutions to (3.23) to (3.26), respectively. In (*d*), grey areas depict DT modes located between two turning surfaces that englobe the shell's inner core and surface. For $m \neq 0$, modes that feature a critical layer inside the shell (where $\tilde{\Omega}_p(r) = 0$) are located between the two orange solid curves.

axisymmetric and of some non-axisymmetric D and DT modes is depicted in figure 3. Contours are obtained upon calculation of (3.19) in a spherical shell with $\eta = 0.35$. As in figure 1, D and DT modes are depicted by blue and white areas, respectively, and no inertial modes exist in the red areas.

The relation $\xi = 0$ defines turning surfaces with colatitude $\theta(r)$ given by

$$\sin^2\theta(r) = \frac{1}{2}\left[1 + \frac{2\tilde{\Omega}_p^2(r)}{\sigma\Omega^2(r)} \pm \mu^{1/2}(r)\right], \tag{3.21}$$

with

$$\mu(r) = 1 + \frac{4(4+\sigma)\tilde{\Omega}_p^2(r)}{\sigma^2 \Omega^2(r)}. \tag{3.22}$$

Another way to find the occurrence of DT modes is to require that, for given values of m, Ω_p and σ, the inequality $0 \leqslant \sin^2\theta(r) \leqslant 1$ is satisfied at least once within the shell. We also point out that the two propositions $\forall \{s, z\}$, $\xi(s, z) > 0$, and $\forall r$, $|\tilde{\Omega}_p(r)| < 2\Omega(r)$, seem to be equivalent numerically (as we have checked). In other words, if the whole shell satisfies the condition for hyperbolicity, it also meets the standard criterion for propagation of inertial waves everywhere locally. Thus, regions with no mode propagation, and those with D modes, can be distinguished by requiring that D modes verify $|\tilde{\Omega}_p(r)| < 2\Omega(r)$ in the whole shell.

The transition curves that separate D and DT modes then satisfy:

(i) $\sin^2\theta(R) = 0$, when the turning surface hits the shell's surface at colatitude $\theta = 0$; it reads $|\tilde{\Omega}_p(R)| = 2\Omega(R)$ or

$$\Omega_p/\Omega_{ref} = -m \pm 2, \tag{3.23}$$

an expression that is depicted by vertical dotted lines in figure 3;

(ii) $\sin^2\theta(R) = 1$, which yields

$$\Omega_p/\Omega_{ref} = -m \pm \sqrt{2(2+\sigma)}, \tag{3.24}$$

which is overplotted by a dashed curve;

(iii) $\sin^2\theta(\eta R) = 0$, which can be recast as

$$\begin{cases} \Omega_p/\Omega_{ref} = (2-m)\eta^\sigma & \text{if } \Omega_p/(2-m) > 0 \\ \Omega_p/\Omega_{ref} = -(2+m)\eta^\sigma & \text{if } \Omega_p/(2+m) < 0, \end{cases} \tag{3.25}$$

and are shown by solid lines;

(iv) $\sin^2\theta(\eta R) = 1$, when the turning surface hits the shell's inner core at colatitude $\theta = \pi/2$, that is when

$$\Omega_p/\Omega_{ref} = \eta^\sigma(-m \pm 2\sqrt{1+\sigma/2}), \tag{3.26}$$

an expression that is shown by dash-dotted curves.

DT modes with $|m| \leqslant 2$ are located between the turning surface and the shell's surface for $\sigma > 0$ (since the background velocity increases with radius), and between the shell's inner core and the turning surface for $\sigma < 0$. A more complex situation arises when $|m| > 2$, where the equation $|\tilde{\Omega}_p(\eta R)| = 2\Omega(\eta R)$ may admit two solutions for a given Ω_p, as can be seen from (3.25). In figure 3(*d*) ($m = 4$), DT modes located between the two solid lines propagate between the shell's inner core and the turning surface, since as D modes they satisfy $|\tilde{\Omega}_p(\eta R)| < 2\Omega(\eta R)$. In contrast, the DT modes above the upper solid curve and those below the lower solid curve, propagate between the turning surface and the shell's surface. Interestingly, modes with $|m| > 2$ may exhibit two turning surfaces that are located between the shell's inner core and the shell's surface. This brings the possibility of waves naturally bouncing between two turning surfaces without interacting with the shell's boundaries. Such modes are depicted by grey areas in figure 3(*d*). Note, however, that this particular set of non-axisymmetric modes will necessarily feature a critical layer (corotation resonance)

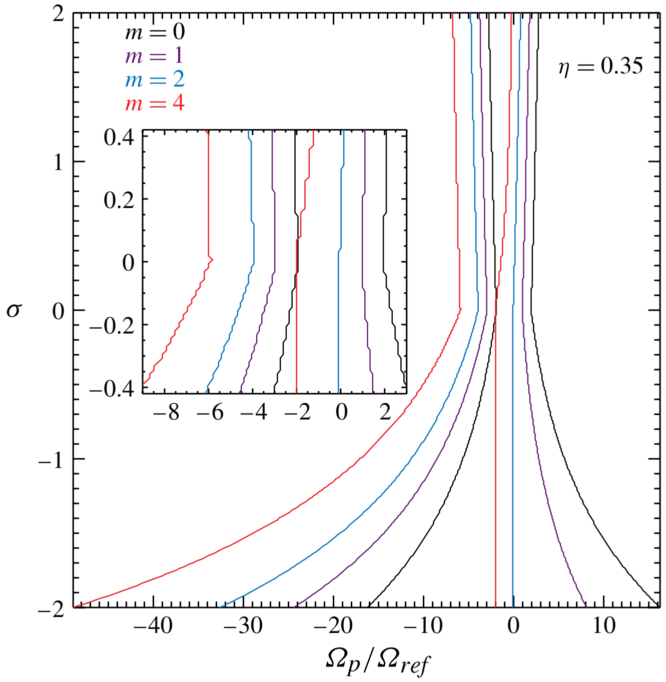

FIGURE 4. (Colour online) Minimum and maximum eigenfrequencies (x-axis) at which inertial modes of oscillation may exist with shellular rotation profile $\Omega(r)/\Omega_{ref} = (r/R)^{\sigma}$, for $m = 0$, 1, 2 and 4 ($\eta = 0.35$). Eigenfrequencies are in units of the angular frequency at the shell's surface. The inset plot focuses on previous range of eigenfrequencies for $\sigma \in [-0.4, 0.4]$.

between both turning surfaces, where $\tilde{\Omega}_p$ vanishes. The location of such critical layers is given by $r = R\,(-\Omega_p/m\Omega_{ref})^{1/\sigma}$. For $m > 0$, modes with $\sigma \leqslant 0$ have a critical layer if $-m\eta^{\sigma} \leqslant \Omega_p/\Omega_{ref} \leqslant -m$ and those with $\sigma \geqslant 0$ if $-m \leqslant \Omega_p/\Omega_{ref} \leqslant -m\eta^{\sigma}$. Modes that exhibit a critical layer within the shell are located between the two orange solid curves in figure 3. They will be further discussed in §§ 3.2.3 and 4.3.2.

The range of eigenfrequencies Ω_p for which inertial modes of oscillation may exist in a spherical shell with $\eta = 0.35$ is displayed in figure 4 for $m = 0$, 1, 2 and 4. Compared with solid-body rotation, inertial modes with shellular rotation may exist at much larger frequencies, especially if the rotation profile is a decreasing function of radius.

Finally, the location of turning surfaces, given by (3.21), is depicted in a meridional slice in figure 5 for $m = 0$ modes with σ ranging from −2 to 2, and increasing by 0.2. Results are shown for $\Omega_p/\Omega_{ref} = 1.5$, 2 and 2.5 in figure 5(*a–c*), respectively. For $\Omega_p = 2\Omega_{ref}$, turning surfaces exist for all values of σ except $\sigma = 0$ (corresponding to solid-body rotation; note however that turning surfaces exist in the limit $|\sigma| \to 0$). In all three figures, DT modes with $\sigma < 0$ exist between the shell's inner core and the turning surface (they may therefore exist without reflexions on the shell's surface). Similarly, DT modes with $\sigma > 0$ exist between the turning surface and the shell's surface, and may therefore exist without reflexions on the shell's inner core. This case will be illustrated in § 4.2.2, where we will show that DT modes may feature shear layers following attractors of characteristics in the absence of an inner core (the necessary reflexion being provided by the shell's surface and the turning surface).

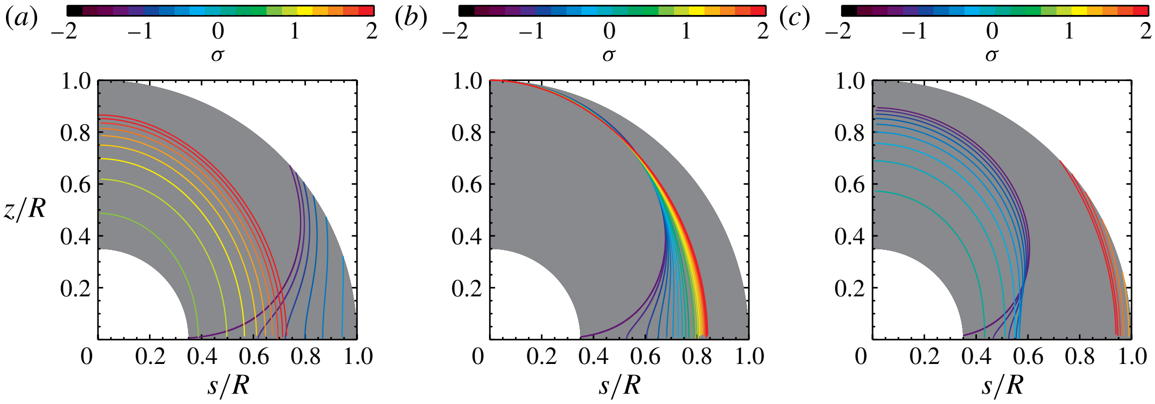

FIGURE 5. (Colour online) Location of turning surfaces for $m = 0$ modes with varying the power-law index of the shellular rotation profile, for $\Omega_p = 1.5\Omega_{ref}$ (*a*), $\Omega_p = 2\Omega_{ref}$ (*b*) and $\Omega_p = 2.5\Omega_{ref}$ (*c*).

3.2.2. *Critical latitudes*

Rays tangent to the shell's inner core define a critical latitude θ_i. They satisfy $\mathrm{d}z/\mathrm{d}s = -s/z$ with $\eta R = \sqrt{s^2 + z^2}$. Combining (3.18)–(3.20), rays intersect the shell's inner core at $s = s_c$, with

$$s_c = \eta R \left(1 - \frac{\tilde{\Omega}_p^2(\eta R)}{4\Omega^2(\eta R)}\right)^{1/2}. \tag{3.27}$$

A critical latitude θ_i at the shell's inner core therefore exists for modes with $|\tilde{\Omega}_p(\eta R)| \leqslant 2\Omega(\eta R)$ and verifies

$$\sin\theta_i = \frac{\tilde{\Omega}_p(\eta R)}{2\Omega(\eta R)}, \tag{3.28}$$

which is a straightforward generalization of the expression for solid-body rotation. For fixed values of η, m and Ω_p, and for $\sigma > 0$, $\sin\theta_i \to 1$ as σ increases. For $\sigma < 0$, $\sin\theta_i \to 0$ as $|\sigma|$ increases.

Similarly, it is easy to show that a critical latitude θ_o exists at the shell's surface for those modes that satisfy $|\tilde{\Omega}_p(R)| \leqslant 2\Omega(R)$, with the expression given by

$$\sin\theta_o = \frac{\tilde{\Omega}_p(R)}{2\Omega(R)}, \tag{3.29}$$

independently of σ. The outer critical latitude has therefore the same value as in the solid-body rotation case.

Critical latitudes also exist with cylindrical rotation. For our cylindrical rotation profile, an inner critical latitude exists if $\xi(s)$, given by (3.9), is positive for $s \in [0, \eta R]$. Similarly, an outer critical latitude exists if $\xi \geqslant 0\, \forall s \in [0, R]$ (that is, for D modes only). There is, however, no simple expressions for the inner and outer critical latitudes with our cylindrical rotation profile.

3.2.3. *Dispersion relation, phase and group velocities*

In the short-wavelength approximation, the wave dispersion relation given by (A 7) becomes

$$\tilde{\Omega}_p^2(r) = 4\Omega^2(r)\frac{k_z^2}{\|\boldsymbol{k}\|^2} \times \left[1 + \frac{\sigma}{2}\frac{s^2}{r^2}\left(1 - \frac{zk_s}{sk_z}\right)\right] \tag{3.30}$$

for our shellular rotation profile, with $\|\boldsymbol{k}\| = \sqrt{k_s^2 + k_z^2}$. We see that the bracket term in the above equation can be negative: inertial waves may become unstable for shellular rotation. As discussed in the Appendix, this is a form of the Goldreich–Schubert–Fricke instability in the limit of an inviscid incompressible fluid (Goldreich & Schubert 1967; Fricke 1968). In that limit, (A 7) indicates that the instability can in principle occur whenever $\partial\Omega/\partial z \neq 0$ (or, equivalently, when $A_z \neq 0$). Assuming that inertial waves remain stable against our shellular rotation profile, we introduce

$$\mathscr{B} = \left[1 + \frac{\sigma}{2}\frac{s^2}{r^2}\left(1 - \frac{zk_s}{sk_z}\right)\right]^{1/2}, \tag{3.31}$$

and (3.30) reduces to $\tilde{\Omega}_p(r) = \pm 2\mathscr{B}\Omega(r)|k_z|/\|\boldsymbol{k}\|$. Note that $\mathscr{B} = 1$ for solid-body rotation. In the rotating frame, the phase velocity reads

$$\boldsymbol{v}_p = \pm 2\mathscr{B}\Omega(r)\frac{k_z\boldsymbol{k}}{\|\boldsymbol{k}\|^3}, \tag{3.32}$$

and the group velocity is given by

$$\boldsymbol{v}_g = \pm 2\Omega(r)\frac{k_s}{\|\boldsymbol{k}\|^3}(-k_z\boldsymbol{e}_s + k_s\boldsymbol{e}_z) \times \left[\mathscr{B} + \frac{\sigma}{4}\frac{sz}{r^2}\frac{\|\boldsymbol{k}\|^2}{k_sk_z}\mathscr{B}^{-1}\right]. \tag{3.33}$$

We now examine the case where a critical layer forms inside the shell, where $\tilde{\Omega}_p(r) = 0$. Inspection of (3.30) shows that there are formally three cases where $\tilde{\Omega}_p(r)$ may vanish:

(i) $k_s \to \infty$ at finite k_z, in which case $\boldsymbol{v}_p = 0$ and $\boldsymbol{v}_g = 0$ at corotation, which is similar to the behaviour obtained with cylindrical rotation (inertial waves do not cross corotation in such a case);

(ii) $k_z \to 0$ at finite k_s, in which case $\boldsymbol{v}_p = \boldsymbol{0}$, $\boldsymbol{v}_g \cdot \boldsymbol{e}_s = 0$ and $|\boldsymbol{v}_g \cdot \boldsymbol{e}_z| \to \infty$; surprisingly, this case indicates that inertial waves may propagate across a critical layer (with locally vertical paths of characteristics);

(iii) $\mathscr{B} \to 0$, which implies that $\boldsymbol{v}_p = \boldsymbol{0}$, $|\boldsymbol{v}_g \cdot \boldsymbol{e}_s| \to \infty$ and $|\boldsymbol{v}_g \cdot \boldsymbol{e}_z| \to \infty$; this case also formally shows that inertial waves may cross a critical layer and the condition $\mathscr{B} = 0$ can be recast as

$$\left.\frac{\mathrm{d}z}{\mathrm{d}s}\right|_{crit} \equiv -\left.\frac{k_s}{k_z}\right|_{\tilde{\Omega}_p(r)=0} = -\frac{s}{z}\left(1 + \frac{2}{\sigma}\frac{r^2}{s^2}\right), \tag{3.34}$$

which shows that, if $\mathscr{B} = 0$ at corotation, then paths of characteristics have a finite slope upon crossing the critical layer.

The propagation properties of inertial waves in viscous fluids with a critical layer will be examined in § 4.3.2 with the results of numerical calculations. We stress again that the fact that the phase speed vanishes at corotation indicates that nonlinear effects should occur near this location, which are not captured by the present linear analysis, nor by the numerical solutions of § 4.3.2.

4. Viscous problem: shear layers, behaviour at corotation resonances, comparison with inviscid analysis

We have described in § 3 the propagation properties of inertial waves in a spherical shell with (specific) cylindrical and shellular rotation profiles. We have shown that in both cases, modes of oscillations satisfy in the inviscid limit a second-order PDE of mixed type. Two families of eigenmodes can therefore be distinguished: D modes, which may propagate throughout the entire shell (the hyperbolic domain covers the whole shell), and DT modes, which feature turning surfaces inside the shell (the hyperbolic domain covers part of the shell). Compared with solid-body rotation, the presence of turning surfaces with differential rotation tends to broaden the range of frequencies at which inertial waves may propagate in a spherical shell.

An interesting result from our analysis in § 3 is that paths of characteristics depend on the azimuthal wavenumber m (through the space-varying Doppler-shifted frequency). In contrast to solid-body rotation, the structure of non-axisymmetric modes cannot be simply inferred from that of axisymmetric modes. However, as far as their dynamical properties are concerned, $m \neq 0$ and $m = 0$ modes only differ by the possible presence of corotation resonances for $m \neq 0$. We will therefore examine the general properties of viscous modes of oscillations for $m = 0$ modes only. This is done in § 4.2, where we take the same rotation profiles as in § 3. We show that the structure of shear layers in the viscous problem closely follows the paths of characteristics derived in the inviscid problem. We particularly focus on singular modes featuring a shear layer that converges towards a short-period attractor. Some of these singular modes form through reflexions at turning surfaces and may therefore exist in the absence of an inner core. A qualitative analysis of the occurrence of modes with quasi-periodic orbits of characteristics is also done at § 4.2.3. We finally examine in § 4.3 a few $m \neq 0$ viscous eigenmodes with corotation resonances.

4.1. *Numerical method*

Our numerical simulations solve the linearized differential system (2.4) and related stress-free boundary conditions, using a spectral approach. Fields are decomposed into spherical harmonics (see, e.g. Rieutord 1987), with the perturbed velocity expanded as

$$\boldsymbol{u}(r,\theta,\varphi) = \sum_{\ell=0}^{\infty} \sum_{m=-\ell}^{\ell} u_m^{\ell}(r)\boldsymbol{R}_{\ell}^{m} + v_m^{\ell}(r)\boldsymbol{S}_{\ell}^{m} + w_m^{\ell}(r)\boldsymbol{T}_{\ell}^{m}, \tag{4.1}$$

with $\boldsymbol{R}_{\ell}^{m} = Y_{\ell}^{m}(\theta,\varphi)\boldsymbol{e}_r$, $\boldsymbol{S}_{\ell}^{m} = \nabla Y_{\ell}^{m}$, and $\boldsymbol{T}_{\ell}^{m} = \nabla \times \boldsymbol{R}_{\ell}^{m}$ and where Y_{ℓ}^{m} denote the usual spherical harmonics normalized on the sphere of unit radius. In the radial direction, equations are discretized on Gauss–Lobatto collocation nodes associated with Chebyshev polynomials. Equations are truncated at order L for the spherical harmonics basis, and at order N_r for the Chebyshev basis. The incomplete Arnoldi–Chebyshev algorithm is used to compute pairs of complex eigenvalues (Ω_p) and eigenvectors, given an initial guess value for Ω_p (for details on this numerical method, see Valdettaro *et al.* (2007)). Values of N_r and L are mode dependent, and will be specified below. Unless otherwise stated, all modes are calculated assuming symmetry with respect to the equatorial plane.

4.1.1. *Shellular rotation*

For the shellular rotation profile that we consider, $\Omega(r)/\Omega_{ref} = (r/R)^{\sigma}$, projecting (2.4) onto $\boldsymbol{R}_\ell^m$ and $\boldsymbol{T}_\ell^m$ gives the following two equations:

$$\left.\begin{aligned}
&E\Delta_\ell w_m^\ell + \left[\frac{2\mathrm{i}m\Omega(r)}{\ell(\ell+1)} - \mathrm{i}\tilde{\Omega}_p(r)\right] w_m^\ell \\
&\qquad = -2\Omega(r)\left[A(\ell,m)r^{\ell-1}\frac{\mathrm{d}(r^{2-\ell}u_m^{\ell-1})}{\mathrm{d}r} + A(\ell+1,m)r^{-\ell-2}\frac{\mathrm{d}(r^{\ell+3}u_m^{\ell+1})}{\mathrm{d}r}\right] \\
&\qquad\quad + r\frac{\mathrm{d}\Omega}{\mathrm{d}r}[-(\ell+1)A(\ell+1,m)u_m^{\ell+1} + \ell A(\ell,m)u_m^{\ell-1}], \\
&E\Delta_\ell\Delta_\ell(ru_m^\ell) + \left[\frac{2\mathrm{i}m\Omega(r)}{\ell(\ell+1)} - \mathrm{i}\tilde{\Omega}_p(r)\right]\Delta_\ell(ru_m^\ell) \\
&\quad = 2\Omega(r)\left[B(\ell,m)r^{\ell-1}\frac{\mathrm{d}(r^{1-\ell}w_m^{\ell-1})}{\mathrm{d}r} + B(\ell+1,m)r^{-\ell-2}\frac{\mathrm{d}(r^{\ell+2}w_m^{\ell+1})}{\mathrm{d}r}\right] \\
&\qquad\quad - \mathrm{i}mr\frac{\mathrm{d}^2\Omega}{\mathrm{d}r^2}u_m^\ell - 2\mathrm{i}m\frac{\mathrm{d}\Omega}{\mathrm{d}r}(u_m^\ell + v_m^\ell) \\
&\qquad\quad + 2\frac{\mathrm{d}\Omega}{\mathrm{d}r}\left[B(\ell,m)w_m^{\ell-1} + B(\ell+1,m)w_m^{\ell+1}\right],
\end{aligned}\right\} \qquad (4.2)$$

where

$$\left.\begin{aligned}
&A(\ell,m) = \frac{1}{\ell^2}\left(\frac{\ell^2-m^2}{4\ell^2-1}\right)^{1/2}, \quad B(\ell,m) = \ell^2(\ell^2-1)A(\ell,m), \\
&\Delta_\ell = \frac{1}{r}\frac{\mathrm{d}^2}{\mathrm{d}r^2}r - \frac{\ell(\ell+1)}{r^2}.
\end{aligned}\right\} \qquad (4.3)$$

In (4.2), since the fluid is incompressible,

$$v_m^\ell = \frac{1}{\ell(\ell+1)r}\frac{\mathrm{d}(r^2u_m^\ell)}{\mathrm{d}r}. \qquad (4.4)$$

For solid-body rotation, $\Omega(r) = \Omega_{ref}$ and (4.2) reduce to equations (2.2) of Rieutord & Valdettaro (1997) (note that these authors defined the Ekman number as $E = \nu/2R^2\Omega_{ref}$, while our definition does not include the factor 2). After projection on the spherical harmonics, stress-free boundary conditions read

$$u_m^\ell = \frac{\mathrm{d}^2(ru_m^\ell)}{\mathrm{d}r^2} = \frac{\mathrm{d}}{\mathrm{d}r}\left(\frac{w_m^\ell}{r}\right) = 0 \qquad (4.5)$$

for the radial functions taken at $r = \eta R$ or $r = R$. Equation (4.2)–(4.5) can be recast as an eigenvalue problem featuring a tridiagonal block matrix, like for solid-body rotation. More details into the numerical scheme can be found in Rieutord & Valdettaro (1997).

4.1.2. *Cylindrical rotation*

For our cylindrical rotation profile, $\Omega(s)/\Omega_{ref} = 1 + \varepsilon\,(s/R)^2$, projecting (2.4) onto $\boldsymbol{R}_\ell^m$ and $\boldsymbol{T}_\ell^m$ gives, after some tedious algebra, two long differential equations, which we do not write for the sake of legibility. The second-order differential equation satisfied by w_m^ℓ can be cast as a linear combination of $u_m^{\ell\pm3}$, $\mathrm{d}u_m^{\ell\pm3}/\mathrm{d}r$, $u_m^{\ell\pm1}$, $\mathrm{d}u_m^{\ell\pm1}/\mathrm{d}r$ and $w_m^{\ell\pm2}$ (the term in front of $w_m^{\ell\pm2}$ vanishes for $m = 0$). The fourth-order differential equation for u_m^ℓ exhibits terms in $w_m^{\ell\pm3}$, $\mathrm{d}w_m^{\ell\pm3}/\mathrm{d}r$, $w_m^{\ell\pm1}$, $\mathrm{d}w_m^{\ell\pm1}/\mathrm{d}r$, $u_m^{\ell\pm2}$, $\mathrm{d}u_m^{\ell\pm2}/\mathrm{d}r$ and $\mathrm{d}^2u_m^{\ell\pm2}/\mathrm{d}r^2$ (the terms in front of $u_m^{\ell\pm2}$, $\mathrm{d}u_m^{\ell\pm2}/\mathrm{d}r$ and $\mathrm{d}^2u_m^{\ell\pm2}/\mathrm{d}r^2$ vanish for $m = 0$). Along with stress-free boundary conditions, these equations take the form of an eigenvalue problem where the matrix to invert has blocks composed of (up to) seven bands. The coupling between harmonics of ranks ℓ, $\ell \pm 1$, $\ell \pm 2$ and $\ell \pm 3$ arises from our particular cylindrical profile.

4.2. *Axisymmetric eigenmodes: a few illustrative cases*

We present in this section the results of simulations for axisymmetric eigenmodes with moderate viscosity, the default Ekman number being $E = 10^{-8}$. Unless otherwise stated, our simulations are carried out with a shell's aspect ratio $\eta = 0.35$. The propagation properties of shear layers for weakly damped eigenmodes is compared with the analytic description based on paths of characteristics, detailed in § 3. Cylindrical and shellular rotation profiles are examined in §§ 4.2.1 and 4.2.2, respectively. A qualitative analysis of the occurrence of modes with quasi-periodic orbits of characteristics follows in § 4.2.3.

4.2.1. *Cylindrical rotation*

We describe in this paragraph three representative $m = 0$ eigenmodes obtained with our cylindrical rotation profile: a D mode (the hyperbolic domain covers the whole shell) and two DT modes (the hyperbolic domain covers a fraction of the shell). All three calculations have a spectral resolution of $N_r = 450 \times L = 800$.

Figure 6 displays the results for a D mode with eigenfrequency $\Omega_p \approx 0.91\Omega_{ref}$, obtained for $\varepsilon = -0.3$ (recall that for cylindrical rotation, Ω_{ref} denotes the shell's angular frequency at the rotation axis). Figure 6(*a*) depicts contours of the mode's kinetic energy in a meridional quarter-plane. Here, as in all other contour plots, the simulation parameters are summarized below the x-axis (spectral resolution $N_r \times L$, azimuthal wavenumber m, Ekman number E, shell's aspect ratio η, differential rotation rate ε or σ for cylindrical or shellular rotation profiles, respectively). Similarly, the complex eigenfrequency is indicated in the bottom-left corner of the shell: the absolute value of its real part is denoted by $|\omega|$ (in units of Ω_{ref}) and its imaginary part by τ (in units of Ω_{ref}^{-1}; negative values of τ correspond to damped modes). Results are shown only for positive values of z for reasons of symmetry exposed in § 3.1. The D mode illustrated in figure 6(*a*) essentially features a shear layer following a short-period wave attractor, which is overplotted by a thick white curve. The mode's kinetic energy is maximum near the rotation axis, as in the case of solid-body rotation (Rieutord & Valdettaro 1997). Note also the presence of another shear layer tangent to the shell's inner core. As already highlighted in § 3.1, rays in a meridional plane are curved by differential rotation. This is also illustrated in figure 6(*b*), which displays the paths of characteristics obtained by solving (3.8), given a particular initial location (here at $s = 0$ and $z = 0.75R$). The patterns of the viscous shear layer (figure 6*a*) and of the paths of characteristics under the short-wavelength approximation (figure 6*b*), are in excellent agreement. Paths of characteristics focus towards the aforementioned wave attractor, depicted by a red curve in figure 6(*b*). Upon varying initial conditions, we have checked that this is the only attractor in the shell for this particular eigenfrequency. Figure 6(*c,d*) shows the good convergence in spectral resolution for this mode.

We present in figure 7 the results for an $m = 0$ DT mode with $\Omega_p \approx 1.33\Omega_{ref}$ and $\varepsilon = -0.4$. Figure 7(*a*) shows a meridional cut of the kinetic energy for this mode, which exhibits again a shear layer following an attractor of characteristics. The mode's pattern features reflexions on the inner and outer edges of the shell, as well as on a turning surface located at $s \sim 0.75R$. The radius at which the shear layer bounces off is in good agreement with the (numerical) solution to $\xi(s) = 0$, shown by a dashed line.

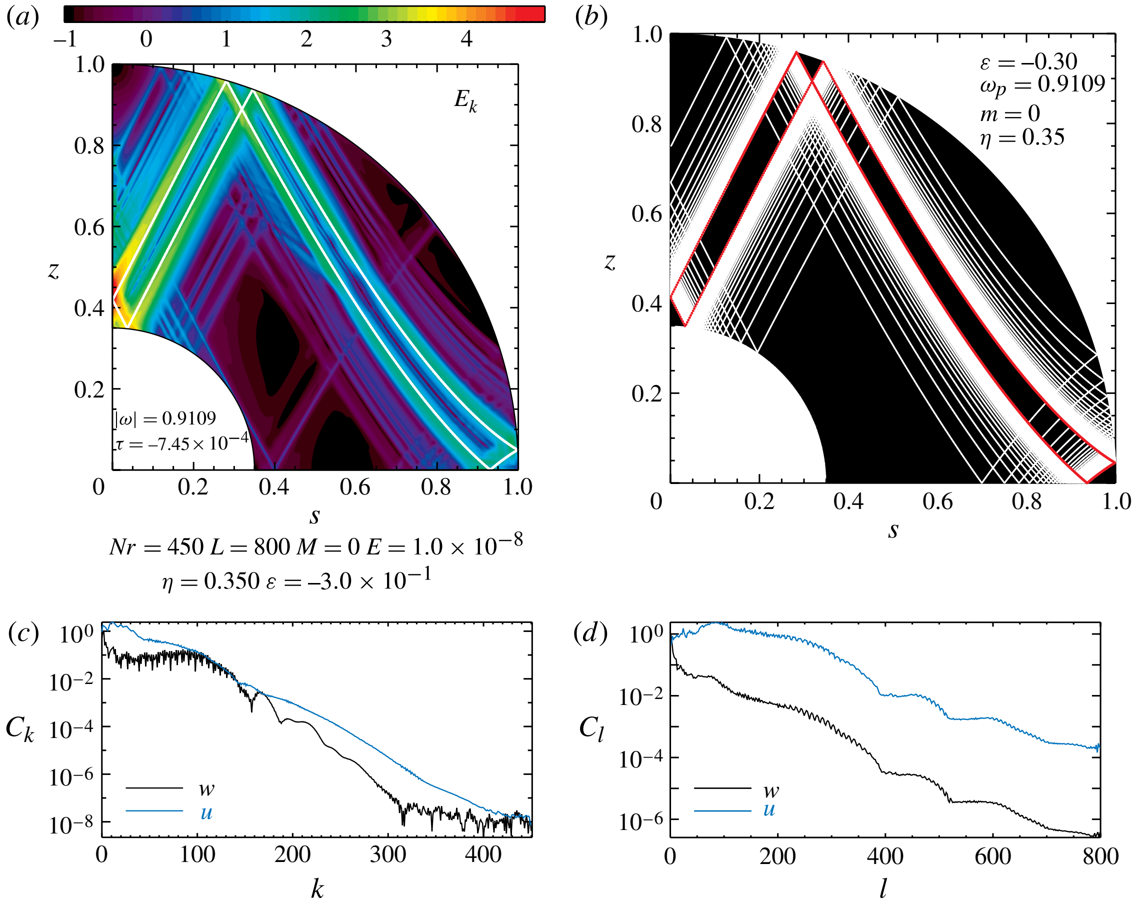

FIGURE 6. (Colour online) (*a*) Meridional cut of the kinetic energy for a D mode with eigenfrequency $\Omega_p \approx 0.91\Omega_{ref}$, obtained with $E = 10^{-8}$ and cylindrical rotation profile $\Omega(s)/\Omega_{ref} = 1–0.3\,(s/R)^2$. An attractor of characteristics is overplotted by a solid white curve. (*b*) A few paths of characteristics are shown to converge towards the aforementioned attractor, which is displayed here by a red curve. Bottom: spectral content of the radial (u) and orthoradial (w) components of the velocity field for this mode. Chebyshev and spherical harmonic coefficients are shown in (*c,d*), respectively.

A few paths of characteristics, obtained again by solving (3.8), are shown by white curves in figure 7(*b*), which rapidly converge toward the above attractor (in red in this figure). We point out that there exists another attractor for this eigenfrequency and this differential rotation rate, which is overplotted by a blue curve.

An interesting DT mode is finally illustrated in figure 8 for $\Omega_p \approx 1.10\Omega_{ref}$ and $\varepsilon = -0.4$, where a shear layer follows an attractor for an arbitrarily small inner core. In this particular calculation, $\eta = 0.05$. This example highlights that, in contrast to solid-body rotation, attractors may be formed by reflexions on one of the shell's edges (the surface in this case) and a turning surface. This property is also shared by gravito-inertial modes in stably stratified rotating fluids (Friedlander 1982; Dintrans *et al.* 1999). The mode shown in figure 8 indicates that, with cylindrical rotation, wave attractors may exist independently of a putative inner core inside the shell. We show below that the same is true with shellular rotation.

4.2.2. *Shellular rotation*

We describe in this paragraph a few axisymmetric ($m = 0$) eigenmodes obtained with our shellular rotation profile, $\Omega(r)/\Omega_{ref} = (r/R)^{\sigma}$ (here, Ω_{ref} denotes the angular

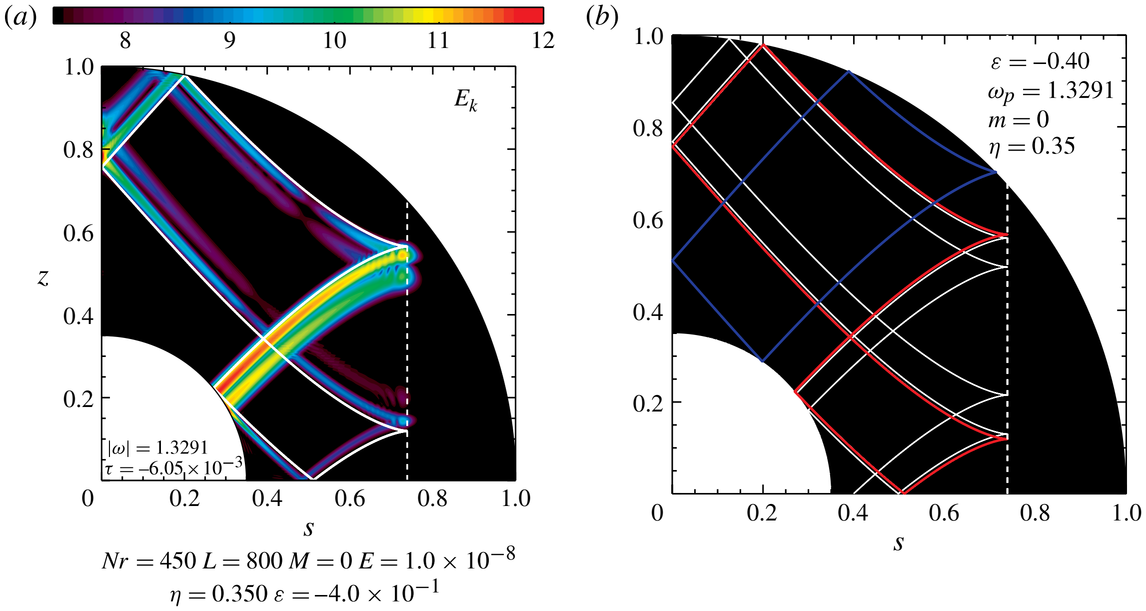

FIGURE 7. (Colour online) (*a*) Meridional slice of the kinetic energy for a DT mode with $\Omega_p \approx 1.33\Omega_{ref}$, $E = 10^{-8}$ and $\varepsilon = -0.4$. The shear layer follows a wave attractor (solid curve). The dashed line shows the location of the turning surface inferred from (3.9). (*b*) A few paths of characteristics are depicted by white curves, which converge toward the aforementioned wave attractor (red curve). A second wave attractor is shown in blue.

frequency at the shell's surface). An overview of the impact of shellular rotation is illustrated in figure 9 for a singular mode with eigenfrequency $\Omega_p \approx 1.11\Omega_{ref}$ for solid-body rotation. Contours of the kinetic energy in a meridional quarter-plane are shown for σ equal to 0 (figure 9*a*), -0.5 (figure 9*b*) and -1.3 (figure 9*c*). Calculations were carried out as a sequence, the eigenfrequency of the least-damped mode obtained with differential rotation rate σ being used as the guess frequency for the next run with differential rotation rate $\sigma - \mathrm{d}\sigma$. In this series of runs, $\mathrm{d}\sigma = 0.01$, $E = 10^{-7}$, and the spectral resolution is $N_r = 250 \times L = 600$. The contour panels in figure 9 show how the shape of the shear layer, and thus that of the wave attractor it focuses on (white curve), is progressively deformed by shellular rotation. Note the presence of a turning surface for $\sigma = -1.3$ (dashed curve). Not surprisingly, the mode's eigenfrequency increases with increasing the steepness σ of the rotation profile. We also observe that the mode's damping rate decreases in absolute value for steeper rotation profiles. Some insight into the asymptotic behaviour of this mode at small Ekman numbers is given by figure 9(*d*). The damping rate of the mode with $\sigma = -1$ is displayed for Ekman numbers varying from 10^{-6} down to $\sim 2 \times 10^{-8}$. Runs were also performed as a series, the eigenfrequency of the least-damped mode obtained at Ekman number E being used as the guess frequency for the run with Ekman number $E - \mathrm{d}E$ (the spectral resolution is progressively increased with decreasing E). The dashed line shows that the damping rate of this particular mode scales proportional to $E^{1/3}$, a scaling that is reminiscent of the solid-body rotation case (Rieutord & Valdettaro 1997).

The aforementioned $E^{1/3}$ scaling of the mode's damping rate is not the only possible scaling for shellular rotation in the limit of vanishing viscosities. This is illustrated in figure 10(*a*) for a particular DT mode having a turning surface that encompasses the inner core, and for which the damping rate is found to be roughly independent of E. This property is reminiscent of quasi-modes associated with critical layers (see, e.g. Le

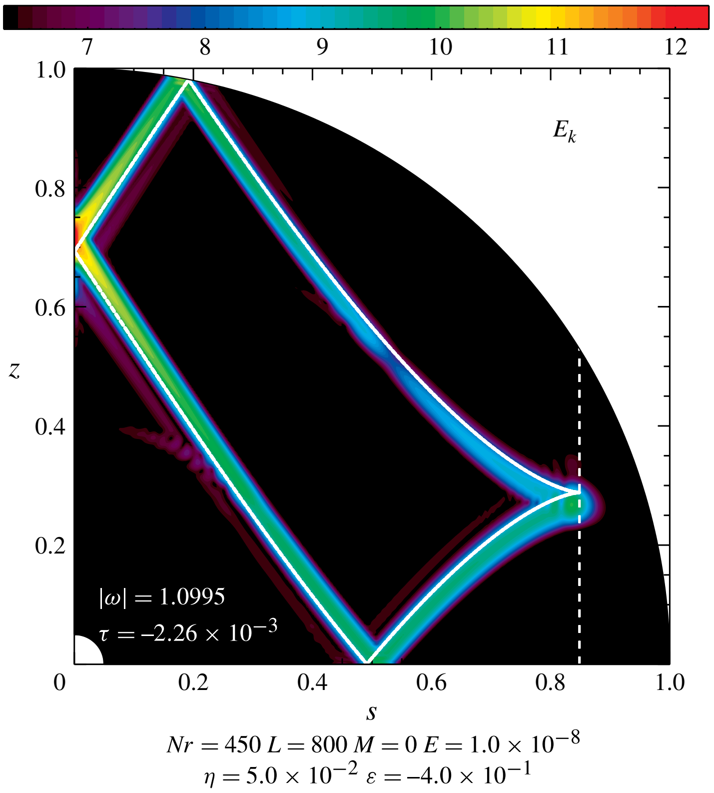

FIGURE 8. (Colour online) Meridional slice of the kinetic energy for a DT mode with $\varOmega_p \approx 1.10\varOmega_{ref}$, $E = 10^{-8}$, $\eta = 0.05$ and $\varepsilon = -0.4$. The turning surface is shown by a dashed line. For an arbitrarily small inner core, the shear layer follows an attractor of characteristics, shown by the solid curve.

Dizès 2004). However, the physical mechanism leading to such a damping rate must be different because the DT mode we consider is axisymmetric, so that no corotation singularity exists. Contours of kinetic energy for this new type of quasi-modes are shown in figure 10(*b*), where we see that the mode is dominated by a shear layer following a wave attractor tangent to the turning surface at the location of the rotation axis (note that, since the turning surface encompasses the inner core at $r = 0.35R$, this mode exists for arbitrarily small inner cores, akin to the mode shown in figure 8 for cylindrical calculation). We have carried out additional calculations with a slightly different eigenfrequency at given Ekman number, such that the wave attractor no longer hits the tangent critical point at the rotation axis. We found that the damping rate is no longer independent of E for the same range of Ekman numbers as in figure 10(*a*). It suggests that the tangent critical point plays a prominent role in getting a damping rate independent of E. Such scaling demands a very thin detached shear layer, namely $\mathscr{O}(E^{1/2})$ wide. This is indeed confirmed by the velocity profiles depicted in figure 10(*c*) at three Ekman numbers (shown by red squares in figure 10*a*). Of course, this numerical result does not prove that this vigorously damped mode survives at vanishingly small viscosities, and that it is thus a new type of quasi-mode. Still, it calls for a detailed analysis of this new type of detached shear layers, which are as thin as Ekman boundary layers.

We now present the results of simulations for two D and DT eigenmodes at smaller Ekman number ($E = 10^{-8}$) and higher spectral resolution ($N_r = 500$ or $N_r = 580$, $L = 1000$). Results are shown in figure 11. A D mode with $\varOmega_p \approx 1.11\varOmega_{ref}$

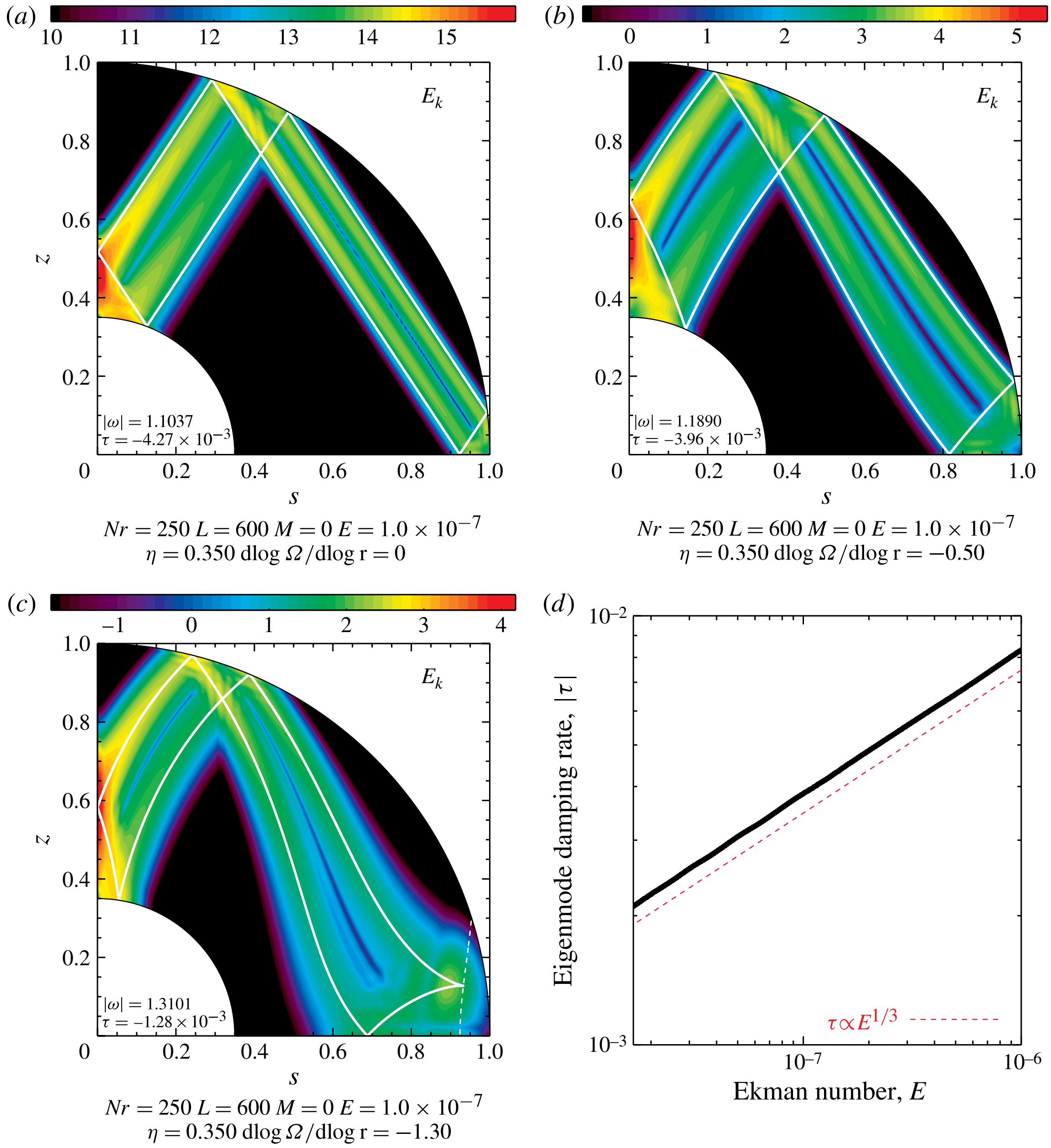

FIGURE 9. (Colour online) Meridional cuts of kinetic energy for a given eigenmode with $E = 10^{-7}$ and $\sigma = 0$ (*a*), -0.5 (*b*) and -1.3 (*c*). The shear layer for this mode follows an attractor overplotted by a solid curve in each of these panels. The dashed curve in (*c*) displays the location of a turning surface, given by (3.21). (*d*) Plot showing that the damping rate of previous mode with $\sigma = -1$ scales as $E^{1/3}$, with E the Ekman number.

and $\Omega \propto r^{-1}$ is shown in figure 11(*a*). A shear layer is clearly visible that follows an attractor of characteristics, calculated through (3.18) and overplotted by a white curve. We note again the excellent agreement between the overall pattern of the viscous shear layer and the paths of characteristics. Owing to its finite width, the shear layer also excites the critical latitude singularity, on both the inner and outer edges of the shell. The location of the inner and outer critical latitudes, given by (3.28) and (3.29), is depicted by red ticks, and it is clear that the shear layer is tangent to the inner and outer edges of the shell at these latitudes. Lastly, figure 11(*b*) shows a DT mode

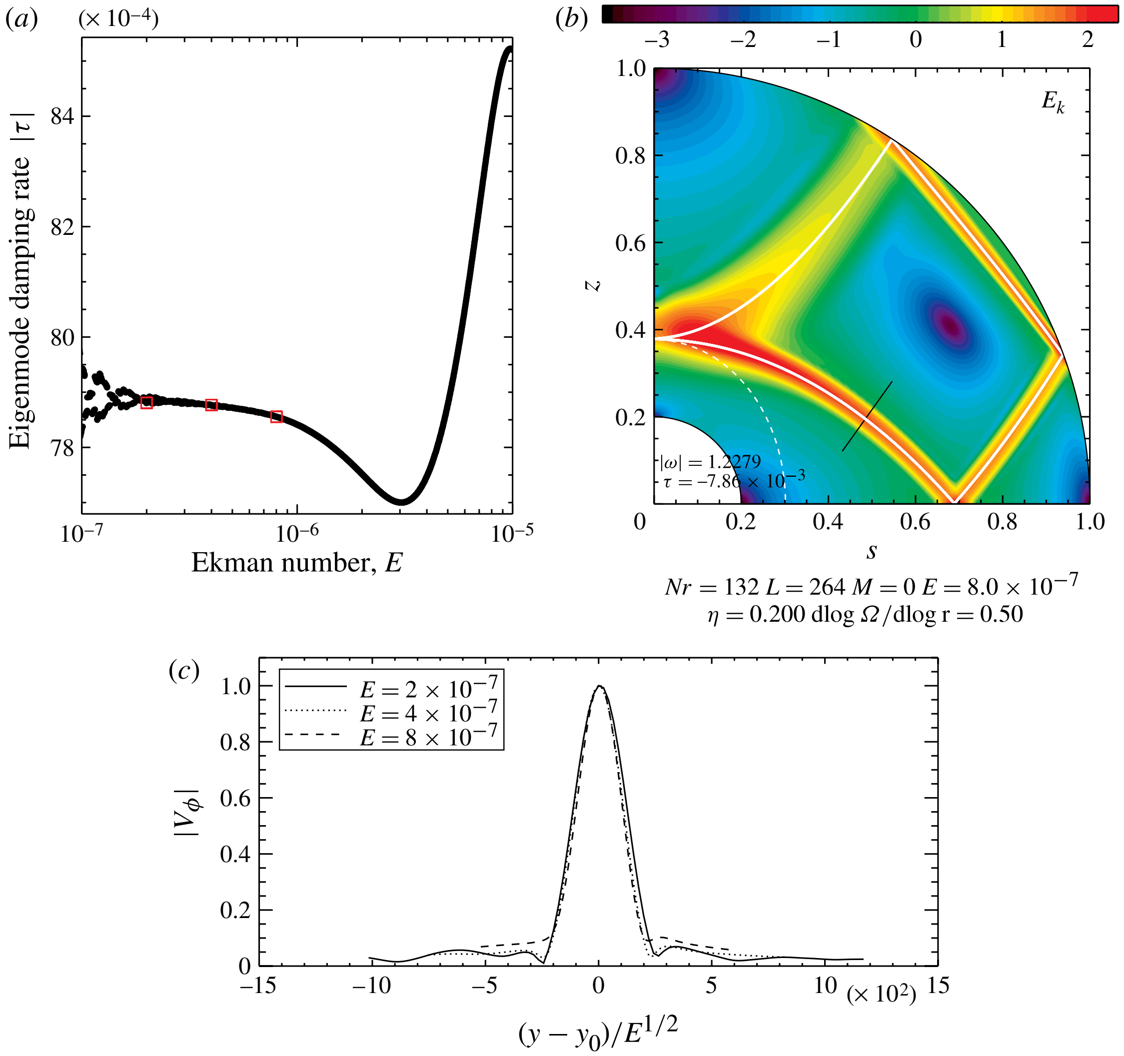

FIGURE 10. (Colour online) (*a*) Evolution of the damping rate ($|\tau|$) with decreasing Ekman number for a DT eigenmode with shellular rotation, $\Omega(r) \propto r^{0.5}$, $\eta = 0.2$, which features a detached shear layer tangent to a turning surface at the location of the rotation axis. (*b*) Contours of kinetic energy for the mode depicted by the rightmost open square in (*a*) ($E \approx 8.0 \times 10^{-7}$). The thick white curve shows the attractor of characteristics followed by the shear layer, and the dashed curve the location of a turning surface that encompasses the inner core. (*c*) Cut of the perturbed velocity across the shear layer (at the location depicted by a black line in *b*) for the three modes displayed with open square symbols in (*a*).

with $\Omega_p \approx 1.90\Omega_{ref}$ and $\Omega \propto r^{-0.5}$. In this case again, the mode's pattern suggests that part of the shear layer approximately follows a wave attractor, shown by a white curve, and that part of it is tangent to both the inner and outer edges of the shell at the critical latitudes.

4.2.3. *Quasi-periodic orbits of characteristics*

The results presented in the previous paragraphs all feature modes that are associated with short-period attractors. These modes are all singular at vanishing viscosity. One may however wonder about the existence of regular modes, which exist in the inviscid case, or at least modes that display shear layers only at unphysically small viscosities. Such modes are necessarily associated with weak attractors or

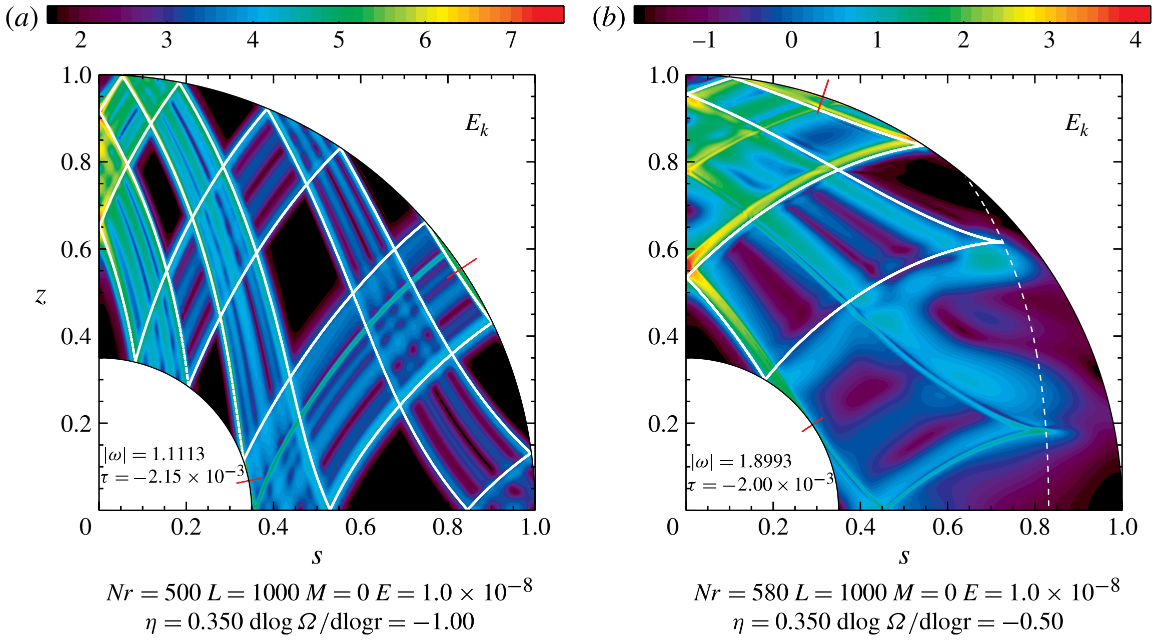

FIGURE 11. (Colour online) Kinetic energy of two axisymmetric D and DT eigenmodes with shellular rotation, for $E = 10^{-8}$. (a) D mode with $\Omega_p \approx 1.11\Omega_{ref}$ and $\Omega(r) \propto r^{-1}$. (b) DT mode with $\Omega_p \approx 1.90\Omega_{ref}$ and $\Omega(r) \propto r^{-0.5}$. Red ticks show the values of the inner and outer critical latitudes given by (3.28) and (3.29): (a) $Nr = 500$ $L = 1000$ $M = 0$ $E = 1.0 \times 10^{-8}$ $\eta = 0.350$ dlog Ω/dlogr $= -1.00$; (b) $Nr = 580$ $L = 1000$ $M = 0$ $E = 1.0 \times 10^{-8}$ $\eta = 0.350$ dlog Ω/dlogr $= -0.50$.

with quasi-periodic orbits of characteristics. To assess the occurrence of such orbits of characteristics, we have evaluated the Lyapunov exponent of various pairs of characteristics. The Lyapunov exponent measures the rate of convergence of two close characteristics after multiple reflections on the inner and outer edges of the shell, and on turning surfaces when present. For solid-body rotation, the latitudes of two successive reflections on the inner or outer edges can be related analytically, and the Lyapunov exponent can therefore be determined semi-analytically (Rieutord *et al.* 2001). This is no longer the case with differential rotation: Lyapunov exponents must be evaluated numerically by integrating paths of characteristics given some initial conditions.

For the symmetry reasons underlined in § 3, paths of characteristics are calculated in a meridional quarter-plane with reflections on to the rotation axis ($s = 0$) and the equatorial axis ($z = 0$). Because turning surfaces may prevent reflections on either axis, we define the two following Lyapunov exponents associated with reflections on the equatorial axis (denoted by Λ_s) and on the rotation axis (Λ_z):

$$\Lambda_s = \lim_{N_s\to\infty} \frac{1}{N_s} \sum_{k=1}^{N_s} \ln \left| \frac{\mathrm{d}s_{k+1}}{\mathrm{d}s_k} \right| \quad \text{and} \quad \Lambda_z = \lim_{N_z\to\infty} \frac{1}{N_z} \sum_{k=1}^{N_z} \ln \left| \frac{\mathrm{d}z_{k+1}}{\mathrm{d}z_k} \right|, \tag{4.6}$$

where $\mathrm{d}s_k$ and $\mathrm{d}z_k$ are the separation between two characteristics after k reflections on the equatorial and rotation axes, respectively.

A negative Lyapunov exponent means that the two characteristics get progressively closer to each other, converging towards an attractor. The more negative this value, the faster the convergence (and the stronger the attractor). In contrast, small-amplitude

Lyapunov exponents may correspond to quasi-periodic orbits of characteristics. Because two attractors may co-exist in the shell at a given eigenfrequency, and for averaging purposes, we have considered five pairs of initial conditions and four regions of the shell located near the rotation or equatorial axes, and near the shell's surface or the inner core (that is, twenty pairs of characteristics). The most negative value amongst the (averaged) Lyapunov exponents obtained in the above four regions defines what we now refer to as the Lyapunov exponent, and which we denote by Λ. If two attractors co-exist in the shell, our method will thus retain that with the shortest period.

Lyapunov exponents obtained for $m = 0$ and a few rotation profiles are displayed in figure 12(a). The range of eigenfrequencies $[0.2\Omega_{ref}, 2\Omega_{ref}]$ is sampled with 1800 values (Ω_{ref} is the angular frequency at the shell's surface). The case with solid-body rotation and $\eta = 0.35$ is depicted by a red curve. It can be compared with the semi-analytic results of Rieutord *et al.* (2001), see the left panel of their figure 6 (where $\Omega_p/2\Omega_{ref}$ is displayed on the x-axis). This comparison shows that our numerical method reproduces qualitatively well the ranges of frequencies at which strong attractors and quasi-periodic orbits of characteristics exist. Quantitative differences inevitably exist, however, and are most significant for attractors with moderate Lyapunov exponents (that is, Λ in the range $[-0.5, -0.2]$), which our method tends to underestimate.

Results obtained with shellular rotation and $\sigma = 0.5$ are overplotted by a black curve in figure 12(a). For this rotation profile, inertial modes exist for eigenfrequencies $|\Omega_p| \lesssim 2.2\Omega_{ref}$ (see, e.g., figure 3) and the transition from D to DT modes occurs at $|\Omega_p| \approx 1.18\Omega_{ref}$ (see (3.25)). For $\Omega_p \leqslant 1.18\Omega_{ref}$ (D modes only), the shellular case features the same attractors as in the case with solid-body rotation. However, attractors are shifted toward lower frequencies with shellular rotation as the shell's interior rotates at a slower pace in this case. Lyapunov exponents also take very similar values since shellular rotation changes the overall shape of these attractors without altering their period. For $\Omega_p \geqslant 1.18\Omega_{ref}$, the shellular case displays many more attractors, which form through reflections on to turning surfaces that encompass the inner core. Finally, results obtained with the same shellular profile, but for the full sphere ($\eta = 0$) are also shown by the blue curve. The full sphere only supports DT modes in this case. For $\Omega_p \gtrsim 1.4\Omega_{ref}$, results are identical to those obtained with $\eta = 0.35$, as in both cases the turning surface occupies radii $r > 0.35R$. Differences for $\Omega_p \lesssim 1.4\Omega_{ref}$ are essentially through the strong attractor at $\Omega_p \sim 0.8\Omega_{ref}$, which is related to a turning surface located at $r < 0.35R$.

Although the above results have been obtained with a fixed profile of shellular rotation, the general conclusion that can be drawn is that, just like for solid-body rotation, a differentially rotating spherical shell may harbour both short-period attractors and quasi-periodic orbits of characteristics. Their occurrence depends on the rotation profile and the sphere's aspect ratio. An example of an $m = 0$ D mode with a weak attractor, obtained for $E = 10^{-8}$, $\sigma = 0.5$ and $\eta = 0.35$, is shown in figure 12(b), and it is clear that the kinetic energy for this mode is more homogeneously distributed than in the modes illustrated in previous figures.

While the calculation of Lyapunov coefficients unambiguously shows the existence of quasi-periodic orbits of characteristics, it is difficult to use it to prove or disprove the existence of regular modes for which Λ should strictly vanish (Dintrans *et al.* 1999; Rieutord *et al.* 2001). We have looked for regular modes with differential rotation, though. It was suggested by Rieutord *et al.* (2001) that toroidal modes, with Doppler-shifted eigenfrequencies of the

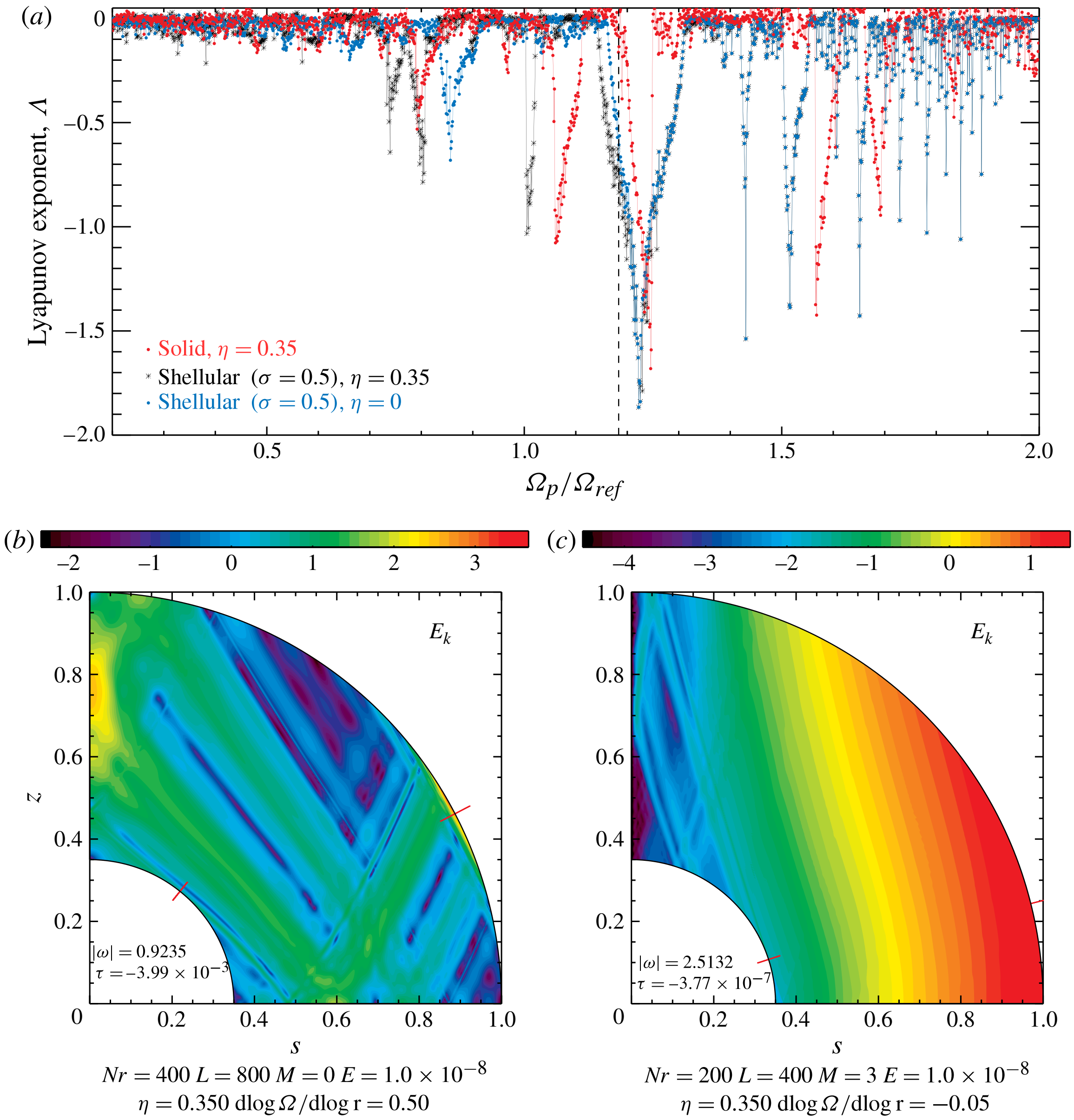

FIGURE 12. (Colour online) (*a*) Lyapunov exponent obtained for $\eta = 0.35$ and $m = 0$. Results with solid-body rotation (red curve) are compared with shellular rotation with $\sigma = 0.5$ (black curve). The vertical dashed line displays the eigenfrequency that separates D and DT modes for this rotation profile. Results with shellular rotation, $\sigma = 0.5$ and for a full sphere ($\eta = 0$) are overplotted in blue. (*b*) Meridional cut of the kinetic energy for an $m = 0$ D mode with $\sigma = 0.5$ and $\Omega_p \approx 0.92\Omega_{ref}$, which features a weak attractor (the Lyapunov coefficient is a few per cent). (*c*) Meridional cut of the kinetic energy for an $m = 3$ D mode with $\Omega_p \approx -2.5\Omega_{ref}$ and $\sigma = -0.05$. This mode has been obtained assuming asymmetry with respect to the equatorial plane.

form $\tilde{\Omega}_p = 2\Omega/(m + 1)$ (m is the azimuthal wavenumber) are the only regular modes in a rigidly rotating spherical shell. We have followed the toroidal mode with $m = 3$ by slowly increasing the differential rotation rate (for shellular rotation). As shown in figure 12(*c*), even for values of σ as small as a few per cent, the mode's regularity fades away. Although most of the kinetic energy remains contained in a smooth structure reminiscent to that of the toroidal mode, ray

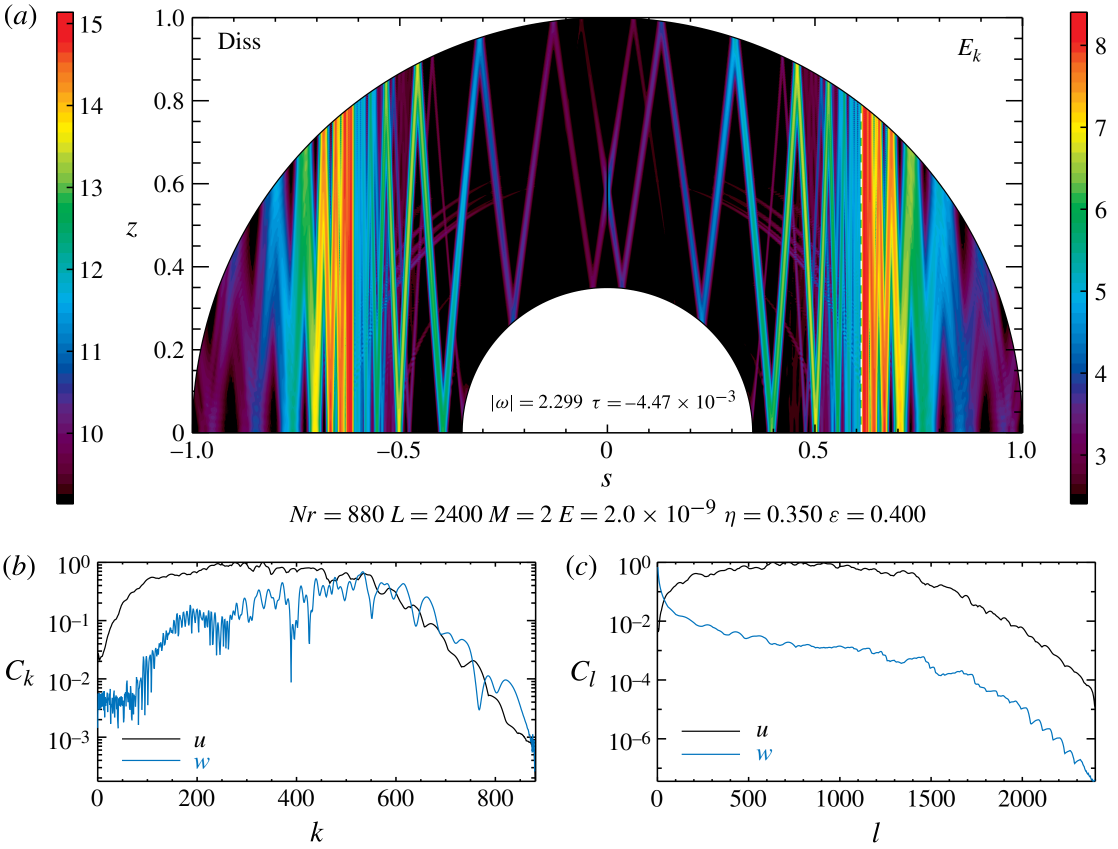

FIGURE 13. (Colour online) (*a*) Meridional cut of the viscous dissipation (left quadrant) and kinetic energy (right quadrant) for a D mode with $m = 2$, eigenfrequency $\Omega_p \approx -2.3\Omega_{ref}$, $E = 2 \times 10^{-9}$ and cylindrical rotation profile $\Omega(s) = 1 + 0.4s^2$. A corotation resonance (critical cylinder) is located at $s \approx 0.6$. (*b,c*) Spectral content of the radial (u) and orthoradial (w) components of the velocity field for this mode. Chebyshev and spherical harmonic coefficients are shown in (*b,c*), respectively.

structures develop, in particular from the inner critical latitude. Therefore, inertial oscillations with differential rotation seem to be all singular in the limit of vanishing Ekman numbers. A similar result was obtained for gravito-inertial modes (Friedlander 1982; Dintrans *et al.* 1999), which also satisfy a PDE of mixed type, analogous to (3.1).

4.3. *Non-axisymmetric eigenmodes: corotation resonances*

We briefly examine in this section the behaviour of viscous, non-axisymmetric inertial waves when their frequency in the rotating frame ($\tilde{\Omega}_p$) vanishes inside the shell. Such corotation resonances will be referred to as critical cylinders for cylindrical rotation, and as critical layers for shellular rotation. We present results of linear numerical calculations, which we compare with the analysis of § 3. Cylindrical and shellular rotation profiles are considered in §§ 4.3.1 and 4.3.2, respectively.

4.3.1. *Cylindrical rotation*

An example of an $m = 2$ D eigenmode with a critical cylinder is displayed in figure 13. This mode is obtained for $\varepsilon = 0.4$, $E = 2 \times 10^{-9}$ and the very high spectral resolution $N_r = 880 \times L = 2400$. Its eigenfrequency $\Omega_p \approx -2.3\Omega_{ref}$ (a negative Ω_p is required for an $m > 0$ eigenmode to have a corotation resonance within the shell).

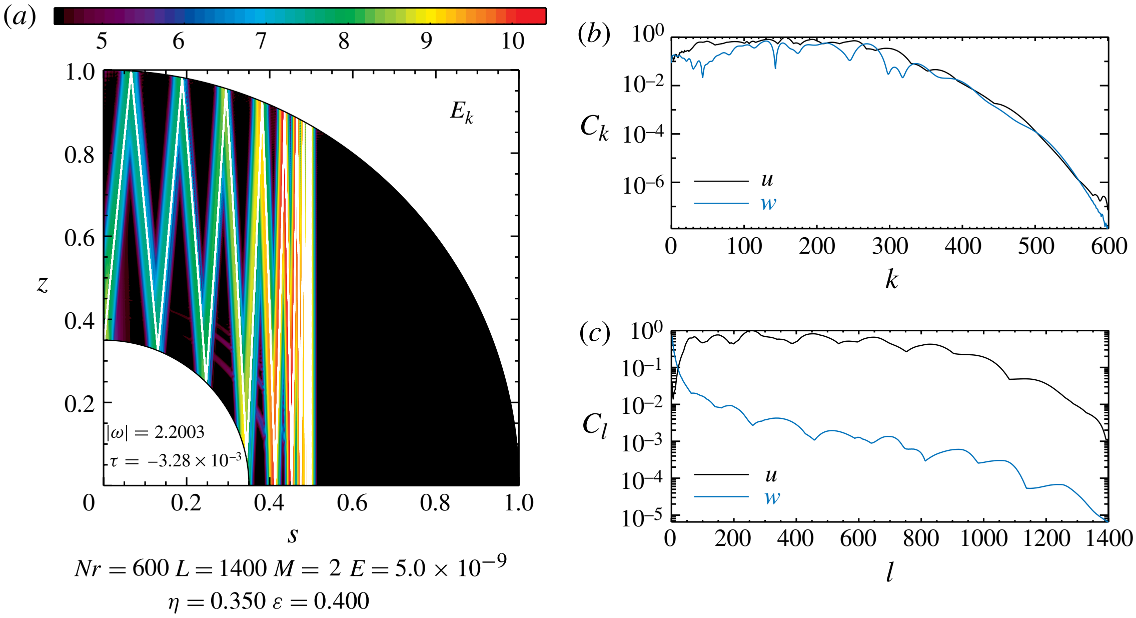

FIGURE 14. (Colour online) (*a*) Meridional cut of the kinetic energy for a D mode with $m = 2$, eigenfrequency $\Omega_p \approx -2.20\Omega_{ref}$, $E = 5 \times 10^{-9}$ and $\varepsilon = 0.4$. A corotation resonance is located at $s \approx 0.5$. A few paths of characteristics are overplotted by white curves. (*b,c*) Spectral content of the radial (u) and orthoradial (w) components of the velocity field for this mode. Chebyshev and spherical harmonic coefficients are shown in (*b,c*), respectively.

Figure 13(*a*) shows a meridional cut of the viscous dissipation (left quadrant) and of the kinetic energy (right quadrant) for this mode. The mode's spectral content is also displayed in figure 13(*b,c*) to highlight the good convergence in spectral resolution obtained for this mode. According to (3.13), a critical cylinder is located at $s_{crit} \approx 0.61R$. Near this location, the mode's kinetic energy and viscous dissipation are discontinuous. Upon approaching corotation from $s > s_{crit}$, the mode's pattern in a meridional quarter-plane becomes more and more parallel to the rotation axis, and according to (3.16), the component of the group velocity perpendicular to the critical cylinder should eventually cancel out at corotation, formally preventing the mode from crossing the critical cylinder. Our simulation indicates that, in a moderately viscous fluid, waves get dramatically absorbed upon crossing corotation, but keep on propagating at $s < s_{crit}$ with a much reduced amplitude.

We point out that the fraction of the mode's amplitude that is effectively transmitted across corotation depends on the mode of interest. A similar $m = 2$ mode with eigenfrequency and Ekman number slightly increased to $\Omega_p \approx -2.20\Omega_{ref}$ and $E = 5 \times 10^{-9}$, respectively, shows no significant transmission in figure 14, as if the incoming wave was fully absorbed at corotation. The contour plot in figure 14(*a*) gives an upper limit for the kinetic energy transmission factor $\sim 10^{-6}$. Note that in the example shown in figure 14, linear inertial waves propagate from the inside outwards, whereas figure 13 shows an opposite direction of propagation (from the outside inwards). It is likely due to a mode selection, with different modes existing on each side of the corotation radius.

4.3.2. *Shellular rotation*

An example of an $m = -6$ eigenmode with a critical layer is depicted in figure 15. For this mode, $E = 6 \times 10^{-9}$, $\Omega(r) \propto r^{-0.2}$ and the spectral resolution

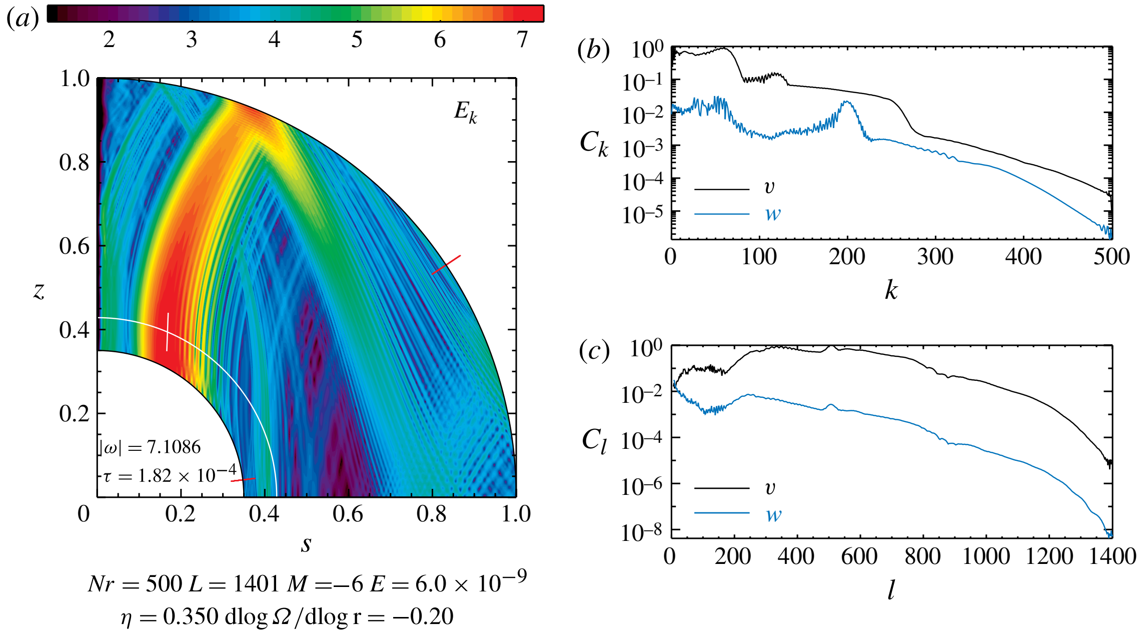

FIGURE 15. (Colour online) (*a*) Meridional cut of the kinetic energy for a growing eigenmode with $E = 6 \times 10^{-9}$, $\sigma = -0.2$, $\Omega_p \approx 7.11\Omega_{ref}$ and $m = -6$. The location of the critical layer is depicted by a solid curve, along which a white tick shows the local slope of characteristics given by (3.34). Red ticks show the inner and outer critical latitudes. (*b,c*) Spectral content of the radial (the quantity $v = xu$ is displayed here) and orthoradial (w) components of the velocity field for this mode. Chebyshev and spherical harmonic coefficients are in (*b,c*), respectively.

is $N_r = 500 \times L = 1401$. This mode's eigenfrequency $\Omega_p \approx 7.11\Omega_{ref}$ (this time, a positive Ω_p is required for an $m < 0$ eigenmode to have a corotation resonance within the shell). Contours of the kinetic energy in a meridional quarter-plane are shown together with the mode's spectral content. The critical layer is depicted by a white solid curve in (*a*), and we see that, in contrast to cylindrical rotation, waves cross the critical layer without experiencing significant absorption. The local analysis carried out for the inviscid case in § 3.2.3 shows that (linear) inertial waves may indeed cross a critical layer with a (formally) divergent group velocity at the critical layer. This occurs if $|k_z| \to 0$ (paths of characteristic then being locally parallel to the rotation axis), or if $\mathscr{B} \to 0$ (paths of characteristics having a finite slope at the critical layer). The white tick displayed on top of the critical layer in figure 15(*a*) shows the local slope of characteristics if $\mathscr{B} = 0$, which is given by (3.34). The large slope obtained in this case (due to the small value of $|\sigma|$) prevents a clear distinction with the case $|k_z| \to 0$. The local analysis also shows the possibility that the group velocity formally vanishes at a critical layer (when $|k_s| \to \infty$ locally), much like in the case of cylindrical rotation. However, we have not found such a situation in our numerical exploration of modes featuring a critical layer.

The most salient feature of the mode shown in figure 15 is that it is found to be unstable: its growth rate, τ, is positive. We have examined in some more detail this particular mode by varying the Ekman number, keeping the same spectral resolution. We have varied E in the range $[4 \times 10^{-9}$–$3.2 \times 10^{-8}]$. Results are shown in figure 16, where the mode's growth rate is depicted as a function of the Ekman number. There is a transition occurring near $E_c \approx 10^{-8}$: $\tau < 0$ (the mode is decaying) for $E > E_c$,

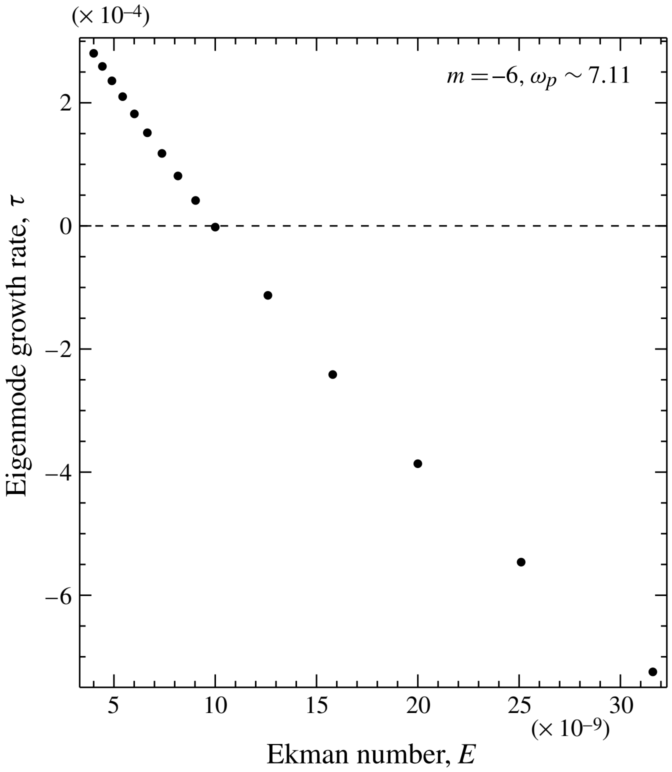

FIGURE 16. Growth rate for the same eigenmode as in figure 15 ($m = -6$, $\sigma = -0.2$, $\Omega_p \approx 7.11\Omega_{ref}$) with varying the Ekman number E. The mode becomes unstable for $E \lesssim 10^{-8}$.

whereas $\tau > 0$ (the mode is growing) for $E < E_c$. The mode's growth rate is actually well approximated by a linear function of E near this transition: $\tau = \alpha(E - E_c)$, with $\alpha < 0$. Although not displayed here, the kinetic energy obtained in the simulations with $E \gtrsim 10^{-8}$ is very similar to that of figure 15(*a*), except for the thick shear layer on each side of corotation, which is found to progressively disappear with increasing E. The very good convergence in spectral resolution obtained in these calculations (as is highlighted by figure 15*b,c*), and the fact we have been able to successfully follow this particular mode with decreasing Ekman number (see figure 16) makes us confident that the positive growth rate that we obtain at small Ekman numbers is physical and not a numerical artifact arising from truncature or round-off errors. It is tempting to interpret this result based on the local dispersion relation obtained at (3.30). It is possible indeed that the instability we have obtained in our simulations is related to the Goldreich–Schubert–Fricke instability in the limit of an incompressible inviscid fluid. The physical mechanism that drives the instability in our model requires a specific investigation that is postponed for future work.

5. Astrophysical implications and concluding remarks

The late evolution of the orbital elements and spin of short-period extrasolar planets, or of close binary-star systems, is primarily driven by tidal interactions. The tidal torque acting on a gravitationally perturbed body encompasses the equilibrium torque, which arises from the quasi-hydrostatic tidal bulge setting around the body, and the dynamical torque, due to tidally forced internal waves propagating inside the body.

Inertial waves may propagate in convective regions of stars and planets, where the Coriolis force is the main restoring force. Gravito-inertial waves may propagate in radiative zones, where buoyancy and rotation act as restoring forces. The magnitude of the dynamical torque is directly related to how much angular momentum is deposited by internal waves, which has a complex dependency upon the forcing potential (amplitude and frequency), and the body's internal properties (see, e.g., Ogilvie & Lin 2004, 2007; Ogilvie 2009; Rieutord & Valdettaro 2010). In many dynamical studies of short-period exoplanets, the tidal torque of the central star is parametrized by a single, dimensionless tidal quality factor Q, which should be thought of, and determined as, a frequency-averaged quantity (Ogilvie 2009).

Prior to an investigation of tidally forced inertial waves in differentially rotating stars and planets, we have examined the propagation properties of linear inertial waves in a rotating fluid body contained in a spherical shell, taking into account the effects of differential rotation. We have used a simple model that consists of an incompressible homogeneous fluid, with dissipation occurring through viscous forces. This fluid model is an intentionally simplified model for the convective zones of stars and planets. We have considered two particular rotation profiles: a cylindrical rotation profile, and a shellular rotation profile. For the sake of simplicity, we have assumed the background flow to be in equilibrium with differential rotation. In the case of shellular rotation, this equilibrium would require additional forces that we have not included. In this respect, the relaxation of the incompressible assumption, or the generalization to stratified fluid bodies, will certainly be an improvement on our model.

Upon linearization of the governing fluid equations, we have revisited the propagation properties of paths of characteristics with differential rotation, in the inviscid limit. Paths of characteristics are shown to obey a second-order PDE of mixed type. Two kinds of inertial modes are thus found to exist with differential rotation: D modes, for which the hyperbolic domain covers the entire shell, and DT modes, for which the hyperbolic domain covers part of the shell. We have analysed the occurrence of axisymmetric ($m = 0$) and non-axisymmetric D and DT eigenmodes for various differential rotation rates and eigenfrequencies. The presence of turning surfaces for DT modes extends the range of frequencies at which inertial modes of oscillation may exist compared with solid-body rotation. We have also discussed the presence of critical latitudes and corotation resonances with differential rotation.

The analytic results based on the dynamics of characteristics are then compared with the results of numerical simulations of linear inertial waves propagating in a viscous fluid contained in a spherical shell. High-resolution calculations, based on a spectral method, have been performed to properly describe the structure of the thin shear layers arising in the physically interesting regime of small Ekman numbers (small viscosities). The Ekman numbers used in our simulations typically range from a few 10^{-9} to 10^{-6}, values that are, however, much larger than what may be expected in stars and planets (Ekman numbers between 10^{-15} and 10^{-10}). The modes that we have primarily focused on are singular modes with a shear layer converging towards a short-period wave attractor. As in the solid-body rotation case, the pattern of these shear layers is well reproduced by the dynamics of characteristics under the short-wavelength approximation. As an interesting side result, we have shown that reflexions on a turning surface, and on the body's outer radius, may form singular modes with short-period wave attractors in the whole sphere (that is, in the absence of an inner core). The damping rate of singular modes with differential rotation is also assessed in the limit of small Ekman numbers. Our results of calculations indicate that an $E^{1/3}$ scaling is to be expected for most D and DT eigenmodes, much similar to the case of solid-body rotation. Still, the case of a DT mode with damping rate approximately independent of the Ekman number is uncovered. In addition, we have carried out a qualitative analysis of the occurrence of modes with quasi-periodic orbits of characteristics for shellular rotation.

We have also briefly examined the behaviour of linear inertial waves with a corotation resonance within the shell (where the wave's frequency vanishes in the frame rotating with the fluid). For cylindrical rotation, our simulations show that inertial waves may cross a corotation resonance, but experience a very large absorption at this location, much like inertial waves propagating in differentially rotating astrophysical discs (Latter & Balbus 2009). For shellular rotation, however, we have found that waves may propagate across a corotation resonance (critical layer) without visible absorption. Such modes are found to be unstable for small enough viscosities. Clearly, these findings appeal for a confirmation with an improved fluid model, where shellular rotation is balanced for by appropriate body forces and where nonlinear effects are taken into account.

Many simplifying assumptions in the fluid model we have considered deserve further investigation to make it more applicable to the fluid flows inside stars or planets. The incompressible and homogeneous assumptions are obvious examples, and naturally a full model including appropriate modelling for the convective and radiative zones would be desirable. Since inertial waves propagate in convective regions of stars and planets, it would be interesting to study the impact of convective turbulence on the propagation and dissipation properties of inertial waves (the formation of large-scale attractors for instance). The nature and quality of wave reflections at the shell's boundaries should be analysed, as it is still unclear for example how inertial waves reflect on the upper atmosphere of stars and planets.

Acknowledgements

We thank H. Latter, R. Nelson and G. Ogilvie for very helpful discussions. M.R. would like to specially thank S. Friedlander who suggested this work during a visit in Toulouse. Many years after, these discussions have borne fruit. We are also grateful to the three anonymous referees for their constructive reports. Numerical simulations were carried out on the CalMip machine of the Centre Interuniversitaire de Calcul de Toulouse, and on the Darwin Supercomputer of the University of Cambridge High Performance Computing Service. C.B. acknowledges support from a Herchel Smith Postdoctoral Fellowship of the University of Cambridge.

Appendix. Equation for the perturbed pressure and dispersion relation

This appendix derives the PDE satisfied by the perturbed pressure, p, in the inviscid limit. It also derives the wave dispersion relation, the phase and the group velocities under the short-wavelength approximation. In cylindrical coordinates (s, φ, z), (2.1) becomes

$$i\tilde{\Omega}_p \boldsymbol{u} + 2\Omega \boldsymbol{e}_z \times \boldsymbol{u} + s(\boldsymbol{u} \cdot \nabla \Omega)\boldsymbol{e}_\varphi = \nabla p, \tag{A 1}$$

with Ω the background angular frequency and $\tilde{\Omega}_p$ the Doppler-shifted frequency. The cylindrical components of the linearized velocity vector, (u_s, u_φ, u_z), can be expressed as a function of p and of its partial derivatives:

$$u_s(s, z) = \frac{1}{i\tilde{\Omega}_p(A_s - \tilde{\Omega}_p^2)} \times \left[\tilde{\Omega}_p^2 \frac{\partial p}{\partial s} + A_z \frac{\partial p}{\partial z} + 2\Omega \tilde{\Omega}_p \frac{mp}{s}\right], \tag{A 2}$$

$$u_\varphi(s,z) = \frac{1}{2\Omega(A_s - \tilde{\Omega}_p^2)} \times \left[A_s \frac{\partial p}{\partial s} + A_z \frac{\partial p}{\partial z} + 2\Omega\tilde{\Omega}_p \frac{mp}{s} \right], \tag{A 3}$$

$$u_z(s,z) = \frac{i}{\tilde{\Omega}_p}\frac{\partial p}{\partial z}, \tag{A 4}$$

and where

$$A_s = \frac{2\Omega}{s}\frac{\partial}{\partial s}\left(s^2\Omega\right) \quad \text{and} \quad A_z = \frac{2\Omega}{s}\frac{\partial}{\partial z}(s^2\Omega). \tag{A 5}$$

For solid-body rotation or cylindrical rotation, $A_z = 0$ and $A_s = 4\Omega^2$. Note the special case where $\tilde{\Omega}_p = 0$ for which a corotation resonance exists in the shell, and that where $A_s = \tilde{\Omega}_p^2$, which is analogous to Lindblad resonances in compressible fluids with cylindrical rotation such as astrophysical discs.

Taking the divergence of (A 1) and using (A 2)–(A 4), we find, after some algebra, that p satisfies

$$\begin{aligned}
&-\tilde{\Omega}_p^2 \frac{\partial^2 p}{\partial s^2} + (A_s - \tilde{\Omega}_p^2)\frac{\partial^2 p}{\partial z^2} - A_z \frac{\partial^2 p}{\partial s \partial z} \\
&\quad = \frac{\partial p}{\partial s}\left[\frac{\tilde{\Omega}_p^2}{s} + \frac{\partial A_s}{\partial s} - \frac{m A_s \tilde{\Omega}_p}{2\Omega s} - \frac{A_s}{A_s - \tilde{\Omega}_p}\frac{\partial}{\partial s}(A_s - \tilde{\Omega}_p^2) \right] \\
&\qquad + \frac{\partial p}{\partial z}\left[\frac{A_z}{s} + \frac{\partial A_z}{\partial s} - \frac{m A_z \tilde{\Omega}_p}{2\Omega s}\left(1 + \frac{4\Omega^2}{\tilde{\Omega}_p^2}\right) - \frac{A_z}{A_s - \tilde{\Omega}_p^2}\frac{\partial}{\partial s}(A_s - \tilde{\Omega}_p^2) \right] \\
&\qquad + \frac{mp}{s}\left[\frac{m}{s}\left(A_s - \tilde{\Omega}_p^2 - 8\Omega^2\right) + \frac{A_s\tilde{\Omega}_p}{\Omega s}\left(1 - \frac{4\Omega^2}{A_s}\right) - \frac{2\Omega\tilde{\Omega}_p}{A_s - \tilde{\Omega}_p^2}\frac{\partial}{\partial s}(A_s - \tilde{\Omega}_p^2) \right],
\end{aligned} \tag{A 6}$$

which reduces to (3.1) when only second-order terms are retained (the short-wavelength approximation).

We now examine the propagation properties of local waves in a meridional plane. Assuming $p \propto \exp(\mathrm{i}\{k_s s + k_z z\})$, (A 6) yields the following wave dispersion relation in the short-wavelength approximation:

$$\tilde{\Omega}_p^2 = \frac{k_z^2}{\|\boldsymbol{k}\|^2}\left[A_s - \frac{k_s}{k_z}A_z \right], \tag{A 7}$$

where $\|\boldsymbol{k}\| = \sqrt{k_s^2 + k_z^2}$. For solid-body rotation, (A 7) reduces to the well-known dispersion relation $\tilde{\Omega}_p = \pm 2\Omega k_z / \|\boldsymbol{k}\|$ (see, e.g., Greenspan 1969). In the bracket term of (A 7), while $A_s > 0$ is required to satisfy Rayleigh's criterion, the sign of $A_z k_s / k_z$ is not known *a priori*. Equation (A 7) therefore indicates that an instability may occur if $A_s - A_z k_s / k_z < 0$. It corresponds in fact to the Goldreich–Schubert–Fricke instability for an incompressible inviscid fluid (Goldreich & Schubert 1967; Fricke 1968), in which case the inequality $A_s - A_z k_s / k_z < 0$ is identical to that in equation (33) (misprinted) of Goldreich & Schubert (1967) (see also Nelson, Gressel & Umurhan 2012). Assuming the fluid is stable against the Goldreich–Schubert–Fricke instability, we introduce

$$\tilde{\mathscr{B}} = \left[A_s - \frac{k_s}{k_z}A_z \right]^{1/2}, \tag{A 8}$$

and (A 7) translates into $\tilde{\Omega}_p = \pm\tilde{\mathscr{B}}|k_z|/\|\boldsymbol{k}\|$. In the frame rotating with the fluid, the phase velocity, $\boldsymbol{v}_p = \tilde{\Omega}_p\boldsymbol{k}/\ \|\boldsymbol{k}\|^2$, satisfies

$$\boldsymbol{v}_p = \frac{\pm\tilde{\mathscr{B}}k_z}{\|\boldsymbol{k}\|^3}\boldsymbol{k}, \tag{A 9}$$

while the group velocity, $\boldsymbol{v}_g = \partial\tilde{\Omega}_p/\partial\boldsymbol{k}$, is given by

$$\boldsymbol{v}_g = \pm\frac{k_s}{\|\boldsymbol{k}\|^3}(-k_z\boldsymbol{e}_s + k_s\boldsymbol{e}_z) \times \left[\tilde{\mathscr{B}} + \frac{A_z}{2}\frac{\|\boldsymbol{k}\|^2}{k_s k_z}\tilde{\mathscr{B}}^{-1}\right]. \tag{A 10}$$

Note that $\boldsymbol{k}\cdot\boldsymbol{v}_g = 0$: the group velocity is perpendicular to the phase velocity for differential rotation as for solid-body rotation.

REFERENCES

Barker, A. J. & Ogilvie, G. I. 2010 On internal wave breaking and tidal dissipation near the centre of a Solar-type star. *Mon. Not. R. Astron. Soc.* **404**, 1849–1868.

Bryan, G. 1889 The waves on a rotating liquid spheroid of finite ellipticity. *Phil. Trans. R. Soc. Lond.* **180**, 187–219.

Cartan, E. 1922 Sur les petites oscillations d'une masse fluide. *Bull. Sci. Math.* **46**, 317–352; 356–369.

Dintrans, B., Rieutord, M. & Valdettaro, L. 1999 Gravito-inertial waves in a rotating stratified sphere or spherical shell. *J. Fluid Mech.* **398**, 271–297.

Fricke, K. 1968 Instabilität stationärer Rotation in Sternen. *ZAp* **68**, 317.

Friedlander, S. 1982 Turning surface behaviour for internal waves subject to general gravitational fields. *Geophys. Astrophys. Fluid Dyn.* **21**, 189–200.

Friedlander, S. 1987 Hydromagnetic waves in the Earth's fluid core. *Geophys. Astrophys. Fluid Dyn.* **39**, 315–333.

Friedlander, S. & Siegmann, W. L. 1982 Internal waves in a rotating stratified fluid in an arbitrary gravitational field. *Geophys. Astrophys. Fluid Dyn.* **19**, 267–291.

Goldreich, P. & Schubert, G. 1967 Differential rotation in stars. *Astrophys. J.* **150**, 571.

Goodman, J. & Lackner, C. 2009 Dynamical tides in rotating planets and stars. *ApJ* **696**, 2054–2067.

Greenspan, H. P. 1969 *The Theory of Rotating Fluids*. Cambridge University Press.

Hollerbach, R. & Kerswell, R. 1995 Oscillatory internal shear layers in rotating and precessing flows. *J. Fluid Mech.* **298**, 327–339.

Kelley, D., Triana, S. A., Zimmerman, D., Tilgner, A. & Lathrop, D. 2007 Inertial waves driven by differential rotation in a planetary geometry. *Geophys. Astrophys. Fluid Dyn.* **101**, 469–487.

Kelley, D. H., Triana, S. A., Zimmerman, D. S. & Lathrop, D. P. 2010 Selection of inertial modes in spherical Couette flow. *Phys. Rev.* E **81** (2), 026311.

Kelvin, Lord 1880 Vibrations of a columnar vortex. *Phil. Mag.* **10**, 155–168.

Kerswell, R. 1995 On the internal shear layers spawned by the critical regions in oscillatory Ekman boundary layers. *J. Fluid Mech.* **298**, 311–325.

Latter, H. N. & Balbus, S. A. 2009 Inertial waves near corotation in three-dimensional hydrodynamical discs. *Mon. Not. R. Astron. Soc.* **399**, 1058–1073.

Le Dizès, S. 2004 Viscous critical-layer analysis of vortex normal modes. *Stud. Appl. Maths* **112**, 315–332.

Maas, L. & Lam, F.-P. 1995 Geometric focusing of internal waves. *J. Fluid Mech.* **300**, 1–41.

Nelson, R. P., Gressel, O. & Umurhan, O. M. 2012 Linear and nonlinear evolution of the vertical shear instability in accretion discs. *Mon. Not. R. Astron. Soc.* arXiv:1209.2753.

Ogilvie, G. I. 2005 Wave attractors and the asymptotic dissipation rate of tidal disturbances. *J. Fluid Mech.* **543**, 19–44.

OGILVIE, G. 2009 Tidal dissipation in rotating fluid bodies: a simplified model. *Mon. Not. R. Astron. Soc.* **396**, 794–806.

OGILVIE, G. I. & LIN, D. N. C. 2004 Tidal dissipation in rotating giant planets. *ApJ* **610**, 477–509.

OGILVIE, G. I. & LIN, D. N. C. 2007 Tidal dissipation in rotating solar-type stars. *Astrophys. J.* **661**, 1180–1191.

RIEUTORD, M. 1987 Linear theory of rotating fluids using spherical harmonics part I: steady flows. *Geophys. Astrophys. Fluid Dyn.* **39**, 163–182.

RIEUTORD, M. 2006 The dynamics of the radiative envelope of rapidly rotating stars. I. A spherical boussinesq model. *A&A* **451**, 1025–1036.

RIEUTORD, M., GEORGEOT, B. & VALDETTARO, L. 2001 Inertial waves in a rotating spherical shell: attractors and asymptotic spectrum. *J. Fluid Mech.* **435**, 103–144.

RIEUTORD, M., TRIANA, S. A., ZIMMERMAN, D. S. & LATHROP, D. P. 2012 Excitation of inertial modes in an experimental spherical Couette flow. *Phys. Rev.* E **86** (2), 026304.

RIEUTORD, M. & VALDETTARO, L. 1997 Inertial waves in a rotating spherical shell. *J. Fluid Mech.* **341**, 77–99.

RIEUTORD, M. & VALDETTARO, L. 2010 Viscous dissipation by tidally forced inertial modes in a rotating spherical shell. *J. Fluid Mech.* **643**, 363–394.

RIEUTORD, M., VALDETTARO, L. & GEORGEOT, B. 2002 Analysis of singular inertial modes in a spherical shell: the slender toroidal shell model. *J. Fluid Mech.* **463**, 345–360.

STEWARTSON, K. 1971 On trapped oscillations of a rotating fluid in a thin spherical shell. *Tellus* **23**, 506–510.

STEWARTSON, K. 1972*a* On trapped oscillations of a rotating fluid in a thin spherical shell II. *Tellus* **24**, 283–287.

STEWARTSON, K. 1972*b* On trapped oscillations in a slightly viscous rotating fluid. *J. Fluid Mech.* **54**, 749–761.

STEWARTSON, K. & RICKARD, J. 1969 Pathological oscillations of a rotating fluid. *J. Fluid Mech.* **35**, 759–773.

VALDETTARO, L., RIEUTORD, M., BRACONNIER, T. & FRAYSSE, V. 2007 Convergence and round-off errors in a two-dimensional eigenvalue problem using spectral methods and Arnoldi–Chebyshev algorithm. *J. Comput. Appl. Math.* **205**, 382–393.

WU, Y. 2005 Origin of tidal dissipation in Jupiter. II. The value of *Q*. *Astrophys. J.* **635**, 688–710.

ZAHN, J.-P. 1992 Circulation and turbulence in rotating stars. *A&A* **265**, 115.

Monthly Notices
of the
ROYAL ASTRONOMICAL SOCIETY

MNRAS **486,** 304–319 (2019) doi:10.1093/mnras/stz802
Advance Access publication 2019 March 19

Dust traps in the protoplanetary disc MWC 758: two vortices produced by two giant planets?

Clément Baruteau,[1★] Marcelo Barraza,[2,3,4] Sebastián Pérez,[2,3] Simon Casassus,[2,3] Ruobing Dong,[5] Wladimir Lyra,[6,7] Sebastián Marino,[4] Valentin Christiaens,[2,3,8] Zhaohuan Zhu,[9] Andrés Carmona,[1] Florian Debras[1] and Felipe Alarcon[2,3]

[1] *IRAP, Université de Toulouse, CNRS, UPS, F-31400 Toulouse, France*
[2] *Departamento de Astronomía, Universidad de Chile, Casilla 36-D, Santiago, Chile*
[3] *Millennium Nucleus 'Protoplanetary Disks', Chile*
[4] *Max Planck Institute for Astronomy, Königstuhl 17, D-69117 Heidelberg, Germany*
[5] *Steward Observatory, University of Arizona, Tucson, AZ 85719, USA*
[6] *Department of Physics and Astronomy, California State University Northridge, 1811 Nordhoff St, Northridge, CA 91130, USA*
[7] *Jet Propulsion Laboratory, California Institute of Technology, 4800 Oak Grove Drive, Pasadena, CA 91109, USA*
[8] *Monash Centre for Astrophysics (MoCA) and School of Physics and Astronomy, Monash University, Clayton Vic 3800, Australia*
[9] *Department of Physics and Astronomy, University of Nevada, Las Vegas, 4505 South Maryland Pkwy, Las Vegas, NV 89154, USA*

Accepted 2019 March 13. Received 2019 March 12; in original form 2018 July 17

ABSTRACT

Resolved ALMA and VLA observations indicate the existence of two dust traps in the protoplanetary disc MWC 758. By means of two-dimensional gas+dust hydrodynamical simulations post-processed with three-dimensional dust radiative transfer calculations, we show that the spirals in scattered light, the eccentric, asymmetric ring and the crescent-shaped structure in the (sub)millimetre can all be caused by two giant planets: a 1.5-Jupiter mass planet at 35 au (inside the spirals) and a 5-Jupiter mass planet at 140 au (outside the spirals). The outer planet forms a dust-trapping vortex at the inner edge of its gap (at ∼85 au), and the continuum emission of this dust trap reproduces the ALMA and VLA observations well. The outer planet triggers several spiral arms that are similar to those observed in polarized scattered light. The inner planet also forms a vortex at the outer edge of its gap (at ∼50 au), but it decays faster than the vortex induced by the outer planet, as a result of the disc's turbulent viscosity. The vortex decay can explain the eccentric inner ring seen with ALMA as well as the low signal and larger azimuthal spread of this dust trap in VLA observations. Finding the thermal and kinematic signatures of both giant planets could verify the proposed scenario.

Key words: accretion, accretion discs – hydrodynamics – planets and satellites: formation – planet–disc interactions – protoplanetary discs – stars: individual: MWC 758 (HD 36112).

1 INTRODUCTION

MWC 758 is a 3.5 ± 2.0 Myr Herbig A5 star (Meeus et al. 2012) located at a distance of 160.2 ± 1.7 pc (Gaia Collaboration et al. 2018). Its mass has been estimated as 1.5 ± 0.2 $M_{\odot}$ (Isella et al. 2010; Reggiani et al. 2018). The disc around MWC 758 is a transition disc with a nearly 50 au (0.30 arcsec) cavity in the submillimetre (Andrews et al. 2011). Recent high angular resolution observations have revealed stunning non-axisymmetric emission features in the MWC 758 disc. These asymmetries so far consist of multiple spiral arms and arcs in near-infrared scattered light (Grady et al. 2013; Benisty et al. 2015; Reggiani et al. 2018; Ren et al. 2018), an asymmetric ring of emission at ∼0.32 arcsec as well as a compact crescent-shaped structure at ∼0.53 arcsec in the (sub)millimetre emission (Marino et al. 2015; Boehler et al. 2018; Dong et al. 2018; Casassus et al. 2019). The asymmetries in the (sub)millimetre emission, which we will refer to as Clump 1 (crescent at ∼0.53 arcsec) and Clump 2 (asymmetric ring at ∼0.32 arcsec; see the right-hand panels in Fig. 4) have been interpreted as dust traps at local pressure maxima arising from two large-scale vortices (Marino et al. 2015). The cm-wavelength VLA observations presented in Casassus et al. (2019) support the dust trapping scenario for Clump 1, and suggest marginal trapping for Clump 2. Still, the mechanism behind the formation of the possible dust-trapping vortices in the MWC 758 disc remains elusive and is the subject of this paper.

One way to form a large-scale vortex in a protoplanetary disc is through the Rossby wave instability (RWI; Lovelace et al. 1999; Li et al. 2000, 2001). This instability can set in when there is a

---

[★] E-mail: clement.baruteau@irap.omp.eu

Published by Oxford University Press on behalf of the Royal Astronomical Society

radial minimum in the gas vortensity,[1] which in practice may occur where there is a radial pressure bump. A radial pressure bump can form for instance at the transition between magnetically active and inactive regions in protoplanetary discs, where a sharp transition in the effective turbulent viscosity occurs (Varnière & Tagger 2006; Regály et al. 2012; Lyra, Turner & McNally 2015), or at the edges of the gap that a massive planet carves in its disc (e.g. Lyra et al. 2009; Lin 2012). More often, it is the gap's outer edge that develops a pressure maximum, but a very massive planet of typically a few Jupiter masses may also form and maintain a pressure maximum at the inner edge of its gap (Bae, Zhu & Hartmann 2016).

Whatever its trigger, the RWI leads to the formation of one or several vortices, which tend to merge and form a single large-scale anticyclonic vortex. An anticyclonic vortex forms a patch of closed elliptical streamlines about a local pressure maximum. The vortex flow tends to maintain dust on the same elliptical streamlines, gas drag tends to drive dust towards the vortex centre, while dust turbulent diffusion tends to spread it out (Chavanis 2000; Youdin 2010; Lyra & Lin 2013). In addition, the vortex's self-gravity causes dust particles to describe horseshoe U-turns relative to the vortex centre, much like in the circular restricted three-body problem, despite the vortex not being a point mass (Baruteau & Zhu 2016). The competition between the aforementioned effects implies that dust particles of increasing size get trapped farther ahead of the vortex centre in the azimuthal direction (Baruteau & Zhu 2016). Vortices triggered by the RWI could play a key role in planet formation by slowing down or stalling the dust's inward drift due to gas drag, while potentially allowing dust to grow to planetesimal sizes or even planetary sizes (Lyra et al. 2009; Sándor, Lyra & Dullemond 2011).

A planetary origin for the two possible vortices in the MWC 758 disc is appealing, as it could also account for the detection of a point-like source inside the submillimetre cavity in the L'-band high-contrast imaging observations of Reggiani et al. (2018), and for the spirals in near-infrared scattered light. The aim of this paper is to present theoretical support for the scenario where the asymmetric structures in the (sub)millimetre and the spirals in scattered light could be due to the presence of two massive planets in the MWC 758 disc. For this purpose, we have carried out two-dimensional (2D) gas+dust hydrodynamical simulations of the protoplanetary disc around MWC 758, and used three-dimensional (3D) dust radiative transfer calculations to compare synthetic maps of continuum and scattered light with observations. In Section 2, we describe the physical model and numerical set-up of the hydrodynamical simulations and the radiative transfer calculations. Their results are then presented in Section 3. Discussion and summary follow in Section 4.

2 PHYSICAL MODEL AND NUMERICAL METHODS

2.1 Hydrodynamical simulations

We carried out 2D gas+dust hydrodynamical simulations using the code Dusty FARGO-ADSG. It is an extended version of the grid-based code FARGO-ADSG (Masset 2000; Baruteau & Masset 2008a,b) with dust modelled as Lagrangian test particles (Baruteau & Zhu 2016; Fuente et al. 2017).

2.1.1 *Planets*

We assume that MWC 758, which we take as a $M_\star = 1.5\mathrm{M}_\odot$ star (Isella et al. 2010; Reggiani et al. 2018), has two planetary companions: a 1.5 Jupiter-mass planet at 35 au and a 5 Jupiter-mass planet at 140 au. The mass of the inner planet is chosen such that it opens a mild gap in the gas around its orbit (see the first paragraph in Section 3.1) to be consistent with the non-detection of a gap in scattered light around this location (∼0.22 arcsec; Benisty et al. 2015). The mass of the outer planet is taken as the upper mass limit for a companion at this location (∼0.87 arcsec), as estimated by Reggiani et al. (2018) based on their L'-band observations and the use of the BT-Settl hot start evolutionary model for planetary luminosities at near-infrared wavelengths (Allard 2014). Section 4.4 contains a discussion on the location and mass of the possible planets in the MWC 758 disc. In our simulations, the planets do not migrate in the disc (they remain on quasi-circular orbits). To avoid a violent relaxation of the disc due to the sudden introduction of the planets, their mass is gradually increased over 20 orbits of the inner planet. In the following, whenever time is expressed in orbits, it refers to the orbital period at the inner planet's location, which is about 170 yr.

2.1.2 *Gas*

A locally isothermal equation of state is assumed for the gas, where its temperature remains fixed in time. Based on Boehler et al. (2018)'s thermal Monte Carlo simulation of the MWC 758 disc (see their fig. 9), we take the mid-plane temperature to decrease as r^{-1} and equal to 85 K at 35 au (r denotes the radial cylindrical coordinate measured from the central star). The disc's aspect ratio h, which is the ratio of the mid-plane isothermal sound speed to the Keplerian velocity, is therefore uniform and equal to 0.088 (we assume a mean molecular weight of 2.4).

The initial surface density of the disc gas, which we denote by Σ_0, is assumed proportional to r^{-1} and equal to $\sim 1.7\ \mathrm{g\,cm^{-2}}$ at 35 au. In a quasi-steady state, when the planets have carved a gap around their orbit, the azimuthally averaged gas surface density varies from 1 to $2\ \mathrm{g\,cm^{-2}}$ between 40 and 90 au, which is overall consistent with the values of the gas surface density obtained by Boehler et al. (2018) based on their ALMA band 7 observations of ^{13}CO and C^{18}O in the MWC 758 disc (see their fig. 8). Despite the Toomre Q-parameter being rather large (it is ∼30 at 85 au, the radial location of Clump 1), gas self-gravity is included, as it is found to impact both the vortex lifetime (Zhu & Baruteau 2016; Regály & Vorobyov 2017) and the dust dynamics (Baruteau & Zhu 2016) given our range of disc parameters. The importance of gas self-gravity will be further emphasized in Section 4.1. To mimic the effect of a finite vertical thickness, a softening length of $0.3H(r)$ is used in the calculation of the self-gravitating acceleration, with $H(r) = h \times r$ the disc's pressure scale height. Likewise, a softening length of $0.6H(r)$ is used in the calculation of the planets acceleration on the gas.

Turbulent transport of angular momentum is modelled by a constant alpha turbulent viscosity, $\alpha = 10^{-4}$. This rather low level of turbulence is representative of the discs mid-plane from a few tens to a hundred au, as suggested by observations of the dust continuum in the submillimetre (see e.g. Pinte et al. 2016, for the modelling of the HL Tau disc), and according to 3D, non-ideal,

---

[1] In 2D, the gas vortensity (or potential vorticity), which we denote by ω, is the ratio of the z-component of the curl of the (2D) velocity to the surface density. We denote by ω_0 the initial radial profile of the gas vortensity. Vortensity tends to be conserved along streamlines, diffused by the action of turbulent viscosity, and created at shocks or at locations where surfaces of constant density and pressure are not aligned (baroclinic source term).

local magnetohydrodynamic (MHD) simulations (although larger α values in the mid-plane can be obtained depending on the disc model, in particular the amplitude of the vertical magnetic field that threads the disc, see e.g. Simon et al. 2015, 2018).

The continuity and momentum equations for the gas are solved on a polar grid centred on the star, and the indirect terms due to the acceleration of the star by the disc and the planets are taken into account. The grid extends from 10.5 to 350 au in the radial direction, and from 0 to 2π in the azimuthal direction. We use 900 cells in the radial direction with a logarithmic spacing (required for the gas self-gravitating acceleration to be computed by Fast-Fourier Transforms; see Baruteau & Masset 2008b). We use 1200 cells evenly spaced in azimuth. Given our initial surface density profile, the initial mass of the disc gas amounts to $\sim$0.01 $M_\star$. To minimize the reflection of the planets wakes, we use wave-killing zones as boundary conditions at the inner and outer radial edges of the grid, where the disc fields are damped towards their initial value. We have checked that a different choice of boundary condition does not affect our results.

2.1.3 Dust

Dust is modelled as Lagrangian test particles that feel the gravity of the star, of the planets, of the gaseous disc (since gas self-gravity is included) and gas drag. Dust turbulent diffusion is also included as stochastic kicks on the particles position following the method in Charnoz et al. (2011) (see Ataiee et al. 2018 for more details). However, the dust self-gravity, dust drag (or feedback), growth, and fragmentation are not taken into account in the simulations.

We use 10^5 particles with a size distribution $n_{\rm simu}(s) \propto s^{-1}$ for the particles size s ranging from 10 μm to 10 cm (the quantity $n_{\rm simu}(s){\rm d}s$ represents the number of superparticles in the size interval $[s, s + {\rm d}s]$ in the simulation). This particular scaling of the dust's size distribution is chosen for computational reasons, as it implies that there is approximately the same number of particles per decade of size. An important note is that the radiative transfer calculations do need a realistic size distribution for the dust, but the only input that they need from the hydrodynamical simulations is the spatial distribution of the dust particles. This is the reason why we can choose any size distribution in the simulations, as long as there is enough particles per bin size to properly resolve their dynamics.

The dust particles are introduced in the disc gas at 300 orbits after the beginning of the simulation, when the planets have already started to open a gap around their orbit. The particles are uniformly distributed between 52 and 102 au, so that they approximately all remain between the gaps over the duration of the simulation. This is meant to maximize the particles resolution at the two dust traps from which Clumps 1 and 2 originate in our scenario. Furthermore, inspired by the dust trapping predictions of Casassus et al. (2019, see their section 3.2.2), we assume that the dust particles have an internal density $\rho_{\rm int} = 0.1\ \ {\rm g\,cm^{-3}}$, independent of particles size, instead of a more conventional internal density of a few ${\rm g\,cm^{-3}}$. Our dust particles can therefore be considered as moderately porous particles. This rather low density is overall consistent with the collection by *Rosetta* of large (>10 μm) porous aggregate particles[2] in the near coma of comet 67P/Churyumov–Gerasimenko (Bentley et al. 2016; Langevin et al. 2016). A brief discussion on how the particles internal density impacts our results is given in Section 4.3.3.

Table 1. Simulations parameters.

Parameter	Value
Star mass	1.5 $M_\odot$
Inner planet's mass	1.5 $M_{\rm Jup}$
Inner planet's location	35 au
Outer planet's mass	5 $M_{\rm Jup}$
Outer planet's location	140 au
Disc's aspect ratio	0.088
Alpha turbulent viscosity	10^{-4}
Dust's initial location	$\in$ [52–102] au
Dust's size range	$\in$ [10 μm – 10 cm]
Dust's internal density	0.1 ${\rm g\,cm^{-3}}$

The dust particles that we simulate are much smaller than the mean free path in our disc model, and the Epstein regime of drag is therefore relevant. In this regime, the particle's Stokes number (St), which is the ratio of the particle's stopping time to the dynamical time, can be expressed as

$$
{\rm St} \approx 0.15 \times \left(\frac{s}{1\ {\rm cm}}\right) \left(\frac{\rho_{\rm int}}{0.1\ {\rm g\ cm^{-3}}}\right) \left(\frac{1\ {\rm g\ cm^{-2}}}{\Sigma}\right), \tag{1}
$$

where Σ denotes here the gas surface density interpolated at the particle's location. When our simulations reach a quasi-steady state, St varies from $\sim 3 \times 10^{-5}$ to $\sim$2. Note that the so-called short-friction time approximation is used in the simulations for the smallest dust particles for which the local stopping time is shorter than the hydrodynamical time-step. A summary of the parameters used in the simulations can be found in Table 1.

2.2 Radiative transfer calculations

Our results of 2D hydrodynamical simulations are post-processed with the 3D radiative transfer code RADMC3D (version 0.41, Dullemond et al. 2015). The dust's spatial distribution obtained in our simulations is used as input to compute continuum emission maps at ALMA band 7 (0.9 mm) and VLA (9.0 mm) wavelengths (Section 2.2.1). The gas surface density is used as input to compute a polarized scattered light image in the Y band (1.04 μm, Section 2.2.2). The spatial grid used in RADMC3D is a 3D extension of the simulations grid in spherical coordinates (the grid's vertical extent and the number of cells in colatitude are specified in Sections 2.2.1 and 2.2.2). We use 10^9 photon packages for the thermal Monte Carlo calculation of the dust temperature and for the ray-tracing computation of the (sub)millimetre continuum and near-infrared polarised scattered light images. We assume that the star has a radius of 2.0 $R_\odot$ and an effective temperature of 7340 K (Gaia Collaboration et al. 2018, or see Gaia archive online). We assume the disc to be located at 160 pc (Gaia Collaboration et al. 2018), with an inclination of 21° and a position angle of 62° (Isella et al. 2010; Boehler et al. 2018). Since the disc is rotating clockwise in the observations, but counterclockwise in the simulation, the effective inclination adopted in the radiative transfer calculations is 201°. The PYTHON program used to compute the (sub)millimetre continuum and near-infrared polarized scattered light images with RADMC3D from the results of Dusty FARGO-ADSG simulations, `fargo2radmc3d`, is publicly available at https://github.com/charango/fargo2radmc3d.

---

[2] More specifically, internal densities between 0.1 and 1 ${\rm g\,cm^{-3}}$ are required to explain the dust's observed accelerations via radiation pressure or by a *rocket force* due to sublimation of surface ice on the day side of ejected grains (see e.g. Güttler et al. 2019 for a review).

2.2.1 *(Sub)millimetre continuum emission*

The calculation of the dust's continuum emission requires to specify (i) the size distribution $n(s)$ and the total mass that the dust that we simulate would have in the MWC 758 disc, (ii) the vertical distribution of the dust's mass volume density, and (iii) the absorption and scattering opacities:

(i) The dust's size distribution and its total mass are free parameters that we have varied to best reproduce the current ALMA and VLA observations of the MWC 758 disc. As will be shown in Section 3, good results are obtained for $n(s) \propto s^{-3}$, a minimum particle size of 10 µm (as in the simulations), a maximum particle size of 1 cm, and a dust-to-gas mass ratio of 2 per cent. This corresponds to a total dust mass $\sim 1.6 \times 10^{-4} M_\star$ (or $\sim 80\ \mathrm{M}_\oplus$) between ∼40 and ∼100 au, which is about five to seven times larger than the value reported in Boehler et al. (2018). The mass difference likely points to optical depth effects (see Section 3). The impact of the dust's size distribution and its total mass will be discussed in Sections 4.3.1 and 4.3.2. In practice, the aforementioned size range, [10 µm–1 cm], is decomposed into 30 logarithmically spaced size bins, and from the spatial distribution of the dust particles in the 2D hydrodynamical simulation we compute the dust's surface density for each size bin i, which we denote by $\sigma_{i,\mathrm{dust}}$. The quantity $\sigma_{i,\mathrm{dust}}$ can be expressed as

$$\sigma_{i,\mathrm{dust}}(r,\varphi) = \frac{N_i(r,\varphi)}{\mathcal{A}(r)} \times \frac{M_{i,\mathrm{dust}}}{\sum\limits_{r,\varphi} N_i(r,\varphi)}, \qquad (2)$$

where N_i denotes the number of dust particles per bin size and in each grid cell of the simulation, $\mathcal{A}$ is the surface area of each grid cell, and $M_{i,\mathrm{dust}}$ is the dust mass per bin size, which takes the form

$$M_{i,\mathrm{dust}} = \xi M_{\mathrm{gas}} \times \frac{s_{i+1}^{4-p} - s_i^{4-p}}{s_{\max}^{4-p} - s_{\min}^{4-p}} = \xi M_{\mathrm{gas}} \times \frac{s_i^{4-p}}{\sum\limits_i s_i^{4-p}}, \qquad (3)$$

where $[s_i, s_{i+1}]$ is the size range of the ith size bin, $s_{\min}$ and $s_{\max}$ are the minimum and maximum particle sizes, $-p$ is the power-law exponent of the dust's size distribution $n(s)$, M_{gas} the total mass of gas in the simulation, and ξ the dust-to-gas mass ratio. As stated above, the synthetic maps of continuum emission shown in Section 3 are for $s_{\min} = 10\ \mu\mathrm{m}$, $s_{\max} = 1$ cm, $p = 3$, and $\xi = 2$ per cent.

(ii) For the vertical distribution of the dust's mass volume density, hydrostatic equilibrium is assumed and for each size bin a Gaussian profile is adopted in which the dust's scale height $H_{i,\,\mathrm{dust}}$ of the ith size bin is given by (see e.g. Riols & Lesur 2018)

$$H_{i,\mathrm{dust}} = H \times \left(\frac{D_z}{D_z + \mathrm{St}_i}\right)^{1/2}, \qquad (4)$$

where H is the gas pressure scale height, St_i is the average Stokes number of the dust particles in the ith size bin, and D_z is a dimensionless turbulent diffusion coefficient for the gas in the vertical direction evaluated at the disc mid-plane, which for simplicity we take equal to the alpha turbulent viscosity in our 2D hydrodynamical simulations (note, however, that D_z may appreciably differ from the alpha turbulent viscosity in 3D MHD simulations, depending on the level of turbulent activity across the disc's vertical extent; see e.g. Yang, Mac Low & Johansen 2018). The spatial grid used to produce the continuum emission maps covers $2H$ on both sides of the disc mid-plane with 36 cells logarithmically spaced in colatitude.

(iii) To compute opacities for dust particles with an internal density of 0.1 g cm^{-3}, we assume that the dust is a mixture of a silicate matrix (internal density of 3.2 g cm^{-3}), water ices (internal density of 1.0 g cm^{-3}), and a vacuum inclusion. Assuming that the mix aggregate has 30 per cent of its solids being silicates and 70 per cent water ices, the level of porosity (volume fraction of vacuum) needed to produce grains with a density of 0.1 g cm^{-3} is ∼92 per cent. We apply the Bruggeman rules to compute the optical constants of the mix. The optical constants of water ices are obtained from the Jena data base, those of astrosilicates are from Draine & Lee (1984). We use the Mie theory to compute the absorption and scattering opacities for anisotropic scattering and the mean scattering angle (Bohren & Huffman 1983). We have checked that both our absorption and scattering opacities are in accordance with those calculated by Kataoka et al. (2014).

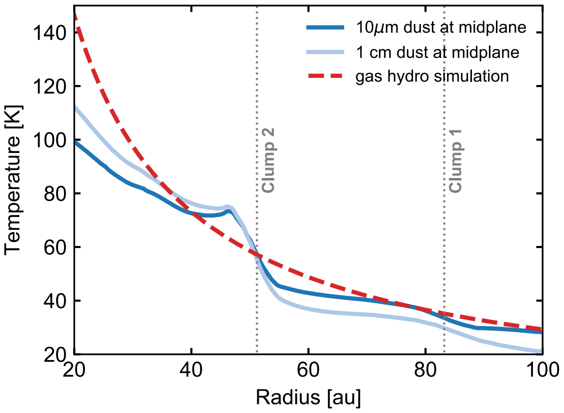

Figure 1. Azimuthally averaged radial profile of the dust's mid-plane temperature (solid curves) for the smallest (10 µm) and largest (1 cm) dust particles contributing to the (sub)millimetre continuum synthetic maps, and radial profile of the gas temperature in the hydrodynamical simulation (dashed curve). The dotted lines mark the location of Clumps 1 and 2.

The raw maps of continuum emission (maps prior to beam convolution) computed by RADMC3D include both absorption and scattering, assuming Henyey–Greenstein anisotropic scattering. The dust temperatures are computed first with a thermal Monte Carlo calculation. As can be seen in Fig. 1, the azimuthally averaged radial profile of the dust's mid-plane temperature obtained with our thermal Monte Carlo calculation for the smallest (10 µm) and largest (1 cm) dust particles is similar to the gas temperature profile of our hydrodynamical simulation near Clumps 1 and 2, where the vast majority of the dust particles is concentrated (it is also consistent with Boehler et al. 2018's temperature profile, see Section 2.1.2, despite different size distributions, masses and opacities for the dust). The continuum image is then computed by ray tracing.

Some of the synthetic maps of continuum emission shown in Section 3 include noise. This is particularly helpful for the maps at 9 mm, since the peak intensities at Clumps 1 and 2 in the VLA image of Casassus et al. (2019), which combines data sets in the A, B, and C array configurations, are only about 15 and 7 times higher than the rms noise level, respectively. Instead of simulating the exact same uv coverage and thermal noise as in the observed data sets, we adopt a much simpler strategy, which is to add white noise to the raw maps of continuum emission. This is done by adding at each pixel of the raw maps a random number that follows a Gaussian probability distribution with zero mean and standard deviation consistent with the rms noise in the observations. For the synthetic maps at 9 mm, the standard deviation is set to 2 µJy beam^{-1}, which is the rms noise level in Casassus et al. (2019)'s VLA image. Similarly, the noise standard deviation in the synthetic maps at 0.9 mm is 20 μJy beam^{-1}, which is the rms noise level in Dong et al. (2018)'s ALMA image.

The raw flux maps at 0.9 mm are finally convolved with the same beam as in the ALMA image of Dong et al. (2018) (0.052 arcsec × 0.042 arcsec PA −7.1°), and the raw flux maps at 9 mm with the same beam as in the VLA image of Casassus et al. (2019) (0.12 arcsec × 0.10 arcsec PA 65°). When included, the noise in the synthetic images thus has a spatial scale that is similar to that of the beam.

2.2.2 *Near-infrared polarized scattered light*

Near-infrared polarized scattered light traces (sub)micron-sized grains at the surface of the disc, which are not included in our hydrodynamical simulations. To produce scattered light predictions, we include 12 bins of small grains ranging from 0.01 to 0.3 μm, and having the same density distribution and scale height as the gas in the simulations (these small grains are expected to be well coupled to the gas in our disc model). We artificially truncate the dust density within 0.15 arcsec (∼24 au) to avoid a strong contribution of the disc's inner parts to the polarized intensity, which is not observed (Benisty et al. 2015). We also reduce the dust density beyond 0.35 arcsec (∼56 au, by a factor ∝ r^{-2}) to decrease the scattering off dust grains outside the inner edge of the outer planet's gap. The outer reduction is meant to mimic shadowing effects due to the gas spirals propagating between the two planets.

We further assume that the small grains are compact monomers forming a mixture of 60 per cent silicate and 40 per cent amorphous carbon, with an equivalent internal density of 2.7 g cm^{-3}. The optical constants for amorphous carbons are taken from Li & Greenberg (1997). The grains have a size distribution $n(s) \propto s^{-3.5}$, and their total mass is $\sim 1.6 \times 10^{-5} M_\star$ (or ∼8 $M_\oplus$) in the results of Section 3. The grid used to compute the polarized scattered light images covers 5 pressure scale heights on both sides of the disc mid-plane with 30 cells evenly-spaced in colatitude.

To obtain the synthetic images of polarized scattered light, the dust temperatures are first computed with a thermal Monte Carlo calculation. We then compute the emergent Stokes maps Q and U at 1.04 μm (Y-band), which represent linear polarized intensities. Scattering is assumed to be anisotropic, and a full treatment of polarization is adopted using the scattering matrix as implemented in RADMC3D. When included, white noise is added to the Stokes maps by adding at each pixel of the maps random numbers that have Gaussian probability distributions with zero mean and a standard deviation of 0.4 per cent the maximum value of each map. This value is found to give a level of noise in the final convolved image of polarized scattered light that is close to that in the Y-band polarized intensity observation of Benisty et al. (2015), which we will compare our synthetic images to. A mask of 0.2 arcsec in radius is further applied to the Stokes maps so as to enhance the brightness of the spirals. The Stokes maps are then convolved with a circular beam of full width at half-maximum (FWHM) 0.026 arcsec, which corresponds to the angular resolution achieved in Benisty et al. (2015). Next, the convolved Stokes maps are post-processed to obtain the local Stokes Q_ϕ following the procedure described in Avenhaus et al. (2017). Each pixel of the Q_ϕ synthetic image is finally scaled with the square of the deprojected distance from the central star in order to compare with the SPHERE image of Benisty et al. (2015).

3 RESULTS

We present in this section the results of our hydrodynamical simulation, starting in Section 3.1 with the time evolution of the gas surface density and of the dust's spatial distribution in response to the two planets. We show that the planets form dust-trapping vortices at the edges of their gap as a result of the RWI. Vortices may not be long-lived structures, however, and dust particles can progressively lose the azimuthal trapping of their vortex when the latter decays on account of the disc's turbulent viscosity. Based on the ALMA and VLA continuum observations of Dong et al. (2018) and Casassus et al. (2019), which are displayed in the right-hand panels of Figs 4 and 5, we argue that Clump 1 is consistent with azimuthal trapping in a vortex, while Clump 2 is more consistent with loss of azimuthal trapping in a decaying vortex. This is what we show in Section 3.2, where we compare our (sub)millimetre continuum synthetic maps with the observations. We then show in Section 3.3 that the two main spirals in the SPHERE image of Benisty et al. (2015), which is displayed in the right-hand panel of Fig. 6, can be reproduced by two of the spiral waves induced by the outer planet in our disc model. Our synthetic maps have a fair number of free parameters, and our aim here is not to find a set of parameters that would fit the observations, but rather show that the two-vortex/two-planet scenario can indeed reproduce the most salient features in the MWC 758 disc.

3.1 Gas and dust evolutions

3.1.1 *Gaps, spirals, and vortices in the gas*

The planets in our disc model progressively carve a gap in the gas around their orbit. This is illustrated in the left-hand panels of Fig. 2, which display the perturbed gas surface density relative to its initial radial profile, $(\Sigma - \Sigma_0)/\Sigma_0$, at 611, 1277, and 2213 orbits after the beginning of the simulation (which is about 0.10, 0.22, and 0.38 Myr after the planets have reached their final mass). Results are shown in polar coordinates with the radius range (x-axis) narrowed to highlight the disc structure between the planets. The white circles spot the position of the planets. At 2213 orbits (near the end of the simulation), the azimuthally averaged surface density of the gas has decreased by about 70 per cent of its initial value at the bottom of the inner planet's gap, and by about 95 per cent at the bottom of the outer planet's gap. The inner edge of the gap carved by the outer planet in the disc gas, which is at ∼90 au, is consistent with the truncation radius of the C^{18}O ring in Boehler et al. (2018)'s ALMA band 7 data (see their fig. 4). The left panels of Fig. 2 also show multiple spiral arms in the disc gas, with some spirals more prominent than others. It is not straightforward to tell from these panels where each spiral originates, since spirals are triggered by the planets and the gas vortices that form in the disc. It is actually not straightforward either to tell where the vortices are, since the gas density perturbation in the spirals is as large, if not larger, than that in the vortices located between the planets.

The presence of gas vortices is more easily seen in the middle panels of Fig. 2, which display the perturbation of the gas vortensity[1] relative to its initial profile [the quantity $\{\omega - \omega_0\}/\omega_0$]. Anticyclonic vortices show up as local minima in the gas perturbed vortensity in both the radial and azimuthal directions. A large-scale vortex is clearly visible at the inner edge of the outer planet's gap (near 85 au) at 611 and 1277 orbits. It is, however, no longer active at 2213 orbits, which can be seen by the fact that the vortensity minimum at this location has turned axisymmetric (based on the gas vortensity,

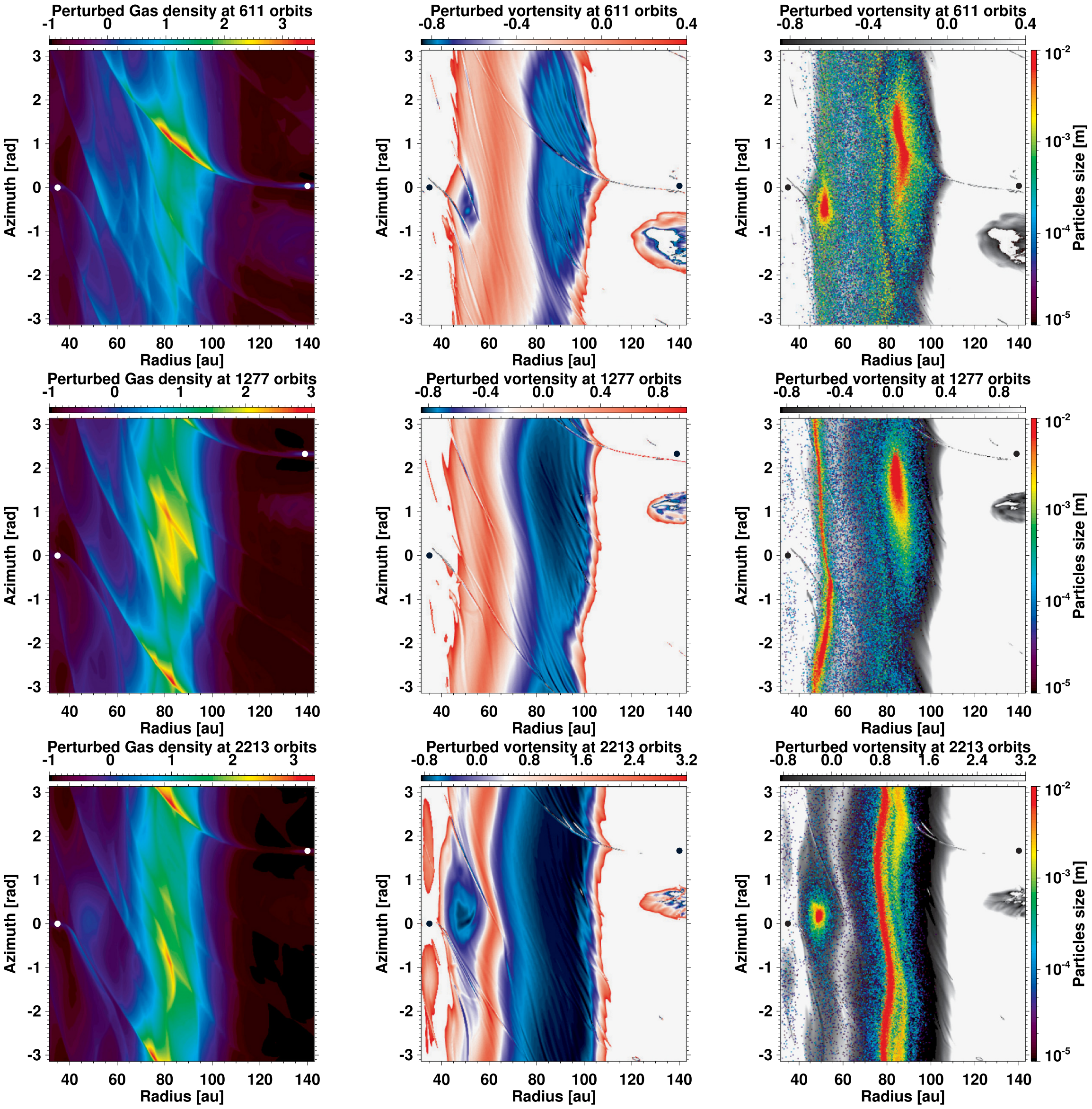

Figure 2. Gas structure and dust spatial distribution in the disc region between the planets. Results are shown in polar cylindrical coordinates at 611, 1277, and 2213 orbits from top to bottom. Left: perturbed gas surface density relative to its initial profile, $(\Sigma - \Sigma_0)/\Sigma_0$. Middle: perturbed gas vortensity relative to its initial profile, $(\omega - \omega_0)/\omega_0$. The colour scale has been adjusted to highlight the large-scale azimuthal minima of vortensity, which trace the gas vortices. Right: same as the middle panels, but with a sequential colourmap for the contours of perturbed vortensity, and with the location of the dust particles overlaid by coloured dots. The colour bar on the right-hand side shows dust size in metres. In each panel, the filled circles at 35 and 140 au mark the position of the planets.

we estimate the lifetime of this vortex to be about 1800 orbits). The fact that the outer planet forms a vortex at the inner edge of its gap via the RWI is the consequence of the rather large planet's mass, which initially allows the persistence of a radial pressure bump (or vortensity minimum) at this location notwithstanding the local turbulent viscosity (Bae, Zhu & Hartmann 2016). We have checked with a dedicated simulation that a very similar vortex structure forms in the absence of the inner planet.

The vortensity panels in Fig. 2 also show a vortex around the L5 Lagrange point located behind the outer planet in azimuth (at 140 au). Although not shown in Fig. 2, another vortex is situated at the outer edge of the outer planet's gap near 230 au. There is no indication for vortices at both these locations in the (sub)millimetre observations of MWC 758, but it could be that the amount of dust trapped there is too small to have a measurable effect on the continuum emission.

A vortex also forms at the outer edge of the inner planet's gap, near 50 au. This vortex has a rather unusual time evolution: it is active during the first 1000 orbits, it then decays and becomes inactive over the next 500 orbits, and finally builds up again and remains active for at least 700 more orbits (until the end of the simulation). This can be seen in the second column of panels in Fig. 2 by the presence at

611 and 2213 orbits of an azimuthal minimum in the gas perturbed vortensity at ∼50 au that is absent at 1277 orbits. The vortex decay coincides with a moderate increase in the eccentricity of the disc gas between the planets. This can be noticed by looking at the contours of perturbed vortensity. For instance, the vortensity maximum that is located around 60 au at 611 orbits is associated with gas on non-circular trajectories at 1277 orbits, with an eccentricity close to 0.1. This point will be further emphasized when describing the dust's spatial distribution in Section 3.1.2.

The gas between the planets retains some level of eccentricity until the end of the simulation, yet the vortex forms again near 50 au from ∼1500 orbits. A possible explanation is the progressive increase in the vortensity maximum around 60 au, due to the eccentric motion of the gas and repeated interactions with the shock wakes of the planets. This evolution makes the vortensity minimum at the outer edge of the inner planet's gap increasingly pronounced, which ultimately allows the RWI to set in again and form a vortex at this location. It does not affect the vortensity near the inner edge of the outer planet's gap, however, and the vortex initially formed at this location progressively decays on account of the gas turbulent viscosity. Vortex decay will be further discussed in Section 4.2.

The reason why the disc gas between the planets becomes moderately eccentric is not clear. The growth of a global eccentric mode with azimuthal wavenumber $m = 1$ has been observed in some simulations of massive self-gravitating discs (e.g. Pierens & Lin 2018; Pérez et al. 2019); however, our Toomre Q parameter seems too high to support this idea (furthermore, the increase in the gas eccentricity is confined to the disc parts between the planets, and is therefore not global). Another possibility is that disc–planet interactions could account for this local increase in the disc eccentricity. This proposal deserves a specific study, which is beyond the scope of this paper.

We finally discuss the aspect ratio χ of the vortices, which measures their elongation. A rough estimate of χ can be obtained by using contours of constant perturbed vortensity in the second column of panels in Fig. 2. For instance, at 611 orbits, the aspect ratio of the vortex near 85 au can be estimated by using the light blue contour which marks a relative perturbation of vortensity of about −0.76. In doing so, the vortex can be approximated as an ellipse that extends from about −1.5 to 2.5 rad in azimuth, and from about 80 to 100 au in radius, which corresponds to $\chi \sim 18$. Interestingly, similar aspect ratios can be estimated for the inner vortex at 611 orbits and for the outer vortex at 1277 orbits. In the same vein, we have checked that similar values for the aspect ratio of the outer vortex can be obtained based on the raw fluxes of continuum emission at 0.9 and 9 mm at 1277 orbits (see also Section 3.2.2) as well as on the reconstructed dust's surface density (by approximating the spatial distribution of aforementioned quantities as ellipses, and measuring their aspect ratio).

3.1.2 Dust trapping in the vortices

The third column of panels in Fig. 2 displays the spatial distribution of the dust particles on top of the vortensity perturbation at 611, 1277, and 2213 orbits. The dust particles have a Stokes number ranging from about 10^{-5} to 0.1 in all the panels. The first thing to notice is that nearly all particles are confined between the planets, and more particularly along two rings. This is because the particles are inserted between the planets at 300 orbits after the beginning of the simulation, when the planets have already started to carve their gap. Particles thus tend to drift towards the inner edge of the outer planet's gap, or towards the outer edge of the inner planet's gap, since both locations are pressure maxima in the radial direction. We see that a few (mostly small) particles can cross the inner planet's gap, which is due to the effect of dust turbulent diffusion kicking particles away from (and inside of) the gap's edge.

The panels further illustrate the dust's azimuthal trapping in the vortices. The top right-hand panel makes it clear that dust trapping correlates with minima in the gas vortensity rather than with maxima in the gas surface density. We also notice in this panel that the large particles trapped in the outer vortex get deflected inwards upon crossing the primary wake induced by the outer planet. We will come back to this effect in Section 4.3.1.

In the middle right-hand panel at 1277 orbits, we see that dust is still trapped in the outer vortex, that it is slightly eccentric, and that the azimuth at which these particles are trapped varies continuously with increasing particles size. By comparison, it is quite clear that the dust particles at the outer edge of the inner planet's gap have lost azimuthal trapping as the inner vortex has decayed. They form a narrow eccentric ring, and from the orbital radius of the largest, cm-sized particles, which range from about 45 to 55 au, we infer a local eccentricity ≈0.1, very similar to that of the background gas (see Section 3.1.1). This eccentricity is consistent with that of the inner ring passing by Clump 2 in the ALMA observation of Dong et al. (2018) (see also Section 3.2). This dust ring is not axisymmetric, which reflects the fact that particles progressively lose memory of their former azimuthal trapping on different time-scales depending on their size, much like in the simulations carried out in Fuente et al. (2017) to account for recent submillimetre observations of the AB Aurigae disc. We also note the presence of a faint eccentric ring of $\lesssim$1 mm dust particles slightly interior to Clump 1, between ∼70 and 80 au, which is reminiscent to the ring of emission at ∼0.43 arcsec seen in the ALMA observation of Dong et al. (2018). Comparison with Fig. 7 (Section 4.3.1) suggests that this ring could be due in part to deflections by the inner wake of the outer planet.

In the bottom right-hand panel of Fig. 2, at 2213 orbits, the inner vortex is formed again and it efficiently traps the dust at the outer edge of the inner planet's gap. The outer vortex is now decayed, and the dust that was trapped at the outer vortex progressively acquires a near axisymmetric spatial distribution. This redistribution is not similar to that of the dust in the inner vortex when the latter had decayed. The dust leaving the outer vortex shifts radially inwards at a rate that depends on dust size. This shift, which arises because of repeated deflections upon crossing the inner wake of the outer planet, will be further described in Section 4.3.1.

Anticipating the results of the radiative transfer calculations in Section 3.2, we find that the faint emission of the inner ring passing by Clump 2 in the VLA observation of Casassus et al. (2019) cannot be accounted for by a compact dust distribution such as the one obtained in the early and late stages of our hydrodynamical simulation when the inner vortex is active. When the inner vortex is active, we find that the predicted peak intensity at 9 mm is indeed 1.5–2 times larger at Clump 2 than at Clump 1, while the observed ratio is ∼0.4 (see Section 3.2.1). We thus need the inner vortex to have decayed for the dust trapped at the outer edge of the inner planet's gap to be distributed along an eccentric ring, and yet have a non-axisymmetric distribution. This is precisely the kind of distribution that the dust has in our simulations between ∼1000 and 1500 orbits, and which we have illustrated at 1277 orbits in the middle row of panels in Fig. 2.

We actually found a fair number of outputs in our simulation between 1000 and 1500 orbits that could account for the main observational features of the continuum maps at 0.9 mm (eccentric

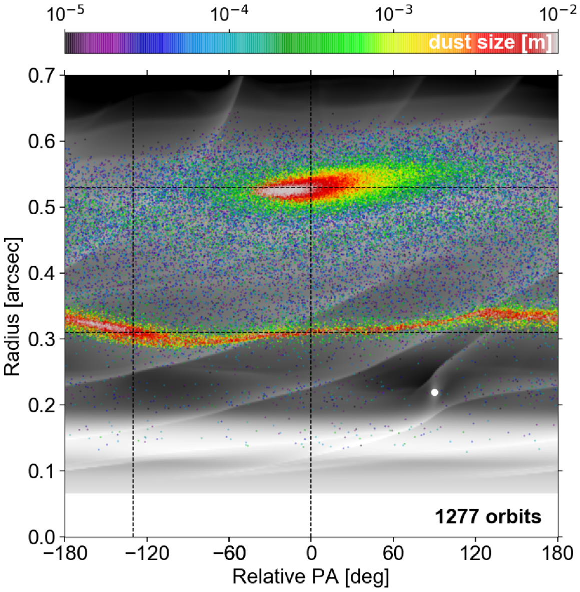

Figure 3. Gas surface density and dust spatial distribution in the hydrodynamical simulation at 1277 orbits (~0.2 Myr). The gas surface density is shown by black and white contours with a logarithmic colour scale (density increases from 0.1 to 10 $\mathrm{g\,cm^{-2}}$ from black to white). The location of the dust particles is marked by coloured dots (colour varies with dust size, see colour bar on top of the image) and that of the inner planet by a white circle. Results are displayed in the disc plane, with the y-axis indicating distance from the central star in arcseconds (assuming a disc distance of 160 pc), and the x-axis the position angle (or azimuth) relative to the approximate location of the largest particles in the outer vortex. The image has been flipped horizontally to reflect that the disc is rotating clockwise in the observations, but counterclockwise in the simulation. The dashed lines show the radius and position angle of the two clumps of emission in the deprojected ALMA continuum image of Fig. 4.

inner ring passing by Clump 2 with Clump 2 near pericentre, compact emission at Clump 1, azimuthal shift of about 130° between Clumps 1 and 2) and at 9 mm (compact emission at Clump 1, faint emission at Clump 2). Out of these outputs, the one that best reproduces the observed maps is that at 1277 orbits.

We finish this section by describing Fig. 3, which depicts again the dust's spatial distribution at 1277 orbits, but now on top of the gas surface density in log scale. Results are displayed in polar coordinates, with the orbital radius in arcseconds in y-axis, and the azimuth (or position angle) relative to the approximate location of the largest particles in the outer vortex in x-axis. The inner planet is visible at $x = 90^{\circ}$, $y \sim 0.22$ arcsec. The figure is meant to be compared with the deprojected synthetic images of the (sub)millimetre continuum emission and of the near-infrared scattered light shown in Figs 4–6. It helps to understand how the dust particles in the simulation contribute to the (sub)millimetre continuum synthetic maps, which are most sensitive to the largest (mm- to cm-sized) particles that lie near the mid-plane. It also helps to see how the spiral density waves in the gas contribute to the polarized intensity image.

3.2 Continuum emission in the (sub)millimetre

A side-by-side comparison of our synthetic maps of continuum emission with the ALMA image of Dong et al. (2018, $\lambda \approx 0.9$ mm) and the VLA image of Casassus et al. (2019, $\lambda \approx 9$ mm) is displayed in Figs 4 and 5, respectively. In each figure, the projected maps (flux maps in the sky plane) are in the upper panels, and the deprojected maps (flux maps in the disc plane) are in the lower panels. Fig. 4 shows only the synthetic map at 0.9 mm with white noise since its amplitude is very small (the predicted peak intensity at Clump 2 is ~200 times larger than the rms noise level). Fig. 5, however, displays the synthetic map at 9 mm without and with white noise since the predicted peak intensity at Clump 1 is only ~12 times the rms noise level. For comparison with our synthetic maps at 9 mm, the star has been subtracted in the VLA images shown in the right column of panels in Fig. 5. We point out that the noise in the VLA observation includes smaller scales than our synthetic map with white noise. This is most likely due to the core of the VLA dirty beam not being perfectly represented by an elliptical Gaussian.

Overall, for the assumed dust properties, our two-vortex model captures the main features of the two clumps of emission observed in the ALMA and VLA images. The dust-trapping vortex at the inner edge of the outer planet's gap can reproduce the compact emission associated with Clump 1 (at ~1 o'clock in both the ALMA and VLA images). In particular, we recover the fact that Clump 1 is azimuthally broader at 0.9 mm than at 9 mm, as expected with azimuthal dust trapping. The decaying vortex at the outer edge of the inner planet's gap reproduces well the eccentric inner ring passing by Clump 2, with Clump 2 near pericentre (at ~5 o'clock in the ALMA image). It also forms a secondary clump of emission near apocentre that could account for the emission seen to the east of the ring in the ALMA image (at ~9 o'clock). And importantly, we recover the more diffuse and rather low level of emission seen in the VLA image for Clump 2. By comparing the synthetic deprojected maps in Figs 4 and 5 with Fig. 3, it is easy to see that the location of the maxima in the synthetic maps corresponds to that of the largest dust particles in the simulation (those ranging from a few mm to a cm in size).

Comparison between the synthetic and observed flux maps at 0.9 mm further indicates that Clump 1 and Clump 2 lie on top of a fainter ring of background emission. This background emission could trace a rather massive population of small dust well coupled to the gas. This idea will be presented in Section 4.3.5 and illustrated in Fig. 8. We also note the presence in our synthetic map at 0.9 mm of a faint ring of emission slightly interior to Clump 1, at a level of emission (~0.1 mJy $\mathrm{beam^{-1}}$) that is close to the rms noise level adopted in the synthetic map. This faint ring of emission traces the dust ring situated between 0.44 arcsec and 0.50 arcsec in Fig. 3 (or, equivalently, between ~70 and 80 au in the middle right-hand panel of Fig. 2). As already stated in Section 3.1.2, this ring is reminiscent to the ring of emission around 0.43 arcsec in the ALMA observation of Dong et al. (2018), and which peaks at about 0.6 mJy $\mathrm{beam^{-1}}$ in the right-hand panels of Fig. 4.

We also briefly comment that the inclusion of anisotropic scattering in the radiative transfer calculations has a minor impact on our (sub)millimetre continuum synthetic maps. At 0.9 mm, anisotropic scattering increases the overall level of flux by only a few per cent compared to a radiative transfer calculation that only includes thermal absorption. At 9 mm, anisotropic scattering increases the overall level of flux by about 20 per cent.

In the following, we provide a more quantitative comparison between our predictions and the observations, in terms of the peak intensities, and the widths and aspect ratio of Clump 1. We also quote the peak absorption optical depths in the synthetic maps.

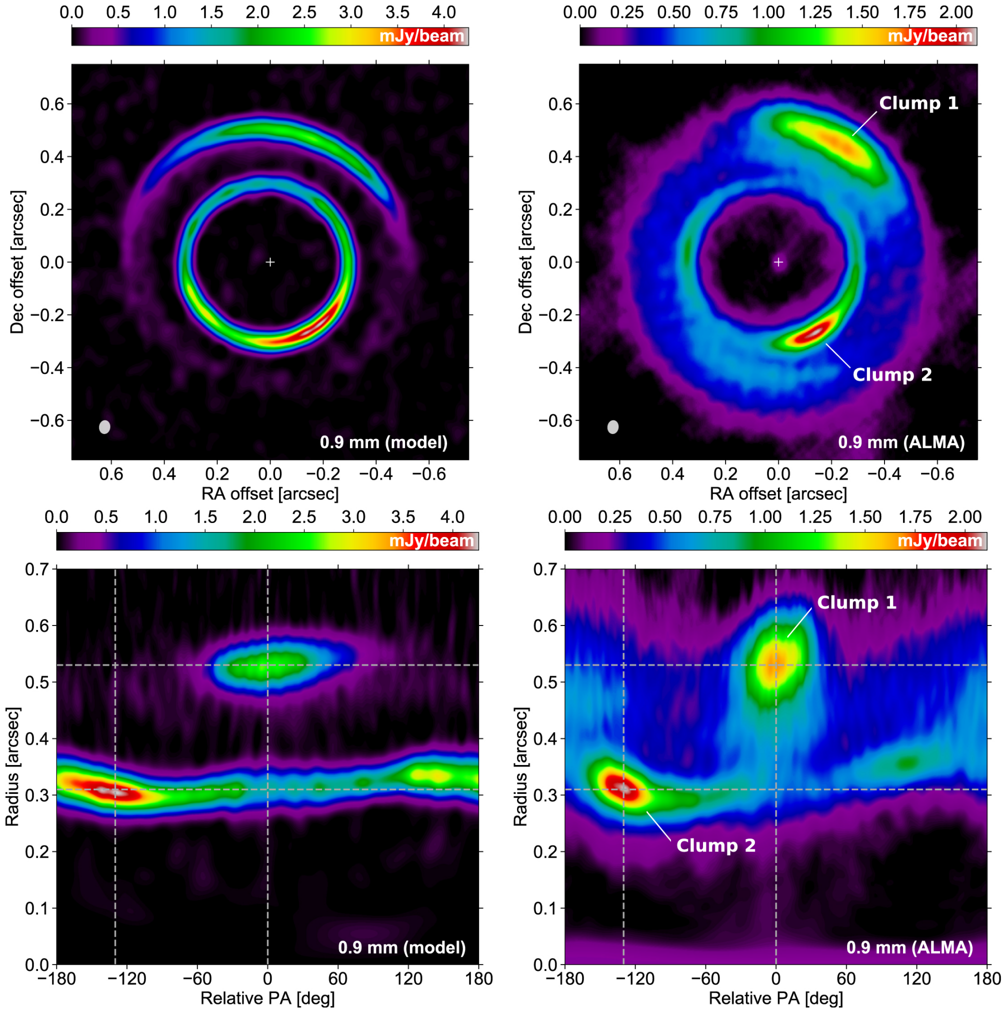

Figure 4. Predicted continuum emission at 0.9 mm with white noise (left-hand panels) compared with the ALMA band 7 observation of Dong et al. (2018, right-hand panels, images in natural weights). Upper panels: projected maps. The *x*- and *y*-axes indicate the offset from the stellar position in the right ascension (RA) and declination (Dec.) in arcseconds, i.e. north is up and east is to the left. The beam (0.052 arcsec × 0.042 arcsec PA −7.1°) is shown by the ellipse in the bottom-left corner in each panel, and the star by a plus symbol. Lower panels: deprojected maps (assuming a disc inclination of 21° and a position angle of 62°). The *y*-axis shows orbital radius in arcseconds, and the *x*-axis shows the position angle in degrees relative to that of Clump 1. The dashed curves mark the position angle (relative to Clump 1) and orbital radius of each clump in the ALMA image.

3.2.1 Peak intensities

At Clump 1, the predicted peak intensity at 0.9 mm is ∼2.6 mJy beam^{-1}, which is ∼50 per cent larger than the observed value, while the predicted peak intensity at 9 mm is ∼24.8 μJy beam^{-1} (without noise), which is close to the observed value of 29.1 ± 2.0 μJy beam^{-1}. At Clump 2, the predicted peak intensity at 0.9 mm is ∼4.2 mJy beam^{-1} (about twice the observed value), that at 9 mm is ∼17.0 μJy beam^{-1} (without noise), which is ∼1.6 times larger than the observed value of 10.8 ± 2.0 μJy beam^{-1}. Our model thus tends to produce a little too much flux at Clump 2, although a direct comparison is not trivial because of different shapes and emitting areas for Clump 2 in the predictions and the observations.

The predicted peak intensity ratio between Clumps 1 and 2 is about 0.6 at 0.9 mm and 1.4 at 9 mm, while the observed values are about 0.8 at 0.9 mm and 2.7 ± 0.3 at 9 mm. We interpret the larger peak intensity ratio at 9 mm as a consequence of the vortex decay that leads to Clump 2 in our model. We have checked this by computing synthetic flux maps at 611 orbits, when the inner vortex is still active (see top panels in Fig. 2), which show that the peak intensity ratio takes very similar values at both wavelengths (it is about 0.5 at 0.9 mm and 0.6 at 9 mm).

We point out that in the ALMA band 7 observations of Boehler et al. (2018), for which the angular resolution is about twice as large as in the ALMA band 7 observations of Dong et al. (2018), Clump 1 has a larger peak intensity than Clump 2. The peak intensity ratio between Clumps 1 and 2 is about 1.6 in Boehler et al. (2018), while it is about 0.8 in Dong et al. (2018). By convolving our raw flux maps with the same beam as Boehler et al. (2018)'s observations (0.11 arcsec × 0.08 arcsec PA 38°), we find a peak intensity ratio between Clumps 1 and 2 of ∼0.85, thus larger than the value of ∼0.6 that we get with the same resolution as in Dong et al. (2018), but still smaller than 1. Our model cannot reproduce the reversal

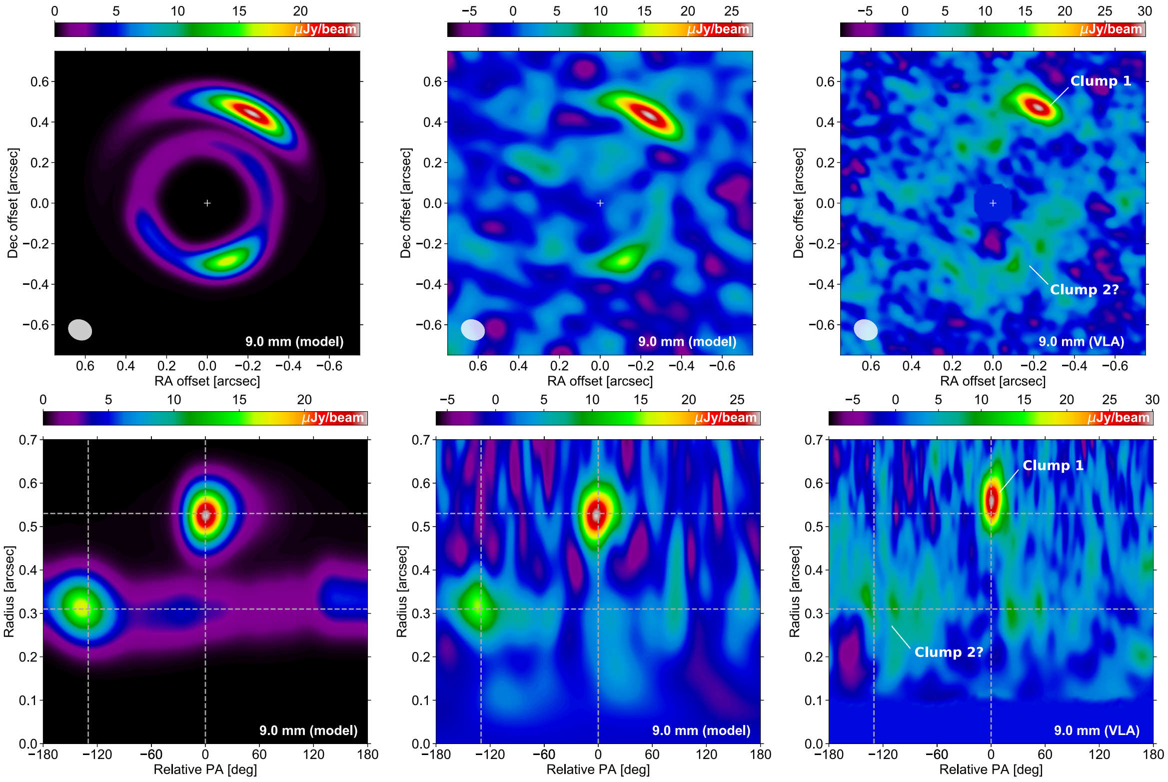

Figure 5. Predicted continuum emission at 9 mm without and with white noise (left and middle panels, respectively) compared with the VLA observation of Casassus et al. (2019, right-hand panels). The star has been subtracted in the VLA images. Upper panels: projected maps (as in the upper panels of Fig. 4). The beam (0.12 arcsec × 0.10 arcsec PA 65°) is shown by the ellipse in the bottom-left corner in each panel, and the star by a plus symbol. Lower panels: deprojected maps (as in the lower panels of Fig. 4). The dashed curves mark the position angle (relative to Clump 1) and orbital radius of each clump in the ALMA image shown in Fig. 4.

in the peak intensity ratio between both aforementioned angular resolutions.

We finally note that Clump 1 is offset by about 0.03 arcsec in the ALMA and VLA images, which is not reproduced in our models. On the contrary, there is no significant azimuthal shift between the positions of Clump 1 in the ALMA and VLA images, whereas the synthetic images show an azimuthal shift by about 10°, with the peak at 9 mm shifted clockwise (in the direction opposite to that of rotation). A very similar azimuthal shift is actually predicted for Clump 2. We stress that this azimuthal shift is not a systematic prediction of our models: at some other outputs in the simulation, the azimuthal shift is in the opposite direction (shift by $\sim -10°$), while at some other outputs we find no azimuthal shift. The predicted azimuthal shift is likely related to Clump 1's eccentricity.

3.2.2 *Widths and aspect ratio of Clump 1*

From the polar maps displayed in Figs 4 and 5, we see that Clump 1 tends to have a slightly larger azimuthal width and smaller radial width in the synthetic maps than in the observations. In the azimuthal direction, the predicted FWHM of the convolved intensity across the peak is about 45° and 19° at 0.9 and 9 mm, respectively, while the observed values are about 28° and 12°. Similarly, in the radial direction, the predicted FWHM of the convolved intensity across the peak is about 0.04 and 0.05 arcsec at 0.9 and 9 mm, respectively, while the observed values are about 0.08 and 0.06 arcsec. A similar analysis can be done for Clump 2, with the same conclusion that, in our model, Clump 2 tends to be a little narrower in radius and somewhat broader in azimuth than in the ALMA observation of Dong et al. (2018). Fine tuning of the disc gas parameters (surface density, temperature, alpha viscosity) and of the dust parameters (size distribution, mass, internal density) could potentially reconcile our predictions and the data. A full parameter search is beyond the scope of this work.

Moreover, from the radial and azimuthal widths of Clump 1 in the emission maps, and the radial location of the peak intensity, we can estimate again the aspect ratio χ for Clump 1. We find that the predicted χ values amount to ∼10.2 and ∼3.5 at 0.9 and 9 mm, respectively, while the observed values are ∼3.2 and ∼1.8 (with about 10 per cent relative uncertainties). These values are much smaller than the one obtained via the gas perturbed vortensity in the vortex from which Clump 1 originates (see the last paragraph in Section 3.1.1). We have checked that this discrepancy comes about because of the beam convolution. Upon calculating the synthetic maps of raw intensity (intensity of continuum emission prior to beam convolution), we obtain $\chi \approx 16 \pm 2$ at both wavelengths, which agrees well with the vortex's aspect ratio measured via the gas vortensity, and also with the value reported in Casassus et al. (2019) where steady-state dust trapping predictions based on Lyra & Lin (2013) are used to model the raw intensity for Clump 1 at 0.9 and 9 mm.

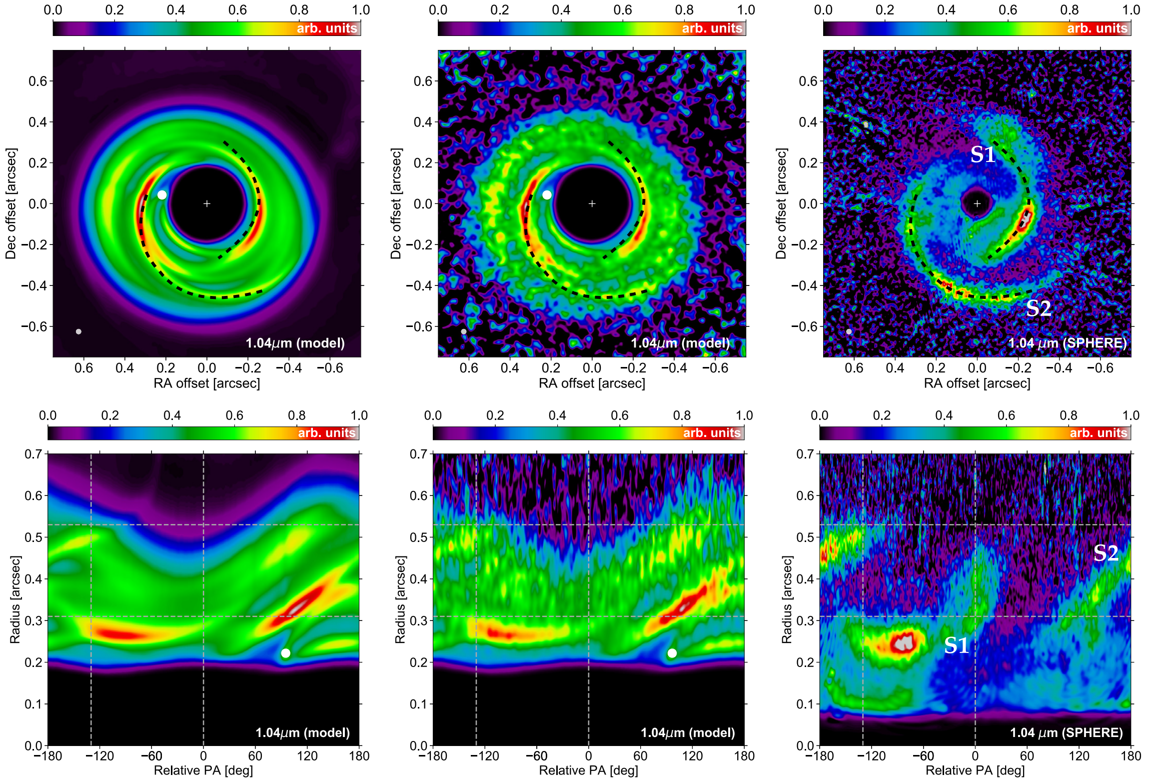

Figure 6. Synthetic scattered light image at 1.04 μm without and with noise (left and middle panels, respectively) compared with the *Y*-band SPHERE image of Benisty et al. (2015, right-hand panels). In each image, the polarized intensity is scaled by the square of the deprojected distance from the central star, and normalized such that the intensity of the strongest pixel is 1. To highlight the spirals structure, a mask of 0.2 arcsec radius is applied to the synthetic images. Upper panels: projected maps (as in the upper panels of Fig. 4). The beam (0.026 arcsec × 0.026 arcsec) is shown by the ellipse in the bottom-left corner in each panel, the star by a plus symbol, and the inner planet by a white circle. The outer planet is outside the image domain (at 0.87 arcsec, PA $-60°$). The dashed curves in all three panels are used to compare the synthetic and observed asymmetries, but they are not fits to the observed spiral traces. Lower panels: deprojected maps (as in the lower panels of Fig. 4). The position of the inner planet is marked by a white circle in the synthetic images. The dashed curves mark the position angle (relative to Clump 1) and orbital radius of each clump in the ALMA image shown in Fig. 4.

3.2.3 *Peak optical depths in absorption*

An interesting information that is accessible with our synthetic maps of continuum emission is the absorption optical depth that our model predicts at the location of the peak intensities. At 0.9 mm, we find maxima in the absorption optical depth of about 30 and 15 for Clumps 1 and 2, respectively. The continuum emission at 0.9 mm is therefore very optically thick near the centre of both clumps. At 9 mm, the absorption optical depth peaks at about 0.9 and 0.4 for Clumps 1 and 2, respectively, which are perhaps surprisingly large values at this wavelength. The peak absorption optical depth at 9 mm near the centre of Clump 1 is a bit larger than the value of $\sim$0.3 predicted by the steady-state dust trapping predictions used in Casassus et al. (2019), but note that the gas vortex and dust distribution assumed to give rise to Clump 1 in Casassus et al. (2019) have different physical parameters than in our simulation (different alpha turbulent viscosity, temperature, dust's internal density and opacity; see Section 3.3.2 in Casassus et al. 2019 for comparison).

3.3 Polarized scattered light in *Y* band

A side-by-side comparison between our synthetic map of polarized scattered light with the *Y*-band ($\lambda = 1.04$ μm) scattered light image of Benisty et al. (2015) is displayed in Fig. 6. The projected maps are in the upper panels, and the deprojected maps in the lower panels. The synthetic maps in the first column of panels do not include noise, those in the second column include white noise with the method described in Section 2.2.2. All images are multiplied by the square of the deprojected distance from the central star, and normalized such that the intensity of the strongest pixel is 1. To highlight the asymmetric structures in our synthetic map, a mask of 0.2 arcsec radius is applied. Recall that the dust density within 0.15 arcsec has been truncated and that beyond 0.35 arcsec has been reduced (see Section 2.2.2). The same dashed curves are superimposed in the upper panels to compare the predicted and observed asymmetries; however, we stress that they are not fits to the observed spiral-like features – they are just drawn to guide the eye.

Overall, we see that our model predicts several spiral arms, but two are more prominent. Just like the spirals in the gas surface density of the simulation (see Figs 2 and 3), the spirals in the synthetic scattered light image do not all have a clear origin, as they trace spiral density waves due to either the planets, the vortices, or a combination thereof. Some insight into the origin of the spirals and/or asymmetries in the synthetic image can be gained by comparing the deprojected maps with the gas surface density contours in Fig. 3. Interestingly, we see that our synthetic map can reproduce both the location and the winding of the observed spiral arm to the south-east very well (see the dashed curve denoted by

S2 in Fig. 6). According to our model, this spiral arm would be the (primary) inner wake of the outer planet, which propagates from the outer planet's position. Our synthetic image shows a second prominent spiral to the west, which corresponds to a secondary spiral density wave induced by the outer planet. This spiral nearly coincides with the bright concentric arc to the west of the SPHERE image (see the lower part of the dashed curve denoted by S1 in Fig. 6). The same spiral is (mainly) responsible for the emission to the east of the synthetic map (near 9 o'clock beyond 0.4 arcsec), but this emission is not observed in the SPHERE image. The arc-shaped peak slightly inside of Clump 1 does not have a clear counterpart in our synthetic map.

The synthetic *Y*-band polarized light images in Dong et al. (2015, 2018), which are obtained from 3D hydrodynamical simulations, had previously shown that the two inner wakes of a planet several times the mass of Jupiter could qualitatively account for the two spiral arms in the SPHERE image of MWC 758. Note, however, that the planet that they considered was located at ∼0.6 arcsec (100 au), which is quite close to Clump 1 in the (sub)millimetre images (∼85 au), and it seems difficult for such a massive planet to form a dust-trapping vortex at this short separation.

We finally stress that a realistic energy equation and 3D effects, which are not taken into account in our hydrodynamical simulations, could well affect the way spirals would look like in polarized intensity images, in particular the appearance of the secondary wake induced by the outer planet (Zhu et al. 2015; Fung & Dong 2015; Dong & Fung 2017). For this reason, we will not press the comparison between our synthetic polarized intensity image and the observed image too far. It could well be that the reproduction of the S2 spiral is actually coincidental.

4 DISCUSSION AND SUMMARY

4.1 Importance of gas self-gravity

The simulations carried out in this study include gas self-gravity, which might seem unnecessary since the (azimuthally averaged) Toomre Q-parameter remains much larger than unity in our disc model. Q reaches a local minimum of about 30 at the inner edge of the outer planet's gap, near 85 au (Clump 1's location). However, as shown in previous studies (Lin & Papaloizou 2011; Lin 2012; Lovelace & Hohlfeld 2013; Zhu & Baruteau 2016; Regály & Vorobyov 2017), gas self-gravity significantly weakens large-scale RWI vortices (with azimuthal wavenumber $m = 1$) when the product of Q and h becomes smaller than $\sim\pi/2$ at the vortex location. Given our uniform aspect ratio $h = 0.088$, vortices become significantly impacted by self-gravity for $Q \lesssim 18$. Had we taken a larger initial surface density for the gas in our simulations, the vortex formed at ∼85 au would have been weaker and would have therefore decayed earlier. Said differently, with gas self-gravity included, a rather low surface density for the gas at the vortex location is necessary for the dust trap to match the high concentration of dust grains inside the vortex core, and consequently the compactness of Clump 1 seen in the ALMA and VLA observations. This rather low surface density is consistent with that estimated by Boehler et al. (2018) based on ALMA band 7 observations of ^{13}CO and C^{18}O.

4.2 Vortex decay

In this study, we present a scenario where the asymmetric eccentric ring and the compact crescent seen in the ALMA band 7 continuum data of the MWC 758 disc are due to planet-induced vortices. To explain the low and diffuse signal obtained with the VLA at the location of the ring, we propose that this ring results from a decaying vortex. In our simulations, vortex decay is mediated by viscous diffusion ($\alpha = 10^{-4}$), and is found to coincide with a moderate increase in the gas eccentricity between the planets (see Section 3.1.1). Notwithstanding this moderate eccentricity of order 0.1, the lifetime of the vortex that gives rise to the asymmetric ring, about a thousand orbits of the inner planet, is consistent with previous 2D simulations of planet-induced vortices for similar disc parameters and planet masses (e.g. Fu et al. 2014a). A smaller turbulent viscosity would increase the lifetime of the vortices in our simulations. However, as we have checked with preliminary simulations, it would also cause a higher concentration of the large dust particles in the vortices, and would therefore increase the compactness of the (sub)millimetre emission at both dust traps in a way that is not consistent with neither the ALMA nor the VLA observations. On the other hand, a larger turbulent viscosity would shorten the lifetime of the vortices, thereby making the dust's azimuthal trapping scenario for Clump 1 less likely. Furthermore, several factors other than the disc's turbulent viscosity affect the growth and decay time-scales of planet-induced vortices in 2D viscous disc models, including the time-scale for planetary growth (Hammer, Kratter & Lin 2017; Hammer et al. 2019), which is taken to be the same for both planets in our model, a non-isothermal energy equation (Les & Lin 2015), gas self-gravity (Lin & Papaloizou 2011), or dust feedback on the gas (Fu et al. 2014b).

About dust feedback, we stress that for the total mass and size distribution of the dust adopted in our radiative transfer calculations, the dust-to-gas mass ratio in the vortices that correspond to Clumps 1 and 2 does not exceed ∼0.1. This rather low value implies that dust feedback should have a small-to-moderate impact on the vortices if it were included in our hydrodynamical simulations (see e.g. Crnkovic-Rubsamen, Zhu & Stone 2015, who showed that vortices could be destroyed for dust-to-gas mass ratios ≥ 0.3–0.5 within the vortices).

The level of viscosity adopted in our simulations is meant to model the effects of MHD turbulence in the outer regions of a protoplanetary disc, where non-ideal MHD effects, in particular ambipolar diffusion, should play an important role. Modelling turbulence as a diffusion process is uncertain when the typical length scale of interest (here, that of the gas vortex) is of the order of the pressure scale height. Zhu & Stone (2014) have investigated growth of and dust trapping in planet-induced vortices via global 3D MHD simulations. One of their simulations including ambipolar diffusion shows that the vortex formed at the outer edge of the gap carved by a nine Jupiter-mass planet decays in about 1000 orbital time-scales, with a similar lifetime found in a 2D hydrodynamical simulation using an equivalent turbulent viscosity. This result gives credit to the vortex's decay time-scales obtained in 2D viscous disc simulations.

Aside from the effects of MHD turbulence, the growth and persistence of vortices in 3D disc models have been intensively examined over the last decade or so. We mention here a few results that are relevant to our study. Lesur & Papaloizou (2009) have found that anticyclonic vortices could be unstable against the elliptic instability, a parametric instability that mainly occurs at small scales, and which is stronger for vortices with small aspect ratios ($\chi \lesssim 4$). The global 3D simulations of Meheut et al. (2012) have shown that a vortex formed by the Rossby–Wave Instability developed meridional circulation and could survive over hundreds of dynamical time-scales before decaying, most probably because of the elliptic instability. Regarding planet-induced vortices in 3D, the impact of gas self-gravity has been examined by Lin (2012), essentially recovering the predictions of 2D simulations, and the impact of a layered disc structure (through a viscosity increasing with height from the mid-plane) has been tackled by Lin (2014), who found that a high ($\alpha \sim 10^{-2}$) viscosity in the disc's upper layers could largely decrease the vortex's lifetime, despite a modest viscosity ($\alpha \sim 10^{-4}$) in the disc mid-plane. About gas self-gravity, we also highlight the recent work of Lin & Pierens (2018), who have shown with 3D shearing box simulations that gas self-gravity could prevent the decay of 3D vortices against elliptic instabilities, which would otherwise destroy them in non-self-gravitating discs.

To our knowledge, the impact of the elliptic instability on the growth and survival of planet-induced vortices has not been investigated yet. This would probably require 3D global, vertically-stratified, high-resolution simulations of planet–disc interactions. It would also be of interest to examine how the elliptic instability behaves in the presence of other sources of turbulence, such as non-ideal MHD turbulence.

We finally discuss to what extent the proposed vortex decay scenario is associated with a transient phenomenon. To interpret the ALMA and VLA observations of MWC 758, the inner vortex is required to have decayed significantly (but with the dust retaining some degree of non-axisymmetry), while the outer vortex has not yet significantly decayed. Given the planets mass and disc parameters in our model, it takes ~0.17 Myr after the planets have reached their final mass for the inner vortex to decay, and ~0.30 Myr for the outer vortex. Both time-scales look short in comparison to the estimated age of the system (5–10 per cent of the age), and one may argue that we are catching the system at a special time. Interestingly, this ratio is actually consistent with the fraction of discs with (sub)millimetre continuum annular substructures that have high-contrast azimuthal asymmetries like in the MWC 758 disc (7 out of 43, or ~16 per cent; see Huang et al. 2018). However, one should bear in mind that it takes time to grow the planets in the first place, and it is unclear how long it should take to form a 1.5 Jupiter-mass planet at 35 au and a 5 Jupiter-mass planet at 140 around an A5-type star. The lifetime of the vortices in our model is also uncertain, and it would be interesting to investigate how slow planetary growth, over a significant fraction of the disc age, would change our scenario, since it has been shown that slow growth tends to produce weaker vortices (Hammer, Kratter & Lin 2017; Hammer et al. 2019). Similarly, the planets in the simulation have been kept on circular orbits, and it is therefore relevant to explore how migration would affect the growth and survival of the vortices, and the eccentricity of the disc gas between the planets.

4.3 Impact of dust parameters

We discuss here how the size distribution, the total mass, the internal density and the opacities of the dust particles affect the results of our simulations and of our (sub)millimetre continuum synthetic maps (Sections 4.3.1–4.3.4). We then present in Section 4.3.5 (sub)millimetre continuum synthetic maps that include a population of small dust between the planets.

4.3.1 Dust's size distribution

Throughout this work, we assume that the size of the dust particles follows a power-law distribution, with thus three parameters: the minimum and maximum sizes, and the power-law exponent. We recall that the results presented in Section 3.2 are for a size distribution $n(s) \propto s^{-3}$ for particles sizes s between 10 μm and 1 cm. Decreasing the minimum size is found to have no impact on our synthetic maps in the (sub)millimetre, as particles smaller than 10 μm have a very small contribution to the continuum emission at both 0.9 and 9 mm. A notable exception will be presented in Section 4.3.5, where we relax the assumption of a power-law size distribution by adding a rather massive population of small dust.

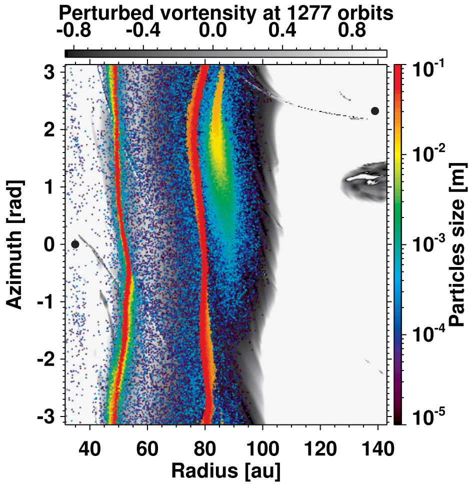

Figure 7. Same as middle right-hand panel of Fig. 2, but including dust particles between 1 and 10 cm in size.

The maximum size assumed for the dust particles has, however, a much higher impact on our results. To see why this is the case, we display in Fig. 7 the dust's spatial distribution at 1277 orbits overlaid on the gas perturbed vortensity, just like in the middle right-hand panel of Fig. 2, except that we now show the location of dust particles up to 10 cm in size (instead of 1 cm). We see that particles larger than about 1.5 cm are not trapped in the vortex at ~85 au, but are shifted radially inwards by about 5–10 au at this time in the simulation. This radial shift stems from the interaction between the large dust particles and the inner wake of the outer planet. Since this wake carries negative fluxes of energy and angular momentum, it pushes dust particles inwards each time they cross the wake. Fig. 7 shows that, at the vortex's orbital radius, the radial deflection caused by the planet wake is larger than the radial drift back towards the vortex for dust particles larger than about 1 cm, which have a Stokes number $\gtrsim 0.1$. These particles thus find an equilibrium location interior to the vortex, where they form a nearly axisymmetric ring. Investigation of dust-wake interactions and their observational implications for the continuum emission in the (sub)millimetre will be detailed in a future paper. For the present work dedicated to MWC 758, we have checked that this ring of $\gtrsim$cm-sized dust particles would make the (sub)millimetre emission near Clump 1 much more extended in the azimuthal direction than predicted in Figs 4 and 5 for the same total dust mass, which would be incompatible with the compactness of Clump 1 as observed by ALMA and especially the VLA. This could have interesting implications for dust growth in the MWC 758 disc, as our model suggests inefficient growth beyond cm sizes around the location of Clump 1, which we speculate might be due to bouncing and/or fragmentation barriers.

Lastly, we have checked that the slope of the dust's size distribution has, overall, a mild impact on the predicted (sub)millimetre emission for Clumps 1 and 2. Qualitatively, we find that the shallower the size distribution, the more compact the emission is for Clump 1 at 0.9 mm as well as at 9 mm.

4.3.2 *Dust's total mass*

For the dust mass adopted in Section 3 ($1.6 \times 10^{-4} M_\star$ between ∼40 and ∼100 au), the peak absorption optical depth at 0.9 mm is ∼30 for Clump 1 and ∼15 for Clump 2 (see Section 3.2.3). We have checked that increasing the total dust mass would result in even larger absorption optical depths at both clumps, and thus more extended emissions in the azimuthal direction, which would be incompatible with the observed compactness of both clumps at 0.9 mm. Increasing the total dust mass too much would also conflict with the assumption that dust feedback has been discarded in the hydrodynamical simulation.

Decreasing the total dust mass would reduce the peak intensity of Clump 2 faster than for Clump 1, thereby increasing the peak intensity ratio between Clumps 1 and 2 at both wavelengths. For instance, by reducing the total dust mass used in Section 3 by a factor of 2, the peak intensity ratio between Clumps 1 and 2 increases from about 0.6 to 0.7 at 0.9 mm (observed value is ∼0.8), and from about 1.4 to 1.7 at 9 mm (observed value is $\sim 2.7 \pm 0.3$). However, since the emission at 9 mm is only marginally optically thick at both clumps, decreasing the dust mass would also decrease the overall flux level, which would reduce the level of agreement between the predicted and observed peak intensities for Clump 1 at 9 mm. In the above example, halving the total dust mass reduces the predicted peak intensity for Clump 1 at 9 mm from ∼24.8 to ∼14.5 mJy beam^{-1} (observed value is 29.1 ± 2 mJy beam^{-1}).

4.3.3 *Dust's internal density*

The particles internal density adopted throughout this study, $\rho_{\rm int} = 0.1\ {\rm g\,cm^{-3}}$, may seem a little surprising as simulations and/or radiative transfer calculations usually model dust as compact grains with an internal density of a few g cm^{-3}. During the course of this project, we carried out a simulation with a more conventional internal density of 1 g cm^{-3}, and obtained synthetic maps in the (sub)millimetre that have nearly the same morphology than for $\rho_{\rm int} = 0.1\ {\rm g\,cm^{-3}}$ *if* the maximum particle size is set to 1 mm instead of 1 cm. This reduced maximum size comes about because the particles dynamics is primarily[3] set by the Stokes number, which scales with the product of particles size and internal density. For $\rho_{\rm int} = 1\ {\rm g\,cm^{-3}}$, particles larger than about 1 mm are shifted interior to the vortex located at ∼85 au because of the inner wake of the outer planet, just like the particles larger than about 1 cm in our simulation with $\rho_{\rm int} = 0.1\ {\rm g\,cm^{-3}}$, as shown in Section 4.3.1.

The main difference between both internal densities is that, in the continuum emission at 0.9 mm, the peak intensity as well as the azimuthal width are a little larger at $\rho_{\rm int} = 1\ {\rm g\,cm^{-3}}$ for both clumps, but probably a similar level of agreement could be attained by fine tuning the other parameters for the dust. Our results therefore cannot rule out that the dust in the MWC 758 disc could be compact, given the degeneracy in the predictions, and the large uncertainties in the dust opacities (at either internal density, actually). It would be interesting to explore the possibility of even smaller internal densities (see e.g. Kataoka et al. 2013).

4.3.4 *Dust opacities*

The dust composition is another free parameter that we have tested for the (sub)millimetre continuum synthetic maps. The dust composition only impacts the calculation of the dust absorption and scattering opacities. Recall that all the results in Section 3 are obtained for porous dust particles for which the solid component comprises 70 per cent water ices and 30 per cent silicates. By testing a different mixture, namely 70 per cent silicates and 30 per cent amorphous carbons, we find that the overall level of flux at 0.9 mm is reduced by only ∼15 per cent, and that at 9 mm by a factor of ∼3. Again, given the degeneracy of the predictions, we would find it difficult to constrain the dust composition from the comparison between the synthetic maps of continuum emission and the observations.

4.3.5 *Inclusion of small dust*

The synthetic and observed flux maps at 0.9 mm shown in Fig. 4 indicate that Clumps 1 and 2 lie on top of a fainter ring of background emission. As alluded to in Section 3.2, this emission might come about because of small dust forming as a result of dust fragmentation between the planets. The spiral shocks and the (moderately) eccentric gas between the planets in our disc model (Section 3.1.1) *a priori* offer an environment ripe for dust fragmentation. Since dust growth and fragmentation are not implemented in our hydrodynamical code, we have tested this idea by simply adding an extra bin of small dust in our radiative transfer calculations. Since the absorption and scattering opacities of our porous dust is largely independent of dust sizes below 10 µm, we need not specify what size range this extra bin of small dust precisely corresponds to. We will just assume these dust particles remain larger than 0.3 µm, to distinguish them from the compact dust particles that contribute to the near-infrared polarized scattered light (Section 2.2.2).

The extra bin of small dust that is added to our synthetic maps of continuum emission is assumed to have a spatial distribution that follows that of the gas between 0.4 and 0.6 arcsec, and a total mass ∼0.6 per cent the mass of the gas (or 24 $M_\oplus$; the total dust-to-gas mass ratio is therefore increased from 2 per cent to ∼2.6 per cent). The results of this numerical experiment are displayed in Fig. 8, where we see a level of background emission at 0.9 mm between Clumps 1 and 2 that resembles that in the ALMA image of Dong et al. (2018). Interestingly, part of this emission has a spiral shape towards the south-west, which is reminiscent of the spiral- or arc-shaped emission seen to the south of Clump 2 in the ALMA image of Dong et al. (2018) (around 6 o'clock in the top right-hand panel of Fig. 4). In our disc model, this spiral, which also has an observational counterpart in polarized intensity (see spiral trace S2 in Fig. 6), corresponds to the primary inner wake of the outer planet. The inclusion of small dust has a minor impact on the synthetic map at 9 mm (the peak intensities at Clumps 1 and 2 are decreased by about 10 per cent).

4.4 On the location and mass of the possible planets in the MWC 758 disc

Reggiani et al. (2018) have recently reported the detection of a point-like source at about 20 au from MWC 758. This source, however, has not been detected in H α line observations with SPHERE/ZIMPOL (Huélamo et al. 2018; Cugno et al. 2019). Assuming this source is a companion candidate, we have investigated under which circumstances it could produce the asymmetric ring at 0.9 mm passing by Clump 2 at ∼50 au. With our disc model, we find that the mass of the companion candidate should be close to $30 M_{\rm Jup}$ so that the pressure maximum located at the outer edge of its gap matches

---

[3] The particles dynamics is primarily set by the Stokes number because gas self-gravity also affects the dynamics, especially when the Stokes number exceeds about 0.1 (Baruteau & Zhu 2016).

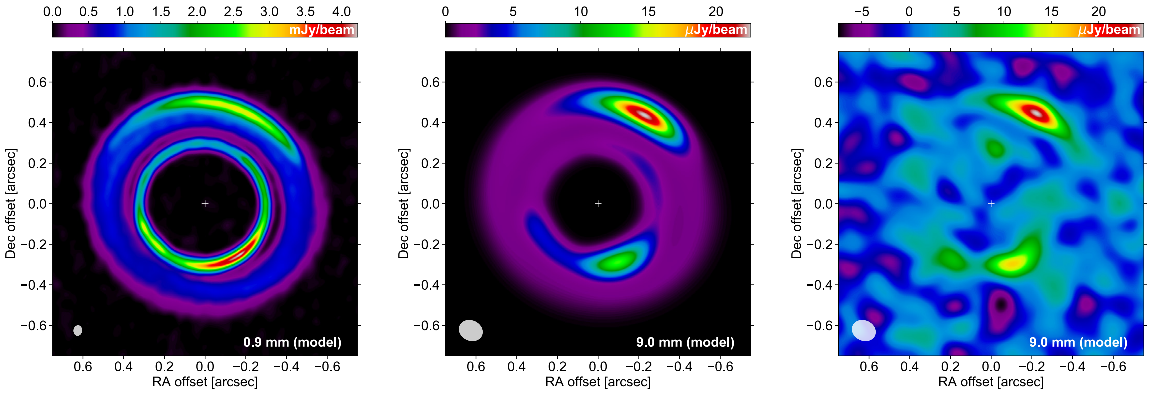

Figure 8. Synthetic maps of continuum emission at 0.9 mm (left-hand panel) and at 9 mm (without and with white noise, middle and right panels) obtained by adding a rather massive (∼24 M$_\oplus$) population of small dust well coupled to the gas between Clumps 1 and 2.

the orbital radius of Clump 2. While such a massive companion could account for the large submillimetre cavity in the disc, it would most likely open a very large gap or even a cavity in the gas which would be devoid of the smallest dust grains. But such a large gap or cavity is not seen in scattered light images of MWC 758, making this scenario less likely. If the companion candidate at about 20 au were present in addition to the planet at 35 au that we think is responsible for Clump 2, then both companions would be close to their 2:1 mean-motion resonance and likely carving a common gap in the gas, which, again, lacks observational support.

With a moderately massive inner planet in the submillimetre cavity, the outer planet is required in our simulations to explain the multiple spiral arms which are observed in polarized scattered light (see Section 3.3). By adopting for the outer planet's mass the upper mass limit obtained by Reggiani et al. (2018), we find that the outer planet should be located at about 140 au to produce the dust trap at the orbital distance of Clump 1 (∼85 au). However, preliminary simulations have shown that a similar dust trap could be achieved by adopting a more massive companion at a larger orbital distance like, for instance, a 0.1M$_\odot$ substellar companion at ∼300 au from the central star.

Despite the fact that the massive outer planet in our scenario has not been detected in the recent Keck L'-band observations of Reggiani et al. (2018), the detection limit was computed assuming a hot start evolutionary model. Assuming a cold start model can dramatically increase the mass detection limit for the same contrast (Spiegel & Burrows 2012). Also, if the planet has a circumplanetary disc or envelope, the material surrounding the planet could affect gas accretion on to the planet and consequently the planet's luminosity (Szulágyi et al. 2014), potentially hindering its direct observation. A direct detection will be possible with future high spatial resolution ALMA observations of molecular lines, where the strong impact that a massive planet could have on the observed kinematics of the gas can be identified (Perez et al. 2015; Pérez, Casassus & Benítez-Llambay 2018). Kinematic evidence for a massive planet in the HD 163296 disc based on ^{12}CO ALMA observations has been recently reported in Pinte et al. (2018).

Based on multi-epoch near-infrared observations of the MWC 758 disc, Ren et al. (2018) have estimated the rotation (or pattern) speed of the two most prominent spirals. Assuming that these spirals are the inner wakes of a massive companion, they find, based on the spirals pattern speed, that the companion's best-fitting orbital distance would be at about 95 au (0.59 arcsec). This is very close to the location of Clump 1 in the (sub)millimetre images (∼85 au), and it seems unlikely that a massive companion at about 95 au could form a dust-trapping vortex at the location of Clump 1. However, we stress that the uncertainty in the estimation of the pattern speed is large, as highlighted in Ren et al. (2018), and that there is actually no constraint on the upper distance of the putative companion. The 3σ lower limit on the pattern speed goes to 0 indeed (that is, no rotation; Ren et al. 2018), which would formally correspond to a companion at infinite distance. The orbital distance that we assume for the outermost planet in our model (140 au) is therefore entirely consistent with the current measurement of the spirals pattern speed.

4.5 Summary

We carried out 2D global hydrodynamical simulations including both gas and dust of a self-gravitating circumstellar disc under the influence of two giant planets. The results of our simulations, which were post-processed with 3D dust radiative transfer calculations, support a scenario where the asymmetries observed in the (sub)millimetre and near-infrared scattered light of the transition disc MWC 758 could be due to the presence of two massive planets moulding the global structure of the disc.

In this scenario, our model suggests the presence of a 5 $M_{\rm Jup}$ planet at 140 au and a 1.5$M_{\rm Jup}$ planet at 35 au. The outer more massive planet triggers several spiral arms, of which two can account for the brightest spirals or arcs seen in Y-band polarized scattered light. It also forms a vortex at the inner edge of its gap (at ∼85 au), where the dust concentration reproduces quite well the compact crescent-shaped structure seen at ∼0.53 arcsec in the ALMA and VLA observations (Clump 1), if assuming moderately porous dust particles, with an internal density of 0.1 g cm^{-3}, up to a centimetre in size. Because it is less massive, the inner planet produces dim spirals in scattered light, and it forms a vortex at the outer edge of its gap (at ∼50 au) that decays due to the disc's turbulent viscosity, as the gas between the planets become moderately eccentric. This decay can explain why the eccentric and asymmetric emission ring seen with ALMA at ∼0.32 arcsec has a weak counterpart in the VLA observations of Casassus et al. (2019). This scenario of a decaying vortex has been recently proposed by Fuente et al. (2017) to explain multiwavelength NOEMA observations of the lopsided emission ring in the AB Aurigae transition disc.

We finally point out the striking similarities between the transition discs around MWC 758, HD 135344B (van der Marel et al. 2016) and V1247 Orionis (Kraus et al. 2017). Similarly to MWC 758, HD 135344B and V1247 Ori have a moderately asymmetric emission ring surrounded by a crescent-shaped structure in ALMA band 7 continuum observations. Both discs also have at least one spiral arm seen in scattered light (see Garufi et al. 2013 for HD 135344B and Ohta et al. 2016 for V1247 Ori). It is therefore tempting to suggest that the asymmetries in the discs around HD 135344B and V1247 Ori could also result from the presence of two massive planets, just like in the proposed scenario for the MWC 758 disc.

ACKNOWLEDGEMENTS

Numerical simulations were performed on the CALMIP Supercomputing Centre of the University of Toulouse. MB, SP, and SC acknowledge support from the Millennium Science Initiative (Chilean Ministry of Economy), through grant 'Nucleus P10-022-F'. MB acknowledges CONICYT-PFCHA/MagísterNacional/2017-22171601 and the support from Departamento de Postgrado y Postítulo de la Vicerrectoría de Asuntos Académicos, Universidad de Chile. This research was partially supported by the supercomputing infrastructure of the NLHPC (ECM-02). SC and SP acknowledge financial support from FONDECYT grants 1130949, 3140601, and 3150643, respectively. FD thanks the European Research Council (ERC) for funding under the H2020 research and innovation programme (grant agreement #740651 NewWorlds). We thank Jérémie Lasue, Romane Le Gal, and Gaylor Wafflard-Fernandez for helpful discussions, as well as our referee for constructive comments.

REFERENCES

Allard F., 2014, in Booth M., Matthews B. C., Graham J. R., eds, IAU Symp. Vol. 299, Exploring the Formation and Evolution of Planetary Systems, Cambridge University Press, Cambridge, UK. p. 271
Andrews S. M., Wilner D. J., Espaillat C., Hughes A. M., Dullemond C. P., McClure M. K., Qi C., Brown J. M., 2011, ApJ, 732, 42
Ataiee S., Baruteau C., Alibert Y., Benz W., 2018, A&A, 615, A110
Avenhaus H. et al., 2017, AJ, 154, 33
Bae J., Zhu Z., Hartmann L., 2016, ApJ, 819, 134
Baruteau C., Masset F., 2008a, ApJ, 672, 1054
Baruteau C., Masset F., 2008b, ApJ, 678, 483
Baruteau C., Zhu Z., 2016, MNRAS, 458, 3927
Benisty M. et al., 2015, A&A, 578, L6
Bentley M. S. et al., 2016, Nature, 537, 73
Boehler Y. et al., 2018, ApJ, 853, 162
Bohren C. F., Huffman D. R., 1983, Absorption and Scattering of Light by Small Particles. Wiley, New York
Casassus S. et al., 2019, MNRAS, 483, 3278
Charnoz S., Fouchet L., Aleon J., Moreira M., 2011, ApJ, 737, 33
Chavanis P. H., 2000, A&A, 356, 1089
Crnkovic-Rubsamen I., Zhu Z., Stone J. M., 2015, MNRAS, 450, 4285
Cugno G. et al., 2019, A&A, 622, A156
Dong R., Fung J., 2017, ApJ, 835, 38
Dong R., Zhu Z., Rafikov R. R., Stone J. M., 2015, ApJ, 809, L5
Dong R. et al., 2018, ApJ, 860, 124
Draine B. T., Lee H. M., 1984, ApJ, 285, 89
Dullemond C., Juhasz A., Pohl A., Sereshti F., Shetty R., Peters T., Commercon B., Flock M., 2015, RADMC3D, http://www.ita.uni-heidelberg.de/ dullemond/software/radmc-3d/
Fu W., Li H., Lubow S., Li S., 2014a, ApJ, 788, L41
Fu W., Li H., Lubow S., Li S., Liang E., 2014b, ApJ, 795, L39
Fuente A. et al., 2017, ApJ, 846, L3
Fung J., Dong R., 2015, ApJ, 815, L21
Gaia Collaboration et al., 2018, A&A, 616, A1
Garufi A. et al., 2013, A&A, 560, A105
Grady C. A. et al., 2013, ApJ, 762, 48
Güttler C. et al., 2019, preprint (arXiv:1902.10634)
Hammer M., Kratter K. M., Lin M.-K., 2017, MNRAS, 466, 3533
Hammer M., Pinilla P., Kratter K. M., Lin M.-K., 2019, MNRAS, 482, 3609
Huang J. et al., 2018, ApJ, 869, L42
Huélamo N. et al., 2018, A&A, 613, L5
Isella A., Natta A., Wilner D., Carpenter J. M., Testi L., 2010, ApJ, 725, 1735
Kataoka A., Tanaka H., Okuzumi S., Wada K., 2013, A&A, 557, L4
Kataoka A., Okuzumi S., Tanaka H., Nomura H., 2014, A&A, 568, A42
Kraus S. et al., 2017, ApJ, 848, L11
Langevin Y. et al., 2016, Icarus, 271, 76
Les R., Lin M.-K., 2015, MNRAS, 450, 1503
Lesur G., Papaloizou J. C. B., 2009, A&A, 498, 1
Li A., Greenberg J. M., 1997, A&A, 323, 566
Li H., Finn J. M., Lovelace R. V. E., Colgate S. A., 2000, ApJ, 533, 1023
Li H., Colgate S. A., Wendroff B., Liska R., 2001, ApJ, 551, 874
Lin M.-K., 2012, MNRAS, 426, 3211
Lin M.-K., 2014, MNRAS, 437, 575
Lin M.-K., Papaloizou J. C. B., 2011, MNRAS, 415, 1426
Lin M.-K., Pierens A., 2018, MNRAS, 478, 575
Lovelace R. V. E., Hohlfeld R. G., 2013, MNRAS, 429, 529
Lovelace R. V. E., Li H., Colgate S. A., Nelson A. F., 1999, ApJ, 513, 805
Lyra W., Lin M.-K., 2013, ApJ, 775, 17
Lyra W., Johansen A., Klahr H., Piskunov N., 2009, A&A, 493, 1125
Lyra W., Turner N. J., McNally C. P., 2015, A&A, 574, A10
Marino S., Casassus S., Perez S., Lyra W., Roman P. E., Avenhaus H., Wright C. M., Maddison S. T., 2015, ApJ, 813, 76
Masset F., 2000, A&AS, 141, 165
Meeus G. et al., 2012, A&A, 544, A78
Meheut H., Keppens R., Casse F., Benz W., 2012, A&A, 542, A9
Ohta Y. et al., 2016, PASJ, 68, 53
Perez S., Dunhill A., Casassus S., Roman P., Szulágyi J., Flores C., Marino S., Montesinos M., 2015, ApJ, 811, L5
Pérez S., Casassus S., Benítez-Llambay P., 2018, MNRAS, 480, L12
Pérez S., Casassus S., Baruteau C., Dong R., Hales A., Cieza L., 2019, preprint (arXiv:1902.05143)
Pierens A., Lin M.-K., 2018, MNRAS, 479, 4878
Pinte C., Dent W. R. F., Ménard F., Hales A., Hill T., Cortes P., de Gregorio-Monsalvo I., 2016, ApJ, 816, 25
Pinte C. et al., 2018, ApJ, 860, L13
Regály Z., Vorobyov E., 2017, MNRAS, 471, 2204
Regály Z., Juhász A., Sándor Z., Dullemond C. P., 2012, MNRAS, 419, 1701
Reggiani M. et al., 2018, A&A, 611, A74
Ren B. et al., 2018, ApJ, 857, L9
Riols A., Lesur G., 2018, A&A, 617, A117
Sándor Z., Lyra W., Dullemond C. P., 2011, ApJ, 728, L9
Simon J. B., Lesur G., Kunz M. W., Armitage P. J., 2015, MNRAS, 454, 1117
Simon J. B., Bai X.-N., Flaherty K. M., Hughes A. M., 2018, ApJ, 865, 10
Spiegel D. S., Burrows A., 2012, ApJ, 745, 174
Szulágyi J., Morbidelli A., Crida A., Masset F., 2014, ApJ, 782, 65
Varnière P., Tagger M., 2006, A&A, 446, L13
Yang C.-C., Mac Low M.-M., Johansen A., 2018, ApJ, 868, 27
Youdin A. N., 2010, in Montmerle T., Ehrenreich D., Lagrange A.-M., eds, EAS Publ. Ser. Vol. 41. Physics and Astrophysics of Planetary Systems, EDP Sciences (Les Ulis). p. 187
Zhu Z., Baruteau C., 2016, MNRAS, 458, 3918
Zhu Z., Stone J. M., 2014, ApJ, 795, 53
Zhu Z., Dong R., Stone J. M., Rafikov R. R., 2015, ApJ, 813, 88
van der Marel N., Cazzoletti P., Pinilla P., Garufi A., 2016, ApJ, 832, 178

This paper has been typeset from a TEX/LATEX file prepared by the author.

Monthly Notices
of the
ROYAL ASTRONOMICAL SOCIETY

MNRAS **493,** 5892–5912 (2020)
Advance Access publication 2020 February 11

doi:10.1093/mnras/staa379

Intermittent planet migration and the formation of multiple dust rings and gaps in protoplanetary discs

Gaylor Wafflard-Fernandez★ and Clément Baruteau★

IRAP, Université de Toulouse, CNRS, UPS, F-31400 Toulouse, France

Accepted 2020 February 6. Received 2020 February 6; in original form 2019 August 13

ABSTRACT

A key challenge for protoplanetary discs and planet formation models is to be able to make a reliable connection between observed structures in the discs emission, like bright and dark rings or asymmetries, and the supposed existence of planets triggering these structures. The observation of *N* dark rings of emission is often interpreted as evidence for the presence of *N* planets which clear dust gaps around their orbit and form dust-trapping pressure maxima in the disc. The vast majority of the models that studied the impact of planets on the dynamics of dust and gas in a protoplanetary disc assumed planets on fixed orbits. Here, we go a different route and examine how the large-scale inward migration of a single planet structures the dust content of a massive disc. In many circumstances, the migration of a partial gap-opening planet with a mass comparable to Saturn is found to run away intermittently. By means of 2D gas and dust hydrodynamical simulations, we show that intermittent runaway migration can form multiple dust rings and gaps across the disc. Each time migration slows down, a pressure maximum forms beyond the planet gap that traps the large dust. Post-processing of our simulations results with 3D dust radiative transfer calculations confirms that intermittent runaway migration can lead to the formation of multiple sets of bright and dark rings of continuum emission in the (sub)millimeter beyond the planet location.

Key words: accretion, accretion discs – hydrodynamics – planets and satellites: formation – planet–disc interactions – protoplanetary discs.

1 INTRODUCTION

Recent observations of substructures in protoplanetary discs have challenged the classical picture of discs being smooth continuous objects. A fair fraction of spatially resolved discs shows indeed substructures, including spirals, axisymmetric, and asymmetric rings when observed from the near-IR to the (sub-)mm. In particular, sequences of dark rings (gaps) and bright rings are the most frequent substructures revealed by radio interferometry with ALMA. In Long et al. (2018), 40 per cent (12/32) of their sample feature axisymmetric rings and gaps. For some discs, such structures have also been observed in SPHERE near-IR polarized observations (e.g. Avenhaus et al. 2018).

If we focus on Discs with Annular Substructures (DAS) in the (sub-)mm continuum from the Disc Substructures at High Angular Resolution Project (DSHARP) in addition to HL Tau, TW Hya, and other DAS listed in table 5 of Huang et al. (2018), we see that around 30 per cent (12/42) of DAS are single-ring systems and 70 per cent (30/42) are multiple-ring systems. This classification is based on the current resolution at which discs are observed. A better resolution could possibly reveal more rings. This is the case for example of the disc around HD 169142, for which the bright ring observed at $\sim0\farcs6$ with an $\sim0\farcs2$ beam by Fedele et al. (2017) turns out to be composed of three narrow rings when observed with an angular resolution ten times better (Pérez et al. 2019). Another bias is the choice of the targets: in the DSHARP sample, targets were deliberately composed of massive and extended discs, and Long et al. (2018) suggest that multiple-ring discs are more massive and larger. This could explain the seemingly large current fraction of multiple-rings discs. In any case, the mechanisms behind the presence of annular substructures should be sufficiently general to occur in a significant fraction of protoplanetary discs and should be able to generate multiple rings.

Bright and dark rings observed in the (sub-)mm are often interpreted as dust overdensities and underdensities. However, generally, radial variations of the observed intensity are not necessarily related to radial variations of the dust density. When scattering is negligible, the specific intensity at frequency ν (I_ν) is linked to the dust temperature $T_{\rm d}$, the dust's surface density $\Sigma_{\rm d}$, and the dust's absorption opacity κ_ν (see e.g. the review by Andrews 2015, his equation 2). Thus, radial variations of I_ν can be due to radial variations of $T_{\rm d}$, $\Sigma_{\rm d}$, and/or κ_ν. Any mechanism able to induce radial variations of these quantities could in principle explain bright and

---

★ E-mail: gwafflard@irap.omp.eu (GW-F); clement.baruteau@irap.omp.eu (CB)

Published by Oxford University Press on behalf of the Royal Astronomical Society

dark rings of emission. Still, we will concentrate in the following on mechanisms that cause radial variations of $\Sigma_{\rm d}$. One such mechanism is dust pile-up due to sintering-induced fragmentation (Okuzumi et al. 2016). Sintering, which bonds dust particles together, occurs efficiently for micro-metric dust monomers slightly outside the snow lines of volatile species. When sintered aggregates collide, they are prone to bouncing, fragmentation and erosion because the collision energy cannot be dissipated, which decreases their sticking efficiency. Sintering thus decreases the size of dust aggregates and therefore their drift velocity, thereby causing a dust pile-up slightly beyond the snow lines.

Several discs show very thin bright rings intercalated between dark rings in the continuum emission, such as HD 163296 or AS 209 (Huang et al. 2018). Assuming these bright rings are dust overdensities, their thinness suggests that they are located at positions of equilibrium for the dust, where radial drift is stalled. These so-called dust traps can be naturally obtained at pressure maxima in a disc. Before mentioning several ways to form pressure bumps in a disc, we note that a pressure maximum is susceptible to the Rossby Wave Instability (RWI; Lovelace et al. 1999), which may trigger the formation of one or several vortices that also trap dust in the azimuthal direction (Barge & Sommeria 1995; Li et al. 2001). Dust trapping in vortices is often invoked to explain the asymmetric crescent-shaped structures in the discs continuum emission at radio wavelengths (e.g. Baruteau et al. 2019).

Various mechanisms have been proposed to generate pressure bumps in protoplanetary discs. One is via the radial changes in the accretion efficiency at the transition between magnetically active regions in discs (where the magnetorotational instability, or MRI, sets in) and magnetically dead zones (where the MRI is quenched due to non-ideal magnetohydrodynamic effects; see e.g. Varnière & Tagger 2006; Flock et al. 2015; Lyra, Turner & McNally 2015). Moreover, when the disc is threaded by a weak magnetic field, a linear instability driven by magnetohydrodynamic winds can induce zonal flows which take the form of axisymmetric rings with alternating minima and maxima in the magnetic pressure, which are associated with maxima and minima in the thermal pressure (Béthune, Lesur & Ferreira 2017; Riols & Lesur 2019). Another popular scenario is planets. A planet that is sufficiently massive to carve an annular gap around its orbit will form pressure maxima at both edges of its gap due to the deposition of the angular momentum flux carried away by the wakes of the planet (Baruteau et al. 2014; Bae, Zhu & Hartmann 2016).

Models that invoke planets to explain annular substructures in discs observations almost always assume a planet on a fixed circular orbit at the middle of each dark ring (see e.g. Dipierro et al. 2015, for the HL Tau disc). Put another way, N gaps would correspond to N planets in a disc (hereafter, NGNP model). Some models have actually proposed to use the radial width of a dark ring to estimate the mass of the planet which created that ring (e.g. Dipierro & Laibe 2017; Zhang et al. 2018). The presence of planets in dark rings still eludes direct detection, with the notable exception of the planet companion in the large gap of the PDS 70 transition disc (Keppler et al. 2018). Other studies have also explored the idea that, in low-viscosity discs, a planet on a fixed circular orbit may form a secondary gap inside its orbit, and even a tertiary gap in some cases (Bae, Zhu & Hartmann 2017; Dong et al. 2017; Zhang et al. 2018).

In this work, we examine how a single planet that migrates in its disc impacts the dust's spatial distribution and continuum emission. A planet will impact the dust structures differently depending on how the planet's migration rate compares with the dust's drift rate. A few studies have recently assessed the effect of planetary migration on the dust dynamics, in particular the presence and location of dust rings on both sides of the planet, the dependence on the dust's size distribution, and how the position of a dust ring relative to the planet can be an indicator of the planet's migration speed (e.g. Meru et al. 2019; Nazari et al. 2019; Pérez et al. 2019; Weber et al. 2019). The parameter space is wide, however, as it involves a range of planet masses, disc's physical properties, (density, temperature profiles etc.) and dust sizes. We shall focus on the migration of moderately massive planets (typically around a Saturn mass) in fairly massive discs, which are subject to rapid runaway migration (Masset & Papaloizou 2003). Such planets can undergo multiple stages of intermittent runaway migration (Lin & Papaloizou 2010; McNally et al. 2019). We find that these multiple stages of intermittent runaway migration lead to the formation of several dust rings and therefore sequences of dark and bright rings in the (sub-)mm continuum.

The plan of this paper is the following. In Section 2, we describe the physical model and numerical methods of the hydrodynamical simulations and the radiative transfer calculations. The results are then presented in Section 3, where we focus on two fiducial cases. A discussion and a summary follow in Section 4.

Table 1. Main parameters of the hydrodynamical simulations.

Parameter	Value(s)
Code's unit of length	$r_0 = 10$ au
Disc's aspect ratio (h) at r_0	$\{0.05{,}0.06\}$
Toomre-Q parameter at r_0	$\in [5.3–64]$
Alpha turbulent viscosity	$\{10^{-4}, 10^{-3}\}$
Planet's initial location	$r_{\rm p,\,0} = 2r_0 = 20$ au
Planet-to-primary mass ratio	$\sim 1.46\, h^3(r_{\rm p,\,0})$
Dust's size range	$\in [10\ \mu\rm m–10\ cm]$
Dust's internal density	$2\ \rm g\,cm^{-3}$

2 PHYSICAL MODEL AND NUMERICAL METHODS

2.1 Hydrodynamical simulations

We performed 2D hydrodynamical simulations of the gas and dust of a protoplanetary disc with an embedded planet. Simulations were carried out with the code DUSTY FARGO-ADSG, which is an extension of the grid-based code FARGO-ADSG (Masset 2000; Baruteau & Masset 2008a,b) with dust grains modelled as Lagrangian test particles (Baruteau & Zhu 2016; Fuente et al. 2017). We adopt a polar coordinate system (r, θ), with r the radial cylindrical coordinate measured from the central star and θ the azimuthal angle. We detail below the physical model and numerical set-up for the gas, dust, and planet in our simulations. A short summary of the main parameters of the simulations is given in Table 1.

2.1.1 Gas

We solve the continuity and the Navier–Stokes equations for the gas on a polar mesh centred on the star, taking into account the indirect terms due to the acceleration of the star by the planet and the disc. In the radial direction, the grid stretches from 2 to 40 au.

We assume for simplicity a locally isothermal equation of state for the gas. This means that the gas temperature, or equivalently the sound speed, is fixed in time but varies with r. This assumption is generally more appropriate to the outer parts of protoplanetary discs, where the radiative cooling and/or diffusion time-scales are short compared to the orbital time-scale. However, we will see in Section 4.4 that allowing the gas temperature to vary with time by solving the energy equation does not qualitatively change our results. In our simulations with a locally isothermal equation of state, the aspect ratio $h(r)$, which is the ratio between the sound speed and the Keplerian speed, is chosen as $h(r) = h_0 \times (r/r_0)^{0.15}$, with $r_0 = 10$ au the code's units of length. Two values for the aspect ratio at r_0 are adopted : $h_0 = 0.05$ and 0.06, which respectively correspond to a temperature of 63 and 91 K for a Sun mass star and a solar composition (mean molecular weight $\mu_\odot = 2.4$).

We model the radial turbulent transport of the disc's angular momentum by an equivalent kinematic viscosity. We parametrize this viscosity as $\nu = \alpha c_{\rm S} H$, with α a dimensionless constant, $c_{\rm S}$ the sound speed, and $H = h(r) \times r$ the disc pressure's scale height (Shakura & Sunyaev 1973). The alpha turbulent viscosity at a few to a few tens of au in the discs mid-plane is highly uncertain. Non-ideal magnetohydrodynamic simulations show that it may vary from a few $\times 10^{-5}$ to as high as a few per cent, depending on the amplitude and sign of the vertical magnetic field that threads the disc (Simon et al. 2015; Béthune et al. 2017). Modelling of the ring-like structures in the (sub)millimeter continuum emission of some protoplanetary discs suggests that the mid-plane alpha at few tens of au should be $\lesssim 10^{-4}$ in order to reproduce the rings sharpness (e.g. Pinte et al. 2016; Pérez et al. 2019). These rather low values are overall consistent with observations of the non-thermal broadening in protoplanetary discs (Flaherty et al. 2015). To reflect this uncertainty, we will adopt two values of α in this study: 10^{-4} and 10^{-3}. We will see that, independently of its effect on planetary migration, the value of α has a clear impact on the dust structures that form because of disc–planet interactions, such as their lifetime, their radial width, or their degree of axisymmetry.

The initial gas surface density profile is $\Sigma_0(r) = \Sigma_0 \times (r/r_0)^{-1}$, with Σ_0 the gas surface density at r_0. We adopt in this work three values for Σ_0: 3×10^{-4}, 10^{-3}, and 3×10^{-3} in code units, which, by choosing a code's unit of mass of 1 $\mathrm{M}_\odot$, correspond to about 27, 89, and 267 g cm^{-2} at $r_0 = 10$ au, respectively. For these three values of Σ_0, the disc-to-star mass ratio amounts to 0.007, 0.02, or 0.07, respectively, while the Toomre Q-parameter at r_0, which is proportional to h_0, initially equals 53, 16, and 5.3, respectively, for $h_0 = 0.05$. Gas self-gravity is included in our simulations, and the disc gas is stable against the gravitational instability throughout the computational domain. Because we perform 2D simulations, a softening length of $0.3H(r)$ is used in the calculation of the self-gravitating acceleration to mimic the vertical extent of the disc (Baruteau & Masset 2008b; Müller, Kley & Meru 2012).

In the azimuthal direction, the grid extends from 0 to 2π and is paved by 900 cells that are evenly spaced. In the radial direction, we use 600 radial cells with a logarithmic spacing, which is necessary for the self-gravitating acceleration to read as a convolution product and be computed via Fast Fourier Transforms (Baruteau & Masset 2008b). For the boundary conditions, we use wave-killing zones near the inner and outer edges of the grid to avoid reflections of the planet wakes. These zones extend from 2 to 3 au, and from 35 to 40 au. The surface density and radial velocity of the gas are damped towards the radial profiles obtained by calculating the pure viscous evolution of the disc on a 1D grid simultaneously to the gas equations solved on the polar grid (the azimuthal velocity of the gas is damped towards its axisymmetric instantaneous profile). This is basically the same boundary condition as that implemented in FARGO-3D by Benítez-Llambay et al. (2016). It is a very simplified way to model the viscous evolution of a global disc in the absence of planets. Given the viscosity adopted in our disc models ($\alpha \le 10^{-3}$) and the duration of our runs (a few thousand planet orbits, at most), this boundary condition is, in practice, nearly identical to damping the gas density and radial velocity towards their initial radial profile. Our 1D grid has 1000 cells logarithmically spaced between 0.4 and 300 au, and the gas surface density is set to zero at the edges of the 1D grid. The choice of boundary conditions does not change significantly the results as long as the planet remains further than ∼4.5 au.

2.1.2 Dust

Dust is modelled as Lagrangian superparticles which feel the gravity of the star, of the disc gas (since gas self-gravity is included), of the planet, and gas drag. However, because we do not take into account dust self-gravity, collisions, dust growth, or fragmentation, particles do not feel each other. Moreover there is no dust backreaction on to the gas. We will discuss this assumption in the simulations results in Sections 3.2 and 3.3. To model the effects of gas turbulence, stochastic kicks are applied to the position ($r_{\rm d}$, $\theta_{\rm d}$) of the dust particles at each hydrodynamical time-step of the simulation [kicks depend on the local kinematic viscosity of the gas and Stokes number of the dust, see Ataiee et al. (2018) for more details].

Particles are assumed to have an internal density of 2 g cm^{-3}, independently of their size. They have a size distribution such that $n(s)\mathrm{d}s$, which corresponds to the number of superparticles in the size interval $[s, s + \mathrm{d}s]$, is a power-law function of the particle size s, going from $s_{\rm min} = 10$ µm to $s_{\rm max} = 10$ cm. The power-law exponent is set to -1 in order to have approximately the same number of particles per decade of size. Even though we need a (more) realistic size distribution exponent to compute the dust emission through radiative transfer calculations, the choice of the power-law exponent has no impact on the hydrodynamical simulations since dust feedback on the gas is discarded. The maximum particles size ($s_{\rm max}$) is consistent with the results of 1D models of dust growth, drift, and fragmentation in planet-less discs having similar physical properties as the background disc in our simulations (Birnstiel, Klahr & Ercolano 2012). The number of particles and their initial location will be specified in Sections 3.2 and 3.3.

2.1.3 Planet ($\mathcal{P}$)

The planet, which we will refer to as $\mathcal{P}$ in this paper, is set initially at $r_{\rm p,0} = 2r_0 = 20$ au from the star. This work focuses on how the migration of $\mathcal{P}$ due to its interactions with the disc gas impacts the formation of dust rings by the spiral wakes of $\mathcal{P}$. The mass of $\mathcal{P}$ is therefore chosen such that its wakes can form pressure maxima on either side of the planet's orbit, where dust particles can be trapped. We have chosen to study planets that carve a partial gap in the gas around their orbit, and which can be subject to fast runaway type III migration if the disc is sufficiently massive (Masset & Papaloizou 2003). Accretion on the planet is discarded in this study.

The range of planet-to-primary mass ratios ($q_{\rm p}$) for which partial gap opening occurs depends on the disc's aspect ratio and turbulent viscosity near the planet's location. Throughout this work, unless otherwise stated, results are obtained for $q_{\rm p} \approx 1.46h^3(r_{\rm p,0})$. More specifically, the simulations with $h_0 = 0.05$ have $q_{\rm p} = 2.5 \times 10^{-4}$, those with $h_0 = 0.06$ have $q_{\rm p} = 4.3 \times 10^{-4}$. These correspond to planets of ∼0.9 and ∼1.5 the mass of Saturn orbiting Solar-mass stars. The mass of the planet is gradually increased over its first 5 orbits, yet it is allowed to migrate from the beginning of the simulations. A softening length of $0.6H(r_p)$ is used to calculate the planet acceleration on the gas, where r_p denotes the (time varying) orbital radius of the planet.

2.2 Dust radiative transfer calculations

We post-process our results of simulations with dust radiative transfer calculations to infer the continuum emission that results from the dust's annular substructures obtained in our simulations. The radiative transfer calculations are carried out with the code RADMC3D (version 0.41, Dullemond et al. 2015). Synthetic maps of continuum emission are computed for a face-on disc at λ = 1.3 mm, which is the same wavelength as in the ALMA survey of discs undertaken by DSHARP (Huang et al. 2018). The procedure to compute RADMC3D synthetic images of the continuum emission from the outputs of the code DUSTY FARGO-ADSG is described in Baruteau et al. (2019) and makes use of the publicly available PYTHON program FARGO2RADMC3D. We recap here the main computing steps for convenience.

The dust's spatial distribution obtained in the hydrodynamical simulations is the key quantity to compute the continuum emission. We first derive the surface density of dust in 30 size bins logarithmically spaced between $s_{\rm min}$ and $s_{\rm max}$, the minimum and maximum particle sizes in the hydrodynamical simulations. This is done by assuming a size distribution $n(s) \propto s^{-3.5}$ and a total dust mass $M_{\rm dust} = 10^{-2} M_{\rm gas}$, where $M_{\rm gas}$ is the mass of the disc gas in the simulations. We then obtain the dust's volume density in each size bin and in each grid cell of the 3D spherical grid used by RADMC3D, which is the 2D polar grid of the simulations extended in colatitude with 36 cells spanning $\pm 2H$ around the mid-plane (a logarithmic spacing is used in colatitude with finer grid cells near the mid-plane). For this, we assume that the vertical distribution of the dust's volume density is Gaussian for each size bin, with a characteristic scale height equal to $H \times (1 + {\rm St}_{\rm bin}/\alpha)^{-1/2}$, where ${\rm St}_{\rm bin}$ is the average Stokes number of dust particles in each size bin.

Opacities are calculated using Mie theory, assuming a dust mixture comprised of 60 per cent astrosilicates and 40 per cent water ices, which corresponds to a mean internal density of $\sim 1.7\,{\rm g\,cm^{-3}}$, close to that assumed in the hydrodynamical simulations. We use the Bruggeman formula to obtain the optical constants of the mixture (the optical constants of water ices are from the Jena database, those of astrosilicates are from Draine & Lee 1984).

Armed with the dust's volume density and opacities, the radiative transfer calculations proceed in two steps: first, the dust temperature is computed via a thermal Monte Carlo calculation, next the specific intensity of continuum emission is calculated by solving the equation of radiative transfer via photon ray tracing. We assume the disc to be located at 150 pc, with zero inclination relative to the line of sight, and a central star with a radius of $2\,{\rm R}_\odot$ and effective temperature of 7000 K. We use 10^9 photon packages for the thermal Monte Carlo and ray-tracing calculations. Scattering off dust grains is discarded as it is found to have a small impact on our final synthetic images. We have checked this by dedicated RADMC3D calculations including anisotropic scattering with the Henyey–Greenstein approximation for the scattering phase function. For the simulation presented in Section 3.3, inclusion of anisotropic scattering results in ∼15 per cent relative difference for the flux of continuum emission compared to a calculation without scattering. Since our disc model is rather optically thick at 1.3 mm, discarding scattering significantly decreases the computation time of the radiative transfer calculations.

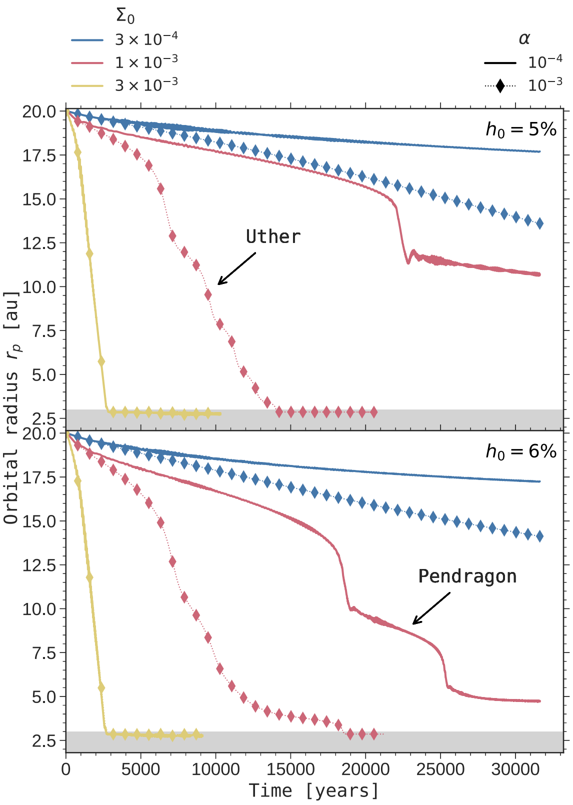

Figure 1. Overview of our results of hydrodynamical simulations: time evolution of the planet's orbital radius for three values of the gas surface density (Σ_0), two values of the alpha turbulent viscosity (α) and of the disc's aspect ratio (h_0). Top: h_0 = 5 per cent. Bottom: h_0 = 6 per cent. The grey bands correspond to the inner wave-killing zone.

Finally, knowing the disc distance, the specific intensity is convolved with a 0.02 arcsec beam in order to obtain a synthetic flux map of continuum emission. In some of the synthetic maps presented in Section 3, white noise is included by adding at each pixel of the synthetic map of specific intensity a random number following a Gaussian distribution with zero mean and a standard deviation set to $50\,\mu{\rm Jy\,beam^{-1}}$. This standard deviation is similar to the rms noise level obtained in recent ALMA observations at 1.3 mm and at similar resolution (see e.g. Pérez et al. 2019).

3 RESULTS

We begin this section with an overview of our results of hydrodynamical simulations in Section 3.1, which delineates the region of parameter space for which intermittent planetary migration is obtained. We then focus in Sections 3.2 and 3.3 on two simulations in which intermittent migration results in the formation of multiple dark and bright rings of emission at millimeter wavelengths.

3.1 Overview

We present in Fig. 1 a general view of 12 simulations characterized by the parameters h_0, α, and Σ_0 described in Section 2.1.1. In this figure, we plot the evolution of the planet's orbital radius as a function of time, with a panel for each value of h_0. For both values of h_0, we remark that the graphs can be separated into three specific areas depending on Σ_0:

(i) *Fast migration:* for the most massive disc model ($\Sigma_0 = 3 \times 10^{-3}$), the four curves (in yellow) almost lie on top of one another, which shows that the migration rate hardly depends on α and h_0. It indicates that migration is mostly driven by a strong dynamical corotation torque, rather than by the wave (Lindblad) torque and the static corotation torque (both of which scale as h_0^{-2} for low-mass planets). The very fast inward migration stalls when the planet ($\mathcal{P}$) reaches the inner damping zone of the grid, where its migration is no longer determined by the physical properties of the disc. This migration regime is so fast that the interaction between $\mathcal{P}$ and the dust particles remains limited, as is illustrated in the first row of Fig. A1 in Appendix A. As $\mathcal{P}$ moves inwards, most dust particles inside the orbit of $\mathcal{P}$ perform indeed an outer horseshoe U-turn relative to $\mathcal{P}$ and end up forming a dust band behind $\mathcal{P}$ that is similar to the initial one. Some of the particles embarking on to horseshoe U-turns also become trapped around the L4 Lagrange point in front of $\mathcal{P}$ in the azimuthal direction. Once the dust band is formed again, it drifts and diffuses radially due to gas drag and turbulence, respectively.

(ii) *Slow migration:* for the least massive disc model ($\Sigma_0 = 3 \times 10^{-4}$, blue curves), migration is slow and the dust rings generated by $\mathcal{P}$ display little evolution over the duration of the simulations. $\mathcal{P}$ actually forms three dust rings: one on each side of its partial gap in the gas, and one that stays coorbital with $\mathcal{P}$. As $\mathcal{P}$ moves inwards, the inner and coorbital dust rings move inward with $\mathcal{P}$ while the outer ring roughly stays at its initial location (Meru et al. 2019; Pérez et al. 2019, see also Section 3.3.1 and the second row of Fig. A1 in Appendix A). This implies that the mutual separation between the three rings increases as $\mathcal{P}$ migrates. This effect may well be observed in the outer parts of the HD 169142 disc, where the radial asymmetry between the three fine bright rings located between ∼0.″5 and ∼0.″7 has been interpreted as the signature of an inward-migrating mini-Neptune planet (Pérez et al. 2019).

(iii) *Intermittent migration:* the intermediate curves for $\Sigma_0 = 10^{-3}$ (in red) show non-steady (or non-smooth) orbital evolution, with several short stages of runaway migration which impart a staircase shape to the curves. Lin & Papaloizou (2010) and McNally et al. (2019) have reported results of hydrodynamical simulations with similar multiple episodes of runaway migration, which were obtained in inviscid or low-viscosity disc models. These intermittent stages of runaway migration are related to the time evolution of the coorbital vorticity-weighted mass deficit of the planet (Masset & Papaloizou 2003). This quantity basically compares the inverse vortensity[1] of the gas crossing the planet's orbit with that of the gas trapped in the planet's horseshoe region (see equation 1 below). Although it has the dimension of a mass, the coorbital vorticity-weighted mass deficit should rather be considered a coorbital vortensity deficit, especially for the low-mass planets considered in our study (Paardekooper 2014). Note in particular that δm may be either positive or negative, depending on the background vortensity profile. We will now call δm the coorbital vortensity deficit. When δm exceeds the mass of the planet ($M_{\rm p}$) plus that of its circumplanetary disc ($M_{\rm cpd}$), $\mathcal{P}$ enters a regime of runaway migration[2] (Masset & Papaloizou 2003; Masset 2008). However, as will be shown via one of our simulations in Section 3.2, δm may decrease during runaway migration, with the consequence that runaway ceases and the migration of $\mathcal{P}$ proceeds at a slower pace. We will show that during this phase of reduced migration, the vortensity inside the horseshoe region gets mixed and runaway can start again.

Table 2. Parameters of simulation Uther (Section 3.2).

Parameter	Value
Planet-to-primary mass ratio $q_{\rm p}$	2.5×10^{-4}
Disc's aspect ratio h_0 at 10 au	0.05
Alpha turbulent viscosity α	10^{-3}
Gas surface density Σ_0 at 10 au [code units]	10^{-3}
Number of dust superparticles	50000
Dust's initial location	∈ [14–21] au

In the following, we focus on the results of two simulations, which are labelled Uther and Pendragon in Fig. 1, for which $\mathcal{P}$ displays intermittent runaway migration. The results of both simulations are described in Sections 3.2 and 3.3.

3.2 Uther simulation ($h_0 = 0.05$, $\alpha = 10^{-3}$)

The simulation that we refer to as Uther displays four episodes of runaway migration in the upper panel of Fig. 1. We begin in Section 3.2.1 by showing that these intermittent stages of runaway migration are due to oscillations in the planet's coorbital vortensity deficit. We then examine the impact of these successive jolts of the planet on the dust's spatial distribution in Section 3.2.2, and on the dust's thermal emission at millimetre wavelengths in Section 3.2.3. The main parameters of the simulation are summarized in Table 2.

3.2.1 Coorbital vortensity deficit

As recalled in the previous section, the coorbital vortensity deficit δm is key to define when migration runs away. When $\delta m < M_{\rm p}$, the dynamical corotation torque is not large enough to trigger runaway migration. On the contrary, when $\delta m > M_{\rm p}$, $\mathcal{P}$ enters a runaway migration regime for which small perturbations to the position of the planet are rapidly amplified. The coorbital vortensity deficit reads (Masset & Papaloizou 2003):

$$\delta m = 4\pi r_{\rm p}\omega(r_{\rm p}) \times \left[x_{\rm s} \frac{\Sigma}{\omega}\left(r_{\rm p} - x_{\rm s}\right) - \int_{r_{\rm p}-x_{\rm s}}^{r_{\rm p}} \frac{\Sigma}{\omega}(r)\,{\rm d}r \right], \qquad (1)$$

with ω the gas vorticity and $x_{\rm s}$ the radial half-width of the planet's horseshoe region. The first term in the square brackets features the inverse vortensity of the gas entering the horseshoe region at orbital radius $r_{\rm p} - x_{\rm s}$, the second term the inverse vortensity of the gas trapped in libration inside the horseshoe region. Equation (1) is valid while the planet's migration time-scale over a radial distance $x_{\rm s}$ remains much longer than the half-libration time-scale of fluid elements at the horseshoe separatrices, located at $r_{\rm p} \pm x_{\rm s}$. In other words, δm can be expressed by equation (1) so long as the migration

---

[1] The gas vortensity, or potential vorticity, refers in this study to the ratio between the vorticity and the surface density, with the vorticity being the z-component of the curl of the 2D velocity.

[2] We have checked that $M_{\rm cpd}$ is always smaller than $M_{\rm p}$ in our simulations, by typically an order of magnitude. Thus, we will now simply use $\delta m > M_{\rm p}$ to define the onset of runaway migration.

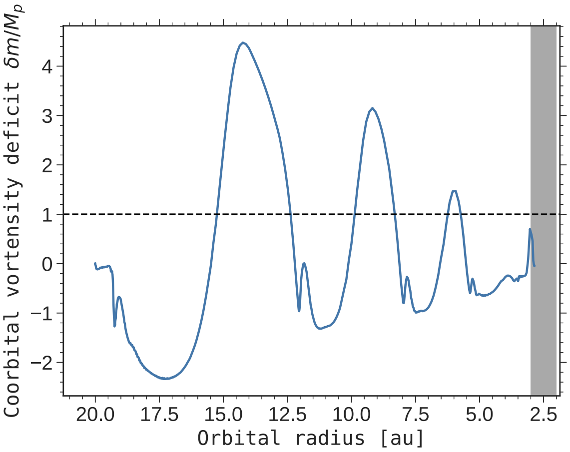

Figure 2. Numerical estimation of the coorbital vortensity deficit (δm) during the inward migration of $\mathcal{P}$ in the Uther simulation. δm is normalized by the planet's mass $M_{\rm p}$. The horizontal dashed line separates the regimes of runaway migration ($\delta m/M_{\rm p} \geq 1$) and non-runaway migration ($\delta m/M_{\rm p} \leq 1$). The grey band corresponds to the inner wave-killing zone.

speed $\dot{a}$ is slow compared to the critical speed $\dot{a}_{\rm c}$:

$$|\dot{a}| \ll \dot{a}_{\rm c} = \frac{3x_{\rm s}^2\Omega_{\rm p}}{4\pi r_{\rm p}}, \qquad (2)$$

with $\Omega_{\rm p}$ the orbital frequency of $\mathcal{P}$. When this is the case, the horseshoe region can be approximated as a rectangle in polar cylindrical coordinates, with a radial width of $2x_{\rm s}$ and an azimuthal width of nearly 2π. We will also assume that the gas vortensity trapped in libration with $\mathcal{P}$ is uniform (see e.g. Paardekooper 2014, and Fig. 3 below). Further denoting by $\mathcal{I}_{\mathcal{V}}$ the inverse vortensity Σ/ω, by $\mathcal{I}_{\mathcal{V}e}$ the inverse vortensity of the gas entering the horseshoe region ($\mathcal{I}_{\mathcal{V}e} = \mathcal{I}_{\mathcal{V}}(r_{\rm p} - x_{\rm s})$), and by $\mathcal{I}_{\mathcal{V}\rm lib}$ that of the gas trapped in libration, equation (1) can thus be recast as

$$\delta m \approx 4\pi r_{\rm p}\omega(r_{\rm p})x_{\rm s} \times [\mathcal{I}_{\mathcal{V}e} - \mathcal{I}_{\mathcal{V}\rm lib}], \qquad (3)$$

which agrees with the simplified version of δm obtained in Lin & Papaloizou (2010; see their section 6.1.1). When equation (2) is no longer satisfied, both the material trapped in libration with $\mathcal{P}$ and the orbit-crossing flow have an azimuthal extent $\Delta\theta < 2\pi$. Assuming that the expression of δm in equation (1) remains valid even when $|\dot{a}| \sim \dot{a}_{\rm c}$, we show in Appendix B that the approximated expression for δm in equation (3) gets multiplied by $\Delta\theta/2\pi$ (see equation B2). A schematic illustration of $\mathcal{I}_{\mathcal{V}e}$ and $\mathcal{I}_{\mathcal{V}\rm lib}$ can be found in the top-middle panel of Fig. 3.

We display in Fig. 2, the coorbital vortensity deficit normalized by the planet's mass $M_{\rm p}$. For simplicity, δm is calculated via equation (3) instead of equation (B2), as an automatic determination of $\Delta\theta$ from the simulation outputs would be quite cumbersome. For $\omega(r_{\rm p})$, we have checked that it can be approximated as the unperturbed (initial) value of the gas vorticity at $r = r_{\rm p}$. For $x_{\rm s}$, we use $x_{\rm s} \approx 2.45 r_{\rm p} \times (q_{\rm p}/3)^{1/3}$, which applies to planets with $q_{\rm p}/h^3(r_{\rm p}) \gtrsim 2$ on fixed circular orbits (Masset, D'Angelo & Kley 2006; Jiménez & Masset 2017). We have checked by a streamline analysis that this expression still works correctly in our simulations. A systematic determination of $\mathcal{I}_{\mathcal{V}e}$ and $\mathcal{I}_{\mathcal{V}\rm lib}$ from the simulation outputs would also be a little tricky. For $\mathcal{I}_{\mathcal{V}e}$, we approximate it as the inverse vortensity radially averaged over horseshoe U-turns just behind the planet in azimuth (since the planet migrates inward), using the fact that the inverse vortensity over a radial U-turn remains essentially unaltered for the range of viscosities in our disc models. This method works generally well, except at the initiation and termination of the runaway stages, where a streamline analysis would be required to estimate $\mathcal{I}_{\mathcal{V}e}$ more accurately. For the quantity $\mathcal{I}_{\mathcal{V}\rm lib}$, it is estimated as the average inverse vortensity of gas in front of the planet in azimuth around $r = r_{\rm p}$, using the fact that, as already stated below, the vortensity of the gas trapped in libration with the planet is roughly uniform. This method is less robust at the termination of runaway stages because of vortensity mixing within the horseshoe region.

Fig. 2 clearly shows that δm oscillates around $M_{\rm p}$, which indicates that $\mathcal{P}$ alternates between stages of runaway and non-runaway migration, and which explains the steps obtained in the migration pattern (Fig. 1). Note that when the planet runs away, the material that remains in corotation (or in libration) with $\mathcal{P}$ shrinks to a trapezoidal region in the radius–azimuth plane, either ahead or behind the planet in azimuth depending on the direction of migration (Masset 2002; Pepliński, Artymowicz & Mellema 2008a,b). The trapezoidal region, which in our case is ahead of the planet as the latter migrates inwards, has an azimuthal width $\Delta\theta < 2\pi$ when migration runs away, as will be illustrated in Fig. 3 (see the libration region labelled with $\mathcal{I}_{\mathcal{V}\rm lib}$ in the top middle panel). Therefore, δm is actually overestimated in Fig. 2 when $\delta m \gtrsim M_{\rm p}$ (see equation B2). But in this case, the hypothesis of slow migration (see equation 2) required to express δm via equations (1), (3), or (B2) may not be verified in the simulation.

To understand what stops and reinstates runaway migration intermittently, we display in Fig. 3 seven screenshots of the gas inverse vortensity ($\mathcal{I}_{\mathcal{V}}$) taken at times $T_{\rm A}$ to $T_{\rm G}$ indicated in the middle right hand panel of the same figure, which shows the temporal evolution of the planet's orbital radius ($r_{\rm p}$) and migration speed ($\dot{a}$). $\mathcal{I}_{\mathcal{V}}$ is calculated in the inertial frame. We now describe each panel of $\mathcal{I}_{\mathcal{V}}$ separately:

(i) $T_{\rm A}$ (top left panel): $\mathcal{P}$ being quite massive ($q_{\rm p}/h^3(r_{\rm p,0}) \sim 1.5$), its wakes turn into shocks within their excitation region (Goodman & Rafikov 2001) and create $\mathcal{I}_{\mathcal{V}}$ maxima on both sides of the planet orbit (Lin & Papaloizou 2010). (Note that the background profile of $\mathcal{I}_{\mathcal{V}}$ increases as $r^{1/2}$, which reflects its initial profile. Note also the $\mathcal{I}_{\mathcal{V}}$ perturbations in the planet's wakes which arise because $q_{\rm p}/h^3(r_{\rm p,0}) > 1$.) We observe an asymmetry in the radial location of the $\mathcal{I}_{\mathcal{V}}$ maxima with respect to $\mathcal{P}$, which comes about because of the inward migration of $\mathcal{P}$. Around the gap's inner edge, the synodic period of the gas relative to the planet remains shorter than the migration time-scale of $\mathcal{P}$ across its gap region. The inner wake of $\mathcal{P}$ can therefore shock the gas near the gap's inner edge multiple times, and sustain an $\mathcal{I}_{\mathcal{V}}$ maximum there (it is like a cumulative effect). Because of the inward migration, the outer wake of $\mathcal{P}$ cannot shock the same fluid elements repetitively near the gap's outer edge, which explains the lack of an $\mathcal{I}_{\mathcal{V}}$ maximum at this location. The $\mathcal{I}_{\mathcal{V}}$ maximum that is visible at around 24 au was triggered by the outer wake of $\mathcal{P}$ when its migration rate was smaller near the beginning of the simulation.

(ii) $T_{\rm B}$ (top middle panel): as migration proceeds, the material that crosses the planet's orbit has increasing inverse vortensity, which therefore increases the dynamical corotation torque and the migration rate (Masset & Papaloizou 2003, and see equation 3). As the migration rate increases, $\mathcal{P}$ enters the runaway migration regime ($\delta m \gtrsim M_{\rm p}$). At some point, migration is fast enough that the synodic period of the gas near the gap's inner edge becomes longer than the migration time-scale of $\mathcal{P}$ across its gap. The cumulative shocks of the inner wake brought about above no longer operate, or, said differently, the inner wake of $\mathcal{P}$ can no longer sustain an

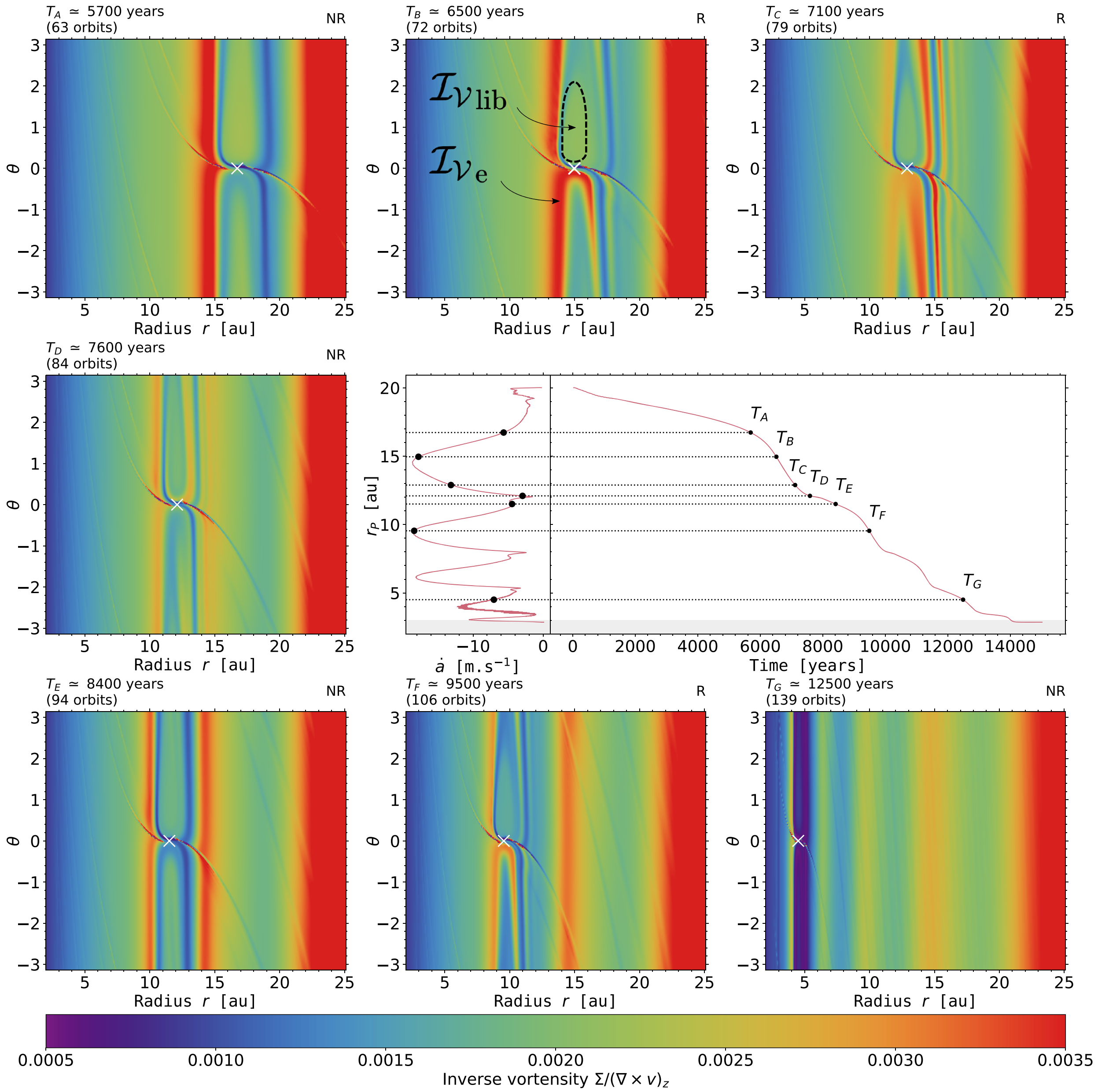

Figure 3. Results of the Uther simulation: time evolution of the planet's orbital radius and migration rate (middle-right panel; the grey band corresponds to the inner wave-killing zone), and screenshots of the inverse vortensity ($\mathcal{I}_\mathcal{V}$) at seven times denoted by T_A to T_G in the panel showing the planet's orbital evolution. In each screenshot, $\mathcal{I}_\mathcal{V}$ is expressed in code units and shown in polar cylindrical coordinates between the inner boundary at 2 and 25 au, and the number of orbits indicated in the upper-left corner corresponds to the number of orbital periods at the planet's initial location (20 au). Note that one orbital period at this location corresponds to ≈90 yr. In the upper-right corner of each $\mathcal{I}_\mathcal{V}$ panel, we specify with 'R' or 'NR' whether the planet is undergoing runaway or non-runaway migration. The planet's position is marked by a white cross.

$\mathcal{I}_\mathcal{V}$ maximum inside the orbit. When the entering inverse vortensity takes its maximum value, $\mathcal{P}$ reaches its maximum migration rate. This is the case shown in this panel (see the 'red' stream of high $\mathcal{I}_\mathcal{V}$ executing an outward U-turn relative to $\mathcal{P}$ at $\theta \lesssim 0$). Meanwhile, the azimuthal extent $\Delta\theta$ of the libration region decreases, which saturates the runaway process by limiting the increase in δm (see the $\Delta\theta$ term in equation B2).

(iii) T_C (top right panel): after the gas with maximum $\mathcal{I}_\mathcal{V}$ has crossed the orbit, $\mathcal{P}$ keeps on migrating and now forces material with unperturbed (and thus smaller) $\mathcal{I}_\mathcal{V}$ to execute outward U-turns. The feedback on migration due to the coorbital vortensity deficit now acts in the opposite way: the inverse vortensity of the material entering the horseshoe region ($\mathcal{I}_{\mathcal{V}_e}$) decreases, δm decreases, and so does the migration rate.

(iv) T_D (middle left panel): migration is now slow enough that part of the high $\mathcal{I}_\mathcal{V}$ material that previously entered the horseshoe region becomes trapped in libration and performs multiple horseshoe U-turns. This panel actually highlights a secondary inward U-turn of high $\mathcal{I}_\mathcal{V}$ material in front of the planet in azimuth. Because the gas executing inward U-turns has a higher $\mathcal{I}_\mathcal{V}$ than the gas doing outward U-turns, a positive corotation torque applies to $\mathcal{P}$, which slows down even more its migration, until the vortensity in the horseshoe region gets progressively mixed. These secondary U-turns will be examined in more detail in Section 4.2.

(v) T_E (bottom left panel): $\mathcal{P}$ is now in a non-runaway migration regime and its wakes can trigger new $\mathcal{I}_\mathcal{V}$ maxima on both sides of the planet's orbit. Inward migration resumes, and a radial asymmetry in the position of the $\mathcal{I}_\mathcal{V}$ maxima with respect to $\mathcal{P}$ can be seen again in this panel, which is similar to the one shown at time T_A. A new cycle of runaway migration begins. The comparison with the panel at T_A highlights that the radial location of the $\mathcal{I}_\mathcal{V}$ maximum outside the planet at T_E (∼14 au) nearly coincides with that of the $\mathcal{I}_\mathcal{V}$ maximum inside the planet at T_A, i.e. just before the onset of runaway migration. We will come back to this point in Section 4.6.

(vi) T_F (bottom middle panel): as previously, runaway stalls as the inner wake ultimately fails to maintain an $\mathcal{I}_\mathcal{V}$ maximum inside the planet's orbit and the azimuthal width of the libration region shrinks. This panel is very similar to the one shown at time T_B, and we notice that the migration rate takes very similar values at both times. A new maximum of $\mathcal{I}_\mathcal{V}$ will form outside the planet's orbit when the migration rate has reached again its minimum value.

(vii) T_G (bottom right panel): at the end of the simulation, when migration stalls near the grid's inner boundary, multiple bands of high-$\mathcal{I}_\mathcal{V}$ material are formed, including one inside the planet's orbit. The bands beyond the planet's orbit trace the transition stages between fast and slow migration. The longevity of these bands will be discussed in Sections 3.2.2 and 4.1.

As already stated in Section 3.1, Lin & Papaloizou (2010) and McNally et al. (2019) have obtained a similar scenario of intermittent migration. Although in these models gas vortices form at the edges of the planet gap due to the Rossby-Wave Instability, the intermittent episodes of runaway migration can also be accounted for by the time evolution of the inverse vortensity of the gas crossing the planet's orbit.

3.2.2 Dust spatial distribution

We have seen in Section 3.2.1 that intermittent planet migration gives structure to the disc gas, with the formation of new maxima in the inverse vortensity profile on each side of the planet's orbit at the end of each stage of runaway migration. These inverse vortensity maxima are intimately related to pressure maxima triggered by the planet wakes when migration decelerates, as we illustrate below (the reader is referred to, e.g. equation 32 in Casoli & Masset 2009 for a formal link between maxima of inverse vortensity and of pressure). We then study how intermittent migration impacts the dust distribution. For the simulation Uther, we use 5×10^4 Lagrangian test particles with initial orbital radius $r_\mathrm{d} \in [14\text{–}21]$ au. This is meant to maximize the particles resolution at the dust structures that form during the inward migration of $\mathcal{P}$.

The upper panels in Fig. 4 show three snapshots of the azimuthally averaged radial profiles of the gas pressure (in blue) and of the dust's surface density (in red). The dust's surface density is calculated with the dust's size distribution and total mass adopted in the radiative transfer calculations (see Section 2.2). We note in passing that the dust-to-gas surface density ratio does not exceed ∼0.1 throughout the simulation, which justifies that dust feedback on the gas can be safely discarded for the Uther disc model. The thick grey lines in Fig. 4 show the location of the pressure maxima beyond the planet's orbital radius. The location of the planet is marked by the dashed line.

Shortly after the beginning of the simulation (Fig. 4, top left), there is only one pressure maximum at the outer edge of the planet's gap, which is built up by the outer wake of $\mathcal{P}$ before the first episode of runaway migration (see also the appendix A of Meru et al. 2019). At the end of the first cycle of runaway migration, when $\mathcal{P}$ has decelerated, a new pressure maximum forms outside the planet orbit (see Fig. 4, top middle, which corresponds approximately to Fig. 3, bottom left, for the inverse vortensity). At the end of the third episode of runaway migration (Fig. 4, top right, corresponding to Fig. 3, bottom right), we obtain four pressure maxima outside the planet orbit, and one inside the orbit. (The fact that the latter is not an inflection point may be partly due to the proximity of the inner wave-killing zone). More precisely, at the position of $\mathcal{P}$ in this last snapshot (∼5 au), the planet braked three times, which gave it time to create three pressure maxima in addition to the initial pressure maximum outside the original position of $\mathcal{P}$ (near 22 au). The pressure maxima that are not sustained by the planet wakes progressively turn into inflection points under the action of turbulent viscosity.

At a given location in the disc, dust and gas do not have the same orbital speed due to the pressure-gradient force acting on the gas. This velocity difference induces an aerodynamic force from the gas to the dust, which eventually leads to the radial drift of the dust. At a pressure maximum, there is no relative motion of the dust and the gas, therefore no aerodynamic force and no resulting drift. A pressure maximum thus defines an equilibrium position where dust accumulates and is trapped in rings. We thus expect an accumulation of dust at each bump in the pressure profile, and this is precisely what can be seen in the upper panels in Fig. 4 by comparing the location of the maxima in the dust surface density (red curves) and in the gas pressure (thick grey lines) beyond the planet.

The bottom panels of Fig. 4 display in black and white the perturbed gas surface density ($\Sigma - \Sigma_0$) relative to its initial profile Σ_0 at the same times as the top panels in the same figure. The red cross spots the location of $\mathcal{P}$. We depict dust superparticles as coloured dots; colour varies with particles size, from red (10 µm) to purple (10 cm). The inward drift of the largest ($s \gtrsim 1$ cm) particles is clearly visible between the bottom left and bottom middle panels of Fig. 4. Note that the small particles are not present in the inner disc due to the choice of initial particles location and the fact that there has not been enough time for the small particles to drift. In the bottom-right panel of Fig. 4, we see that dust particles are trapped in axisymmetric rings at the location of the pressure maxima (around 22, 14, 9, 6, and 4 au for this simulation at 12 500 yr), and that larger particles get more concentrated at these locations on account of their larger Stokes number (larger particles, with Stokes number $\lesssim 1$, drift more rapidly towards equilibrium locations).

To examine the longevity of the dust rings, we display in Fig. 5 the space–time diagram of the dust's radial location versus dust size for the Uther simulation. Each dot marks the orbital radius of a sample of superparticles as a function of time, with colour varying with particles size (see colour bar on the right-hand side). This graph clearly shows the progressive disappearance of the dust rings formed prior to each stage of inward runaway migration. Dust rings typically last between 3000 and 10 000 yr. It is also instructive to examine the time evolution of the radial location of the largest particles (dark-blue dots). Some of these large particles are initially located around the planet's orbital radius before the first episode of runaway migration at ∼6000 yr, and going back to the bottom-left panel in Fig. 4 we see that these correspond to the

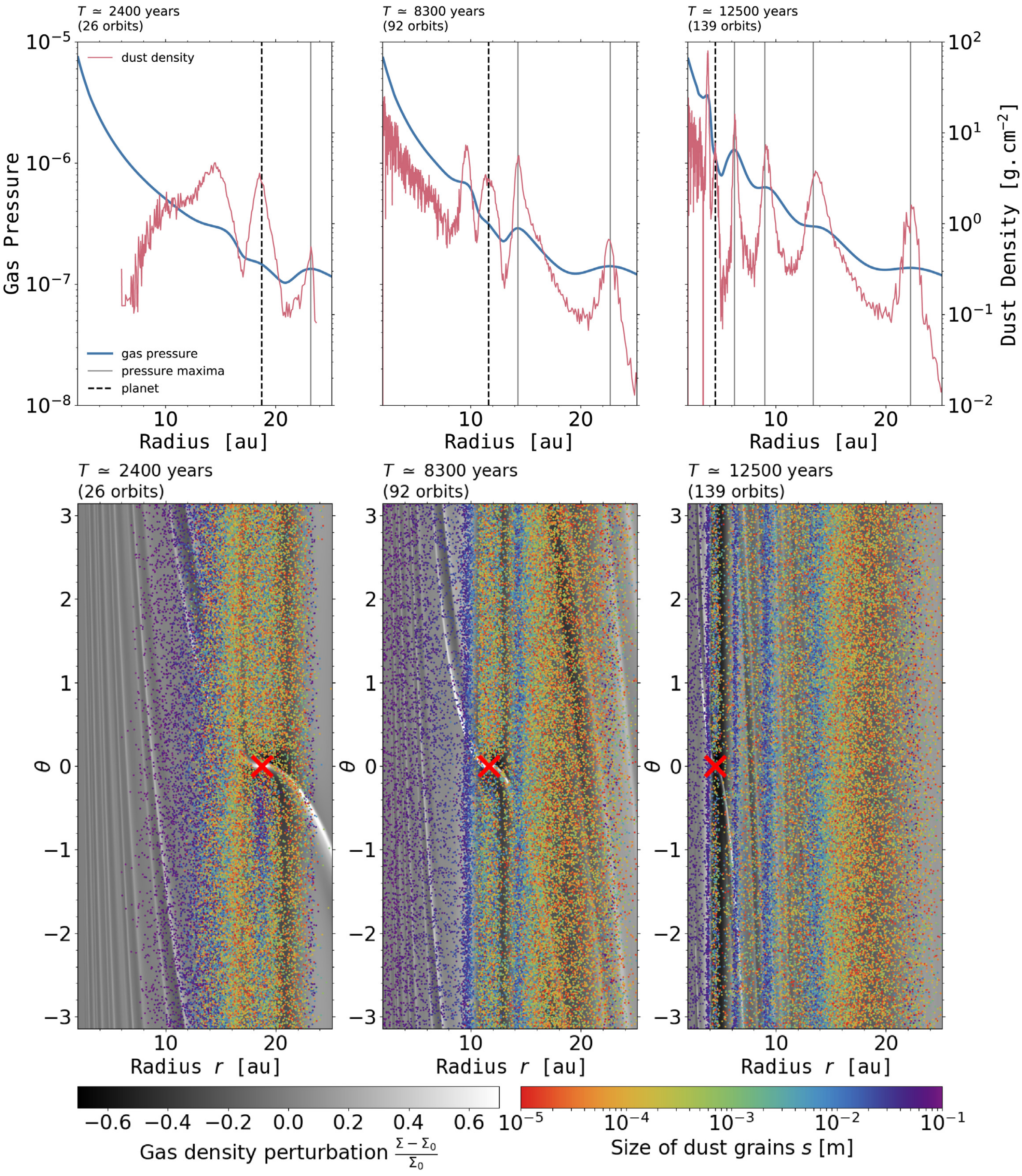

Figure 4. Results of the Uther simulation: gas structure and dust spatial distribution in polar cylindrical coordinates in the disc region between the inner boundary at 2 and 25 au. Results are shown at 2400 yr in the left-hand panels, at 8300 yr in the middle panels, and at 12 500 yr in the right-hand panels (same time as in Fig. 3, bottom right). Top: azimuthally averaged radial profiles of the gas pressure (*blue*) and of the dust's surface density (*red*). The planet's orbital radius is spotted by a vertical dashed line. Pressure maxima outside the planet position are depicted by the thick grey lines. Bottom: perturbed gas surface density relative to its initial profile, $(\Sigma - \Sigma_0)/\Sigma_0$, in black and white. The location of dust particles is overlaid by coloured dots. The rainbow colour bar shows dust size in meters, with purple dots for the largest particles (10 cm) and red dots for the smallest (10 μm). In each panel, the red cross at zero azimuth marks the position of the planet.

particles trapped around the L5 Lagrange point behind the planet in azimuth. As the runaway proceeds, these particles escape the Lagrange point and a large fraction of them become trapped at the pressure maximum outside the planet's orbit which forms at the end of this first runaway. Similarly, close inspection at the second stage of runaway migration at ~9000 yr shows that the large particles that become trapped at the newly formed pressure maximum outside the planet's orbit mainly originate from the reservoir of large particles

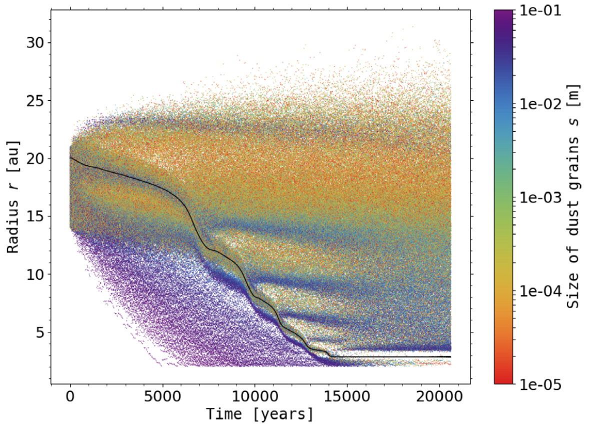

Figure 5. Space–time diagram for the Uther simulation, illustrating the longevity of dust rings formed by multiple stages of runaway planet migration. This panel displays the orbital radius of a sample of superparticles as a function of time, with colour varying with particles size. The planet's orbital radius is shown by a black curve.

Table 3. Parameters of the dust radiative transfer calculations.

Parameter	Value
Wavelength	1.3 mm
Dust size range	$s \in [10^{-5}$–$10^{-1}]$ m
Dust size distribution	$n(s) \propto s^{-3.5}$
Dust-to-gas mass ratio	10^{-2}
Dust composition	60 per cent silicates, 40 per cent water ices
Scattering	Discarded
Disc distance	150 pc
Stellar radius	2 $R_\odot$
Star effective temperature	7000 K

initially inside the orbit. A similar observation can be made with the subsequent stages of runaway migration. It is interesting to realize that not all the reservoir of large particles inside the orbit ends up populating the dust trap triggered outside the orbit. Part of the particles embarking on to outward U-turns perform secondary U-turns inward, the same secondary U-turns that we have illustrated on the gas inverse vortensity in the middle left panel ($T_{\rm D}$) of Fig. 3. This process allows to maintain a contingent of large particles inside the planet's orbit which will progressively fill the dust traps outside the planet's orbit formed after each jolt of the planet. We finally notice that the dust traps formed outside the planet's orbit seem to have a geometrical radial spacing (there is a factor $\sim$1.5 between the radial locations of successive dust rings, we will come back to this point in Section 4.6).

3.2.3 Continuum emission at $\lambda = 1.3$ mm

The dust spatial distribution obtained in the Uther simulation was post-processed with the 3D radiative transfer code RADMC3D to produce synthetic flux maps of continuum emission at $\lambda = 1.3$ mm according to the procedure detailed in Section 2.2. The main parameters of the dust radiative transfer calculations are summed up in Table 3.

The synthetic flux map of continuum emission based on the results of the Uther simulation at 12 500 yr is displayed in the upper panel in Fig. 6. Three bright rings of emission are clearly visible in the flux map. The outermost visible ring, which is located at $\sim 0\overset{''}{.}09$ ($\sim$14 au), corresponds to the maximum in the dust's surface density located near 14 au in the top-right panel in Fig. 4. The dust density maximum located near 22 au does not produce a visible bright ring in the flux map. The second visible ring in the upper panel of Fig. 6 mostly corresponds to the dust density maximum located near 9 au in the top-right panel in Fig. 4. Finally, the innermost bright ring corresponds to the beam dilution of the three dust density maxima which are located at the planet's orbit radius and on both sides of the planet's gap. Furthermore, we notice azimuthal variations of the flux along the bright rings, which are of the order of 50 μJy beam^{-1}. We have checked that, at the location of the bright rings, the dust's thermal emission is optically thick (the absorption optical depth varies between about 2 and 4). These azimuthal variations in the intensity thus convey azimuthal variations in the dust temperature obtained by the thermal Monte Carlo calculation.

The middle panel in Fig. 6 shows the same flux map obtained by adding white noise to the raw flux map prior to beam convolution (see Section 2.2). It is clear that the three bright rings are still discernible despite the realistic level of noise that we consider. These rings are also clearly visible in the lower panel of Fig. 6, where we display the azimuthally averaged radial profile of the convolved intensity.

3.3 Pendragon simulation ($h_0 = 0.06$, $\alpha = 10^{-4}$)

We now present the results of the Pendragon simulation, which differs from the Uther simulation by a slightly increased disc's aspect ratio ($h_0 = 0.06$ instead of 0.05) and a reduced alpha turbulent viscosity ($\alpha = 10^{-4}$ instead of 10^{-3}). Having a smaller α implies that the structures that we obtain in the dust spatial distribution are sharper and less subject to turbulent diffusion, which leads to structures that last longer in the disc. However, because a low turbulence favours the RWI, the formation of vortices that can interact with $\mathcal{P}$ makes the interpretation of the planet's orbital evolution a priori harder. These vortices can appear for example when a stream of high $\mathcal{I}_{\mathcal{V}}$ material mixes with low $\mathcal{I}_{\mathcal{V}}$ non-perturbed regions, which is typical of the fast migration stages presented in Section 3.2.1. Nevertheless, the important quantities presented in that same section, mainly the coorbital vortensity deficit and the inverse vortensity of the orbit-crossing material, allow a good understanding of what happens in the low turbulent case that we present in this section. For the dust, we use this time 10^5 Lagrangian test particles initially distributed in a larger band $r_{\rm d} \in [14$–$23]$ au, in order to have more particles trapped at the outermost pressure maximum formed by the planet shortly after the beginning of the simulation. Table 4 sums up the main parameters of this simulation.

3.3.1 Dust spatial distribution

The upper panel in Fig. 7 shows the time evolution of the planet's orbital radius (right-hand side) and its migration speed (left-hand side). The migration pattern is similar to that in the Uther simulation, with a succession of fast (runaway) and slow (non-runaway) migration episodes. Compared to the Uther simulation, the steps occur at a later time because of a slower initial migration due to a deeper gap. Also, the steps are less numerous and more pronounced, foretelling there should be less bright rings in the continuum emission.

In the lower part of Fig. 7 is shown the dust spatial distribution (coloured dots) superimposed on the perturbed gas surface density

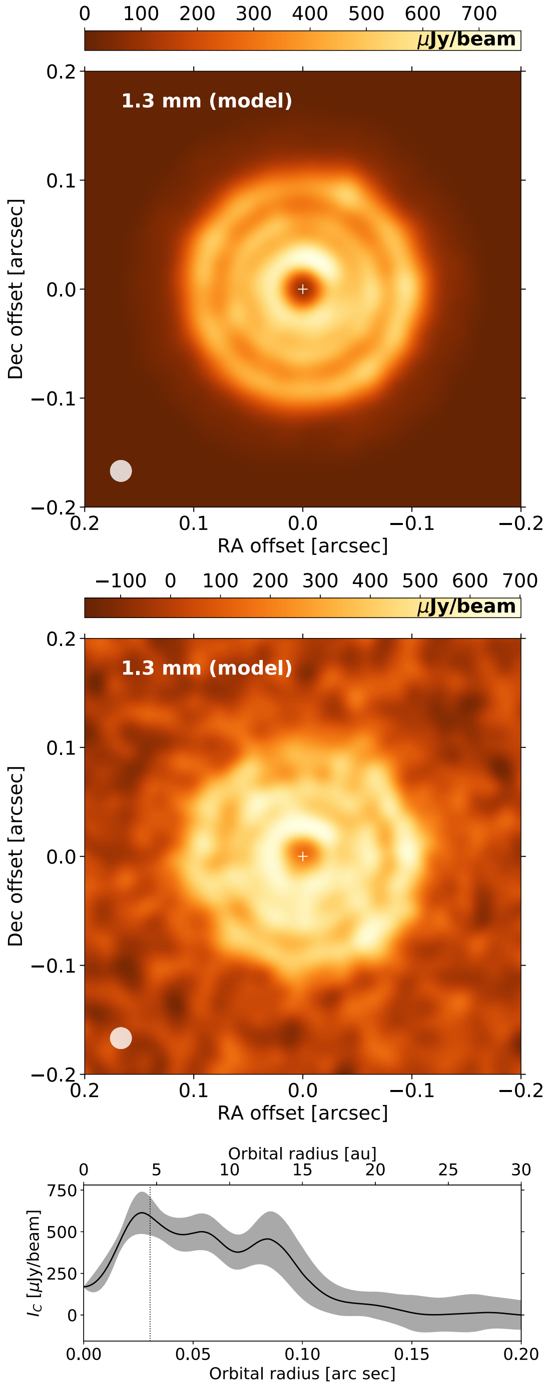

Figure 6. Predicted continuum emission at 1.3 mm for the Uther simulation at 12 500 yr (or 139 planet orbits). Top: Synthetic flux map obtained after convolution with a $0\farcs02$ circular beam. The beam is shown by the circle in the bottom left corner. The *x*- and *y*-axes indicate the offset from the stellar position in the RA and Dec. in arcsec, i.e. north is up and west is to the right. Middle: Same as upper panel, but with white noise of 50 μJy beam^{-1} standard deviation added to the raw flux maps (prior to beam convolution). Bottom: Azimuthally averaged convolved intensity as a function of distance to the star. The grey shaded area around the profile corresponds to $\pm 2\sigma$ dispersion around the mean. The vertical dotted line shows the location of the planet.

Table 4. Parameters of simulation Pendragon (Section 3.3).

Parameter	Value
Planet to primary mass ratio $q_{\rm p}$	4.3×10^{-4}
Disc's aspect ratio h_0 at 10 au	0.06
Alpha turbulent viscosity	10^{-4}
Gas surface density Σ_0 at 10 au [code units]	10^{-3}
Number of dust superparticles	100 000
Dust's initial location	$\in$ [14–23] au

(black and white contours) at the four times marked by black circles in the upper panel: $T_{\rm A} = 14\,900$, $T_{\rm B} = 20\,600$, $T_{\rm C} = 30\,000$, and $T_{\rm D} = 59\,900$ yr. Initially, $\mathcal{P}$ migrates slowly. Due to this slow migration, the dust structures in the disc follow the planet's orbital motion. We can highlight two important behaviours: first, $\mathcal{P}$ forms a dust ring ($\mathcal{R}_p$) centred on its orbital radius with an accumulation of particles around the Lagrange point L5 behind the planet in azimuth. The ring $\mathcal{R}_p$ is surrounded by two rings: an internal ring $\mathcal{R}_i$ and an external ring $\mathcal{R}_{e,1}$. Secondly, we observe the rapid inward drift of the largest grains. While $\mathcal{P}$ migrates inward gently, it gets closer to $\mathcal{R}_i$ as it pushes particles inwards. Particles that were initially trapped at $\mathcal{R}_{e,1}$ drift slowly because the location of the corresponding pressure maximum does not change much. This progressively leads to a radial asymmetry of $\mathcal{R}_i$ and $\mathcal{R}_{e,1}$ compared to $\mathcal{R}_p$ (Meru et al. 2019; Pérez et al. 2019). For instance, at time $T_{\rm A}$, $\mathcal{R}_i$, $\mathcal{R}_p$, and $\mathcal{R}_{e,1}$ are located at around 12, 15, and 24 au, respectively. As we have seen in Section 3.2.1, this asymmetry enables material with higher $\mathcal{I}_{\mathcal{V}}$ to enter the coorbital region, making $\mathcal{P}$ move faster inward. When the fast migration regime is triggered, $\mathcal{P}$ overtakes the internal ring $\mathcal{R}_i$ at around 10 au, and part of the dust that was trapped at $\mathcal{R}_i$ and at the Lagrange points perform a horseshoe U-turn. These particles then follow a complex dynamics due to the presence of small vortices arising because of the Rossby-Wave Instability, and form a new outer dust ring $\mathcal{R}_{e,2}$ at 12 au (see second lower panel from the left at time $T_{\rm B}$). The same behaviour happens again during each jolt in the planet migration. During this evolution, the external rings $\mathcal{R}_e$ that are left behind $\mathcal{P}$ do not drift significantly. After the *N*th jump, $N + 1$ outer dust rings have been created. Since two stages of runaway migration occur in the simulation, three dust rings form outside the planet's location (here at around 7, 12, and 24 au).

Each jolt is associated with an increase in the migration speed (Fig. 7, top left): between $T_{\rm A}$ and $T_{\rm B}$, and between $T_{\rm B}$ and $T_{\rm C}$. The rather large amplitude oscillations in the planet's migration speed are most probably due to the formation of several vortices that carry away sporadically high $\mathcal{I}_{\mathcal{V}}$ material from the inner to the outer edges of the planet's gap ($T_{\rm B}$, see Lin & Papaloizou 2010). These vortices interact with the planet before merging and forming a single large-scale vortex ($T_{\rm C}$) in which dust particles larger than about a millimeter are trapped. The vortex gradually disappears and becomes an axisymmetric dust ring. At the time $T_{\rm D}$ shown in the lower right panel of Fig. 7, which is a long time after the planet has stalled its migration upon reaching the inner wave-killing zone, the three dust rings are still present. The external ring created last ($\mathcal{R}_{e,3}$ at 7 au) is located at the outer edge of the final planet's position $\mathcal{R}_{\rm p} \sim 5$ au.

We display in Fig. 8 the space–time diagram for the Pendragon simulation, which shows that the dust rings have a much longer lifetime than in the Uther simulation, since some dust rings are maintained over more than 10^5 yr. We notice that the dust ring at ~12 au gets disrupted at ~ 60 000 yr onward and the largest dust particles that were initially trapped there start drifting inward.

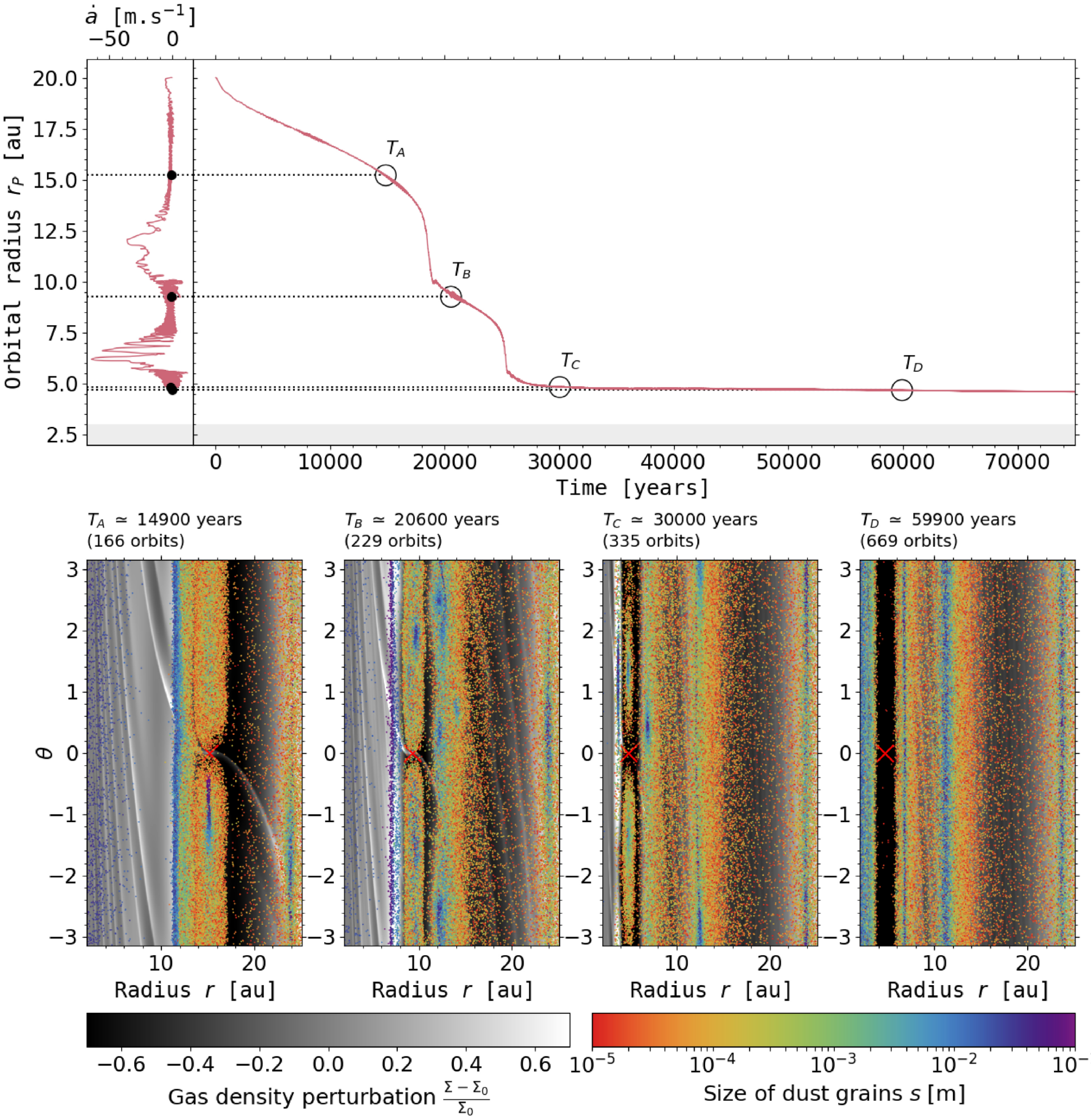

Figure 7. Results of the Pendragon simulation: planet's orbital evolution, gas structure, and dust spatial distribution in the disc region between the inner boundary at 2 and 25 au. Top right: evolution of the planet's orbital radius as a function of time. The four circles indicate four different times in the simulation : $T_A = 14\,900$, $T_B = 20\,600$, $T_C = 30\,000$, and $T_D = 59\,900$ yr. Top left: evolution of the planet's migration speed as a function of its position in the disc. The grey band corresponds to the inner wave-killing zone. Bottom: same as lower panel of Fig. 4, but for the four aforementioned times in the Pendragon simulation.

They ultimately reach the dust trap at ~7 au. Similarly, the dust ring initially at ~24 au disappears after ~ 200 000 yr. As will be further emphasized in Section 4.1, the longevity of the dust rings is intimately related to the sharpness of the pressure profile around the maxima, which turbulent viscosity progressively smooths out. It therefore depends on how strong the shock of the outer planet's wake is initially during each stage of non-runaway migration. The shorter this stage, the weaker the shock will be, and the earlier the dust ring formed beyond the planet's orbit will disappear. We finally point out that, for the size distribution and total mass of dust in the radiative transfer calculation, the dust-to-gas surface density ratio can reach up to 0.5–0.6 throughout the Pendragon simulation, and discarding dust feedback remains a safe approximation for this disc model.

3.3.2 *Continuum emission at λ = 1.3 mm*

The synthetic map of the 1.3 mm continuum emission obtained from the Pendragon simulation at 59 900 yr is displayed in the upper panel in Fig. 9. The low level of turbulence in this simulation implies sharp

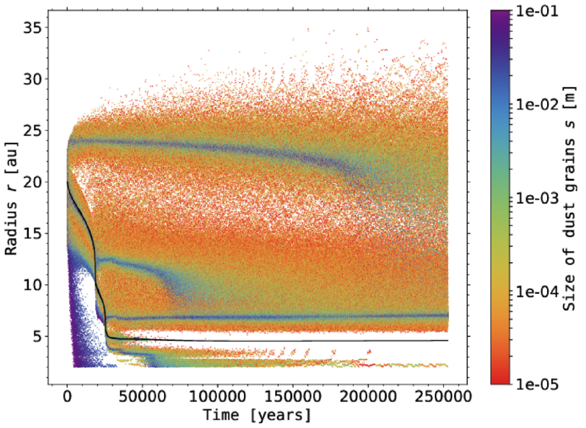

Figure 8. Same as Fig. 5 for the Pendragon simulation.

structures in the continuum emission. Four bright rings of emission are clearly visible in the synthetic flux map. The two innermost bright rings correspond to the dust rings at the pressure maxima located on both sides of the planet's orbit (which are at around 4 and 7 au, see bottom-right panel of Fig. 7). The two outermost bright rings correspond to the dust rings that formed outside the planet's orbit prior to each stage of runaway inward migration (they are at about 12 and 24 au, see again the bottom-right panel of Fig. 7).

We notice that the flux along the bright rings decreases with increasing distance from the star, which mostly reflects the radial decrease in the dust temperature (the emission at the bright rings is optically thick). The intensity of the outermost bright ring at around 24 au is actually quite low (around 100 μJy beam^{-1}). Thus, when white noise with a rms level of 50 μJy beam^{-1} is added to the raw flux map, the outermost ring is almost not visible anymore, whereas the innermost rings are still clearly visible (see middle and bottom panels of Fig. 9).

4 DISCUSSION AND SUMMARY

4.1 Longevity of the dust rings

We discuss in this section, the longevity of the dust rings induced by intermittent runaway migration. When the planet starts a new episode of runaway migration, the pressure maximum that the planet has formed beyond its orbit is no longer sustained by the planet's outer wake. The pressure maximum is therefore progressively smoothed out by the disc's turbulent viscosity, and so is the dust ring that coincides with the pressure maximum. As we have seen in Figs 5 and 8, the dust rings last between 3000 and 10 000 yr in the Uther simulation ($\alpha = 10^{-3}$), whereas some dust rings survive for more than 10^5 yr in the Pendragon simulation ($\alpha = 10^{-4}$).

This comparison highlights that the lifetime of the dust rings does not simply scale inversely proportional to the gas turbulent viscosity. The main reason is that the lifetime of a dust trap partly depends on how sharp the radial pressure profile is around the pressure maximum, which is related to the duration of the stage of decelerated migration between two successive runaways. This duration is sensitive to the disc's turbulent viscosity, but also to the disc's physical model (e.g. the background gas density profile, see Section 4.2) and the numerical resolution (see Section 4.5).

Finally, Fig. 10 presents the space–time diagram of the dust's radial location for an additional simulation with a set-up identical to that of the Pendragon run, but a turbulent viscosity reduced to $\alpha = 10^{-5}$. It shows that all dust rings, except the one coorbital with the planet, last over the entire duration of the simulation ($\gtrsim 3 \times 10^5$ yr). We notice in this case that the planet slowly migrates outwards after having reached the proximity of the inner wave-killing zone, and so do the dust rings formed inside and outside the planet's orbit after the last episode of runaway migration.

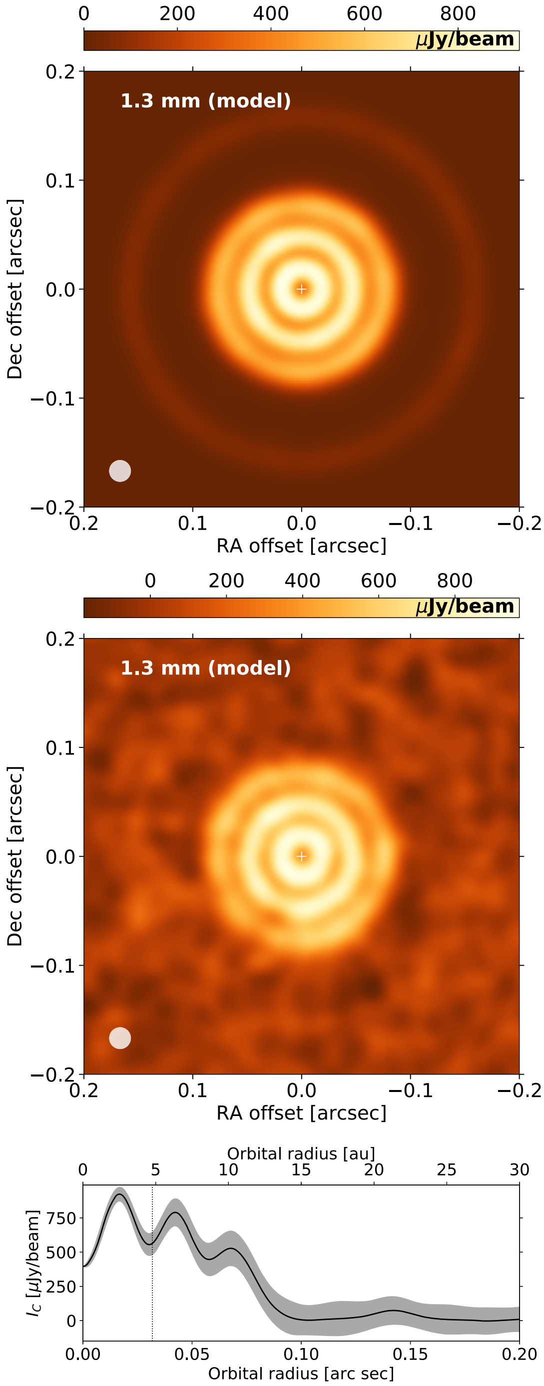

Figure 9. Same as Fig. 6, but for the Pendragon simulation at 59 900 yr (669 planet orbits).

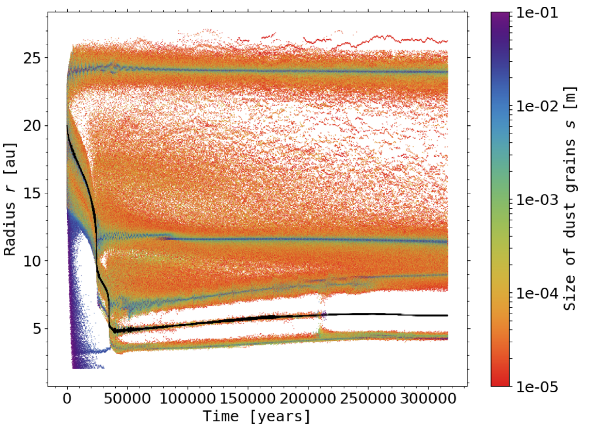

Figure 10. Same as in Fig. 5 for an extra run with the same setup as Pendragon but with a turbulent viscosity $\alpha = 10^{-5}$.

4.2 Initial gas surface density profile

We have seen in Fig. 1 that increasing the initial surface density Σ_0 from 3×10^{-4} to 3×10^{-3} radically changes the migration pattern of $\mathcal{P}$, as well as the dust spatial distribution (Fig. A1). According to fig. 14 of Masset & Papaloizou (2003), which shows the occurrence of runaway migration as a function of disc mass and planet mass, the slow migration case in Fig. 1 (Section 3.1) corresponds to non-runaway type I migration, whereas the intermittent and fast cases correspond to type III runaway migration. We now show in this section that, for a given value of Σ_0, inward runaway migration can also be smooth or discontinuous depending on the slope of the initial gas density profile.

By varying the power-law exponent of the initial surface density profile of the gas, that is σ in $\Sigma_0(r) = \Sigma_0 \times (r/r_0)^{-\sigma}$, we change the unperturbed (i.e. initial) inverse vortensity profile, $\mathcal{I_V}_0(r) = \Sigma_0(r)/\omega_0(r) \propto r^{3/2-\sigma}$, and thus the inverse vortensity of the material entering the horseshoe region ($\mathcal{I_V}_e$) as the planet migrates. To examine how different values of σ impact our results, we performed two additional simulations with the Uther disc model for $\sigma = 0$ and $\sigma = 2$, the fiducial Uther simulation presented in Section 3.2 having $\sigma = 1$. In the following, we refer to these simulations as the σ_0, σ_1, and σ_2 runs. The upper panel of Fig. 11 compares the time evolution of the planet's orbital radius (r_p) and migration speed ($\dot{a}$) in these three simulations.

We see that, initially, $|\dot{a}|$ takes very similar values in all three runs ($|\dot{a}| \sim 2\ \mathrm{m\,s^{-1}}$). From this we argue that the static corotation torque plays a minor role in the initial migration rate. This is confirmed by inspection at equation (51) of Paardekooper, Baruteau & Kley (2011), which indicates that the static corotation torque saturates for the values of q_p, h_0, and α in the Uther simulation. The migration behaviour changes dramatically, however, after the first episode of runaway: in the σ_2 run, migration remains smooth and fast, whereas in the σ_0 run migration is intermittent, with stages of decelerated migration that last longer than in the σ_1 run. These behaviours boil down again to the radial profile of inverse vortensity.

In the σ_2 run, the background inverse vortensity profile decreases with radius (as $r^{-1/2}$). The unperturbed material that crosses the orbit has an inverse vortensity comparable to, if not larger than that of the gas initially shocked by the inner wake. The coorbital vortensity deficit thus does not decrease when the planet starts interacting with the unperturbed gas inside its orbit, and migration does not decelerate. Shock formation is impeded, and runaway migration is fuelled solely by the increasing inverse vortensity of the background material that crosses the orbit as $\mathcal{P}$ moves inwards. A similar result was predicted by Lin & Papaloizou (2010; their section 6.1.1). Consequently, migration becomes increasingly fast, and it is clear in the upper panel of Fig. 11 that $|\dot{a}|$ increases nearly continuously in the σ_2 simulation until $\mathcal{P}$ reaches the grid's inner boundary.

On the contrary, in the σ_0 and σ_1 runs, the background inverse vortensity increases with radius. The unperturbed material crossing the orbit has an inverse vortensity smaller than that of the gas initially shocked by the inner wake. The coorbital vortensity deficit therefore decreases when $\mathcal{P}$ starts interacting with this unperturbed material, runaway stalls, and $\mathcal{P}$ is able to generate an $\mathcal{I_V}$ maximum inside its orbit that fuels the next episode of runaway migration.

The maximum migration rate is determined by the difference between the $\mathcal{I_V}$ maximum of the gas shocked by the inner wake (which we denote by $\mathcal{I_V}_\mathrm{max}$) and $\mathcal{I_V}_\mathrm{lib}$ (which is close to $\mathcal{I_V}_0(r_\mathrm{p})$). Both quantities are annotated in the lower left panel of Fig. 11. This difference of inverse vortensity increases upon lowering σ, and we see in the upper left panel of Fig. 11 that the maximum migration rate increases for smaller σ, at least in the first episode of runaway migration. Likewise, the braking is determined by the difference between $\mathcal{I_V}_\mathrm{max}$ and the $\mathcal{I_V}_0$ of the material orbiting inside the shocked gas (denoted by $\mathcal{I_V}_0^-$ in the lower left panel of Fig. 11). Again, this difference increases (in absolute value) for smaller σ. The braking also depends on the ability of the material entering the horseshoe region to perform secondary U-turns, which slows down migration by adding a positive corotation torque.

We have already mentioned the existence of secondary U-turns for the Uther simulation in Section 3.2 (see the panel at time T_D in Fig. 3). A smaller σ favours multiple U-turns of the material entering the horseshoe region, a larger induced corotation torque, and therefore a more abrupt braking of the migration. A short episode of outward migration is even observed at the end of the first runaway in the σ_0 run, as highlighted by the inset plot in the upper panel of Fig. 11. The three panels of inverse vortensity in Fig. 11 help understand this short episode. The left-hand panel at time $T_\mathrm{A} = 5900$ yr is when $|\dot{a}|$ is maximum. A trapezoidal region of material trapped in libration with $\mathcal{P}$ forms at $0 \lesssim \theta \lesssim 2$ rad, whereas the inner material with maximum $\mathcal{I_V}$ executes primary U-turns outwards, contributing to the planet's runaway. Part of this material with maximum $\mathcal{I_V}$ crosses the orbit, but when $\mathcal{P}$ starts slowing down, part of it stays in the horseshoe region and performs secondary U-turns. This situation is illustrated in the middle panel at time $T_\mathrm{B} = 6700$ yr, where the $\mathcal{I_V}$ difference of the gas just in front of the planet in azimuth (high $\mathcal{I_V}$) and just behind it (low $\mathcal{I_V}$) is large enough for the (positive) corotation torque to allow outward migration. This $\mathcal{I_V}$ difference changes sign in the right-hand panel at time $T_\mathrm{C} = 7000$ yr. Progressive advection-diffusion of vortensity in the horseshoe region, and shock formation inside the gap's inner edge, reinstate inward migration. The oscillations in the planet's orbital radius described by McNally et al. (2019) after each runaway phase correspond in our work to secondary U-turns of high-$\mathcal{I_V}$ material in the coorbital region. These secondary U-turns help at once brake the planet's migration and replenish the reservoir of dust particles ahead of the planet before the pending runaway phase.

Concerning the impact of σ on the dust, we point out that the number of rings is smaller in the σ_0 run than in the σ_1 run, due to the reduced number of episodes of runaway migration. Moreover, because the phases of non-runaway migration last longer for σ_0, the pressure maxima are sharper, and the intensity ratio between bright

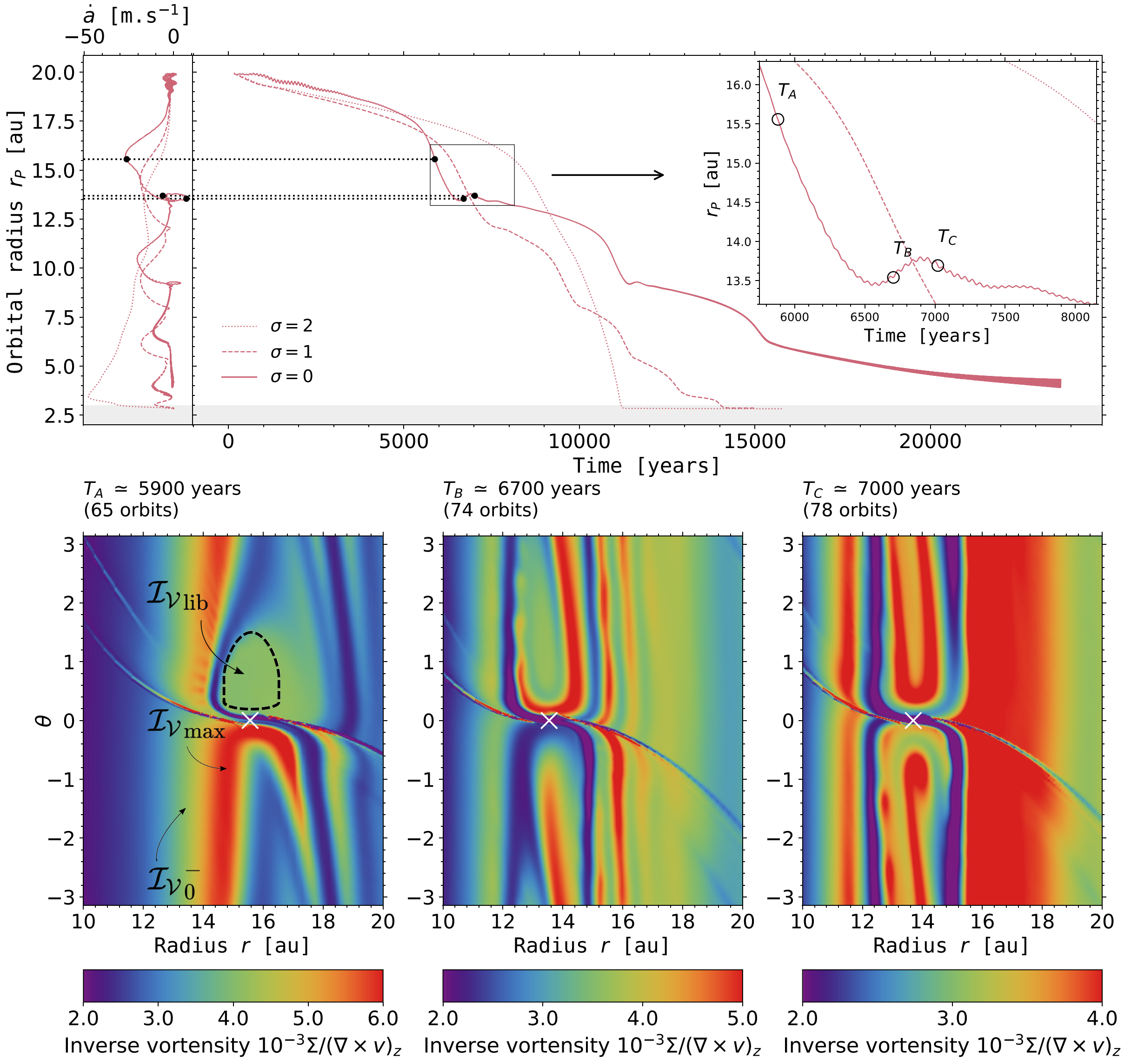

Figure 11. Impact of the initial surface density profile of the gas ($\Sigma_0(r) \propto r^{-\sigma}$) on the planet's orbital evolution in the Uther disc model. The upper panel compares the time evolution of the planet's orbital radius and migration rate in the simulation presented in Section 3.2 (dashed curves, $\sigma = 1$), with those obtained in two additional simulations for $\sigma = 0$ (solid curves) and $\sigma = 2$ (dotted curves). The grey band corresponds to the inner wave-killing zone. The lower panels display three screenshots of the gas inverse vortensity in the $\sigma = 0$ simulation at the three times denoted by $T_{\rm A}$, $T_{\rm B}$, and $T_{\rm C}$ in the upper panel. The planet's position is marked by a white cross.

and dark rings is larger. We have checked this by a dedicated dust radiative transfer calculation for the σ_0 run (not shown here). The sharper pressure maxima in the σ_0 run also imply longer lived dust rings.

To conclude this section, we stress again that, for a given planet mass and disc's aspect ratio, inward runaway migration comes in two flavours: (i) smooth and fast, or (ii) intermittent and globally slower. Getting one behaviour or the other depends on the profile of inverse vortensity in the disc, in particular across the inner edge of the planet gap. As we have seen, a low turbulent viscosity and a shallow gas surface density profile favour intermittent runaway with sharper stairs in the migration pattern.

4.3 Impact of gas self-gravity

Depending on the disc's aspect ratio h_0, the disc models for which intermittent runaway migration is observed in Fig. 1 have an initial Toomre Q-parameter in the range [16–19] at 10 au, which is about half way between the planet's initial location and the outer edge of the inner damping boundary. These values of Q are large enough to wonder whether gas self-gravity should be included in the simulations. To show that gas self-gravity actually matters despite these rather large Q values, we compare in Fig. 12 the planet's orbital evolution in the Pendragon run (blue curve, Section 3.3) with that in two additional simulations: one that discards gas self-gravity (yellow curve), and another one where only the axisymmetric part

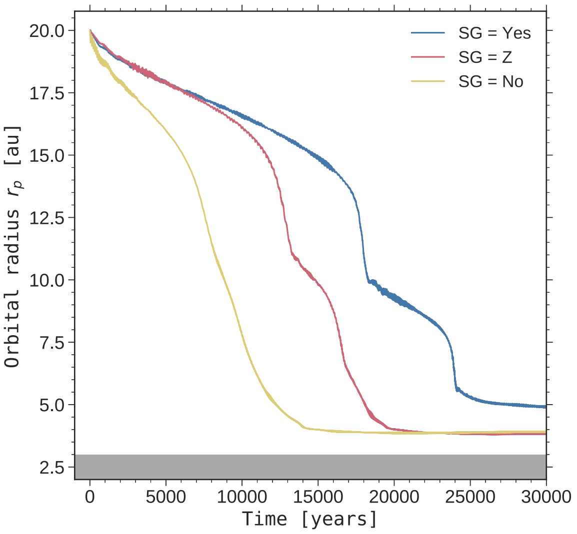

Figure 12. Impact of including gas self-gravity on the planet's orbital evolution in the Pendragon simulation. Results are shown with full inclusion of the gas self-gravity (blue curve labelled as SG = Yes), with only the axisymmetric part of the gas self-gravity (red curve, SG = Z), and without self-gravity (yellow curve, SG = No). The grey band shows the inner wave-killing zone.

of the gas self-gravity is accounted for (red curve, see Baruteau & Masset 2008b). These two additional simulations use otherwise the same setup as Pendragon.

We see that the initial migration rate is substantially larger in the run without self-gravity. This is due to a spurious inward shift of the Lindblad resonances when the planet feels the gravitational potential of the disc but the disc does not feel its own potential (Pierens & Huré 2005; Baruteau & Masset 2008b). This inward shift causes an increase in the magnitude of the net Lindblad torque that scales with $(Qh)^{-1}$, and which becomes significant when $Qh \lesssim 1$, as is the case in the Pendragon and Uther simulations (see Baruteau & Masset 2008b, whose results were obtained for non-gap-opening planets). As a consequence of the faster (initial) migration, the steps in the migration pattern are much less visible in the run without self-gravity (see Section 4.2). To understand why this is the case, one has to dwell again on the inverse vortensity profile ($\mathcal{I_V}$). Without self-gravity, we find that the planet is able to maintain a small $\mathcal{I_V}$ bump inside its orbit all over its migration course. The orbit-crossing gas has an $\mathcal{I_V}$ which is high enough to sustain runaway migration, but not high enough that the planet can overcome this $\mathcal{I_V}$ bump, which would cause gas with unperturbed, smaller $\mathcal{I_V}$ to start crossing the orbit, and which would therefore cease runaway, as explained in Section 3.2.1. The smaller amplitude of the $\mathcal{I_V}$ bump inside the planet orbit without self-gravity is due to the artificially faster migration rate in that case, which weakens the shock driven by the planet's inner wake (the synodic period of the gas around the gap's inner edge being too short in comparison to the planet's migration time-scale over its horseshoe region). In the run without self-gravity, the planet's migration rate ($|\dot{a}|$) stays around 10 m s^{-1}, while with self-gravity $|\dot{a}|$ oscillates between approximately 0 and 20 m s^{-1}.

In the simulation with the axisymmetric part of the gas self-gravity, the initial migration rate is very similar to that with full self-gravity, in agreement again with past studies on the Lindblad torque (Pierens & Huré 2005; Baruteau & Masset 2008b). We notice, however, that runaway migration starts earlier in the run with axisymmetric self-gravity. Comparison with full self-gravity points to the presence of stronger (high-$\mathcal{I_V}$) vortices in the run with axisymmetric self-gravity, in particular along the inner separatrix of the horseshoe region, which fuels the runaway process. This is due to the fact that the non-axisymmetric part of the gas self-gravity significantly damps large-scale vortices induced by the Rossby-Wave Instability (with azimuth wavenumber $m = 1$) when $Q \times h \lesssim 1$, as is the case in these simulations (e.g. Lovelace & Hohlfeld 2013; Zhu & Baruteau 2016).

We finally point out that, in some of our simulations with full self-gravity, growth of a global $m = 1$ mode is observed (hints of this behaviour can be seen in the σ_0 run displayed in Fig. 11, through oscillations of increasing amplitude visible in the planet's orbital radius after ~18 000 yr). Similar findings have been recently reported (Pierens & Lin 2018; Baruteau et al. 2019; Pérez et al. 2019). The nature and implications of such mode growth require a dedicated study.

4.4 Inclusion of an energy equation

As already stated in Section 2.1.1, a locally isothermal equation of state is more relevant to the outer parts of protoplanetary discs, typically beyond a few tens of au, where the radiative diffusion and/or cooling time-scales become shorter than the orbital time-scale. This section aims at examining the impact of an energy equation on the results of the Pendragon simulation. The energy equation solves the time evolution of the gas thermal energy density, and it includes viscous heating, radiative cooling, and stellar irradiation. However, radiative diffusion is discarded for simplicity. Our energy equation is thus the same as, e.g. equation (1) of Pierens & Raymond (2016), but without the radiative diffusion term. The Rossland mean opacity is taken from Bell & Lin (1994). The gas adiabatic index is set to 5/3, and for our fiducial profiles of initial surface density and temperature, the initial entropy profile happens to be nearly flat ($\propto r^{-1/30}$). Since viscous heating is small in the Pendragon disc model ($\alpha = 10^{-4}$), the gas temperature very quickly evolves towards the temperature profile set by stellar irradiation. For comparison purposes, the radial profile of the irradiation temperature ($T_{\rm irr}$) is chosen such that the radial profile of the gas adiabatic sound speed approximately matches that of the isothermal sound speed in the Pendragon run, which led us to adopt $T_{\rm irr}(r) = 80\,{\rm K} \times (r/r_0)^{-0.7}$ (recall that $r_0 = 10$ au). In the following, simulations that include the above energy equation are referred to as radiative simulations, those that do not as isothermal simulations.

In the upper panel of Fig. 13, we compare the time evolution of the planet's orbital radius in the isothermal and radiative Pendragon simulations. The migration pattern of $\mathcal{P}$ is similar in both simulations, with basically two stages of runaway migration that cease at about the same locations in the disc (near 10 and 5 au). The initial migration rate is somewhat higher in the radiative run, however, and the first runaway occurs earlier. The origin of this behaviour is not entirely clear. One possible lead is the absence of vortices observed in the radiative run, or the fact the planetary shocks appear to be smoother in that run. A detailed investigation would require a specific study. In agreement with the results presented in Section 4.2, this overall faster migration results in smoother stairs. None the less, the similar pattern of intermittent migration leads to the formation of similar dust structures at the end of the radiative simulation, and therefore a similar sequence of bright and dark rings of continuum emission, as illustrated in the middle and bottom panels in Fig. 13. Because the stage of decelerated migration at ~10 au lasts shorter

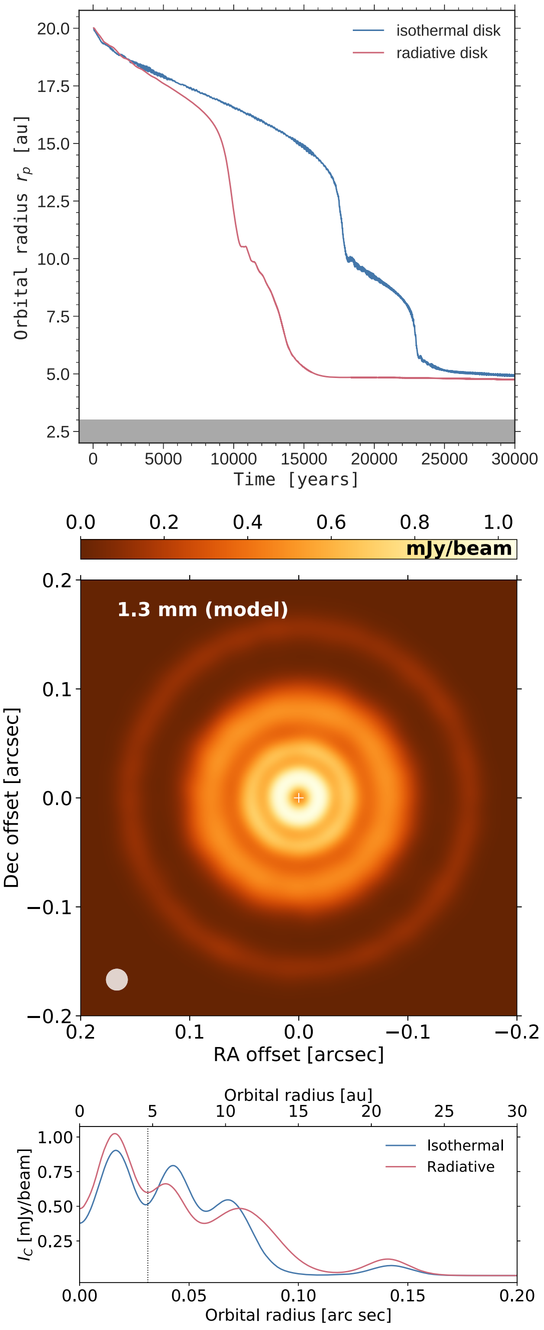

Figure 13. Top: Time evolution of the planet's orbital radius in the Pendragon run (blue curve, labelled as isothermal disc) and in an additional run that includes an energy equation (red curve, labelled as radiative disc; see text). The grey band shows the inner wave-killing zone. Middle: Synthetic flux map of the continuum emission at $\lambda = 1.3$ mm in the radiative run, convolved with a $0\farcs02$ circular beam, at $\sim 40\,000$ yr ($\sim$25 000 yr after migration halted). Bottom: Azimuthally averaged convolved intensity versus distance to the star in the isothermal and radiative runs. The intensity of the isothermal run is at 59 900 yr (also $\sim$25 000 yr after migration stopped in that run). The vertical dotted line shows the planet location.

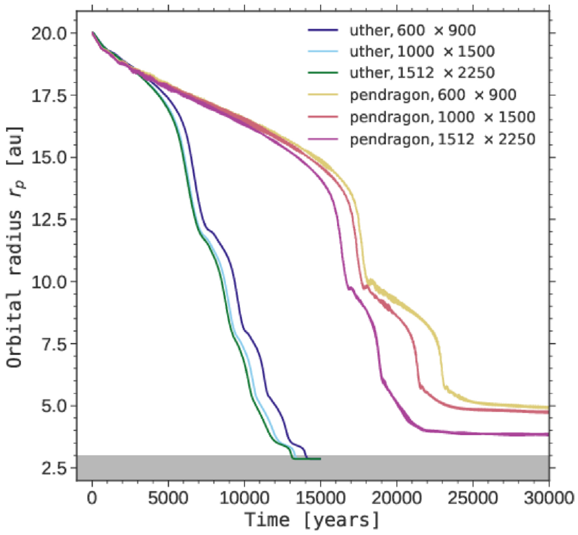

Figure 14. Impact of increasing grid resolution on the planet's orbital evolution in the Uther and Pendragon simulations. Results are shown for three grid resolutions: 600 × 900 (fiducial), 1000 × 1500, and 1512 × 2250. The grey band shows the inner wave-killing zone.

in the radiative simulation, the dust ring that forms at the pressure maximum outside the planet (near 12 au) fades away faster than in the isothermal simulation. The lower panel in Fig. 13 actually makes it clear that the bright ring of continuum emission near 12 au is broader in the radiative simulation.

For the sake of completeness, we also performed a radiative simulation with the Uther disc model ($\alpha = 10^{-3}$). The profile of irradiation temperature was chosen as $T_{\rm irr}(r) = 60\,{\rm K} \times (r/r_0)^{-0.7}$. Although not shown here, the migration pattern in this radiative simulation is very smooth, and the absence of clear steps in the migration, along with the higher level of disc turbulence, preclude the formation of well-defined dust rings in the disc. Still, we have checked that intermittent migration and the formation of multiple dust rings are recovered in the Uther radiative simulation by simply increasing the planet mass.

4.5 Grid resolution

When the grid resolution is increased, we find that the planet migrates globally faster, and that, as we have seen in Section 4.2, the stages of decelerated migration last shorter. This is illustrated in Fig. 14 for the Uther and Pendragon simulations, where the fiducial grid resolution is increased to 1000 × 1500 and 1512 × 2250. The convergence in resolution is more easily achieved in the Uther run due to the larger disc's turbulent viscosity. Increasing resolution allows to better resolve small-scale structures in the gas vortensity within or near the planet's horseshoe region. This is particularly critical to the simulations at low viscosity, like in the Pendragon run with $\alpha = 10^{-4}$, for which increasing resolution tends to form smaller, high-$\mathcal{I}_\mathcal{V}$ vortices along the inner separatrix of the horseshoe region, which therefore embark more easily on to U-turns, and boost the planet's migration rate. These small-scale vortices, which are better resolved in the 1512 × 2250 simulation, thus tend to extend the runaway phase, and bring the planet closer to the grid's inner boundary. Similar results have been obtained by McNally et al. (2019), who examined intermittent runaway migration in low-viscosity and inviscid disc models, and found that convergence in resolution was increasingly difficult to achieve, if achievable at all, upon decreasing viscosity.

Although, in our simulations, stages of decelerated migration last shorter when increasing resolution, a pressure maximum does form when migration decelerates, but it is smoother, the density of dust trapped at this location is therefore smaller, and so is the intensity of the corresponding bright ring. For Pendragon, for instance, when the number of grid cells is increased from 600 × 900 to 1000 × 1500, the intensity of the three innermost bright rings is decreased by a few per cent up to 30 per cent, depending on the ring. Concerning the longevity of dust rings, for example the ring at 12 au in the Pendragon simulation, its lifetime is shorter when increasing resolution because the preceding stage of slow migration is shorter and the corresponding pressure maximum therefore smoother. For the 1512 × 2250 run, the ring's disruption starts at ~50 000 yr, while it does so at ~70 000 yr at 600 × 900.

4.6 Concluding remarks

We have shown in this study that a single planet undergoing multiple episodes of runaway inward migration could form several dust rings and gaps in its protoplanetary disc, and therefore sequences of bright and dark rings of continuum emission at (sub)mm wavelengths. We have seen that the gas inverse vortensity is the key quantity that grasps the planet's orbital evolution all over the stages of runaway migration, and that the formation of the dust rings boils down to the creation of a pressure maximum or an inflection point on both sides of the planet's orbit every time runaway migration ceases. As runaway stalls, the gas that enters the planet's horseshoe region exerts a positive corotation torque through secondary U-turns, which further decelerates the planet migration. When the planet decelerates, its wakes have enough time to shock the gas and thus rebuild a pressure maximum or an inflection point on both sides of the planet's orbit, which efficiently trap the largest dust particles. It is the trapping of these large particles at the pressure maximum outside the planet's partial gap which causes a new bright ring in the continuum emission at radio wavelengths. By lengthening the stages of non-runaway migration, the aforementioned secondary U-turns help enhance the pressure maximum outside the planet gap, which increases the density contrast between the dust gap and the dust ring, and therefore the intensity contrast between the corresponding dark and bright rings of emission. A longer stage of non-runaway migration also helps increase the longevity of the dust ring that forms at the pressure maximum.

The *N Gaps N Planets* (NGNP) model mentioned in Section 1 needs as many fixed planets as observed dark rings in the disc's continuum emission. However, with our scenario of intermittent runaway migration, planet-induced bright rings can be obtained without expecting planets in the vicinity of gaps in the continuum emission. As already stated by McNally et al. (2019), an intermittently migrating planet can wind up close to the star and be unresolved for the current observing facilities, and still have given rise to lasting multiple rings, depending on the disc's turbulent viscosity.

It has been shown that a single planet on a fixed circular orbit could form more than three bright rings and two dark rings of continuum emission in low-viscosity discs, due to the formation of a tertiary gap inside the planet's orbit (Bae et al. 2017; Dong et al. 2017; Zhang et al. 2018). We do not find this behaviour with the regime of parameters that we have adopted in this study, whether the planet migrates slowly (see Appendix A) or even remains on a fixed circular orbit. Although numerical artefacts due to the inner damping region play a role, we think that it is likely due to the values of α that we consider in this work, which are too high to allow for a tertiary gap to form.

Our work extends previous studies on intermittent runaway migration by including the full calculation of the gas self-gravity, by testing the effects of an energy equation for the gas, by considering a broad range of sizes for dust particles, and by analysing the impact of intermittent migration on the disc's continuum emission through dust radiative transfer calculations. In agreement with previous works, we find that runaway migration can be either smooth or discontinuous (intermittent). We actually find a wide range of disc parameters for which runaway migration is intermittent. Intermittence is favoured for smaller α turbulent viscosities, flatter gas surface density profiles (smaller σ, see Section 4.2), which is globally in line with discs' observational constraints. Although not shown here, we find that intermittence is also favoured for larger planet-to-primary mass ratios q_{p} (but still in the partial gap-opening regime). We have checked the latter dependence for the Uther disc model presented in Section 3.2 by increasing the planet mass from 0.9 to 2.7 Saturn masses. For all these reasons, we believe that the intermittent runaway migration of a giant planet is a viable mechanism to account for the multiple rings and gaps observed in massive protoplanetary discs. Still, rapid planet growth beyond the mass range of intermittent runaway migration may occur, which needs to be examined to further assess the robustness of our mechanism.

Among the possible extensions of this work, it would be interesting to examine how the formation of multiple dust rings and gaps due to intermittent runaway migration would look like in scattered light at near-IR wavelengths. This question would probably be best addressed by dust radiative transfer calculations based on 3D gas and dust hydrodynamical simulations (instead of 2D, as presented in this work). It is possible that intermittent migration may leave imprints in scattered light as radial minima and maxima in the polarized intensity, which would reflect more or less the radial variations of the gas density in the superficial layers of the disc. It would also be interesting to examine the impact of additional planets on our results. Furthermore, we have discarded dust drag on to the gas in our simulations, which we have justified a posteriori by showing that the dust-to-gas density ratio remains smaller than unity for the dust mass and size distribution adopted in our dust radiative transfer calculations. A larger dust mass or a shallower size distribution could well lead to larger dust-to-gas density ratios, and future work on our migration scenario should therefore aim at including the backreaction of the dust on to the gas.

Finally, we have seen in the Uther simulation that the dust rings have a geometric spacing $\delta = r_{i+1}/r_i \sim 1.5$, with r_i the radial location of the ith bright ring. Additional simulations indicate that, when intermittent runaway migration is at work, this geometric spacing mainly depends on the disc's aspect ratio h_0, but hardly on q_{p}, α (fig. 11 in Lin & Papaloizou 2010), the initial location of the planet $r_{\mathrm{p,0}}$, Σ_0 (fig. 18 in Lin & Papaloizou 2010), and even σ. A simple estimate of δ can be obtained by assuming (i) an ideal staircase migration pattern, and (ii) that the radial location of the $\mathcal{I}_{\mathcal{V}}$ maximum outside the planet just after runaway migration coincides with that of the $\mathcal{I}_{\mathcal{V}}$ maximum inside the planet just before runaway migration (Section 3.2.1). This leads to $\delta = (r_{\mathrm{p}} + \epsilon)/(r_{\mathrm{p}} - \epsilon)$, with ϵ the radial separation between the planet and the $\mathcal{I}_{\mathcal{V}}$ maxima. The precise value of ϵ is uncertain, but roughly $\epsilon \gtrsim x_{\mathrm{s}}$ (recall that x_{s} denotes the radial half-width of the planet's horseshoe region). We thus expect $\epsilon \propto r_{\mathrm{p}}$, and therefore δ independent of r_{p}, which accounts for the geometric spacing of the dust rings. By adopting

$\epsilon = x_s$, we obtain $\delta \approx 1.25$. This is smaller than the typical value $\sim$1.5 found in our simulations, which is due in part to the fact that the migration pattern is not an ideal staircase (due to the stages of non-runaway migration in-between the runaway phases). Interestingly, some protoplanetary discs display a very similar geometric spacing for the radial location of successive bright rings in the continuum emission. For RU Lup, we infer $\delta \sim 1.4$ by considering the four bright rings reported in Huang et al. (2018), and for HD 163296, we infer $\delta \sim 1.5$ by selecting the three outermost rings in Huang et al. (2018). This spacing could be an interesting quantity to look at in future works to discriminate between different models of multiple rings formation, for a given disc observation. Another quantity worth looking at is the deviation of the gas azimuthal velocity from Keplerian rotation (Pérez, Casassus & Benítez-Llambay 2018; Teague et al. 2018). It would be interesting to see whether measuring this deviation across the multiple gaps could help differentiate between observations of multiple gaps formed by a single slowly migrating planet, a single planet experiencing intermittent runaway migration (as in this paper), and by multiple planets (NGNP model).

ACKNOWLEDGEMENTS

We acknowledge Florian Thuillet's contribution to the early stages of this work, as part of his Master's thesis (University of Toulouse, 2016). We thank Quentin Kriaa for providing PYTHON scripts that were used to produce some of the figures in this paper. We thank Olivier Berné, Andrés Carmona and Frédéric Masset for stimulating discussions. We extend special thanks to Frédéric Masset for a thorough reading of a first draft of this manuscript. We also thank the referee for a thorough review and constructive comments. Numerical simulations were performed on the CALMIP Supercomputing Center of the University of Toulouse.

REFERENCES

Andrews S. M., 2015, PASP, 127, 961
Ataiee S., Baruteau C., Alibert Y., Benz W., 2018, A&A, 615, A110
Avenhaus H. et al., 2018, ApJ, 863, 44
Bae J., Zhu Z., Hartmann L., 2016, ApJ, 819, 134
Bae J., Zhu Z., Hartmann L., 2017, ApJ, 850, 201
Barge P., Sommeria J., 1995, A&A, 295, L1
Baruteau C., Masset F., 2008a, ApJ, 672, 1054
Baruteau C., Masset F., 2008b, ApJ, 678, 483
Baruteau C., Zhu Z., 2016, MNRAS, 458, 3927
Baruteau C. et al., 2014, Protostars and Planets VI, Univ. Arizona Press, Tucson, AZ, p. 667
Baruteau C. et al., 2019, MNRAS, 486, 304
Bell K. R., Lin D. N. C., 1994, ApJ, 427, 987
Benítez-Llambay P., Ramos X. S., Beaugé C., Masset F. S., 2016, ApJ, 826, 13
Béthune W., Lesur G., Ferreira J., 2017, A&A, 600, A75
Birnstiel T., Klahr H., Ercolano B., 2012, A&A, 539, A148
Casoli J., Masset F. S., 2009, ApJ, 703, 845
Dipierro G., Laibe G., 2017, MNRAS, 469, 1932
Dipierro G., Price D., Laibe G., Hirsh K., Cerioli A., Lodato G., 2015, MNRAS, 453, L73
Dong R., Li S., Chiang E., Li H., 2017, ApJ, 843, 127
Draine B. T., Lee H. M., 1984, ApJ, 285, 89
Dullemond C., Juhasz A., Pohl A., Sereshti F., Shetty R., Peters T., Commercon B., Flock M., 2015, RADMC3D. http://www.ita.uni-heidelberg.de/ dullemond/software/radmc-3d/
Fedele D. et al., 2017, A&A, 600, A72
Flaherty K. M., Hughes A. M., Rosenfeld K. A., Andrews S. M., Chiang E., Simon J. B., Kerzner S., Wilner D. J., 2015, ApJ, 813, 99
Flock M., Ruge J. P., Dzyurkevich N., Henning T., Klahr H., Wolf S., 2015, A&A, 574, A68
Fuente A. et al., 2017, ApJ, 846, L3
Goodman J., Rafikov R. R., 2001, ApJ, 552, 793
Huang J. et al., 2018, ApJ, 869, L42
Jiménez M. A., Masset F. S., 2017, MNRAS, 471, 4917
Keppler M. et al., 2018, A&A, 617, A44
Li H., Colgate S. A., Wendroff B., Liska R., 2001, ApJ, 551, 874
Lin M.-K., Papaloizou J. C. B., 2010, MNRAS, 405, 1473
Long F. et al., 2018, ApJ, 869, 17
Lovelace R. V. E., Hohlfeld R. G., 2013, MNRAS, 429, 529
Lovelace R. V. E., Li H., Colgate S. A., Nelson A. F., 1999, ApJ, 513, 805
Lyra W., Turner N. J., McNally C. P., 2015, A&A, 574, A10
Masset F., 2000, A&AS, 141, 165
Masset F. S., 2002, A&A, 387, 605
Masset F. S., 2008, in Goupil M. J., Zahn J. P., eds, EAS Publ. Ser. Vol. 29, Planet Disk Interactions. Cambridge Univ. Press, Cambridge. p. 165
Masset F. S., Papaloizou J. C. B., 2003, ApJ, 588, 494
Masset F. S., D'Angelo G., Kley W., 2006, ApJ, 652, 730
McNally C. P., Nelson R. P., Paardekooper S.-J., Benítez-Llambay P., 2019, MNRAS, 484, 728
Meru F., Rosotti G. P., Booth R. A., Nazari P., Clarke C. J., 2019, MNRAS, 482, 3678
Müller T. W. A., Kley W., Meru F., 2012, A&A, 541, A123
Nazari P., Booth R. A., Clarke C. J., Rosotti G. P., Tazzari M., Juhasz A., Meru F., 2019, MNRAS, 485, 5914
Okuzumi S., Momose M., Sirono S.-i., Kobayashi H., Tanaka H., 2016, ApJ, 821, 82
Paardekooper S.-J., 2014, MNRAS, 444, 2031
Paardekooper S. J., Baruteau C., Kley W., 2011, MNRAS, 410, 293
Pepliński A., Artymowicz P., Mellema G., 2008a, MNRAS, 386, 179
Pepliński A., Artymowicz P., Mellema G., 2008b, MNRAS, 387, 1063
Pérez S., Casassus S., Benítez-Llambay P., 2018, MNRAS, 480, L12
Pérez S., Casassus S., Baruteau C., Dong R., Hales A., Cieza L., 2019, AJ, 158, 15
Pierens A., Huré J.-M., 2005, A&A, 433, L37
Pierens A., Lin M.-K., 2018, MNRAS, 479, 4878
Pierens A., Raymond S. N., 2016, MNRAS, 462, 4130
Pinte C., Dent W. R. F., Ménard F., Hales A., Hill T., Cortes P., de Gregorio-Monsalvo I., 2016, ApJ, 816, 25
Riols A., Lesur G., 2019, A&A, 625, A108
Shakura N. I., Sunyaev R. A., 1973, A&A, 24, 337
Simon J. B., Lesur G., Kunz M. W., Armitage P. J., 2015, MNRAS, 454, 1117
Teague R., Bae J., Bergin E. A., Birnstiel T., Foreman-Mackey D., 2018, ApJ, 860, L12
Varnière P., Tagger M., 2006, A&A, 446, L13
Weber P., Pérez S., Benítez-Llambay P., Gressel O., Casassus S., Krapp L., 2019, ApJ, 884, 178
Zhang S. et al., 2018, ApJ, 869, L47
Zhu Z., Baruteau C., 2016, MNRAS, 458, 3918

APPENDIX A: ADDITIONAL RESULTS FOR FAST AND SLOW MIGRATION

We have seen in Section 3.1 via Fig. 1 that for our disc model and range of planet masses, migration could be either fast, slow, or intermittent, depending on the background surface density of the gas. While the main body of the paper focuses on intermittent migration, we illustrate in this section our main findings in the fast and slow migration regimes. Results are shown in Fig. A1 for the same disc setup as in the Pendragon simulation (see Table 4), but for different initial surface densities of the gas at 10 au (Σ_0).

The upper panels are for $\Sigma_0 = 3 \times 10^{-3}$, that is for the fast migration case highlighted in Section 3.1. After $\mathcal{P}$ has moved through the initial dust band (upper left panel), some particles get

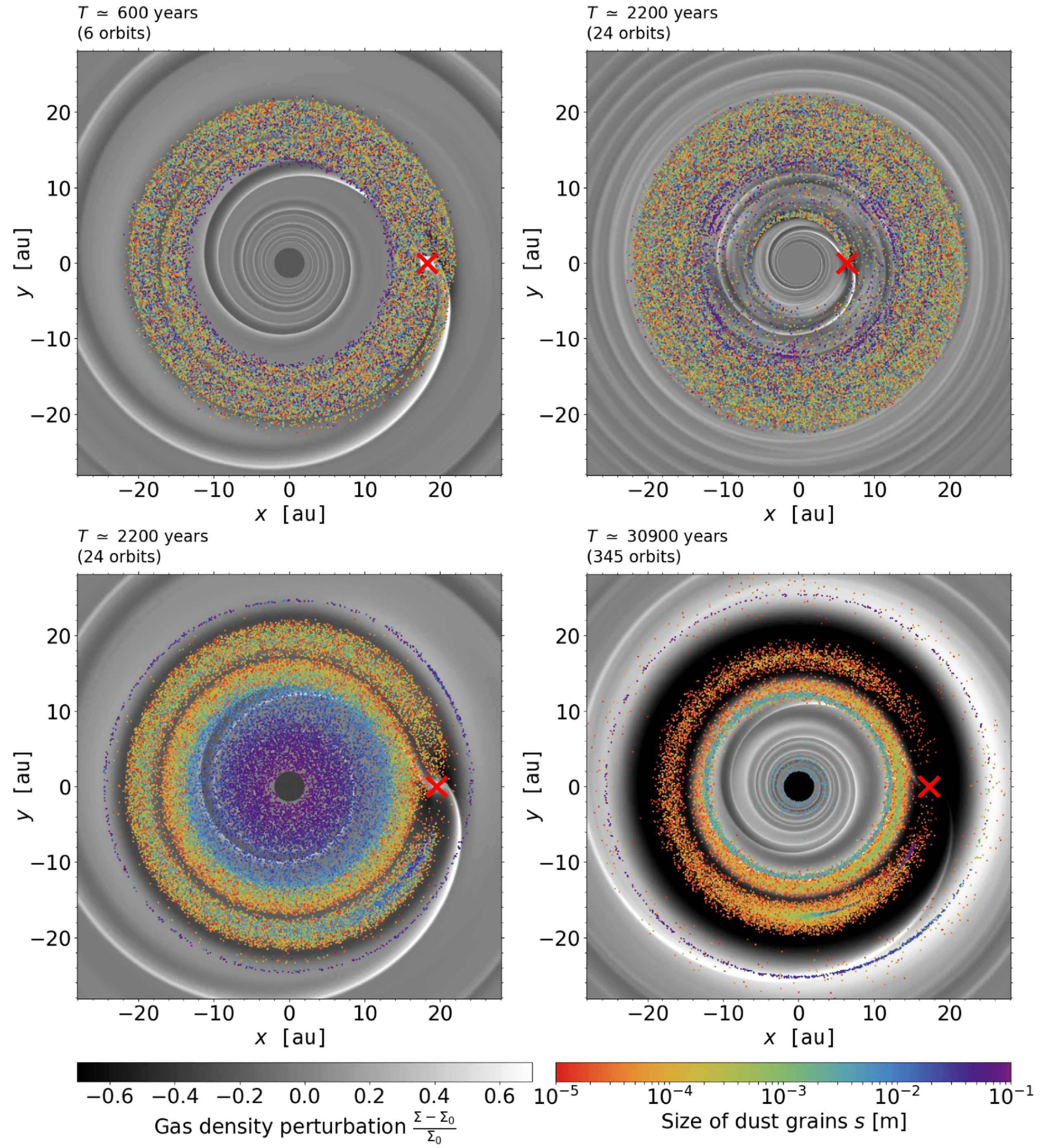

Figure A1. Perturbed gas surface density relative to its initial profile, $(\Sigma - \Sigma_0)/\Sigma_0$, in black and white and in Cartesian coordinates. The location of the dust particles is overlaid by coloured dots (see rainbow colour bar below the bottom-right panel). In each panel, the red cross marks the position of the planet. Results are shown for a simulation with a disc setup similar to that of the Pendragon run, but for two different initial surface densities: $\Sigma_0 = 3 \times 10^{-3}$ (upper panels, fast planet migration) and $\Sigma_0 = 3 \times 10^{-4}$ (lower panels, slow migration).

trapped around the L4 Lagrange point located ahead of $\mathcal{P}$ in the azimuthal direction, which is clearly seen in the upper right panel. Comparison between both panels shows that, apart from the dust trapped near L4, most of the dust particles ultimately forms a band behind $\mathcal{P}$ that is similar to the initial one, except that it drifts radially due to gas drag, and diffuses radially due to turbulence.

The lower panels are for $\Sigma_0 = 3 \times 10^{-4}$ (slow migration). The bottom-right panel shows that the planet forms three rings: (i) an outer ring that is mostly comprised of large particles, and which roughly stays at its initial location (compare with the bottom-left panel), (ii) a coorbital ring, and (iii) an inner ring that builds up at the pressure maximum between the main gap around the planet orbit and a secondary gap inside the orbit. Concerning the outer ring, a different choice of initial particles location could have led to more particles being trapped there, which would have made this ring more visible and/or thicker. Both the coorbital and the inner rings move inward together with the planet. Note that the inner ring only forms at low viscosities (it does not form for $\alpha = 10^{-3}$). The bottom-right panel indicates that some large particles remain in the inner disc parts. We attribute this seeming trapping to a numerical artefact of the grid's inner wave-killing zone rather than to a physical pressure maximum arising from a tertiary gap carved by the planet's inner wake.

APPENDIX B: A SIMPLE MODIFICATION TO THE EXPRESSION OF THE COORBITAL VORTENSITY DEFICIT FOR FAST MIGRATION

The aim of this section is to propose a simple generalized expression for the coorbital vortensity deficit δm when the assumption of slow migration in equation (2) is not satisfied. We shall still assume, however, that δm can be defined by equation (1). By dividing the right-hand side of equation (1) by $2\pi r_{\rm p}$, and integrating over θ, we get

$$\delta m \approx 4\pi r_{\rm p}\omega(r_{\rm p}) \times \left[\frac{x_{\rm s}}{2\pi r_{\rm p}}\int_{\theta_1}^{\theta_2} \mathcal{I}_{\mathcal{V}}\left(r_{\rm p}-x_{\rm s},\theta\right) r_{\rm p}{\rm d}\theta \right.$$
$$\left. - \frac{1}{2\pi r_{\rm p}}\int_{\theta_1}^{\theta_2}\int_{r_{\rm p}-x_{\rm s}}^{r_{\rm p}} \mathcal{I}_{\mathcal{V}}\left(r,\theta\right) r_{\rm p}{\rm d}\theta{\rm d}r\right], \quad \text{(B1)}$$

which assumes $r \approx r_{\rm p}$, and where $[\theta_1, \theta_2]$ defines the azimuthal extent of the material trapped in libration with $\mathcal{P}$ and of the orbit-crossing flow ($\Delta\theta = \theta_2 - \theta_1$). Further assuming that the material trapped in libration has uniform $\mathcal{I}_{\mathcal{V}}$ over a rectangular domain of extent $2x_{\rm s} \times \Delta\theta$ in polar cylindrical coordinates, and that $\mathcal{I}_{\mathcal{V}}\left(r_{\rm p}-x_{\rm s},\theta\right)$ is independent of θ over $[\theta_1, \theta_2]$ (see Fig. 3 and lower left panel in Fig. 11), equation (1) can be recast as

$$\delta m \approx 4\pi r_{\rm p}\omega(r_{\rm p}) \times \left[\frac{x_{\rm s}}{2\pi r_{\rm p}}\mathcal{I}_{\mathcal{V}e} r_{\rm p}\Delta\theta - \frac{1}{2\pi r_{\rm p}}\mathcal{I}_{\mathcal{V}\,{\rm lib}} r_{\rm p}\Delta\theta x_{\rm s}\right]$$
$$\approx 4\pi r_{\rm p}\omega(r_{\rm p})x_{\rm s} \times \frac{\Delta\theta}{2\pi} \times \left[\mathcal{I}_{\mathcal{V}e} - \mathcal{I}_{\mathcal{V}\,{\rm lib}}\right]. \quad \text{(B2)}$$

Recall that $\mathcal{I}_{\mathcal{V}e}$ is the inverse vortensity of the gas entering the horseshoe region ($\mathcal{I}_{\mathcal{V}e} = \mathcal{I}_{\mathcal{V}}(r_{\rm p}-x_{\rm s})$), and $\mathcal{I}_{\mathcal{V}\,{\rm lib}}$ that of the gas trapped in libration with $\mathcal{P}$. The r.h.s. of equation (B2) is therefore that of equation (3) multiplied by $\Delta\theta/2\pi$.

This paper has been typeset from a TEX/LATEX file prepared by the author.

Résumé

Ce mémoire d'Habilitation à Diriger des Recherches décrit mes activités de recherche sur la formation et l'évolution orbitale des systèmes planétaires et la dynamique des disques protoplanétaires. Mon travail porte sur les interactions gravitationnelles entre planètes, le disque protoplanétaire de gaz et de poussières où elles se forment, et leur(s) étoile(s). Je cherche à comprendre dans quelle mesure la migration planétaire résultant des interactions entre planètes et leur disque protoplanétaire peut rendre compte des propriétés orbitales des exoplanètes, dont la diversité révèle que les planètes peuvent se former et évoluer dans des conditions variées, parfois extrêmes. Je cherche également à comprendre si les structures observées dans l'émission du gaz et des poussières des disques protoplanétaires (succession d'anneaux sombres et brillants, spirales, asymétries etc.) peuvent être dues à des planètes, et ce que de telles structures peuvent nous apprendre sur les premières étapes de la formation planétaire. Pour cela, j'ai recours à la théorie en dynamique des fluides astrophysiques, aux simulations hydrodynamiques multi-dimensionnelles et aux calculs de transfert radiatif.

Une part importante de mes travaux vise à déterminer la direction et la vitesse de migration des planètes dans leur disque protoplanétaire. Mon travail a notamment permis (i) de trouver comment ralentir la migration rapide des planètes terrestres vers leur étoile, qui pendant longtemps avait rendu les prédictions des modèles de formation et d'évolution planétaires incompatibles avec les propriétés orbitales des exoplanètes détectées, (ii) de montrer que les planètes géantes formées à grande distance de leur étoile par instabilité gravitationnelle migrent très rapidement vers les parties internes des disques protoplanétaires, et qu'il est là aussi question de devoir ralentir leur migration afin de rendre compte des planètes observées par imagerie directe, et (iii) de montrer que la diversité des rapports de période orbitale dans les systèmes multi-planétaires détectés par le satellite spatial *Kepler* peut être expliquée par les modèles de migration planétaire.

Stimulé par les observations multi-longueurs d'onde de disques protoplanétaires, je travaille plus récemment sur la dynamique et l'émission du gaz et des poussières dans les disques. Mon travail ici a pour but de prédire d'une part le type de structures qu'une planète peut génèrer dans l'émission de son disque, et d'examiner d'autre part si les structures réellement observées peuvent s'expliquer par la présence de planètes enfouies dans ces disques. Les modèles que j'ai développés ont permis notamment (i) de proposer un scénario où la présence d'anneaux multiples sombres et brillants dans l'émission radio des poussières pourrait être due à la migration rapide d'une seule planète dans le disque protoplanétaire, et (ii) de montrer que les observations de l'émission radio de plusieurs disques (AB Aurigae, MWC 758, HD 169142) suggèrent fortement la présence de planètes massives structurant la poussière de leur disque à grande distance de l'étoile, ce qui permettrait, si ces prédictions étaient confirmées à l'avenir, d'apporter de nouvelles contraintes sur la formation et l'évolution de planètes jeunes.

Le nombre croissant d'exoplanètes très proches de leur étoile, dont certaines ont une obliquité orbitale très élevée ou un rayon physique anormalement grand, demande de mieux comprendre les effets de marée entre étoiles et planètes. C'est dans cette optique que j'étudie la propagation et la dissipation d'ondes de marée dans les fluides en rotation modélisant l'intérieur d'étoiles ou de planètes géantes, ce qui m'a permis notamment de trouver un mécanisme capable d'augmenter considérablement l'efficacité des effets de marée étoile-planète.

Mots clé : formation et migration planétaires, dynamique et émission des disques protoplanétaires, effets de marée, analyse linéaire, simulations hydrodynamiques, transfert radiatif